

# **Geology and Genesis of the Cerro la Mina Porphyry - High Sulfidation Epithermal Prospect, Mexico**

by

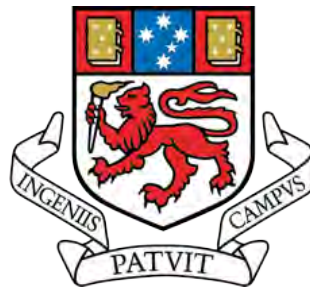
Nicholas H. Jansen

BSc. Hons. (Saint Mary's University, Halifax, Canada)

Submitted in fulfilment of the requirements for the degree of

Doctor of Philosophy

March, 2012



University of Tasmania



ARC Centre of Excellence in Ore Deposits



## **Declaration**

This thesis contains no material which has been accepted for the award of any other degree or diploma in any tertiary institution and, to the best of my knowledge and belief, contains no copy or paraphrase of material previously published or written by another person, except where due reference is made in the text of this thesis.

Nicholas H. Jansen

Date:

## **Confidentiality**

This thesis is not to be made available for loan or copying for 18 months from the date this statement was signed; after that time limited copying is permitted in accordance with the *Copyright Act 1968*

Nicholas H. Jansen

Date:



## Abstract

The Cerro la Mina prospect is located in Chiapas State, southern Mexico. In 2006, exploration drilling at Cerro la Mina intersected a near surface oxide gold zone and significant Au (Cu-Mo) sulfide mineralisation with porphyry alteration and thick advanced argillic alteration with associated epithermal mineralisation. A total of 64 drill holes totalling approximately 22,000 m were drilled at Cerro la Mina before exploration ceased.

Cerro la Mina is located in a tectonic setting characterized by a complex triple junction between the North American, Caribbean, and Cocos plates. The state of Chiapas has a pre-Mesozoic metamorphic, sedimentary, and igneous basement, overlain by Mesozoic detrital-calcareous units and Cenozoic interbedded sandstone and siltstone.

The Chiapanecan volcanic arc began around 3 Ma, when volcanism on the Pacific coast parallel to the trench moved inland and approximately 30° oblique to the Middle American trench using the northwest orientated strike-slip fault zone as magma conduits. The strike-slip fault zone is a continuation of the Motagua-Polochic sinistral fault zone which separates the North American and Caribbean plates. The Selva Negra volcanic rocks, part of the north-westernmost Chiapanecan volcanic arc, comprise widespread monzodiorite to diorite intrusions with a crystallization age of ~1.0 Ma (zircon U-Pb), trachyandesite volcanic rocks and rare basalt flows of shoshonitic composition. The shoshonitic and LILE-rich composition of the Selva Negra volcanic rocks is the result of low degree partial melts which have ascended along the inland faults of the strike-slip zone 300 to 330 km from the trench. The radiogenic isotope data suggest that the ascending magmas interacted with the thick crust (~50 km) through MASH processes. The combination of low degree partial melts of a heterogeneous mantle enriched in LILE and LREE and crustal contamination resulted in a shoshonitic and enriched LILE geochemistry for the Selva Negra volcanic rocks.

The geology of the Cerro La Mina prospect, hosted in the Selva Negra volcanic rocks, comprise four major units. The volcanic stratigraphy consists of ignimbrites (Unit 1) that are intruded by monzodiorites to diorites (Unit 2). Unit 1 is overlain by debris flows or lahars and trachyandesite synvolcanic domes and associated autoclastic rocks (Unit 3). U-Pb ages for volcanic rocks in the Selva Negra region indicate volcanism occurred from ~1.2 to at least ~0.75 Ma. The matrix-rich, granule breccia (Unit 4) cross cuts the volcanic rocks (Units 1 to 3) and is inferred to be a breccia pipe formed by the explosive release of hydrothermal fluids from an intrusion at depth causing brecciation of the overlying rocks. A major northwest fault off-sets the stratigraphy and the breccia pipe and is probably part of the regional strike-slip fault zone of the region.

Early porphyry-style alteration includes potassic (quartz + potassium feldspar ± biotite) veins and wall rock alteration (Stage A), and later sericitic alteration (Stage B). The potassic veins are infilled with late fractured pyrite (Stage 1) that has been fractured to a jigsaw-fit texture, consistent with its pre-brecciation timing. Potassic alteration also occurred after breccia pipe formation, altering the matrix of the breccia pipe (Unit 4).

A late sericitic alteration (Stage B) comprises quartz, muscovite, illite, illite/smectite, chlorite, calcite, gypsum (after anhydrite), and tourmaline. The sericitic alteration (Stage B) is zoned, with a quartz + muscovite core centred on the breccia pipe and transition to lower temperature clay assemblages distally. Sericitic alteration (Stage B) is associated with Stage 2 mineralisation comprising inclusion-rich pyrite ± chalcopyrite ± molybdenite veins and disseminations that are most abundant in the quartz-muscovite core. Stage 2 molybdenite yielded an age of  $0.780 \pm 0.010$  Ma (Re-Os). The Cu and Mo ore grade shells have a vertical orientation coincident with the shape of the breccia pipe.

Sulfur isotope data suggest that Stage 1 and 2 pyrite precipitated from magmatic fluids and are enriched in Co, Ni and Se, have oscillatory zoning and local arsenic-rich zones. The high temperature quartz-muscovite alteration is associated with the highest Co, Ni and Se concentrations which decrease distally, coincident with decreasing temperature clay assemblages.

The hydrothermal system cooled below 300°C at  $0.689 \pm 0.013$  Ma (hydrothermal biotite Ar-Ar age) with the onset of Stage 3 and 4 mineralisation associated with advanced argillic kandite alteration (Stage C). The kandite alteration (Stage C) is hosted in the breccia pipe and is telescoped onto the early porphyry system. The kandite alteration (Stage C) grades between the quartz + dickite ± pyrophyllite ± alunite ± kaolinite (Stage C<sub>OD</sub>) at the surface and halloysite + kaolinite zones (Stage C<sub>HK</sub>) extending 800 metres below the surface. The advanced argillic alteration is not typical of a lithocap with no vuggy quartz and very little alunite, consistent with fluids interacting with the basement evaporite and limestone.

The kandite-altered rocks host the most significant Au-Cu mineralisation. Mineralisation in Stage C<sub>OD</sub> consists of arsenian-pyrite + enargite + galena + sphalerite + barite (Stage 3 and 4). In the Stage C<sub>HK</sub> zone mineralisation consists of marcasite + arsenian-pyrite ± sphalerite ± galena ± barite (Stage 3 and 4). The sulfides occur in breccia cement, veins, and disseminations. Stages 3 and 4 mineralisation have similar geochemistry, being enriched in As, Cu, Au, Zn, Mn, Sb, Pb, Ag, Tl, Te and Bi, typical of high sulfidation epithermal systems. Sulfur isotope data of epithermal mineralisation (Stages 3 and 4) suggests a mix of magmatic waters and meteoric waters that have interacted with volcanic rocks and/or evaporite units in the basement.

The kandite alteration (Stage C) contains abundant halloysite. Traditionally the low temperature halloysite clay is thought to be a supergene mineral. However, at Cerro la Mina the halloysite occurs in veins and wall rock alteration associated with gold-bearing sulfides below the oxide zone. In addition, the halloysite is developed to at least 800 m below the present day surface in the fluid pathway of the breccia pipe, deeper than the hypogene clay minerals dickite, alunite, and pyrophyllite. A TerraSpec study showed that the relative abundance of halloysite to kaolinite changes in association with the thickness of rimming pyrite (Stage 4). A SEM study revealed the transition from halloysite to kaolinite. All the above evidence indicates that the halloysite is hypogene in origin.

The Cerro la Mina prospect has potassic and advanced argillic alteration and heavy sulfur isotopic values consistent with a reduced calc-alkaline porphyry system. This is unusual as the

geochemistry of the volcanic rocks and intrusions are alkalic, therefore calc-alkaline magmatism, not yet recognized in the district, may be related to the alteration and mineralisation. Abundant hypogene halloysite is unusual although the identification of halloysite is complicated by dehydration and may be underestimated in high sulfidation deposits.

In summary, the Cerro la Mina prospect consists of a breccia pipe with weakly developed porphyry Cu-Mo mineralisation and associated potassic alteration overprinted by hypogene advanced argillic alteration and epithermal Au-Cu mineralisation. The geological and geochemical features of the prospect are not consistent with traditional models with its calc-alkaline alteration and mineralisation with alkalic rocks and the abundant low temperature hypogene halloysite. The results of the thesis add to the understanding of advanced argillic alteration telescoped onto porphyry systems. The increased understanding of Cerro la Mina will also give explorers new insights for discoveries in an under explored region of Mexico.



## Acknowledgements

This study was initiated as part of AMIRA International project P765A “Geochemical Halos in Green Rocks and Lithocaps: The Explorers’ Toolbox for Porphyry and Epithermal Districts” at the Centre for Ore Deposit Research (CODES). Sincere thanks are owed to the sponsors of P765A including AngloGold Ashanti, Anglo American, Barrick, Buenaventura, Codelco, Dundee, Equinox, Freeport-McMoran, Gold Fields, Kinross, MMG, Newcrest, Newmont, St. Barbara Rio Tinto, Teck, Vale, and Xstrata. We gratefully acknowledge Kinross and Brigus Gold for providing field support and access to the Cerro la Mina prospect. I would also like to thank the SEG for the graduate student research fellowship award in support of this thesis.

This thesis is the result of support and encouragement from Bruce Gemmell, Zhaoshan Chang, Peter Hollings, Dave Cooke and Noel White. Individually they have been crucial to the completion of this project and together they are a superb supervisory team. I am grateful for the opportunity to have been part of the ARC Centre of Excellence in Ore Deposit (CODES) at the University of Tasmania.

A special thank-you to the geologists on site Jean-Pierre Londero, Rolando Arias, Francisco Martinez Lopez, Scott Gaffri, Julio Gama, Alejandro Gómez Avilés, Mike Martinez, Gabriel Hernandez, core shed crew and administrative staff who have assisted with the fieldwork. I will also like to thank Roisin Kyne for her honours thesis that contributed to the understanding of clay alteration. Also, I’d like to extend a hearty and sincere thanks to Rosio and Sandra at ‘la iluminación’ restaurant for your delicious tacos after long field days.

I give special thanks to those kind people who have donated their time, expertise and enthusiasm: Karsten Goemann (Microprobe and SEM imaging), Sebastien Meffre (geochronology) and Sarah Gilbert (laser mapping) and David Braxton (isotopes). Invaluable technical and organisational assistance was provided by Peter Cornish, Nilar Hilang, Di Steffens, Helen Scott, Karen Mollross, Katie McGoldrick, Phil Robinson and Simon Stevens.

Finally, I would to thank my family and friends; without your continued support and distractions to keep me sane and smiling, an achievement like this would not have been possible. My Dad for the daily phone calls of encouragement and video calls with my sisters, nieces and nephews kept me smiling and often gave me the boost to start the day. To my housemates present and past, I don’t think it’s appropriate to say thanks, but rather to give an apology. Living with a PhD student isn’t the easiest! To Malcolm Robinson, Jon Ettershank and Julie Hunt and the rest of the Wildfire crew, thank-you for the opportunities to get away for a sail and let me forget about a thesis for a while.

“From little things, big things grow” - *Paul Kelly and Kev Carmody*

☞ Dedicated to C.H.M Weststeyn ☞



# Table of Contents

|  |              |
|--|--------------|
| <b>Declaration and Confidentiality .....</b>     | <b>i</b>     |
| <b>Abstract.....</b>                             | <b>iii</b>   |
| <b>Acknowledgements .....</b>                    | <b>vii</b>   |
| <b>List of Figures.....</b>                      | <b>xv</b>    |
| <b>List of Tables .....</b>                      | <b>xxi</b>   |
| <b>Appendices.....</b>                           | <b>xxiii</b> |
| <b>Nomenclature and Abbreviations .....</b>      | <b>xxv</b>   |
| <b>Chapter 1 - Introduction</b>                  |              |
| 1.1 Preamble .....                               | 1            |
| 1.2 Project Aims and Objectives.....             | 2            |
| 1.3 Area of Study .....                          | 3            |
| <i>1.3.1 Access and Working Conditions.....</i>  | <i>3</i>     |
| <i>1.3.2 Exploration and Mining History.....</i> | <i>4</i>     |
| <i>1.3.3 Previous Research.....</i>              | <i>5</i>     |
| <i>1.3.4 Field Work.....</i>                     | <i>5</i>     |
| 1.4 Thesis Organization .....                    | 5            |
| <b>Chapter 2 - Regional Geology</b>              |              |
| 2.1 Introduction.....                            | 7            |
| 2.2 Tectonic Setting .....                       | 7            |
| 2.3 Volcanism of Mexico and Central America..... | 10           |
| 2.4 Geology of Chiapas .....                     | 11           |
| <i>2.4.1 Volcanism of Chiapas.....</i>           | <i>12</i>    |
| 2.5 District Geology.....                        | 15           |
| 2.6 Metallogeny of Chiapas State.....            | 15           |
| <i>2.6.1 Porphyry-Epithermal Deposits.....</i>   | <i>15</i>    |
| <i>2.6.2 Campamento Au-Ag Deposit .....</i>      | <i>18</i>    |
| <i>2.6.3 Cerro la Mina Prospect .....</i>        | <i>20</i>    |
| <i>2.6.4 Santa Fé Mine District .....</i>        | <i>20</i>    |
| <i>2.6.5 Tolimán Porphyry-Cu .....</i>           | <i>21</i>    |
| 2.7 Conclusions.....                             | 21           |

**Chapter 3 - Igneous Geochemistry of the Selva Negra**

|   |    |
|---|----|
| 3.1 Introduction.....   | 23 |
| 3.2 Research Methods.....   | 23 |
| 3.2.1 <i>Sampling Program</i> .....                                 | 23 |
| 3.2.2 <i>Petrographic Microscopy</i> .....                          | 25 |
| 3.2.3 <i>Major and Trace Element Analysis</i> .....                 | 25 |
| 3.2.4 <i>Radiogenic Isotopes</i> .....                              | 25 |
| 3.3 Selva Negra Volcanic Rocks.....                                 | 27 |
| 3.4 Petrography .....   | 28 |
| 3.4.1 <i>Basalt Flows (Group A)</i> .....                           | 28 |
| 3.4.2 <i>Diorite to Monzodiorite Plutonic Rocks (Group B)</i> ..... | 28 |
| 3.4.3 <i>Trachyandesite Volcanic Rock (Group C)</i> .....           | 28 |
| 3.5 Geochemistry Results .....                                      | 30 |
| 3.5.1 <i>Discrimination of Altered Samples</i> .....                | 30 |
| 3.5.2 <i>Geochemistry of the Selva Negra</i> .....                  | 30 |
| 3.6 Discussion .....  | 34 |
| 3.6.1 <i>Selva Negra Distribution</i> .....                         | 34 |
| 3.6.2 <i>Selva Negra Harker Diagrams</i> .....                      | 34 |
| 3.6.3 <i>Selva Negra and Regional Volcanism</i> .....               | 39 |
| 3.6.4 <i>Formation of K-Rich Lavas</i> .....                        | 41 |
| 3.6.5 <i>Crustal versus Sediment Contamination</i> .....            | 41 |
| 3.6.6 <i>Melt Fluid Metasomatism</i> .....                          | 46 |
| 3.6.7 <i>Adakite</i> .....  | 46 |
| 3.7 Conclusions.....  | 49 |

**Chapter 4 - Prospect Geology**

|   |    |
|---|----|
| 4.1 Introduction.....   | 51 |
| 4.2 Research Methods.....   | 51 |
| 4.2.1 <i>Graphic Logging</i> .....  | 51 |
| 4.3 Lithofacies Description.....  | 51 |
| 4.3.1 <i>Unit 1 - Trachyandesite Fiamme Breccias</i> .....                                      | 53 |
| 4.3.1.1 <i>Unit 1A - Clast-Supported Breccia</i> .....  | 53 |
| 4.3.1.2 <i>Unit 1B<sub>M</sub> and 1B<sub>S</sub> - Moderate to Strong Fiamme Breccia</i> ..... | 53 |
| 4.3.1.3 <i>Unit 1C - Volcaniclastic Sandstone</i> .....   | 53 |
| 4.3.1.4 <i>Unit 1D - Basalt</i> .....   | 55 |
| 4.3.2 <i>Unit 2 - Monzodiorite to Diorite</i> .....   | 55 |
| 4.3.3 <i>Unit 3 - Trachyandesite Coherent to Matrix-Supported Breccias</i> .....                | 55 |

|   |    |
|---|----|
| 4.3.3.1 Unit 3A <sub>T</sub> and 3A <sub>S</sub> - Feldspar-Phyric Trachyandesite ..... | 55 |
| 4.3.3.2 Unit 3B - Monomictic Breccias .....   | 55 |
| 4.3.3.3 Unit 3C - Matrix-Supported Breccias .....                                       | 56 |
| 4.3.4 Unit 4 - Breccia Complex.....   | 57 |
| 4.3.4.1 Unit 4A - Matrix-Rich, Granule Breccia .....                                    | 57 |
| 4.3.4.2 Unit 4B - Brecciated Volcanic Wall Rocks .....                                  | 57 |
| 4.3.4.3 Unit 4C - Monomictic Breccia .....  | 60 |
| 4.4 Lithofacies Distribution .....  | 61 |
| 4.4.1 Surface Geology.....  | 61 |
| 4.4.2 Cross Sections .....  | 62 |
| 4.5 Structure .....   | 70 |
| 4.6 Discussion .....  | 70 |
| 4.6.1 Genetic Interpretation.....   | 70 |
| 4.6.2 Paragenesis.....  | 71 |
| 4.6.3 Interpretations of Other Authors.....   | 71 |
| 4.6.4 Geologic Setting.....   | 72 |
| 4.7 Conclusions.....  | 73 |
| <br><b>Chapter 5 - Wall Rock Alteration</b>   |    |
| 5.1 Introduction.....   | 75 |
| 5.2 Research Methods.....   | 75 |
| 5.2.1 Graphic Core Logging.....   | 75 |
| 5.2.2 Petrographic Microscopy.....  | 75 |
| 5.2.3 Potassium Feldspar Staining .....   | 75 |
| 5.2.4 TerraSpec Analyses .....  | 76 |
| 5.2.5 X-ray Diffraction.....  | 76 |
| 5.2.6 Scanning Electron Microscope .....  | 79 |
| 5.3 Alteration Description.....   | 79 |
| 5.3.1 Potassic Alteration (Stage A).....  | 79 |
| 5.3.2 Sericitic Alteration (Stage B).....   | 82 |
| 5.3.3 Kandite Alteration (Stage C) .....  | 84 |
| 5.3.3.1 Quartz-Dickite Alteration (Stage C <sub>QD</sub> ).....                         | 84 |
| 5.3.3.2 Halloysite-Kaolinite Alteration (Stage C <sub>HK</sub> ) .....                  | 84 |
| 5.3.4 Oxide Zone .....  | 85 |
| 5.4 Spatial Distribution.....   | 88 |
| 5.5 Discussion of Cerro la Mina Alteration.....   | 96 |
| 5.6 Halloysite .....  | 98 |

---

|   |     |
|---|-----|
| 5.6.1 <i>KH Index</i> .....                                       | 98  |
| 5.6.2 <i>Kaolinite-Halloysite Zoning</i> .....                    | 100 |
| 5.6.3 <i>SEM Imaging of Stage C<sub>HK</sub> Alteration</i> ..... | 102 |
| 5.6.4 <i>Halloysite Dehydration</i> .....                         | 104 |
| 5.7 Discussion .....  | 107 |
| 5.8 Conclusions.....  | 109 |
| <br><b>Chapter 6 - Mineralisation</b>                             |     |
| 6.1 Introduction.....   | 111 |
| 6.2 Research Methods.....   | 111 |
| 6.2.1 <i>Graphic Logging</i> .....                                | 111 |
| 6.2.2 <i>Petrographic Microscopy</i> .....                        | 111 |
| 6.2.3 <i>Acid Etching</i> .....                                   | 111 |
| 6.2.4 <i>Scanning Electron Microprobe</i> .....                   | 111 |
| 6.2.5 <i>Sulfide Imaging</i> .....                                | 112 |
| 6.2.5.1 <i>Image Conversion for cps to ppm</i> .....              | 113 |
| 6.2.5.2 <i>Data Reduction with ioGas</i> .....                    | 114 |
| 6.3 Macro Scale Description.....                                  | 114 |
| 6.4 Petrographic Descriptions.....                                | 115 |
| 6.4.1 <i>Stage 1</i> .....  | 117 |
| 6.4.2 <i>Stage 2</i> .....  | 117 |
| 6.4.3 <i>Stages 3 and 4</i> .....                                 | 120 |
| 6.4.3.1 <i>Stage 3</i> .....                                      | 120 |
| 6.4.3.2 <i>Stage 4</i> .....                                      | 121 |
| 6.5 Vein Textures.....  | 126 |
| 6.6 Spatial Distribution .....                                    | 126 |
| 6.7 Discussion.....   | 136 |
| 6.8 Sulfide Imaging.....  | 140 |
| 6.8.1 <i>Stage 1</i> .....  | 140 |
| 6.8.2 <i>Stage 2</i> .....  | 140 |
| 6.8.3 <i>Stage 3</i> .....  | 150 |
| 6.8.4 <i>Stage 4</i> .....  | 150 |
| 6.9 Discussion of Laser Map Imaging.....                          | 150 |
| 6.9.1 <i>As versus Au Plot</i> .....                              | 156 |
| 6.10 Conclusions.....   | 158 |
| <br><b>Chapter 7 – Geochronology</b>                              |     |
| 7.1 Introduction.....   | 161 |

---

|  |     |
|--|-----|
| 7.2 Research Methods.....  | 161 |
| 7.2.1 <i>U-Pb Geochronology</i> .....  | 161 |
| 7.2.1.1 Zircon Separation and Preparation.....   | 161 |
| 7.2.1.2 LA- ICP-MS Method .....  | 161 |
| 7.2.1.3 Data Collection and Reduction .....  | 162 |
| 7.2.2 <sup>40</sup> Ar/ <sup>39</sup> Ar Methods .....                                   | 163 |
| 7.2.3 <i>Re-Os Analysis</i> .....  | 164 |
| 7.3 Results.....   | 164 |
| 7.3.1 <i>U/Pb Age Results</i> .....  | 164 |
| 7.3.1.1 Trachyandesite Fiamme Breccia (Unit 1B <sub>S</sub> ) .....                      | 165 |
| 7.3.1.2 Monzodiorite (Unit 2) .....  | 165 |
| 7.3.1.3 Unit 4 with Dickite-Cemented Hydrothermal Breccia (Stage C <sub>QD</sub> ) ..... | 166 |
| 7.3.1.4 Trachyandesite Matrix-Supported Breccia (Unit 3C).....                           | 169 |
| 7.3.2 <sup>40</sup> Ar/ <sup>39</sup> Ar Results .....                                   | 169 |
| 7.3.3 <i>Re-Os Results</i> .....   | 170 |
| 7.4 Discussion.....  | 170 |
| 7.5 Conclusions.....   | 176 |
| <br><b>Chapter 8 - Stable Isotopes</b>   |     |
| 8.1 Introduction.....  | 177 |
| 8.2 Research Methods.....  | 177 |
| 8.2.1 <i>Oxygen-Deuterium Isotopes</i> .....   | 177 |
| 8.2.1.1 Halloysite Separation .....  | 177 |
| 8.2.1.2 Quantitative X-ray diffraction Analysis.....                                     | 177 |
| 8.2.1.3 Oxygen-Deuterium Analysis.....   | 177 |
| 8.2.2 <i>Sulfur Isotope Methods</i> .....  | 178 |
| 8.3 Oxygen-deuterium Results .....   | 178 |
| 8.4 Sulfur Isotope Results.....  | 178 |
| 8.5 Oxygen-Deuterium Discussion.....   | 181 |
| 8.5.1 <i>Comparison with Supergene and Hypogene Halloysite</i> .....                     | 181 |
| 8.5.2 <i>Fractionation Factor for Cerro la Mina Halloysite</i> .....                     | 181 |
| 8.5.3 <i>Formation Temperature of Halloysite</i> .....                                   | 183 |
| 8.5.4 <i>Halloysite Hydrogen Exchange</i> .....  | 184 |
| 8.5.5 <i>Deep Position of Cerro la Mina Halloysite</i> .....                             | 185 |
| 8.6 Sulfur Isotope Discussion.....   | 185 |
| 8.7 Conclusions.....   | 186 |

**Chapter 9 - Genesis of the Cerro la Mina Prospect**

|   |     |
|---|-----|
| 9.1 Introduction.....                                 | 187 |
| 9.2 Genesis.....                                      | 187 |
| 9.2.1 <i>Tectonic Setting and Volcanism</i> .....     | 187 |
| 9.2.2 <i>Geologic Framework</i> .....                 | 188 |
| 9.2.3.1 Hydrothermal System .....                     | 188 |
| 9.2.3.2 Porphyry Cu-Mo Stage .....                    | 189 |
| 9.2.3.3 Epithermal Au-Cu Stage .....                  | 189 |
| 9.2.3.4 Halloysite Formation.....                     | 191 |
| 9.2.3 <i>Present Day</i> .....                        | 191 |
| 9.3 Cerro la Mina in Relation to World Deposits ..... | 192 |
| 9.3.1 <i>Alkalic Affinity</i> .....                   | 192 |
| 9.3.2 <i>Breccia Pipes</i> .....                      | 193 |
| 9.3.3 <i>Halloysite</i> .....                         | 193 |
| 9.3.4 <i>Lithocap</i> .....                           | 193 |
| 9.4 Conclusions.....                                  | 194 |

**Chapter 10 - Conclusions**

|   |     |
|---|-----|
| 10.1 Tectonic Setting .....                             | 195 |
| 10.2 Selva Negra Geochemistry .....                     | 195 |
| 10.3 Cerro la Mina Geology .....                        | 195 |
| 10.4 Alteration and Mineralisation .....                | 196 |
| 10.4.1 <i>Porphyry System</i> .....                     | 196 |
| 10.4.2 <i>Epithermal System</i> .....                   | 197 |
| 10.5 Genesis.....                                       | 198 |
| 10.6 Exploration Implications .....                     | 199 |
| 10.6.1 <i>Tectonics and Geology</i> .....               | 199 |
| 10.6.2 <i>Porphyry Vectors</i> .....                    | 199 |
| 10.6.3 <i>High Sulfidation Epithermal Vectors</i> ..... | 200 |
| 10.7 Further Work.....                                  | 200 |
| 10.7.1 <i>Geology</i> .....                             | 200 |
| 10.7.2 <i>Halloysite Isotopes</i> .....                 | 200 |

|                               |            |
|-------------------------------|------------|
| <b>References Cited .....</b> | <b>201</b> |
|-------------------------------|------------|

## List of Figures

|  |    |
|--|----|
| Figure 1.1 Schematic illustration of relationships between porphyry and epithermal mineralisation styles .....   | 1  |
| Figure 1.2 Location of the Cerro la Mina Au (Cu-Mo) prospect, Ixhuatán concession, Chiapas State, Mexico.....  | 3  |
| Figure 1.3 Photograph of the Cerro la Mina Au (Cu-Mo) prospect.....  | 4  |
| Figure 2.1 Tectonic map and distribution of volcanic arcs of Mexico and Central America from Cenozoic till recent .....  | 8  |
| Figure 2.2 Generalized structural map of southeast Mexico.....   | 8  |
| Figure 2.3 Generalized geologic map of Chiapas State .....   | 11 |
| Figure 2.4 Magnetic anomaly map of Chiapas State .....   | 13 |
| Figure 2.5 Volcanism of the Chiapanecan volcanic arc and its association with strike-slip faults.....  | 14 |
| Figure 2.6 Generalized geologic map and geochronology of El Chichón, and the Santa Fé mining district - Selva Negra region.....  | 16 |
| Figure 2.7 Distribution of porphyry and epithermal deposits of Mexico .....  | 17 |
| Figure 2.8 Metallogeny of Chiapas State highlighting the Santa Fé, Campamento, Cerro la Mina and Tolimán porphyry-epithermal occurrences and other polymetallic prospects..... | 17 |
| Figure 2.9 Geology of the Campamento deposit.....  | 18 |
| Figure 3.1 Geologic Map of the Selva Negra volcanic rocks and locations of whole-rock geochemistry samples .....   | 24 |
| Figure 3.2 The major and trace elements concentrations of five duplicate analysis plotted against each other.....  | 26 |
| Figure 3.3 UTM N versus elevation for the Selva Negra volcanic rocks .....   | 27 |
| Figure 3.4 Hand sample and petrographic images of Selva Negra rock types. ....   | 29 |
| Figure 3.5 Distinguishing altered from unaltered samples (highlighted in grey) using primitive mantle-normalized patterns and REE patterns.....                                | 31 |
| Figure 3.6 Hawker diagrams for the major oxides illustrating unaltered versus altered samples. ....  | 32 |
| Figure 3.7 LOI versus mobile elements Rb, Ba, U, Cs, Pb, and Sr. ....  | 33 |
| Figure 3.8 Plot of immobile elements for the altered and unaltered Selva Negra volcanic rocks.....   | 33 |
| Figure 3.9 SiO <sub>2</sub> versus total alkalis diagram (Le Maitre et al., 1989) comparing the Selva Negra suite with the regional volcanism .....                            | 35 |
| Figure 3.10 Hawker diagrams for the Chiapanecan volcanic arc .....   | 36 |
| Figure 3.11 SiO <sub>2</sub> versus K <sub>2</sub> O diagram for the Selva Negra.....  | 37 |
| Figure 3.12 Alternative diagrams for discriminating rocks of alkaline composition .....  | 37 |
| Figure 3.13 Average primitive mantle diagrams for the Selva Negra compared with the regional volcanism.....  | 38 |
| Figure 3.14 LILE/HFSE (Ba/Hf and Rb/Ta) versus SiO <sub>2</sub> . ....   | 38 |
| Figure 3.15 La/Yb <sub>CN</sub> , La/Sm <sub>CN</sub> and Sm/Yb <sub>CN</sub> ratios for the Selva Negra compared with the regional volcanism.....                             | 40 |
| Figure 3.16 La/Yb <sub>CN</sub> , La/Sm <sub>CN</sub> and Sm/Yb <sub>CN</sub> for the Selva Negra suite. ....  | 40 |

---

|  |    |
|--|----|
| Figure 3.17 Eu/Eu* versus silica diagram for the Selva Negra. ....   | 40 |
| Figure 3.18 Silica versus $^{87}\text{Sr}/^{86}\text{Sr}$ for the Selva Negra, El Chichón, and El Chichón mafic xenoliths...<br>.....  | 43 |
| Figure 3.19 $^{87}\text{Sr}/^{86}\text{Sr}$ versus $\epsilon_{\text{Nd}}$ for the Selva Negra and regional volcanism. ....   | 43 |
| Figure 3.20 $^{87}\text{Sr}/^{86}\text{Sr}$ versus $^{206}\text{Pb}/^{204}\text{Pb}$ for the Selva Negra compared with the TMVB and TVF .....                                | 45 |
| Figure 3.21 Pb isotopes for the Selva Negra compared with the Trans-Mexican volcanic belt and Los Tuxtlas volcanic field .....   | 45 |
| Figure 3.22 $^{87}\text{Sr}/^{86}\text{Sr}$ versus Rb/Cs for the Selva Negra suite. A positive trend is consistent with increasing crustal contamination.....                | 47 |
| Figure 3.23 U/Th versus Ba/La diagram to identify sediment input. ....   | 47 |
| Figure 3.24 Adakite discrimination diagrams for the Selva Negra, El Chichón and central CVA.....   | 48 |
| Figure 3.25 Sr/Y versus $\text{SiO}_2$ diagram for Selva Negra and El Chichón .....  | 48 |
| Figure 4.1 Characteristics of fiamme breccias (Unit 1).. ....  | 54 |
| Figure 4.2 Characteristics of monzodiorite to diorite intrusions (Unit 2).....   | 56 |
| Figure 4.3 Characteristics of trachyandesite coherent rocks and matrix-supported breccias (Unit 3)....<br>.....  | 59 |
| Figure 4.4 Characteristics of the breccia complex (Unit 4). ....   | 61 |
| Figure 4.5 Images of lineations seen in the matrix-rich, granule breccia in thin section, drill core and outcrop.....  | 62 |
| Figure 4.6 Fine-grained zones of quartz - potassium feldspar - plagioclase.....  | 62 |
| Figure 4.7 Surface geology and aeromagnetic image of the Cerro la Mina prospect.....   | 63 |
| Figure 4.8 Topography image of Cerro la Mina.....  | 63 |
| Figure 4.9 Geology of cross section A-A' .....   | 65 |
| Figure 4.10 Geology of cross section B-B' .....  | 66 |
| Figure 4.11 Geology of cross section C-C' .....  | 67 |
| Figure 4.12 Geology of cross section D-D' .....  | 68 |
| Figure 4.13 Geology of long section E-E' .....   | 69 |
| Figure 4.14 Cerro la Mina stratigraphic column illustrating the paragenesis of the volcanic stratigraphy .....   | 72 |
| Figure 5.1 Examples of SWIR spectra collected from the Stage A potassic and Stage B sericitic alteration .....   | 77 |
| Figure 5.2 Examples of SWIR spectra collected from quartz-dickite alteration (Stage $C_{\text{QD}}$ ). X-axis is wavelength (nm) and Y-axis is normalised hull quotient..... | 78 |
| Figure 5.3 Examples of SWIR spectra collected from halloysite-kaolinite alteration (Stage $C_{\text{HK}}$ ).....   | 78 |
| Figure 5.4 Drill core examples of Stages A, B, $C_{\text{QD}}$ , and $C_{\text{HK}}$ alteration.....   | 80 |
| Figure 5.5 Characteristics of Stage A potassic alteration. ....  | 81 |
| Figure 5.6 Characteristics of Stage B sericitic alteration .....   | 83 |
| Figure 5.7 Characteristics of quartz-dickite alteration (Stage $C_{\text{QD}}$ ) .....   | 86 |
| Figure 5.8 Characteristics of halloysite-kaolinite (Stage $C_{\text{HK}}$ ) alteration.....  | 87 |

---

|   |     |
|---|-----|
| Figure 5.9 Drill hole illustrating the distribution of Stage $C_{HK}$ alteration in relation to the oxide zone and pyrite.....  | 88  |
| Figure 5.10 The Cerro la Mina and regional surface alteration.....  | 89  |
| Figure 5.11 Crystallinity and Al-OH zonation of the sericitic alteration (Stage B) versus distance from the breccia pipe centre.....  | 90  |
| Figure 5.12 Alteration of cross section A-A`.....   | 91  |
| Figure 5.13 Alteration of cross section B-B`.....   | 92  |
| Figure 5.14 Alteration of cross section C-C`.....   | 93  |
| Figure 5.15 Alteration of cross section D-D`.....   | 94  |
| Figure 5.16 Alteration of long section E-E`.....  | 95  |
| Figure 5.17 Depth below surface contour of kandite alteration (Stage C).....  | 96  |
| Figure 5.18 Paragenetic sequence of alteration for the Cerro la Mina prospect.....  | 97  |
| Figure 5.19 Comparison of TSG v.5 reference library spectra for kaolinite and halloysite.....   | 99  |
| Figure 5.20 KH index versus QXRD analysis of samples containing halloysite/kaolinite.....   | 99  |
| Figure 5.21 KH index of cross section C-C`.....   | 101 |
| Figure 5.22 Zoning of the Stage $C_{QD}$ and Stage $C_{HK}$ alteration illustrated with SWIR spectral identification, KH Index, XRD mineral identification, and QXRD data.....                    | 102 |
| Figure 5.23 SEM image of the < 1 $\mu\text{m}$ fraction of a halloysite-kaolinite altered rock.....   | 103 |
| Figure 5.24 SEM images of halloysite-kaolinite altered samples.....   | 105 |
| Figure 5.25 SEM image of halloysite aggregates intergrown with fine-grained sulfides.....   | 106 |
| Figure 5.26 KH index versus heating and time graph for H-K altered samples.....   | 107 |
| Figure 5.27 Illustration showing the transformation from halloysite to kaolinite.....   | 108 |
| Figure 6.1 Zonation of Au, Cu, Mo, As, Zn and Pb at the Cerro la Mina prospect in relationship to the breccia pipe (Unit 4).....  | 115 |
| Figure 6.2 Simplified log of drill hole IXCM07-44 illustrating the relationship of high Au-Cu grades with structures, quartz-dickite alteration (Stage $C_{QD}$ ) and breccia pipe rock type..... | 116 |
| Figure 6.3 Outcrop of grey quartz-dickite alteration (Stage $C_{QD}$ ) with brown oxide.....  | 116 |
| Figure 6.4 Mineralisation in drill core commonly observed at the Cerro la Mina prospect.....  | 117 |
| Figure 6.5 Characteristics of Stage 1 mineralisation.....   | 118 |
| Figure 6.6 Characteristics of Stage 2 mineralisation.....   | 119 |
| Figure 6.7 Characteristics of Stage 3 mineralisation.....   | 122 |
| Figure 6.8 Characteristics of Stage 4 mineralisation.....   | 124 |
| Figure 6.9 Veins textures of Cerro la Mina.....   | 127 |
| Figure 6.10 Rare phosphorous veins of Cerro la Mina.....  | 128 |
| Figure 6.11 Mineralisation of cross section A-A`.....   | 129 |
| Figure 6.12 Mineralisation of cross section B-B`.....   | 130 |
| Figure 6.13 Stage 1 and 2 mineralisation of cross section C-C`.....   | 131 |
| Figure 6.14 Stage 3 and 4 mineralisation of cross section C-C`.....   | 132 |

---

|   |     |
|---|-----|
| Figure 6.15 Mineralisation of cross section D-D' .....  | 133 |
| Figure 6.16 Stage 1 and 2 mineralisation of long section E-E' .....   | 134 |
| Figure 6.17 Stage 3 and 4 mineralisation of long section E-E' .....   | 135 |
| Figure 6.18 Schematic illustrating the paragenesis of the Cerro la Mina Stages 1 to 4 mineralisation and associated alteration.....   | 138 |
| Figure 6.19 Parageneses of mineralisation for the Cerro la Mina prospect.....   | 139 |
| Figure 6.20 Tukey box plot showing the composition of a Cerro la Mina standard pyrite .....   | 141 |
| Figure 6.21 Laser map image of fractured pyrite (Stage 1) with Co- and Se-rich zones .....  | 142 |
| Figure 6.22 Laser map image of fractured pyrite with an arsenic-rich core (units in ppm) .....  | 143 |
| Figure 6.23 Tukey box plot showing the trace element concentrations for fractured pyrite (Stage 1) mineralisation with Co-, Se- and As-rich zones.....                            | 144 |
| Figure 6.24 Laser map image of inclusion-rich pyrite (Stage 2; units in ppm) .....  | 145 |
| Figure 6.25 Laser map image of inclusion-rich pyrite (Stage 2; units in ppm) with an arsenic-rich core (units in ppm) .....   | 146 |
| Figure 6.26 Laser map image of chalcopyrite (Stage 2; units in cps).....  | 146 |
| Figure 6.27 Tukey box plot showing the trace element concentrations for inclusion-rich pyrite (Stage 2) with Co-, Se- and As-rich zones .....                                     | 147 |
| Figure 6.28 Concentrations of Co, Ni, Cu, Se, Mo, Te, and Au in Stage 2 pyrite versus horizontal distance from breccia pipe. ....   | 148 |
| Figure 6.29 Concentrations of Co, Ni, Cu, Se, Mo, Te, and Au in Stage 2 pyrite vs elevation in the breccia pipe. ....   | 149 |
| Figure 6.30 Laser map image marcasite (Stage 3; units in ppm).....  | 151 |
| Figure 6.31 Laser map image sphalerite (Stage 3; units in cps) .....  | 151 |
| Figure 6.32 Tukey box plot showing the trace element concentrations for Stage 3 marcasite.....  | 152 |
| Figure 6.33 Laser map image ragged pyrite (Stage 4; units in ppm).....  | 152 |
| Figure 6.34 Laser map image rimming pyrite (Stage 4; units in ppm). inclusion-rich pyrite.....  | 153 |
| Figure 6.35 Laser map image enargite (Stage 4; units in cps) .....  | 154 |
| Figure 6.36 Tukey box plot showing the trace element concentrations for Stage 4 ragged, and rimming pyrite of the upper and lower arsenic-rich zones .....                        | 155 |
| Figure 6.37 Tukey box plot of the various stages illustrating an increase in As concentration with each stage of mineralisation .....   | 157 |
| Figure 6.38 As versus Au diagram for fractured (Stage 1) and inclusion-rich pyrite (Stage 2) .....  | 157 |
| Figure 6.39 As versus Au diagram showing the distribution of ragged pyrite (Stage 4) and rimming pyrite (Stage 4) from the upper and lower arsenic-rich zones.....                | 158 |
| Figure 7.1 Cathodoluminescence images of typical zircon grains with weak oscillatory zoning.....  | 165 |
| Figure 7.2 $^{207}\text{Pb}$ corrected $^{206}\text{Pb}/^{238}\text{U}$ zircon ages on Tera-Wasserburg concordia diagrams.....  | 167 |
| Figure 7.3 $^{207}\text{Pb}$ corrected $^{206}\text{Pb}/^{238}\text{U}$ zircon ages corrected for $^{230}\text{Th}$ disequilibrium.....   | 168 |
| Figure 7.4 Image of sample with hydrothermal biotite veinlets in potassium feldspar altered rock in which biotite was extracted for $^{40}\text{Ar}/^{39}\text{Ar}$ analysis..... | 169 |
| Figure 7.5 Age spectrum and inverse isochron plots for $^{40}\text{Ar}/^{39}\text{Ar}$ analysis of biotite.....   | 169 |

---

---

|  |     |
|--|-----|
| Figure 7.6 Comparison of U-Pb, Re-Os and Ar-Ar ages completed in this study .....  | 171 |
| Figure 7.7 Probability charts for old zircons analysed in Unit 1B <sub>s</sub> (samples IXCM07-23 221.0 and 327.0) and their correlation to basement ages from the Chiapas massif .....              | 172 |
| Figure 7.8 Compilation of geology, mineralisation and alteration ages for the Cerro la Mina prospect .....   | 173 |
| Figure 7.9 Simplified geologic map indicating the location ages from the literature and new ages from this study .....   | 174 |
| Figure 8.1 Sample locations for oxygen-deuterium and sulfur isotope analyses on long section E-E' ..   | 179 |
| Figure 8.2 Extrapolation of $\delta^{18}\text{O}$ values for pure halloysite from samples with varying abundances of halloysite to impurities .....  | 179 |
| Figure 8.3 Histograms illustrating the $\delta^{34}\text{S}$ values for the total, Stage 1, Stage 2 and Stage 4 sulfides ..  | 180 |
| Figure 8.4 $\delta^{18}\text{O}$ versus $\delta\text{D}$ diagram showing the composition of Cerro la Mina halloysite compared to the fields of supergene and hypogene halloysite.....                | 182 |
| Figure 8.5 $\delta^{18}\text{O}$ versus $\delta\text{D}$ diagram showing the fractionation trend of water in equilibrium with Cerro la Mina halloysite in relation to possible sources of water..... | 183 |
| Figure 9.1 Schematic presentation of the geologic setting for the Cerro la Mina prospect.....  | 188 |
| Figure 9.2 Schematic diagrams illustrating the formation of the Cerro la Mina Au (Cu-Mo) prospect ..   | 190 |
| Figure 9.3 Schematic illustrating Cerro la Mina prospect at present day where geology, alteration and mineralisation are off-set horizontally and vertically by the northwest fault.....             | 191 |



## List of Tables

|   |     |
|---|-----|
| Table 4.1 Description and interpretation of lithofacies for the Cerro la Mina prospect. ....  | 52  |
| Table 5.1 Summary of the Cerro la Mina alteration assemblages and their relationship to rock lithofacies .....  | 80  |
| Table 5.2 Whole rock quantitative XRD data of sericitic altered (Stage B) samples in relation to their distance from the breccia pipe.....                                  | 82  |
| Table 5.3 Summary for SEM imaging of alunite .....  | 85  |
| Table 5.4 Summary of whole rock, vein and clay separate of Stage ( $C_{HK}$ ) altered samples observed with the SEM.....  | 103 |
| Table 5.5 Quantitative XRD analysis of bulk rock, <10 $\mu\text{m}$ , <4 $\mu\text{m}$ and <1 $\mu\text{m}$ fractions of a halloysite-kaolinite altered samples .....       | 103 |
| Table 5.6 The size range, parent mineral, and dominant quantitative XRD mineralogy for different morphologies of the Cerro la Mina halloysite-kaolinite altered rocks ..... | 106 |
| Table 6.1 Comparison of Au-Cu-Mo grades for breccia pipe (Unit 4), volcanic wall rocks (Units 1 to 3) and quartz-dickite alteration (Stage $C_{QD}$ ).....                  | 115 |
| Table 6.2 Summary of the number of laser maps created for each mineral.....   | 141 |
| Table 7.1 Summary of new U-Pb geochronology for the Cerro la Mina prospect and Ixhuatán concession .....  | 166 |
| Table 7.2 Summary of standards analysed during U-Pb age dating and their recommended ages ...   | 166 |
| Table 7.3 Summary of data for Re-Os dating of molybdenite .....   | 170 |
| Table 7.4 Summary table of regional dating from literature and new ages from this study.....  | 175 |
| Table 8.1 $\delta^{18}\text{O}$ and $\delta\text{D}$ data for separated Cerro la Mina halloysite and rain water from Tapilula, Chiapas. ....                                | 179 |
| Table 8.2 $\delta^{34}\text{S}$ data for sulfates and sulfates from the four stages of mineralisation. ....   | 180 |



# Appendices

Appendices are provided electronically on accompanying CD.

## **Appendix I - Graphic Logging**

I.1 Graphic logging technique

I.2 Graphic logs

## **Appendix II - Igneous Petrology**

II.1 Sample location details

II.2 Rock photos

II.3 Petrography

II.4 Whole rock geochemistry data

II.5 Isotope data

## **Appendix III - Alteration**

III.1 Potassium feldspar staining images

III.2 Spectral database

III.3 Spectra interpretation

III.4 XRD database

III.5 SEM images of alunite

III.6 SEM images of halloysite and kaolinite

## **Appendix IV - Mineralisation**

IV.1 Petrography

IV.2 Raw LA-ICP-MS cps laser images

IV.3 Converted LA-ICP-MS ppm laser images

## **Appendix V - Geochronology**

V.1 Zircon analyses data and CL images

V.2 Ar isotopic data

V.3 Ar-Ar plateau ages

## **Appendix VI - Rock Catalogue**



# Nomenclature and Abbreviations

## Units of measurement

nm - nanometre  
µm - micrometre  
mm - millimetre  
cm - centimetre  
m - metre  
km - kilometre

## Abbreviations

|         |                               |          |                                 |
|---------|-------------------------------|----------|---------------------------------|
| Alu     | alunite                       | Kao      | kaolinite                       |
| Au      | gold                          | KH index | kaolinite-halloysite index      |
| At      | aligned tubes                 | Ksp      | potassium feldspar              |
| Ba      | barite                        | MAT      | Middle American Trench          |
| Bt      | biotite                       | Mc       | marcasite                       |
| CAVA    | Central American volcanic arc | Mo       | molybdenite or molybdenum       |
| CP      | Cordilleran Province          | MPSF     | Motagua-Polohic sinistral fault |
| Cpy     | chalcopyrite                  | Musc     | muscovite                       |
| Cu      | copper                        | Pyr      | pyrophyllite                    |
| Cv      | covellite                     | Qtz      | quartz                          |
| CVA     | Chiapanecan volcanic arc      | RgPy     | ragged pyrite                   |
| Dik     | dickite                       | RmPy     | rimming pyrite                  |
| EAP     | Eastern Alkaline Province     | Rt       | rutile                          |
| En      | enargite                      | Sh       | subhedral                       |
| Eu      | euohedral                     | Smc      | smectite                        |
| FgPy    | fine-grained pyrite           | SMVA     | Sierra Madre volcanic arc       |
| FrPy    | fractured pyrite              | SN       | Selva Negra                     |
| Ft      | flat tubes                    | Sp       | spheroids                       |
| Ga      | galena                        | Sph      | sphalerite                      |
| Hall    | halloysite                    | Sulf     | sulfide,                        |
| HK      | halloysite + kaolinite        | TMVB     | Trans-Mexican volcanic belt     |
| Ill     | illite                        | TVF      | Los Tuxtlas volcanic field      |
| Ill/Smc | illite/smectite               | TR       | Tehuantepec ridge               |
| IrPy    | inclusion-rich pyrite         | Vt       | vertical tubes                  |
| It      | intermediate tubes            | WR       | wall rock                       |



# Chapter 1 - Introduction

## 1.1 Preamble

Exploration in porphyry-related mineral districts can be complicated by shallow level lithocap formation which can obscure the alteration, mineralisation and geochemical footprint of an underlying porphyry deposit (Fig. 1.1; Holliday and Cooke, 2007). Lithocaps are further complicated when they are formed in a dynamic tectonic, volcanic and erosional environment and by syn- to post-mineralisation structural movements. There are also considerable difficulties associated with assessing the depth to potentially mineralised zones, be they porphyry or epithermal in character, due to the challenges of determining the thickness and extent and the internal structural and stratigraphic architecture of the lithocap (Sillitoe, 1995, 1999; Hedenquist, 2000).

A lithocap, as defined by Sillitoe (1995), is a large zone of pyritic advanced argillic and argillic alteration found between the subvolcanic intrusive environment and the paleosurface. They are topographically prominent, can extend for several kilometres and can have a hypogene, steam heated, or supergene origin or combination thereof. Lithocaps are formed by strongly acidic and oxidized

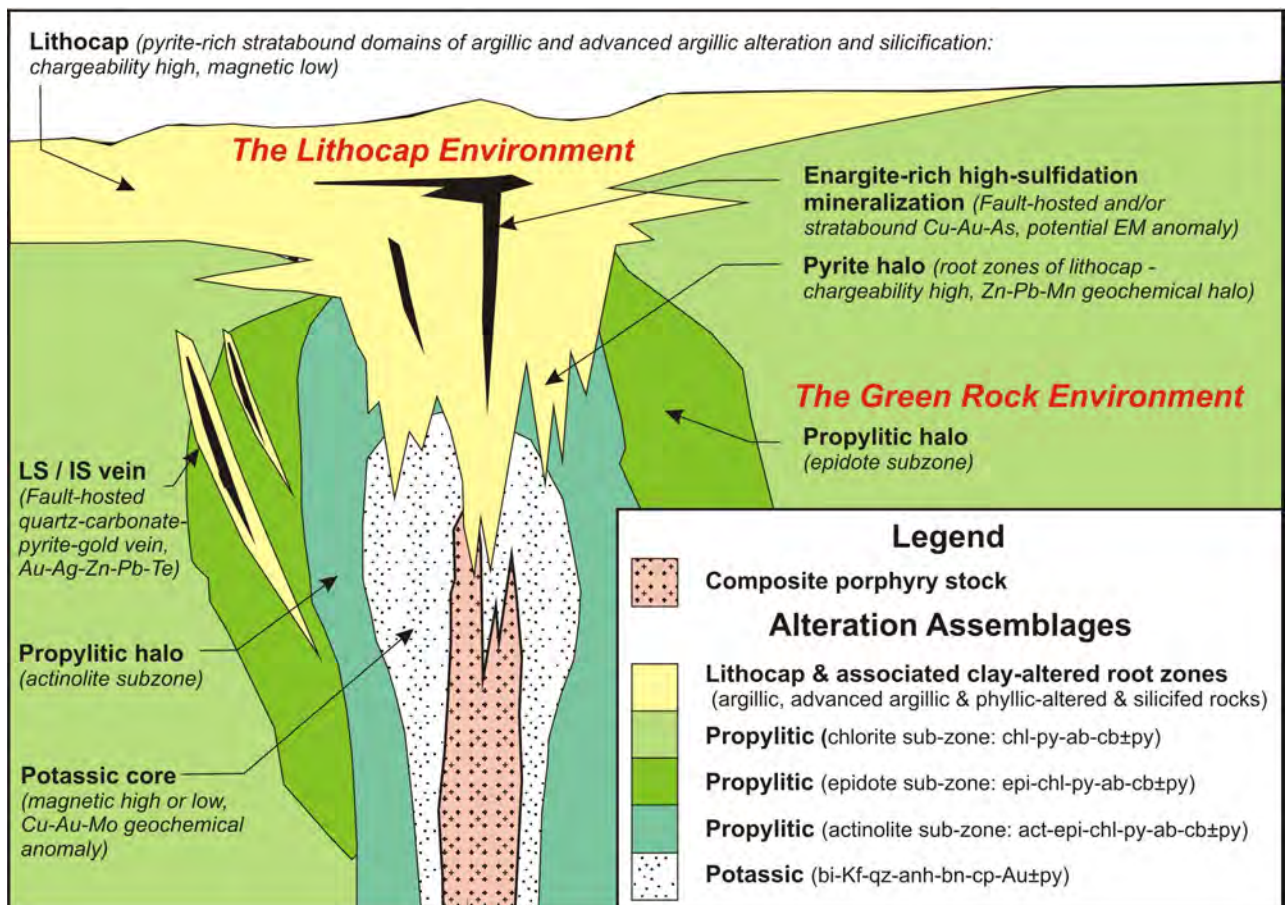


**Figure 1.1** Schematic illustration of relationships between porphyry and epithermal mineralisation styles. The “green rock environment” comprises three propylitic alteration sub-facies (actinolite, epidote and chlorite zones) that occur around the porphyry system and also peripheral to epithermal veins. In this model, the green rock environment has been partially overprinted by a lithocap and related epithermal mineralisation styles, and the roots of the lithocap produces a pyrite halo to the porphyry system. The degree of superposition of the lithocap into the porphyry system is contingent on uplift and erosion rates at the time of mineralisation. From Holliday and Cooke (2007).

fluids interacting with rocks above one or more subvolcanic stocks that may host porphyry Cu or Au deposits (Hedenquist et al., 1998). Late high sulfidation character fluids with a magmatic parentage are thought to be responsible for much of the epithermal Au mineralisation within early formed lithocaps (Sillitoe and Hedenquist, 2003).

The Cerro la Mina Au (Cu-Mo) prospect, southern Mexico, was a greenfields discovery in 2005 by Brigus Gold (formerly Linear Gold Corp.) and considered to have a well developed lithocap (Miranda-Gasca et al., 2009). The site was initially chosen for study by the AMIRA International project P765A “Geochemical Halos in Green Rocks and Lithocaps: The Explorers’ Toolbox for Porphyry and Epithermal Districts” for testing and applying exploration vectors for porphyry mineralisation below lithocaps. P765A was an industry-funded project involving collaborative research between the Centre for Ore Deposit Research (CODES – University of Tasmania), Lakehead University and the University of Ottawa. Sponsors were AngloGold Ashanti, Anglo American, Barrick, Buenaventura, Codelco, Dundee, Equinox, Freeport-McMoran, Gold Fields, Kinross, MMG, Newcrest, Newmont, St. Barbara Rio Tinto, Teck, Vale and Xstrata.

## 1.2 Project Aims and Objectives

The Ph.D. study aims and objectives were to characterise and evaluate the genesis of the Cerro la Mina Au (Cu-Mo) prospect and its relationships to porphyry and epithermal mineralisation. The aim was also to test, refine, modify and apply exploration vectors and discriminators that were developed at CODES in AMIRA International project P765 “Transitions and Zoning in Porphyry-Epithermal Districts: Indicators, Discriminators and Vectors”, which proved effective at detecting mineralised centres beneath the Mankayan lithocap.

The P765 and P765A projects focused on mineral chemistry of alunite and whole rock geochemistry of alunite bearing rocks as discriminators for vectoring towards porphyry targets. Cerro la Mina offered different challenges with abundant kandite clay minerals (halloysite, kaolinite and dickite) compared with other lithocap study sites that contained large zones of vuggy quartz and alunite. In addition, the kandite alteration contains abundant low temperature halloysite clay that is traditionally considered to be a supergene mineral (e.g., Hedenquist, 2000), however, at Cerro la Mina it is associated with sulfides to at least 800 m below the present day surface suggesting a hypogene origin.

In addition to gaining a baseline understanding of the geology and alteration of the Cerro la Mina prospect and its relationship to porphyry and epithermal mineralisation the main aims of this Ph.D. project included the following:

- Multi-element geochemical analyses of regional volcanic rocks
- Evaluate whether Cerro la Mina is a lithocap
- Determine the origin of the abundant halloysite using mineral assemblages, zonation, textures and oxygen-deuterium analysis

- Structural mapping and determination of structural and stratigraphic controls on thickness variations in the lithocap
- Geochronological and isotopic studies of alunite to constrain the timing of lithocap formation, fluid sources and fluid flow directions within the lithocap
- Shortwave infrared analyses of surface and drill core samples using the TerraSpec
- Mineral chemistry analyses of alunite, pyrite, enargite and other appropriate minerals
- Sulfur isotopic analyses of sulfides to test for isotopic zonation patterns that can be used as exploration vectors (e.g., Wilson et al., 2007)
- Geochronology on volcanic rocks, mineralisation and alteration

### 1.3 Area of Study

#### 1.3.1 Access and Working Conditions

The Cerro la Mina prospect is part of Brigus Gold's Ixhuatán concession located in Chiapas State, southern Mexico (Fig. 1.2A), 55 km north of the capital city Tuxtla Gutiérrez (Fig. 1.2B). The property is accessed by highway 195 from either Tuxtla Gutiérrez in the south or Villahermosa, Tabasco State in the north (Fig. 1.2C). At the town of Rayón, dirt roads are taken to the Laguna Chica village where the property can then be accessed by all terrain vehicles and/or walking trails.

The topography in northern Chiapas is steep and rugged with elevations between 350 and 2470 m above sea level (Fig. 1.3). Dense tropical rainforest covers the region, however, some of the areas have been degraded by logging and cultivation. The area has a tropical climate, temperatures are consistent throughout the year between 20 and 35°C and receives a high average rainfall of

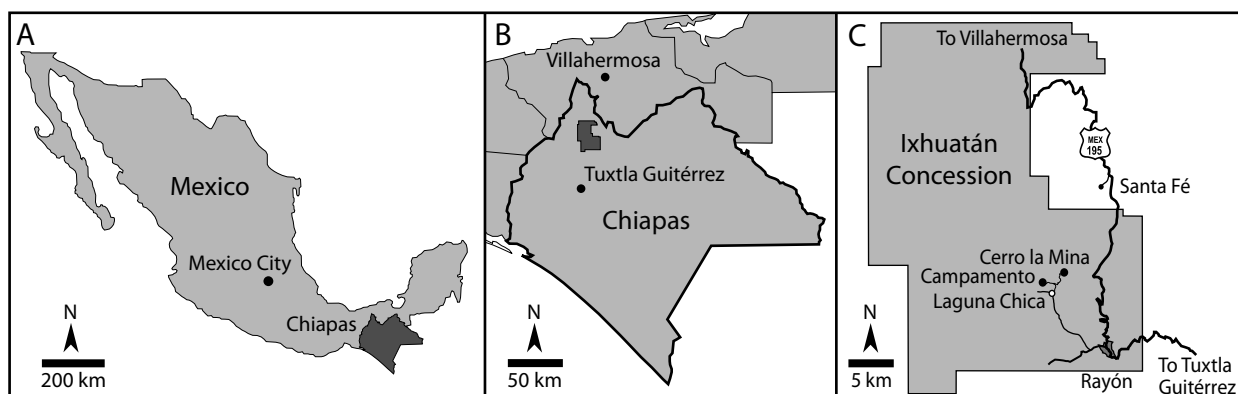


**Figure 1.2** Location of the Cerro la Mina Au (Cu-Mo) prospect, Ixhuatán concession, Chiapas State, Mexico. **A.** Map of Mexico showing the location of Mexico City and Chiapas State in dark grey. **B.** Map of Chiapas State showing the location of the capital Tuxtla Gutiérrez, Villahermosa, and the Ixhuatán concession in dark grey. **C.** Map of Brigus Gold's Ixhuatán concession. The locations of the Santa Fé mine, Campamento deposit and Cerro la Mina prospect are shown. Modified from Linear Gold Corp. (2007).

approximately 4 m per annum (Wallén, 1955).

The working conditions are affected mostly by dense vegetation and steep topography making outcrops sparse and access difficult (Fig. 1.3). Most of the outcrops are limited to trail cuts and ravines. The steep terrain is susceptible to frequent landslides and washouts during the rainy season from June to October. Changing agreements with land owners or “ejidos” restricted access to various locations in the Ixhuatán concession including restricted field access to Cerro la Mina for the last two field seasons. As a result the majority of geological information was gathered from diamond drill hole logging.



**Figure 1.3** Photograph of the Cerro la Mina Au (Cu-Mo) prospect. Access trails are in dense tropical forest with steep topography.

### 1.3.2 Exploration and Mining History

Northern Chiapas does not have a significant exploration and mining history unlike other major metallogenic provinces of Mexico (Camprubí, 2009) due to the remoteness, difficult terrain and lack of geologic information. Evidence of early Spanish exploitation of resources in the Ixhuatán concession are indicated by localities named Cerro la Mina - “Mine Hill”, Monte de Oro - “Gold Mountain” and Mina Valtierra - “Valtierra Mine”. In addition, old mine adits found at the base of Cerro la Mina could have been developed by these early explorers. Mineralisation was first described in northern Chiapas during the 1890’s (MacCarthy, 1897) when Cu-Au mineralisation was mined at the Santa Fé mine 10 km to the northeast of Cerro la Mina (Fig. 1.2C). Early records show that the Santa Fé mine was bought by the Chiapas Mining Company and Mexican Company of London in 1889 (New York Times, 1889). The Santa Fé mine was abandoned in 1905 and limited exploration and mining took place around the Santa Fé area from the 1950’s to 1970’s by various companies (Cano Mendoza, 2008). The nearby La Victoria deposit was discovered and mined during this time (Cano Mendoza, 2008). Minera Frisco currently holds the property with limited exploration activities having been undertaken (Cano Mendoza, 2008).

MIM holdings of Australia staked the Ixhuatán concession (Fig. 1.2C) in 2000 after a review

of the Santa Fé mine which indicated a high sulfidation environment and the potential for a porphyry system at depth. A stream sediment geochemical study in the area indicated strong gold anomalies in the Ixhuatán concession (Pyle, 2009). A ridge and spur soil-sampling program followed by grid soil sampling resulted in the definition of a number of strong soil and outcrop Au anomalies associated with hydrothermal alteration including the Campamento and Cerro la Mina anomalies (Fig. 1.2C; Pyle, 2009). The concession was then sold to Brigus Gold from Canada in 2003; they subsequently discovered the Campamento Au-Ag deposit in 2004. Significant mineralisation was discovered at the Cerro la Mina Au (Cu-Mo) prospect in 2006. From 2008 to 2010 a joint venture was formed with Kinross Gold Corporation to explore the Cerro la Mina Au (Cu-Mo) prospect and test other Au in soil anomalies on the Ixhuatán concession. In 2010 Kinross terminated the joint venture and Brigus Gold continues to hold the concession but currently has no exploration program. Over the years a total of 64 drill holes totalling approximately 21,900 m were drilled at Cerro la Mina, but no resource estimate has been calculated.

### *1.3.3 Previous Research*

Most of the previous work undertaken at the Ixhuatán concession was completed by Brigus Gold exploration geologists consisting mainly of drill hole logging and exploration-based reporting. Three studies were completed on the Campamento deposit included a fluid inclusion study (Richards, 2006a), a mineral paragenesis and gold distribution report (Rainbow and Kyser, 2005) and a Honours thesis on the clay alteration (Jansen, 2007). At Cerro la Mina detailed work consisted of petrography reports describing geology, alteration and mineralisation by Richards (2006b) and Harris (2007). Cumming (2008) described the volcanic facies at Cerro la Mina based on 15 drill holes. In addition, a honours thesis on the Cerro la Mina clay alteration using X-ray diffraction was completed in conjunction with this study by Kyne (2009). An overview of the mineralisation of the Ixhuatán concession and Santa Fé mining district was presented by Miranda-Gasca et al. (2009).

### *1.3.4 Field Work*

The field work consisted of detailed core logging, surface mapping, sampling and spectral analysis of the Cerro la Mina prospect. Field work at Cerro la Mina was completed over four field seasons totalling 4.5 months in 2008 and 2009. Access to the field area was inhibited by the outbreak of Swine Flu from April to May, 2010, which caused the termination of field work. Another field season was cut short when logistical support was lost in September, 2010 as the joint venture agreement between Brigus Gold and Kinross Gold Corporation ceased and the project could no longer be accessed.

## **1.4 Thesis Organization**

The thesis starts with description of the regional geology and mineralisation of Mexico. Chapter 3 describes the geochemistry of the Selva Negra intrusions and volcanic rocks in which the Cerro la Mina prospect is hosted. Chapter 4 describes the Cerro la Mina prospect geology. Chapter 5 describes the wall rock alteration and the halloysite clay in detail. Chapter 6 describes the mineralisation of the prospect and LA-ICP-MS mapping of the mineralisation. Chapter 7 presents U-Pb, Ar-Ar

and Re-Os ages obtained for geology, alteration and mineralisation. Chapter 8 describes oxygen-deuterium work completed on the halloysite clay and sulfur isotopes on sulfides and sulfates. Chapter 9 brings the observations of all the chapters together and discusses the genesis of the Cerro la Mina prospect. The thesis ends with conclusion of the main points.

## Chapter 2 - Regional Geology

### 2.1 Introduction

The complex regional geology of southeast Mexico was highlighted by the surprise eruption of the previously unknown El Chichón volcano in March, 1982. The unique geochemistry and position of El Chichón with respect to surrounding volcanoes highlights the unusual tectonic setting of southeastern Mexico (Nixon, 1982; García-Palomo et al., 2004). In addition, the recognition of potassically-altered accidental lithic clasts as eruption products suggested the potential for a porphyry-type hydrothermal system below El Chichón (Luhr et al., 1984; Rye et al., 1984; Luhr, 2002).

The eruption of El Chichón made apparent to the scientific community the geologic intricacy of the region and to mineral explorers the potential for the region to host porphyry-epithermal deposits. With the Cerro la Mina prospect located only 20 km to the southeast of El Chichón, the understanding of the tectonics, basement geology and volcanism of the region is crucial to understanding the genesis of the Cerro la Mina prospect and to further mineral exploration in the region.

This chapter will first outline the tectonic setting and structure of southeastern Mexico. Second the volcanism of Mexico and Central America is discussed to provide a background to Chapter 3 which discusses the igneous geochemistry of the Selva Negra where the Cerro la Mina prospect is hosted. This is followed by the geology and volcanism of Chiapas and a discussion of how Cerro la Mina fits in the regional metallogensis of Mexico.

### 2.2 Tectonic Setting

Southeastern Mexico is characterized by a complex triple junction of the North American, Caribbean and Cocos plates (Fig. 2.1). The tectonic setting is characterized by a regional zone of left-lateral strike-slip faults known as the Motagua-Polochic sinistral fault which separates the North American and Caribbean plates. The sinistral fault was created by the eastward migration of the Caribbean plate relative to the North American plate. A zone of convergence is created by the subduction of the Cocos plate under the North American and Caribbean plates along the Middle American trench (Nixon, 1982; Burbach et al., 1984). The Cocos plate is marked by a prominent bathymetric feature called the Tehuantepec ridge (Manea et al., 2005).

Structure is characterized by a Neogene fold and thrust belt and strike-slip fault zone in Mesozoic and Tertiary sedimentary rocks located in the central and northeast portions of Chiapas State (Fig. 2.2; Guzman-Speziale and Meneses-Rocha, 2000; Meneses-Rocha, 2001). The Neogene fold and thrust belt and strike-slip fault zone formed at the beginning of the middle Miocene as a result of a northeast-oriented maximum horizontal stress of the subducted Cocos plate (Meneses-Rocha, 2001). The structural zone is bounded to the south by the Chiapas massif and to the north by the Yucatan platform (Fig. 2.2). The fold and thrust fault belt is an elongated structural trend, convex to the northeast, formed by long, narrow anticlines offset along their flanks by reverse faults that generally overthrust the intervening synclines (Fig. 2.2; Mandujano-Velazquez and Keppie, 2009).

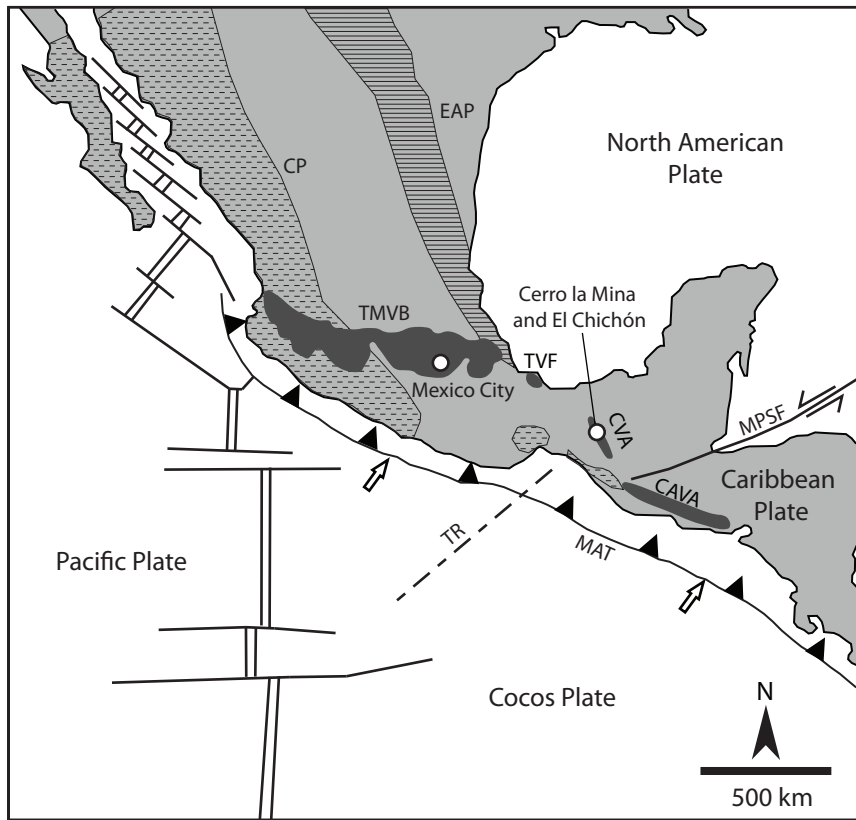


**Figure 2.1** Tectonic map and distribution of volcanic arcs of Mexico and Central America from Cenozoic till recent. **Abbreviations:** CAVA - Central American volcanic arc, CVA–Chiapanecan volcanic arc, CP - Oligocene to Miocene Cordilleran Province, EAP - Eastern Alkaline Province, MAT - Middle American Trench, MPSF - Motagua-Polochic Sinistral Fault, TMVB –Trans Mexican Volcanic Belt, TVF –Tuxtla volcanic field, TR - Tehuantepec ridge. Modified from Robin (1982) and García-Palomo et al. (2004).

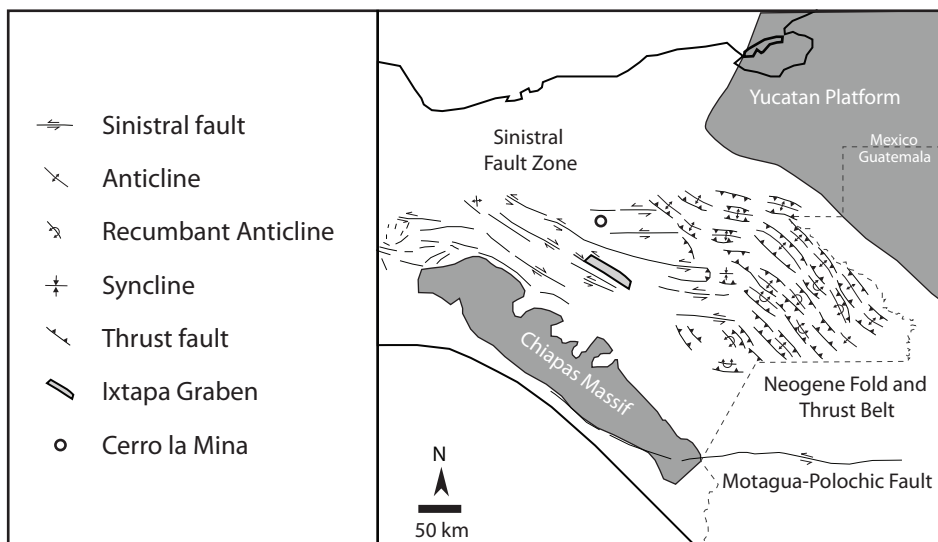


**Figure 2.2** Generalised structural map of southeast Mexico. The Motagua-Polochic sinistral fault is a diffuse boundary of faults that starts in northern Guatemala and continues into southeastern Mexico where the Neogene fold and fault belt and strike-slip zone occurs. This shear belt distributes the interplate strain along reverse and strike-slip faults and is bounded by the Yucatan platform and the Chiapas Massif. Modified from Guzman-Speziale et al. (2000) and Meneses-Rocha et al. (2001).

The fold axes trend northwest and generally plunge beneath the Pliocene and younger sedimentary rocks of the coastal Tabasco plain of the Gulf of Mexico (Duffield et al., 1984; Meneses-Rocha, 2001; García-Palomo et al., 2004). The strike-slip fault zone is 130 km wide and 360 km long formed by a set of up thrown and down thrown blocks, bounded by left-lateral strike-slip faults (Fig. 2.2; Meneses-Rocha, 2001).

The Ixtapa graben is located in the centre of the strike-slip fault zone and exposes rocks of Middle Cretaceous (Albian-Cenomanian) to Pleistocene age (Fig. 2.2; Meneses-Rocha, 2001). Since the initiation of the subducting trench, the Ixtapa graben has been mainly under transtension until the early Pliocene and shifted to transpression by the late Pliocene (Meneses-Rocha, 2001). The Quaternary is marked by an extension in the Ixtapa graben that was contemporaneous with the initiation of the Chiapanecan Volcanic arc (CVA), during which time volcanic derived sediments were deposited (Meneses-Rocha, 2001).

The nature of the triple junction between the North American, Caribbean and the Cocos plates is controversial, as some (e.g., Burkart, 1983) interpreted it as a simple trench-trench-transform, whereas others (e.g., Guzman-Speziale and Meneses-Rocha, 2000; Meneses-Rocha, 2001) do not consider the triple junction of the three plates to be a classic triple point, but rather propose that the continuation of the western-most part of the Motagua-Polochic sinistral fault is a diffuse boundary of faults that starts in northern Guatemala and continues into southeastern Mexico (Figs. 2.1 and 2.2). According to this model, the Neogene fold and fault belt and strike-slip zone is a shear belt that distributes the interplate strain along reverse and strike-slip faults in northeast and central Chiapas (Fig. 2.2).

The subduction architecture in southern Mexico consists of the Cocos plate subducting beneath the North American and Caribbean plates toward N45°E at an average rate of 76 mm/year (Fig. 2.1; De Mets et al., 1990). The plate is marked by a fracture zone called the Tehuantepec ridge, which began subducting around 8 Ma (Manea et al., 2005) and onshore propagation intercepts El Chichón volcano and the Cerro la Mina prospect (Fig. 2.1). The ridge is a narrow linear feature with a maximum vertical relief of 2000 m from the sea bottom that separates shallower sea floor (−3900 m) to the northwest from the deeper Guatemala basin sea floor (−4800 m) toward the southeast (Manea and Manea, 2008). The geometry of Wadati-Benoiff zone shows that the dip of subduction increases from 25° northwest of the Tehuantepec ridge to 40° southeast and the ridge itself dips at 30 to 35° according to Rebollar et al. (1999). Despite the different subduction angles of the down going Cocos plate there is no evidence for any major tear in the subducted plate associated directly with the Tehuantepec ridge (Burbach et al., 1984; Pardo and Suárez, 1995). The age of the Cocos plate increases from northwest to southeast of the Tehuantepec ridge by approximately 7 Ma (Manea et al., 2005). The depth of the slab below the Cerro la Mina prospect region is calculated to be 225 km (Havskov et al., 1982).

The Cocos plate subducts below the Maya terrane in southern Mexico, a crustal block that comprises mainly the Yucatan Peninsula, the Mexican states of Chiapas, Veracruz and parts of Oaxaca. Basement rocks of northern Chiapas are thought to be granitic and metamorphic, similar

in age and composition to rocks exposed in the Chiapas Massif (described below; Meneses-Rocha, 2001). The Chiapas crust ranges in thickness from 17 to 28 km near the Middle American trench and 49 to 53 km further inland and in the proximity of the Cerro la Mina prospect (Narcía-López et al., 2004).

### 2.3 Volcanism of Mexico and Central America

The distribution of volcanic arcs of Mexico is shown in Figure 2.1. Initial igneous activity occurred during the Oligocene-Miocene in the Cordilleran Province located along the Pacific coast parallel to the Middle American trench, from northwest to southern Mexico. Since the Miocene, volcanism has migrated inland forming the Trans-Mexican Volcanic Belt (TMVB) and the CVA (Robin and Tournon, 1978). Tertiary to Recent volcanism continues into Central America along the Pacific coast in the Central American volcanic arc (CAVA; Fig. 2.1; Carr et al., 1982). Abundant alkaline rocks occur in the Eastern Alkaline Province (EAP) that runs north-south in eastern Mexico (Fig. 2.1; Robin and Tournon, 1978; Robin, 1982). The Miocene to Recent volcanism of the TMVB, EAP including Los Tuxtlas volcanic field (TVF) and the CAVA are discussed here, as their geochemical data sets will be compared with the Selva Negra geochemical data in Chapter 3.

The TMVB includes approximately 8,000 volcanic centres (stratovolcanoes, cinder cones, maars, etc.) of Miocene to Recent age, is approximately 1,000 km long and 50 to 300 km wide and extends east–west from Veracruz to Puerto Vallarta at an angle of approximately 20° with respect to the Middle American trench (Fig. 2.1; Verma, 2006; Vigouroux et al., 2008). Since the Pliocene, the TMVB has erupted mainly calc-alkaline volcanic rocks that are interpreted to be related to the subducting Cocos plate (Luhr, 2006).

The EAP is a roughly north-south belt of Tertiary mafic alkaline volcanic rocks that runs from the United States border to southern Veracruz State and its distribution intersects the subduction related TMVB (Fig. 2.1; Robin, 1982; Ferrari et al., 1999). The EAP alkaline magmatism is related to extensional faults adjacent to the Gulf of Mexico (Robin, 1982). The TVF is part of the most southern portion of the EAP and is close to intersection with the TMVB. The TVF is an isolated area of volcanic centres (cinder cones and stratovolcanos) of late Miocene to Recent age that has erupted basanitic and alkaline basaltic rocks (Verma, 2006). Verma (2006) has suggested that the TVF shows more affinity to the EAP than the TMVB. The TVF has erupted both primitive alkaline to calc-alkaline magmas with picrites, basanitoids and hawaiites, and is interpreted to be an extensional environment similar to a back arc basin that has allowed the juxtaposition of mantle derived alkaline and subduction derived calc-alkaline magmatism (Nelson et al., 1995).

The CAVA is a late Tertiary-Quaternary volcanic province that is 1100 km long extending from Mexico-Guatemala border to central Costa Rica parallel to the Middle American trench (Fig. 2.1; Carr et al., 1982). The active volcanoes, most of which are probably younger than 100 Ka were preceded by an earlier Quaternary volcanic front and by several pulses of volcanic activity during the Tertiary (Carr et al., 1982). The Quaternary volcanic rocks of the CAVA have a clear calc-alkaline

affinity and have relatively little regional variation along the volcanic front (Carr et al., 1982). This volcanic chain is interpreted to be the result of plate convergence between the Cocos and Caribbean plates (Carr et al., 1982). The Tacaná volcano is the north-westernmost volcano of the CAVA occurring in southeast Chiapas (Fig. 2.3). The volcano is built on Pliocene–Pleistocene caldera block-and-ash flows, ignimbrites, lavas and debris flow deposits that overlie older Sierra Madre volcanic arc rocks. The Tacaná volcanic complex began its formation during the late Pleistocene and comprises basaltic-andesite to dacitic lava flows and domes and pyroclastic deposits. The entire volcanic sequence has a calc-alkaline signature with medium K contents, negative anomalies of Nb, Ti and P, and enrichment in light rare earth elements, typical of subduction zones.

## 2.4 Geology of Chiapas

The regional geology of the state of Chiapas comprises a pre-Mesozoic metamorphic, sedimentary and igneous basement, overlain by Mesozoic sedimentary rocks and Cenozoic sedimentary, igneous and volcanic rocks (Fig. 2.3; Sánchez-Montes De Oca, 1979; Escandón Valle et al., 2006).

Pre-Mesozoic rocks crop out in the southwest portion of Chiapas and consist of Proterozoic granites, diorites and gneisses which are discordantly overlain by a sequence of metamorphic units including serpentinites, schists, quartzites and gneisses as well as non-metamorphosed sandstones, conglomerates and other detrital units of middle to upper Paleozoic age (Fig. 2.3; Damon and Motesinos, 1978). The metamorphic units have been metamorphosed to amphibolite to granulite

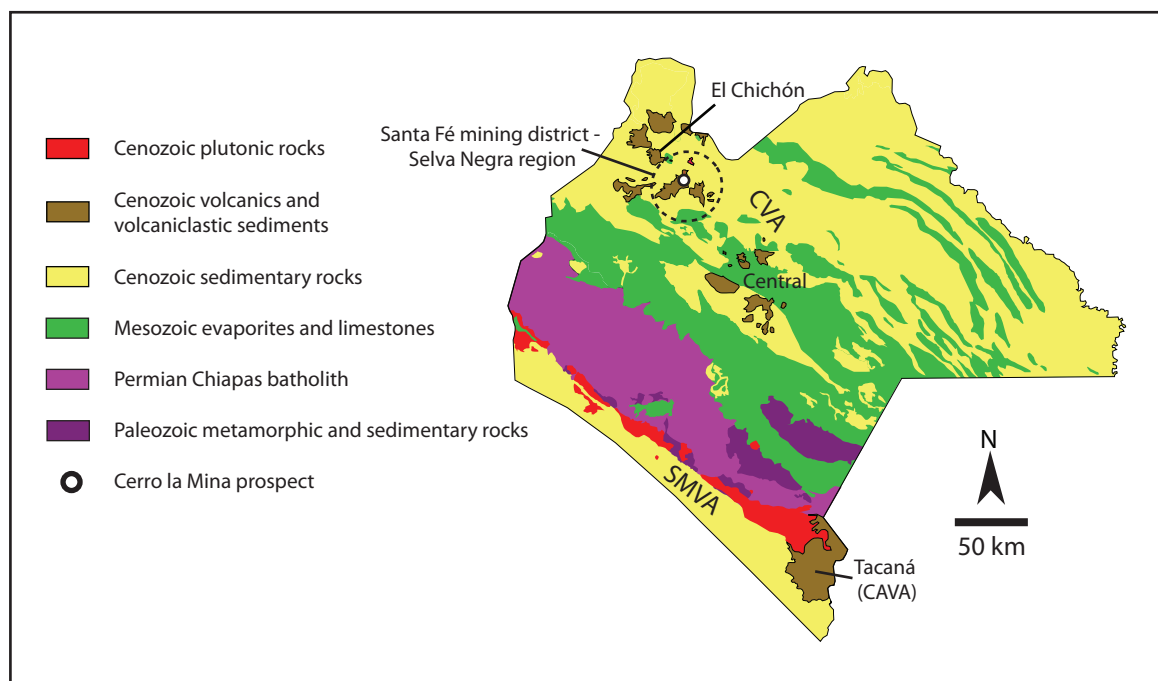


**Figure 2.3** Generalized geologic map of Chiapas State. The Cerro la Mina prospect is part of the Santa Fé mining district - Selva Negra region hosted in the Chiapanecan volcanic arc (CIVA). The volcanism of Chiapas has two stages; the first began in the early Miocene with the initiation of the Sierra Madre volcanic arc (SMVA) along the Pacific coast and ceased around 9 Ma. The distribution of volcanism moved inland and approximately 30° oblique to the middle American trench with the onset of the modern CIVA around 3 Ma (Damon and Motesinos, 1978; Manea and Manea, 2006). **Abbreviations:** CAVA - Central American volcanic arc, CIVA - Chiapanecan volcanic arc, SMVA - Sierra Madre volcanic arc. Modified from Geologic Map of Chiapas and Tabasco State Servicio Geológico Mexicano (2006).

facies (Sánchez-Montes De Oca, 1979; Schaaf et al., 2002; Weber et al., 2005). The final event in the Paleozoic was the intrusion of a late Permian batholithic complex referred to as the Chiapas Massif, consisting of gabbros, granodiorite, diorite and granite intrusions aligned in a northwest direction (Fig. 2.3).

Unconformably overlying the pre-Mesozoic rocks are Triassic-Jurassic red beds to Upper Cretaceous detrital-calcareous units which occur in the north-central portion of the state and have a wide distribution in the uppermost 4 km of the Chiapas crust (Fig. 2.3; Hernández-García, 1973; Taran et al., 1998). They are strongly deformed but not metamorphosed, forming a mountain range exposed as northwest trending anticlinoriums/synclinoriums in the Neogene fold and thrust belt (Figs. 2.2 and 2.3; Meneses-Rocha, 2001). The lower Cretaceous rocks consist of gypsum, interbedded with dolomitic limestone, some breccias, halite and bentonitic beds. A Petrólios Mexicanos (PEMEX) bore hole that was drilled 15 km to the northwest of Cerro la Mina indicated a minimum thickness of 770 m for the Lower Cretaceous evaporite deposits that consisted mainly of anhydrite and halite (Duffield et al., 1984). The Middle and Upper Cretaceous sequences consist of massive, dolomitic, gray limestone.

Cenozoic rocks consist principally of Paleocene to Pliocene interbedded sandstones and siltstones that unconformably overlie the Cretaceous rocks (Sánchez-Montes De Oca, 1979; Escandón Valle et al., 2006). Marine Paleocene units form flysch type rhythmic deposits. Eocene rocks are siltstone and sandstone of mixed continental and marine origin and are overlain by Oligocene units composed mainly of limestone, sandstone and shale. Miocene rocks are mainly calcareous units of marl, conglomerate, sandstone and shale in addition to granodiorite, quartz monzonite and granitic stocks of the Sierra Madre volcanic arc. Pliocene-Holocene units comprise silt, sand and clay deposits together with pyroclastic deposits derived from the CVA and recent volcanic activity of El Chichón and Tacaná volcanoes (García-Palomo et al., 2004; García-Palomo et al., 2006).

#### *2.4.1 Volcanism of Chiapas*

The volcanism of Chiapas has two stages; the first began in the early Miocene with the onset of subduction of the Cocos plate and the initiation of the Sierra Madre volcanic arc along the Pacific coast parallel to the Middle American trench and ceased around 9 Ma (Fig. 2.3; Damon and Motesinos, 1978; Meneses-Rocha, 2001). Much of the volcanic cover of the Sierra Madre volcanic arc has been removed exposing granodiorite, quartz monzonite and granitic stocks (Damon and Motesinos, 1978). Around 3 Ma, the volcanic arc moved inland and approximately 30° oblique to the Middle American trench with the onset of the modern CVA around 3 Ma (Fig. 2.3; Damon and Motesinos, 1978; Manea and Manea, 2006).

The CVA is a 150 km stretch of Pliocene to recent volcanoes (Fig. 2.3) consisting of El Chichón volcano which has been active from 372,000 years to recent (Layer et al., 2009), the Santa Fé mining district - Selva Negra region (2.79 Ma; Damon and Motesinos, 1978) and the central CVA which includes Cerro Tzontehuitz (2.14 Ma; Damon and Motesinos, 1978), the Cerro Lanza (0.85 Ma; Damon and Motesinos, 1978) and the Navenchauc volcano (0.43 Ma; Damon and Motesinos,

1978). Intrusions of granodiorite associated with the CVA crop out in the Santa Fé mining district - Selva Negra region are associated with a large magnetic high (Fig. 2.4).

The position of the CVA is unusual, as it lies well inland and 300 to 350 km from the Middle American trench. The subducted portion of the Cocos plate is ~200 km below the arc (Manea and Manea, 2006). The CVA consists of low profile (< 850 m high), small-volume (3 to 4 km<sup>3</sup>) volcanic domes with associated pyroclastic flow deposits comprising rare basalts, porphyritic hornblende andesites, trachyandesites and minor rhyodacites and rhyolites (Damon and Motesinos, 1978; Duffield et al., 1984; Mora et al., 2007). This differs from the TMVB or the CAVA which are characterized by large stratovolcanos that undergo large plinian eruptions.

The CVA lies in the strike-slip zone and evidence that these faults are used as magma conduits is indicated by the presence of

Pliocene intrusions and Pliocene-Quaternary volcanoes at the ends of some faults or at zones of maximum-extension-produced fault stepping volcanism commonly associated with strike-slip faults (Damon and Motesinos, 1978; Medina et al., 1990; García-Palomo et al., 2004; Mora et al., 2007). García-Palomo et al. (2004) have suggested that the formation of El Chichón volcano is favoured by the structural junction of the extensional zone called the Chapultenango Fault System, forming a half-graben structure and the left lateral, strike-slip east trending San Juan Fault, transecting the volcano (Fig. 2.5A). The emplacement of at least 10 volcanic structures in the central CVA form an irregular northwest alignment generally lying on north–northwest trending faults splayed from the Motagua-Polochic fault system (Fig. 2.5B; Mora et al., 2007).

With the exception of El Chichón, the volcanic structures and deposits of the CVA are calc-alkaline in composition with a medium to high content of potassium (Mora et al., 2007). CVA volcanic rocks vary from andesite to dacite with SiO<sub>2</sub> between 57 and 66 wt.%, low concentrations of Ti, P, Nb and Ta, are enriched in light rare earth elements, depleted in heavy rare earths and show a small Eu anomaly; all indicative of arc-related volcanism associated with subduction of the Cocos plate (Mora et al., 2007).

El Chichón volcano is the only Holocene volcano in the CVA (Fig. 2.3). El Chichón is an

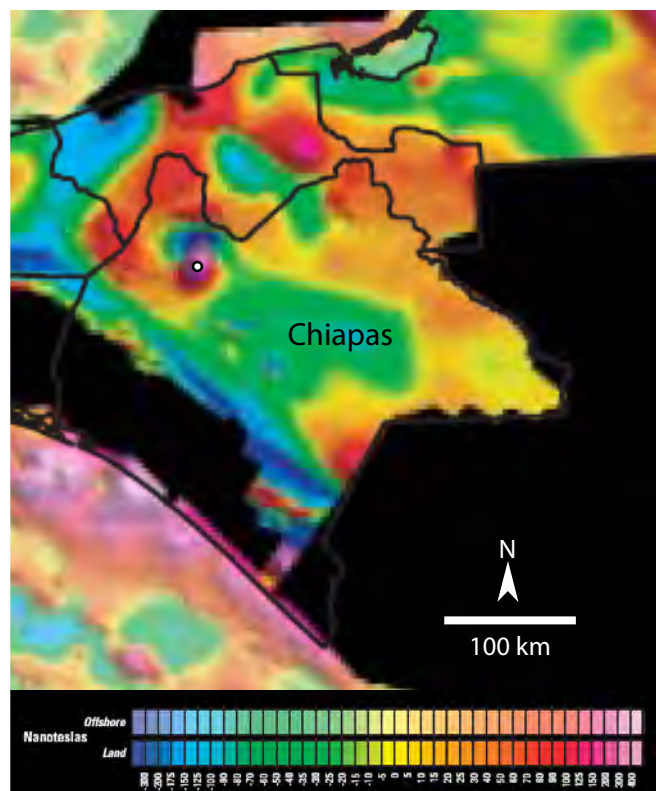


**Figure 2.4** Magnetic anomaly map of Chiapas State. A large magnetic high occurs in northwest Chiapas. The circle indicates location of the Santa Fé mining district - Selva Negra region and the Cerro la Mina prospect. Modified after North American Magnetic Anomaly Group (2002).

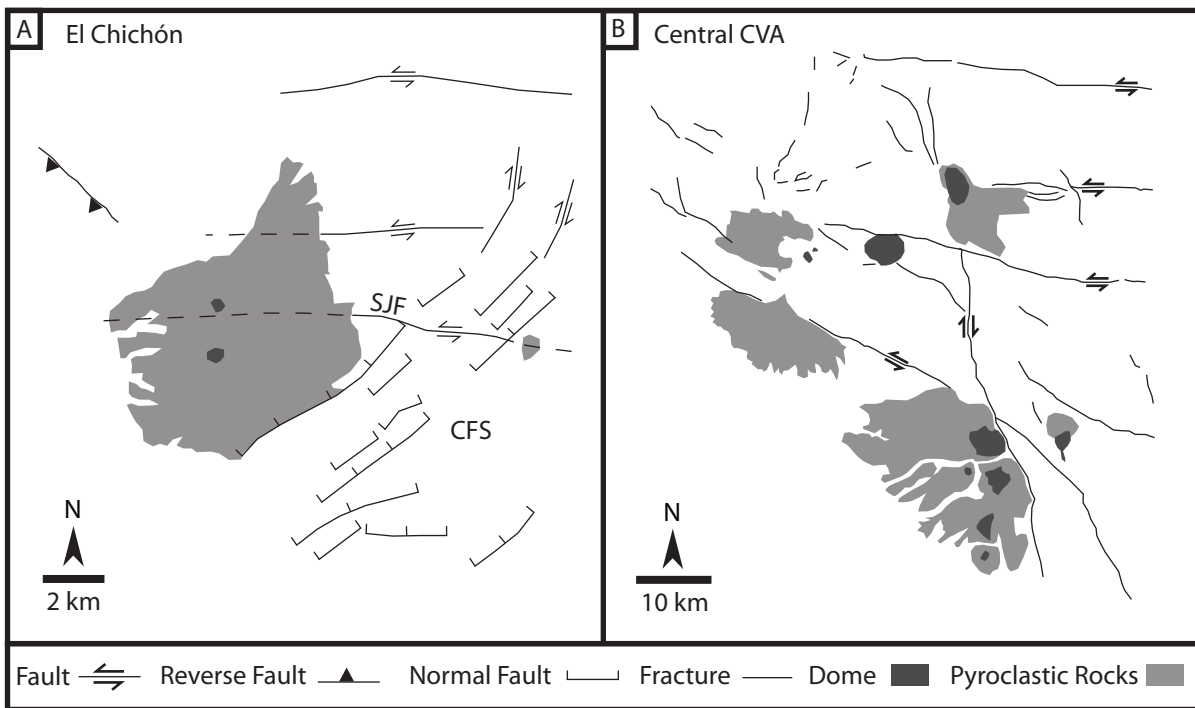


**Figure 2.5** Volcanism of the Chiapanecan volcanic arc and its association with strike-slip faults. **A.** Formation of El Chichón volcano is favoured by the structural junction of an extensional zone, forming a half-graben structure called the Chapultenango Fault System and the left lateral, strike-slip east trending San Juan Fault, transecting the volcano. Modified after García-Palomo et al. (2004). **B.** The emplacement of at least 10 volcanic structures in the central CVA form an irregular northwest alignment generally lying on north–northwest trending faults splayed from the Motagua-Polochic fault system. Modified after Mora et al. (2007). **Abbreviations:** CFS - Chapultenango Fault System, CVA - Chiapanecan volcanic arc, SJF - San Juan Fault.

anomaly in southeast Mexico due to its K-rich alkaline geochemistry and isolated location. The nearest Holocene volcanoes are 275 km and 200 km to the southeast and northwest respectively (Duffield et al., 1984). El Chichón is a low profile (< 850 m) cluster of domes and associated pyroclastic deposits (Duffield et al., 1984) which are geochemically distinct from the TMVB to the northwest, the CAVA to the southeast and the rest of the CVA which are composed mainly of calc-alkaline volcanic rocks (García-Palomo et al., 2004; Manea and Manea, 2008).

El Chichón volcano has only erupted K-rich alkaline trachyandesites and K-rich trachybasalts (Luhr et al., 1984; García-Palomo et al., 2004; Jones et al., 2008) and it has been suggested to have transitional adakite-like geochemistry (De Ignacio et al., 2003). El Chichón trachyandesites are relatively enriched in  $K_2O$ , Rb, Sr, Th, U, Cs and LREE compared to other andesites from Mexico and Central America (Luhr et al., 1984). The TR is thought to affect the anomalous high-K geochemistry of El Chichón volcano. The serpentinized root beneath the TR strongly dehydrates (> 90%) at depths of 180–200 km comparable with the slab depths beneath El Chichón suggesting possible fluid related mantle metasomatism that may play a significant role in the origin of the K-rich rocks (Manea and Manea, 2008).

## 2.5 District Geology

The Cerro la Mina prospect is situated in northern Chiapas where the oldest unit in the region is an Early to Late Cretaceous limestone which crops out as a northwest trending anticline near El Chichón Volcano and is not metamorphosed (Fig. 2.6). Folded Palaeogene limestone with interbedded shales to sandstones are overlain by the Pliocene to Pleistocene CVA volcanic rocks (Fig. 2.6). The Holocene El Chichón volcanic dome complex occurs 20 km to the northwest of the Cerro la Mina prospect (Fig. 2.6). El Chichón's most recent eruptions occurred between 1982-5 and the resulting ash layer is observed in the first metre of the soil profile in the district. The Cerro la Mina prospect is hosted in Selva Negra volcanic rocks of the CVA and in a region of sinistral strike-slip faults (Figs. 2.2 and 2.3; Damon and Motesinos, 1978; Meneses-Rocha, 2001). The geologic map for the area shows northwest trending sinistral faults and a northeast trending dextral faults (Fig. 2.6; Islas Tenorio et al., 2005).

## 2.6 Metallogeny of Chiapas State

### 2.6.1 Porphyry-Epithermal Deposits

Magmatic activity along the North American Cordillera during the late Mesozoic and Palaeogene are related to important porphyry Cu deposits (Valencia-Moreno et al., 2007). Magmatic activity began around 200 Ma in western Canada and gradually migrated south, arriving in north-western Mexico between 64 and 55 Ma (Valencia-Moreno et al., 2007). Subsequently, the migration reached the central and southern region of western Mexico between 45 and 31 Ma and the southernmost tip of the country around 6 Ma. (Fig. 2.7A; Damon et al., 1983). The most important metallogenetic pulse for porphyry deposits occurred during the Laramide event in north-western Mexico and south-western United States (90-40 Ma.; Valencia-Moreno et al., 2007). The continuation of the porphyry copper belt through central and southern Mexico, where the Cerro la Mina prospect occurs, is located in a significantly younger Miocene-Pliocene belt and is poorly documented (Fig. 2.7A; Damon and Motesinos, 1978; Camprubí and Albinson, 2007; Valencia-Moreno et al., 2007; Camprubí, 2009).

The epithermal deposits of Mexico are Tertiary, ranging mainly from middle Eocene to early Miocene in age and are dominated by intermediate to low sulfidation types (Camprubí and Albinson, 2007). Only four high sulfidation deposits have been described in the northwest part of the country (Fig. 2.7B; Camprubí and Albinson, 2007). The space and time distribution of Mexican epithermal deposits follow the evolution of continental arc volcanism of the Sierra Madre Occidental and Sierra Madre del Sur by moving from the north to the south of Mexico (Camprubí and Albinson, 2007). The epithermal deposits in Chiapas are located outside major metallogenic provinces in central Mexico and are both low and high sulfidation (Campamento and Cerro la Mina respectively) occurring in volcanic rocks less than  $2.79 \pm 0.08$  Ma (Fig. 2.7; Damon and Motesinos, 1978).

The Campamento deposit, Cerro la Mina prospect, Santa Fé mine and Tolimán deposit are the only documented porphyry-epithermal deposits in Chiapas and are genetically associated with

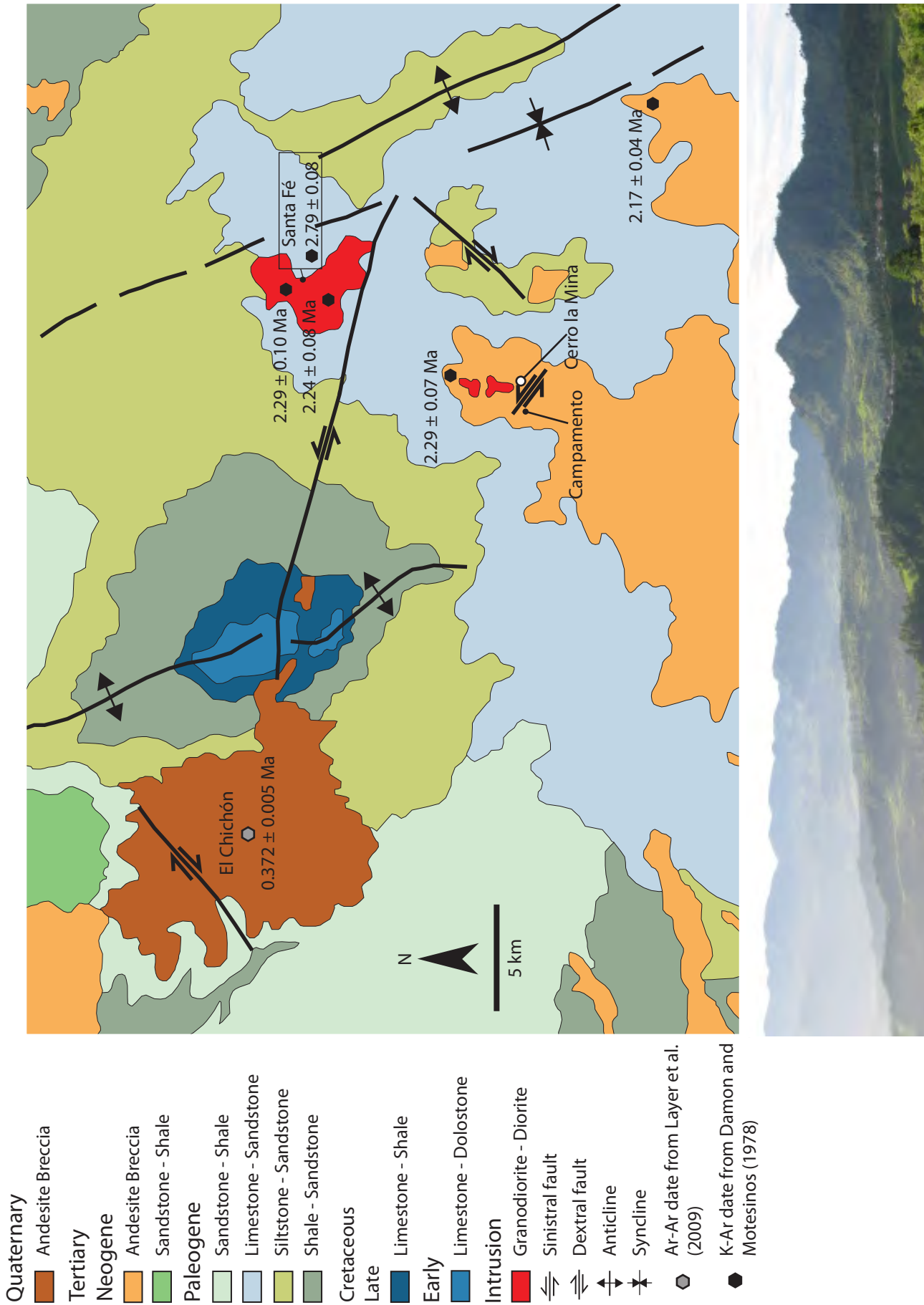


**Figure 2.6** Generalized geologic map and geochronology of El Chichón, and the Santa Fé mining district - Selva Negra region. Modified from Islas Tenorio et al. (2005). Landscape picture looking south from the Cerro la Mina prospect.

plutons of the Miocene Sierra Madre and the late Pliocene CVA (Fig. 2.8). Other unclassified polymetallic prospects in the Arriaga, Mapastepec, Motozintla and Chicomuselo mineralised zones contain Au, Ag, Cu, Pb, Zn and Sb (Fig. 2.8). Fe-skarn are also mostly found close to the contact of Miocene Sierra Madre granodiorite or CVA granodiorite with limestone (Fig. 2.8; Escandón Valle et al., 2006).

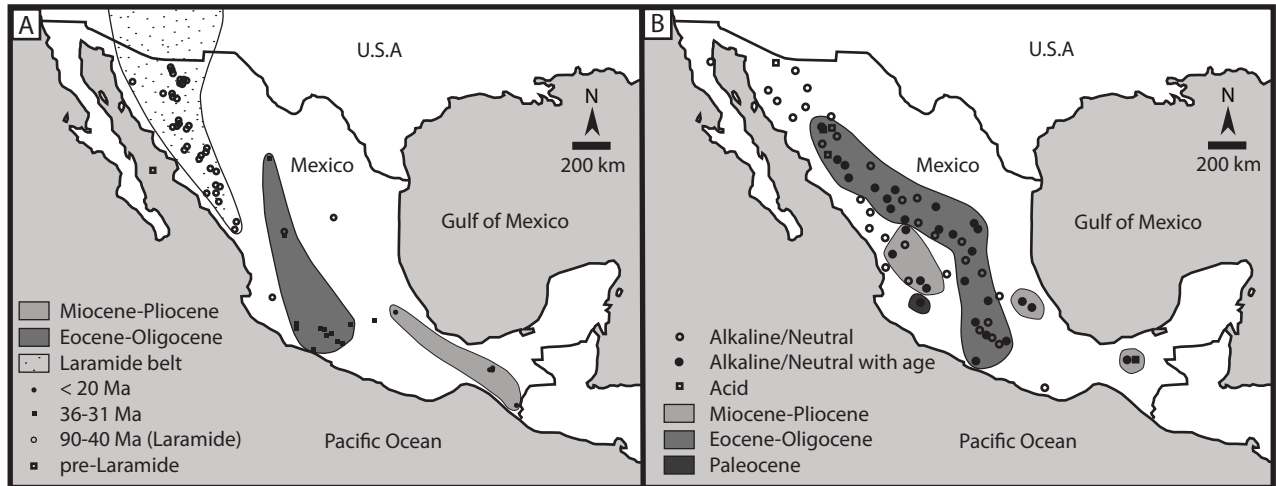


**Figure 2.7** Distribution of porphyry and epithermal deposits of Mexico. **A.** Distribution and age of porphyry deposits in Mexico. Modified from Valencia-Moreno (2007). **B.** Distribution and age of epithermal deposits in Mexico. Modified from Camprubi (2007).

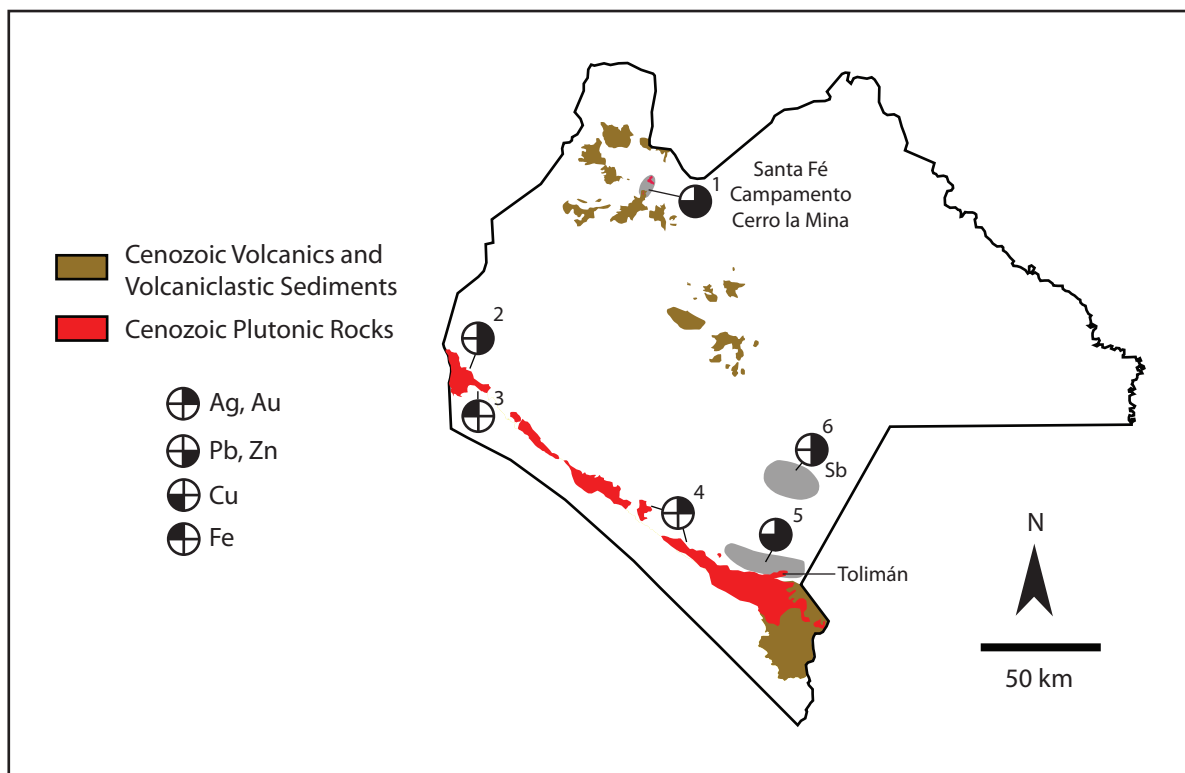


**Figure 2.8** Metallogeny of Chiapas State highlighting the Santa Fé, Campamento, Cerro la Mina and Tolimán porphyry-epithermal occurrences and other polymetallic prospects. **Mining Zones:** 1 - Santa Fé - La Victoria. **Mineralised Zones:** 2 and 3 - Arriaga, 4 - Mapastepec, 5 - Motozintla, 6 - Chicomuselo. Modified from Damon and Montesinos (1978) and Escandón Valle et al. (2006).

### 2.6.2 Campamento Au-Ag Deposit

The Campamento Au-Ag deposit is located 1.5 km west of the Cerro la Mina prospect (Fig. 2.6). Campamento is hosted by a sequence of Pleistocene-Pliocene andesitic volcanic rocks that have been intruded by a feldspar-phyric andesite. The deposit is controlled by sub-vertical intense fracturing (Miranda-Gasca et al., 2009). Measured and indicated resources are 852,000 oz Au and 3.46 Moz Ag with inferred resources of 374,000 ounces Au and 920,000 ounces Ag (Linear Gold Corp., 2007). Resources were estimated at a 1.0 g/t Au equivalent cut-off (Linear Gold Corp., 2007). The description of the geology, mineralisation and veining and alteration is taken from Linear Gold Corp. (2007) unless otherwise referenced.

The geology of the Campamento deposit comprises a sequence of andesitic volcanic rocks consisting mainly of interlayered pyroclastic rocks ranging from tuff to lappilli to breccia-size fragments with minor lavas. On the surface, there is a general progression from coarser pyroclastic phases at higher elevations in the east to finer tuff and flow phases at lower elevations toward the west. The coarser pyroclastic unit to the east contains a variety of volcanic fragments which have probably originated as a pyroclastic flow, lahar or agglomerate. An east-west cross section shows approximately 450 m of coarse pyroclastic phases that are locally interlayered with finer 30 to 50 m thick andesitic tuffs to andesitic flows (Fig. 2.9A). There is also a minor layer of epiclastic reworked

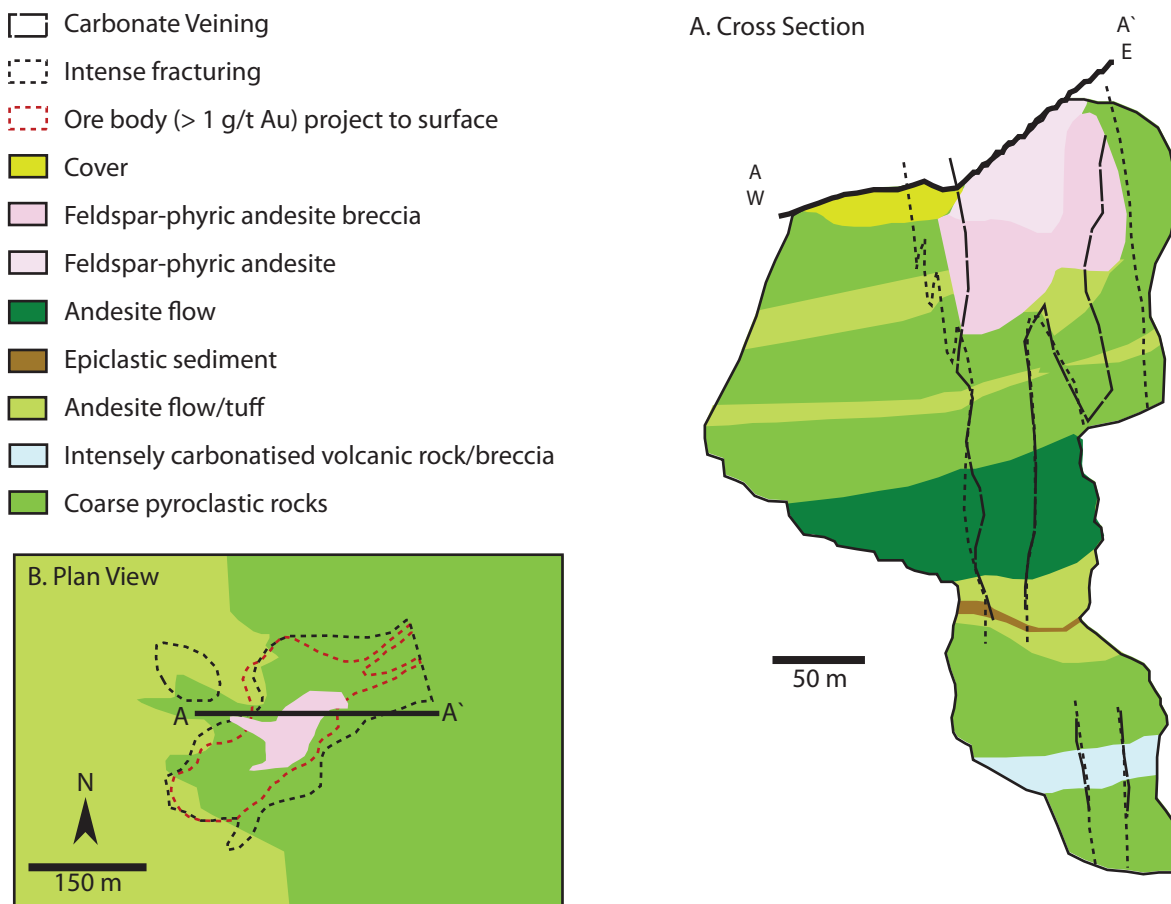


**Figure 2.9** Geology of the Campamento deposit. **A.** Cross section A-A' through the Campamento deposit. **B.** Plan view of the Campamento deposit showing the location of cross section A-A'. Modified from Linear Gold Corp. (2007).

tuffaceous sedimentary rocks at depth. Overall, the sequence dips 10 to 30° to the west. A dominantly sub-vertical feldspar porphyry complex intrudes the core of the deposit. Extrusive phases related to the feldspar porphyry complex include porphyritic flows and pyroclastic breccia phases with a feldspar crystal tuff matrix.

The deposit occurs in a sub-vertical zone of intense fracturing (Fig. 2.9B). On the surface, the fracturing occurs in many orientations that are juxtaposed against each other and are highly discontinuous over a few metres. The zone of intense fracturing forms a linear northeast trending zone that is 130 to 150 m wide that has been traced for at least 450 m along strike (Fig. 2.9B). The highly fractured zone shows areas of strong bleaching and there is argillic clay alteration developed throughout.

A paragenesis study by Rainbow and Kyser (2005) describes an early potassic alteration comprising a fine-grained assemblage of potassium feldspar + biotite/phlogopite + pyrite ± apatite. As well, a late calcite vein event shows Mn enrichment with the presence of kutnahorite (Ca(Mn,Mg,Fe)(CO<sub>3</sub>)<sub>2</sub>). Virtually all the calcite veins host some precious and/or base metal mineralisation. The ore assemblage hosted in the veins include pyrite + chalcopyrite + sphalerite + native gold ± tennantite - tetrahedrite ((Cu,Ag,Fe,Zn)<sub>12</sub>As<sub>4</sub>S<sub>13</sub> - (Cu,Fe,Ag,Zn)<sub>12</sub>Sb<sub>4</sub>S<sub>13</sub>) ± galena ± acanthite ± marcasite ± several unidentified opaque phases tentatively identified as Ag-sulfosalts (Rainbow and Kyser, 2005).

The deposit comprises abundant narrow carbonate ± clay ± rare quartz veins developed throughout. The carbonate-rich veinlets tend to be spatially associated with the feldspar-phyric andesite whereas the clay-rich veinlets are distal. The high-grade core of the deposit, characterized by >5 g/t Au is centered on the feldspar-phyric andesite and the associated carbonate veining. The lower grade zone defined as 1-5 g/t Au envelops the high-grade core and is associated with the highly fractured, coarser pyroclastic phase. A fluid inclusion study of the carbonate veins indicated the mineralising fluid was of moderately high temperature (261 ± 17°C) and salinity (23 to 27 equiv. wt.% NaCl), moderately oxidized and near neutral pH (Richards, 2006a).

An infrared spectral reflectance study of alteration minerals from Campamento (Jansen, 2007) indicates early, deep, neutral-pH, high-temperature (>250°C) biotite, muscovite and chlorite alteration that has been overprinted by shallow, late, neutral-pH, low- to medium-temperature (ambient to 250°C) smectite, illite/smectite and illite alteration. The occurrence of hydrothermal biotite and muscovite at the surface indicates lowering of the paleo-water table by 750 to 1200 m.

Mineralisation at Campamento shows both porphyry affinities with secondary biotite alteration, and epithermal affinities with extensive clay-carbonate alteration inferred to have formed at shallow depths (Jansen, 2007). Fluid inclusion analyses indicate a depth of formation less than 1 km (Richards, 2006a) although the deposit lacks typical epithermal features such as crustiform veining (Jansen, 2007). The high salinities in the fluid inclusions are consistent with either a porphyry-related system or with fluid interaction from the basement evaporites (Jansen, 2007). The carbonate veining comprises calcite, which can form either by fluid cooling and boiling or by fluid mixing (Simmons and Christenson, 1994). There is no textual evidence for boiling or silica polymorphs being deposited by fluid cooling at Campamento (Jansen, 2007). Therefore, it is probable that CO<sub>2</sub>-rich waters close to

calcite saturation were mixed with higher temperature waters causing the precipitation of calcite due to its retrograde solubility, e.g. Simmons and Christenson, (1994) (Jansen, 2007).

### 2.6.3 Cerro la Mina Prospect

The Cerro la Mina Au (Cu-Mo) prospect is located in northern Chiapas and is the topic of this thesis (Fig. 2.8). The prospect has a near surface oxide Au zone and significant Au (Cu-Mo) sulfide mineralisation at depth. The prospect has porphyry affinities with extensive potassium feldspar and biotite alteration and epithermal affinities with a thick zone of intense kaolinite clay alteration.

A volcanic facies report by Cumming (2008) divided the Cerro la Mina volcanic succession into three major units. Coherent andesitic rocks and associated auto-breccias in the lower part of the succession are overlain by abundant, thick beds of polymictic andesitic-dacitic breccias (lapilli tuff and agglomerates), interpreted to represent debris and mass flows of mixed provenance, are interbedded with and gradational to massive dacitic tuffaceous sandstones and minor flow banded dacite. The upper part of the succession is capped by a coarse andesitic-dacitic agglomerate. The Cumming (2008) study was done mostly in intensely altered rock and did not include observations on least altered rock as undertaken in this study.

An XRD study completed by Kyne (2009) in conjunction with the TerraSpec data collected in this study confirmed the presence of alunite, halloysite 7Å, halloysite 10Å, kaolinite, illite, dickite, chlorite and pyrophyllite. Richards (2006b) described eight thin sections that indicated an early chalcopyrite-pyrite-molybdenite assemblage that is partially to completely replaced by covellite, digenite and idaite ( $\text{Cu}_3\text{FeS}_4$ ) where minor enargite was observed with covellite and digenite replacements.

Harris (2007) described the geology, alteration and mineralisation from 35 thin sections. The geology comprised micro-quartz syenite porphyry (to fine-grained trachytic) intrusions, volcanogenic rocks that include broadly trachytic to dacitic, vesicular, coherent volcanic and volcanoclastic rocks, including polymictic breccias and crystal-rich sandstone. The alteration comprised potassium feldspar-rich potassic alteration assemblages that occur as coarse- to fine-grained pervasive potassium feldspar replacement of igneous groundmass and biotite-rich potassic alteration assemblages comprising unusually coarse-grained pervasive replacement of the igneous groundmass by biotite (up to 0.4 mm). Chalcopyrite + pyrite ± bornite was reported to be associated with the potassic alteration zones, occurring as subhedral to euhedral crystals. Weak propylitic alteration assemblages overprint potassic alteration assemblages as chlorite ± muscovite-actinolite with rare epidote. Advanced argillic alteration assemblages occur as shallow-level pervasive alteration zones. Alunite occurs as coarse isolated and clustered crystals intergrown with quartz and clays, either as vugs or replacement assemblages of the igneous groundmass. Pyrite in zones of most pervasive clay alteration has distinctly rounded and amoeboid forms and occurs as clusters.

### 2.6.4 Santa Fé Mine District

The Santa Fé mine is located in northern Chiapas, 10 km to the northeast of the Cerro la Mina

prospect (Figs. 2.6 and 2.8). The mine has irregular ore bodies with a metasomatic origin associated with the contact between Oligocene limestone and a granodioritic to dioritic stock where Cu-Au-Ag mineralisation occurs in a wollastonite halo (MacCarthy, 1897; Damon et al., 1983; Pantoja, 1991; Barton et al., 1995).

The hypogene mineralisation comprises chalcopyrite, bornite, enargite and argentite with supergene malachite and chrysocolla and the gangue comprises wollastonite, quartz, calcite and garnet (MacCarthy, 1897; Damon et al., 1983; Pantoja, 1991). The calculated reserves are 10,000 t at 6 g/t Au, 189 g/t Ag and 2.46% Cu (Pantoja, 1991; Barton et al., 1995). Biotite in a mineralised diorite intruding Oligocene limestone was dated using K-Ar at  $2.29 \pm 0.10$  Ma and biotite in an argillic-altered granodiorite dyke was dated using K-Ar at  $2.24 \pm 0.08$  Ma (Damon and Motesinos, 1978). Additional mineralisation has been encountered at the nearby La Victoria mine that has hypogene mineralisation consisting of chalcopyrite, tetrahedrite-tennantite, sphalerite, molybdenite, stibnite, scheelite, covellite and jamesonite (Islas Tenorio et al., 2005).

### 2.6.5 Tolimán Porphyry-Cu

The Tolimán Cu porphyry deposit is located in southeastern Chiapas (Fig. 2.8). Tolimán is related to a quartz monzonite porphyry stock and hypogene Cu-Mo-Zn-Ag mineralisation and grades less than 0.8% Cu (Sillitoe, 1976; Damon et al., 1983; Barton et al., 1995; Valencia-Moreno et al., 2007). The wall rocks comprise a Miocene granodiorite batholith overlain by post-batholith volcanic rocks and intercalated sedimentary rocks. The mineralisation has both stockwork and disseminated textures with chalcopyrite-pyrite-molybdenite-pyrite veinlets with quartz-biotite-chlorite anhydrite selvages (Sillitoe, 1976; Damon et al., 1983; Barton et al., 1995). The alteration in the ore zone comprises intense biotite, potassium-feldspar, sericite and quartz-pyrite with an epidote-chlorite-pyrite-goethite halo (Sillitoe, 1976; Damon et al., 1983; Barton et al., 1995). Biotite in the quartz-monzonite porphyry was dated with K-Ar at  $5.75 \pm 0.10$  Ma (Damon and Motesinos, 1978).

## 2.7 Conclusions

The Cerro la Mina Au (Cu-Mo) prospect is located at a complex triple junction tectonic setting between the North American, Caribbean and Cocos plates. The prospect is hosted in the Selva Negra volcanic rocks of the CVA and comprised mostly of small-volume volcanic domes with associated pyroclastic flow deposits. The northwest trending sinistral strike-slip fault zone controls the emplacement of volcanic structures in the CVA. The Selva Negra volcanic rocks are located 20 km to the southeast of El Chichón volcano which has erupted anomalous high-K alkaline trachyandesites that are thought to be the result of the complex tectonic setting and/or the subducting Tehuantepec ridge. Porphyry and epithermal mineralisation of Chiapas is poorly documented and occurs outside the major metallogenic provinces of Mexico in significantly younger volcanic rocks ( $< 5$  Ma; Damon and Motesinos, 1978). The Cerro la Mina Au (Cu-Mo) prospect has both porphyry and epithermal affinities.



## Chapter 3 - Igneous Geochemistry of the Selva Negra

### 3.1 Introduction

Damon and Motesinos (1978) described the volcanic rocks of northern Chiapas the Santa Fé mining district - Selva Negra region as basaltic-andesites, andesites, dacites and diorites (Chapter 2; Fig. 2.3). The volcanic rocks of the Santa Fé mining district - Selva Negra region will herein be referred to as the Selva Negra volcanic rocks (SN). K-Ar dating of whole rock from a basaltic-andesite dyke, andesite and augite andesite and biotite from diorite and granodiorite yielded ages between 2.79 to 1.95 Ma (Damon and Motesinos, 1978). The SN volcanic rocks are part of the Chiapanecan volcanic arc (CVA) for which geochemical data has been published (Fig. 2.3; Luhr et al., 1984; Rose et al., 1984; Capaul, 1987; McGee et al., 1987; Espindola et al., 2000; Tepley et al., 2000; Macías et al., 2003; García-Palomo et al., 2004; Mora et al., 2007; Layer et al., 2009); however, no whole rock geochemical data has been published for the SN region.

The SN volcanic rocks are located in a complex tectonic triple junction setting (Chapter 2; Fig. 2.1). The SN is part of the CVA which is attributed to the subduction of the Cocos Plate under the North American plate (García-Palomo et al., 2004; Mora et al., 2007). The subducting plate includes the prominent Tehuantepec ridge, the onshore propagation of which lies directly below the anomalous high-K El Chichón volcano and the SN suggesting an influence from the ridge (Chapter 2; Fig. 2.1).

The SN volcanic rocks occur 20 km to the southeast of El Chichón, therefore, a study was undertaken on the SN volcanic rocks to understand their genesis and to test if any signature of ridge subduction could be identified in these rocks, as ridge subduction has been suggested to be important for the formation of porphyry deposits (Cooke et al., 2005; Hollings et al., 2005; Sun et al., 2010; Hollings et al., 2011). None of the units had been analysed by previous studies.

The organisation of this chapter comprises a description of research methods used, description of the SN volcanic rocks including aeromagnetic data. This is followed by petrography of the SN and major and trace element geochemistry results. The chapter ends with a discussion.

### 3.2 Research Methods

#### 3.2.1 Sampling Program

A suite of 47 samples (including five duplicates) collected from the SN volcanic rocks were analysed for major and trace elements (Table 3.1). The sample locations are shown in Figure 3.1. The samples were collected by the author, Peter Hollings (Lakehead University), Francisco Martinez Lopez (Kinross) and Scott Gaffri (Kinross). Where possible least altered rocks were sampled, although proximity to mineralisation made it necessary, in some cases, to analyse samples that had undergone alteration. Samples were trimmed to remove oxidised exteriors or fracture surfaces. Rock images and location information are compiled in Appendix II.1 and II.2.

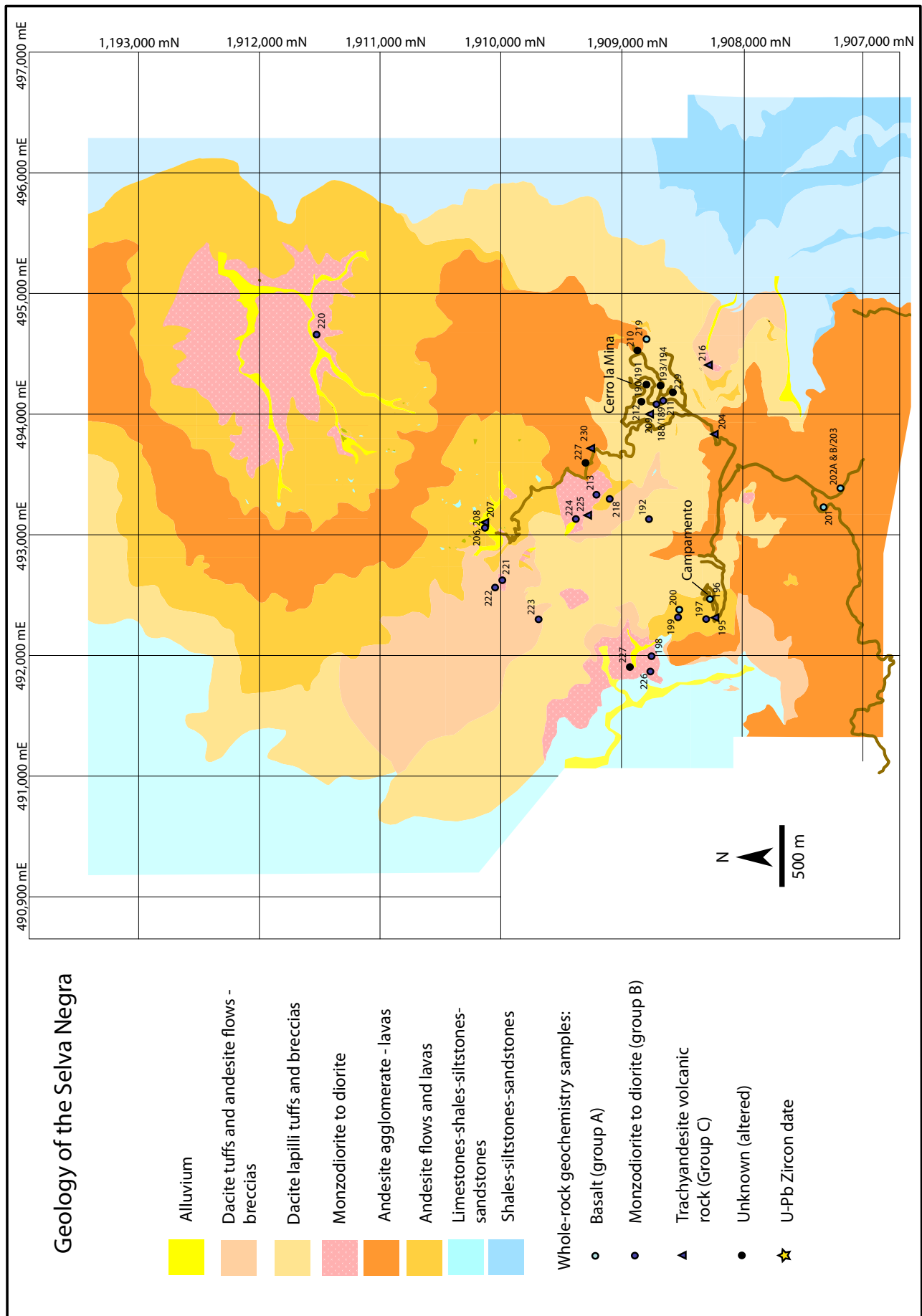


**Figure 3.1** Geologic Map of the Selva Negra volcanic rocks showing the locations of whole-rock geochemistry samples. Location of the Campamento Au-Ag deposit and the Cerro la Mina Au (Cu-Mo) prospect is indicated. Modified after Martinez Lopez (2009).

### 3.2.2 Petrographic Microscopy

Thin sections were cut in-house at the University of Tasmania for all samples and petrography was completed using a Nikon Labophot-2® Pol Standard Polarizing Microscope and an Olympus ColorView imaging system. Descriptions of the primary rock mineralogy and secondary alteration minerals are provided for all samples in Appendix II.3.

### 3.2.3 Major and Trace Element Analysis

Forty-two samples were analysed at the ALS Chemex lab in Vancouver using the CCP-PKG01 package. The rocks were crushed in agate and the major elements were measured using lithium metaborate fusion, C and S measured by Leco, trace using OREAS 45P standard. elements and REE's measured by lithium borate fusion and ICP-MS and volatiles (As, Bi, Hg, Sb, Se, Te) measured by aqua regia and ICP-MS. Accuracy of measurements, were determined by analyses of standards comprising G2000, GBM3961c, GEOMS-03, MA-1b, OREAS-13P, OREAS-45P, SARM-16, SRM88B, SY-4 and UTS-1.

An additional five samples were crushed in agate and analysed using X-ray fluorescence for major and some trace elements at the School of Earth Sciences, University of Tasmania, using a PANalytical Axios Advanced X-Ray Spectrometer (2009). Accuracy of measurements, as determined by analyses of international standards, is better than 5% for all elements, except Ba, Ni, Zn, Cu and Cr for which accuracy is better than 10%. Trace element and REE analyses were carried out using an Agilent 7700 ICP-MS by high-pressure dissolution of sample aliquots in hydrofluoric and sulfuric acid, and dilution to a standard volume in ultrapure water using the methodology of Yu et al. (2001). Trace element compositions were measured using an Agilent HP4500 quadrupole ICP-MS, following the methods and instrument settings of Yu et al. (2000) and Robinson et al. (1999).

The suite of 47 samples includes five duplicates. The duplicate values of all five samples are plotted against each other and have a tight trend with a coefficient of determination  $R^2 = 0.99$  (Fig. 3.2). All of the major elements plot within 5% error whereas Bi, Ni, Co, Cu, Rb, Sn and Cs are within 10% error and As, W, Hg and Sb are greater than 10% error for trace elements. Whole rock geochemistry data is listed in Appendix II.4.

### 3.2.4 Radiogenic Isotopes

Five samples were analysed (Appendix II.5) for radiogenic isotopes at the Isotope Geochemistry and Geochronology Research Centre, Ottawa using a ThermoFinnigan Triton TI thermal ionization mass spectrometer. Samples were washed or leached before dissolution, then 100 and 200 milligrams of powder was dissolved in 50% HF-12N HNO<sub>3</sub>, then attacked with 8N HNO<sub>3</sub> and finally 6N HCl. The residue was taken up in 1N HBr for Pb, Sr and Nd.

Pb was separated in Bio-Rad 10-ml polyethylene columns and Dowex AG1-8X anion resin, using 1N HBr to elute other elements and 6N HCl to elute Pb. The collected Pb solution was dried, redissolved in 1N HBr, and the above procedure was repeated with a small volume resin bed. Total

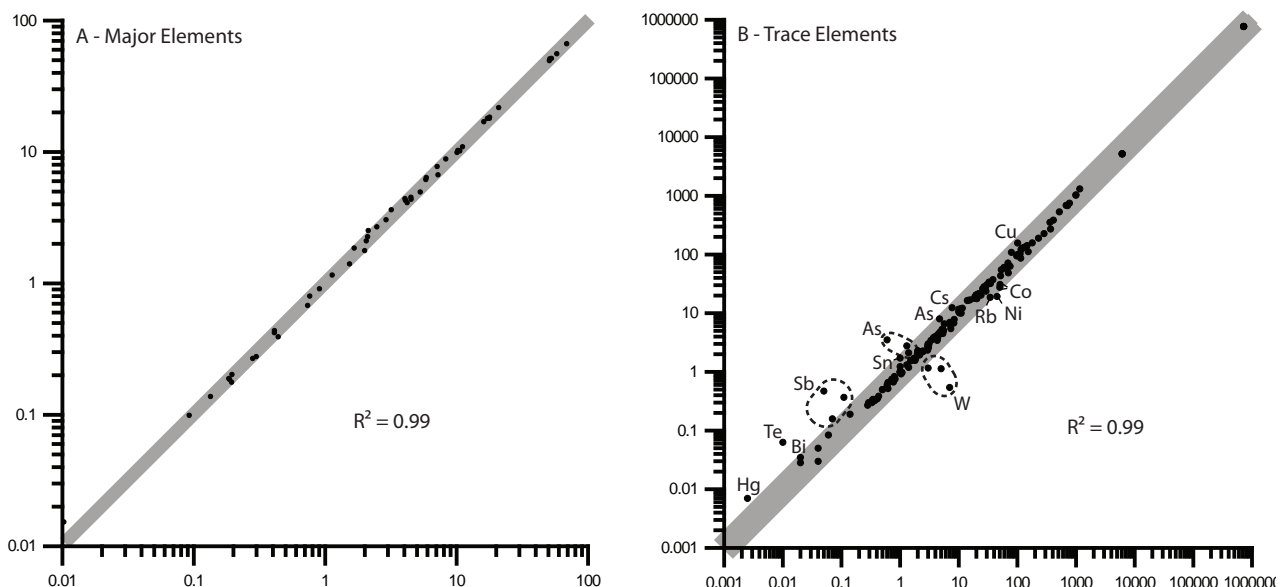


**Figure 3.2** The major and trace elements concentrations of five duplicate analysis plotted against each other. **A.** Major elements. **B.** Trace Elements. Grey zone denotes 5% error. Elements below detection limits are not plotted.

procedural blanks for Pb were < 450 picograms. A  $^{208}\text{Pb}$  spike (J. Blenkinsop, Carleton University) was used for Pb concentrations. Concentrations were precise to  $\pm 0.5\%$ . Samples were loaded onto single Re filaments with  $\text{H}_3\text{PO}_4$  and silica gel, and were run at filament temperatures of 1250–1350°C, depending on the gel-type used. Analysis of USGS Standard BCR-1 yielded Pb = 13.56 ppm,  $^{206}\text{Pb}/^{204}\text{Pb} = 18.818$ ,  $^{207}\text{Pb}/^{204}\text{Pb} = 15.633$  and  $^{208}\text{Pb}/^{204}\text{Pb} = 38.633$  (average of 2 runs according to Tatsumoto et al., 1972). All mass spectrometer runs were corrected for fractionation using NIST SRM981. The average ratios measured for SRM981 were:  $^{206}\text{Pb}/^{204}\text{Pb} = 16.888 \pm 0.013$ ,  $^{207}\text{Pb}/^{204}\text{Pb} = 15.425 \pm 0.017$  and  $^{208}\text{Pb}/^{204}\text{Pb} = 36.494 \pm 0.057$  ( $2\sigma$ ), based on 20 runs between October 2007 – May 2009. The subsequent fractionation correction was based on the values of Todt et al. (1984).

Rb/Sr was separated by dissolution in 2.5N HCl, the solution was pipetted into a 14-ml Bio-Rad borosilicate glass chromatography column containing 3.0 ml of Dowex AG50-X8 cation resin. Rb and Sr were eluted in succession using 2.5 N HCl. The rare earth elements were then eluted using 6N HCl. The REE solution was dried and the residue dissolved in 0.26N HCl. Total procedural blanks for Sr were < 250 picograms. A  $^{87}\text{Rb}/^{84}\text{Sr}$  spike for mafic to intermediate rocks was used before dissolution. Sr was loaded onto a single Ta filament with  $\text{H}_3\text{PO}_4$  and was run at filament temperatures of 1380 to 1600°C. Isotope ratios were normalized to  $^{86}\text{Sr}/^{88}\text{Sr} = 0.11940$  to correct for fractionation. One standard was run at Carleton, NIST SRM987 ( $^{87}\text{Sr}/^{86}\text{Sr} = 0.710234 \pm 14$ ,  $n=22$ ). Rb was loaded with  $\text{H}_3\text{PO}_4$  onto one side of a double Re filament assembly and run at temperatures of 1250 to 1300°C. No correction for fractionation was made.

Sm/Nd were separated by being dissolved in 0.26N HCl and loaded onto Eichrom Ln Resin chromatographic columns containing Teflon powder coated with Bis-(2-Ethylhexyl) phosphoric acid (Richard et al., 1976). Nd was eluted using 0.26N HCl, followed by Sm in 0.5N HCl. Total procedural blanks for Nd were < 50 picograms; < 6 picograms for Sm. Samples were spiked with a mixed  $^{148}\text{Nd}$ - $^{149}\text{Sm}$  spike before dissolution. Concentrations are precise to  $\pm 1\%$ , but  $^{147}\text{Sm}/^{144}\text{Nd}$  ratios are

reproducible to 0.5%. Samples were loaded with  $\text{H}_3\text{PO}_4$  on one side of a Re double filament and run at temperatures of 1700-1800°C. Isotope ratios were normalized to  $^{146}\text{Nd}/^{144}\text{Nd} = 0.72190$ . Analyses of the USGS standard BCR-1 yielded Nd = 29.02 ppm, Sm = 6.68 ppm and  $^{146}\text{Nd}/^{144}\text{Nd} = 0.512668 \pm 20$  (n=4). The international La Jolla standard produced:  $^{143}\text{Nd}/^{144}\text{Nd} = 0.511847 \pm 7$ , n = 26. Internal lab standard =  $0.511818 \pm 8$ , n = 28 and  $0.511819 \pm 10$  n = 94.

### 3.3 Selva Negra Volcanic Rocks

As described in Chapter 2, the SN volcanic rocks lie at the northwest end of the continental calc-alkaline and relatively young (< 3Ma) Chiapanecan volcanic arc (except for the K-rich El Chichón volcano; Damon and Motesinos, 1978; García Palomo et al., 2004; Mora et al., 2007). The Cocos slab depth is calculated to be at 200 to 220 km depth below the SN (Syracuse and Abers, 2006). The SN is located 300 to 330 km from the Middle America Trench (MAT) considerably further than most volcanic arcs that generally occur within 200 km of the trench for continental arcs (Thorpe, 1982). The crust thickness is approximately 49 to 53 km in the SN region (Narcía-López et al., 2004).

A geologic map for the SN volcanic rocks was produced by Francisco Martinez Lopez, a geologist working for Kinross (Fig. 3.1). However, Martinez Lopez (2009) only included the distribution of the volcanic rocks and not their detailed description. The SN volcanic rocks overlie Oligocene limestones, shales, siltstones and sandstones. The volcanic rocks consist of lower dacite tuffs and andesite flows to breccias, to andesite flows and lavas, to dacite lapilli tuffs and breccias and capped by coarse andesite agglomerates which form the resistant hill tops. The volcanic rocks are intruded by equigranular diorite to monzodiorite intrusions. The volcanic rocks are similar to the remainder of the CVA in that they consist mainly of pyroclastic flows with associated domes and minimal lava flows (e.g., García Palomo et al., 2004; Mora et al., 2007).

The volcanic rocks are divided into three groups based on rock texture and location comprising Group A (basalts), Group B (monzodiorite to diorite) and Group C (trachyandesite volcanic rock) and described below. Group A occurs mainly in the south at high elevations, whereas Group B occurs in the north at lower elevations (Figs. 3.1 and 3.3). None of groups have been observed to be related to mineralisation.

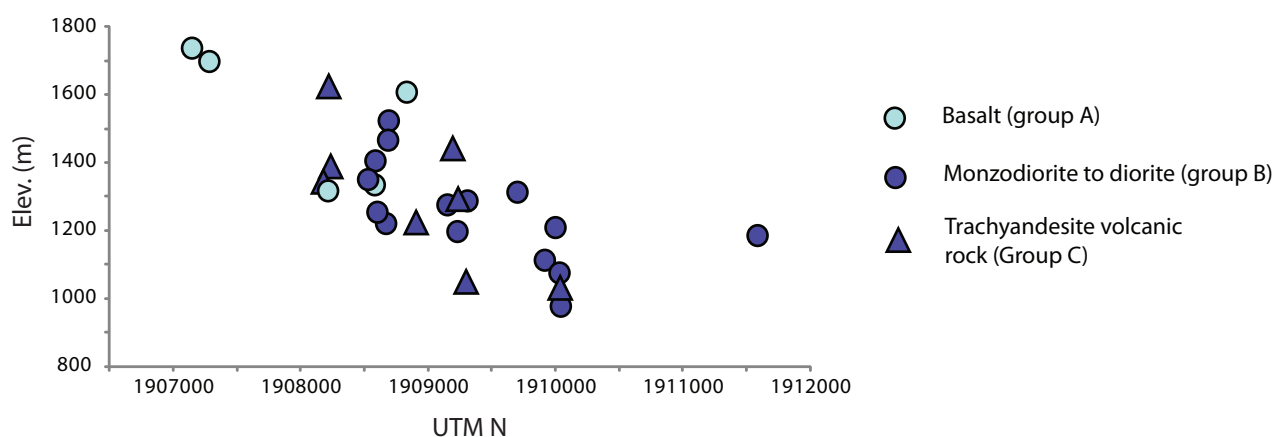


**Figure 3.3** UTM N versus elevation for the Selva Negra volcanic rocks. Basalts occur in the south and at higher elevations than the monzodiorites to diorite and trachyandesite volcanic rocks.

### 3.4 Petrography

The suite comprises fine-grained basalt flows, equigranular diorite to monzodiorite plutonic rocks and feldspar-phyric trachyandesite volcanic rocks. Many of the samples show evidence of hydrothermal alteration including plagioclase altered to clay, potassium feldspar and chlorite; hornblende, clinopyroxene and biotite altered to chlorite, secondary biotite and pyrite; and titanomagnetite altered to rutile and titanite.

#### 3.4.1 Basalt Flows (Group A)

The basalt displays a holocrystalline texture of plagioclase, clinopyroxene and magnetite (Figs. 3.4A, B and F). Plagioclase is tabular and elongate typically displaying albite extinction from 35 to 46°. Plagioclase crystals range from 100 to 500  $\mu\text{m}$  in a coarse-grained matrix of plagioclase that are 50 to 100  $\mu\text{m}$  across. Plagioclase is the most abundant mineral with up to 65% by volume, clinopyroxene 20-30% and magnetite forming the remainder. The rocks sometimes display a vesicular texture with vesicles infilled with calcite, quartz and an unidentified brown mineral (Fig. 3.4A). Basalt flows are rare in the volcanic stratigraphy and individual basalt flows were not identified by Martinez Lopez (2009).

#### 3.4.2 Diorite to Monzodiorite Plutonic Rocks (Group B)

The plutonic rock mineralogy comprises plagioclase + clinopyroxene + biotite + orthoclase + apatite + titanomagnetite  $\pm$  hornblende  $\pm$  quartz  $\pm$  olivine (Figs. 3.4C and F). Plagioclase makes up 60%, whereas clinopyroxene and biotite each contribute approximately 5-15%, and apatite and titanomagnetite contributed up to 5%. Plagioclase is tabular and elongate, typically displaying albite extinction from 24 to 33°. Coarse-grained variants have 500  $\mu\text{m}$  to 2 mm plagioclase, whereas finer grained examples have 100 to 500  $\mu\text{m}$  crystals but maintain the same mineralogy. Clinopyroxene commonly occurs as clusters but also occurs with titanomagnetite and biotite all occurring as grains less than 500  $\mu\text{m}$ . Large apatite crystals up to 300  $\mu\text{m}$ , were observed along with many fine-grained apatite (<20  $\mu\text{m}$ ) crystals within plagioclase, biotite and clinopyroxene and can comprise 5% of the modal abundance (Fig. 3.4H). Hornblende is not common and is observed to be interstitial and generally occurring with biotite. Hornblende only occurs in low concentrations in mafic rocks (< 52%  $\text{SiO}_2$ ), whereas orthoclase increases but apatite decreases in concentration as  $\text{SiO}_2$  increases. Quartz occurs in small concentrations in more felsic rocks (> 58%  $\text{SiO}_2$ ). Olivine is rare and occurs in more mafic rocks (< 52%). Using the IUGS classification (Le Bas and Streckeisen, 1991) these rocks are classified as monzodiorite to diorite.

#### 3.4.3 Trachyandesite Volcanic Rock (Group C)

In thin section, the trachyandesite consists predominantly of medium-grained (0.5 cm) plagioclase phenocrysts, small phenocrysts of biotite and clinopyroxene in a fine-grained groundmass (< 25  $\mu\text{m}$ ; Fig. 3.4D and G). The plagioclase feldspar occurs as subhedral and euhedral phenocrysts, sometimes zoned and typically displaying albite extinction around 29°. Fine-grained apatite crystals occur in

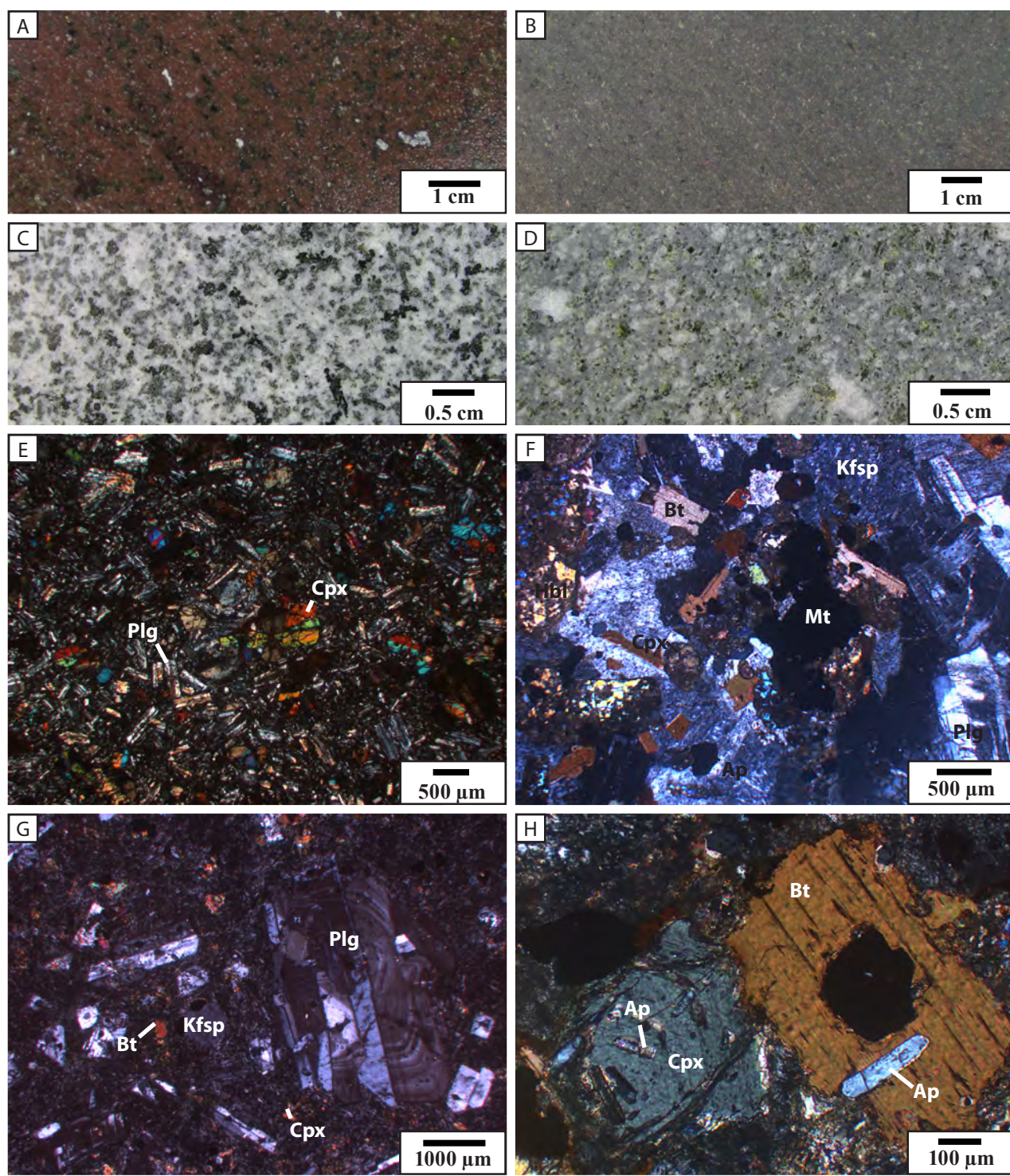


**Figure 3.4** Hand sample and petrographic images of Selva Negra rock types. **A.** Vesicular basalt flow. **B.** Fine grained basalt flow. **C.** Equigranular diorite to monzodiorite plutonic rock. **D.** Trachyandesite volcanic rock. **E.** Cross-polar microscope image of fine-grained basalt flow with fine-grained plagioclase and clinopyroxene. **F.** Cross-polar microscope image of an equigranular diorite to monzodiorite plutonic rock with intergrown plagioclase, potassium feldspar, biotite, clinopyroxene, titanomagnetite and hornblende. **G.** Cross-polar microscope image of trachyandesite volcanic rock with plagioclase, potassium feldspar, biotite and clinopyroxene in a fine-grained matrix. **H.** Cross-polar microscope image apatite crystals in biotite and clinopyroxene. **Sample ID:** A. NJ08IX-202B, B. NJ08IX-203, C. NJ08IX-224, D. NJ08IX-230, E. NJ08IX-203, F. NJ08IX-198, G. NJ08IX-230, H. NJ08IX-222.

plagioclase. Plagioclase (~60%) is more abundant than orthoclase (~30%). Biotite and clinopyroxene are equally abundant (~10%). The trachyandesite occasionally hosts xenoliths of monzodiorite to diorite. The trachyandesite commonly displays a moderate to strong trachytic or a square to elongate crystal texture (Fig. 3.4D).

### 3.5 Geochemistry Results

#### 3.5.1 Discrimination of Altered Samples

In addition to problems associated with weathering in tropical climates, many of the samples have undergone hydrothermal alteration. To select unaltered samples this study only considered the samples fulfilling the following requirements: i.) Petrography was undertaken to characterize the degree of alteration and only samples that contained a modal abundance of secondary alteration minerals < 5% were used in this study; ii.) smooth REE patterns and coherent primitive mantle-normalized patterns (Fig. 3.5; Kerrich and Wyman, 1996).

Eighteen of the samples fit the petrological and geochemical classification previously described, comprising three Group A, 14 Group B and one Group C. As indicated in Figure 3.6, samples considered to be altered fall outside of trends for unaltered samples for one or more of major oxides when plotted on Harker diagrams. The unaltered samples have a loss on ignition < 3.5 wt% and a trend is observed in relation to LOI and SiO<sub>2</sub> in which the altered samples fall above the line formed between approximately 5%, 48.5% and 0%, 65.0% (Fig. 3.6). Cs, Rb, Ba, Sr, U and Pb are considered to be mobile elements in hydrothermal alteration (e.g., Hollings and Wyman, 2005). As indicated in Figure 3.7 only Rb and Sr become more sporadic with increasing LOI and the ranges for Cs, Ba, U and Pb are similar for the altered and unaltered samples except for a few points. The trend suggests that only Rb and Sr have become mobile during alteration. The samples were also plotted using Zr, Nb, Ta and Hf which are considered to be immobile elements (e.g., Hollings and Wyman, 2005). The unaltered rocks have coefficient of determination R<sup>2</sup> values of 0.88, 0.83 and 0.93 for Nb, Ta and Hf, respectively, suggesting coherent data for unaltered samples (Fig. 3.8). The altered samples have similar R<sup>2</sup> suggesting that these elements have remained immobile during alteration (Fig. 3.8). As a result we will be focussing on the immobile elements for this study.

#### 3.5.2 Geochemistry of the Selva Negra

The SN igneous rocks are alkaline and mafic to intermediate in composition (SiO<sub>2</sub> = 47 to 58 wt.%; Fig. 3.9). Group A comprises three samples and plot in the basalt to basaltic trachyandesite field, Group B comprises 14 samples and plot in the basalt to trachyandesite fields (one sample in phonotephrite field) and Group C comprises one sample and plots in the trachyandesite field on the total alkalis diagram (Fig. 3.9; Le Maitre, 1989). The Selva Negra suite display decreasing MgO, Fe<sub>2</sub>O<sub>3</sub>t and CaO and increasing K<sub>2</sub>O and Na<sub>2</sub>O with SiO<sub>2</sub> (Fig. 3.10). Group A has lower Al<sub>2</sub>O<sub>3</sub> than Group B and both have a decreasing trend with SiO<sub>2</sub>. P<sub>2</sub>O<sub>5</sub> remains constant for Group A but decreases for Group B with SiO<sub>2</sub>. The only Group C sample plots on the same trend as Group B on Harker diagrams (Fig. 3.10). The SN suite is characterized by high K<sub>2</sub>O contents (1.4 to 5.0%) and all samples

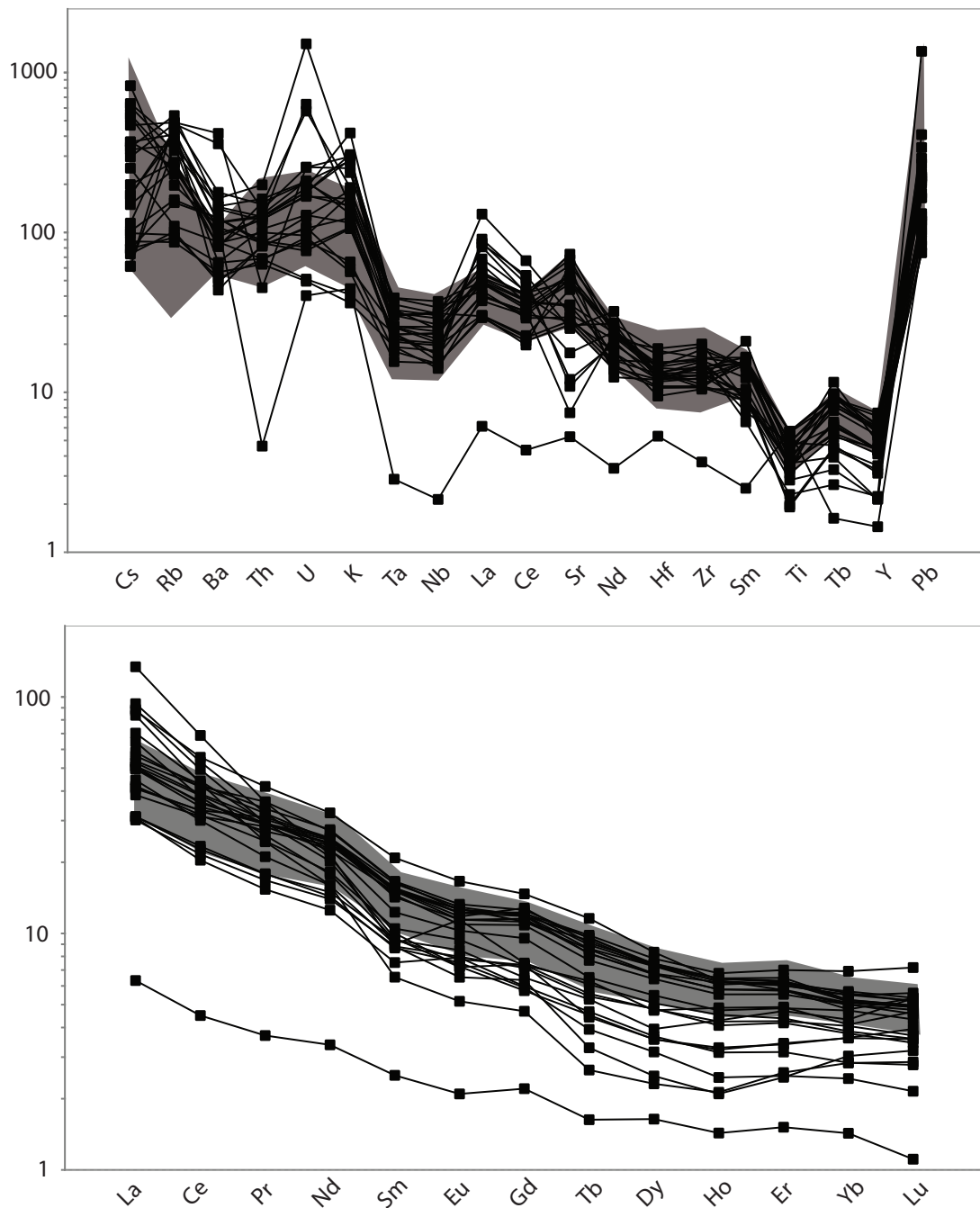


**Figure 3.5** Distinguishing altered from unaltered samples (highlighted in grey) using primitive mantle-normalized patterns and REE patterns. **A.** The altered primitive mantle-normalized patterns are not coherent and varies widely compared to unaltered samples that are highlighted in grey. **B.** The REE pattern for altered samples is not smooth and varies widely from the unaltered samples that are highlighted in grey.

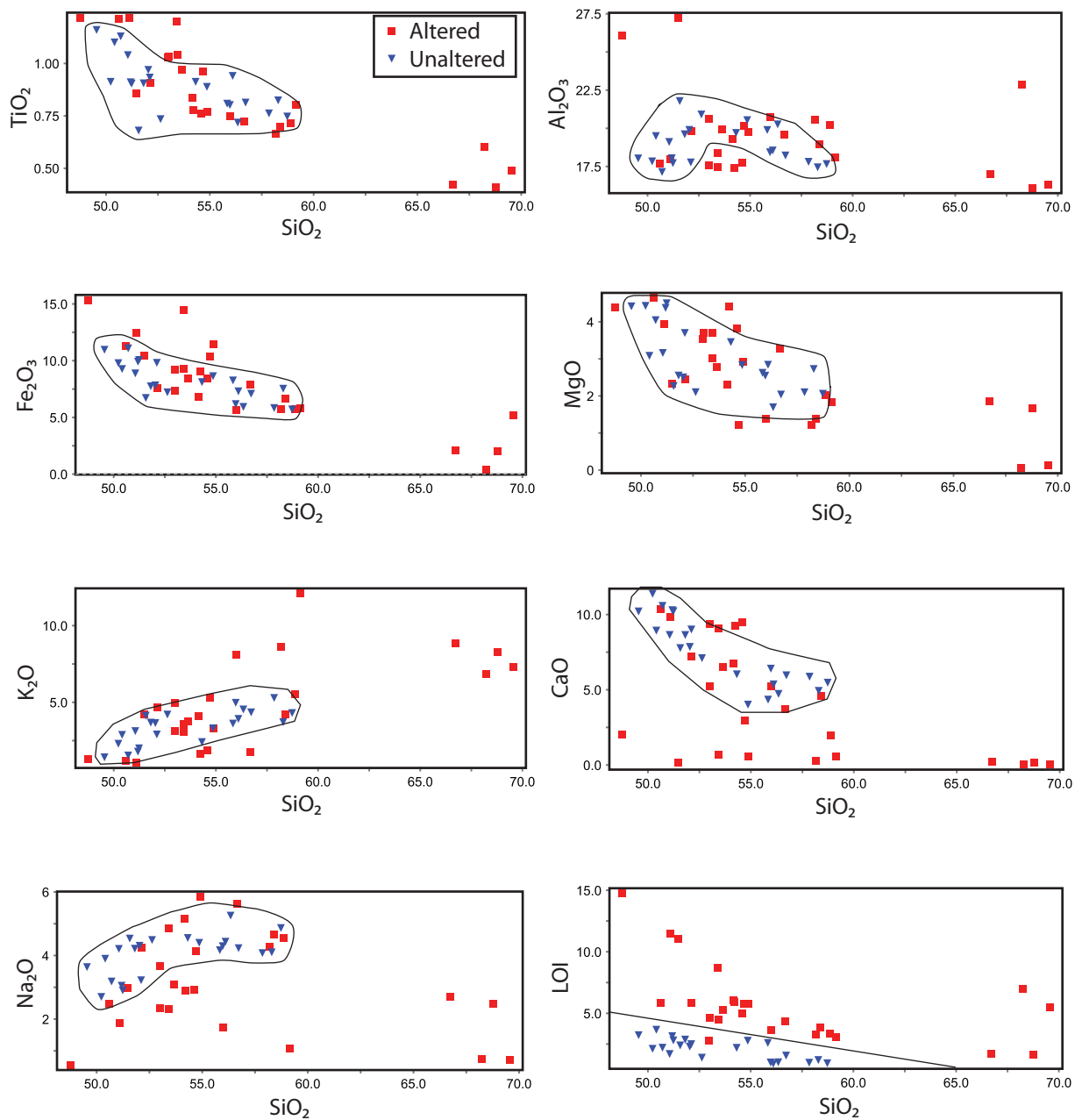


**Figure 3.6** Harker diagrams for the major oxides illustrating unaltered versus altered samples. A line distinguishes most altered versus unaltered samples on a  $\text{SiO}_2$  versus LOI diagram. The outlined area highlights the composition at which all of the unaltered samples plot. Most of the samples considered to be altered using the selection criteria explained in the text plot outside of this area.

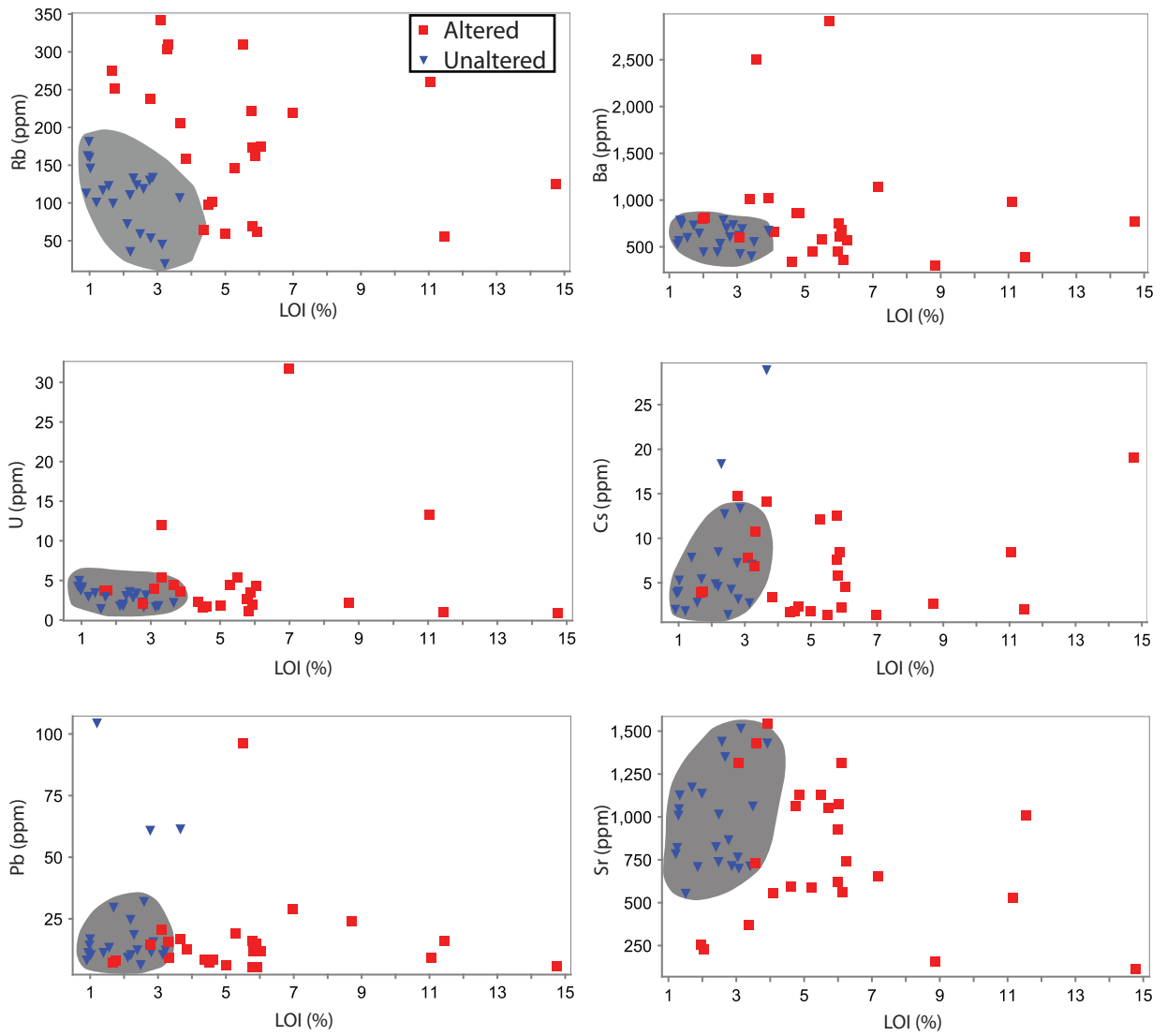


**Figure 3.7** LOI versus mobile elements Rb, Ba, U, Cs, Pb, and Sr. Grey field denotes close cluster of unaltered samples.

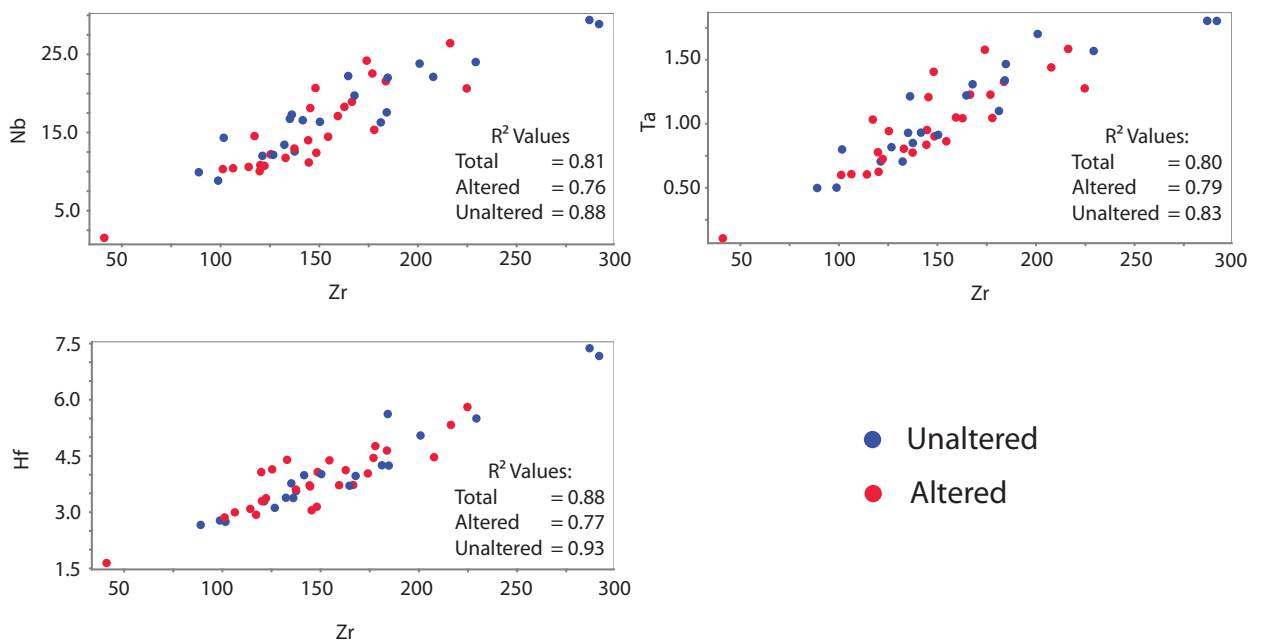


**Figure 3.8** Plot of immobile elements (Zr versus Nb, Ta and Hf) for the altered and unaltered Selva Negra volcanic rocks.

except for three plot in the high-K to shoshonitic fields on a  $\text{SiO}_2$  versus  $\text{K}_2\text{O}$  diagram (Fig. 3.11; Peccerillo and Taylor, 1976). The molecular K/Na ratios range from 0.4 to 1.2 supporting an alkalic and shoshonitic nature (Joplin, 1968; Morrison, 1980). As traditional plots discriminating alkalinity rely on the highly mobile elements potassium and sodium, a number of other plots have been developed to test for an alkaline composition (e.g., Crawford et al., 2007; Hastie et al., 2007). On a  $\text{P}_2\text{O}_5/\text{Al}_2\text{O}_3$  versus  $\text{K}_2\text{O}/\text{Al}_2\text{O}_3$  plot (Crawford et al., 2007) based on the accepted immobility of  $\text{Al}_2\text{O}_3$  the SN occur in the high-K to mainly shoshonitic fields (Fig. 3.12A). Hastie et al. (2007) developed an alternative method using Th and Cr as proxy elements to substitute for  $\text{K}_2\text{O}$  and  $\text{SiO}_2$ . The SN suite falls mostly in the high-K and shoshonitic field with four samples in the calc-alkaline field (Fig. 3.12B).

The SN suite is enriched in LILE (K, Rb, Sr, Th, U and Cs; Fig. 3.13C). Group B and C are more enriched in HFSE and LILE than Group A (Fig. 3.13C). All suites are characterised by negative Nb, Ti, Hf and Zr anomalies on primitive mantle-normalized diagrams (Fig. 3.13C). LILE/HFSE ratios are high for the Selva Negra (Fig. 3.14). All suites are characterized by LREE enrichment with  $\text{La}/\text{Yb}_{\text{CN}}$  ratios that range from 6.8 to 12.9 (mean 9.2),  $\text{La}/\text{Sm}_{\text{CN}}$  ratios range from 2.6 to 3.9 (mean 3.3) and the  $\text{Sm}/\text{Yb}_{\text{CN}}$  ranges from 2.2 to 3.6 (mean 2.8; Fig. 3.15). The  $\text{La}/\text{Yb}_{\text{CN}}$  and  $\text{La}/\text{Sm}_{\text{CN}}$  ratios increase from Group A toward Group C whereas  $\text{Sm}/\text{Yb}_{\text{CN}}$  ratio remains the same for all three groups (Fig. 3.16). Group A, B and C have similar  $\text{Eu}/\text{Eu}^*$  values between 0.8 and 1.1 (Fig. 3.17).

Isotope data is only available for Group B. The SN  $^{143}\text{Nd}/\text{Nd}^{144}$  ranges from 0.512598 to 0.512895 and  $^{87}\text{Sr}/^{86}\text{Sr}$  ranges from 0.7037 to 0.7060. On a  $\text{SiO}_2$  versus  $^{87}\text{Sr}/^{86}\text{Sr}$  plot the SN becomes more radiogenic with increasing  $\text{SiO}_2$  (Fig. 3.18). There is one anomalous SN value with high  $^{87}\text{Sr}/^{86}\text{Sr}$  outside the general trend for the SN. On a  $^{87}\text{Sr}/^{86}\text{Sr}$  versus  $\epsilon_{\text{Nd}}$  plot the SN plots between MORB and Mexican crust and Pacific sediments (Fig. 3.19). Pb isotopes values of  $^{206}\text{Pb}/^{204}\text{Pb}$  range from 18.710 to 18.824 (Figs. 3.20 and 3.21),  $^{207}\text{Pb}/^{204}\text{Pb}$  range from 15.575 to 15.613 (Fig. 3.21) and  $^{208}\text{Pb}/^{204}\text{Pb}$  range from 38.418 to 38.601 (Fig. 3.21).

## 3.6 Discussion

### 3.6.1 Selva Negra Distribution

The geologic map for northern Chiapas identifies large granodiorites outcrops (Islas Tenorio et al., 2005). However, the rocks mapped as granodiorite sampled by this study are monzodiorite to diorite. The distribution of basalts (Group A) at higher elevations and monzodiorite to diorite and trachyandesite (Groups B and C) at lower elevations toward the north probably represents a deeper erosion level. The monzodiorite to diorite (Group B) is the most voluminous unit and has been identified in many drill holes throughout the Ixhuatán concession.

### 3.6.2 Selva Negra Harker Diagrams

The major elements of the Selva Negra follow variation trends commonly observed in calc-alkaline series rocks and usually interpreted as reflecting fractionation of olivine - plagioclase - clinopyroxene - amphibole - titanomagnetite - apatite phenocryst assemblages (Gill, 1981) and is consistent

with petrographic observations of the SN (Fig. 3.10). The decrease in MgO, Fe<sub>2</sub>O<sub>3</sub>t and CaO as SiO<sub>2</sub> increases is consistent with the removal of early-forming plagioclase, plus olivine and or clinopyroxene from the cooling liquid as MgO and FeO are incorporated into the typically early-forming mafic minerals (Fig. 3.10). A weak increase then decrease of Al<sub>2</sub>O<sub>3</sub> and a continuous CaO decrease suggests that clinopyroxene was removed early on and a decrease in Al<sub>2</sub>O<sub>3</sub> is consistent with crystallization of plagioclase (Fig. 3.10). Hornblende is present in more mafic rocks and is considered to be a major mafic mineral crystallizing from magmas ranging from basic to acid in composition with its abundance in the plutonic rocks reflecting the increased stability of amphibole at depth in the crust (Thorpe, 1982). Group A is spatially separated from Groups B and C but have similar major element geochemical trends except for phosphorous (Fig. 3.10).

The primitive mantle normalised diagrams are similar for all three groups (Fig. 3.13C). The Hf-Zr slope increases from Groups A to C (Fig. 3.13C) and the LREE elements become increasingly enriched from Groups A to C (Fig. 3.16). The major and trace element geochemistry therefore suggest they have the same parental magma. Group A does not show fractionation of P<sub>2</sub>O<sub>5</sub> on the Harker diagram consistent with the absence of apatite in its mineralogy (Fig. 3.10). The basalt (Group A) is generally higher in CaO and MgO and lower Al<sub>2</sub>O<sub>3</sub> than Group B consistent with a higher content of clinopyroxene consistent with petrographic observations.

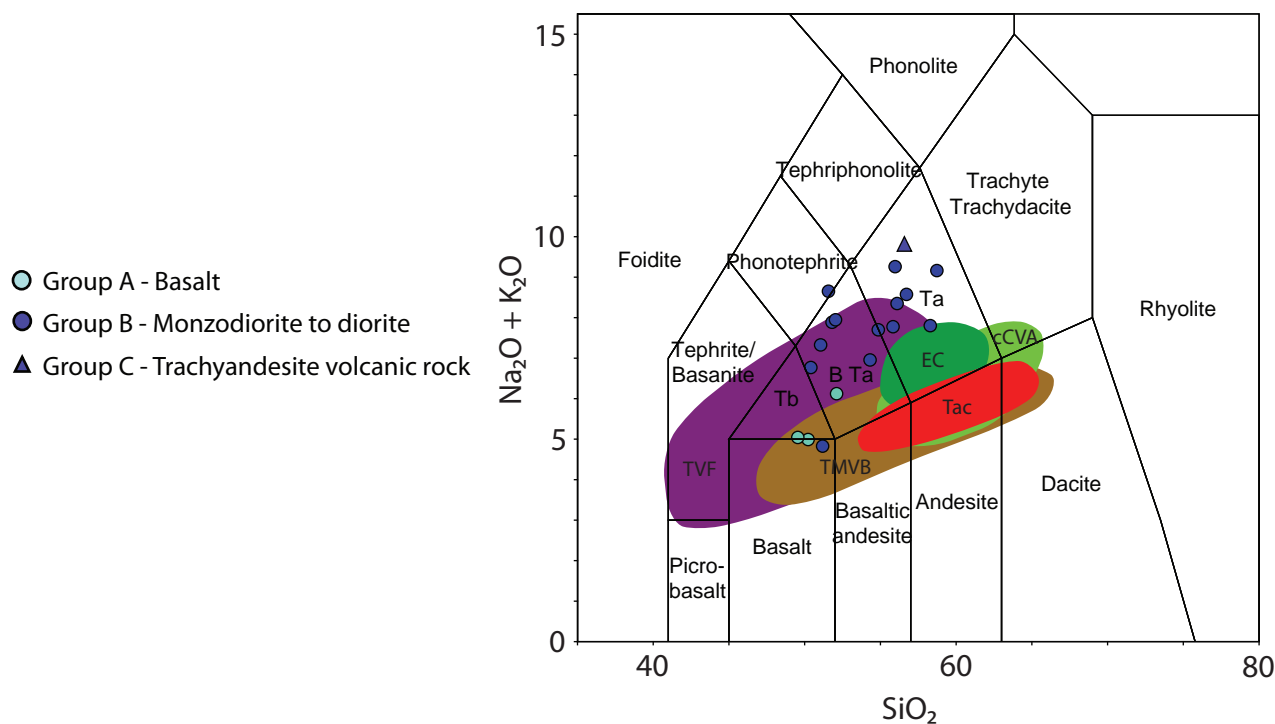


**Figure 3.9** SiO<sub>2</sub> versus total alkalis diagram (Le Maitre et al., 1989) comparing the Selva Negra suite with the regional volcanism. Trans-Mexican Volcanic Belt from Luhr et al. (2006), Tuxtlas volcanic field from Nelson and Gonzalez-Caver (1992) and Nelson et al. (1995), Tacaná volcano from Mercado and Rose (1992), Macías et al. (2000) and García-Palomo et al. (2006), and the central CVA from Mora et al. (2007). El Chichón from Luhr et al. (1984), Rose et al. (1984), Capaul (1987), McGee et al. (1987), Espindola et al. (2000), Tepley et al. (2000), Macías et al. (2003), García-Palomo et al. (2004), and Layer et al. (2009). **Abbreviations:** B Ta - Basaltic trachyandesite, cCVA - central Chiapanecan volcanic arc, EC - El Chichón, Ta - Trachyandesite, Tac - Tacaná, Tb - Trachybasalt, TMVB - Trans Mexican Volcanic Belt, TVF - Los Tuxtlas volcanic field.

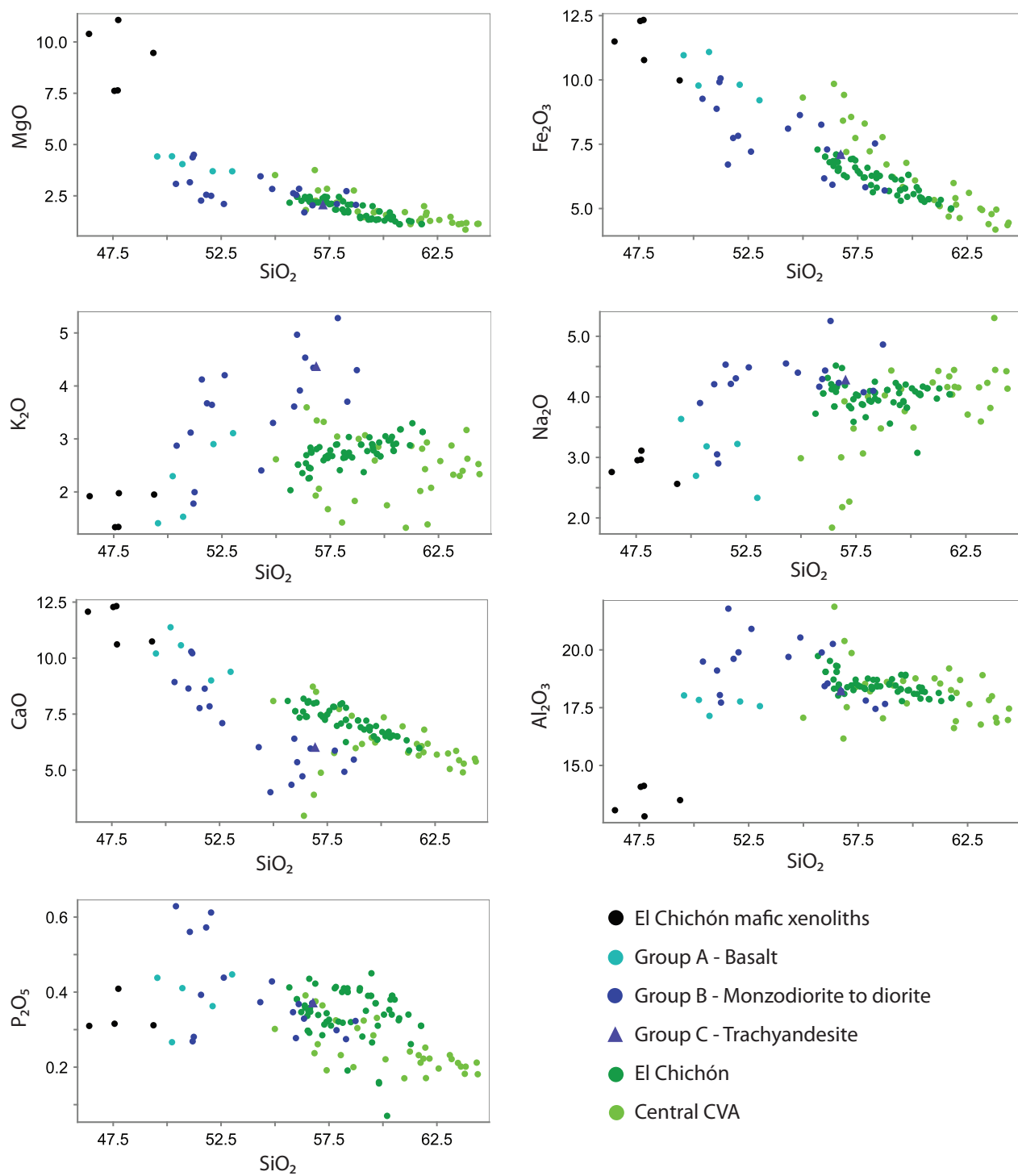


**Figure 3.10** Harker diagrams for the Chiapanecan volcanic arc. References the same as Figure 3.9.

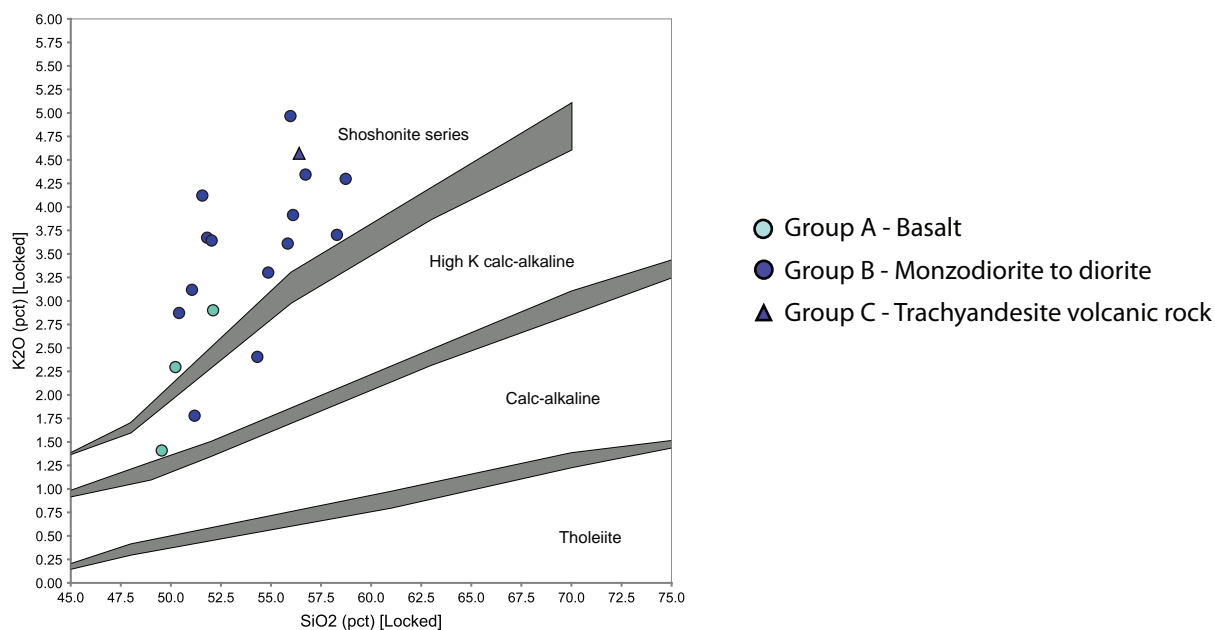


**Figure 3.11**  $\text{SiO}_2$  versus  $\text{K}_2\text{O}$  diagram for the Selva Negra (Peccerillo and Taylor, 1976).

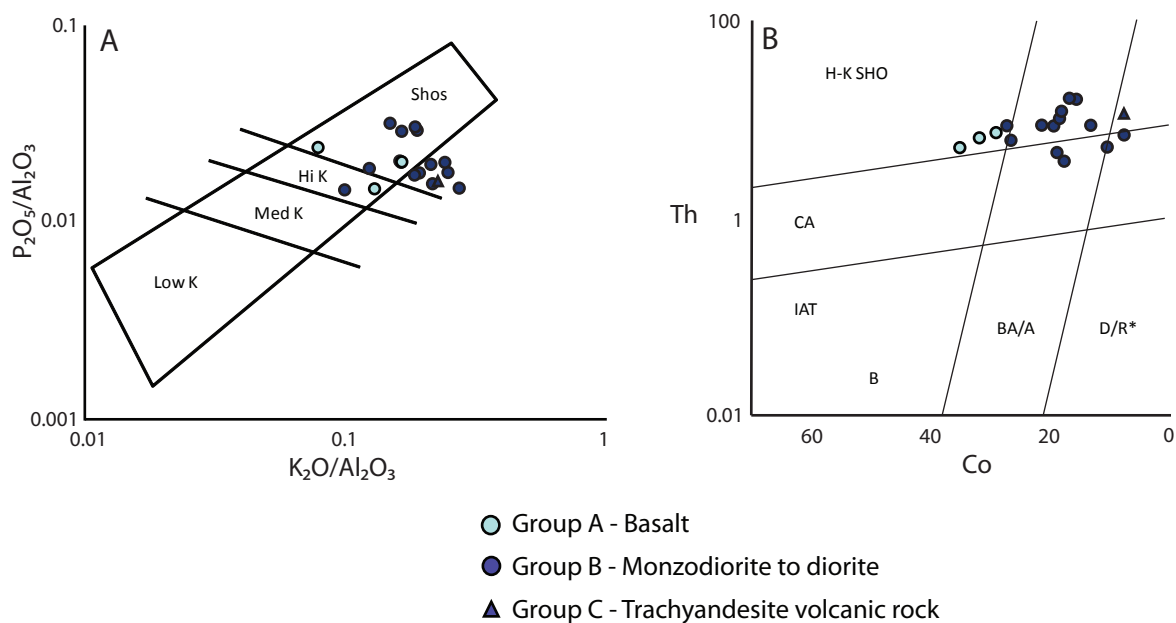


**Figure 3.12** Alternative diagrams for discriminating rocks of alkaline composition **A.**  $\text{K}_2\text{O}/\text{Al}_2\text{O}_3$  versus  $\text{P}_2\text{O}_5/\text{Al}_2\text{O}_3$  plot of Crawford et al. (2007) for the Selva Negra. **B.** The Th versus Co plot Hastie et al. (2007) for the Selva Negra. **Abbreviations:** B, basalt; BA/A, basaltic andesite and andesite, CA - calcalkalinite, D/R\*, dacite and rhyolite, H-K SHO - high-K shoshonitic, IAT - island arc tholeiites, Shos - shoshonitic.

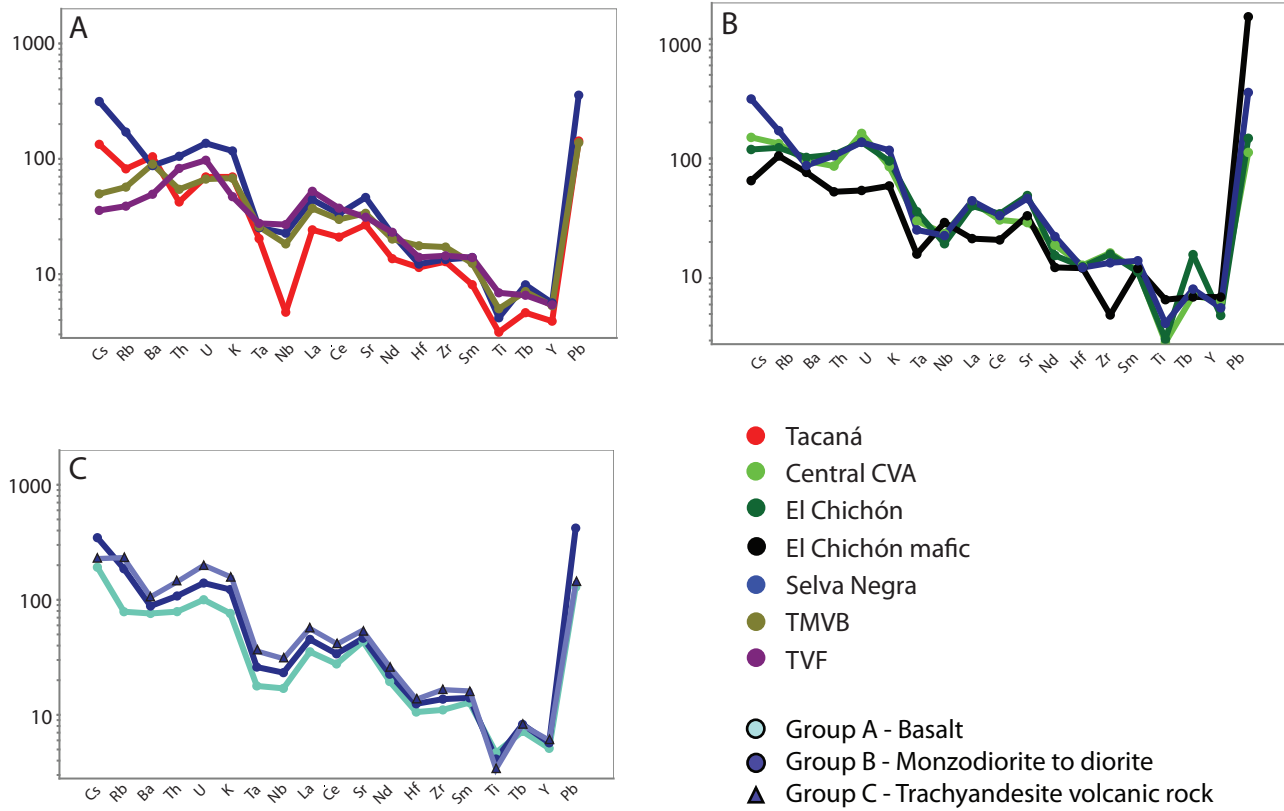


**Figure 3.13** Average primitive mantle diagrams for the Selva Negra compared with the regional volcanism. **A.** The Selva Negra in relation to Tacaná, TMVB, and TVF. **B.** Selva Negra in relation to El Chichón, El Chichón mafic xenoliths and the central CVA. **C.** Group A, B, and C of the Selva Negra. Normalised to primordial mantle of McDonough et al. (1992). References the same as Figure 3.9. **Abbreviations:** CVA - Chiapanecan volcanic arc, TMVB - Trans-Mexican volcanic belt, TVF - Lost Tuxtlas volcanic field.

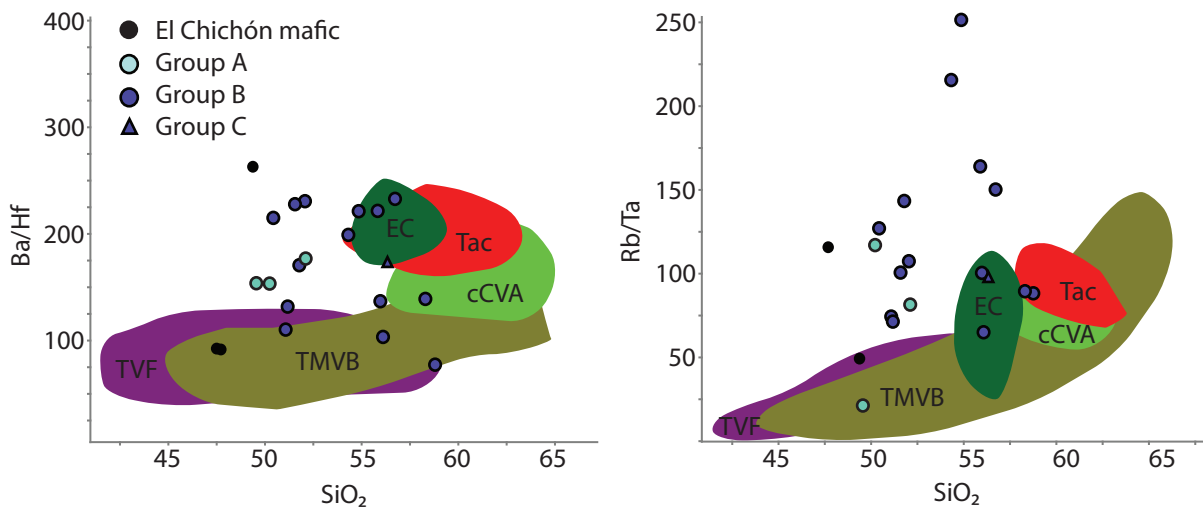


**Figure 3.14** LILE/HFSE (Ba/Hf and Rb/Ta) versus  $SiO_2$ . The Selva Negra is more enriched in LILE to HFSE than most of the other volcanic centres in the region. References the same as Figure 3.8.

### 3.6.3 Selva Negra and Regional Volcanism

The major element geochemistry of the SN suite can be compared with the Late Miocene to recent volcanic rocks of the Trans Mexican Volcanic Belt (TMVB; Luhr et al., 2006; Gómez-Tuena et al., 2007), the Late Miocene to recent Los Tuxtlas volcanic field (TVF; Nelson and Gonzalez-Caver, 1992; Nelson et al., 1995), the late Pliocene to recent Tacaná volcano of the Central America volcanic arc (CAVA; Mercado and Rose, 1992; Macías et al., 2000; García-Palomo et al., 2006) and the Pleistocene to Holocene CVA which is separated into the central CVA, anomalous high-K volcanism of the El Chichón volcano, mafic xenoliths and a nearby basaltic dyke located to the east near the village of Chapultanengo (Luhr et al., 1984; Rose et al., 1984; Capaul, 1987; McGee et al., 1987; Espindola et al., 2000; Tepley et al., 2000; Macías et al., 2003; García-Palomo et al., 2004; Layer et al., 2009). The El Chichón trachybasaltic xenoliths have a mineral assemblage composed of hornblende > augite > olivine > enstatite > plagioclase (Espindola et al., 2000). The geology and tectonic setting of the comparative data sets are described in Chapter 2.

The SN has a distinct alkaline composition compared to the TMVB, Tacaná and the central CVA (Fig. 3.9), extends to more mafic compositions than the CVA, El Chichón and Tacaná and is more felsic than the alkaline TVF. When compared with the other volcanic centres of the CVA, the SN generally plot in a distinct field, especially CaO and K<sub>2</sub>O, are on a different trend than the majority of the CVA (Fig. 3.10). The SN suite is strongly enriched in alkalis compared with the remainder of the CVA (Figs. 3.9 and 3.10). El Chichón generally plots in the similar range with CVA albeit with some rocks moderately enriched in alkalis (Fig. 3.10).

The SN suite has similar primitive mantle normalized diagrams compared to other volcanic belts (TMVB, TVF, central CVA, El Chichón, Tacaná; Fig. 3.13A) except that the SN is more enriched in LILE (K, Rb, Sr, Th, U and Cs) similar to the moderately LILE enriched El Chichón (Figs. 3.13B and 3.14). The rocks of the CVA (including the SN) are enriched in LREE elements with La/Yb<sub>CN</sub> ratios ranging from 2 to 15 (mean 9), similar to the Tacaná (5 to 12; mean 8) and the TMVB (6 to 10 with outliers to 1 to 70; mean 9) and significantly lower than the TVF (5 to 30; mean 16.0; Fig. 3.15). The La/Sm<sub>CN</sub> and Sm/Yb<sub>CN</sub> ratios are similar for all volcanic centres except for the TVF which has a noticeably higher Sm/Yb<sub>CN</sub> and the TMVB that has far outliers but most of the data ranges from 1 to 11 (Fig. 3.15).

The trace element geochemistry for SN is similar to most of the regional (TMVB, CVA, Tacaná) volcanism characterized by LREE enrichment and negative Nb, Ti, Hf, Zr anomalies on primitive mantle-normalized diagrams characteristic of a subduction zone environment (Pearce and Peate, 1995), however, the SN is strongly enriched in LILE and similar to El Chichón (Fig. 3.13). The trace element chemistry is different with lower La/Sm<sub>CN</sub> and Sm/Yb<sub>CN</sub> ratios for the SN than what is typical for back-arc settings like the TVF alkaline volcanism (Nelson et al., 1995).

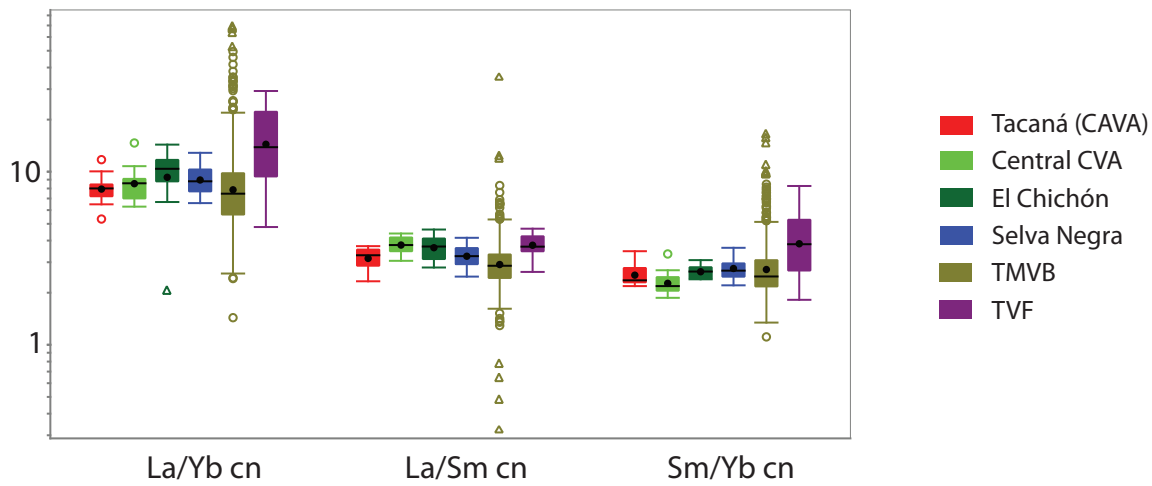


**Figure 3.15** La/Yb<sub>CN</sub>, La/Sm<sub>CN</sub> and Sm/Yb<sub>CN</sub> ratios for the Selva Negra compared with the regional volcanism. References the same as Figure 3.9.

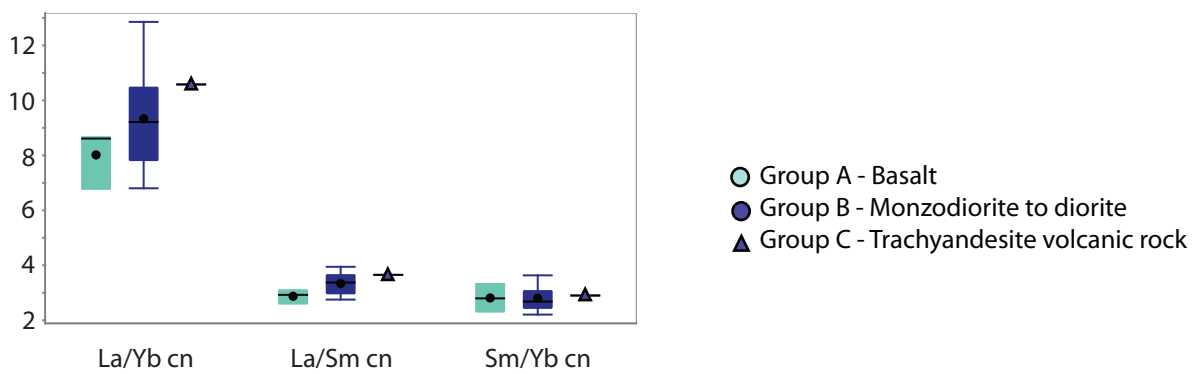


**Figure 3.16** La/Yb<sub>CN</sub>, La/Sm<sub>CN</sub> and Sm/Yb<sub>CN</sub> for the Selva Negra suite.

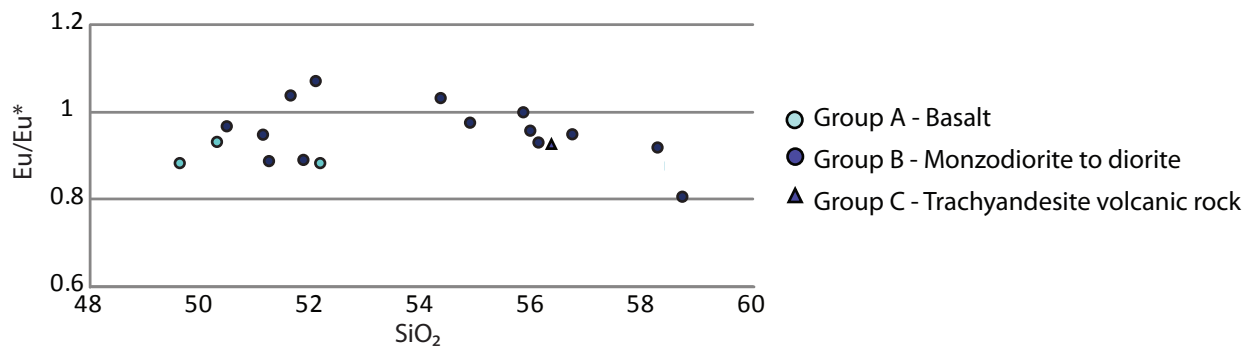


**Figure 3.17** Eu/Eu\* versus silica diagram for the Selva Negra.

### 3.6.4 Formation of K-Rich Lavas

The formation of K-rich lavas can be achieved by several processes including crystal fractionation, sediment subduction, crustal contamination, melt/fluid-related metasomatism and involvement of continental lithospheric mantle (e.g., Varne, 1985; Rogers et al., 1987; Foley, 1992a, 1992b; Edwards et al., 1994; Luhr, 1997; Peccerillo, 1999; Carlson and Nowell, 2001).

There is debate as to the origin of the K-rich composition and location of El Chichón volcano which has erupted juvenile trachyandesitic products of essentially the same chemical composition since the formation of the volcano 372,000 years ago (Rose et al., 1984; McGee et al., 1987; Layer et al., 2009). The inland location of the CVA and El Chichón is the result of volcanic activity moving from the Pacific coast (Sierra Madre volcanic arc) to its current location inland (Manea and Manea, 2006). De Ignacio et al. (2003) suggest the movement is attributed to the clock-wise rotation of the isolated Yucatan block formed by the sinistral Tehuantepec fault to the west and the Motogua-Polochic fault to the east. However, the more widely accepted explanation of the movement of volcanic activity is the result of slab flattening in central Mexico during the middle Miocene (Damon and Motesinos, 1978; Manea and Manea, 2006). Nixon (1982) proposed that extensional tectonics related to the triple junction of the North American, Cocos and Caribbean plates may account for alkaline volcanism of El Chichón.

More recently, marine magnetic anomalies over the Tehuantepec ridge show with high amplitudes of 200–300 nT and wavelengths of 20–30 km, whereas the rest of marine magnetic anomalies have shorter wavelengths (8–10 km) and lower amplitudes 100–200 nT (Manea and Manea, 2008). The magnetic anomaly has been interpreted to indicate that the upper mantle beneath the Tehuantepec ridge having undergone strong serpentinization, and carrying significant amounts of water into the subduction zone (Manea et al., 2005; Manea and Manea, 2008). Phase diagrams for sediments, basalt and peridotite and the thermal structure of the subduction zone indicate that ~40% of sediments and basalt dehydrate at ~80 km depth corresponding with the location of the serpentinized mantle wedge, whereas the serpentinized root beneath the Tehuantepec ridge strongly dehydrates (~90%) at depths of 180 to 200 km comparable with the slab depths beneath El Chichón (200 to 220 km; Manea and Manea, 2008). Manea and Mean (2008) suggest that the arrival of the highly serpentinized Tehuantepec ridge and its strong dehydration triggers partial melting in the mantle above the subducting slab, and may explain the composition of the El Chichón volcano.

### 3.6.5 Crustal versus Sediment Contamination

Crustal contamination can increase LILE content through melting, assimilation, storage, and homogenization (MASH) in the lowermost crust or the mantle crust transition zone (Hildreth and Moorbath, 1988). MASH occurs when basaltic magmas arising from the mantle wedge, become neutrally buoyant at the crust-mantle transition, and mix with each other, as well as with the array of magmas derived from the induced partial melting of heterogeneous deep-crustal rocks.

Subducted sediment can also increase the LILE content by increases in availability of subducted sedimentary pile or temporal increase of their LILE contents. Dominguez et al. (1998a; 1998b) demonstrated that in the wake of a subducting high a large shadow zone develops behind the seamount trailing slope because the seamount deflects the basal decollement upward in the reentrant area. As a consequence frontal accretion is inhibited and part of the frontal margin and the trenchfill sediments are subducted. The subducting Tehuantepec ridge could effectively be acting as a conveyor belt introducing significant amounts of sediments into the arc mantle wedge enriching the melts with LILE.

Distinguishing between crustal contamination and sediment contribution in the mantle is difficult (e.g., Hildreth and Moorbath, 1988; Gasparon and Varne, 1998). Sediments subducting along the active continental margin of the CVA are partly derived from the erosion of Chiapas Massif, the Miocene Sierra Madre volcanic arc and the continental basement along the Pacific coast. As a result magmas will retain the isotopic composition of their source, a mixture of mantle-derived and crustal components (e.g., Lucassen et al., 2010). Thus, crustal contamination and sediment recycling may have similar effects on the isotopic composition of magmas in the CVA (e.g., Lucassen et al., 2010).

However, in the CAVA, sediment versus crustal contamination can be distinguished (Carr et al., 1990; Patino et al., 2000). The CAVA isotopes have two distinct trends (Fig. 3.19): The trend for CAVA 1 occurs where the crust is sufficiently thin in Nicaragua (32 to 40 km), or the assimilant sufficiently young, that the Sr and Nd isotopic systematics of a mantle modified by sediment contribution from the subducting slab are still visible (Carr et al., 1990). The CAVA 2 trend is interpreted to be the result of crustal contamination along the volcanic front in Guatemala and Central Costa Rica where the crust is thick (40 to 58 km; Carr et al., 1990). If both sediment and crustal contamination are occurring, the isotopic systematics of the mantle could be overwhelmed by crustal contamination as they are at continental margins such as central Chile (e.g., Hildreth and Moorbath, 1988).

Sr, Nd and Pb isotopic ratios of magmatic rocks are unchanged by partial melting and closed-system fractional crystallization processes (Polve et al., 2007). Therefore, trends observed in isotopic diagrams are indicative of source heterogeneities. Magmatic rocks in the Chiapanecan volcanic arc are relatively young (<3 Ma), which implies that no correction for radioactive decay is needed and thus can be assumed to represent source characteristics.

Crustal contamination of the SN rocks can be demonstrated by radiogenic Sr isotope values that increase with  $\text{SiO}_2$  (Fig. 3.18) and are also consistent with the high LILE content (Fig. 3.13). An increase of Rb/Cs with increasing  $^{87}\text{Sr}/^{86}\text{Sr}$  is also consistent with crustal contamination (Fig. 3.22; e.g., Hildreth and Moorbath, 1988) On a  $\text{SiO}_2$  versus  $^{87}\text{Sr}/^{86}\text{Sr}$  plot the rocks of SN becomes more radiogenic with increasing  $\text{SiO}_2$  similar to the TMVB and distinctly more radiogenic than the TVF (Fig. 3.18). There is one anomalous SN value with high  $^{87}\text{Sr}/^{86}\text{Sr}$  outside the general trend for the SN that is probably caused by alteration, as hydrothermal fluids would have a radiogenic  $^{87}\text{Sr}/^{86}\text{Sr}$  signature of the crustal rocks in which they have interacted. El Chichón samples have a narrow range of  $\text{SiO}_2$  contents and  $^{87}\text{Sr}/^{86}\text{Sr}$  values except for a mafic xenolith and basaltic dyke which have  $^{87}\text{Sr}/^{86}\text{Sr}$

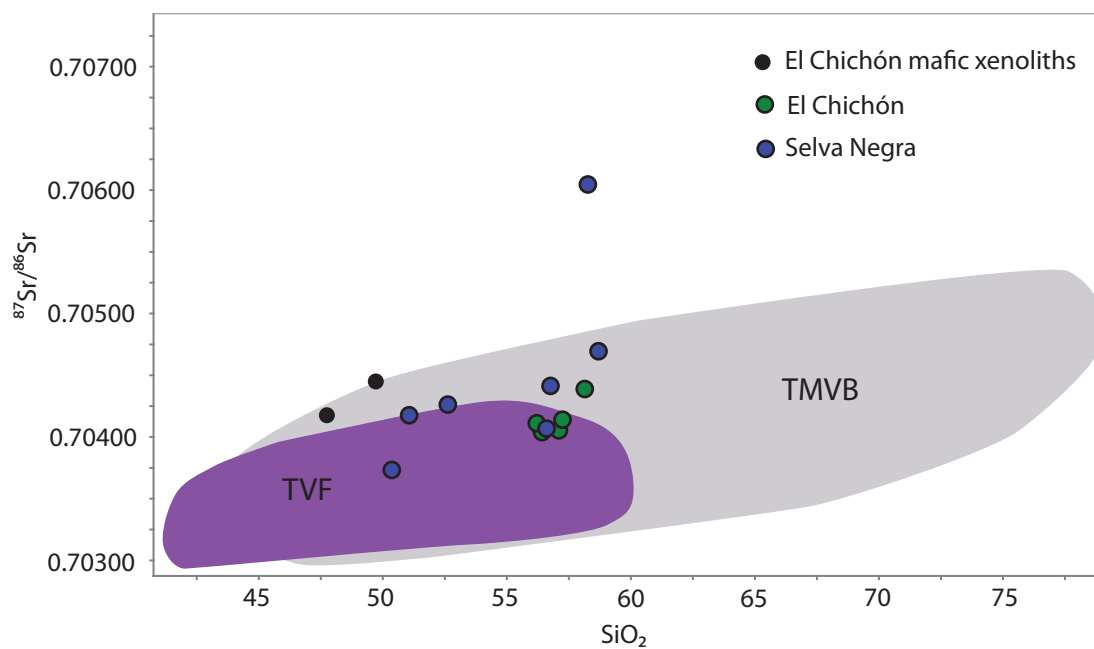


**Figure 3.18** Silica versus  $^{87}\text{Sr}/^{86}\text{Sr}$  for the Selva Negra, El Chichón, and El Chichón mafic xenoliths. TMVB field from Luhr et al. (2006), TVF field from Nelson et al. (1995), El Chichón points from García-Palomo et al. (2004).

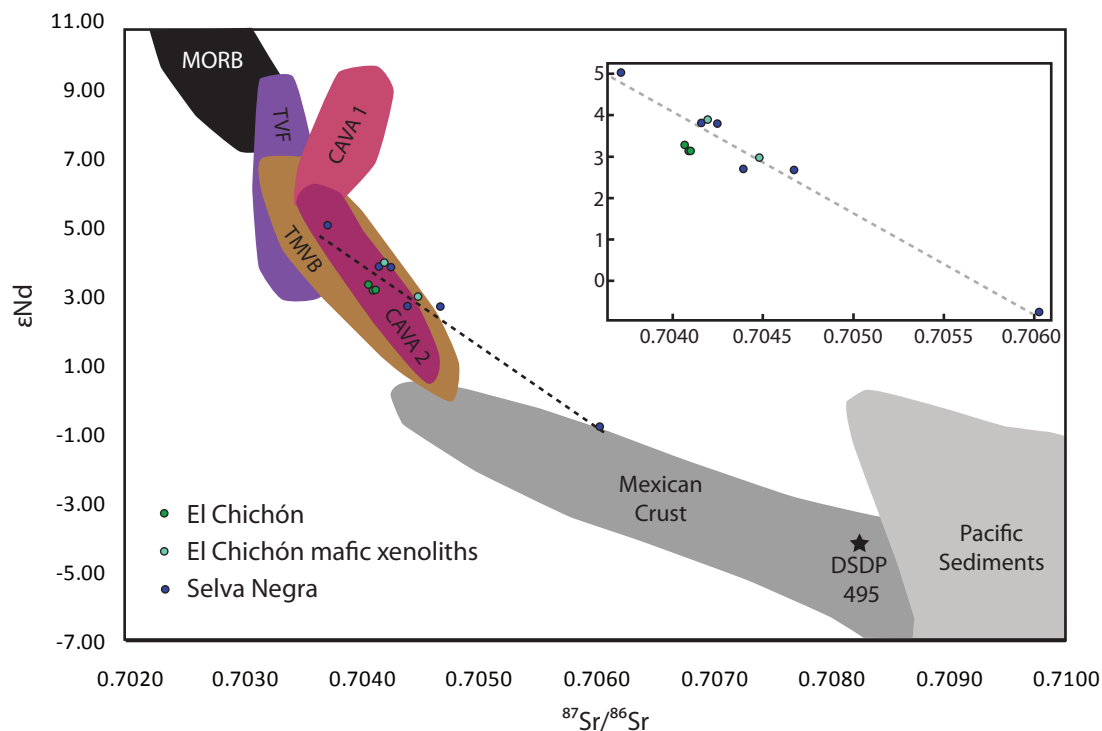


**Figure 3.19**  $^{87}\text{Sr}/^{86}\text{Sr}$  versus  $\epsilon_{\text{Nd}}$  for the Selva Negra, El Chichón and El Chichón mafic xenoliths volcano compared with the regional volcanism. CAVA fields from Carr et al. (2003), El Chichón data from García-Palomo et al. (2004), Selva Negra (This Study), TMVB field from Luhr et al. (2006) and TVF field from Nelson et al. (1995). MORB, Mexican crust, Pacific sediments from Ben Othman et al. (1989). DSDP 495 from Carr et al. (1990). **Abbreviations:** TMVB - Trans Mexican Volcanic Belt, TVF - Los Tuxtlas volcanic field.

values that are high for their low  $\text{SiO}_2$  contents compared to the TMVB and TVF distribution (Fig. 3.18).

On a  $^{87}\text{Sr}/^{86}\text{Sr}$  versus  $\epsilon_{\text{Nd}}$  plot, the SN display a shallow trend between depleted mantle and crustal and/or subducted sediments (DSDP 495) compared to the TMVB, CAVA and the TVF (Fig. 3.19). Site DSDP 495 is a sediment sample from offshore of Guatemala. The major trend for the TMVB is attributed to crustal contamination (Figs. 3.18 and 3.19; Luhr et al., 2006). El Chichón has small ranges for  $\epsilon_{\text{Nd}}$  (3.0 to 3.9) and  $^{87}\text{Sr}/^{86}\text{Sr}$  (0.7041 to 0.7045; García Palomo et al., 2004) and on a  $^{87}\text{Sr}/^{86}\text{Sr}$  versus  $\epsilon_{\text{Nd}}$  plot, the data overlap with the fields of TMVB and CAVA 2 (Fig. 3.19). The El Chichón mafic xenoliths and basaltic dyke plot on the same trend as the SN samples. On a  $^{87}\text{Sr}/^{86}\text{Sr}$  versus  $^{206}\text{Pb}/^{204}\text{Pb}$  plot, the SN suite has a different trend to the TVF (Fig. 3.20). The SN has a slightly steeper trend than the TMVB when ignoring the sample that plots off the main SN trend as a result of alteration (Fig. 3.20).  $^{207}\text{Pb}/^{204}\text{Pb}$  and  $^{208}\text{Pb}/^{204}\text{Pb}$  show an increase with respect to  $^{206}\text{Pb}/^{204}\text{Pb}$  similar to the TMVB (Figs. 3.21A and B). The Pb isotopes for the TMVB are attributed to crustal contamination and the same is probable for the SN which displays a similar trend (Luhr et al., 2006). The more radiogenic Sr and less radiogenic Nd (Fig. 3.19) reflect not only larger crustal contributions but also the greater average age of the thicker northern crust. The radiogenic trend for the SN is therefore attributed to crustal contamination, however subducted sediment cannot be discounted as the thick crust may be diluting the signal from the subducted sediment.

The strong enrichment of LILE compared to other volcanic centres (Fig. 3.13) for the Selva Negra suite is probably from crustal contamination, however, it can also be a result from an increase in the amount of subducted sediments contributing to the mantle source (White and Patchett, 1984; Defant and Drummond, 1990). Sediment subduction was proposed in the CAVA by Patino et al. (2000) by analysing a sedimentary section (at DSDP Site 495) on the subducting Cocos Plate which they propose would most closely resemble the current sediments in the subduction zone. Marine sediment control on some geochemical characteristics of the lavas is evidenced by variations in Ba/Th and U/La ratios within individual volcanic centres in Central America which are interpreted to increase in response to the intensity of sediment flux from the subducting slab. The sediment contribution is also evidenced in radiogenic isotopes (CAVA 2; Fig. 3.19). Assuming that the sediment geochemistry DSDP Site 495 is the same for the Cocos plate subducting below the Chiapas region, the Ba/Th and U/La ratios were applied and compared with the CAVA to find evidence of sediment contribution (Fig. 3.23). As indicated in Figure 3.23, the carbonate sediments (CS) and the hemipelagic sediments (HS) from DSDP Site 495 on the Cocos plate plot close to each other and the CAVA lavas are distributed between UAOC/EMORB and the sediments implying a binary mixture (Patino et al., 2000). The Selva Negra, central CVA and El Chichón plot between the TVF and the back-arc lavas of the CAVA field which Patino et al. (2000) interpreted to indicate sediment input from the Cocos plate.

The isotopes suggest that SN has undergone crustal contamination as it falls on the same trends as the TMVB and CAVA 2 which are also attributed to crustal contamination (Fig. 3.19; Carr et al., 1990; Luhr et al., 2006). Radiogenic crustal contamination is consistent with limestone xenoliths hosted by a plagioclase-rich trachyandesite at El Chichón (Espindola et al., 2000) and a

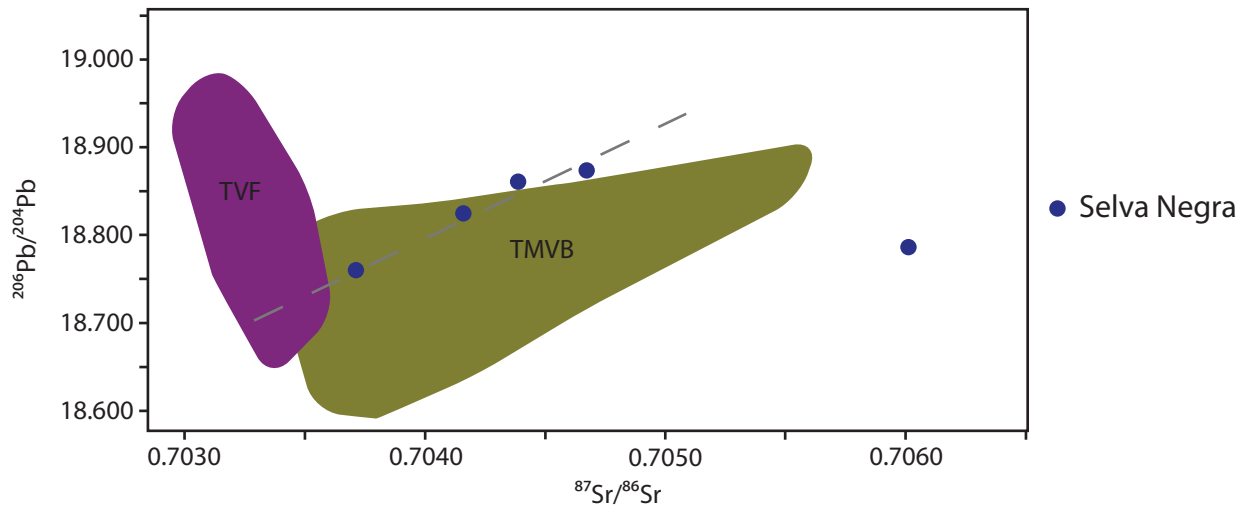


**Figure 3.20**  $^{87}\text{Sr}/^{86}\text{Sr}$  versus  $^{206}\text{Pb}/^{204}\text{Pb}$  for the Selva Negra compared with the TMVB and TVF. TMVB from Luhr et al. (2006), TVF from Nelson et al. (1995). **Abbreviations:** TMVB - Trans Mexican Volcanic Belt, TVF - Los Tuxtlas volcanic field.

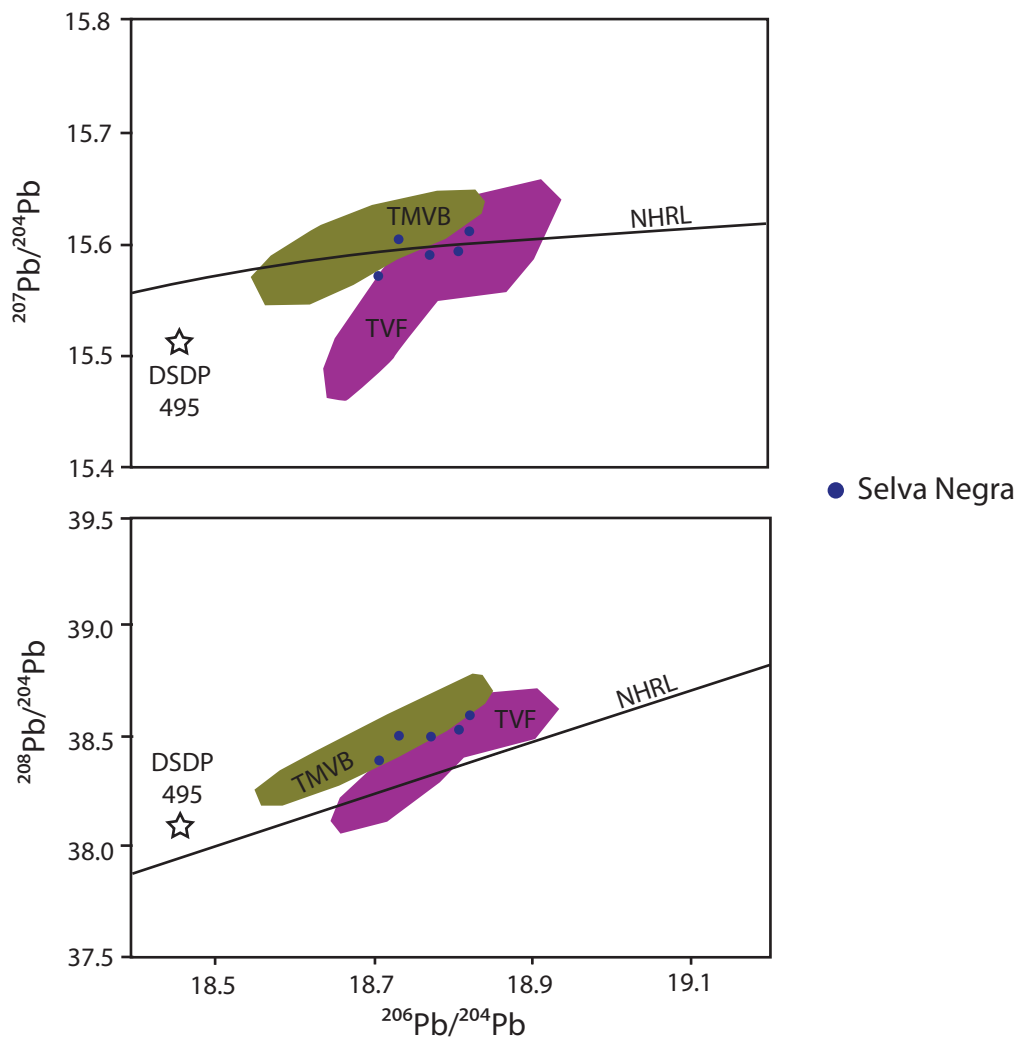


**Figure 3.21** Pb isotopes for the Selva Negra compared with the Trans-Mexican volcanic belt and Los Tuxtlas volcanic field. **A.**  $^{206}\text{Pb}/^{204}\text{Pb}$  versus  $^{207}\text{Pb}/^{204}\text{Pb}$  for the TMVB, El Chichón, TVF, CAVA and Selva Negra. **B.**  $^{206}\text{Pb}/^{204}\text{Pb}$  versus  $^{208}\text{Pb}/^{204}\text{Pb}$  for the TMVB, El Chichón, TVF, CAVA and Selva Negra. MORB and Pacific Sediment fields from Nelson et al. (1995), TMVB field from Luhr et al. (2006), TVF field from Nelson et al. (1995). **Abbreviations:** TMVB - Trans Mexican Volcanic Belt, TVF - Los Tuxtlas volcanic field.

radiogenic mafic xenolith that is probably derived from the lower crust and plots on the same trend as the SN. The SN is different to CAVA 1 which is attributed to a mantle modified by subducting sediment (Fig. 3.19). However, as discussed crustal contamination may be obscuring the systematics of mantle processes given the thick crust below the SN compared to the thin crust below the volcanic rocks for the CAVA 1 trend (Carr et al., 1990).

### 3.6.6 Melt Fluid Metasomatism

Manea and Manea (2008) have suggested that the arrival of the highly serpentized Tehuantepec ridge and its strong dehydration triggers partial melting in the mantle above the subducting slab, may explain the composition of the El Chichón volcano. Potassic melts are generally attributed to low degrees of partial melting in areas of the mantle wedge that have been previously enriched in LILE by slab-derived fluids or melt (Thorpe, 1982; Foley, 1992b). This metasomatic enrichment may be achieved by overprinting the mantle wedge by either LILE-enriched fluids or LILE-enriched partial melts, both derived during dehydration of the subducted oceanic slab (Menzies and Hawkesworth, 1987; Peccerillo, 1992). Partial melting of these enriched harzburgitic areas, under hydrous conditions, would yield potassic melts, with partial melting of normal lherzolitic peridotite considered unable to produce extensive LILE enrichment (e.g., Kay and Gast, 1973).

The depth of slab below the SN is deep (200 to 220 km) compared with global subduction zones when averaged over 500-km-long arc ranges from 72 to 173 km with a global average of 105 km (Syracuse and Abers, 2006). The slab below the SN is also a considerable distance from the trench (300 to 300 km). The position is probably controlled by the strike-slip province which the magmas are using as conduits (described in Chapter 2; García Palomo et al., 2004; Mora et al., 2007). Therefore, the shoshonitic composition of the SN could be a result of large distance from the trench where a decreasing degree of partial melting effects a heterogeneous mantle (Dostal et al., 1977).

### 3.6.7 Adakite

Most volcanic rocks in continental arcs are probably derived from melting of the mantle wedge by hydrous fluids released from the subducting slab. In contrast, adakite melts can be derived directly from the subducted slab where relatively young and hot lithosphere can be easily melted during subduction (e.g., Defant and Drummond, 1990; Richards and Kerrich, 2007). The Cocos plate subducting below the Selva Negra is less than 16 Ma making it a candidate for slab melting.

De Ignacio et al. (2003) argue that El Chichón has a transitional calc-alkaline to adakitic-like magmatism interpreted to be the result of a torn slab allowing the mixing of slab derived and mantle-derived melts. De Ignacio et al. (2003) showed on a Sr/Y versus Y plot that most of the El Chichón samples plot between normal andesite-dacite-rhyolite and the adakite fields with only two samples occurring in the adakite field (Fig. 3.24A). As a result De Ignacio et al. (2003) suggested that the El Chichón reflects a transitional geochemical character between “normal” calc-alkaline and adakitic-like magmas based on higher Sr and lower Y contents in addition to the presence of magmatic anhydrite, high sulfur contents; and high  $fO_2$ .

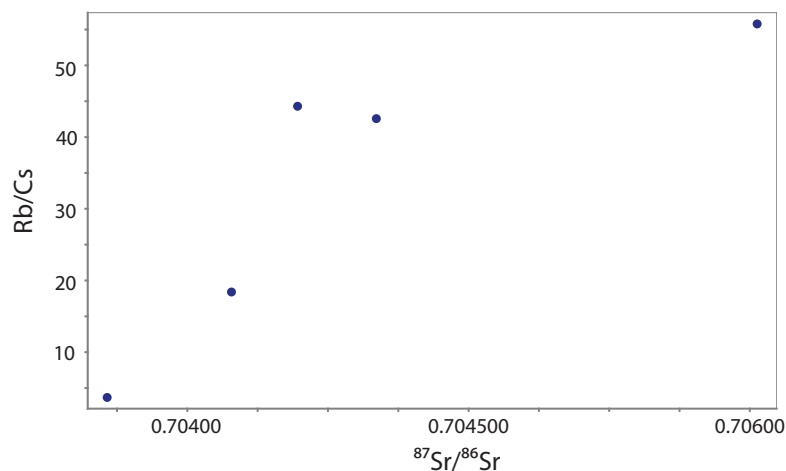


**Figure 3.22**  $^{87}\text{Sr}/^{86}\text{Sr}$  versus Rb/Cs for the Selva Negra suite. A positive trend is consistent with increasing crustal contamination.

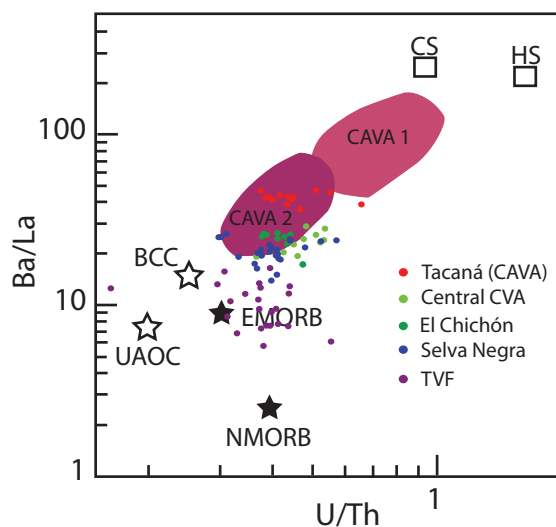


**Figure 3.23** U/Th versus Ba/La diagram to identify sediment input (modified from Patino et al., (2000)). The carbonate sediments (CS) and the hemipelagic sediments (HS) from DSDP Site 495 on the Cocos plate plot close to each other and the CAVA lavas are distributed in a linear array, implying a binary mixture between the mantle and the sediments (Patino et al., 2000). The larger sediment contribution is observed in the samples from western Nicaragua and the smallest contribution in the back-arc lavas (Patino et al., 2000). The Selva Negra, central CVA and El Chichón plot between the back-arc lavas of the CAVA field and the TVF suggesting no sediment input from the Cocos plate. BCC - Taylor and McLennan (1985), CAVA fields from Carr et al. (1990), Patino et al. (2000), EMORB from Sun and McDonough (1989), UAOC from Alt et al. (1996) and references therein, other fields the same as Figure 3.9. **Abbreviations:** BCC - bulk continental crust, CAVA - Central American volcanic arc, CVA - Chiapanecan volcanic arc, EMORB - enriched mid-oceanic ridge basalt, NMORB - normal mid-oceanic ridge basalt, UAOC - upper altered oceanic crust.

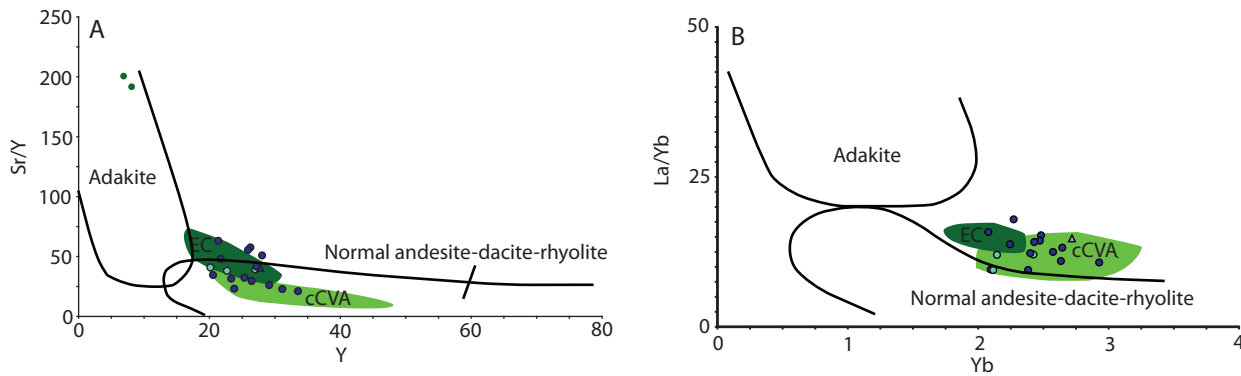


**Figure 3.24** Adakite discrimination diagrams for the Selva Negra, El Chichón and central Chiapanecan volcanic arc. **A.** Sr/Y versus Y plot after Richards and Kerrich (2007) and Defant and Drummond (1993). **B.** La/Yb versus Yb plot after Richards and Kerrich (2007) and Castillo et al., (1999). The references for the central CVA and El Chichón are the same as Figure 3.8. **Abbreviations:** cCVA - central Chiapanecan volcanic arc, EC - El Chichón. References same as Figure 3.9.

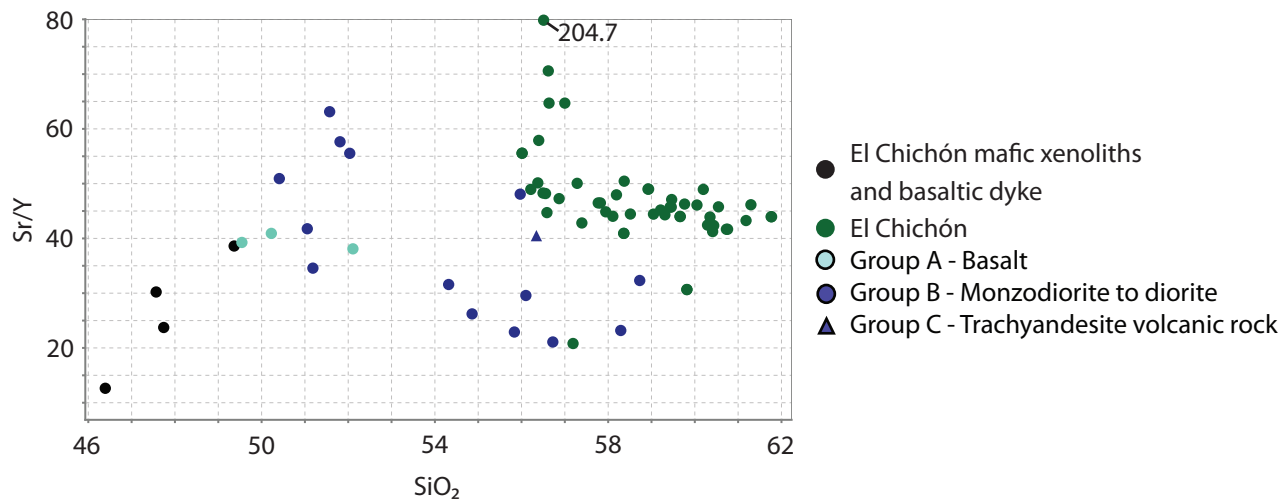


**Figure 3.25** Sr/Y versus SiO<sub>2</sub> diagram showing a decreasing trend of Sr/Y with SiO<sub>2</sub> for Selva Negra and El Chichón. References same as Figure 3.9.

On a Yb versus La/Yb chart (Castillo et al., 1999; Richards and Kerrich, 2007) the Selva Negra, CVA and El Chichón plot outside the adakite and normal andesite-dacite-rhyolite field at higher La/Yb values (Fig. 3.24B). According to Richards and Kerrich (2007) the SN volcanic rocks do not fit the adakite classification, as they do not plot in the adakite field using Sr/Y versus Y and La/Yb versus Yb charts (Figs. 3.24A and B; Defant and Drummond, 1993; Castillo et al., 1999; Richards and Kerrich, 2007). Radiogenic isotopes suggest crustal contamination and the El Chichón probably has a false Sr/Y characteristic for transitional adakites, as the concentration of Sr would increase with crustal contamination (e.g., Richards and Kerrich, 2007). In addition the Sr/Y ratio should increase with SiO<sub>2</sub> content consistent with the fractionation of garnet, amphibole,

clinopyroxene, titanite and apatite, however, this ratio decreases with fractionation for both SN and El Chichón (Fig. 3.25). The complexities of a continental arc, including contamination, mean that it is difficult to conclude that volcanic rocks of the El Chichón and SN are adakites.

### 3.7 Conclusions

The SN igneous rocks are shoshonitic with a basic to intermediate composition ( $\text{SiO}_2 = 47$  to 58 wt.%; Fig. 3.9). The suite comprises basalts to basaltic trachyandesites. The suites plot on the same trends on Harker diagrams and primitive mantle normalised diagrams suggesting a similar petrogenesis. The SN is enriched in LILE (K, Rb, Sr, Th, U and Cs) and LREE. All SN suites are characterized by LREE enrichment and negative Nb, Ti, Hf, Zr anomalies on primitive mantle-normalized diagrams (Fig. 3.13) characteristic of a subduction zone environment (Pearce and Peate, 1995) and different to the alkaline TVF geochemistry typical of a back-arc setting. The SN and El Chichón are high-K to shoshonitic and enriched in LILE and together show that the northwest end of the CVA is distinctly K-rich and distinct from regional volcanism (TMVB, CVA, Tacaná).

The nature and distribution of magmatic activity in the overriding plate is a function of the convergence rate, the age of the subducted lithosphere and the presence of features such as seamount chains or aseismic ridges (Wilson, 1989). The entire CVA is located in a structural setting characterised by a sinistral strike-slip zone which controls where the volcanism erupts (Meneses-Rocha, 2001; García-Palomo et al., 2004; Mora et al., 2007). The entire CVA also has similar crustal thicknesses of 49 to 53 km (Narcía-López et al., 2004) comprising Cenozoic sedimentary rocks and Mesozoic evaporites and limestones (Fig. 2.3; Islas Tenorio et al., 2005). The Permian Chiapas batholith and Paleozoic metamorphic and sedimentary rocks do not crop out in the area of the CVA but are inferred to occur below the CVA (Meneses-Rocha, 2001). The style of volcanism comprising low-profile (< 850 m high), small-volume (3 to 4 km<sup>3</sup>) volcanic domes with associated pyroclastic flow deposits is a characteristic of the entire CVA. The depth of the slab below SN/El Chichón and the central CVA is the same 200 to 220 km (Rebollar et al., 1999) and the slab convergence rate 6.6 cm/year is the same (Pardo and Suárez, 1995). The only obvious distinction at the northwest end of the CVA where K- and LILE-rich volcanism of SN and El Chichón is associated with the occurrence of the onshore propagation of Tehuantepec ridge.

The shoshonitic and LILE-rich composition of the Selva Negra is the result of low degree partial melts which have ascended along the inland faults of the strike-slip zone 300 to 330 km from the trench. The radiogenic isotope data suggest that the ascending magmas interacted with the thick crust (~50 km) through MASH processes. The combination of low degree partial melts of a heterogeneous mantle enriched in LILE and LREE and crustal contamination resulted in a shoshonitic and enriched LILE geochemistry for the Selva Negra volcanic rocks. The affects of the Tehuantepec ridge on the geochemistry are uncertain as crustal contamination may be diluting the signal.



## Chapter 4 - Prospect Geology

### 4.1 Introduction

The Cerro la Mina Au (Cu-Mo) prospect is hosted in the Pliocene to Pleistocene Selva Negra volcanic rocks of the Chiapanecan volcanic arc. Chapter 3 described the Selva Negra as composed of basalt to trachyandesite volcanoclastic rocks and equigranular monzodiorite to diorite intrusions.

One of the primary aims of this Ph.D. was to determine stratigraphic and structural controls on alteration and mineralisation. The geology of the Cerro la Mina prospect therefore needed to be constrained and was determined by core logging and supplemented by limited outcrop information. One internal Kinross study was undertaken to propose a geologic model for the Cerro la Mina prospect (Cumming, 2008). The Kinross study was constructed by logging a section through the most intensely altered rocks where primary textures are difficult to observe. In this study, the protolith was recorded by mapping the most distal holes to the intense alteration where primary textures could be observed. Geologic relationships and interpretations of this study were based mainly on drill core observations.

The chapter is organised by beginning the research methods followed by a description of each lithofacies followed by their distribution. The chapter ends with a discussion for the genetic rock type for each lithofacies, paragenesis of the volcanic stratigraphy and an interpretation of the geologic setting for the Cerro la Mina prospect.

### 4.2 Research Methods

#### 4.2.1 Graphic Logging

Methods for drill core graphic logging and graphic logs are in Appendix I.1 and II.2.

### 4.3 Lithofacies Description

The Cerro la Mina volcanic succession comprises volcanoclastic rocks as well as syn-volcanic porphyritic and equigranular intrusions. The succession is divided into four major lithofacies based on rock textures and lithofacies association (Table 4.1). A lower succession of clast-supported to matrix-supported, fiamme breccias (Unit 1A and B) interbedded with volcanoclastic sandstone (Unit 1C) and rare basalt (Unit 1D) is intruded by equigranular monzodiorite to diorite intrusions (Unit 2). These units are overlain by feldspar-phyric, trachyandesite syn-volcanic intrusions (Unit 3A) and associated monomictic breccias (Unit 3B) that transition distally to abundant, thick beds of matrix-supported breccias (Unit 3C). Unit 4 cross-cuts all of the previous units and forms a predominantly matrix-rich, granule breccia (Unit 4A) to distal brecciated volcanic wall rocks (Unit 4B) and rare monomictic breccias (Unit 4C). The matrix-rich, granule breccia (Unit 4A) is an important rock type, as it hosts all of the significant alteration and mineralisation drilled to date. The units are summarized in Table 4.1.

Table 4.1 Description and interpretation of lithofacies for the Cerro la Mina prospect.

| Unit   | Lithofacies                       | Characteristics  | Crystal/grain/lithic populations   | Ground-mass/matrix | Interpretation                   |
|--|-----------------------------------|--|--|--------------------|----------------------------------|
| Unit 1A  | Clast-supported breccia           | Polymictic, clast-supported, with <10% fiamme clasts. Normal grading.      | 0.5-5 cm clasts that are sub-rounded to sub-angular, and are sparsely feldspar-phyric white - cream dacite, grey-cream mudstone, feldspar-phyric andesite                      | Minor              | Ignimbrite (pyroclastic deposit) |
| Unit 1B <sub>M</sub><br>Unit 1B <sub>S</sub>   | Moderate to strong fiamme breccia | Polymictic, matrix-supported with 10-50% fiamme clasts                     | Same as above. Moderate 10-30% and strong 30-50% fiamme clasts   | 1-3 mm             | Ignimbrite (pyroclastic deposit) |
| Unit 1C  | Volcaniclastic sandstone          | Fine-grained, well sorted  | The crystals are 1-2 mm, 25% in abundance, anhedral to euhedral. Occasional fragments up to 3 cm of pumice, feldspar-phyric clasts and grey (lithic?) clasts                   |                    | Air fall deposit                 |
| Unit 1D  | Basalt                            | Fine-grained, coherent   | Holocrystalline texture of plagioclase, clinopyroxene and magnetite. Occasional vesicular texture with amygdules filled with calcite, quartz and an unidentified brown mineral | None               | Basalt flow                      |
| Unit 2   | Monzodiorite to diorite           | Fine- to coarse-grained, equigranular, coherent                            | Plagioclase, clinopyroxene, biotite, magnetite, hornblende   | None               | Intrusion                        |
| Unit 3A <sub>T</sub><br>Unit 3A <sub>S</sub>   | Feldspar-phyric trachyandesite    | Feldspar-phyric, coherent  | The feldspar-phyric andesite contains 30% - 50% blocky to tabular feldspar phenocrysts and lesser tabular euhedral biotite, clinopyroxene and hornblende crystals              | None               | Syn-volcanic dome                |
| Unit 3B  | Monomictic breccia                | Monomictic, poorly sorted  | 0.5 to 4 cm, subangular clasts of Unit 3A  | 1-2 mm             | Dome autobreccia                 |
| Unit 3C <sub>FG</sub><br>Unit 3C <sub>CG</sub> | Matrix-supported breccia          | Polymictic, poorly sorted  | 0.5 to 5.0 cm subangular clasts of predominantly aphanitic cream, with lesser feldspar-phyric and minor fine-grained lithic. Rare bedding                                      | 1-2 mm             | Debris or mass flows             |
| Unit 4A  | Matrix-rich, granule breccia      | Massive, fine-grained (< 1 cm) and well sorted with clasts of Units 1 to 3 | Plagioclase and potassium feldspar grains and clasts of quartz - potassium feldspar - plagioclase  | < 50 µm            | Breccia pipe core                |
| Unit 4B  | Brecciated volcanic wall rocks    | Polymictic breccia   | Clasts of Units 1 to 3. Common clasts of Unit 3B (clasts within clasts) and Unit 2   | 1-2 mm             | Breccia pipe rim                 |
| Unit 4C  | Monomictic breccia                | Monomictic, poorly sorted  | 0.5 to 2cm, subangular clasts of monzodiorite or feldspar-phyric andesite clasts. Occasional jig-saw fit texture   | 1-2 mm             | Breccia pipe rim                 |

### 4.3.1 Unit 1 - Trachyandesite Fiamme Breccias

Unit 1 contains a range of volcanoclastic rocks that are mainly distinguished by the occurrence of fiamme clasts. Clast-supported breccias (Unit 1A) contain <10% fiamme clasts, and the moderate (Unit 1B<sub>M</sub>) to strong fiamme (Unit 1B<sub>S</sub>) breccia is matrix-supported and contains approximately 10-30% and 30-50% fiamme clasts, respectively. Volumetrically minor fine-grained volcanoclastic sandstone (Unit 1C) and rare basalt (Unit 1D) are interbedded with Units 1A and 1B.

In thin section Unit 1 is moderately to strongly altered with illite, muscovite and chlorite. In least altered zones Unit 1 contains clasts which are variably plagioclase, orthoclase and clinopyroxene phyrics hosted in a fine-grained groundmass. Apatite is sometimes observed as grains or as fine-grained inclusions in plagioclase. Clinopyroxene, biotite and magnetite are locally observed in least altered zone and observed to be replaced by pyrite and rutile. The phenocryst assemblage (feldspar - biotite - orthoclase - clinopyroxene - apatite) indicates that Unit 1 is trachyandesite to trachydiorite in composition.

#### 4.3.1.1 Unit 1A - Clast-Supported Breccia

This unit is a coarse, poorly sorted, clast-supported, polymictic breccia (Fig. 4.1A). Clasts are 0.5 to 5 cm (rare > 5 cm) and sub-rounded to sub-angular and consist of (in order from most to least common) of fine-grained, sparsely feldspar-phyric white/cream dacite clasts, variably silicified grey-cream mudstone clasts, feldspar-phyric trachyandesite and rare amygdaloidal trachyandesite. Occasional fiamme or 'whispy' clasts (< 10%) are observed in this unit. The feldspar-phyric, trachyandesite clasts have tabular euhedral to subhedral feldspar laths in an equigranular and fine-grained grey, groundmass. Normal grading is occasionally observed in the clast-supported breccia (Fig. 4.1E).

#### 4.3.1.2 Unit 1B<sub>M</sub> and 1B<sub>S</sub> - Moderate to Strong Fiamme Breccia

The moderate to strong fiamme volcanoclastic rocks are coarse and poorly sorted with a eutaxitic texture formed by abundant fiamme textured clasts (Figs. 4.1C and D). The facies is matrix-supported with 1 to 3 mm matrix and 0.5 to 1.0 cm (occasional oversized) sub-rounded clasts and elongated fiamme-like clasts. The clasts comprise (in order from most to least common) fine-grained, sparsely feldspar-phyric white/cream dacite clasts, variably silicified grey/cream mudstone clasts and feldspar-phyric trachyandesite. The feldspar-phyric trachyandesite has tabular euhedral to subhedral feldspar laths in an equigranular fine grey groundmass. The moderate (Unit 1B<sub>M</sub>) and strong fiamme (Unit 1B<sub>S</sub>) breccia contains 10 to 30% (Fig. 4.1C) and 30 to 50% (Fig. 4.1D) fiamme-textured clasts and are aligned sub-horizontally. In thin-section the rock is too altered to observe glass shards and evidence of welding or diagenetic compaction.

#### 4.3.1.3 Unit 1C - Volcanoclastic Sandstone

The volcanoclastic sandstone is crystal-rich, well sorted and massive (Fig. 4.1B). The crystals are 1 to 2 mm, 25% in abundance, anhedral to euhedral and hosted in a fine-grained (< 1mm) matrix. Occasional pumice fragments up to 3 cm (Fig. 4.1B), feldspar-phyric clasts and grey aphanitic clasts

## Unit 1: Trachyandesite fiamme breccias

**Subunits:** Unit 1A: Clast-supported breccia

Unit 1B<sub>M</sub> and 1B<sub>S</sub>: Moderate to strong fiamme breccia

Unit 1C: Volcaniclastic sandstone

Unit 1D: Basalt

### Description

**Distinguishing Features:** Volcaniclastic rock with fiamme clasts, polymictic, clast to matrix-supported.

**Distribution:** The northeast block and greater than 500 m below the surface in the southeast block. The clast-supported to moderate to strong fiamme breccias (Unit 1A and 1B) are the most voluminous in Unit 1 and are interbedded with minor volcaniclastic sandstone (unit 1C) and rare basalt (unit 1D).

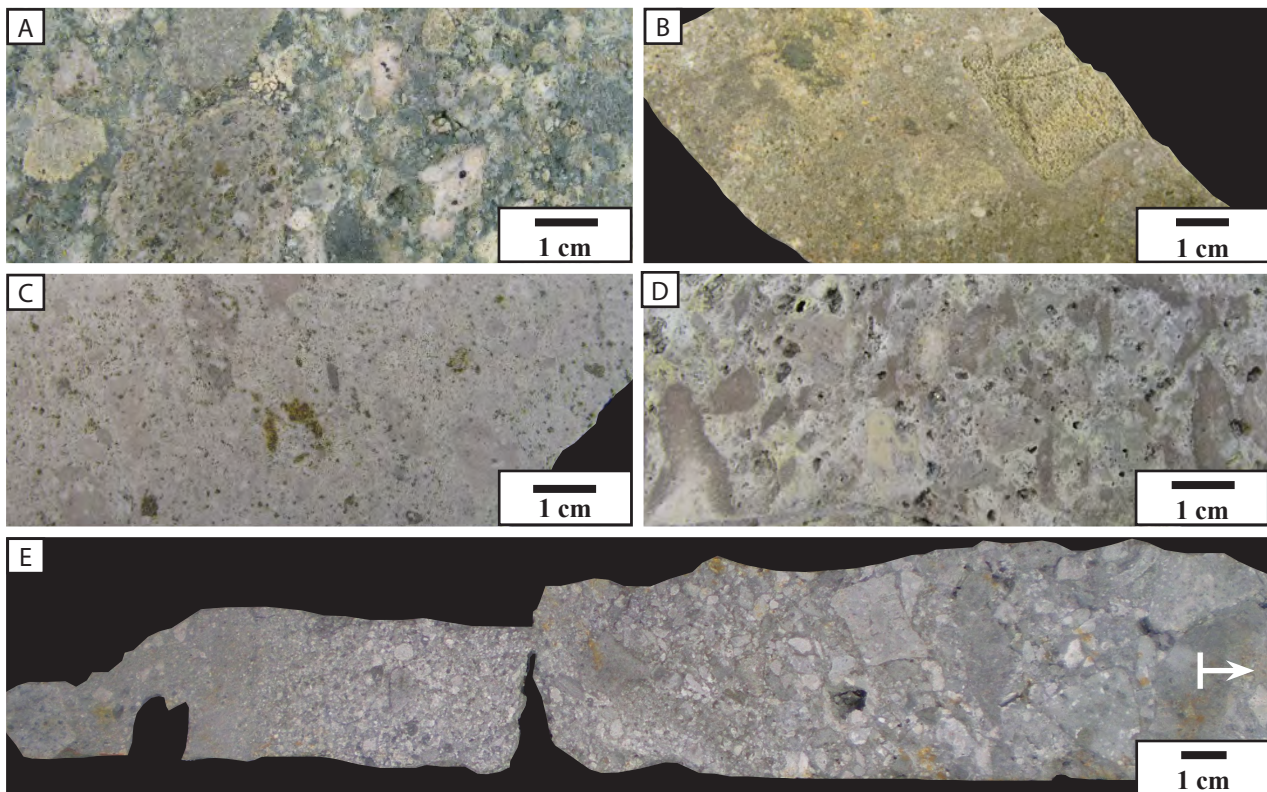
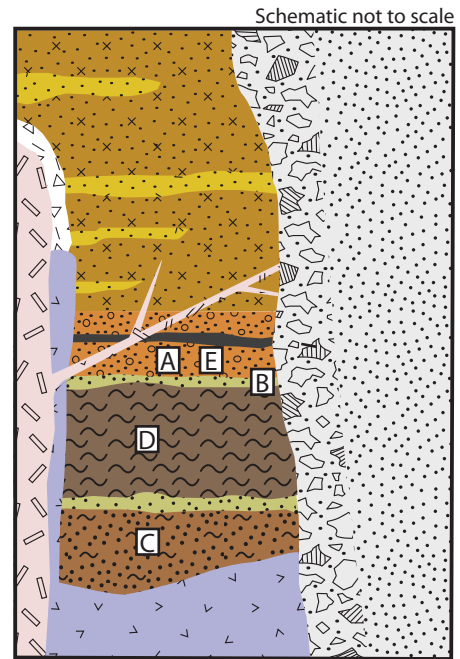


**Figure 4.1** Characteristics of fiamme breccias (Unit 1). **A.** Clast supported breccia (Unit 1A). **B.** Volcaniclastic sandstone with pumice clast (Unit 1C). **C.** Moderate fiamme breccia (Unit 1B<sub>M</sub>). **D.** Strong fiamme breccia (Unit 1B<sub>S</sub>). **E.** Clast supported breccia (Unit 1A) showing normal grading. Legend for stratigraphic column in Figure 4.14. **Sample ID:** A. IXCM08-59 245.4, B. IXCM08-59 278.8, C. IXCM08-59 324.6, D. IXCM08-46 225.2, E. IXCM07-23 64.5.

occur in this rock. This unit is interbedded within Units 1A and B.

#### *4.3.1.4 Unit 1D - Basalt*

The basalt displays a holocrystalline texture of plagioclase, clinopyroxene and magnetite. The rocks sometimes display a vesicular texture with vesicles infilled with calcite, quartz and an unidentified brown mineral. Unit 1D is rare at Cerro la Mina and only occurs once within Unit 1A. Unit 1D is part of Group B geochemistry whose petrography, geochemistry and description of this rock type were described in Chapter 3.

#### *4.3.2 Unit 2 - Monzodiorite to Diorite*

The equigranular monzodiorite to diorite is composed of plagioclase, clinopyroxene, biotite, magnetite, hornblende and olivine. A fine-grained and coarse-grained variety is observed at Cerro la Mina with crystal sizes of 0.5 to 1 mm and 1 to 2 mm, respectively (Figs. 4.2A and B). Plagioclase veins lined with hornblende - biotite - magnetite are rarely observed (Figs. 4.2C and D). This rock type crops out and is intersected in many drill holes throughout the Ixhuatán concession. Unit 2 is part of Group B geochemistry whose petrography, geochemistry and description of this rock type were described in Chapter 3.

#### *4.3.3 Unit 3 - Trachyandesite Coherent to Matrix-Supported Breccias*

Unit 3 comprises a coherent feldspar-phyric trachyandesite that transitions towards monomictic feldspar-phyric breccias then to abundant, thick beds of polymictic matrix-supported breccias.

##### *4.3.3.1 Unit 3A<sub>T</sub> and 3A<sub>S</sub> - Feldspar-Phyric Trachyandesite*

This coherent rock type contains plagioclase, clinopyroxene, biotite and hornblende phenocrysts in a fine-grained plagioclase groundmass. Unit 3A commonly displays a moderate to strong trachytic (Unit 3A<sub>T</sub>; Fig. 4.3A) or a square crystal texture (Unit 3A<sub>S</sub>; Fig. 4.3B). The feldspar-phyric trachyandesite contains 30 to 50 % blocky to tabular feldspar phenocrysts and less than 30 % tabular, euhedral biotite and columnar hornblende crystals. Xenoliths of the equigranular monzodiorite are observed in this rock type (Fig. 4.3K). Coherent domains have gradational contacts towards monomictic (Unit 3B), trachyandesitic breccias (Unit 3C). Unit 3A<sub>T</sub> and 3A<sub>S</sub> are part of Group C geochemistry whose petrography, geochemistry and description of this rock type were described in Chapter 3.

##### *4.3.3.2 Unit 3B - Monomictic Breccias*

The monomictic breccia ranges from a weak clastic texture in an igneous matrix to jigsaw-fit texture and is clast-supported to weakly clast-supported (Figs. 4.3C and F). The clasts are typically less than 4 cm, angular (Figs. 4.3C and D) to cusped (Figs. 4.3E and F) and are sparsely to highly porphyritic. The unit cannot be easily distinguished between a clastic or coherent rock (Fig. 4.3D). The monomictic breccia clasts are feldspar-phyric trachyandesite (Unit 3A) in composition with minor proportions

## Unit 2: Monzodiorite to diorite

### Description

**Distinguishing Features:** Equigranular plagioclase, clinopyroxene, biotite, magnetite and hornblende.

**Distribution:** Crop out to the northwest of Cerro la Mina, fine-grained in the southwest block and commonly occurs as clasts in Unit 4.

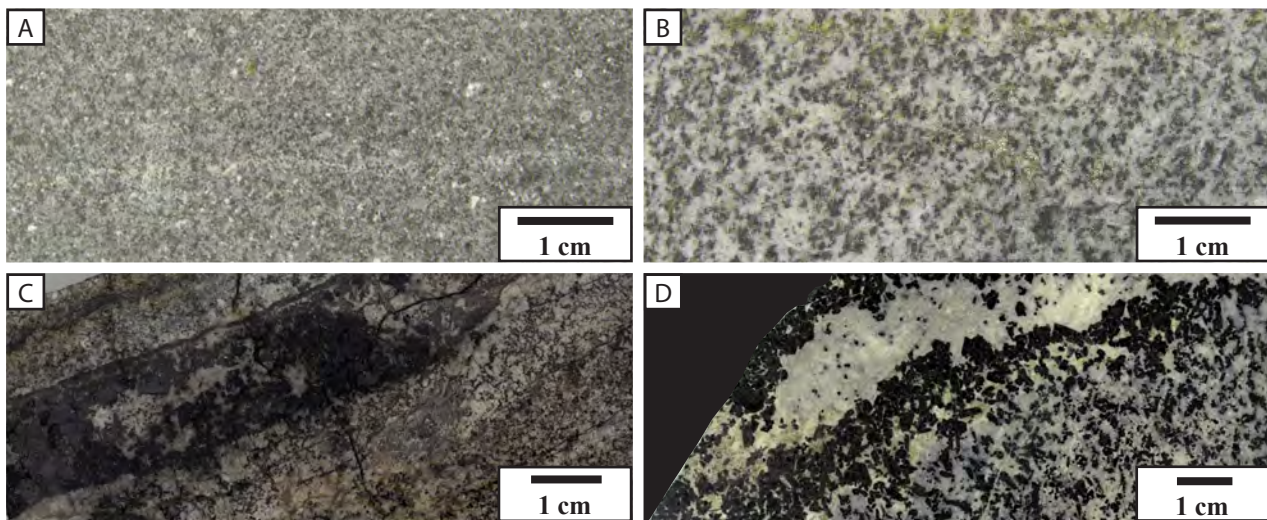
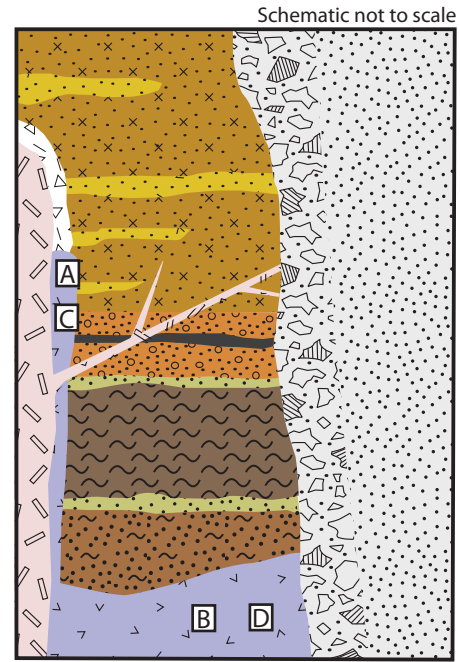


**Figure 4.2** Characteristics of monzodiorite to diorite intrusions (Unit 2). **A.** Fine grained, equigranular monzodiorite. **B.** Coarse grained, equigranular monzodiorite. **C.** Magnetite-plagioclase vein in a monzodiorite. **D.** Plagioclase - biotite - clinopyroxene - hornblende vein in a coarse-grained monzodiorite. Legend for stratigraphic column in Figure 4.14. **Sample ID:** A. IXCM08-55 183.7, B. IXCM08-55 275.3, C. IXCM08-55 170.6, D. IXCA08-16 137.5.

of fine-grained lithic and aphanitic clasts. Unit 3B is generally intensely altered, especially the matrix, which is gradational into polymictic, matrix-supported domains of Unit 3C over a distance of 0.30 to 25 m (Fig. 4.3G and H).

### 4.3.3.3 Unit 3C - Matrix-Supported Breccias

The fine- to coarse-grained polymictic matrix-supported rocks have clasts that are 0.5 to 5.0 cm with occasional oversized clasts (Figs. 4.3I and J). The fine- and coarse-grained facies clast size ranges from 0.5 to 1.0 cm and 1.0 to 5.0 cm, respectively. The clasts form 5 to 20% of the rock and are rounded to sub-angular. The clasts consist of predominantly aphanitic cream clasts, with lesser feldspar-phyric and minor fine-grained lithic clasts in a 1 to 2 mm matrix. The grain size of the rock changes sporadically and not in a regular manner, however, graded beds, thin volcanoclastic

sandstone (ash) layers (< 10 cm) and erosional surfaces are occasionally observed. The matrix-supported breccias occur distal to the monomictic breccias and coherent trachyandesite rocks. Outcrop photos of this rock type are shown in Figures 4.3L and M. In thin section Unit 3C has the same observations as described for Unit 1.

#### *4.3.4 Unit 4 - Breccia Complex*

Unit 4 cross-cuts all of the previous lithofacies and its distribution is in a vertical pipe orientation. Three lithofacies occur in Unit 4 comprising matrix-rich, granule breccia (Unit 4A), brecciated volcanic wall rocks (Unit 4B) and monomictic breccia (Unit 4C). The matrix-rich, granule breccia (Unit 4A) is the most voluminous rock and the less common polymictic and monomictic breccias occur distal to it. The core of the matrix-rich, granule breccia (Unit 4A) is dominantly granule (2 to 4 mm) and towards the margins the clast size and abundance increases (Unit 4B and 4C). Unit 4A is commonly strongly altered and mineralised and is the most difficult unit to identify because of intense alteration.

##### *4.3.4.1 Unit 4A - Matrix-Rich, Granule Breccia*

Unit 4A is fine-grained (< 4mm), massive, moderately sorted with occasional oversized clasts (Figs. 4.4A to C). This lithofacies is strongly altered by all stages of alteration (predominately kandite alteration) and occasionally there is an unaltered glimpse of primary textures (Fig. 4.4A). The rock contains grains < 4 mm and occasionally clasts of rounded to sub-angular equigranular monzodiorite to diorite (Unit 2) up to 5 cm diameter (Fig. 4.4C). The matrix-rich, granule breccia is well sorted with angular to sub-rounded plagioclase grains typically less than 500  $\mu\text{m}$  in a fine-grained matrix < 50  $\mu\text{m}$  (Fig. 4.4D). In thin section, drill core and outcrop the rock commonly displays lineations. From drill core and outcrop observations these lineations are sub-vertical (Figs. 4.5A to C). Thin section observations indicate that the plagioclase grains are generally (or weakly) aligned (Fig. 4.5A). Megacrystic monzodiorite clasts (Figs. 4.4I and J) are commonly observed in Unit 4A. The clasts are a megacrystic version of Unit 2 with plagioclase, biotite, clinopyroxene, magnetite and hornblende. Clusters of potassium feldspar - plagioclase - quartz grains (< 3 mm) also occur in this rock type (Fig. 4.6).

##### *4.3.4.2 Unit 4B - Brecciated Volcanic Wall Rocks*

Unit 4B comprises clasts of Units 1 to 3, but is predominantly clasts of Unit 3 (matrix-supported breccias). The clasts range from pebble (4 to 64 mm) to boulder (> 256mm), and has a matrix that is typically < 4 mm (Fig. 4.4E). The clasts are sub-rounded to angular and comprise predominantly aphanitic, cream, feldspar-phyric trachyandesite, equigranular monzodiorite, clasts within a clast and minor fine-grained lithic clasts in. A xenolith of a fiamme breccia in contact with a monzodiorite to diorite (Unit 2) is observed in this unit (Fig. 4.4F). Distinguishing between Unit 3C and Unit 4B is difficult especially where there is strong clay alteration and intense fracturing. Even where the drill core is reasonably intact it is rarely possible to be certain about identification. However, the lithofacies can sometimes be distinguished from Unit 3C by clasts within a clast (Fig. 4.4E) and clasts of coarse-

### Unit 3: Trachyandesite coherent rocks and matrix-supported breccias

**Subunits:** Unit 3A<sub>r</sub> and 3A<sub>s</sub>: Feldspar-phyric trachyandesite

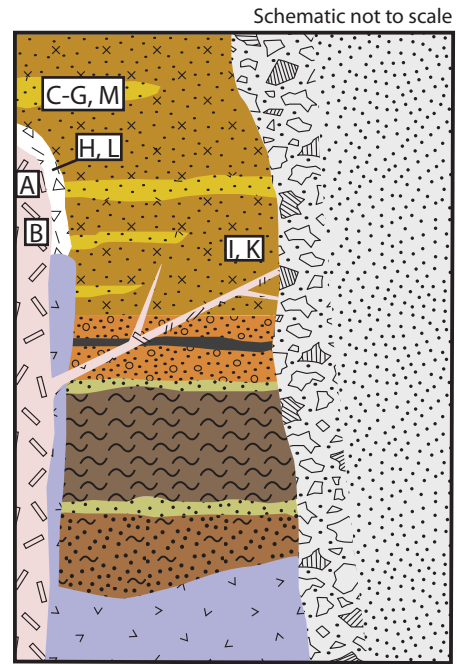
Unit 3B: Monomictic breccias

Unit 3C: Matrix-supported breccias

#### Description

**Distinguishing Features:** Unit 3A - a coherent feldspar-phyric rock. Unit 3B - monomictic breccia of feldspar-phyric clasts. Unit 3C - Matrix-supported polymictic breccia with abundant matrix.

**Distribution:** The southwest block. Unit 3C is the most voluminous rock unit at Cerro la Mina.



## Unit 3 continued

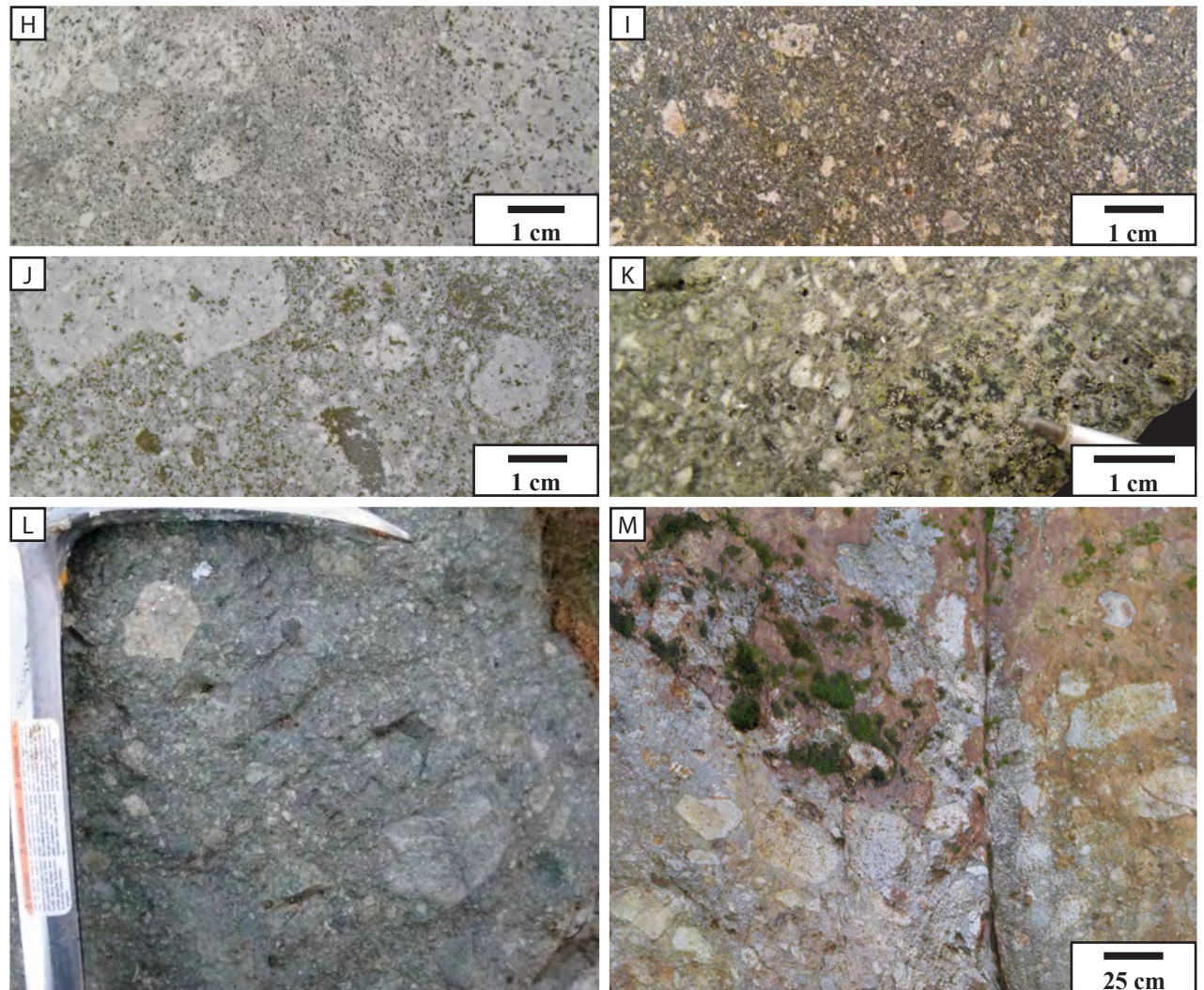


**Figure 4.3 (this and opposite page)** Characteristics of trachyandesite coherent rocks and matrix-supported breccias (Unit 3). **A.** Square feldspar trachyandesite. **B.** Trachytic, feldspar trachyandesite. **C.** Hematite cemented monomictic breccia of square feldspar trachyandesite with angular clasts. **D.** Monomictic breccia of square feldspar trachyandesite. **E/F.** Monomictic breccia of cusped sparsely porphyritic trachyandesite clasts in a fine-grained matrix. **G.** Monomictic breccia becoming increasing polymictic distal to plagioclase phyric trachyandesite (left to right). **H.** Transition right to left from coherent feldspar-phyric trachyandesite to a sparse monomictic breccia of square feldspar-phyric trachyandesite. **I.** Fine-grained matrix-supported breccia. **J.** Coarse-grained matrix-supported breccia. **K.** Xenolith of monzodiorite in a square feldspar-phyric trachyandesite. **L.** Outcrop photo of fine-grained matrix-supported breccia. **M.** Outcrop photo of coarse-grained, matrix-supported breccia. Legend for stratigraphic column in Figure 4.14. **Sample ID:** A. IXCM08-58 280.0, B. IXCM08-55 167.3, C. NJ08IX-500, D. IXCM08-58 173.2, E. IXCM08-63 194.9, F. IXCM08-63 201.4, G. IXCM08-63 245.3, H. IXCM08-63 259.6, I. IXCM08-45 42.9, J. IXCM08-63 30.4, K. IXCM08-58 308.7, L. Outcrop near drill hole collar IXCM08-62, M. Outcrop near drill hole collar IXCM08-63.

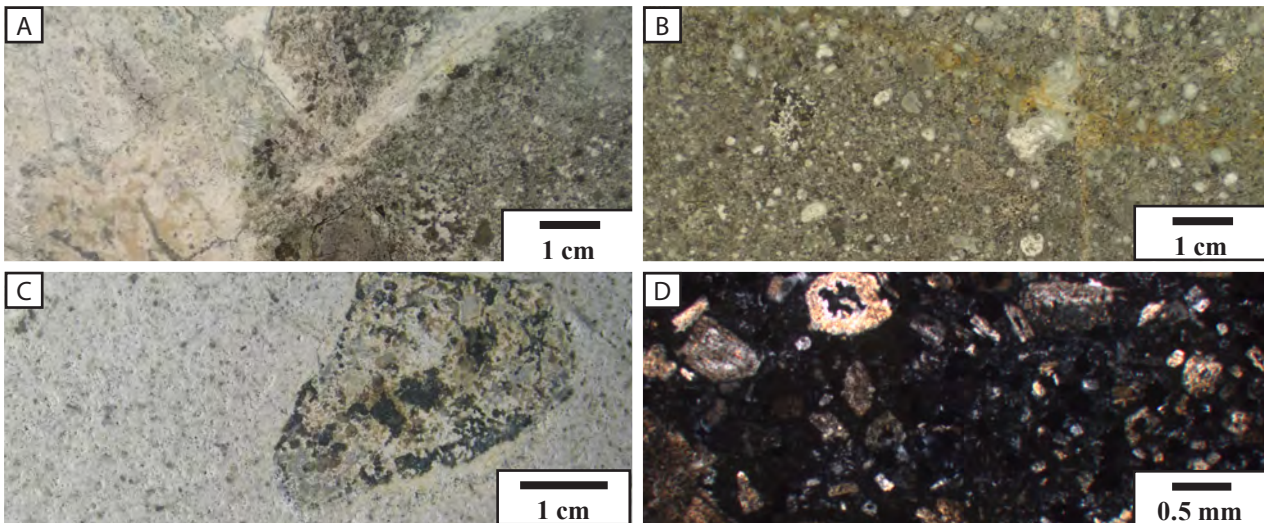
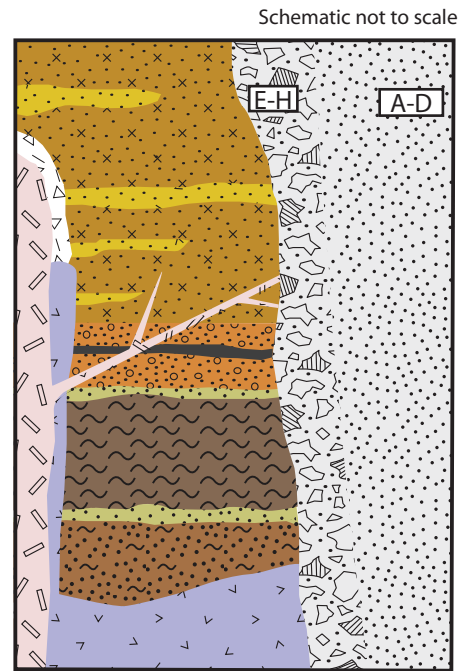
## Unit 4 - Breccia complex

- Subunits:** Unit 4A - Matrix-rich granule breccia  
 Unit 4B - Brecciated volcanic wall rocks  
 Unit 4C - Monomictic breccia

### Description

**Distinguishing Features:** Unit 4A - Fine-grained granule breccia with abundant clasts of Unit 2. Unit 4B has a similar texture to Unit 3C and distinguished by the occurrence of clasts within clasts. Unit 4C is distinguished by monomictic breccia on the breccia pipe rim.

**Distribution:** Vertically orientated with Unit 4A in the core and Units 4B and 4D distal.



grained equigranular dacite (Unit 2; Fig. 4.4F). Additionally, occasional graded beds, ash layers and erosional surfaces are observed in Units 1 and 3 but are absent in Unit 4B.

### 4.3.4.3 Unit 4C - Monomictic Breccia

Localized rare monomictic breccias occur on the margins of the matrix-rich, granule breccia (Unit 4A). The clasts are angular from chaotic to jig-saw fit texture and less than 2 cm in diameter. The clasts are monzodiorite to diorite (Unit 2; Fig. 4.4G) or feldspar-phyric trachyandesite clasts in a fine-

## Unit 4 continued

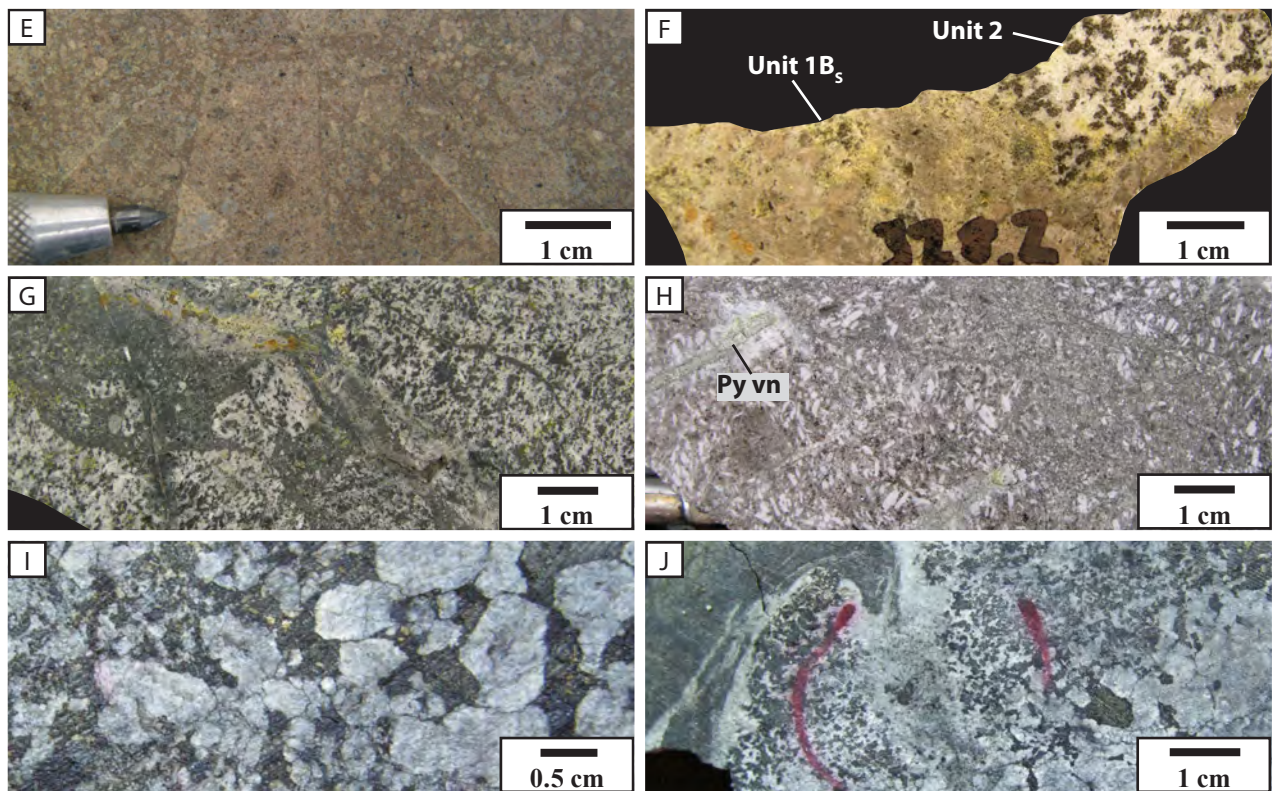


**Figure 4.4 (this and opposite page)** Characteristics of the breccia complex (Unit 4). **A.** Massive matrix-rich, granule breccia with cross-cutting kandite alteration. **B.** Massive matrix-rich, granule breccia. **C.** Kaolin altered matrix-rich, granule breccia with clast of monzodiorite. **D.** Transmitted light image of matrix-rich, granule breccia showing fine-grained nature of rounded and angular feldspar grains. **E.** Brecciated matrix-supported breccia highlighting a clast within an angular clast. **F.** Xenolith of a fiamme breccia (unit 1B<sub>s</sub>) and monzodiorite to diorite (unit 2) observed in Unit 4. **G.** Monomictic breccia of monzodiorite. **H.** Monomictic breccia showing pyrite veins cut by margin of clast. **I.** A large coarse-grained monzodiorite clast in the matrix-rich, granule breccia. **J.** Irregular contact of monzodiorite and matrix-rich, granule breccia. Red lines are marker. Legend for stratigraphic column in Figure 4.14. **Sample ID:** A. IXCM07-29 111.2, B. IXCM07-29 114.5, C. IXCM08-61 363.0, D. IXCM08-47 139.8, E. IXCM07-34 87.1, F. IXCM07-26 328.2, G. IXCM08-55 275.3, H. IXCM08-52 188.0, I. IXCM07-20 750.6, J. IXCM07-20 720.6.

grained matrix (Unit 3A; Fig. 4.4H). The monomictic breccias of Unit 3B and Unit 4C can only be distinguished by the occurrence of pyrite veins cut by the clast margin (Fig. 4.4H).

## 4.4 Lithofacies Distribution

### 4.4.1 Surface Geology

Figure 4.7A shows the surface geology for the Cerro la Mina prospect based mostly on the upper 50 m of drill holes (due to limited outcrop) and regional mapping by Martinez Lopez, (2009). The geology is separated into a southwest block and a northeast block by a northwest trending sinistral fault.

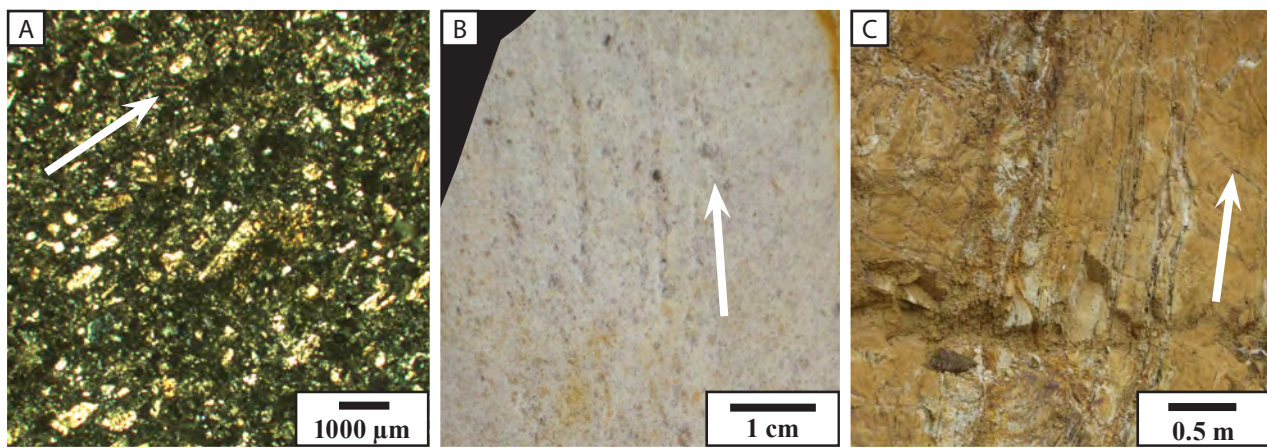


**Figure 4.5** Images of lineations seen in the matrix-rich, granule breccia in thin section, drill core and outcrop. **A.** Thin section image showing a weak alignment of plagioclase grains. **B.** Lineations seen in a drill core sample. **C.** Lineations observed at outcrop scale. **Sample ID:** A. IXCM08-51 285.6, B. IXCM06-08 28.8, C. Outcrop near drill hole collar XCM08-51.

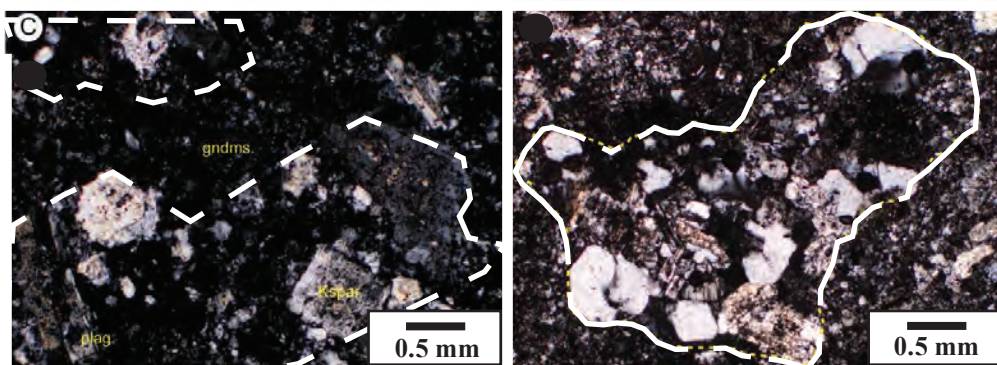


**Figure 4.6** Fine-grained zones of quartz - potassium feldspar - plagioclase. Modified from Harris (2006)

The southwest block is predominantly matrix-supported breccias (Unit 3), whereas the northeast block is fiamme breccias (Unit 1). Unit 4 forms a circular shape at the surface which has been split in half, as it is offset by the sinistral northwest fault (Fig. 4.7A). The surface distribution of Unit 4 in the northeast block has been inferred from deep drill holes (IXCM07-41, IXCM07-43 and IXCM08-63), and from the aeromagnetic image (Fig. 4.7B) as there is no outcrop information at the surface. The surface distribution of Unit 4 corresponds to an oblique circular topographical feature on the surface (Fig. 4.8). The off-set created by the northwest fault can also be observed in the aeromagnetic image (Kinross Gold, 2008) where magnetic highs are off-set by approximately 200 m (Fig. 4.7B). A monzodiorite to diorite intrusion crops out to the northwest of the Cerro la Mina prospect and associated with a magnetic high.

#### 4.4.2 Cross Sections

Four cross sections were developed throughout the prospect to describe the geology (Figs. 4.9 to 4.12). Three cross sections (A to C) are situated mostly in the southwest block, from distal to proximal locations relative to the intense alteration and one cross section (D) in the northeast block. A long section (E) combines cross sections A to C in the southwest block to better illustrate the geology of

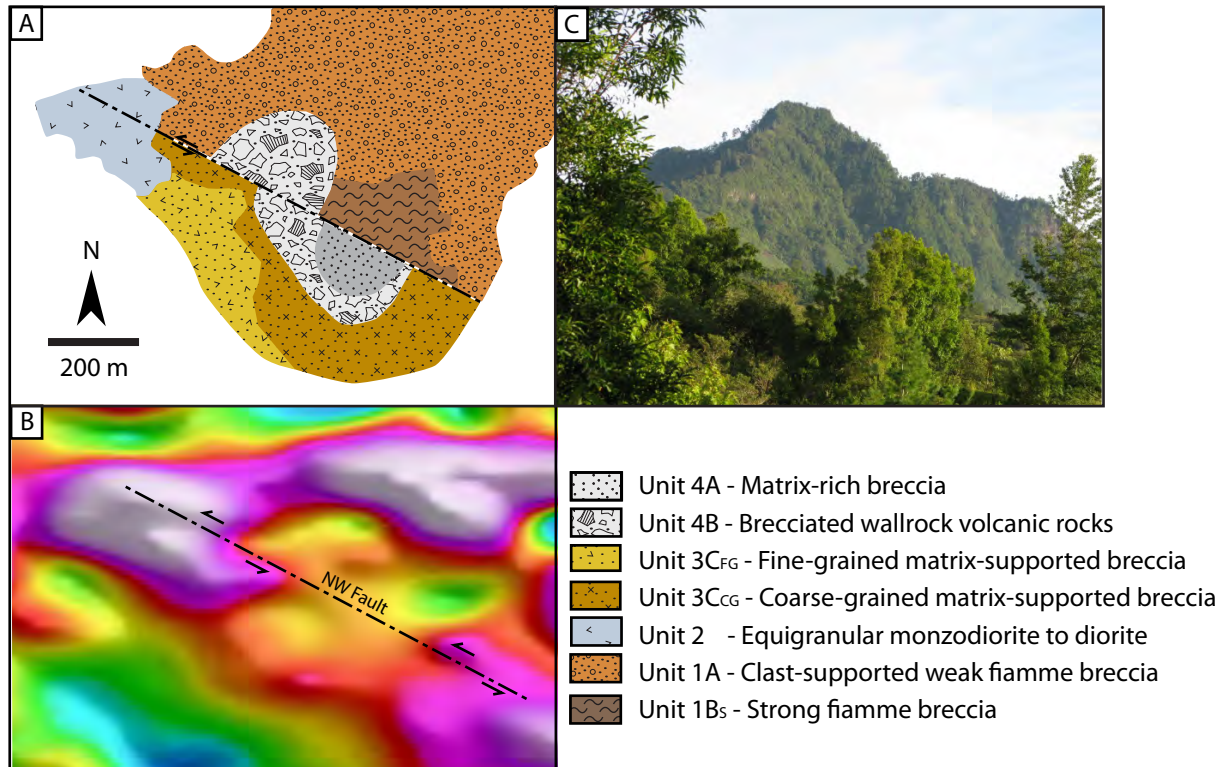


**Figure 4.7** Surface geology and aeromagnetic image of the Cerro la Mina prospect. **A.** Plan view of the surface geology for the Cerro la Mina prospect. A northwest fault off-sets the geology. The map is based on mapping by author and Martinez Lopez (2009). **B.** Aeromagnetic image of the Cerro la Mina prospect showing the off-set of magnetic highs created by the northwest fault. Modified from Kinross Gold (2008). **C.** Landscape photo looking south from Laguna Chica village.

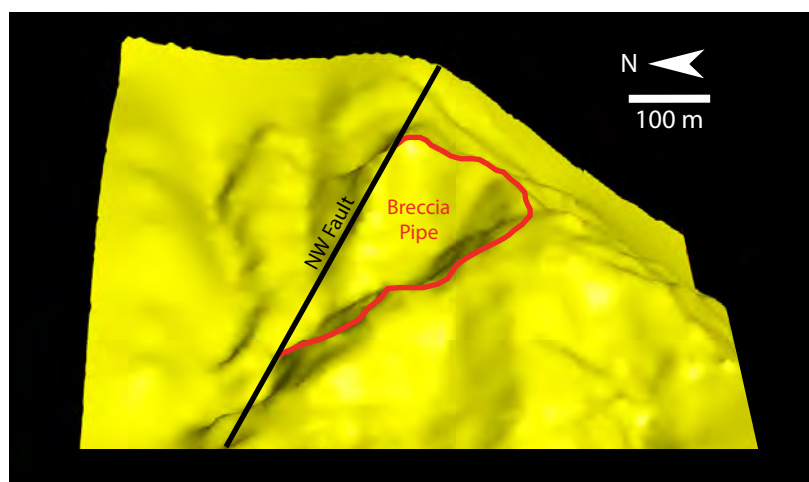


**Figure 4.8** Topography image of Cerro la Mina. Modified after Kinross (2008b). The limit of the breccia pipe (Unit 4) shown in red corresponds to an oblique circular topographical feature that is cut by the northwest fault.

the Cerro la Mina prospect (Fig. 4.13)

Cross section A-A' is based on one drill hole located distal to the intense alteration (Fig. 4.9). The geology is broken by the northwest fault where abundant matrix-supported breccias (Unit 3C) and coherent trachyandesite (Unit 3A) with their associated monomictic breccias (Unit 3B) occur to the southwest and a matrix-rich, granule to brecciated volcanic wall rocks (Unit 4B) occurs northeast of the fault.

Cross section B-B', situated distal to the intense clay alteration, is based on four drill holes (Fig. 4.10). The south-western block comprises a thick sequence of fine- to coarse-grained matrix-supported breccias (Unit 3C) with feldspar-phyric trachyandesite (Unit 3A) and associated monomictic breccias (Unit 3B). Cross section B-B' illustrates that the feldspar-phyric trachyandesites are vertically orientated and are not laterally continuous. A matrix-rich, granule to brecciated volcanic wall rock (Unit 4) crosscuts the stratigraphy in a vertical orientation. The matrix-rich, granule breccia (Unit 4A) dominates in the core and becomes increasing clast-rich (Unit 4B) towards the southwest and closer to the matrix-supported breccia (Unit 3C). A xenolith occurs in Unit 4B containing the contact between fiamme breccia (Unit 1B<sub>s</sub>) and the monzodiorite to diorite (Unit 2; Figs. 4.4F and 4.10). Unit 4A in this cross section is weakly altered and its distribution is easily observed. The northwest fault cross-cuts the stratigraphy indicated by a change in lithology from a matrix-rich, granule breccia (Unit 4A) to a moderate fiamme breccia (Unit 1B).

Cross section C-C', located in moderate to intense clay alteration, is based on 12 drill holes (Fig. 4.11). The cross section illustrates the vertical orientation of the matrix-rich, granule breccia (Unit 4A) and the occurrence of matrix-supported breccias (Unit 3C) in the southwest block. The matrix-rich, granule breccia (Unit 4A) dominates in the core and becomes increasing clast-rich towards the southwest and closer to the matrix-supported breccia (Unit 3C). The distribution of the matrix-rich, granule breccia (Unit 4A) in cross section C-C' is largely interpreted due to strong alteration. Unit 4A is inferred to occur here because of its distribution in nearby cross section B-B', its occurrence on the margins of intense alteration; and it is occasionally observed in weaker altered zones in the intense alteration. The northwest fault cross-cuts the stratigraphy with a change in lithology from the matrix-rich, granule breccia (Unit 4A) to a moderate fiamme breccia (Unit 1B<sub>M</sub>).

Cross section D-D' illustrates the geology of the northeast block (Fig. 4.12) which was crucial in delineating the location of the northwest fault, as these rock types were encountered when crossing the fault from the southwest (Figs. 4.10 and 11). The cross section contains clast-supported (Unit 3A) to fiamme breccias (Unit 3B) that are interbedded with volcanoclastic sandstone (Unit 3C) and a rare basalt flow (Unit 3D). Unit 3A occurs as feldspar-phyric dykes cross-cutting the stratigraphy in the northeast block (Fig. 4.12) contrary to its occurrence as distinct intrusions in the southwest block (Figs. 4.9 to 4.11).

Long section E-E' (Fig. 4.13) illustrates the overall geology of Cerro la Mina with a lower succession of fiamme breccias (Unit 1) overlain by thick intervals of Unit 3C and associated trachyandesite feldspar-phyric intrusions (Unit 3A) and monomictic breccias (Unit 3B). The volcanic rocks

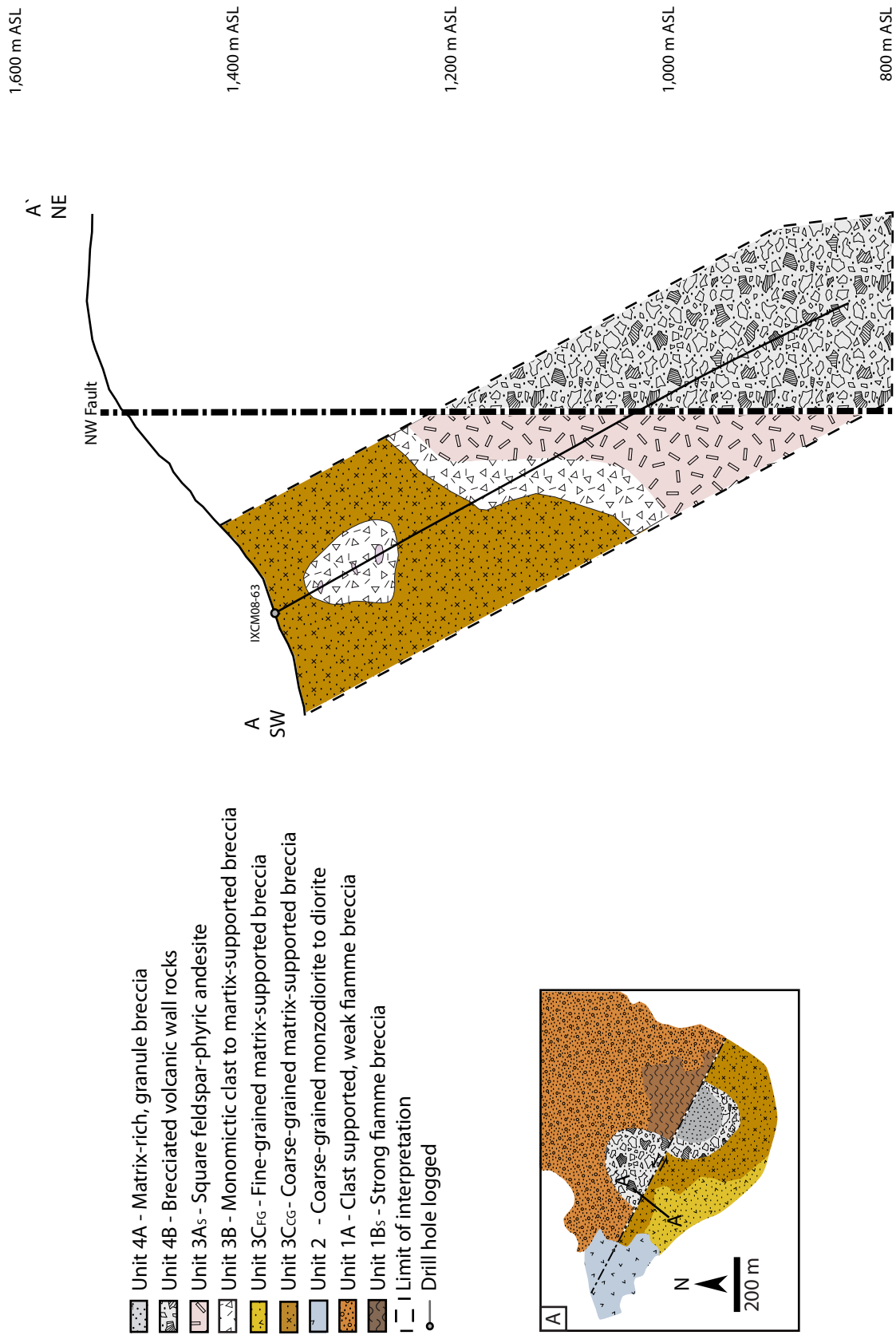
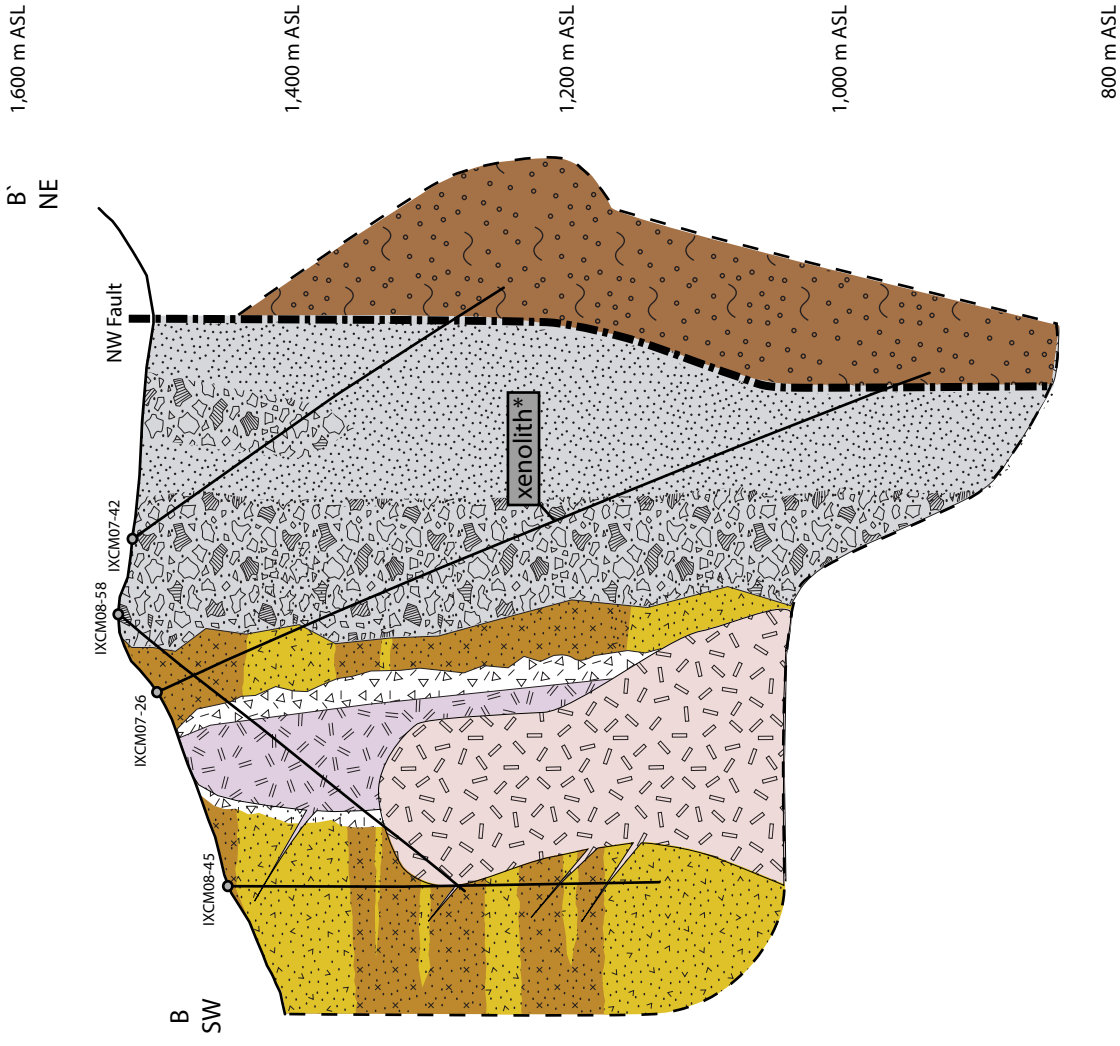


Figure 4.9 Geology of cross section A-A'. Cross section location shown on plan view in inset A.



- Unit 4A - Matrix-rich, granule breccia
- Unit 4B - Brecciated volcanic wall rocks
- Unit 3A<sub>T</sub> - Trachytic, feldspar-phyric andesite
- Unit 3A<sub>S</sub> - Square feldspar-phyric andesite
- Unit 3B - Monomictic clast to matrix-supported breccia
- Unit 3C<sub>FG</sub> - Fine-grained matrix-supported breccia
- Unit 3C<sub>CG</sub> - Coarse-grained matrix-supported breccia
- Unit 2 - Coarse-grained monzodiorite to diorite
- Unit 1A - Clast supported, weak flame breccia
- Unit 1B<sub>M</sub> - Moderate flame breccia
- Unit 1B<sub>S</sub> - Strong flame breccia
- Limit of interpretation
- Drill hole logged

Xenolith\* - Unit 1Bs in contact with unit 2 (Fig. 4.4F)

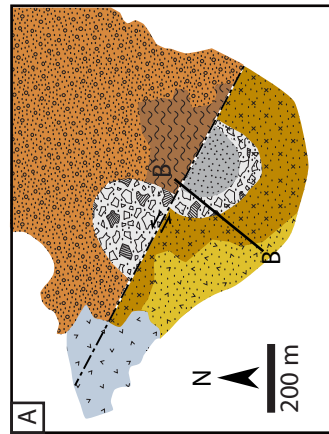


Figure 4.10 Geology of cross section B-B'. Cross section location shown on plan view in inset A.

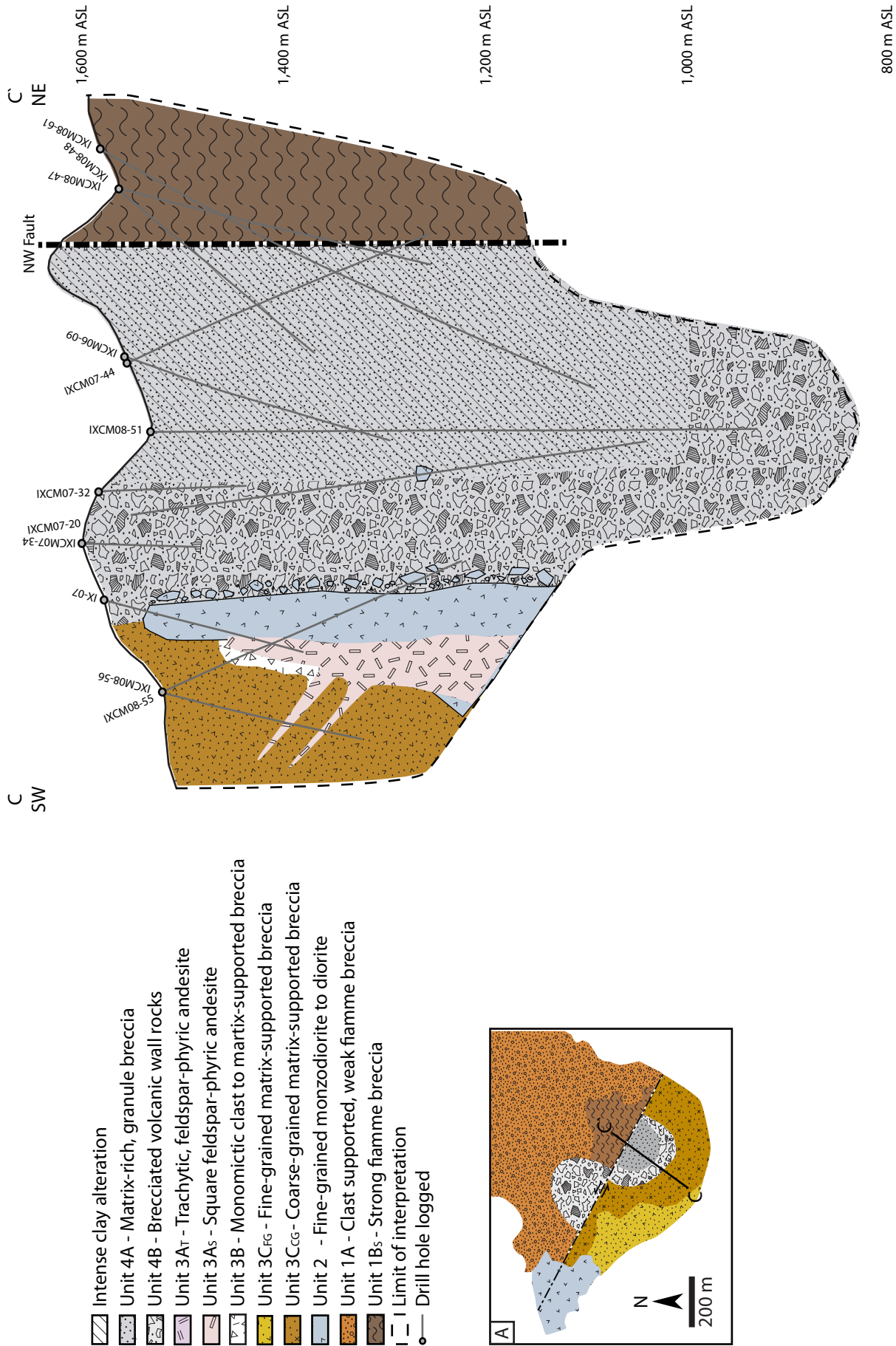
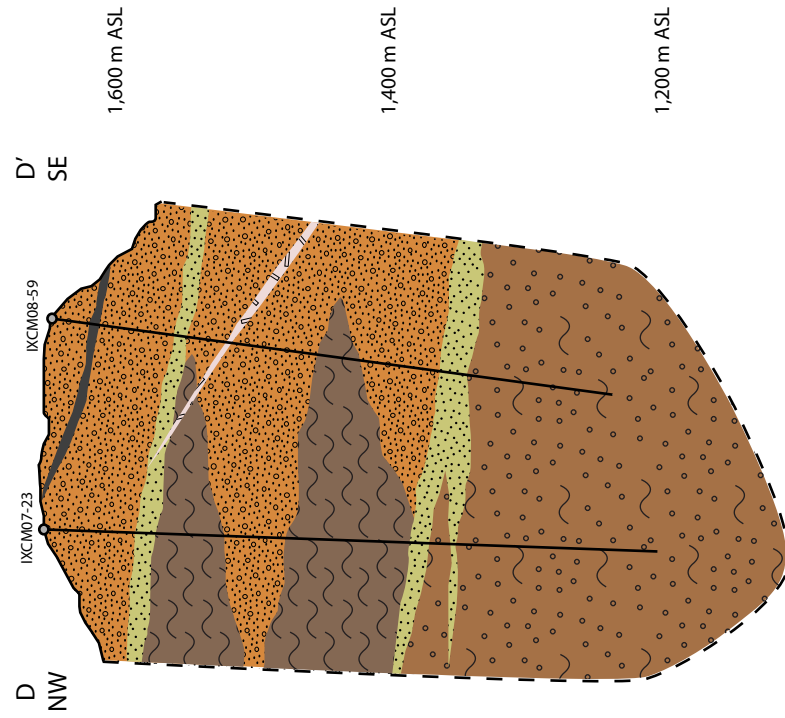


Figure 4.11 Geology of cross section C-C'. Cross section location shown on plan view in inset A.



- Unit 4A - Matrix-rich, granule breccia
- Unit 4B - Brecciated volcanic wall rocks
- Unit 3As - Square feldspar-phyric andesite
- Unit 3CEG - Fine-grained matrix-supported breccia
- Unit 3CCG - Coarse-grained matrix-supported breccia
- Unit 2 - Coarse-grained monzodiorite to diorite
- Unit 1A - Clast supported, weak flame breccia
- Unit 1BM - Moderate flame breccia
- Unit 1Bs - Strong flame breccia
- Unit 1C - Volcanoclastic sandstone
- Unit 1D - Basalt
- Limit of interpretation
- Drill hole logged

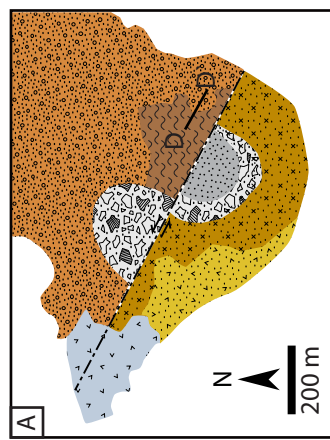


Figure 4.12 Geology of cross section D-D'. Cross section location shown on plan view in inset A.

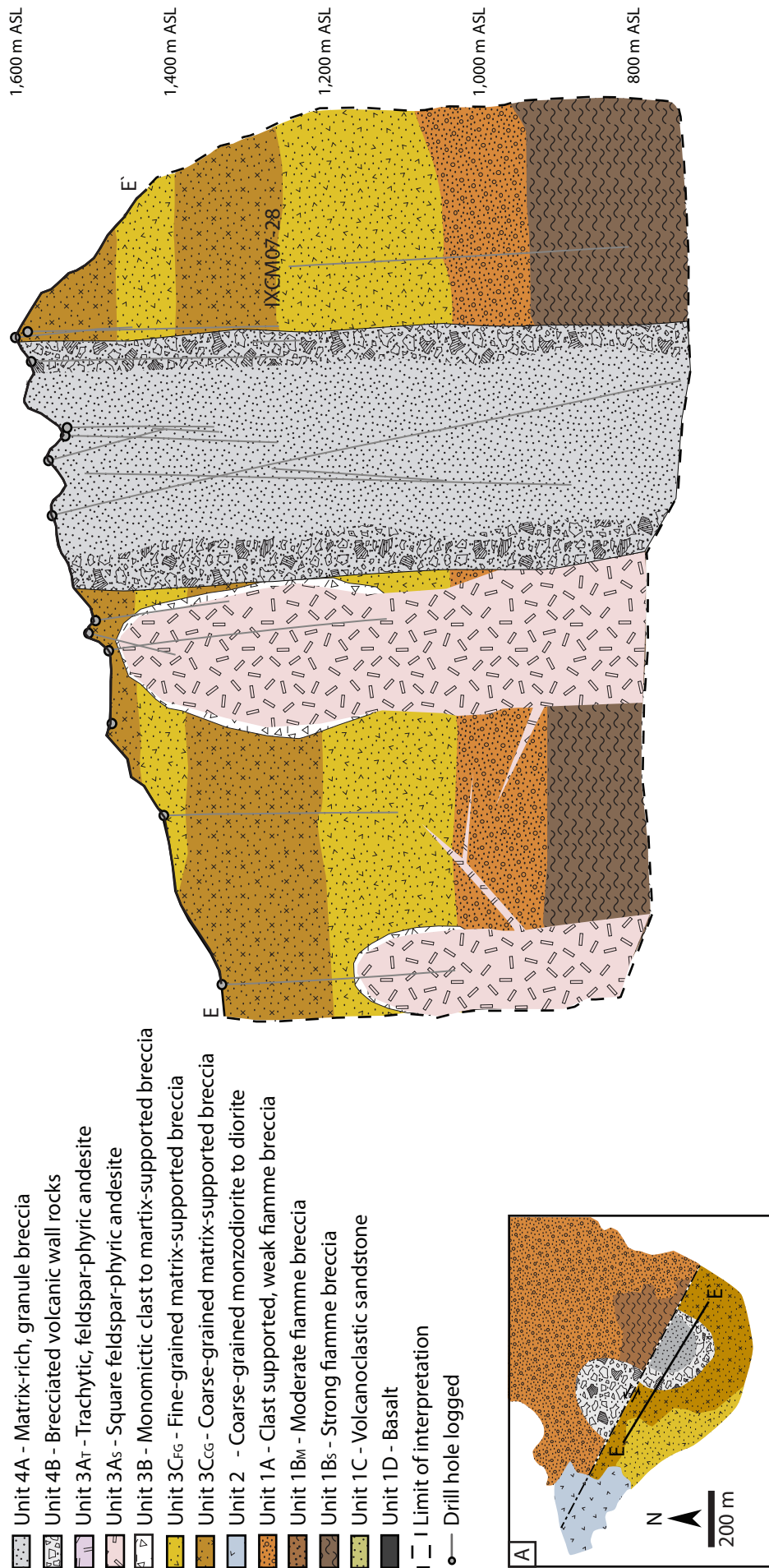


Figure 4.13 Geology of long section E-E'. Long section location shown on plan view in inset A.

are crosscut by a vertically orientated breccia pipe complex (Unit 4).

## 4.5 Structure

Structures at Cerro la Mina comprise fault gouge, fractured rock and slicken slides. The strongly, fractured nature of the volcanic rocks at the Ixhuatán concession is confirmed by an average drill core recovery of 78% for all diamond drilling. No structural observations (i.e. orientated core) were recorded by company geologists. The general homogeneity and lack of marker horizons in the host volcanic rocks and the intensity of alteration make structural off-sets of stratigraphy difficult to observe.

One major northwest fault was recognized by change in lithology. The fault is typically recognized with a change from a matrix-supported breccia (Unit 3C) to a fiamme breccia (Unit 1B) when drilling in a northeast direction. This fault breaks the prospect into southwest and northeast blocks. The orientation of the northwest fault was calculated using a three point calculation of a plane using drill hole intercepts of the fault. The northwest fault has a strike orientation of 308° and is sub-vertical. The fault has sinistrally offset the stratigraphy by approximately 200 m horizontally, as indicated by spatial distribution of lithology and on an aeromagnetic image (Figs. 4.7A and B). Logging of a deep drill hole in the southwest block (IXCM07-28) indicates that the matrix-supported breccia (Unit 3C) overlies the fiamme breccia (Unit 1) suggesting approximately 500 m of vertical movement on the fault. Structures (fault gouge, slicken-slides, fractured core) increase in abundance closer to the northwest fault. These structures commonly host mineralisation suggesting a pre- or syn-mineralisation timing for the deformation. The mineralisation and alteration are offset suggesting movement on the fault post mineralisation.

## 4.6 Discussion

### 4.6.1 Genetic Interpretation

The geology of the Cerro la Mina prospect was divided into four major units and described with non-genetic terminology. The genetic interpretation of the volcanic rocks is discussed here to determine the volcanic setting.

The lower succession of fiamme breccias (Unit 1) is interpreted to be an ignimbrite (pyroclastic deposits; Units 1A and 1B) interbedded with air fall deposits (Unit 1C) and basalt flows (Unit 1D). Unit 1B displays eutaxitic textures but is too altered to distinguish between a welding or diagenetic compaction origin. An equigranular monzodiorite to diorite (Unit 2) intrudes a fiamme breccia (Unit 1B) as observed in a xenoliths occurring in Unit 4B. The overlying coherent feldspar-phyric trachyandesite (Unit 3A) and associated monomictic breccias (Unit 3B) are interpreted to be a syn-volcanic intrusion or dome with associated autobreccia margins, respectively. The occurrence of abundant blocky angular clasts and granulated aggregates is consistent with the fracturing, quench fragmentation and auto-brecciation of a dome. Unit 3B transitions to distal thick beds of matrix-supported breccias (Unit 3C). Unit 3C is matrix-rich and has rare gradational zones indicating movement via mass flow processes. The coarse nature, poor sorting and large volumes of the breccia reflects a high

supply rate of clasts. The little to moderate amount of clast abrasion and reworking indicates that the material was generally rapidly deposited. Unit 3C probably represent debris and mass flows (lahar) of mixed provenance.

Unit 4 distribution comprises an inner core of matrix-rich, granule breccia (Unit 4A) and outer zone of brecciated volcanic wall rocks (Unit 4B) and monomictic breccias (Unit 4C). Xenoliths of Units 1 to 3 occurring in Unit 4 suggests that this Unit cross-cuts the wall rock stratigraphy. The abundance of monzodiorite to diorite (Unit 2) clasts suggests a deep source for the clasts, probably from the basement where Unit 2 is abundant. Unit 4 is recognized at various elevations from the surface to the maximum drill hole depth of 800 m (Figs. 4.9 to 4.13) and a circular distribution at the surface (Figs. 4.7) implying a vertical pipe-shaped emplacement. Unit 4 is therefore inferred to be a breccia pipe formed by the explosive release of hydrothermal fluids from an inferred intrusion at depth causing brecciation of the overlying rocks. The distribution of facies in Unit 4 suggests a higher energy in the core with complete brecciation of the rock to a granule size (Unit 4A). The brecciation becomes weaker closer to the wall rocks with increasing size of clasts (Units 4B and C). The lineations in Unit 4A are sub-vertical suggesting vertical movement.

The distribution of Unit 4 has cylindrical shape that is evidenced in the topography of Cerro la Mina (Fig. 4.8). The topographical feature probably formed as a result of the intense clay alteration making the breccia pipe more susceptible to erosion than the less altered surrounding volcanic wall rocks. The stratigraphy is offset by a major northwest fault that has an orientation and movement consistent with the regional left-lateral strike-slip structural regime in which it occurs as discussed in Chapter 2 (Fig. 2.2; Meneses-Rocha, 2001; García-Palomo et al., 2004).

#### 4.6.2 Paragenesis

The paragenesis of the rock units is determined from stratigraphic position and rock textures. Matrix-supported breccias (Unit 3C) are observed to overlie fiamme breccias (Unit 1) in a single deep drill hole on the southwest block (Fig. 4.13; IXCM07-28). The contact between the fiamme breccia (Unit 1) and the monzodiorite (Unit 2) has not been intercepted in drilling but is observed in a xenoliths of Unit 4 where a fiamme breccia (Unit 1B<sub>s</sub>) is in contact with a monzodiorite to diorite (Unit 2) suggesting that Unit 2 has intruded Unit 1 (Fig. 4.4F). The late, feldspar-phyric trachyandesite (Unit 3A) contain xenoliths of the earlier equigranular monzodiorite to diorite (Unit 2; Fig. 4.3K). Unit 4 contains clasts of Units 1 to 3 suggesting Unit 4 is the youngest rock unit. A stratigraphy column is provided in Figure 4.14 illustrating the paragenetic relationships of the four units.

#### 4.6.3 Interpretations of other Authors

Unit 4A is difficult to observe and much of its distribution is interpreted. Despite occasional textures reflective of Unit 4 being observed in the intense alteration it is possible that other rock types could occur in the intense clay alteration. Cumming (2008) suggests evidence for a flow banded dacite which could explain the lineations in Unit 4A, however, the author favours a breccia pipe interpretation, as there is no flow banded dacite observed in unaltered rocks or elsewhere in the district.

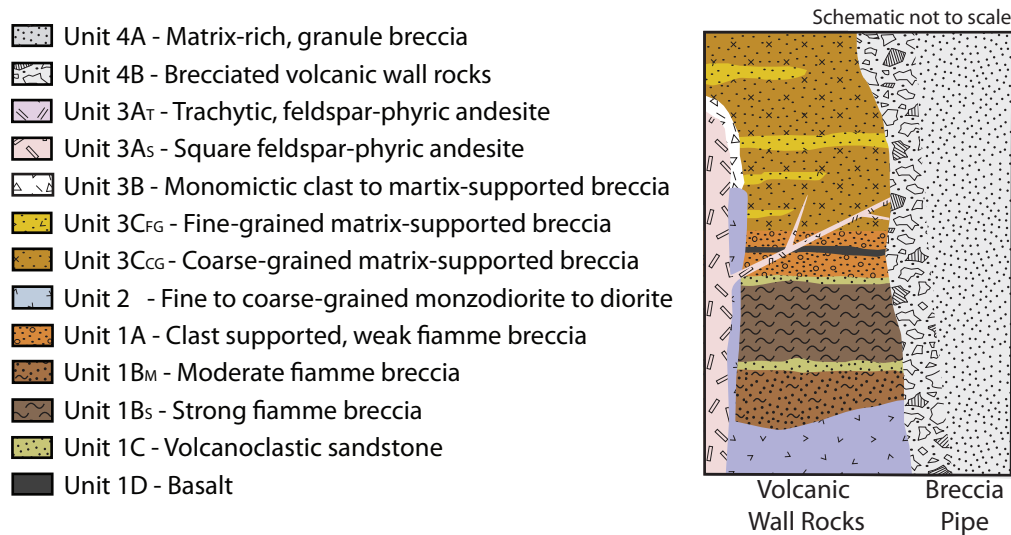


**Figure 4.14** Cerro la Mina stratigraphic column illustrating the paragenesis of the volcanic stratigraphy.

Fine-grained zones (< 5 mm) of quartz - potassium feldspar - plagioclase observed in Unit 4A was interpreted by Harris (2007) as miarolitic cavities comprising euhedral intergrowths of quartz and feldspar surrounded by finer graphic quartz–alkali feldspar intergrowths. Interconnected miarolitic cavities have been recognized in intrusions related to porphyry Cu mineralisation (Harris et al., 2004). Pods of saccharoidal quartz are connected by narrow, anastomosing zones of graphic quartz–alkali feldspar intergrowths and ragged biotite with lesser apatite and magnetite (Harris et al., 2004). In contrast, the interpretation in this thesis is that these textures are clasts in the matrix-rich, granule breccia and not miarolitic cavities (Fig. 4.6).

#### 4.6.4 Geologic Setting

The Cerro la Mina stratigraphy dominantly comprises ignimbrites (Unit 1), syn-volcanic intrusions (Unit 3A and 3B), debris and mass flows (Unit 3C) and is similar to the Campamento deposit volcanic rocks, as described in Chapter 2, that are thick beds of debris and mass flows (lahar) of mixed provenance and associated syn-volcanic domes. The only exception is a breccia pipe (Unit 4) which cross-cuts the stratigraphy at Cerro la Mina. The Campamento and Cerro la Mina stratigraphy (Fig. 2.9 and Fig. 4.14) does not suggest a central volcanic setting and implies that volcanism occurred in a relatively low relief, multiple-vent volcanic sedimentary rift basin or graben, a setting similar to the Bajo de la Alumbrera porphyry Cu-Au deposit (Harris et al., 2006). At Bajo de la Alumbrera sheet-like, laterally continuous debris-flows and other coarse-grained sedimentary deposits are dominant with volumetrically minor mafic-intermediate composition lavas (Harris et al., 2006). The geology of Cerro la Mina prospect and the Campamento deposit (Chapter 2) reflect the regional geology of the Chiapanecan volcanic arc including El Chichón volcano. The Chiapanecan volcanic arc volcanic rocks, consist of low profile, small-volume, volcanic domes with associated pyroclastic flow deposits with rare basalts, porphyritic hornblende trachyandesite and trachyandesite (Damon and Motesinos, 1978; Duffield et al., 1984; Mora et al., 2007).

The regional map of the Selva Negra volcanic rocks shows that there is a large intrusion flanked by concentric rims of volcanic rocks including the trachyandesite agglomerate/lavas capping the stratigraphy and also form the topography and resistant rock unit of the area (Fig. 3.1). This zonation may represent a volcanic edifice similar to El Chichón volcano. Geological interpretations suggests that Cerro la Mina developed on the flanks of volcano similar to El Chichón volcano and probably in a graben setting where there is large input of debris flows.

#### **4.7 Conclusions**

The Cerro la Mina stratigraphy was divided into four units. Fiamme breccias (Unit 1A, 1B) interpreted to be ignimbrites (pyroclastic deposits) are interbedded with air fall deposits (Unit 1C) and rare basalt flows (Unit 1D). Unit 1 is intruded by equigranular monzodiorite to diorite intrusions (Unit 2). Coherent feldspar-phyric trachyandesite (Unit 3A) and associated monomictic breccias (Unit 3B) are interpreted to be a syn-volcanic domes with associated autobreccia margins, respectively. Unit 3B transitions distally to thick massive beds of matrix-supported breccia (Unit 3C) which represent debris and mass flows of mixed provenance. Crosscutting the volcanic stratigraphy is a vertically orientated breccia pipe (Unit 4) formed by the explosive release of hydrothermal fluids from an inferred intrusion at depth causing brecciation of the overlying rocks.

A major fault with a strike orientation of  $308^{\circ}$  and sub-vertical offsets the stratigraphy by approximately 200 m horizontally and 500 m vertically. The northwest fault is consistent with the regional, left-lateral, strike-slip structural regime in which it occurs (Fig. 2.2; Meneses-Rocha, 2001; García-Palomo et al., 2004).

The geology the Cerro la Mina prospect and the Campamento deposit (Chapter 2) is consistent with the style of volcanism of the Chiapanecan volcanic arc including El Chichón volcano located 20 km to the northwest. The geology suggests that Cerro la Mina developed on the flanks of volcano similar to El Chichón volcano and probably in a graben setting where there was a large input of debris flows.



## Chapter 5 - Wall Rock Alteration

### 5.1 Introduction

The Cerro la Mina Au (Cu-Mo) prospect consists of porphyry-style alteration that is superimposed on by advanced argillic alteration. The porphyry style alteration consists of early quartz, potassium feldspar and biotite alteration (Stage A), and later quartz, muscovite, illite, illite/smectite, smectite, chlorite, calcite, gypsum, and tourmaline alteration (Stage B). The most evident and abundant alteration is the latest advanced argillic (Stage C) overprint which consists predominantly of the kandite group minerals halloysite, kaolinite and dickite and lesser pyrophyllite, alunite and kaolinite. The Stage C alteration is entirely hosted in the breccia pipe extending approximately 250 metres wide and 600 metres deep, turning the rock colour to uniformly grey-white. The occurrence of halloysite is traditionally regarded as supergene (e.g. Hedenquist, 2000), however at Cerro la Mina its occurrence is unusual due to its deep extent and association with sulfides that suggest a hypogene origin.

This chapter is divided into two parts. The first describes research methods, alteration assemblages, distribution followed by a discussion and paragenesis of the Cerro la Mina alteration. The second part will present detailed research on halloysite followed by a discussion. The chapter ends with a conclusion summarising the main points for the alteration at Cerro la Mina.

### 5.2 Research Methods

The alteration mineralogy was determined using thin section petrography, potassium feldspar staining, TerraSpec instruments, quantitative X-ray diffraction (QXRD) and scanning electron microprobe (SEM) methods.

#### 5.2.1 Graphic Core Logging

Graphic core logging methods for alteration and graphic logs are in Appendix I.1 and I.2.

#### 5.2.2 Petrographic Microscopy

Thin sections were made in the lapidary lab at the University of Tasmania for selected samples and petrographic observations were completed using a Nikon Labophot-2<sup>®</sup> Pol Standard Polarizing Microscope and an Olympus ColorView imaging system.

#### 5.2.3 Potassium Feldspar Staining

To determine whether potassium feldspar is present at Cerro la Mina, 43 samples were acid etched using hydrofluoric acid following the methods described in Bailey and Stevens (1960). Hydrofluoric acid was applied on the sample with a brush, removed and washed after 30 seconds, followed by a re-immersion in sodium cobaltinitrite ( $\text{Na}_3\text{Co}(\text{NO}_2)_6$ ) for roughly one minute. This process stains potassium feldspar to be bright yellow. Results and pictures of the potassium feldspar staining are shown in Appendix III.1.

### 5.2.4 TerraSpec Analyses

TerraSpec instruments were used to measure SWIR (Short Wavelength Infra-Red) spectra of rocks and characterize clay assemblages. This study contributed approximately 1000 samples (13,000 metres of drill core coverage) and 30 surface spectral samples to the database. The spectral database currently contains more than 200 surface samples and covers 19,929 metres of Cerro la Mina drill core (~1600 samples; 91% of total drilling).

The drill core was analysed every 10 to 20 metres. Each sample was analysed at three to five spots. Where veins occurred 1 to 2 readings were taken of the vein and 1 to 2 readings were taken of the wall rock. The spectrum average parameter of the spectral acquisition software was set to be 60 for light coloured rocks, 100 for medium coloured rocks and 200 for dark coloured rocks and the white balance parameter was set to be twice of spectrum average.

A spectral interpretation software, the Spectral Geologist Professional was used to assist reinterpreting the old company spectral database and interpreting the newly collected spectra. The Spectral Geologist identifies up to two minerals in a spectrum. I made my own interpretations for each spectrum and in some cases identified up to four minerals in a spectrum. The program was also used to extract numerical values from the spectra including the Al-OH absorption peak position at ~2200 nm, white mica crystallinity (depth of Al-OH/depth of water absorption) and alunite absorption peak position at ~1480 nm (Pontual, 2001). Examples of the common alteration minerals observed are shown in Figures 5.1 to 5.3. The spectral database and interpretations are contained in Appendix III.2 and III.3.

### 5.2.5 X-ray Diffraction

The X-ray diffraction (XRD) analysis was used to supplement the SWIR spectral data and thin section petrography. Initially Kyne (2009) analysed 45 samples and this study added a further 20 samples using semi-quantitative X-ray diffraction (Appendix III.4).

The quantitative XRD data was analysed at the University of Ballarat, Australia. X-ray diffraction traces were obtained using Siemens D500 and D501 diffractometers with Fe-filtered  $\text{CoK}_\alpha$  radiation. Operating conditions were 40kV/25mA, step scan  $0.03^\circ$  ( $2\theta$ ) at  $1^\circ$  ( $2\theta$ )/min, fixed  $1^\circ$  divergence and receiving slits and  $0.15^\circ$  scatter slit. Mineral phases present were identified by computer-aided (EVA<sup>TM</sup>-X'Pert Pro<sup>TM</sup>) searches of the 2009 ICDD PDF4-Minerals subfile. Quantitative XRD results were obtained using SiroQuant<sup>TM</sup> version 3.0 and refinement of the most suitable mineral structures available in the current software package databank. SiroQuant<sup>TM</sup> is a "whole pattern" Rietveld analysis technique. XRD traces were obtained from air-dried (AD) sedimented mounts prepared from all samples after settling in 1 wt% sodium polyphosphate aqueous solution for eight hours. Sample mounts producing traces indicating the presence of kandite group clay minerals have been treated with formamide and XRD scans were run again within 20 minutes of exposure to confirm the presence or absence of halloysite. Sample mounts producing peaks indicating the presence of smectite clay or of illite-smectite (IS) interlayer clays have been treated with glycol and traces were

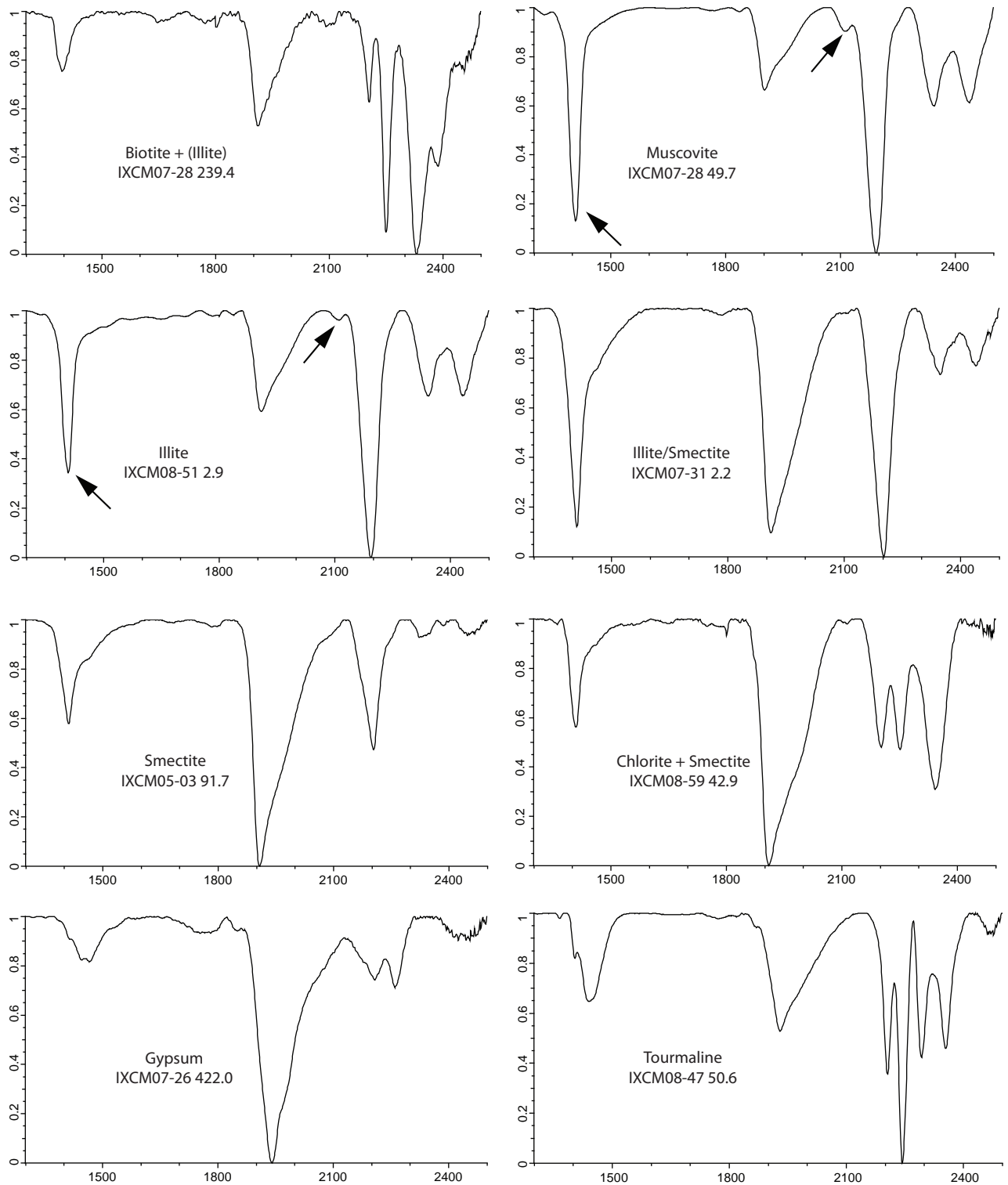


**Figure 5.1** Examples of SWIR spectra collected from the Stage A potassic and Stage B sericitic alteration. X-axis is wavelength (nm) and Y-axis is normalised hull quotient. The first spectra, biotite, is from Stage A and the remainder are from Stage B. Muscovite and illite is distinguished by absorption peak position at ~2110 nm and ~1410 nm. The crystallinity (depth of Al-OH/depth of water absorption) increases from muscovite towards illite, illite/smectite and smectite.

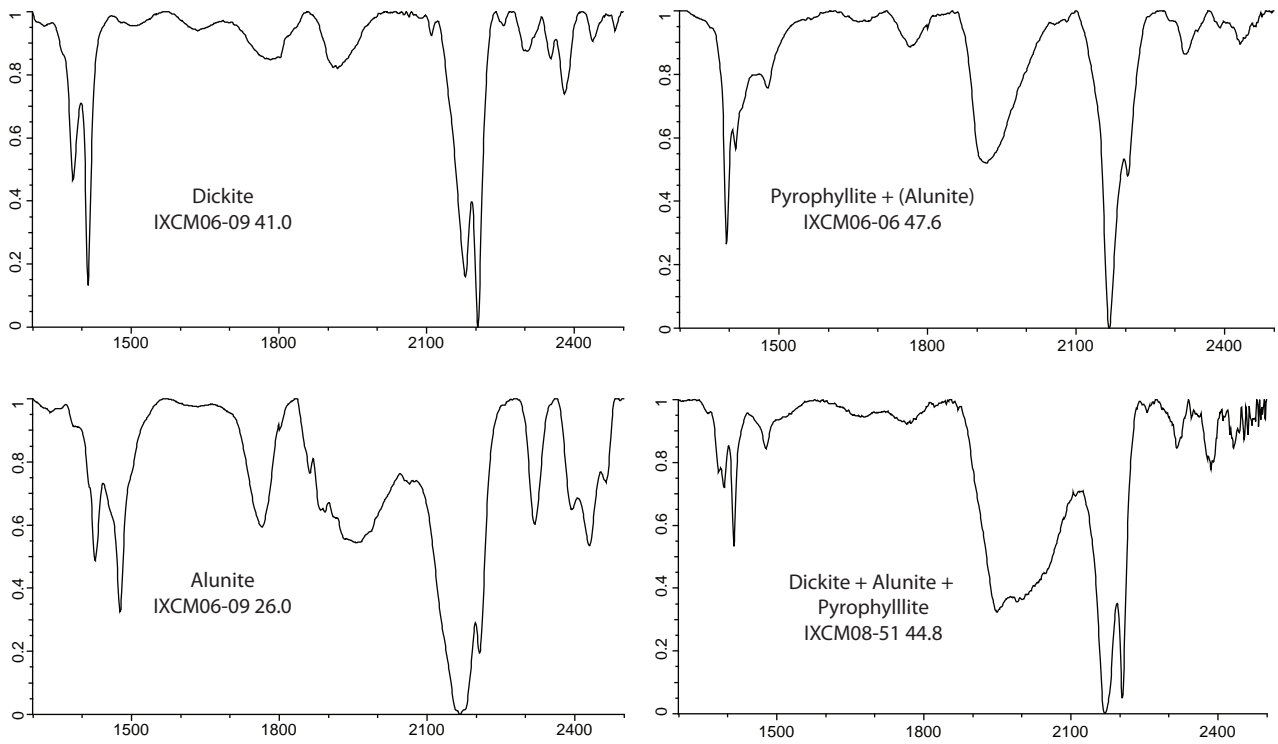


**Figure 5.2** Examples of SWIR spectra collected from quartz-dickite alteration (Stage C<sub>QD</sub>). X-axis is wavelength (nm) and Y-axis is normalised hull quotient.

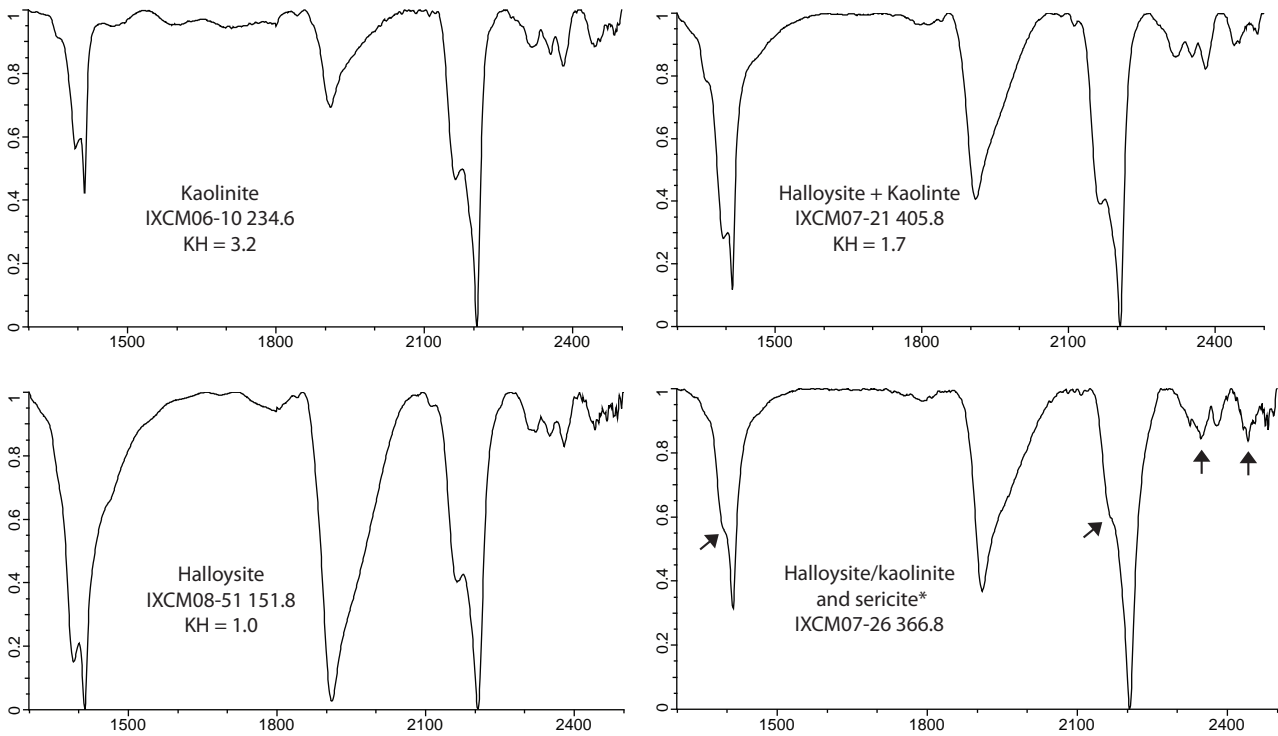


**Figure 5.3** Examples of SWIR spectra collected from halloysite-kaolinite alteration (Stage C<sub>HK</sub>). X-axis is wavelength (nm) and Y-axis is normalised hull quotient. KH index is explained in text. **Notation:** \* - sericite is identified by shoulders 1413 nm and 2207 nm suggesting a mix between sericite and halloysite/kaolinite. In addition weak development of absorption peak position at ~2340 and ~2430 nm suggests sericite.

obtained after 24 hours exposure at 60°C.

### 5.2.6 Scanning Electron Microscope

The scanning electron microscope (SEM) at the Central Science Laboratory of the University of Tasmania was used to observe the crystal morphology of alunite, halloysite and kaolinite at micron scale to determine the origin of these minerals. The SEM Petrology Atlas (Welton, 1984) was the primary reference book for this study. A FEI Quanta 600 scanning electron microscope was used in conjunction with an EDAX Genesis 7000 EDS (energy dispersive X-ray spectrometry) system with two Sapphire SUTW Si(Li) detectors, with a MnK $\alpha$  130 eV resolution. A spot size of 3 to 5, 15 to 25 kV high-voltage and secondary electron or back scatter electron imaging was used.

Samples were prepared by mounting rock chips with fractured surface onto an aluminum plug with conducting silver paint and conductive carbon tape, and then coating them with gold. For samples that were separated using clay separation, a clay/water mixture was made and applied to a glass surface. The sample was then dried, leaving a clay residue that was then carbon- or gold-coated for conductivity. Gold coating provided the best resolution for imaging.

Mineral identification with the SEM was done by observing the crystal morphology, using EDS, and reference to quantitative XRD and SWIR data when available. The EDS cannot obtain quantitative data on a broken surface because the uneven surface causes the electrons to scatter. Instead element peaks were compared with the chemical formula of the suspected mineral. The correlation of the peak heights of Si, Al, K, and Ca with the mineral chemical formula is possible, as their peak heights are roughly proportional to their concentration (Welton, 1984). The Au coating produces Au peaks in the EDS spectra but do not affect any of the elements probably present. Observations and SEM images of halloysite, kaolinite and alunite are in Appendix III.5 and III.6

## 5.3 Alteration Description

The Cerro la Mina alteration is divided into three stages, potassic (Stage A), sericitic (Stage B) and kandite (Stage C<sub>QD</sub> and C<sub>HK</sub>). The characteristics of each alteration stage are summarised in Figures 5.4 to 5.8, Table 5.1 and described in detail below. In drill core quartz + biotite  $\pm$  potassium feldspar alteration (Stage A) turns the rock brown and is commonly cross cut by grey quartz + sericite (Stage B) altered vein margins (Fig. 5.4). Quartz + dickite  $\pm$  pyrophyllite  $\pm$  alunite  $\pm$  kaolinite (Stage C<sub>QD</sub>) and halloysite + kaolinite (Stage C<sub>HK</sub>) alter the rock to white grey colour and much of the primary texture is removed by this alteration (Fig. 5.4).

### 5.3.1 Potassic Alteration (Stage A)

Stage A alteration was identified using thin-section petrography, staining and quantitative XRD (Fig. 5.5). Stage A consists of quartz + potassium feldspar + biotite. By analysing the textures of the stained potassium feldspars, a primary or secondary origin can be established. Grains with rims of stained feldspar are consistent with a secondary alteration origin and grains that are fully stained can be not be distinguished between a primary or secondary origin.

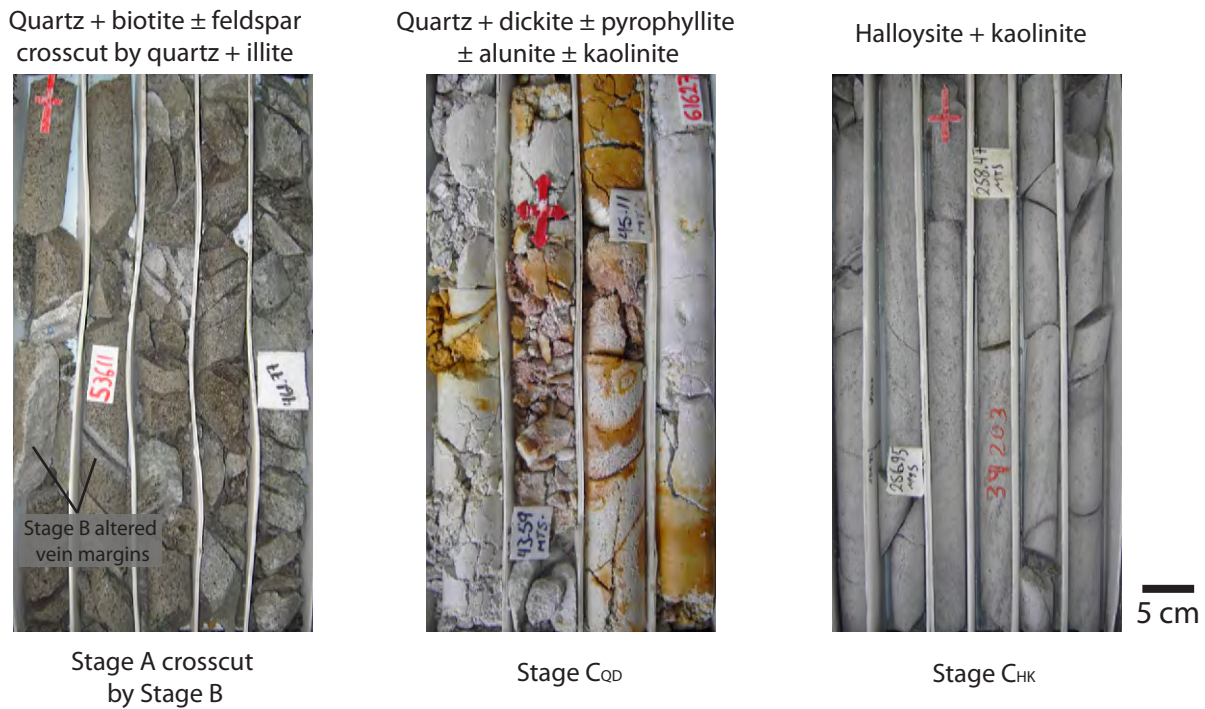


**Figure 5.4** Drill core examples of Stages A, B, C<sub>QD</sub>, and C<sub>HK</sub> alteration. **Sample ID left to right:** IXCM07-28 459.9 to 462.0 m, IXCM07-44 43.0 to 45.10 m, and IXCM06-10 256.2 to 259.6 m.

| Alteration   |                            |  |                                   |                             |
|--|----------------------------|--|-----------------------------------|-----------------------------|
| Stage  | Stage A                    | Stage B  | Stage C <sub>QD</sub>             | Stage C <sub>HK</sub>       |
| Classification   | Potassic                   | Sericitic  | Kandite                           | Kandite                     |
| Mineral Assemblage   | qtz + Ksp + bt             | qtz, musc, ill<br>ill/smc, chl, ct,<br>gyp, tou      | qtz + dik ± pyr<br>± alu ± kao    | hall + kao                  |
| Location and extent  | Proximal-medial            | Proximal to distal                                   | Proximal, small<br>pod at surface | Proximal, to 800 m<br>depth |
| Zonation   | Ksp core<br>bt distal      | qtz + musc core<br>ill/smc + chl distal              | None                              | kao-rich close to<br>CQD    |
| Alteration Style   | Per, Vn                    | Per, Vn  | Per, HBx, F                       | Per, Vn, HBx                |
| Texture Destructive  | Weak to Moderate           | Weak to Moderate                                     | Strong                            | Strong                      |
| Identification   | bt: TS, SWIR, V<br>Ksp: ST | SWIR, XRD  | SWIR, XRD                         | SWIR, SEM, XRD              |
| Lithofacies  |                            |  |                                   |                             |
| Unit 1 - Fiamme breccias   | Minor                      | Common, Per, ~Vn<br>1A - chl, 1B <sub>s</sub> - musc |                                   | Rare                        |
| Unit 2 - Monzodiorite to diorite                                 | Minor, Vn                  | Common, Per, ~Vn                                     |                                   | Rare                        |
| Unit 3 - Trachyandesite Coherent<br>to Matrix-Supported Breccias | Minor, Vn                  | Common, Per, ~Vn                                     |                                   | Rare                        |
| Unit 4 - Breccia Complex   | Common, Per                | Common, Per, Vn                                      | Common, Per,<br>HBx               | Common, Per, HBx,<br>Vn     |

**Table 5.1** Summary of the Cerro la Mina alteration assemblages and their relationship to rock lithofacies.

**Abbreviations:** alu - alunite, chl - chlorite, ct - calcite, dik - dickite, F - fault related, gyp - gypsum, hall - halloysite, HBx - hydrothermal breccia, ill - illite, ill/smc - illite/smectite, kao - kaolinite, Ksp - potassium feldspar, musc - muscovite, Per - pervasive, pyr - pyrophyllite, qtz - quartz, smc - smectite, SWIR - shortwave infrared spectroscopy, tou - tourmaline, TS - thin section, Vn - vein, XRD - X-ray diffraction

## Potassic Alteration (Stage A)

### Alteration description

**Minerals:** Quartz + potassium feldspar + biotite

**Texture:** Pervasive alteration of breccia pipe matrix (Unit 4) and potassium feldspar alteration of plagioclase rims. Disseminated and veinlets of shreddy biotite.

**Distribution:** Potassium feldspar alteration is strong in the breccia pipe (Unit 4) and weak in surrounding volcanic rocks. Biotite is rare in breccia pipe and is widespread in surrounding volcanic wall rocks (Units 1 to 3).

**Intensity:** Strong in breccia pipe and weak in volcanic wall rocks.

**Timing:** Early Porphyry

**Distinguishing Features:** Potassium feldspar is distinguished with thin section, staining, and XRD. Biotite forms small round booklets and sometimes veinlets.

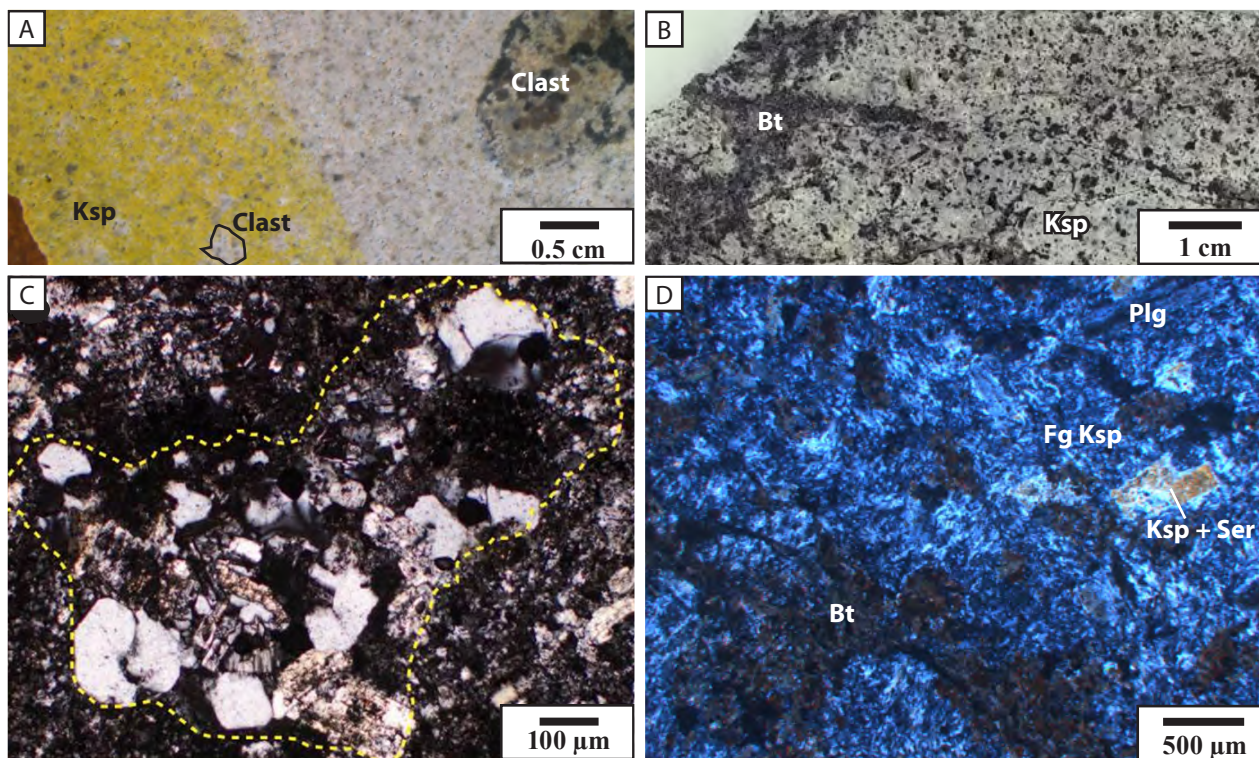
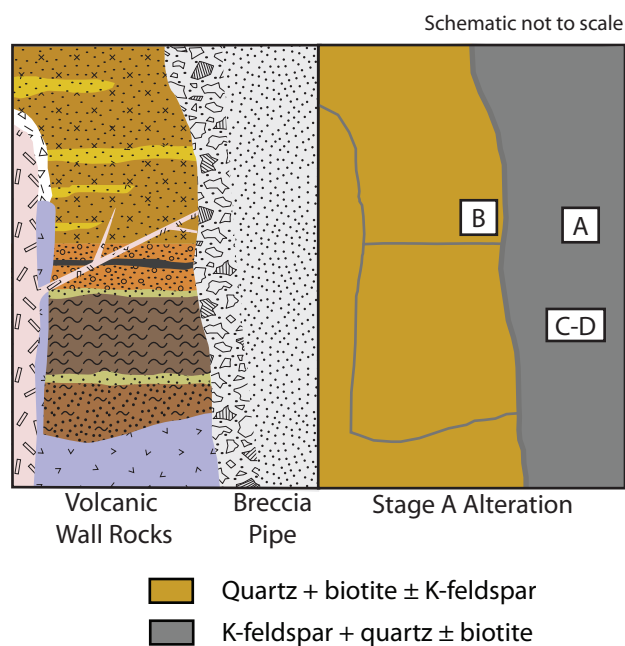


**Figure 5.5** Characteristics of Stage A potassic alteration. **A.** Matrix-rich breccia (Unit 4) with potassium feldspar staining highlighting potassium feldspar alteration of matrix and clast outlines. **B.** Veinlets and booklets of biotite with potassium feldspar. **C.** Clast of quartz - potassium feldspar in breccia pipe. **D.** Cross polarized image showing a biotite veinlet and abundant fine-grained potassium feldspar and potassium feldspar replacement of plagioclase. Potassium feldspar is being replaced by sericite clays (Stage B). Legend for geology in Figure 4.14. **Abbreviations:** Bt - biotite, Fg - fine-grained, Ksp - potassium feldspar, Plg - plagioclase, Ser - sericite. **Sample ID:** A. IXCM08-61 439.0, B. IXCM07-25.6.10.3, C. IXCM06-16.313.0, D. IXCM07-25.6.10.3.

The potassium feldspar alteration is the strongest in the breccia pipe where it occurs as a fine-grained matrix hosting plagioclase phenocrysts with potassium feldspar altered rims and clasts of the matrix-rich, granule breccia (Unit 4A; Fig. 5.5A). Clasts of hydrothermal potassium feldspar inter-grown with quartz also occur in the fine-grained matrix (Fig. 5.5C). Outside the breccia pipe in the volcanic wall rocks, hydrothermal biotite is dominant with weak to rare potassium feldspar. The biotite forms < 2 mm shreddy aggregates, fine-grained disseminations and veinlets (Fig. 5.5B). Quantitative XRD data of rocks that occur in the zone where staining indicates abundant potassium feldspar report 25 to 72 percent potassium feldspar and 10 to 22 percent quartz and is greater than the content of quartz observed in least altered volcanic wall rocks (<1%).

### 5.3.2 Sericitic Alteration (Stage B)

Stage B alteration consists of quartz, muscovite, illite, illite/smectite, chlorite, calcite, gypsum and tourmaline (Fig. 5.6). The alteration has quartz-muscovite-rich and chlorite-rich varieties and typically occurs as weak to moderate intensity and is pervasive in all rock types observed at Cerro la Mina. Stage B also commonly alters vein margins (Fig. 5.6A). Stage B alteration turns the volcanic wall rocks to grey (quartz-muscovite-rich) and green (chlorite-rich) but still preserves the primary texture of the rock (Figs. 5.6B-C).

The presence of calcite was determined with dilute hydrochloric acid and occurs mainly along fractures. In thin-section, sericite is commonly observed to replace plagioclase and hydrothermal potassium feldspar (Fig. 5.5D). Chlorite is observed to replace feldspar and hydrothermal biotite. Gypsum only occurs in the sericitic altered rocks, and anhydrite is rarely observed (Kyne, 2009). Tourmaline is not common and mostly occurs close to the northwest fault forming black disseminated acicular needles. In one sample oxidized brown tourmaline is observed replacing volcanic clasts in a quartz-muscovite matrix (Fig. 5.6D). Table 5.2 shows quantitative XRD data from pervasive sericitic alteration where the quartz and sericite content decreases away from the breccia pipe. A sericitic altered vein margin contains abundant quartz (17.2% quartz; sample IXCM08-55.75.1) and greater than least altered volcanic wall rock quartz (< 1%; sample IXMC08-58 127.8 and IXCM08-63 47.5).

| Sample          | Distance from muscovite core | Description | Qtz  | Musc | Ill | Ill/Smc | Tou | Gyp | Sulf | Other |
|-----------------|------------------------------|-------------|------|------|-----|---------|-----|-----|------|-------|
| IXCM06-15.72.0  | 150 m                        | Pervasive   | 28.0 | 63.7 |     |         |     |     | 6.7  | 1.6   |
| IXCM07-42 49.1  | 225 m                        | Pervasive   | 0.5  | 16   |     | 3       |     | 0.2 | 1.5  | 78.8  |
| IXCM08-58 127.2 | 275 m                        | Pervasive   | 0.7  |      | 8.1 | 2.4     |     |     | 6.8  | 82.0  |
| IXCM08-63 47.5  | 325 m                        | Pervasive   | 0.5  |      | 3.5 | 0.9     |     |     | 12.1 | 83.0  |
| IXCM08-55.75.6  | 275 m                        | Vein Halo   | 17.2 | 52.5 |     |         |     |     | 4.5  | 25.9  |

**Table 5.2** Whole rock quantitative XRD data of sericitic altered (Stage B) samples in relation to their distance from the breccia pipe. Sericite and quartz content decreases from the muscovite core. Other includes plagioclase, albite, kaolinite, halloysite, rutile, and titanite. Abbreviations: Qtz - quartz, Musc - muscovite, Ill - illite, Ill/Smc - illite/smectite, Tou - tourmaline, Gyp - gypsum, Sulf - sulfides.

## Sericitic Alteration (Stage B)

### Alteration description

**Minerals:** Quartz, muscovite, illite, illite/smectite, chlorite, calcite, gypsum and tourmaline

**Texture:** Alteration halo to veins

**Distribution:** Widespread in all rock types

**Intensity:** Weak to moderate, texture preserving

**Timing:** Late Porphyry, Stage B

**Distinguishing Features:** Commonly texture preserving, muscovite/illite-rich assemblages alter rock to grey, chlorite-rich assemblages alter rock to green. Silicified grey halo to veins.

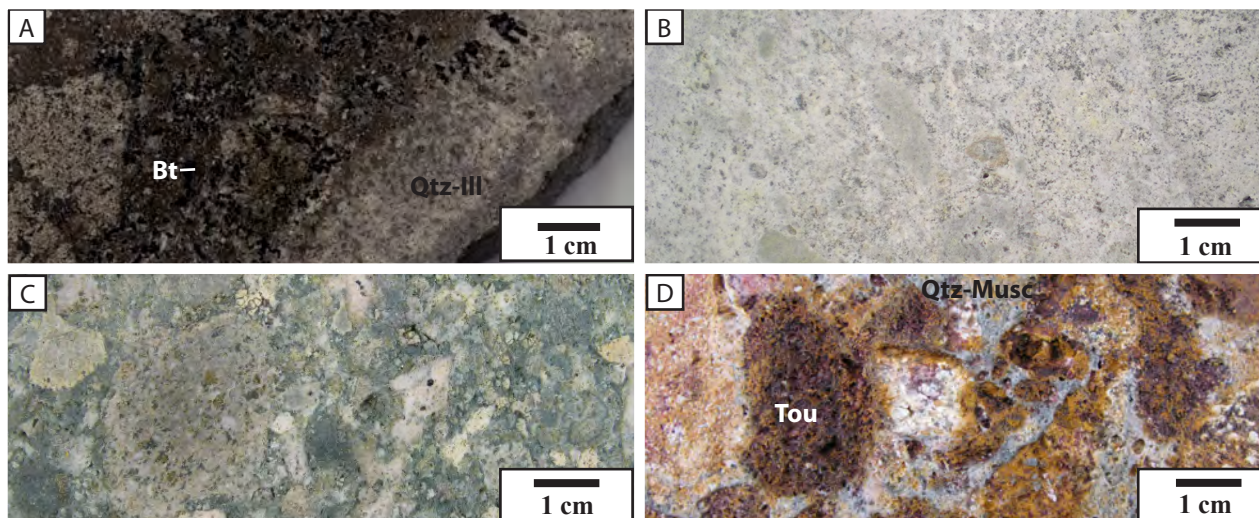
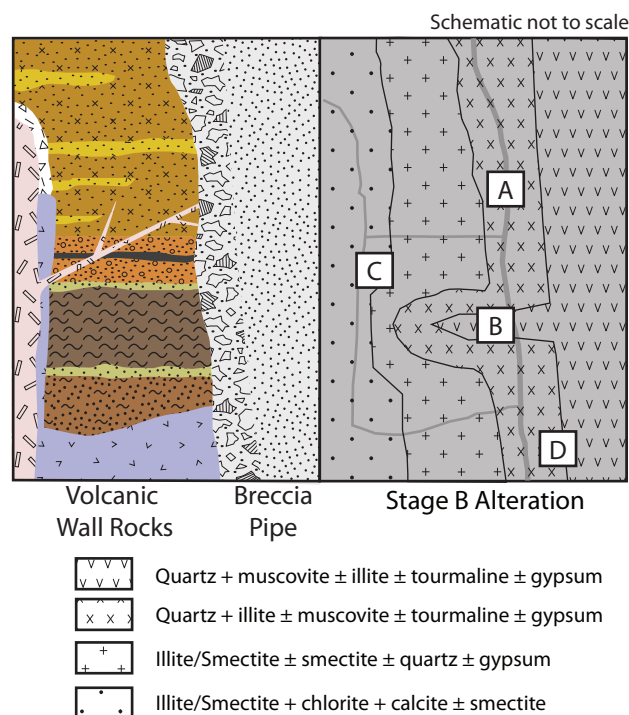


**Figure 5.6** Characteristics of Stage B sericitic alteration. **A.** Grey quartz-illite alteration occurring on vein margin crosscutting early Stage A biotite alteration. **B.** Grey quartz-illite alteration of a fiamme breccia. **C.** Green illite/smectite + chlorite alteration of a clast-supported breccia. **D.** Oxidized brown tourmaline crystals altering clasts with a quartz-muscovite altered matrix. Legend for geology in Figure 4.14. **Abbreviations:** Bt - biotite, Ill - illite, Musc - muscovite, Qtz - quartz, Tou - tourmaline. **Sample ID:** A. IXCM07-28 487.4, B. IXCM07-23 233.5, C. IXCM08-59 245.5, D. IXCM08-47 65.1.

### 5.3.3 *Kandite Alteration (Stage C)*

Stage C alteration at Cerro la Mina consists dominantly of kandite group minerals halloysite 10Å ( $\text{Al}_2\text{Si}_2\text{O}_5(\text{OH})_4 \cdot 2\text{H}_2\text{O}$ ), halloysite 7Å ( $\text{Al}_2\text{Si}_2\text{O}_5(\text{OH})_4$ ), kaolinite ( $\text{Al}_2\text{Si}_2\text{O}_5(\text{OH})_4$ ) and dickite ( $\text{Al}_2\text{Si}_2\text{O}_5(\text{OH})_4$ ). Stage C alteration is the most abundant alteration at Cerro la Mina mainly altering early potassium feldspar in the breccia pipe and changing the rocks to grey-white. The surrounding volcanic rocks have weak Stage C alteration. The alteration is largely pervasive and kandite + pyrite + marcasite cemented breccias are common. Individual kandite alteration clay minerals could not be identified by visual inspection and were identified using the combination of SWIR instruments (TerraSpec), quantitative X-ray diffraction and imaging with a scanning electron microscope. Stage C alteration comprises two distinct and coeval alteration sub-types. The first consists of quartz + dickite ± pyrophyllite ± alunite ± kaolinite (Stage  $C_{\text{QD}}$ ) and the second of halloysite + kaolinite (Stage  $C_{\text{HK}}$ ).

#### 5.3.3.1 *Quartz-Dickite Alteration (Stage $C_{\text{QD}}$ )*

Stage  $C_{\text{QD}}$  quartz-dickite alteration consists of quartz + dickite ± pyrophyllite ± alunite ± kaolinite. The strong pervasive nature of Stage  $C_{\text{QD}}$  alters mainly the breccia pipe rock to grey obscuring most of the primary texture of the rock. Dickite + pyrite cemented breccias are common with mosaic, jigsaw-fit, and chaotic textures (Figs. 5.7A-C). The clasts of the breccias are also quartz + dickite altered. Stage  $C_{\text{QD}}$  can be pervasive or limited to faults/structures. Quantitative XRD analysis shows that Stage  $C_{\text{QD}}$  alteration comprises 34-36% quartz, 28-37% dickite, 3-8% pyrophyllite and 1-18% alunite. The quartz is greater than all other alteration stages and least altered volcanic wall rocks (<1%). Stage  $C_{\text{QD}}$  alteration zones are close to current surface and mostly occurs in the oxide zone. No vuggy quartz is observed at the Cerro la Mina prospect. Occasionally a texture similar to vuggy quartz is observed in drill core; however, it was formed by the flushing out of clay minerals by fluids when the drill core quartz-clay altered porphyritic volcanic rock was cut for assay purposes.

The alunite at Cerro la Mina is fine-grained (< 150 μm) and cannot be observed with a hand lens and occurs in and 100 metres outwards from the oxide zone. To further study the origin of the alunite, six samples containing alunite collected from in and outside the oxide zone were observed with a SEM (Table 5.3; Appendix III.5). Alunite with various 1480 nm absorption peak positions were also selected to determine if there was an association of the 1480 nm absorption peak position with the oxide zone and/or size of alunite. The alunite was found to be euhedral, hexagonal, tabular crystals ranging from 5 to 150 μm (Fig. 5.7C). The largest alunite crystal size of 150 μm (IXCM08-51 62.5) occurs in association with pyrophyllite. No relationship between the position of the 1480 nm absorption peak position and its location to the oxide zone or to size of the alunite was observed.

#### 5.3.3.2 *Halloysite-Kaolinite Alteration (Stage $C_{\text{HK}}$ )*

Stage  $C_{\text{QD}}$  halloysite-kaolinite alteration consists of halloysite + kaolinite with predominant halloysite. Halloysite was first described by Berthier (1826) as a dioctahedral 1:1 clay mineral of the kandite group. Halloysite occurs widely in both weathered rocks and soils and it has been identified as having

| Sample          | Location         | Crystal form | Alunite size ( $\mu\text{m}$ ) | 1480 position | SWIR Ident  |
|-----------------|------------------|--------------|--------------------------------|---------------|-------------|
| NJ08IX-61       | Oxide            | Eu           | 30                             | 1485          | Dik-Alu-Kao |
| NJ08IX-5.8      | Oxide            | Eu           | 30                             | 1489          | Ill-Alu     |
| IXCM06-09 22.8  | Oxide            | S            | 25 - 90                        | 1478          | Alu         |
| IXCM07-25.23.5  | Oxide            | n/a          | n/a                            | 1481          | Alu         |
| IXCM08-51 62.5  | 30 m below oxide | Eu           | 100 - 150                      | 1478          | Alu-Pyr     |
| IXCM06-10 140.3 | 50 m below oxide | Eu           | 5 - 40                         | 1479          | Alu         |

**Table 5.3** - Summary for SEM imaging of alunite. **Abbreviations:** Alu - alunite, Dik - dickite, Eu - euhedral, Kao - kaolinite, Pyr - pyrophyllite, S - subhedral.

formed by the alteration of a variety of rock types (Joussein et al., 2005). Halloysite may occur in partially hydrated forms as well as in a fully hydrated and a fully dehydrated form (Churchman and Carr, 1972). The terms halloysite (10Å) and halloysite (7Å) are used for the hydrated and dehydrated forms, respectively. Churchman and Carr (1972) reports that halloysite 10Å can easily dehydrate to 7Å under ambient conditions. Kaolinite and halloysite 7Å produce the same peak under XRD and the presence of halloysite 7Å is detected by the use of formamide intercalation which separates the XRD peaks (Joussein et al., 2007). Cerro la Mina halloysite was first identified with a TerraSpec in this study and Kyne (2009) confirmed it with XRD. Kyne (2009) reported the presence of both hydrated (10Å) and halloysite (7Å) whereas this study reports only the presence of halloysite (7Å). I will refer to halloysite 10Å and 7Å collectively as halloysite.

Stage  $C_{\text{HK}}$  alteration is pervasive and mainly alters the breccia pipe rock to grey-white, similar to the Stage  $C_{\text{QD}}$ . Stage  $C_{\text{HK}}$  cannot be distinguished without the aid of a SWIR instrument or XRD. Stage  $C_{\text{HK}}$  also occurs as breccia cement (Figs. 5.8A and B). The halloysite + kaolinite + marcasite + pyrite cemented breccias are mosaic to jig-saw fit whose clasts are also Stage  $C_{\text{HK}}$  altered. In hand specimen Stage  $C_{\text{HK}}$  alteration does not preserve much of the primary texture (Fig. 5.4); however in thin section the primary texture can still be observed. Quantitative XRD indicates that the Stage  $C_{\text{HK}}$  alteration minerals form up to 17.5 percent of the rock. This study selected 10 samples in the Stage  $C_{\text{HK}}$  alteration and used quantitative XRD to determine the relative abundances of halloysite and kaolinite. The samples showed varying abundances of halloysite to kaolinite (0.6 to 40), with kaolinite in greater abundance close to the Stage  $C_{\text{QD}}$  alteration zone.

#### 5.3.4 Oxide Zone

At the Cerro la Mina prospect the upper 1 to 3 metres of the oxide zone is a soil horizon formed by the intense weathering of the bedrock to smectite, halloysite and gibbsite. In bedrock, the oxide zone continues on average to 50 metres below the surface with a maximum depth of 175 metres where opal (XRD), goethite, hematite and barite occur without sulfides. Weaker oxidation, where minor sulfides occur, extends to depths of 5.6 metres below the surface in structures that are less than 0.5 metres

**Kandite Alteration  
Quartz-dickite (Stage C<sub>QD</sub>)**

**Alteration description**

**Minerals:** Quartz + dickite ± pyrophyllite ± alunite ± kaolinite

**Colour:** Grey

**Texture:** Massive

**Hydrothermal breccias:** Dickite + pyrite cement and quartz-dickite altered clasts. Mosaic, jig-saw fit and chaotic breccias.

**Distribution:** Small pod at the surface and in breccia pipe. Often oxidized due to close proximity to the surface. Sometimes limited to fault/structures.

**Intensity:** Strong texturally destructive

**Timing:** High sulfidation overprint (Stage C)

**Distinguishing Features:** Massive grey and can only be distinguished from halloysite-kaolinite with SWIR/XRD.

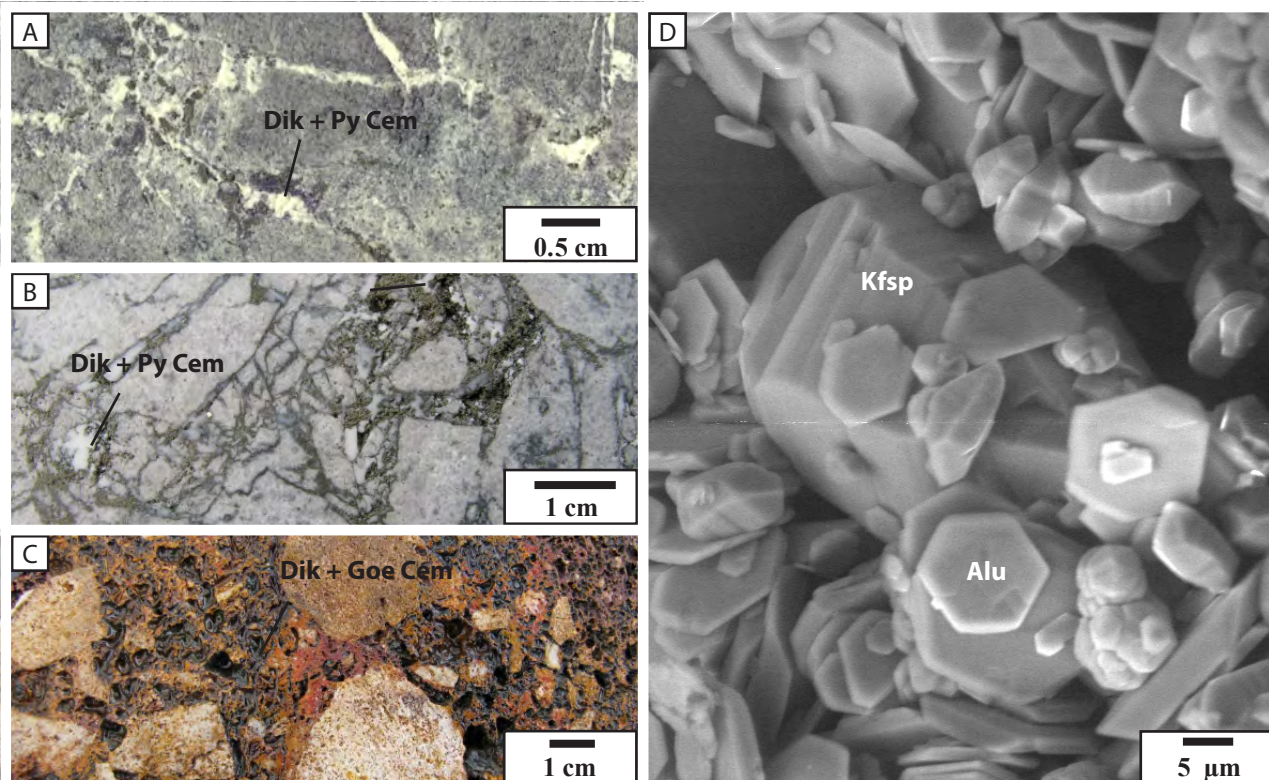
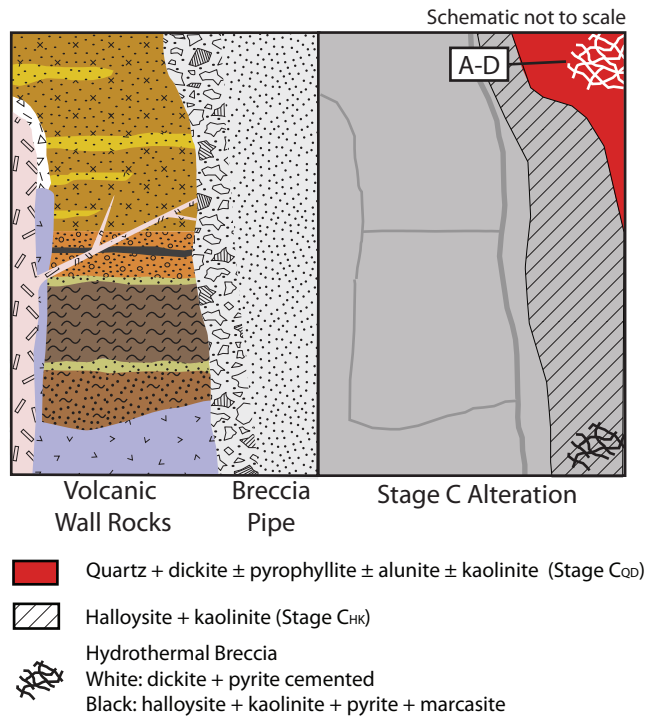


**Figure 5.7** Characteristics of quartz-dickite alteration (Stage C<sub>QD</sub>). **A.** Mosaic dickite + pyrite cemented hydrothermal breccia. **B.** Jigsaw fit dickite + pyrite cemented hydrothermal breccia. **C.** Chaotic dickite + goethite (after pyrite) cemented hydrothermal breccia. **D.** SEM image of abundant hexagonal and tabular alunite around a larger feldspar. Legend for geology in Figure 4.14. **Abbreviations:** Alu - alunite, Cem - cement, Dik - dickite, Goe - goethite, Kfsp - potassium feldspar, Py - pyrite. **Sample ID:** A. IXCM06-09 100.7, B. IXCM08-47 238.4, C. IXCM07-44 26.9, D. IXCM06-10 140.3.

## Kandite Alteration Halloysite-Kaolinite (Stage C<sub>HK</sub>)

### Alteration description

**Minerals:** Halloysite + kaolinite

**Colour:** Grey-white

**Texture:** Infill in veins.

**Hydrothermal Breccias:** Halloysite+ kaolinite + marcasite + pyrite cement and halloysite + kaolinite altered clasts. Mosaic and jig-saw fit breccias.

**Distribution:** From surface to at least 800 metres depth in breccia pipe. Hydrothermal breccias occur at depth

**Intensity:** Moderate to strong texture destructive

**Timing:** High sulfidation overprint, Stage C

**Distinguishing Features:** Massive grey-white and can only be distinguished from dickite with SWIR/XRD

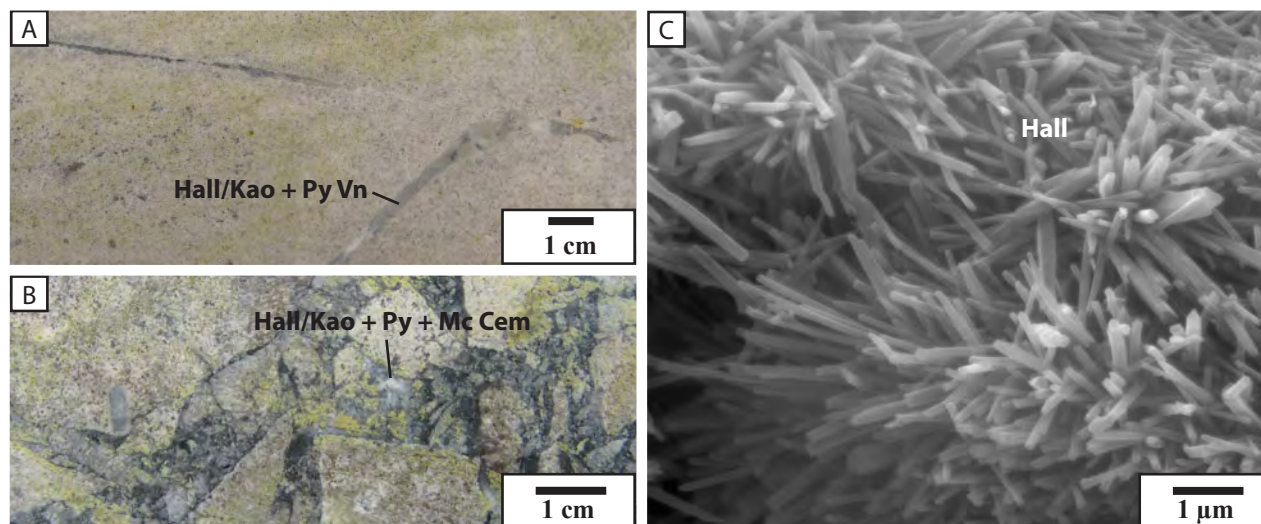
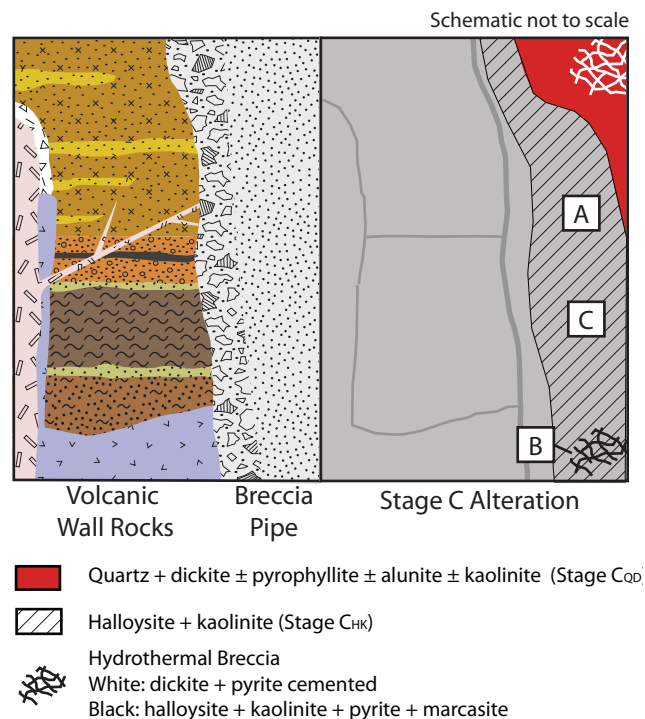


**Figure 5.8** Characteristics of halloysite-kaolinite (Stage C<sub>HK</sub>) alteration. **A.** Halloysite-kaolinite vein. **B.** Jigsaw fit halloysite + kaolinite + pyrite + marcasite cemented hydrothermal breccia. **C.** SEM image of halloysite cylindrical tubes. Legend for geology in Figure 4.14. **Abbreviations:** Cem - cement, Hall - halloysite, Kao - kaolinite, Mc - marcasite, Vn - vein. **Sample ID:** A. IXCM08-51 109.5, B. IXCM08-51 531.5, C. IXCM08-51 151.0.

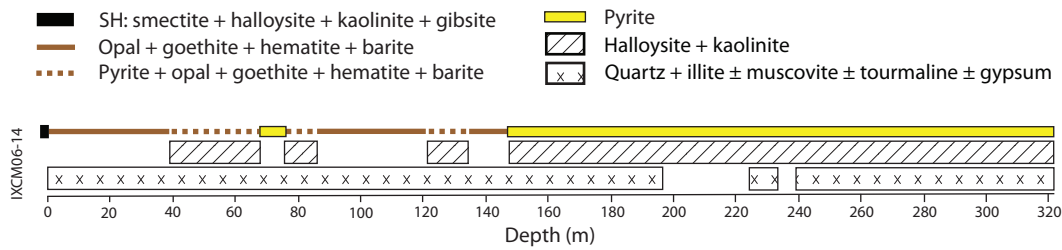


**Figure 5.9** Drill hole illustrating the distribution of Stage  $C_{HK}$  alteration in relation to the oxide zone and pyrite. Stage  $C_{HK}$  does not occur in the oxide zone but occurs in zones of weak oxidation with pyrite and with pyrite below the oxide zone. On the contrary sericitic alteration (Stage B) occurs in the oxide zone creating a resistant opal and sericite-rich zone at the surface and also at depth with pyrite. The actual drill hole does not include the soil horizon but is present from field based observations. **Abbreviations:** SH - soil horizon.

wide and close to the northwest fault. Stage  $C_{HK}$  does not occur in the oxide zone but occurs in zones of weak oxidation with pyrite and with pyrite below the oxide zone. On the contrary sericitic alteration (Stage B) occurs in the oxide zone creating a resistant opal and sericite-rich zone at the surface and also at depth with pyrite (Fig. 5.9).

## 5.4 Spatial Distribution

The Cerro la Mina surface alteration is shown in Figure 5.10. Stage B alteration is zoned over 2.5 kilometres with a quartz + muscovite ± illite ± tourmaline ± gypsum core centred on the breccia pipe transitioning to quartz + illite ± muscovite ± tourmaline ± gypsum, illite/smectite ± smectite ± gypsum ± quartz, and illite/smectite + calcite + chlorite ± smectite distally. Stage C consists of a small pod of Stage  $C_{QD}$  quartz + dickite ± pyrophyllite ± alunite ± kaolinite centred on the breccia pipe that is zoned over 250 metres outwards to Stage  $C_{HK}$  halloysite + kaolinite. Insufficient sampling does not permit mapping of the potassic alteration at a district scale. Figure 5.11 shows a decrease and increase in the Al-OH peak position and crystallinity respectively towards the breccia pipe. All alteration assemblages decrease in intensity away from the breccia pipe.

Cross section A-A' (Fig. 5.12) is located distal to the Cerro la Mina breccia pipe and associated strong clay alteration. The section shows contrasting alteration on either side of the northwest fault where the southwest side has illite/smectite + chlorite + calcite ± smectite alteration (Stage B) and the northeast side has biotite ± potassium feldspar alteration (Stage A).

Cross section B-B' (Fig. 5.13) comprises of biotite ± potassium feldspar (Stage A) that is overprinted by illite/smectite ± smectite ± quartz ± gypsum alteration (Stage A). A zone of halloysite + kaolinite (Stage  $C_{HK}$ ) occurs from surface to 100 m depth.

Cross section C-C' (Fig. 5.14) shows a quartz + potassium feldspar ± biotite altered core (Stage A) and a distal zone of biotite ± potassium feldspar (Stage A). Biotite is absent in the breccia pipe. Stage B alteration consists of an inner zone of muscovite ± illite and outer zone of illite ± muscovite. The overprinting Stage C alteration extends to 600 metres below the surface and consists of a small pod of Stage  $C_{QD}$  alteration near the surface and Stage  $C_{HK}$  alteration deeper. Dickite + pyrite cemented breccias are located near the surface in Stage  $C_{QD}$  alteration. Halloysite + pyrite cemented breccias (Stage  $C_{HK}$ ) are located below 1200 metres ASL (~600 metres below surface).

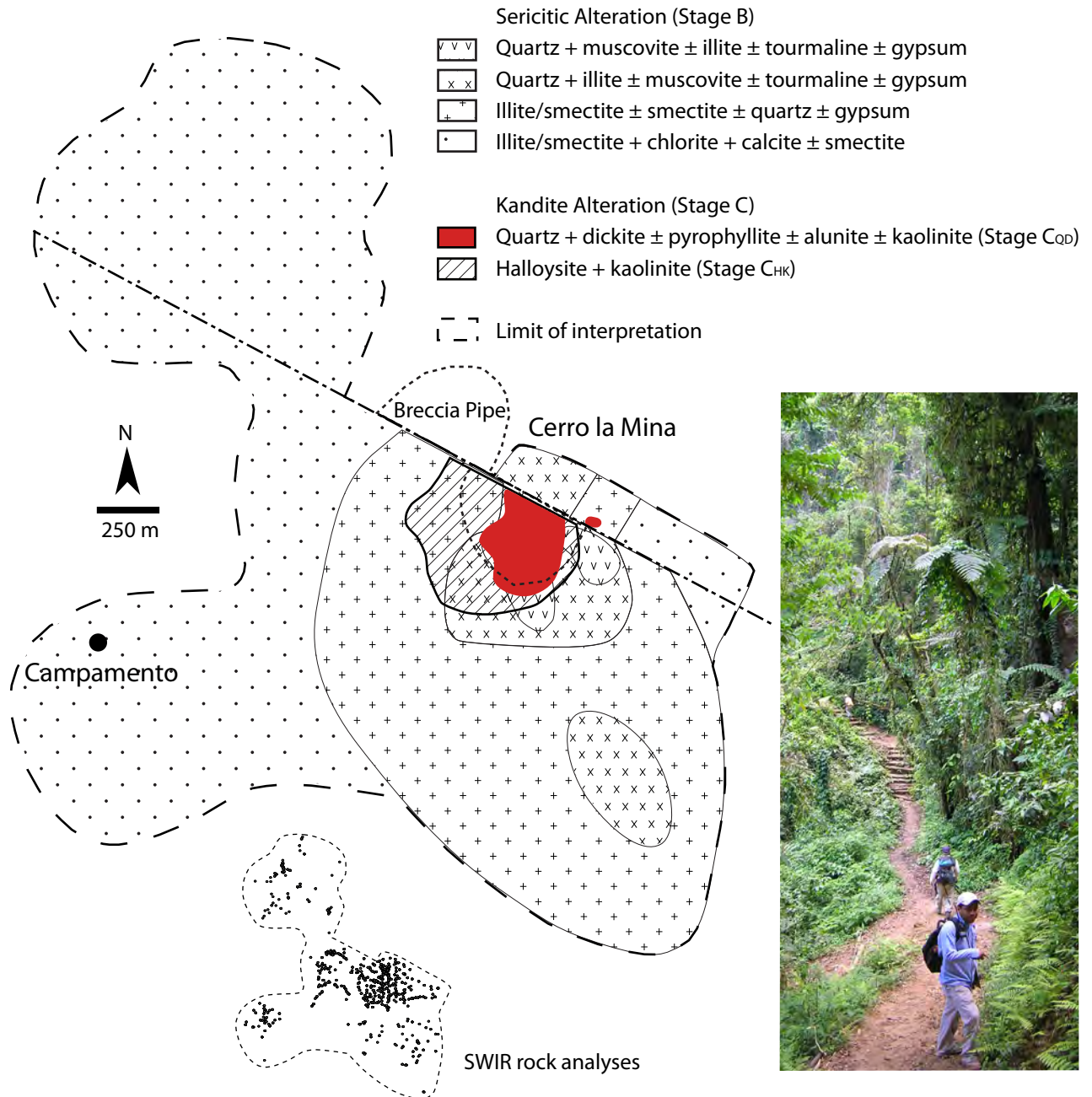


**Figure 5.10** The Cerro la Mina and regional surface alteration. Both the sericitic and kandite alteration show a “fried egg” pattern with both centres located on the breccia pipe (Unit 4). The northwest fault offsets the alteration. Distribution of SWIR rock analyses shown on bottom of image. The location of the Campamento Au/Ag deposit is indicated. Bottom right is a photograph of an access trail at the Cerro la Mina prospect.

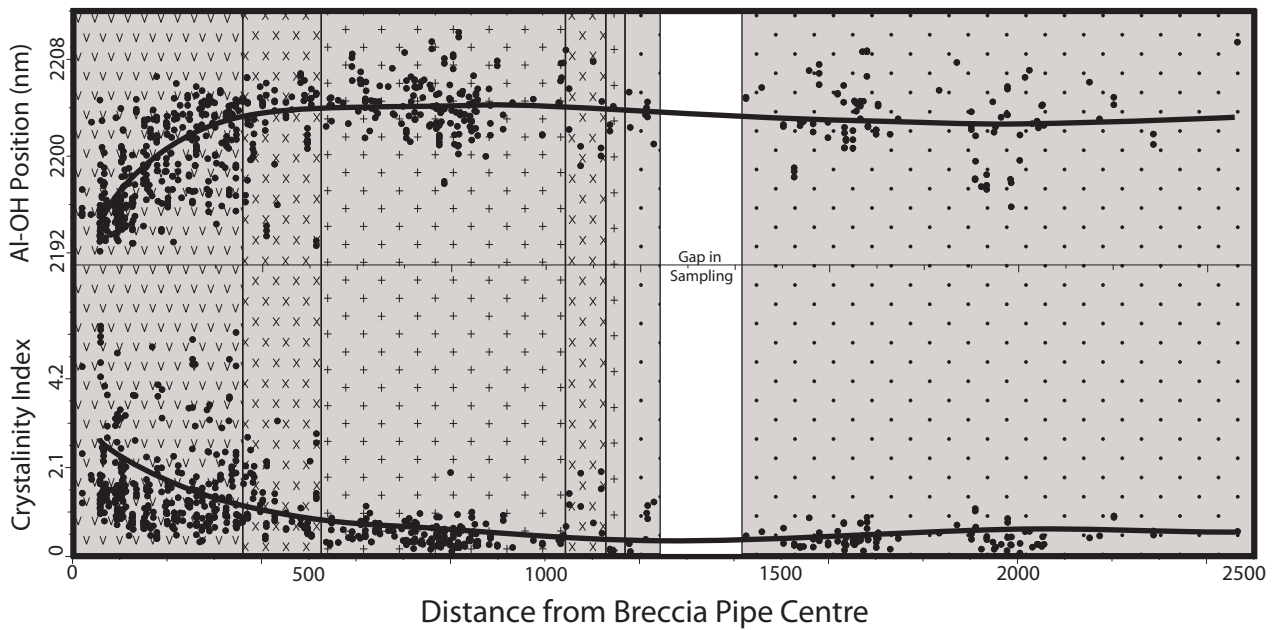


**Figure 5.11** Crystallinity and Al-OH zonation of the sericitic alteration (Stage B) versus distance from the breccia pipe centre. The Al-OH shifts to lower wavelengths and the crystallinity of the sericite increases closer to the breccia pipe. Legend is the same as Figure 5.10. Circles are SWIR analysis of surface rock samples.

Cross section D-D' (Fig. 5.15) is on the northeast side of the northwest fault and has a biotite  $\pm$  potassium feldspar alteration (Stage A) overprinted by a zoned sericitic alteration (Stage B) from a muscovite core transitioning outwards to predominantly illite/smectite + chlorite alteration to the southwest. The alteration changes according to the lithology with quartz-muscovite associated with the strong fiamme breccia Unit 1B<sub>s</sub> and chlorite-rich assemblages associated with clast-supported breccia (Unit 1A; Figs 4.12 and Fig. 5.15).

Long section E-E' was compiled from cross sections A, B and C (Fig. 5.16) and illustrates the lateral distribution of alteration assemblages and their vertical orientation. Stage A alteration consists of a vertically orientated potassium feldspar core surrounded by a zone of biotite  $\pm$  potassium feldspar. Stage B alteration consists of a vertically orientated quartz + muscovite  $\pm$  illite  $\pm$  tourmaline  $\pm$  gypsum core centred on the breccia pipe transitioning to quartz + illite  $\pm$  muscovite  $\pm$  tourmaline  $\pm$  gypsum, illite/smectite  $\pm$  smectite  $\pm$  gypsum  $\pm$  quartz, and illite/smectite + calcite + chlorite  $\pm$  smectite distally. Stage C consists of a small pod of quartz + dickite  $\pm$  pyrophyllite  $\pm$  alunite  $\pm$  kaolinite (Stage C<sub>QD</sub>) at the surface and halloysite + kaolinite (Stage C<sub>HK</sub>) extending to 600 metres blanketing the early potassium feldspar alteration.

To better illustrate the dimensions of the Stage C alteration, a depth below surface contour map was made by logging the location of Stage C alteration. The strong alteration forms a bowl shape with a diameter of approximately 250 metres and extends from the surface to approximately 600 metres below the surface (Fig. 5.17). Stage C alteration occurs entirely within the breccia pipe and a weak north-northwest trend can be observed in its orientation. The maximum depth of reported Stage C alteration extends to at least 800 metres below the surface at the end of drill hole IXCM07-20 791.8 where a weak Stage C<sub>HK</sub> alteration is observed.

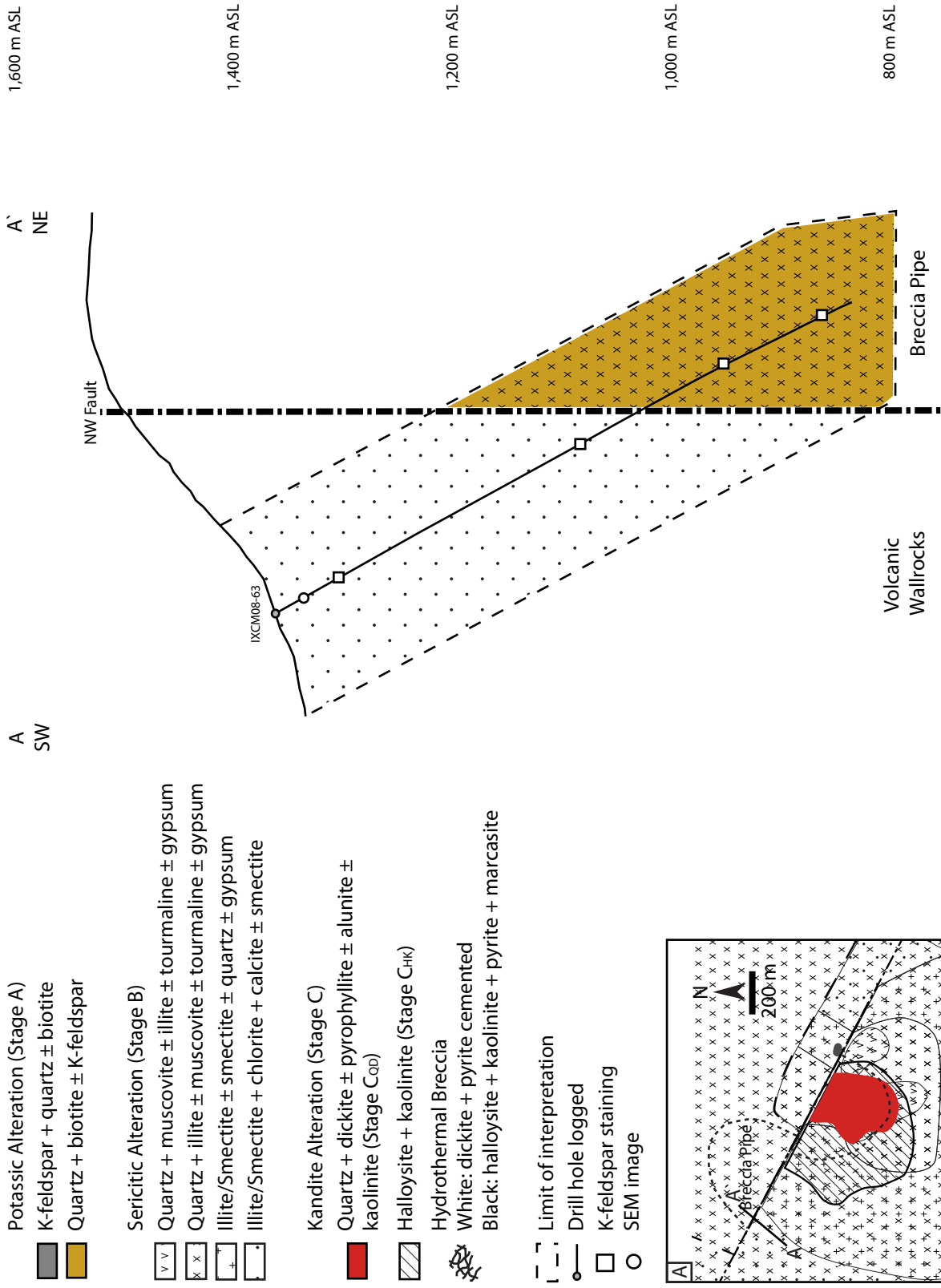


Figure 5.12 Alteration of cross section A-A'. Cross section location shown on plan view in inset A.

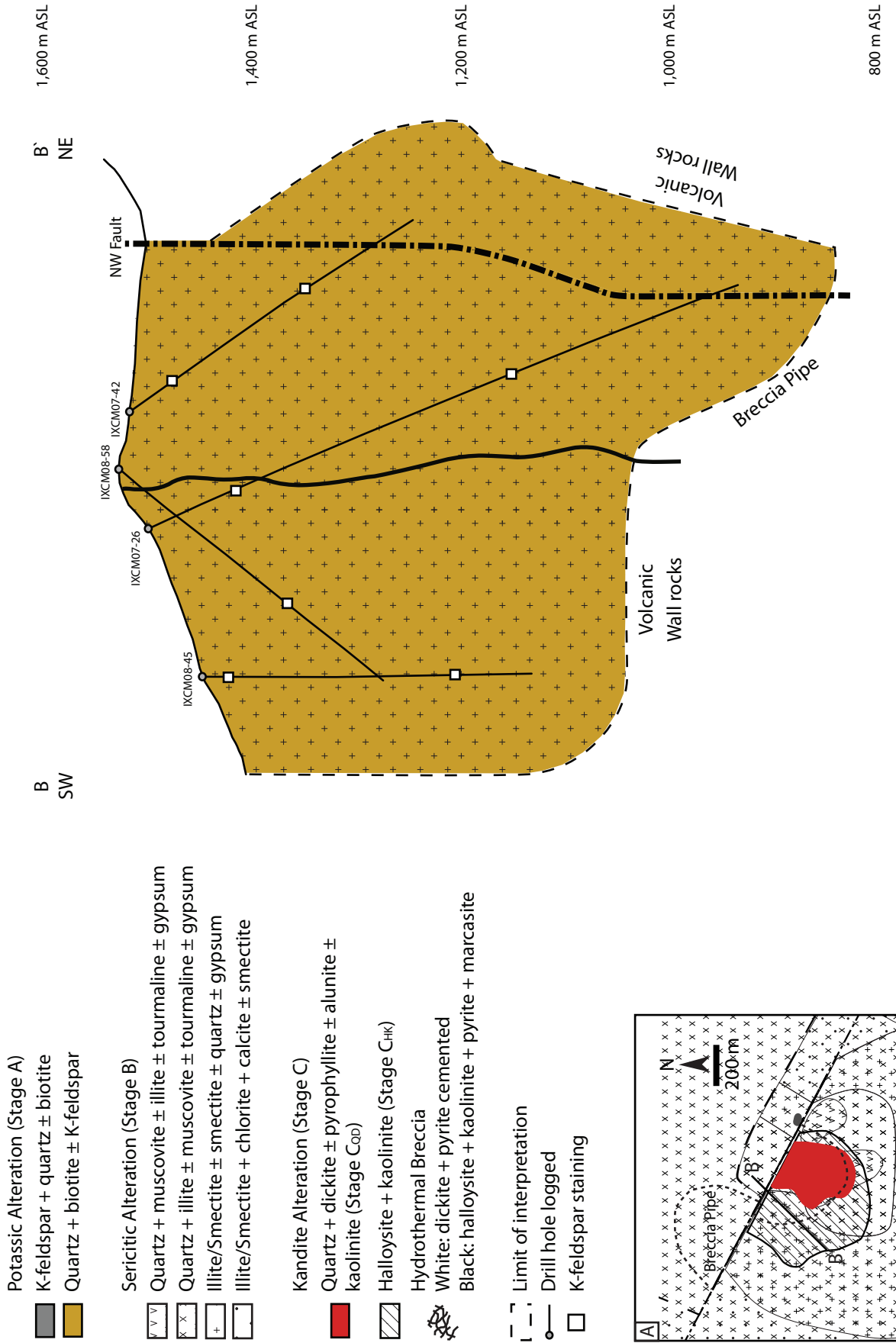


Figure 5.13 Alteration of cross section B-B'. Cross section location shown on plan view in inset A.

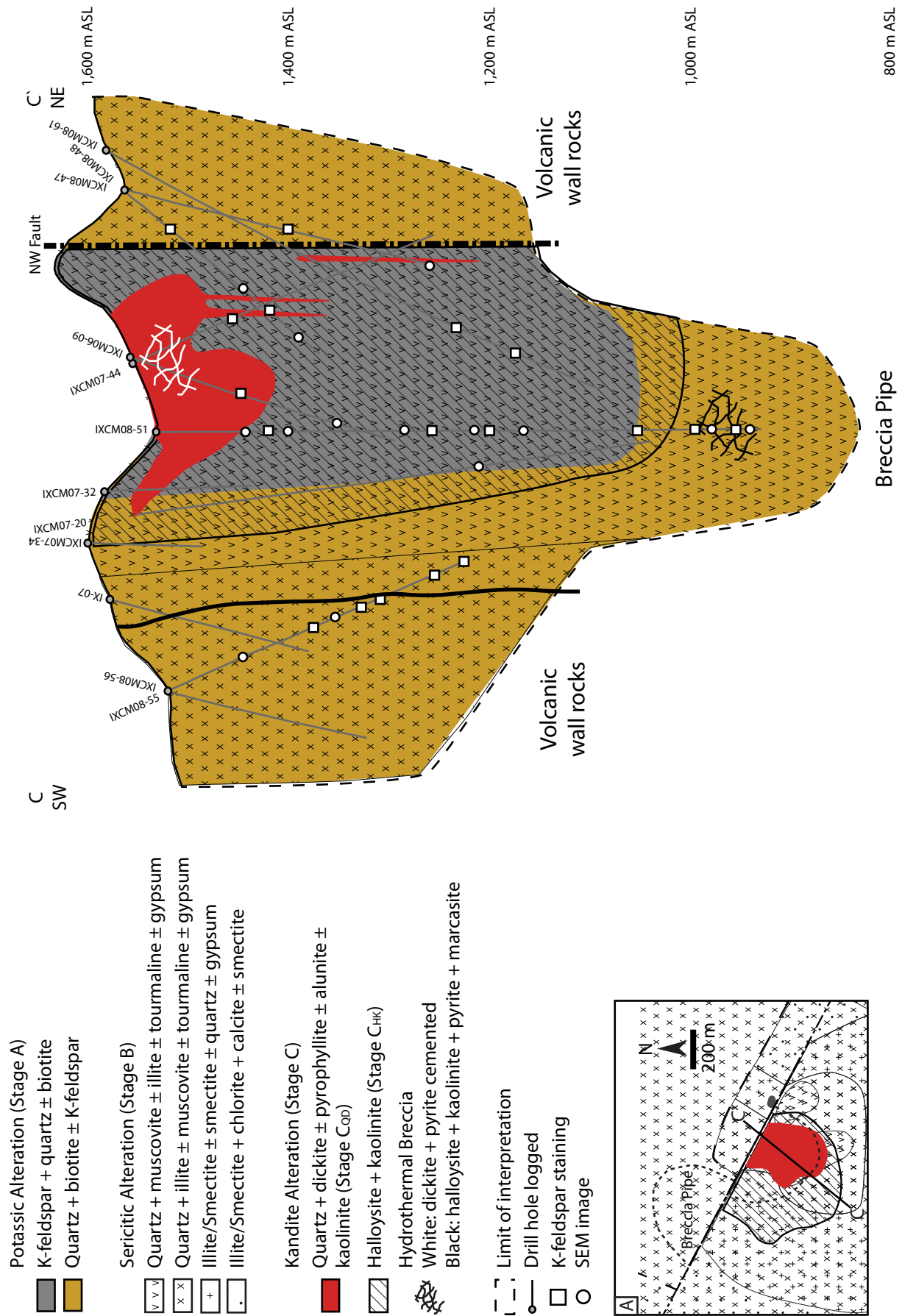


Figure 5.14 Alteration of cross section C-C'. Cross section location shown on plan view in inset A.

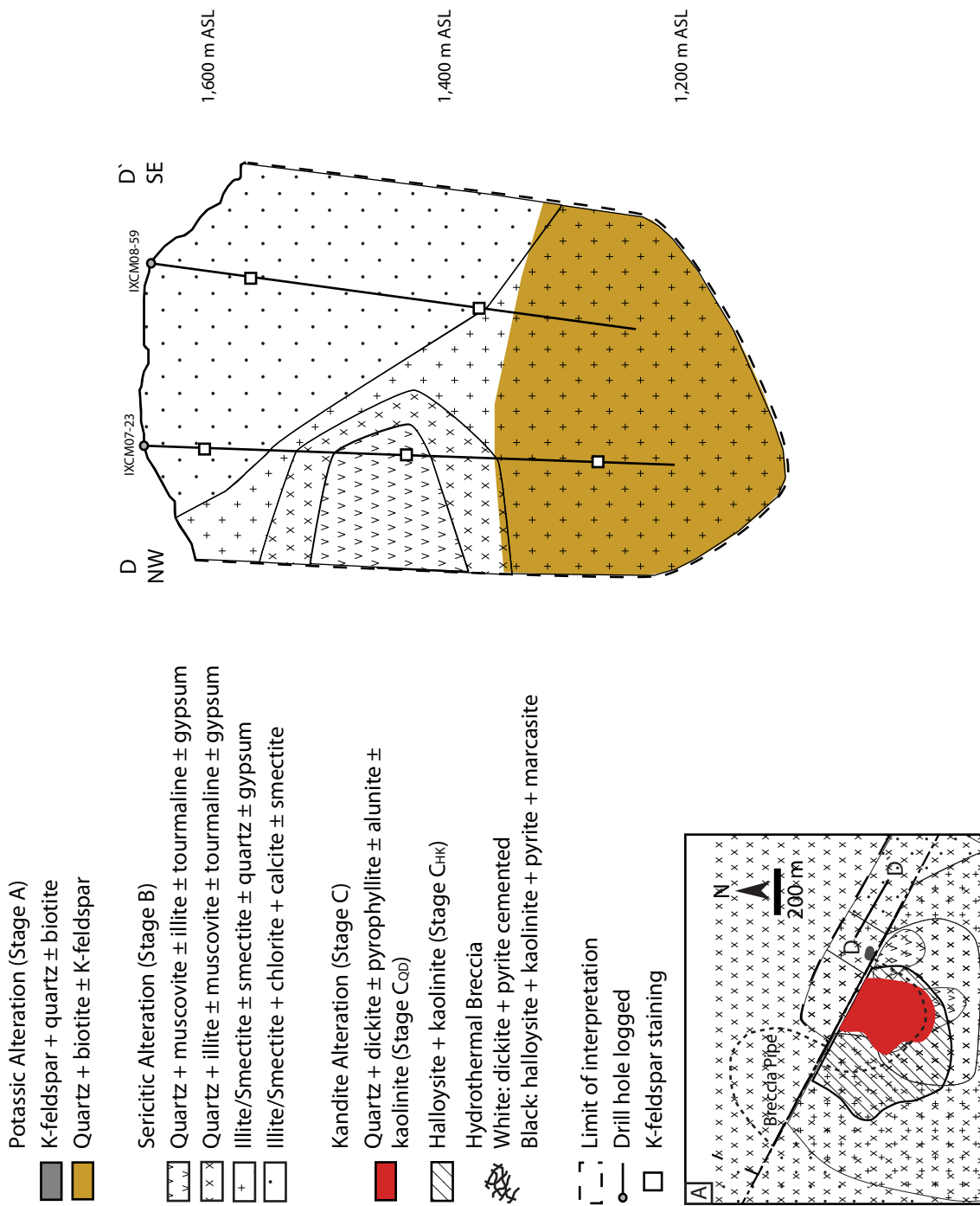
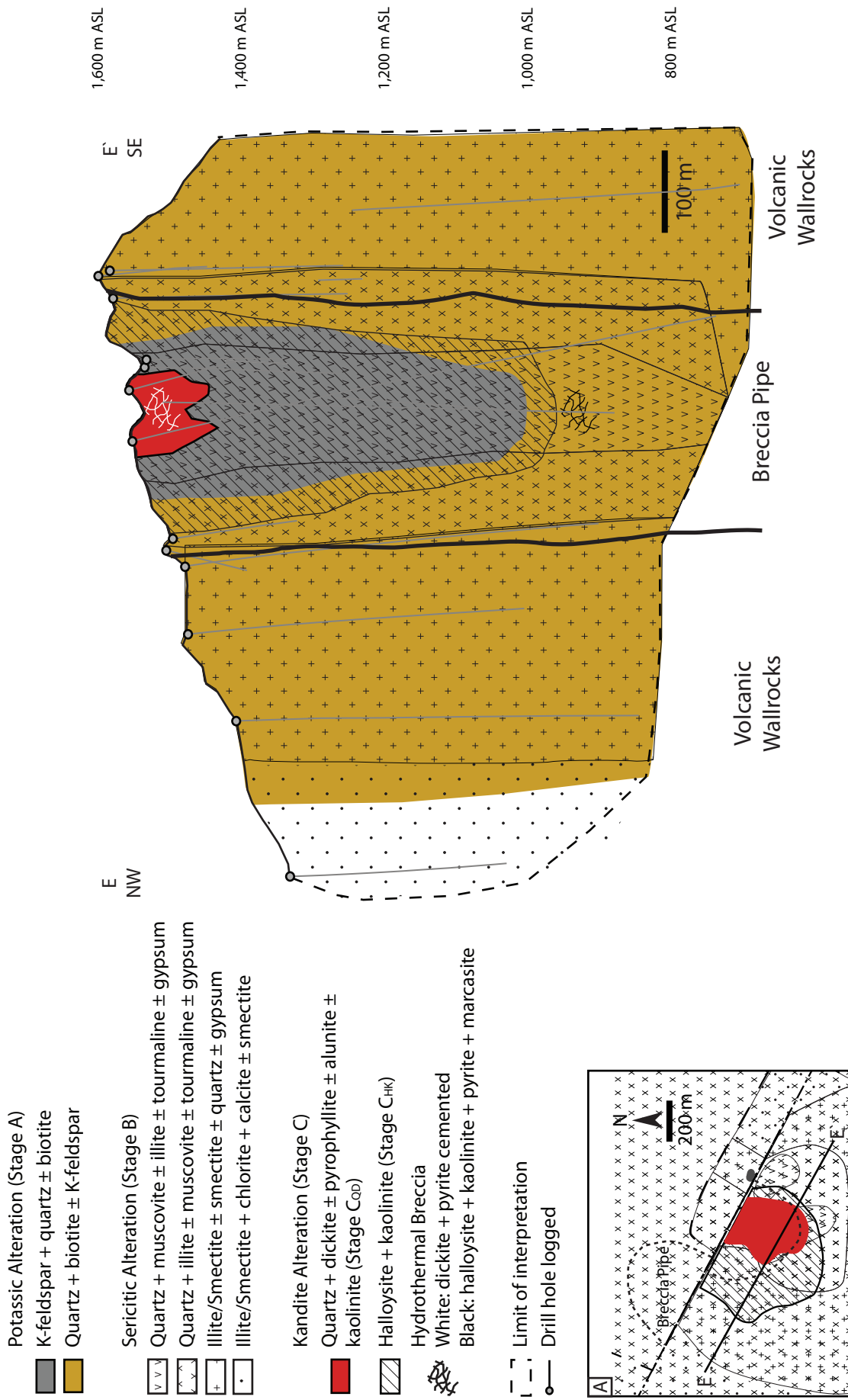
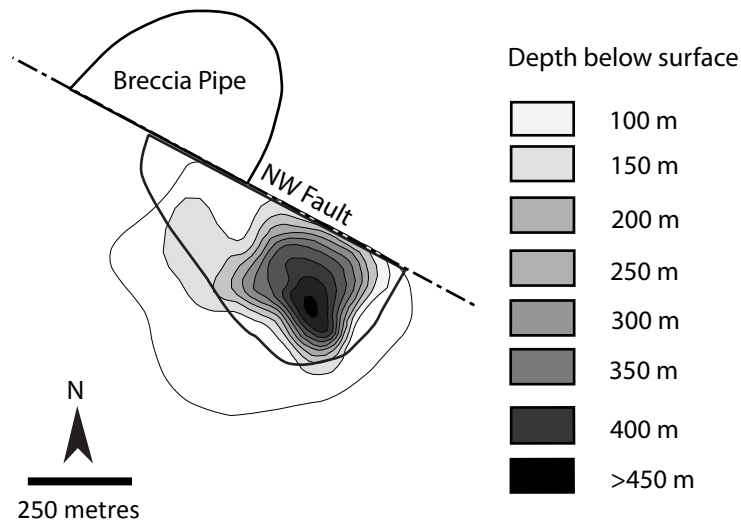


Figure 5.15 Alteration of cross section D-D'. Cross section location shown on plan view in inset A.



**Figure 5.16** Alteration of long section E-E'. Long section location shown on plan view in inset A.



**Figure 5.17** Depth below surface contour of kandite alteration (Stage C).

## 5.5 Discussion of Cerro la Mina Alteration

The alteration comprises potassic (Stage A) overprinted by sericitic (Stage B) and kandite (Stage C). The telescoping of advanced argillic alteration onto a porphyry system would require significant uplift of at least one kilometre via erosion or sector collapse (Sillitoe, 1994). All of the strong alteration occurs in the breccia pipe (Unit 4). The volcanic wall rocks contain less than 1 percent quartz consistent with a mafic composition for the Selva Negra volcanic rocks discussed in Chapter 3. Therefore, the high abundance of quartz in Stage A, Stage B and Stage C<sub>OD</sub> is interpreted to be hydrothermal.

The Cerro la Mina alteration consists of an early porphyry style alteration with a potassium feldspar + biotite alteration assemblage (Stage A) that is overprinted by a predominantly muscovite + illite assemblage (Stage B; Fig. 5.18). These assemblages are consistent with the potassic and phyllic zone respectively of a porphyry system (Lowell and Guilbert, 1970). The potassic zone is characterized by a potassium feldspar core in the breccia pipe and surrounded by biotite predominantly in the volcanic wall rocks. The timing of the potassic alteration (Stage A) is interpreted to have formed after breccia pipe formation. Clasts of quartz-potassium feldspar are observed in the breccia pipe and the breccia pipe matrix is strongly altered to potassium feldspar, indicating post-breccia timing. However, based on vein textures described in Chapter 6 the potassic alteration is interpreted to have also occurred before breccia pipe formation. A pre-breccia pipe timing suggests that the clasts of quartz-potassium feldspar probably formed during breccia pipe formation. In thin-section sericite is commonly observed to alter potassium feldspar and hydrothermal biotite.

The sericitic alteration (Stage B) is zoned with a quartz + muscovite ± illite ± gypsum core centred on the breccia pipe transitioning to quartz + illite ± muscovite ± tourmaline ± gypsum, illite/smectite ± smectite ± gypsum, and illite/smectite + calcite + chlorite ± smectite distally (Fig. 5.10).

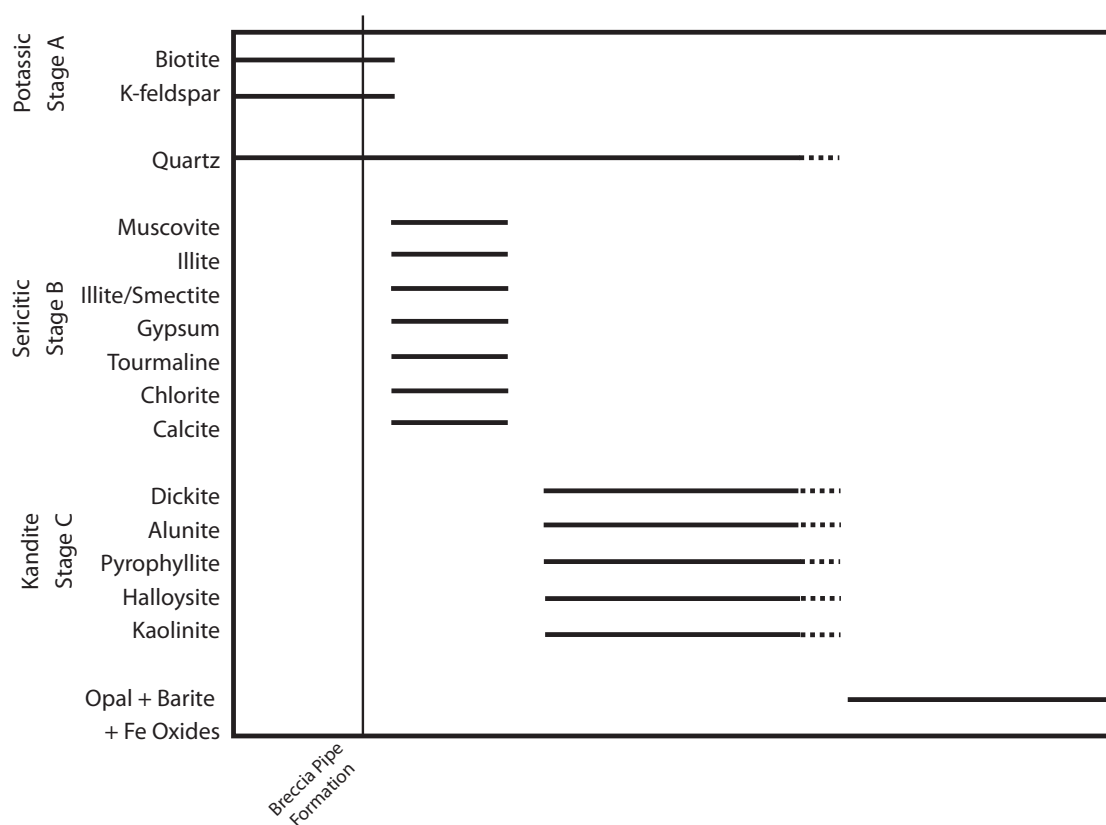


**Figure 5.18** Paragenetic sequence of alteration for the Cerro la Mina prospect.

This zonation reflects a decreasing temperature moving distally (Reyes, 1990; Corbett and Leach, 1998; Hedenquist, 2000). The zonation is also reflected in the Al-OH and crystallinity shifts in the spectra data. The zoned sericitic alteration indicates that the high temperature source is within the Cerro la Mina breccia pipe.

Gypsum is common and has probably resulted from the hydration of anhydrite by ground-water and/or after drilling due to the high humidity of northern Chiapas. The anhydrite could be an alteration product or a primary feature of the volcanoclastic rocks. Fresh pumice from the nearby El Chichón volcano contained approximately 1 vol. % anhydrite microphenocrysts (Luhr, 2002). The content of anhydrite at Cerro la Mina is uncertain because it has hydrated to gypsum which is easily removed during sample handling.

The extensive advanced argillic overprint is characterized by Stage C alteration comprising predominantly halloysite, kaolinite and dickite and abundant hydrothermal breccias (Figs. 5.7 and 5.8). Pyrophyllite and alunite also occur. Kandite (Stage C<sub>QD</sub>) is late, as it forms the cement of brecciated quartz + muscovite altered clasts (Stage B). In addition, halloysite + kaolinite (Stage C<sub>HK</sub>) is observed to alter potassium feldspar (Stage A) and muscovite (Stage B) under the SEM. Stage C<sub>HK</sub> alteration is developed to at least 800 metres below the present day surface in the fluid pathway of the breccia pipe, deeper than the hypogene clay minerals dickite + alunite + pyrophyllite (Stage C<sub>QD</sub>). Intense Stage C alteration occurs at deeper and deeper positions in the middle of the breccia pipe

(Figs. 5.16 and 5.17), suggesting that the source of the fluids is probably an underlying intrusive body. The Stage C alteration contains abundant kandite clay cemented breccias that are interpreted to be the result of breccia by hydrothermal fluids.

Hedenquist (2000) described hypogene alunite to be coarse-grained (visible with a hand lens) with tabular crystals while supergene and steam heated alunite to be fine-grained with a pseudo cubic or rhombohedral shape. The Cerro la Mina alunite are euhedral, hexagonal, tabular crystals up to 150  $\mu\text{m}$  and associated with dickite and pyrophyllite consistent with a hypogene origin. The Stage  $C_{\text{HK}}$  only occurs where pyrite is present and is absent where the oxide is well developed (no pyrite) and is consistent with a hypogene origin for halloysite. The absence of Stage  $C_{\text{HK}}$  alteration in the oxide zone suggests that it is unstable in supergene environment. The sericitic alteration, however, is stable in the oxide zone resulting in a sericite-rich and resistant (opal) oxide zone.

The mineral assemblages indicate that the Stage C fluids were acidic (Hedenquist, 2000). Stage C alteration is different from the typical alteration in most high sulfidation epithermal deposits in that there is no vuggy quartz and rare alunite but abundant halloysite. A thick sequence of evaporites and limestone in the basement rocks (described in Chapter 2) has probably buffered the fluid acidity that produces intensely leached rocks and vuggy quartz.

## 5.6 Halloysite

The Stage C alteration contains abundant halloysite to at least 800 metres below the present day surface. Halloysite typically forms at low temperatures ( $< 100^\circ\text{C}$ ; Marumo and Hattori, 1999) and is traditionally thought to be a supergene mineral (e.g., Hedenquist, 2000), however at Cerro la Mina, it occurs at depth and is association with sulfides, suggesting a hypogene origin. To constrain the origin of the unusual halloysite alteration at Cerro la Mina it has been studied with SWIR, QXRD and SEM analysis.

### 5.6.1 KH Index

The Stage  $C_{\text{HK}}$  alteration at Cerro la Mina is extensive and QXRD data shows that the relative abundances of halloysite to kaolinite changes in samples. The author developed a KH index in this study to determine the relative abundance using much less expensive SWIR spectral data that can be acquired at faster speed. The KH index uses the relative depth of the water absorption peak to the depth of the Al-OH peak from SWIR spectra to measure the relative abundance of halloysite to kaolinite.

In short wave infrared spectra the kandite group minerals halloysite and kaolinite have two doublets occurring at  $\sim 1400$  and  $\sim 2200$  nm, according to the TSG v. 5 library (Fig. 5.19). Halloysite and kaolinite form doublets consisting of a shallow 1412 nm and a deeper 1390 nm absorption peak and a second doublet consisting of a shallow 2175 nm and deep 2207 nm absorption peak. Halloysite is distinguished from kaolinite by a deeper water absorption peak ( $\sim 1900$  nm).

The relative abundance of halloysite and kaolinite is believed to be determinable by measuring the depth of their water absorption peak which increases from kaolinite to halloysite (Fig. 5.19). These minerals have the same chemical composition and are believed to have the same SWIR spectral sensitivity. The change in water absorption depth can be measured by dividing the depth of the Al-OH absorption peak (2207 nm) by the depth of the ~1900 nm peak, herein referred to as the KH index. Figure 5.19 shows the TSG v. 5 library spectra for kaolinite and halloysite, their increasing depth of the water absorption peak at 1910 nm and their decreasing KH index of 4.2 and

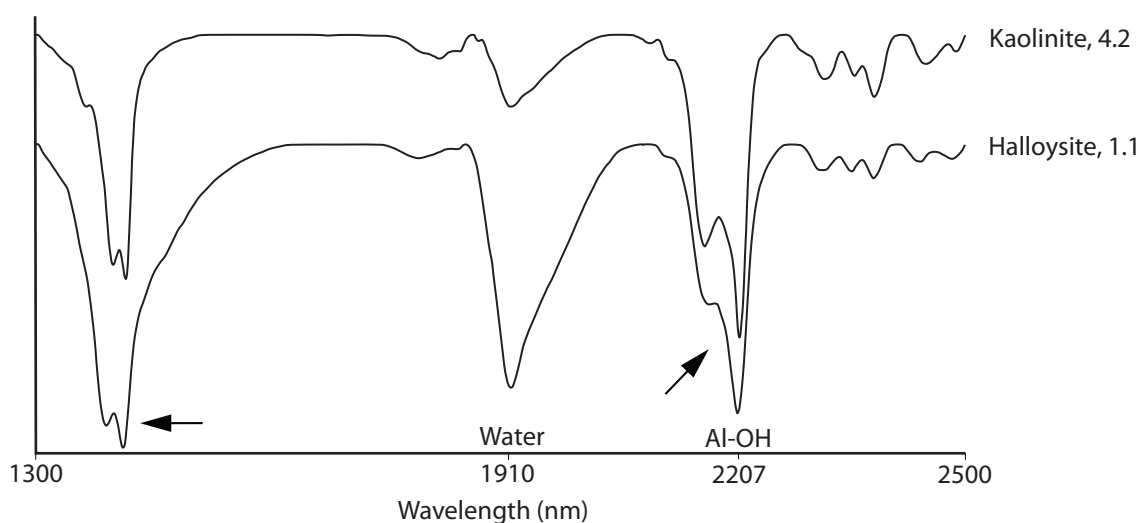


**Figure 5.19** Comparison of TSG v.5 reference library spectra for kaolinite and halloysite. Arrows point to the doublets in halloysite and kaolinite SWIR spectra. The water absorption peak position is deeper for halloysite than it is for kaolinite and is reflected in the KH index value.

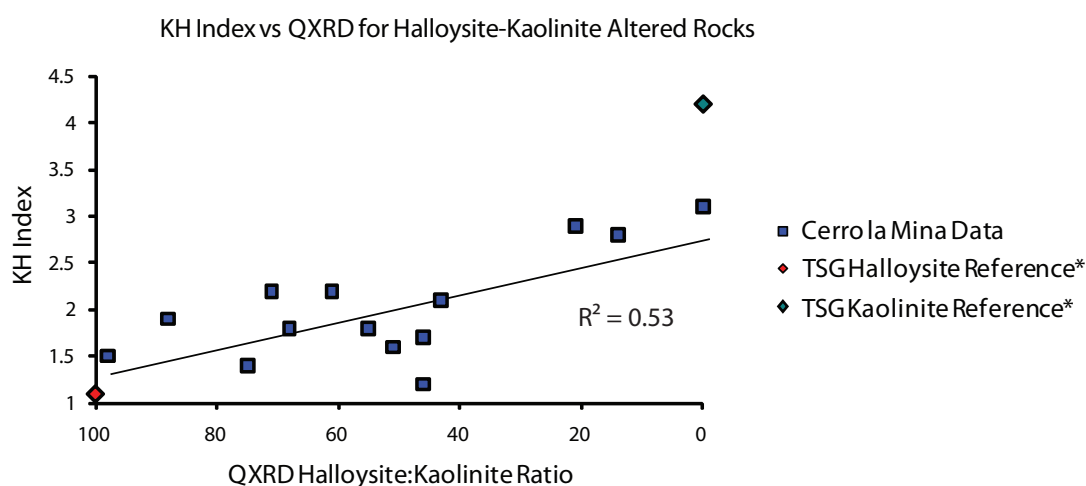


**Figure 5.20** KH index versus QXRD analysis of samples containing halloysite/kaolinite. \* The Spectral Geologist version 5.

1.1, respectively. The KH index for the Cerro la Mina kandite group clays varies slightly from the TSG library where HK altered samples range from 0.5 to 3.0. A halloysite and kaolinite-rich sample (>80%) is considered to have a range from 0.5 to 1.0 and 2.5 to 3.0, respectively (Fig. 5.20). A 50/50 mixture would have a value of 1.8 (Fig. 5.20).

To validate the accuracy of the KH index a comparison with quantitative XRD analysis was done on whole rock and on clay separates with varying abundances of halloysite to kaolinite. The data shows a correlation of increasing KH index with increasing kaolinite content in the samples (Fig. 5.20). The data has an  $R^2$  value of 0.53 and the scatter is probably from moisture content in the samples creating a larger water absorption peak (~1900 nm).

Caution should be used when applying the KH index. The water absorption depth can change if the sample has been heated and/or has not been stored in 100 percent humidity, as halloysite can readily dehydrate in ambient conditions (Churchman and Carr, 1972). Only samples containing halloysite and/or kaolinite can be used as other minerals with a water absorption feature will affect the KH index. All of the samples used in this study were measured shortly after drilling and were stored in the high humidity environment of northern Chiapas.

### 5.6.2 Kaolinite-Halloysite Zoning

Figure 5.21 shows cross section C-C' with a contoured map of the KH index. The KH index values have two highs, one at the surface where the KH index increases toward the Stage  $C_{QD}$  alteration and a weak anomaly below 1200 metres elevation associated with a kaolinite > halloysite assemblage. Quantitative XRD analysis also confirms the corresponding mineralogy. The KH anomaly at the surface transitions over a short distance from a dickite zone, toward kaolinite and predominantly halloysite alteration. The upper KH anomaly also occurs at lower elevations close to the northwest fault.

To study the transition from the upper Stages  $C_{QD}$  to  $C_{HK}$  alteration in detail, the distribution of kandite minerals was plotted across the contact with SWIR, XRD, and quantitative XRD data (Fig. 5.22). The transition from the Stages  $C_{QD}$  to Stage  $C_{HK}$  alteration is marked by the loss of dickite and halloysite and kaolinite becoming the dominant minerals. A total of eight drill holes were used and the diagram represents an average representation for the distribution of mineralogy. The distance of the sample from the Stages  $C_{QD}$  to  $C_{HK}$  contact was measured from the contact observed in their respective drill hole.

The transition from the Stages  $C_{QD}$  to  $C_{HK}$  alteration occurs over a distance of < 1 metre. Kaolinite and occasionally halloysite also occur in the Stage  $C_{QD}$  alteration. In Stage  $C_{HK}$  alteration, kaolinite is the dominant mineral within five metres of the contact (KH range = 1.7 to 2.8; mean 2.4). A ~50/50 halloysite and kaolinite mixture occurs for ~60 metres from the contact (KH range = 1.0 to 3.0; mean = 1.7). A halloysite > kaolinite assemblage occurs from ~60 to ~180 metres and remains relatively constant (KH range = 1.0 to 1.7; mean = 1.3). Overall a zoning comprising a dickite core surrounded by kaolinite and more distal halloysite-rich assemblage is observed.

Cerro la Mina Contour Map of the KH Index  
Cross Section C-C'

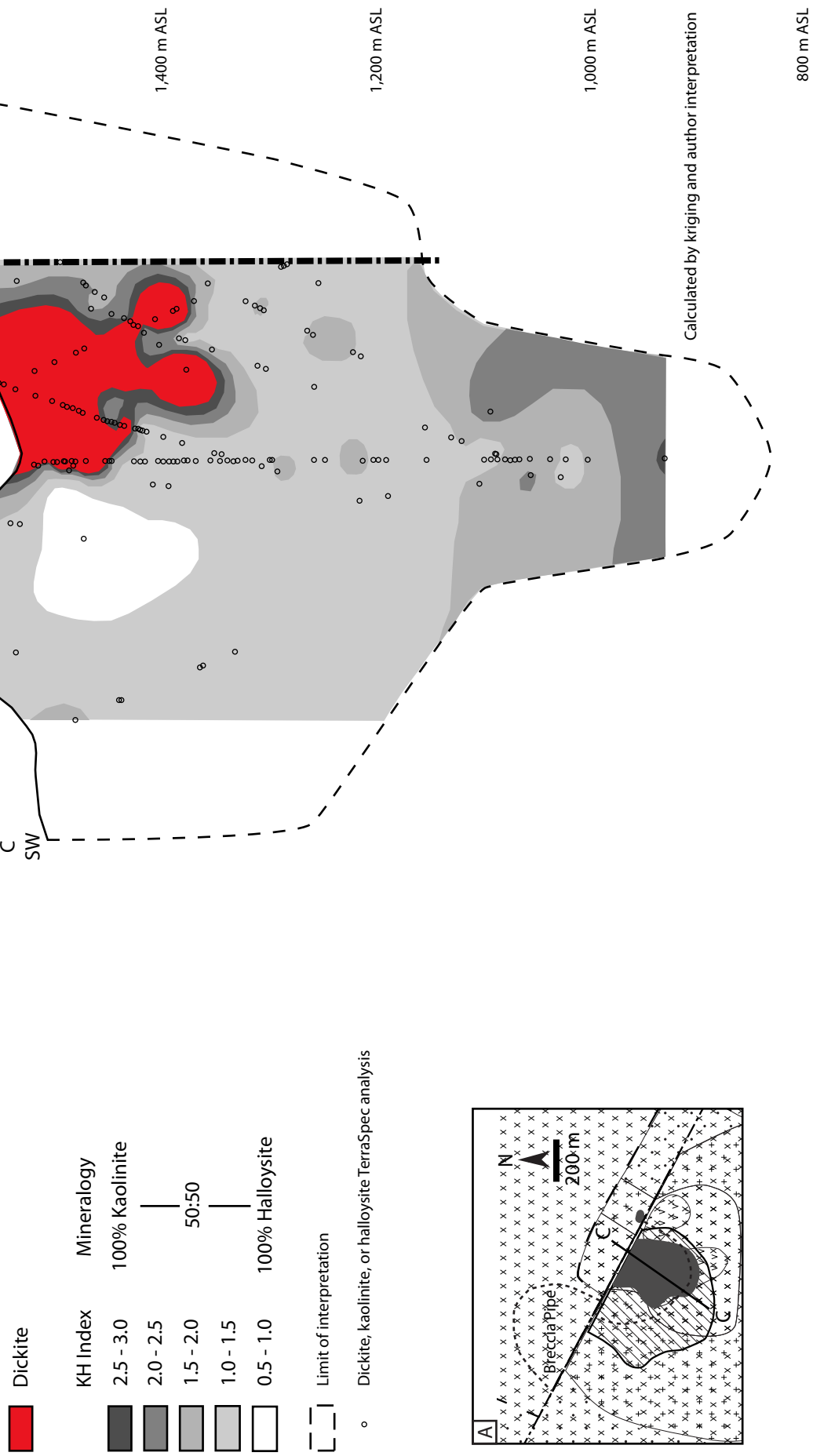
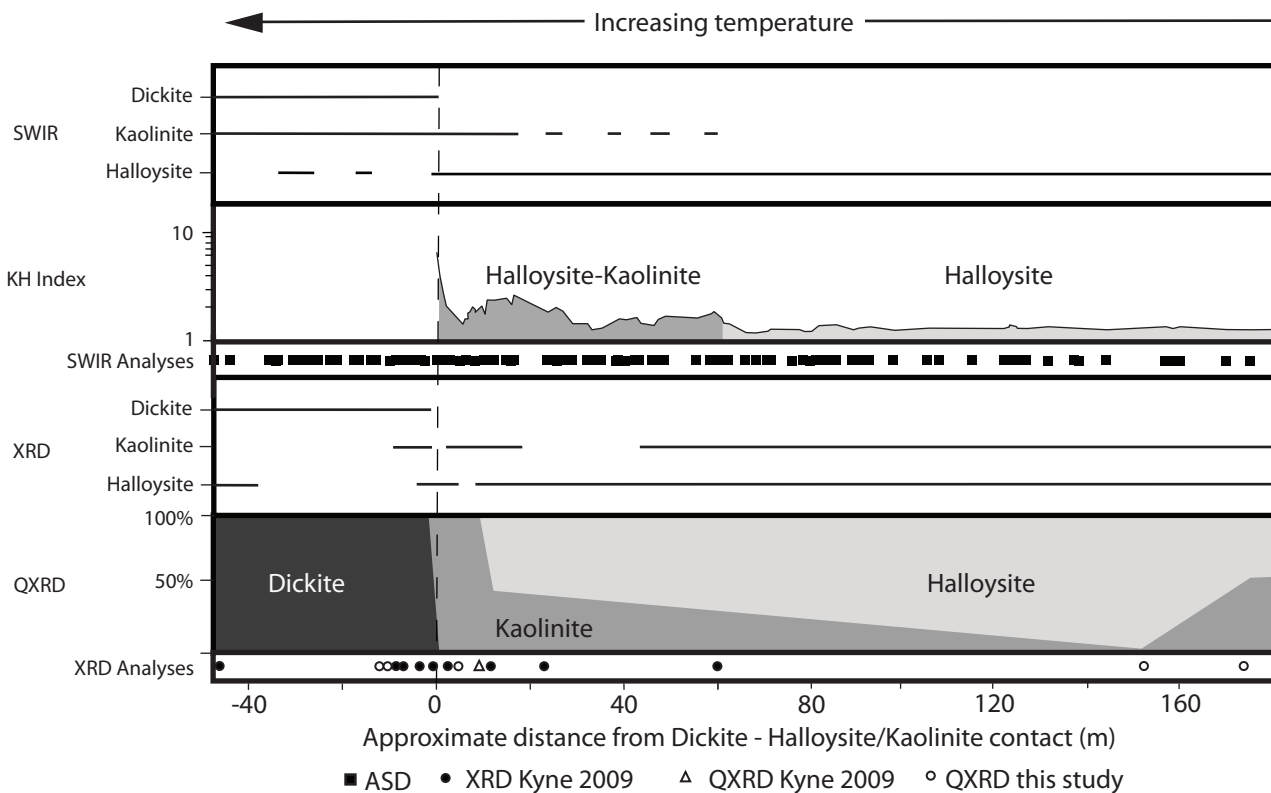


Figure 5.21 KH index of cross section C-C'. Location of cross section shown in plan view map (inset A).



**Figure 5.22** Zoning of the Stage  $C_{QD}$  and Stage  $C_{HK}$  alteration illustrated with SWIR spectral identification, KH Index, XRD mineral identification, and QXR D data. The quartz-dickite to halloysite-kaolinite contact is defined by the disappearance of the dickite. Increasing temperature for the minerals dickite, kaolinite and halloysite from Corbett and Leach (1998). For the QXR D data, only the relative abundances of dickite-kaolinite-halloysite are presented. For the KH index data, only spectra that closely resembled the TSG reference library kaolinite and halloysite or a mixture were used. QXR D and SWIR spectral identification taken from drill holes from IXCM06-05, IXCM06-06, IXCM06-09 and IXCM08-51.

### 5.6.3 SEM Imaging of Stage $C_{HK}$ Alteration

Rocks with Stage  $C_{HK}$  alteration and mineral separates of such rocks were imaged using the SEM to examine the crystal morphology, parent mineral and paragenesis of the halloysite and kaolinite. 183 SEM images of whole rock, vein and clay separate samples throughout the halloysite alteration zone were taken (Table 5.4; Appendix III.6).

In general kaolinite typically has hexagonal platy crystal morphology and halloysite typically has an elongate tubular morphology (Keller et al., 1975; Joussein et al., 2005). However, halloysite can also occur as plates and much debate has been put forth on how to differentiate halloysite from kaolinite based on morphology (Joussein et al., 2005). To determine the crystal morphology of halloysite at Cerro la Mina, SEM imaging and quantitative XRD analysis was done on a Stage  $C_{HK}$  altered rock that was separated to  $<10 \mu\text{m}$ ,  $<4 \mu\text{m}$ , and  $<1 \mu\text{m}$  size fractions (Table 5.5). The  $<1 \mu\text{m}$  size fraction for sample IXCM08-51 317.0 reported the highest content of halloysite at 73.9 percent (QXR D) and contained the most abundant elongate crystals (Fig. 5.23) compared to the other size fractions. The positive correlation between the abundance of halloysite measured by QXR D and the abundance of tubes in SEM images indicate that the halloysite at Cerro la Mina mainly has a tubular shape.

| Drill Hole | Depth  | No. of Carbon Coated Images | No. of Gold Coated Images | Type  |
|------------|--------|-----------------------------|---------------------------|---|
| IXCM06-09  | 214.9  | 2                           | 22                        | Vein  |
| IXCM07-20  | 377.9  | 4                           | 9                         | Whole rock                                    |
| IXCM08-47  | 315.8  | 6                           |                           | Clay separates < 10 and < 4 $\mu\text{m}$     |
| IXCM08-48  | 147.1  | 6                           |                           | Clay separates < 10 and < 4 $\mu\text{m}$     |
| IXCM08-48  | 206.2  | 4                           | 9                         | Whole rock                                    |
| IXCM08-51  | 73.5   | 7                           | 33                        | Whole rock                                    |
| IXCM08-51  | 144.1  | 6                           |                           | Clay separate < 10 $\mu\text{m}$              |
| IXCM08-51  | 238.1  | 9                           | 20                        | Whole rock                                    |
| IXCM08-51  | 317.0  | 17                          |                           | Clay separates < 4, < 2 and < 1 $\mu\text{m}$ |
| IXCM08-51  | 380.1  | 5                           | 24                        | Whole rock                                    |
| IXCM08-51  | 5.10.1 | 7                           |                           | Clay separates < 2 and < 1 $\mu\text{m}$      |
| IXCM08-51  | 5.10.5 | 7                           | 39                        | Whole rock                                    |
| IXCM08-55  | 65.6   |                             | 27                        | Vein  |
| IXCM08-55  | 170.6  | 4                           | 6                         | Whole rock                                    |
| IXCM08-63  | 47.5   |                             | 4                         | Whole rock                                    |
|            | Total  | 66                          | 117                       |   |

**Table 5.4** Summary of whole rock, vein and clay separate of halloysite-kaolinite altered samples observed with the SEM.

| Phase        | Bulk Rock | <10 $\mu\text{m}$ | <4 $\mu\text{m}$ | <1 $\mu\text{m}$ |
|--------------|-----------|-------------------|------------------|------------------|
| Orthoclase   | 67.5      | 66                | 60.1             | 14.2             |
| Plagioclase  | 16        | 14.8              | 15.7             | 9                |
| Quartz       | 9.6       | 4.8               | 3.8              | 0.6              |
| Halloysite   | 2.5       | 11.5              | 18.2             | 73.9             |
| Kaolinite    | 1.2       | 1.3               | 0.7              | 1.8              |
| Chalcopyrite | 2.4       | 1.3               | 1.4              | 0.2              |
| Molybdenite  | 0.9       | 0.3               | 0.3              | 0.2              |

**Table 5.5** Quantitative XRD analysis of bulk rock, <10  $\mu\text{m}$ , <4  $\mu\text{m}$  and <1  $\mu\text{m}$  fractions of a halloysite-kaolinite altered samples. **Sample ID:** IXCM08-51 317.0.

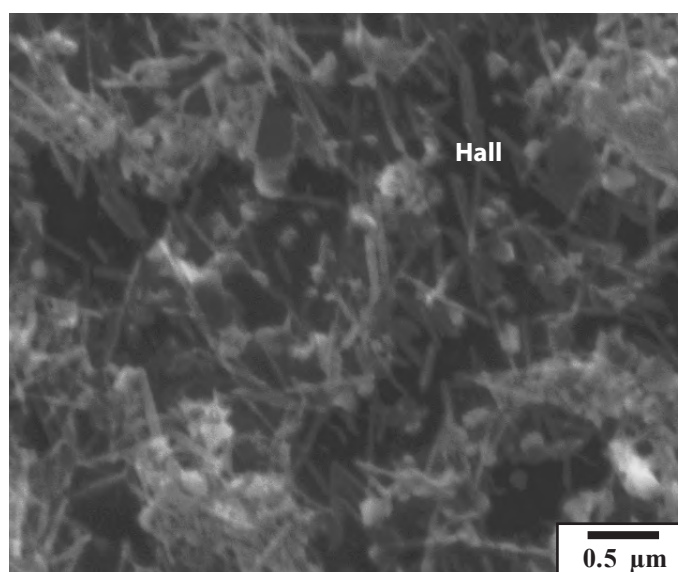


**Figure 5.23** SEM image of the < 1  $\mu\text{m}$  fraction of a halloysite-kaolinite altered rock. The shape of the minerals is predominately elongate crystals indicative of halloysite. **Abbreviations:** Hall - halloysite. **Sample ID:** IXCM08-51 317.0.

The whole rock samples contained halloysite of seven morphologies. Spheroids (1) form on the surfaces of the parent mineral and occur in association with flat tubes (Fig. 5.24A). They are less than 0.3  $\mu\text{m}$  size and due to their small size no EDS signal was obtained to determine their composition. Flat, intermediate, and vertical classification (2 to 4) are based on the position of the tube in relation to the parent mineral, with flat being tubes parallel to the parent mineral (Figs. 5.24A and E) and vertical having sub-vertical to vertical orientation in relation to the parent mineral (Figs. 5.24B to D).

The intermediate classification is a cylindrical tube that is in between a flat and vertical orientation (Figs. 5.24A to B). The flat to vertical tubes range from 0.3 to 8.1  $\mu\text{m}$  in length and are approximately  $<0.6 \mu\text{m}$  in width (Table 5.6). The tubes are observed to be filling voids and their growth direction is controlled by the void formed by the surrounding minerals into which they grew (Fig. 5.24B). Aggregates (5) are a collection of extended tubes that have grown into radial bushes with random orientation (Figs. 5.24B to D). Fine grained sulfides ( $< 1 \mu\text{m}$ ) are observed in the aggregates of cylindrical tubes (Fig. 5.25). An anhedral sheet-like morphology (6) is observed at the base of well developed cylindrical crystal aggregates (Fig. 5.24D). The sheet like morphology produces Al-Si-O peaks in EDS spectra. Aligned tubes (7) are parallel and orientated in the same direction (Fig. 5.24F). A transition from spheroid toward flat, intermediate, extended, aggregates of cylindrical tubes and sheet-like morphologies is observed respectively.

The crystal morphology of kandite minerals observed under the SEM correlate with the dominant mineralogy reported in the quantitative XRD data (Table 5.6). The flat to extended morphologies are the dominant morphology when the XRD reports a significant amount of halloysite ( $>60\%$  relative to kaolinite). When aggregates are observed the XRD reports a mixture of halloysite and kaolinite ( $\sim 50:50$  ratio). Aligned tubes are the dominant morphology when XRD reports a significant amount of halloysite and muscovite in the sample. When the cylindrical tubes are well developed and the sheet-like morphology is observed both halloysite and kaolinite are reported in the quantitative XRD.

The dominant parent mineral to which the halloysite and kaolinite crystals are associated with is potassium feldspar. Albite, muscovite, pyrite, quartz were also observed to have tubes growing on their surfaces. The cylindrical tubes are commonly found forming in the vugs of their parent minerals and occur in the gaps or voids between mineral boundaries (Fig. 5.24B).

#### 5.6.4 Halloysite Dehydration

Halloysite readily loses its inter-layer water even under ambient conditions of temperature and humidity (Churchman and Carr, 1972). Joussein et al. (2007) showed that a fresh soil sample with fully hydrated halloysite  $10\text{\AA}$  appeared to become completely dehydrated after storage for 21 years at  $20^\circ\text{C}$  and 30 percent humidity. The dehydration of halloysite shows that it does not proceed via a single transformation between phases but rather through the formation of a continuous series of hydration states of the mineral with the loss of successive increments of water (Churchman and Carr, 1972). In addition, the irreversibility of the dehydration process implies that the fully dehydrated form

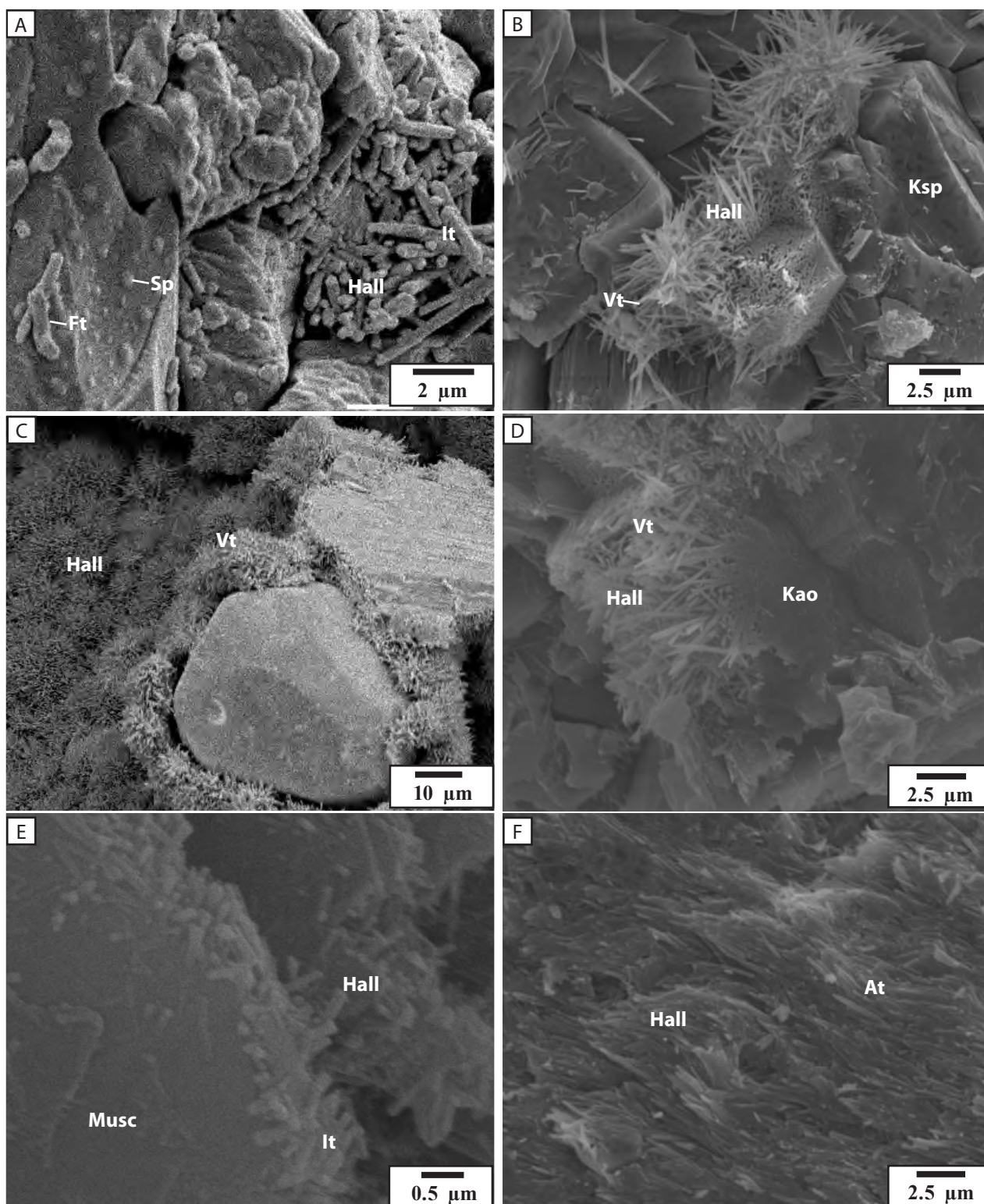


**Figure 5.24** SEM images of halloysite-kaolinite altered samples. A. Spheroids and flat cylindrical crystals developed on the surface of a potassium feldspar (left side of image) and extending to intermediate cylindrical crystals (Kyne, 2009). B. Cylindrical crystals controlled by a void created by the surrounding potassium feldspar and flat to intermediate cylindrical crystals on the surface of a potassium feldspar. C. Aggregates of coalesced cylindrical crystals. D. Aggregate of coalesced cylindrical crystals that transition to sheet like morphology (Kyne, 2009). E. Cylindrical crystals growing on the surface and edge of a muscovite crystal. F. Strong alignment of tubes and associated sheet like morphology developed at the base of the tubes. **Abbreviations:** At - aligned tubes, Ft - flat tubes, Hall - halloysite, It - intermediate tubes, Kao - kaolinite, Ksp - potassium feldspar, Musc - Muscovite, Sp - spheroids, Sulf - sulfide, Vt - vertical tubes. **Sample ID:** A - IXCM07-25 330.0, B - IXCM08-51 238.1, C - IXCM06-05.129.2, D - IXCM08-51 238.1, E - IXCM08-55.75.6, F - IXCM08-51 73.5.

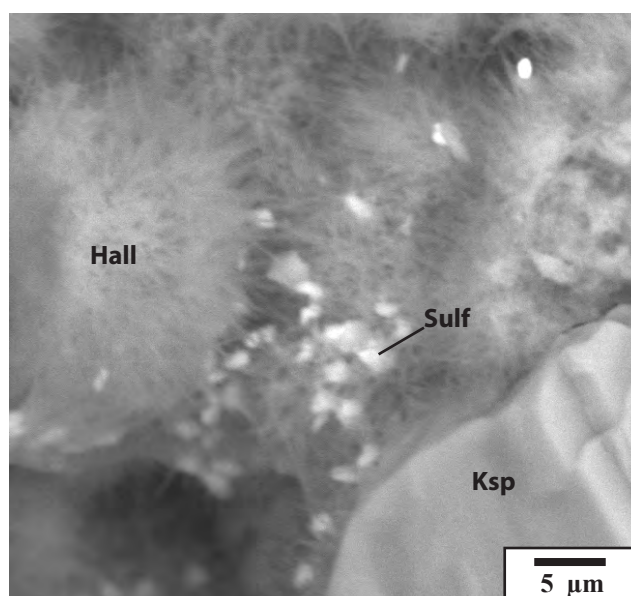


**Figure 5.25** SEM image of halloysite aggregates intergrown with fine-grained sulfides. **Abbreviations:** Hall - halloysite, Sulf - sulfide, Ksp - potassium feldspar. **Sample ID:** IXCM08-51 238.1.

| Morphology   | Tube Length   | Parent Mineral | Dominant mineralogy in QXRD |
|--------------|---------------|----------------|-----------------------------|
| Spheroids    | <0.3 μm       | Plag, Ksp, py  | Halloysite                  |
| Flat         | 0.3 to 3.3 μm | Plag, Ksp      | Halloysite                  |
| Intermediate | 3.3 to 4.8 μm | Plag, Ksp      | Halloysite                  |
| Extended     | 4.8 to 8.1 μm | Plag, Ksp      | Halloysite                  |
| Aggregates   | 4.8 to 8.1 μm | Plag, Ksp      | Halloysite-Kaolinite        |
| Aligned      |               | Musc           | Kaolinite                   |
| Sheet-like   |               | not observed   | Kaolinite                   |

**Table 5.6** The size range, parent mineral, and dominant quantitative XRD mineralogy for different morphologies of the Cerro la Mina halloysite-kaolinite altered rocks. **Abbreviations:** Ksp - potassium feldspar, Musc - muscovite, Plag - plagioclase, Py - pyrite.

is the only stable phase in the halloysite dehydration series (Churchman and Carr, 1972).

Kyne (2009) reported the presence of both halloysite species (7Å and 10Å), however this study has only found halloysite 7Å. The samples used by Kyne (2009) were analysed shortly after leaving high humidity conditions of southern Mexico, whereas the samples from this study were stored for at least 1 year in relatively low humidity conditions in Hobart, Australia, before analysis. This suggests that during storage in Hobart the halloysite 10Å could have dehydrated to halloysite 7Å.

A study was done on the Cerro la Mina Stage C<sub>HK</sub> altered samples to test if the samples had undergone dehydration. Three samples were measured after being stored for 1 year and two samples were measured after being heated in an oven. Samples were analysed with a TerraSpec instrument and the KH index was used to measure dehydration. Out of the three samples that were stored for one year, two samples did not show a change within analytical error of ± 0.08 and one sample showed an increase of KH index value by 0.30. The two samples that were analysed after being placed in an

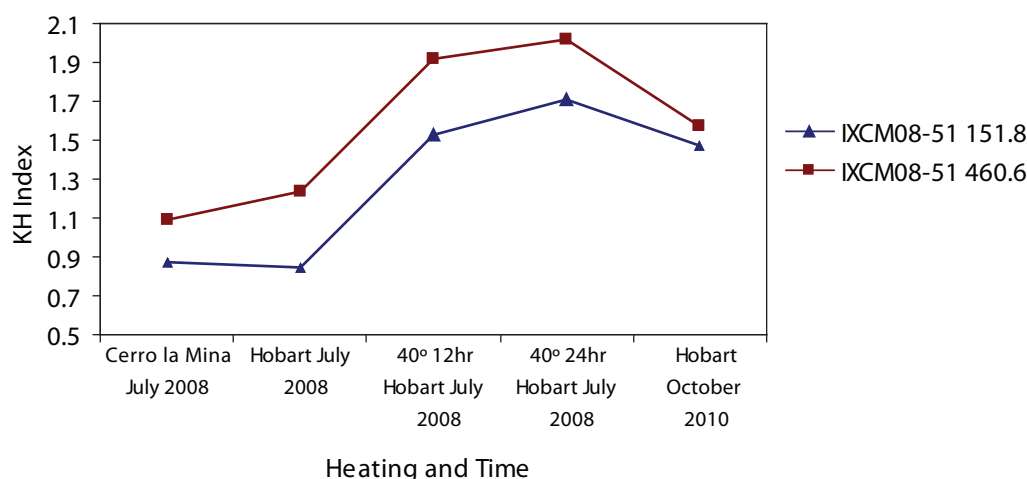


**Figure 5.26** KH index versus heating and time graph for H-K altered samples. Dehydration of halloysite was measured using the KH index after heating to 40° for 12 and 24 hours, then measured after 2 year in storage. Hobart is located in the state of Tasmania, Australia. Drill hole for samples was completed on April 2008.

oven showed significant change. Initially these samples were measured at Cerro la Mina and then in Hobart, Australia after transportation during the month of July, 2008. They were then measured after being placed in an oven for 12 hours at 40°C, after 24 hours at 40°C, and after being stored for 1 year at room temperatures. The results show that the KH index changed negligibly during transportation, increased significantly with heating and decreased following one year storage (Fig. 5.26).

## 5.7 Discussion

The relative abundance of halloysite to kaolinite changes with distance from Stage  $C_{QD}$  alteration, as indicated by the KH index. Kaolinite becomes the dominant mineral close to the dickite core and below 1200 m elevation. Together the dickite, kaolinite, and halloysite form a zonation probably reflecting a change in temperature from high to low temperature, respectively. The zonation is consistent with temperatures of formation for dickite (110°C to 260 °C; Reyes, 1990), kaolinite (< 200°C; Reyes, 1990) and halloysite (< 110°C; Marumo and Hattori, 1999). A kaolinite-rich zone below 1200 m suggests that there is potential for another Stage  $C_{QD}$  at depth or laterally similar to the zonation observed at the surface.

A SEM study shows that Stage  $C_{HK}$  alteration at Cerro la Mina comprises halloysite cylindrical tubes that develop into sheet-like morphology of kaolinite with the progression of alteration. The observed trend is interpreted to be the paragenetic evolution of halloysite to kaolinite that occurs with increasing alteration. The same development and transition of halloysite to kaolinite is observed in the weathering profile of anorthosite (Fig. 5.27; Jeong, 1998) and in hydrothermal alteration (Papoulis et al., 2009). The dominant parent minerals for the halloysite at Cerro la Mina are potassium feldspar and muscovite, indicating that the Stage  $C_{HK}$  alteration is late stage. The aligned halloysite forming on sericite is similar to Singh and Gilkes (1992) observations of laterite profiles from Western Australia, where they inferred that halloysite formed from the alteration of micas. The halloysite

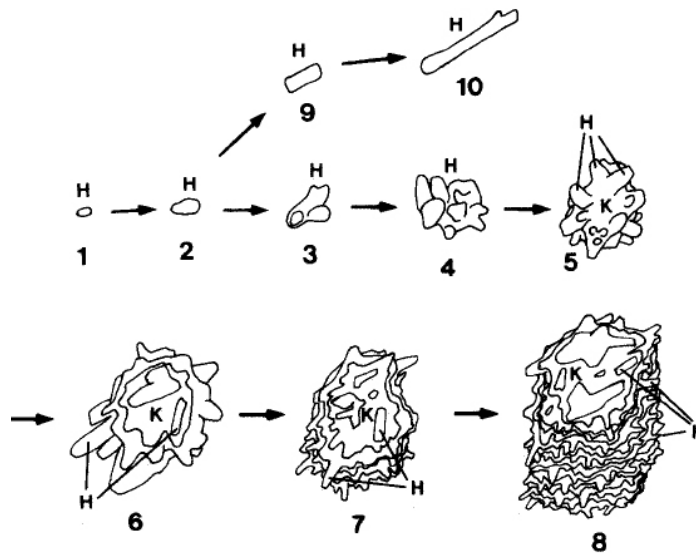


**Figure 5.27** Illustration from Jeong (1998) showing the transformation from halloysite to kaolinite. The transformation starts with an ellipsoid (1) which develops into tubular halloysite (10) and vermicular kaolinite (8) with further progress of anorthosite weathering. **Abbreviations:** H- halloysite, K - kaolinite.

formed parallel-oriented tubes aligned perfectly with the orientation of the mica plates (Singh and Gilkes, 1992). The SEM images also show fine-grained sulfides found in association with the halloysite aggregates, consistent with a hypogene origin for halloysite; otherwise the sulfides would have been oxidized. The halloysite is observed to form small ( $< 15 \mu\text{m}$ ) tubes in voids created by mineral boundaries.

The SWIR data in this study suggest that it is possible for halloysite to partially dehydrate during storage at room temperatures and in relatively less humid conditions for 1 year and by heating at low temperatures of  $\sim 40\text{C}$ . The XRD data also suggest dehydration during storage as Kyne (2009) reports presence of dehydrated and hydrated halloysite species ( $7\text{\AA}$  and  $10\text{\AA}$  respectively), however this study, performed later than Kyne (2009), only reports halloysite  $7\text{\AA}$ . The KH index relies on the water absorption peak and dehydration would affect its accuracy. However, the author is confident in the results of this study as the SWIR spectra was obtained from the core samples shortly after drilling.

Halloysite can be distinguished from kaolinite by its XRD pattern (Brindely and Comer, 1956; Brindley et al., 1963; Joussein et al., 2005). The identification of halloysite  $10\text{\AA}$  is straightforward, however, halloysite  $7\text{\AA}$  and kaolinite produce the same peaks in XRD spectra. The presence of halloysite  $7\text{\AA}$  is detected by the use of formamide intercalation which separates the XRD peaks (Joussein et al., 2007). Joussein (2007) observed that the formamide test greatly underestimates the halloysite content of the clay fractions separated soil that has been stored for a period of 21 years at  $20\text{C}$  and 30 percent humidity. Joussein et al. (2007) suggested due care should be taken in using the formamide test to determine the halloysite content of samples that are not kept in a wet state. SWIR techniques are equally complicated by halloysite dehydration effects. The SWIR spectra for

halloysite and kaolinite are essentially the same except for the depth of the water absorption peak (~1900 nm) which would vary on the moisture content of the rock and amount of halloysite dehydration. Therefore it could be possible for a dehydrated halloysite to produce a SWIR spectra similar to kaolinite.

Given the complications of halloysite dehydration and the problems associated with the identification of dehydrated halloysite  $7\text{\AA}$  with XRD and SWIR techniques, exploring in halloysite-kaolinite altered rocks could be problematical. Post-drilling heating or storage may cause halloysite to dehydrate and potentially cause the false identification of halloysite for kaolinite. Halloysite could be a common hypogene mineral in epithermal deposits but could be underestimated due to the difficulties in its identification, i.e. dehydrated halloysite is identified as kaolinite.

## 5.8 Conclusions

The breccia pipe provided a fluid pathway for three stages of alteration, potassic (Stage A), sericitic (Stage B) and kaolinite (Stage C) alteration. Stage A and B are interpreted to occur in a porphyry environment and is overprinted with Stage C advanced argillic style alteration suggesting significant uplift has occurred (e.g., Sillitoe, 1994).

Stage A comprises quartz, potassium feldspar and biotite and is representative of a potassic zone in a porphyry Cu alteration (Lowell and Guilbert, 1970; Seedorff et al., 2005). The potassic alteration is formed by a quartz - potassic feldspar core surrounded by a biotite-rich assemblage. The alteration distribution suggests that Stage A has a post-brecciation timing, however, vein textures described in Chapter 6 suggest that Stage A also occurred before breccia pipe formation. Abundant potassium feldspar alteration in the breccia pipe matrix suggests that the potassic alteration continued after breccia pipe formation.

Stage B comprises quartz, muscovite, illite, illite/smectite, chlorite, calcite, gypsum, tourmaline typical of phyllic alteration zone of a porphyry Cu deposit (Lowell and Guilbert, 1970; Seedorff et al., 2005). The zoned sericitic alteration (Stage B) indicates that the high temperature source is within the Cerro la Mina breccia pipe and is reflected in SWIR spectra with decreasing Al-OH and increasing crystallinity towards the breccia pipe.

Stage C is separated into two coeval zones, Stage  $C_{\text{QD}}$  comprising quartz, dickite and lesser pyrophyllite, alunite and kaolinite, and Stage  $C_{\text{HK}}$  comprising halloysite and kaolinite. Stage C alteration contains abundant halloysite alteration developed to at least 800 metres below the present day surface, deeper than the hypogene clay minerals dickite + alunite + pyrophyllite. Stage  $C_{\text{HK}}$  is unstable in the oxide zone consistent with a hypogene origin for halloysite. The Cerro la Mina alunites are euhedral, hexagonal, tabular crystals up to 150  $\mu\text{m}$  and associated with dickite and pyrophyllite consistent with a hypogene origin. A TerraSpec study shows that the relative abundance of halloysite to kaolinite decreases towards the hypogene Stage  $C_{\text{QD}}$  alteration and below 1200 m elevation. SEM imaging revealed the transition from halloysite to kaolinite in Stage  $C_{\text{HK}}$  with increasing alteration. The halloysite clay is susceptible to and its identification is hindered by dehydration if not kept in 100 percent humidity.



## Chapter 6 - Mineralisation

### 6.1 Introduction

Exploration drilling at the Cerro la Mina Au (Cu-Mo) prospect intersected a near surface oxide Au zone and significant Au (Cu-Mo) sulfide mineralisation with porphyry and epithermal affinities at depth. Before this study mineralisation was recorded using drill core logging for the purposes of exploration and as a result the distribution and paragenesis of mineralisation was poorly understood. This chapter describes the mineralisation observed in drill core, thin section and using laser mapping of trace elements. The knowledge gained from this helped with understanding of the origin of the halloysite alteration.

A total of 7800 m of drill core was graphically logged and 85 thin sections were investigated. In addition, 43 laser maps were generated to determine the trace element distribution for pyrite, marcasite, chalcopyrite, enargite and sphalerite to provide insights into the chemistry of the fluids from which the mineralisation was precipitated.

The chapter is in two parts; the first part discusses the research methods used followed by a macro scale description of mineralisation, petrographic description of the four mineralising stages, vein textures, and the spatial distribution of the four stages. The first part ends with a discussion of the paragenesis of the Cerro la Mina mineralisation. The second part of the chapter comprises a description of laser maps, followed by an interpretation of the sulfide geochemistry of the Cerro la Mina prospect.

### 6.2 Research Methods

#### 6.2.1 Graphic Logging

Graphic logging methods of mineralisation and graphic logs are in Appendix I.1 and I.2.

#### 6.2.2 Petrographic Microscopy

Polished mounts and slabs were made at the University of Tasmania for selected samples and petrography was completed using a Nikon Labophot-2<sup>®</sup> Pol Standard Polarizing Microscope and an Olympus ColorView imaging system. Petrographic observations are recorded in Appendix IV.1.

#### 6.2.3 Acid Etching

Acid etching with 70% water/HNO<sub>3</sub> mixture placed on a polished slab or polished mount for 5 to 20 seconds allowed for the observation of textural zonation in pyrite.

#### 6.2.4 Scanning Electron Microprobe

The scanning electron microprobe (SEM) was used to identify unknown minerals observed using the petrographic microscope. Samples were carbon coated and placed in a FEI Quanta 600 scanning

electron microscope (SEM) at the Central Science Laboratory, University of Tasmania. The SEM was used in conjunction with an EDAX Genesis 7000 Energy Dispersive Spectroscopy (EDS) system with two Sapphire SUTW Si (Li) detectors, MnK $\alpha$  130 eV resolution, voltage 15 to 25 kV, and secondary electron or back scatter electron imaging was used.

### 6.2.5 Sulfide Imaging

Laser mapping of pyrite, marcasite, enargite, chalcopyrite and sphalerite was done to observe trace element zoning. Sulfide imaging data and images are recorded in Appendix IV.2 and IV.3. The instruments used included a New Wave 213-nm solid-state laser microprobe coupled to an Agilent 7500s or 7500a quadrupole ICPMS housed at the Centre of Excellence in Ore Deposits LA-ICP-MS analytical facility, University of Tasmania. The laser microprobe was equipped with a constant geometry ablation cell characterized by <1-s response time and <2-s wash-out time. Ablation was performed in an atmosphere of pure He (0.8 l/min). Immediately after ablation the products were mixed with Ar (0.8 – 0.9 l/min) and the mix was passed through 3 m nylon tubing before direct introduction into the torch.

The ICPMS was optimized daily to maximize sensitivity on mid- to high-mass isotopes (in the range 130–240 a.m.u.). Production of molecular oxide species (e.g.,  $^{232}\text{Th}^{16}\text{O}/^{232}\text{Th}$  and doubly charged ion species (i.e.,  $^{44}\text{Ca}^{2+} / ^{22}\text{Ne}^{+}$ ) was maintained at <0.2 percent. Due to the low level of molecular oxides and doubly charged ions, no correction was introduced to the analysed signal intensities for these potential interfering species. Each analysis was performed in the time-resolved mode, which involves sequential peak hopping through the mass spectrum.

Imaging of sulfides was completed by ablating parallel sets of lines arranged in a grid across the samples. Depending on the samples size, lines were ablated with a laser beam size of 10 or 22  $\mu\text{m}$  and the spacing between the lines was the same size as the beam. All lines were pre-ablated before the main mapping burn at double the rate used during mapping. The lines were ablated with the repetition rate of 10 Hz, rastering at 10 or 22  $\mu\text{m}/\text{s}$ , depending on the spot size. Thus, every position in the sample was ablated 10 times and its composition contributed to five consecutive pixels in the image, resulting in an unprocessed effective resolution matching the beam size. Every sweep recorded in the mass spectrometer forms a separate pixel in the map. For a normal sweep time of  $\sim 0.2$  s, with an image speed of 25  $\mu\text{m}/\text{s}$ , one pixel equals 5  $\mu\text{m}$ .

Depth of ablation during mapping was around 5  $\mu\text{m}$ . This is estimated from the known depth of ablation by a single shot (0.5  $\mu\text{m}$ ) and the known number of shots in a single point in pyrite ( $n = 10$ ), which is determined by the relationship between the speed with which the sample moves under the laser beam and the spot size used.

Imaging of pyrite, marcasite, enargite, chalcopyrite and sphalerite used a set of 28 to 33 elements analysed with acquisition time for most masses set to 0.002 s, however, to improve their detection limits, Se, Cd, In, Sn, Sb and Tl were measured for 0.004 s, Th and U for 0.005 s and Ag, Te, Pt and Au for 0.04 s. The total sweep time was  $\sim 0.3$ s. To allow for cell wash-out, a delay of 15 s was

used after each line. Background levels and the primary sulfide standard (Danyushevsky et al., 2011) were measured before and after each image. Typically images were analysed over 1 to 2 h where sensitivity drift was negligible. Standards were analysed immediately before and after the image to assess drift. Images were corrected for drift when necessary, but not routinely, and drift was assumed to be linear between the two sets of standards.

The image was processed according to the techniques outlined in Large et al. (2009) and elements were reported in counts per second (cps). The effect of redeposition during mapping was minimized by pre-ablating each line before the main mapping burn. However, this does not remove the redeposited material completely. Redeposition can be a factor when looking at concentration variations between two mineral phases where one contains high concentration and the other low. The redeposited material from the high concentration mineral can mask small variations in the second mineral and is a function of distance, e.g., the greatest effect is seen close to the grain boundary. On images with a concentration scale of several orders of magnitude (including those presented here), redeposition is generally not an issue; however, some Au contamination is evident on some maps around large native gold inclusions.

#### 6.2.5.1 Image Conversion for cps to ppm

The LA-ICP-MS imaging reports elements in counts per second (cps). The cps can vary from image to image depending on machine conditions including spot size and daily variation in instrument settings. To compare images and calculate a quantifiable number the cps are converted to parts per million (ppm).

The conversion process comprises measuring the average count rates for each element on the STDGL2b2 standard (Danyushevsky et al., 2011) analysed before and after image acquisition, then subtracting the background counts collected after the image acquisition to calculate a cps/ppm value. A representative line from the image is chosen and a region in this line is selected to obtain a representative Fe value (the internal standard element) in the pyrite or marcasite. A ratio of elements to Fe is then calculated for this region and a cps to ppm correction factor is calculated using:

$$\text{correction factor} = \frac{1}{\text{bgcorCPS}(\text{elem.std}) / \text{ppm}(\text{elem.std})} \times \frac{\text{bgcorCPS}(\text{IS.sample}) / \text{ppm}(\text{IS.sample})}{\text{bgcorCPS}(\text{IS.std}) / \text{ppm}(\text{IS.std})}$$

Where  $\text{ppm}(\text{elem.std})$  is the concentration of an element in the standard,  $\text{bgcorrCPS}$  is background corrected count rate and  $IS$  denotes the internal standard element (Fe in this case). An in house Python script applies the correction factor to each line and subtracts the background counts to plot a ppm image.

There are several limitations to this method including 1) there is no drift correction as the average values of the standards are used; 2) variation in the background counts are not taken into account, as one background analysis is used throughout; 3) it uses a single representative line from

the image for the value of Fe, instead of using Fe from each individual line as the internal standard element, which does not correct for drift or other sensitivity changes across the image; 4) to make the process simple only pyrite and marcasite were accurately quantified. Other minerals (chalcopyrite, enargite, sphalerite, silicates) which ablate differently were reduced as if they were pyrite thus underestimating their concentration by up to an order of magnitude. As a result only pyrite and marcasite were converted from counts per second to parts ppm and enargite, chalcopyrite and sphalerite remained in cps.

#### 6.2.5.2 Data Reduction with ioGas

Data reduction was undertaken using ioGas (version 4.3) which can select representative points from various zones in pyrite or marcasite for calculation of the average concentration in each of the zones. Due to the large volume of data points the data were filtered to only include Fe concentrations between 45,000 and 48,000 ppm.

The concentration of elements in the various pyrite types are displayed in Tukey Plots (Tukey, 1977). The Tukey plots are created by dividing the ordered values of the data into four equal parts, by finding the median and then the 25<sup>th</sup> and 75<sup>th</sup> percentiles or inter quartile range (IQR). The median is defined by a horizontal line within a box that spans the IQR and contains approximately 50% of the data. The mean is represented by a large black circle. The fence is defined as the central box (IQR) extended by 1.5 times the length of the box towards the maximum and the minimum. The upper and lower 'whiskers' are then drawn from each end of the box to the fence position. Samples outside of the fence are assumed to be Outliers and those that are three times the central box length from the upper or lower quartile boundaries are considered highly anomalous (in a univariate sense) and are called Far Outliers. The elements are distributed on the diagram according to their median value.

### 6.3 Macro Scale Description

At the macro scale, the most significant mineralisation occurs mainly in the breccia pipe (Unit 4; Fig. 6.1; Table 6.1). The ore grade shells for Au, Cu, and Mo are vertical and hosted almost entirely in the breccia pipe (Figs. 6.1A to C). Whereas As has two distinct zones; one at the surface and one at depth (Fig. 6.1D) and Au has a similar trend for As (Fig. 6.1A and D). Zn and Pb show similar distributions in the breccia pipe (Fig. 6.1E and F).

The grades are strongly controlled by lithology (Unit 4; Fig. 6.1) and quartz-dickite alteration (Stage C<sub>QD</sub>) host the highest average grades of 0.7 g/t Au and 0.23% Cu (Fig. 6.2; Table 6.1). Higher grades also occur in structures probably related to the northwest fault and are associated with Stage C<sub>QD</sub> alteration (Fig. 6.2). High Au/Cu ratios occur in the oxide zone resulting from the breakdown of sulfides. No resource estimate has been carried out.

A large outcrop of Stage C<sub>QD</sub> alteration at the surface is grey and oxidized to brown, and has high Au, Cu and Mo grades (Fig. 6.3). Mineralisation associated with potassic and sericitic alteration (Stages A and B) is not easily recognizable in outcrop. In drill core however, abundant veins with sericitic altered margins with chalcopyrite and molybdenite are commonly infilled with late

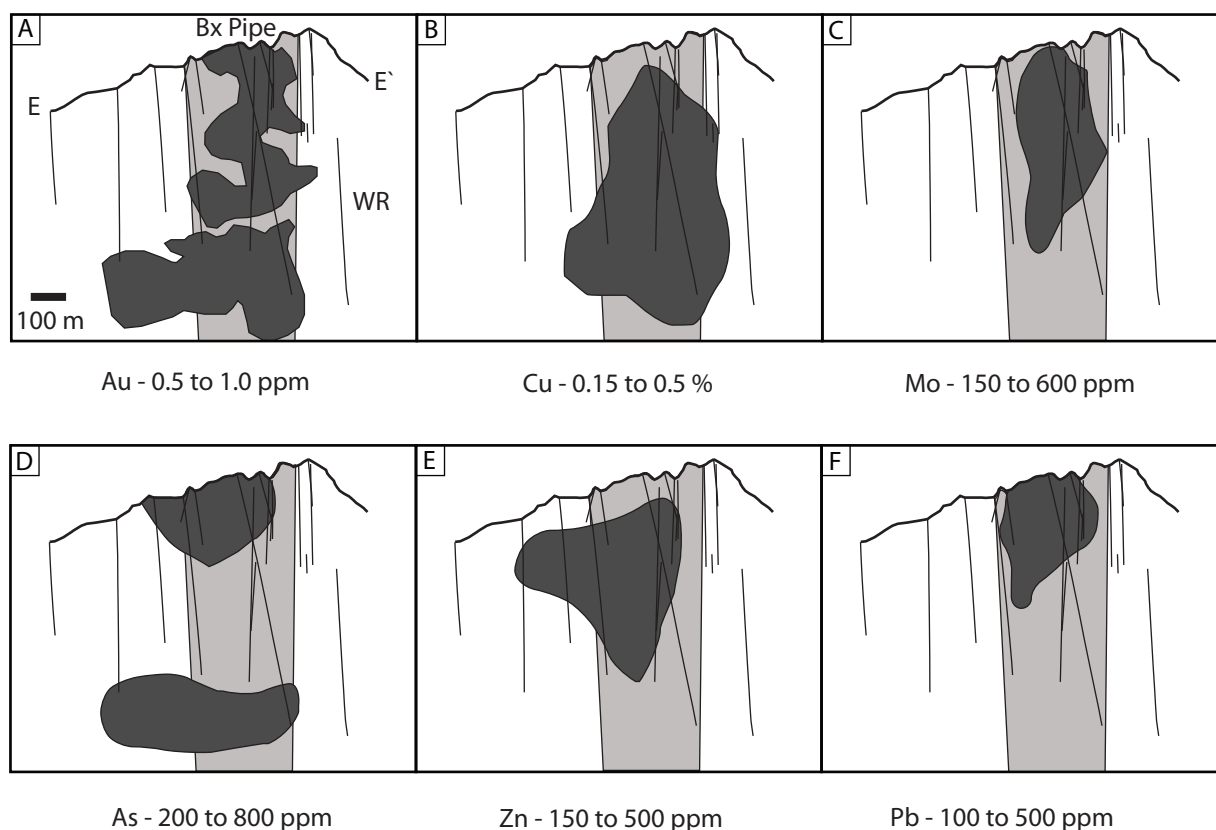


**Figure 6.1** Zonation of Au, Cu, Mo, As, Zn and Pb at the Cerro la Mina prospect in relationship to the breccia pipe (Unit 4). Long section E-E' location shown in Figure 6.15. Light grey is the breccia pipe (Unit 4) and dark grey is the distribution of the respective element. Compiled from company data consisting of 2 m interval sampling, Au 50 g fire assay with atomic absorption finish and 35 element aqua regia digestion ICP-MS. **Abbreviations:** Bx Pipe - breccia pipe, WR - volcanic wall rocks.

| Rock Type/Alteration                               | No. of analyses | Au g/t<br>Mean (Range) | Cu %<br>Mean (Range) | Mo ppm<br>Mean (Range) |
|--|-----------------|------------------------|----------------------|------------------------|
| Breccia pipe (Unit 4)                              | 4657            | 0.4 (0 to 87.7)        | 0.16 (0 to 4.2)      | 131 (0.5 to 4800)      |
| Volcanic wall rocks (Units 1 to 3)                 | 2525            | 0.1 (0 to 4.1)         | 0.03 (0 to 1.1)      | 12 (0 to 615)          |
| Quartz-dickite alteration (Stage C <sub>QD</sub> ) | 160             | 0.7 (0.1 to 5.0)       | 0.23 (0 to 11.6)     | 345 (11 to 4230)       |

**Table 6.1** Comparison of Au-Cu-Mo grades for breccia pipe (Unit 4), volcanic wall rocks (Units 1 to 3) and quartz-dickite alteration (Stage C<sub>QD</sub>). Compiled from company data consisting of 2 m interval sampling, Au 50 g fire assay with atomic absorption finish and 35 element aqua regia digestion ICP-MS.

halloysite + kaolinite + pyrite (Stage C<sub>HK</sub>; Fig. 6.4A). Higher Au-Cu grades are commonly associated with dickite-cemented hydrothermal breccias and pyrite ± enargite (Fig. 6.4B). Mineralisation mainly occurs as disseminated fine-grained (< 500 µm) sulfides, sulfosalts and sulfates (Fig. 6.4C).

## 6.4 Petrographic Descriptions

Five types of pyrite were identified based on their texture and mineral associations; fractured pyrite, inclusion-rich pyrite, ragged pyrite, rimming pyrite and fine-grained pyrite. At Cerro la Mina the preservation of veins is limited due to the highly fractured nature of the core. Where preserved, the core predominantly contained veinlets to veinlet stockworks with occasional veins greater than 1 cm in width.

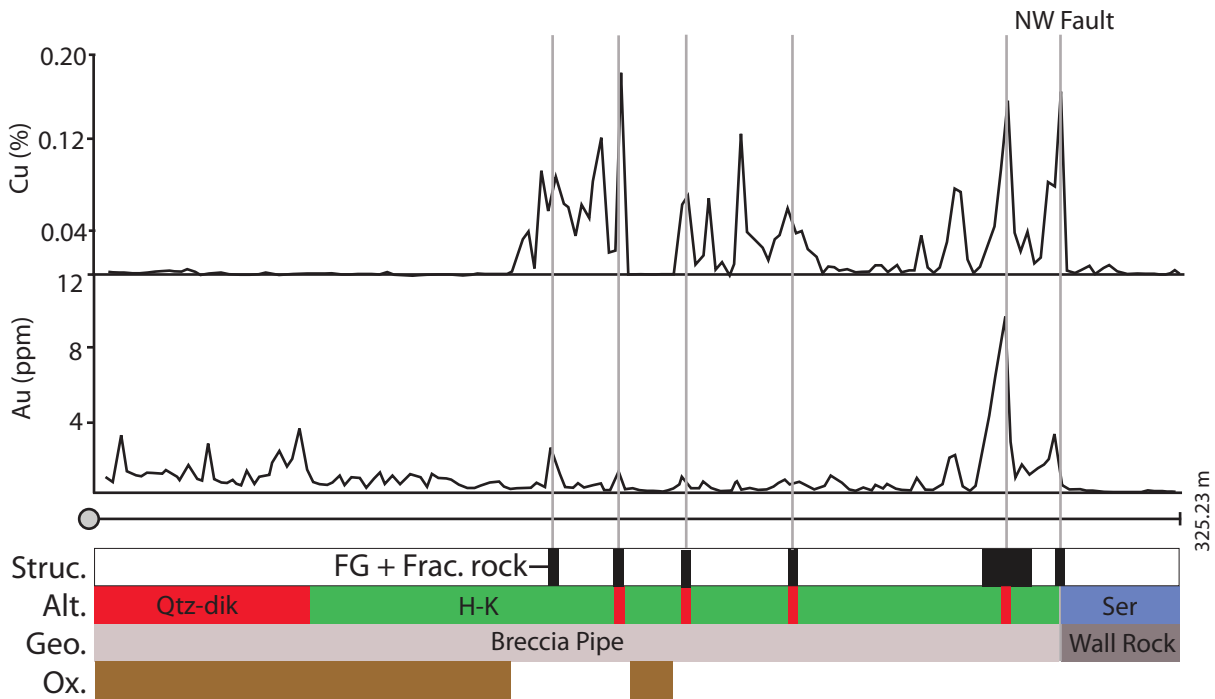


**Figure 6.2** Simplified log of drill hole IXCM07-44 illustrating the relationship of high Au-Cu grades with structures, quartz-dickite alteration (Stage C<sub>QD</sub>) and breccia pipe rock type. Structural zones contain fault gouge and/or strongly fractured rock. **Abbreviations:** Alt. - alteration, FG - fault gouge, Frac. Rock - fractured rock, Geo. - geology, H-K - halloysite-kaolinite alteration (Stage C<sub>HK</sub>), Ox. - oxide, Qtz-dik - quartz-dickite alteration (Stage C<sub>QD</sub>), Ser - sericitic alteration (Stage B), Struc. - structure.

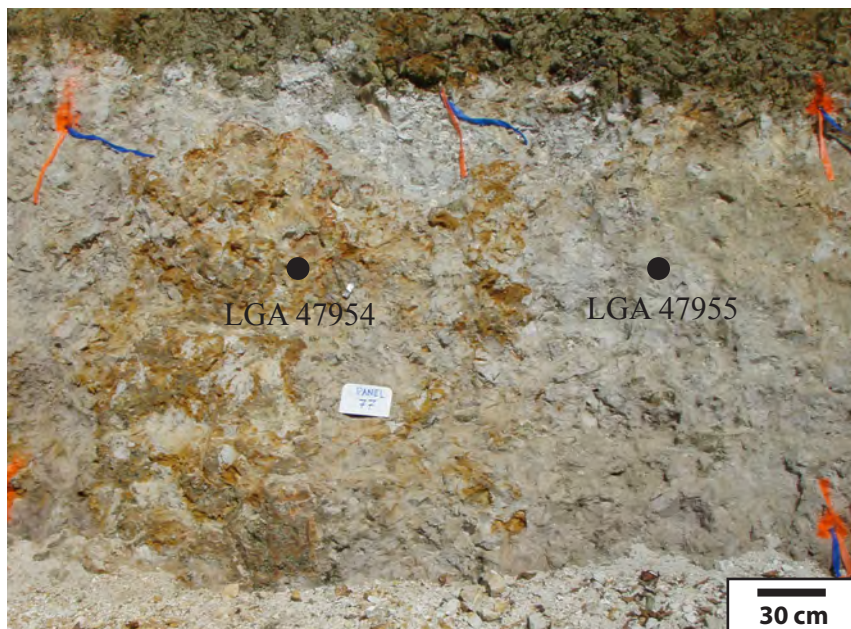


**Figure 6.3** Outcrop of grey quartz-dickite alteration (Stage C<sub>QD</sub>) with brown oxide. Sample LGA 37954 with 0.8 g/t Au, 0.23 % Cu, 984 ppm Mo, 1 ppm Zn, 147 ppm Pb. Sample LGA 47955 1.4 g/t Au, 0.02 % Cu, 32 ppm Mo, 2 ppm Zn, 126 ppm Pb. Data and photo from Kinross database, Au 50 g fire assay with atomic absorption finish and 35 element aqua regia digestion ICP-MS.

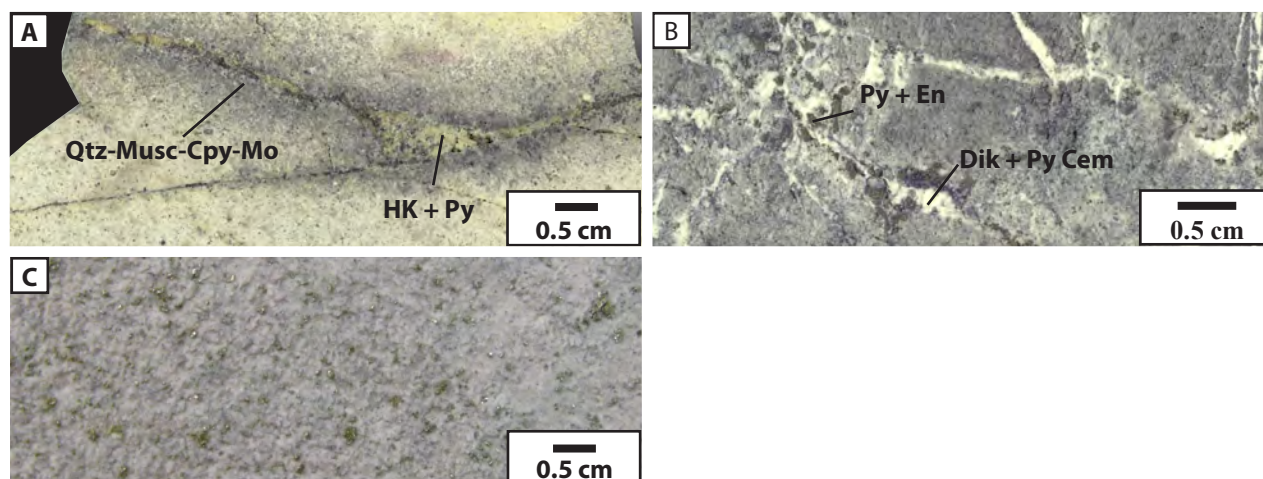


**Figure 6.4** Mineralisation in drill core commonly observed at the Cerro la Mina prospect. **A.** A quartz + muscovite altered vein margin associated with chalcopyrite and molybdenite mineralisation. The vein is infilled with late halloysite + kaolinite associated with pyrite. **B.** A dickite-cemented breccia associated with pyrite ± enargite. **C.** Fine-grained disseminated fine-grained pyrite, chalcopyrite and molybdenite. **Sample ID:** A. IXCM08-61 375.1, B. IXCM06-09 100.7, C. IXCM06-05 97.6. **Abbreviations:** Cem - cement, Cpy - chalcopyrite, Dik - dickite, En - enargite, HK - halloysite + kaolinite, Mo - molybdenite, Musc - muscovite, Py - pyrite, Qtz - quartz.

#### 6.4.1 Stage 1

Stage 1 contains fractured pyrite that is typically 50 to 200  $\mu\text{m}$ , hosts no inclusions and has a jigsaw fit texture (Fig. 6.5A). No other pyrite type at Cerro la Mina has a fractured texture. The fractured pyrite only occurs as infill in early quartz + potassium feldspar  $\pm$  biotite veins associated with potassic alteration (Stage A), which are together fractured into a jigsaw-fit texture breccia. The quartz + potassium feldspar  $\pm$  biotite veins are uncommon. The fractured pyrite is the only sulfide observed to have gold inclusions, with one sample (IXCM07-21 281.0) containing 30 to 70  $\mu\text{m}$  gold grains (Fig. 6.5B).

#### 6.4.2 Stage 2

Stage 2 mineralisation is associated with the distribution of the sericitic alteration (Stage B) and comprises inclusion-rich pyrite, chalcopyrite, molybdenite and rare bornite that occur in veins and as disseminations (Fig. 6.6). Stage 2 veins are common and have sericitic vein selvages, commonly with quartz + muscovite  $\pm$  illite (Stage B alteration). The vein selvage is commonly light grey extending up to 2 cm from the vein into the wall rock.

Inclusion-rich pyrite is the most abundant sulfide at the Cerro la Mina prospect. It is 50 to 300  $\mu\text{m}$  in diameter and is very irregular in shape with many embayments and cusped edges, and contains inclusions predominantly of clay and rutile with lesser pyrrhotite, chalcopyrite, bornite and molybdenite (Figs. 6.6A). The inclusions occasionally show a concentric pattern (Fig. 6.6A). Inclusion-rich pyrite is commonly found in contact with chalcopyrite (Fig. 6.6B).

## Stage 1

**Minerals:** Fractured pyrite

**Texture:** Jig-saw fit texture

**Distribution:** Veins and disseminations in volcanic wall rocks (unit 1 to 3). No veins in breccia pipe (unit 4).

**Associated Alteration:** In fills earlier potassic alteration (Stage A) veins.

**Timing:** Late porphyry mineralisation

**Distinguishing features:** Jig-saw fit texture.

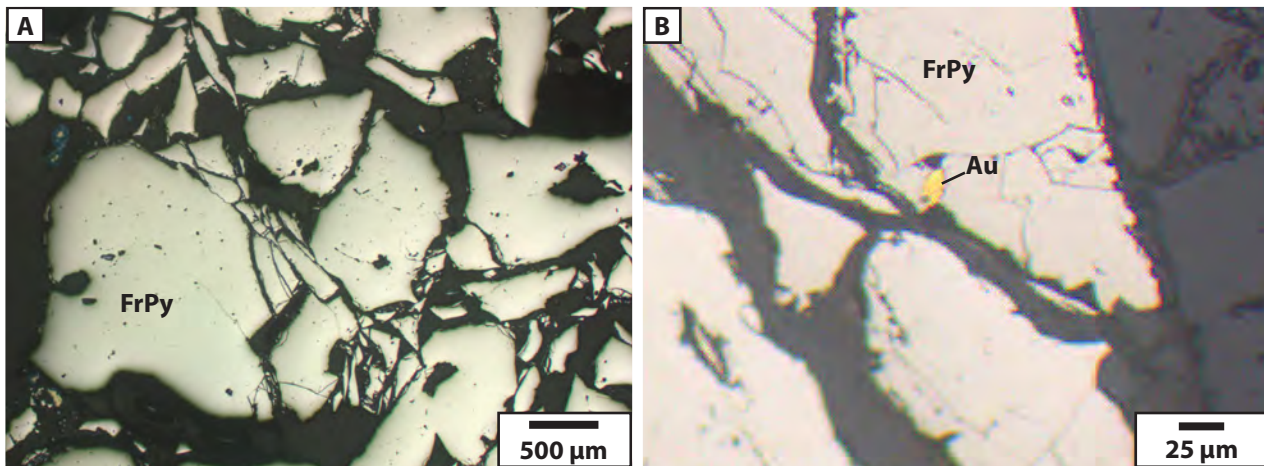
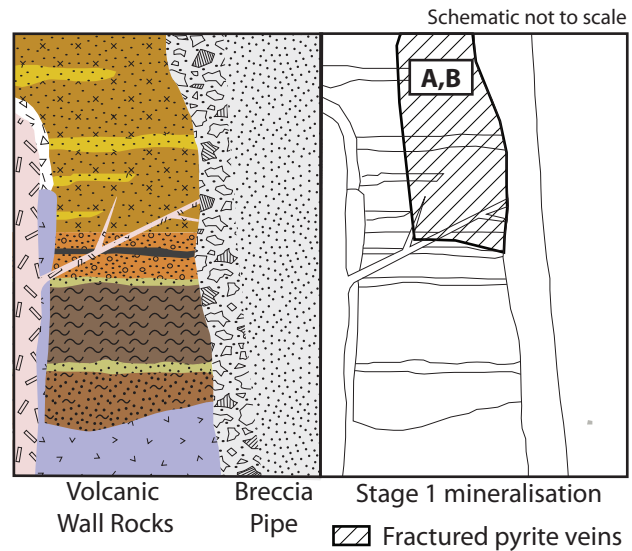


**Figure 6.5** Characteristics of Stage 1 mineralisation. **A.** Stage 1 fractured pyrite showing distinct jig-saw fit texture. **B.** Stage 1 fractured pyrite with a gold inclusion. Stratigraphic column is explained Chapter 4 and legend is in Figure 4.14. All images are reflected light. **Sample ID:** A. IXCM08-48 130.3A, B. IXCM07-21 281.0. **Abbreviations:** Au - gold inclusion, FrPy - fractured pyrite.

Chalcopyrite ranges from 100 to 500 µm and is very irregular with many embayments and cusped edges similar to the inclusion-rich pyrite (Fig. 6.6C). Chalcopyrite is commonly found rimming or in association with inclusion-rich pyrite. Bornite is rare and forms inclusions in chalcopyrite and pyrite.

Molybdenite forms long stubby booklets or slender needles depending on the orientation of the crystal axis ranging from 25 to 250 µm (Figs. 6.6C and D) and commonly has an irregular appearance (Fig. 6.6C). Molybdenite is only observed in association with chalcopyrite in sericitic altered margins of veins or more commonly as disseminations.

## Stage 2

**Minerals:** Inclusion-rich pyrite + chalcopyrite + molybdenite

**Texture:** Strongly embayed and irregular.

**Distribution:** Breccia pipe (unit 4) and becomes predominantly inclusion-rich pyrite in volcanic wall rocks (unit 1 to 3).

**Associated alteration:** Sericitic alteration (Stage B)

**Timing:** Late porphyry

**Distinguishing features:** Inclusion-rich pyrite is the most predominant sulfide. Stage 2 is strongly irregular.

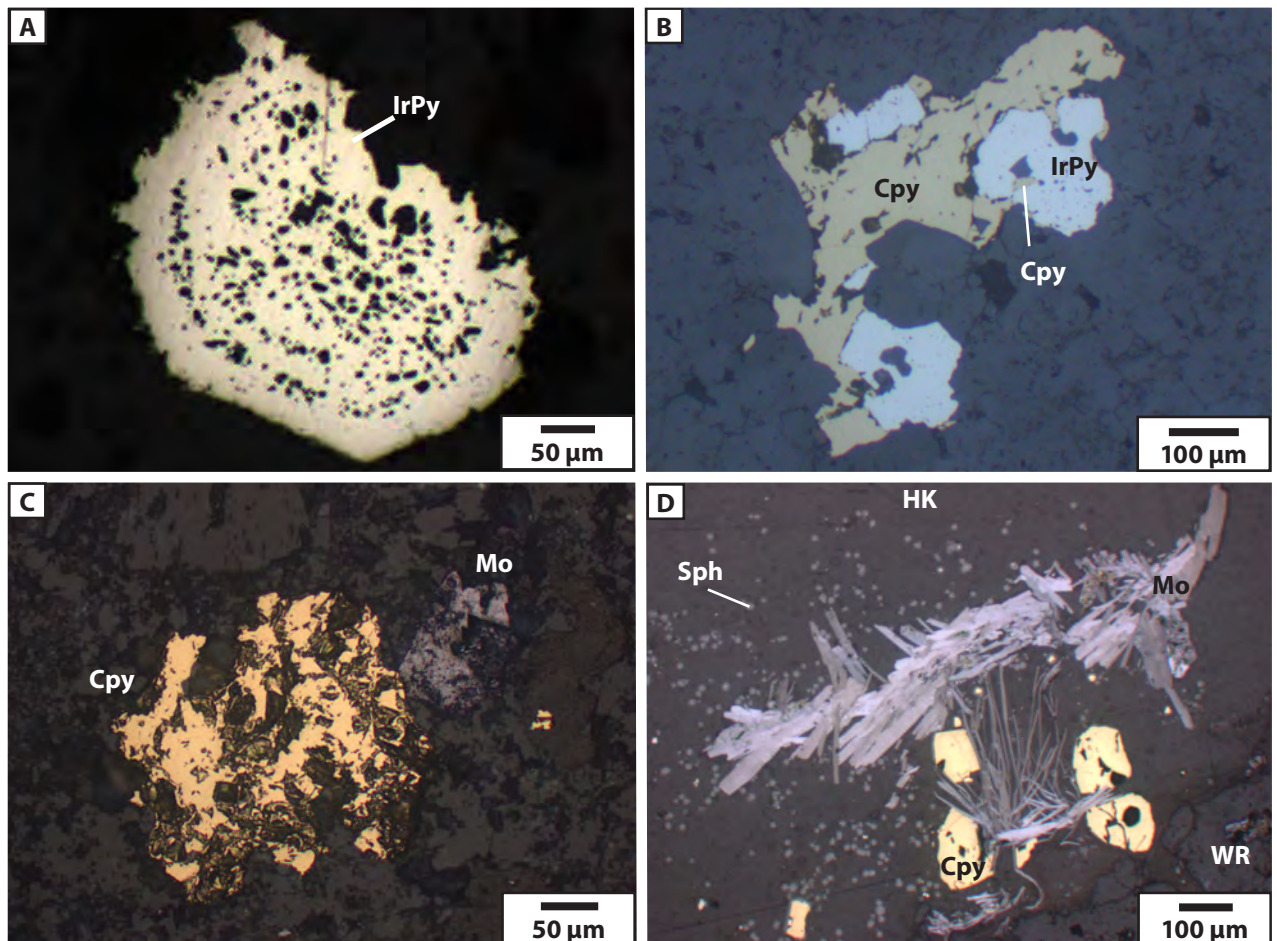
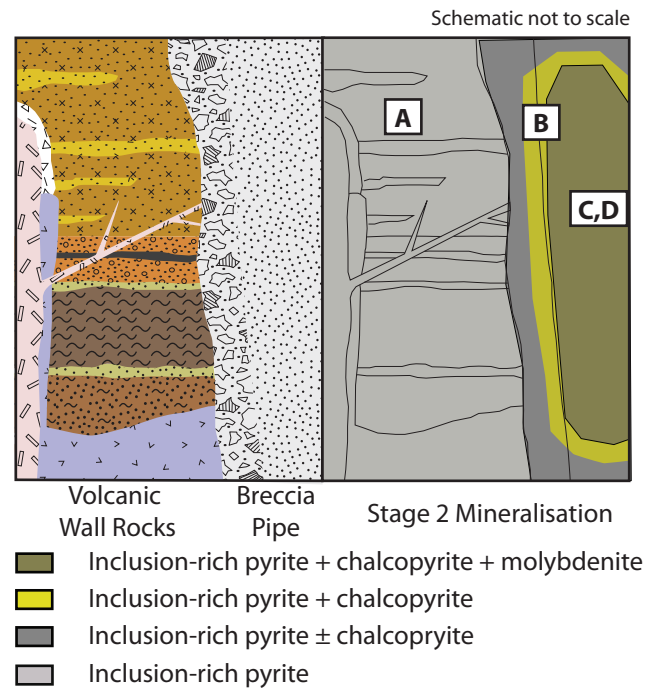


**Figure 6.6** Characteristics of Stage 2 mineralisation. **A.** Stage 2 inclusion-rich pyrite displaying a concentric pattern and cusped edges. **B.** Inclusion-rich pyrite (Stage 2) with chalcopyrite inclusions and intergrown with chalcopyrite (Stage 2). **C.** Stage 2 strongly irregular chalcopyrite with cusped edge and ratty molybdenite. **D.** Long slender molybdenite with chalcopyrite cross-cut by a late Stage 3 halloysite-kaolinite vein with small globules of sphalerite. All images are reflected light. Stratigraphic column is explained Chapter 4 and legend is in Figure 4.14. **Sample ID:** A. IXCM08-63 489.4, B. IXCM06-09 136.9, C. IXCM08-51 285.6, D. IXCM06-09 214.9. **Abbreviations:** Cpy - chalcopyrite, IrPy - inclusion-rich pyrite, HK - halloysite + kaolinite, Mo - molybdenite, Sph - sphalerite, WR - wall rock.

### 6.4.3 Stages 3 and 4

Stages 3 and 4 occur as disseminations associated with kandite alteration (Stage C) or in halloysite + kandite veins. Halloysite + kaolinite veins are the most abundant vein type and commonly infill veins of Stages 1 and 2. The veins are typically < 1 cm in width and are mainly white halloysite + kaolinite clay.

#### 6.4.3.1 Stage 3

Stage 3 mineralisation comprises marcasite, sphalerite, galena, and barite. Stage 3 occurs as disseminations in the kandite altered rocks, in halloysite-kaolinite veins and in halloysite-kaolinite or dickite-cemented hydrothermal breccias (Stage C alteration). Stage 3 mineralisation occurs in larger abundances and is coarser grained near the surface in association with the quartz-dickite alteration (Stage C<sub>QD</sub>) than in the halloysite-kaolinite alteration (Stage C<sub>HK</sub>). In halloysite-kaolinite veins sphalerite, galena and barite are inter-grown and develop from the vein wall to the vein centre (Fig. 6.7F). Marcasite forms 1-5% of the rock and does not occur where ragged pyrite + enargite occurs in the quartz-dickite alteration (Stage C<sub>QD</sub>). Sphalerite, galena and barite comprise less than 1% of the rock and Zn and Pb concentrations are less than 500 ppm in whole rock assays.

Stage 3 mineralisation contains marcasite with a wide range of habits including frayed, concentric rims, wispy, or long slender needles (Figs. 6.7A to D). Marcasite is most commonly found as fine-grained disseminations (< 50 µm) but can be up to 200 µm in diameter. When acid etched the marcasite is observed to form bands rimming chalcopyrite and inclusion-rich pyrite (Fig. 6.7C). Marcasite locally forms rims on sphalerite and hosts inclusions of sphalerite (Fig. 6.7G). Marcasite is also observed to rim early fractured pyrite, inclusion-rich pyrite (Fig. 6.7C) and chalcopyrite.

Disseminated sphalerite forms fine (< 50 µm) rounded grains that are commonly indistinguishable from fine-grained rutile (Fig. 6.7D). In veins it forms clusters of fine grains (< 1 µm) that have concentric banding (Fig. 6.7E) or occurs as needles when intergrown with barite that extend into halloysite-kaolinite (Stage C<sub>HK</sub>) veins (Fig. 6.7F). Sphalerite hosts fine-grained inclusions of, and rims, galena, chalcopyrite, pyrite and marcasite (Figs. 6.7E and H). In the quartz-dickite alteration (Stage C<sub>QD</sub>) sphalerite forms coarse grains from 100 to 1000 µm in diameter.

Disseminated galena is typically fine-grained, < 100 µm in diameter, occurring as small rounded inclusions in sphalerite (Fig. 6.7H) and enargite. Rare coarse-grained galena is observed in veins associated with sphalerite, barite and halloysite-kaolinite (Fig. 6.7F). Galena is also locally observed to be in contact with chalcopyrite (Fig. 6.7H).

Barite is rare and typically fine-grained (< 10 µm) (Fig. 6.7I). Coarse barite up to 1 cm long and 0.25 cm wide (Fig. 6.7J) is occasionally observed in veins inter-grown with sphalerite and galena (Fig. 6.7F).

#### 6.4.3.2 Stage 4

Stage 4 comprises arsenian-pyrite, enargite and covellite. The arsenian-pyrite is divided into ragged, rimming and fine-grained pyrite based on texture. Rimming pyrite and ragged pyrite constitutes 5 to 10% and enargite less than 1% of the rock. Covellite is rare and occurs in fractures and rims chalcopyrite and is inter-grown with enargite. The pyrite in Stage 4 was identified as arsenian by acid etching, which highlighted arsenic-rich zones and the association with enargite. The arsenic-rich sulfides are reactive and oxidize to jarosite after drilling due to the high humidity climate of northern Chiapas, often within days of drilling.

The ragged pyrite has about 40% inclusions, is irregular with rounded edges, and commonly contains inclusions of and rims enargite (Fig. 6.8A). The ragged pyrite commonly occurs in dickite-cemented hydrothermal breccias (described in Chapter 5). The ragged pyrite can also take a similar appearance to inclusion-rich pyrite (Fig. 6.8B).

Rimming pyrite forms bands on marcasite, inclusion-rich pyrite, sphalerite and molybdenite (Figs. 6.7C and 6.8D). Where it forms a rim on inclusion-rich pyrite it is commonly only observed with the aid of acid etching (Fig. 6.7C). The thickness of the rimming pyrite varies from 5 to 30  $\mu\text{m}$ . Locally, two rims of rimming pyrite can be observed (Fig. 6.8J). Fine-grained pyrite ( $< 5 \mu\text{m}$ ) is found on the surfaces of chalcopyrite in association with fine-grained enargite. Due to its fine-grained nature it is difficult to observe.

Enargite is irregular with many embayments and ranges from 100 to 500  $\mu\text{m}$  (Fig. 6.8A). Fine-grained zones with different shades of grey are observed in reflected light. Enargite is commonly in contact with ragged pyrite in the upper arsenic-rich zone (Fig. 6.8A). Enargite can also be fine-grained in chalcopyrite (Fig. 6.8E and F); it is also observed rimming chalcopyrite. Enargite development varies from weak on the rim of chalcopyrite or as fine grains on the surface of chalcopyrite, to totally engulfing the chalcopyrite (Figs. 6.8E to F). Multiple episodes of enargite development are shown in Figure 6.8I, where chalcopyrite has enargite + fine-grained pyrite on its surface and it is then rimmed by a second generation of enargite. Enargite is observed to rim and be inter-grown with covellite indicating that they are coeval (Stage 3; Fig. 6.8H).

Covellite is not common and occurs with rimming pyrite, enargite and chalcopyrite. Covellite is fine-grained and forms in the fractures of chalcopyrite, as radial needles in vugs of inclusion-rich pyrite and on the surface of chalcopyrite and enargite (Figs. 6.8G to H). Covellite and enargite form complex intergrowths (Fig. 6.8H). In Figure 6.8H, covellite is found on chalcopyrite and as needles radiating away from the chalcopyrite followed by a thin rim of enargite that is developed on the edge of the covellite.

### Stage 3

**Minerals:** Marcasite + sphalerite + galena + barite

**Texture:** Fine grained and forms banded rims on earlier stages and is fine-grained. Marcasite is the most common. Sphalerite, galena and barite are commonly intergrown. Stage 3 is coarser grained at near the surface.

**Distribution:** Breccia Pipe (unit 4), and lesser abundance in volcanic wall rocks (unit 1 to 3).

**Associated Alteration:** Kandite alteration (Stage C)

**Timing:** Early epithermal

**Distinguishing features:** Fine grained and commonly rims other minerals.

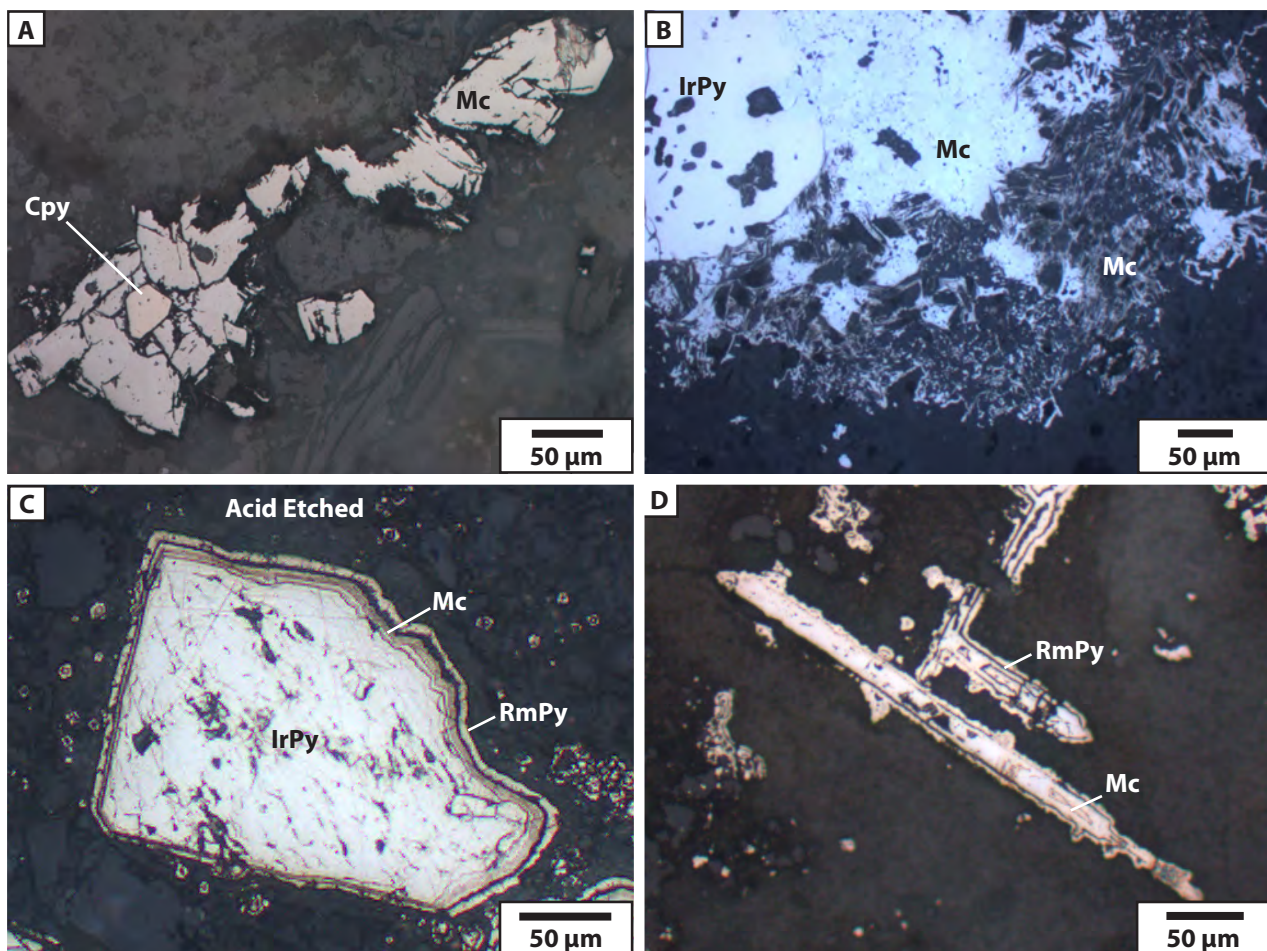
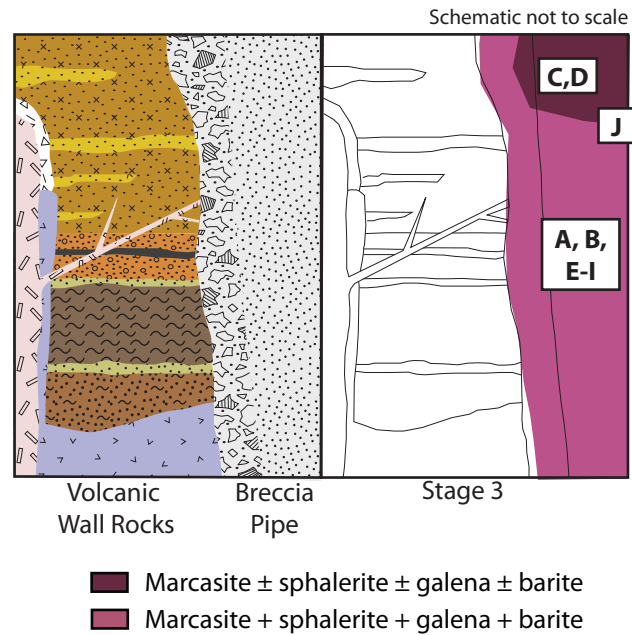


**Figure 6.7** Characteristics of Stage 3 mineralisation. **A.** Marcasite forming on the rim of chalcopyrite with a frayed appearance. **B.** Marcasite with a wispy texture forming on the edge of an inclusion-rich pyrite. **C.** Acid etched image that shows marcasite forming concentric rims on an inclusion-rich pyrite and rimmed by rimming pyrite. **D.** Marcasite forming long slender needles and rimmed by rimming pyrite of Stage 4. All images are reflected light. Stratigraphic column is explained Chapter 4 and legend is in Figure 4.14. **Sample ID:** A. IXCM07-20 324.5, B. IXCM06-14 255.7, C. IXCM08-48 130.3, D. IXCM06-09 113.5. **Abbreviations:** Cpy - chalcopyrite, IrPy - inclusion-rich pyrite, Mc - marcasite, RmPy - rimming pyrite.

## Stage 3 continued

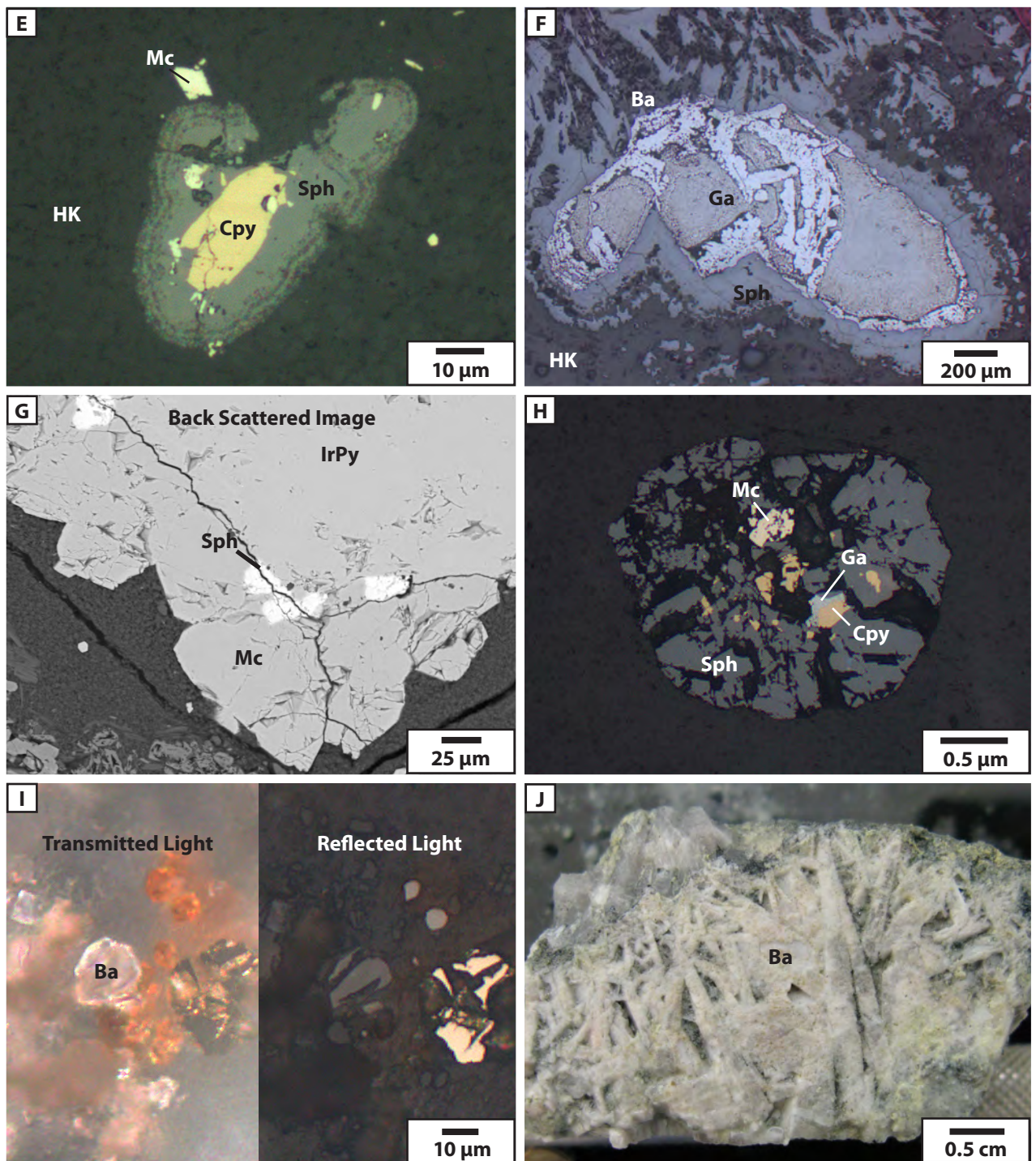


**Figure 6.7** Characteristics of Stage 3 mineralisation continued. **E.** Sphalerite forming concentric rims on a chalcopyrite in a haloysite-kaolinite + marcasite vein. **F.** Galena with sphalerite and chalcopyrite inclusions in intergrown with barite in a haloysite + kaolinite vein. **G.** Back scattered image of marcasite hosting sphalerite inclusions and rimming inclusion-rich pyrite. **H.** Sphalerite with chalcopyrite and marcasite inclusions. Galena is replacing the chalcopyrite. **I.** Fine grained barite in transmitted and reflected light. **J.** Coarse grained barite forming long slender needles. All images are reflected light unless otherwise indicated. Stratigraphic column is explained Chapter 4 and legend is in Figure 4.14. **Sample ID:**E. IXCM06-09 214.9, F. IXCM087-51 478.2, G. IXCM06-09 106.8, H. IXCM06-09 106.8 I. IXCM06-09 106.8, J. IXCM07-21 284.3. **Abbreviations:** Ba - barite, Cpy - chalcopyrite, FrPy - fractured pyrite, Ga - galena, HK - haloysite + kaolinite, IrPy - inclusion-rich pyrite, Mc - marcasite, Mo - molybdenite, RmPy - rimming pyrite, Sph - sphalerite, WR - wall rock.

## Stage 4

**Minerals:** Ragged pyrite, rimming pyrite, enargite, covellite

**Texture:** Ragged pyrite is irregular commonly intergrown with enargite. Rimming pyrite forms distinct rims on earlier stages. Enargite and fine-grained pyrite form in or on the rims of chalcopyrite.

**Distribution:** Breccia pipe (unit 4), thin rimming pyrite in volcanic wall rocks (unit 1 to 3). Rimming pyrite and ragged pyrite are the most common.

**Associated alteration:** Kandite alteration (Stage C)

**Timing:** Late epithermal.

**Distinguishing features:** Acid etching highlights rimming pyrite. Irregular pyrite in association with enargite.

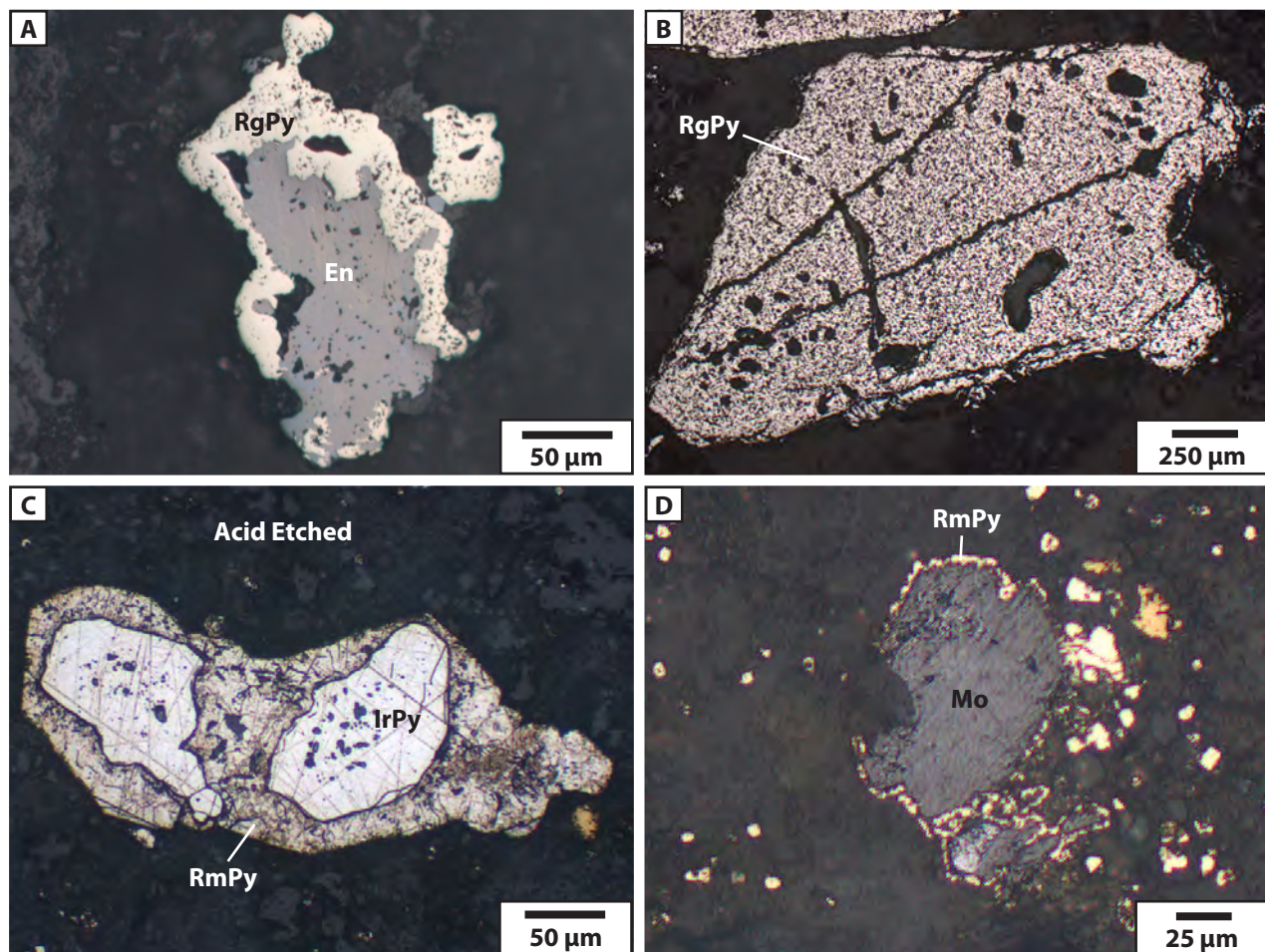
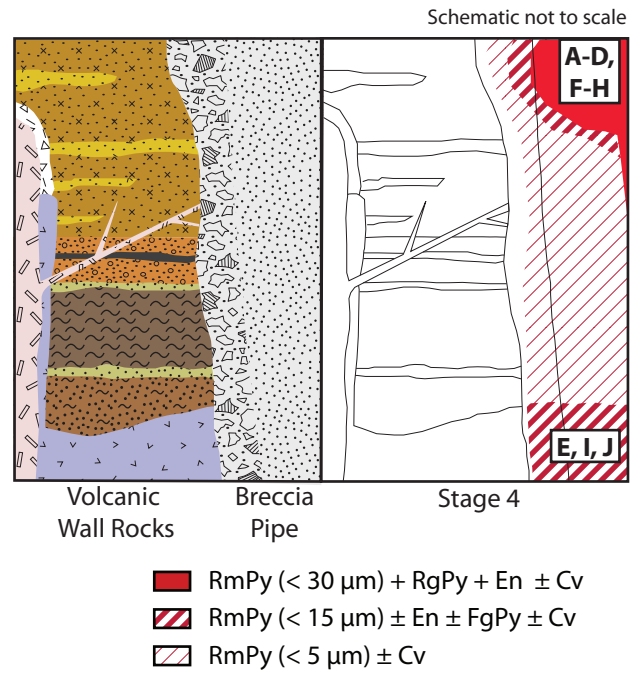


**Figure 6.8** Characteristics of Stage 4 mineralisation. **A.** Enargite rimmed by ragged pyrite. **B.** Ragged pyrite taking the appearance of a inclusion-rich pyrite. **C.** A thick 30 µm rim forming on inclusion-rich pyrite revealed with acid etching. **D.** Rimming pyrite on molybdenite. All images are reflected light. Stratigraphic column is explained Chapter 4 and legend is in Figure 4.14. **Sample ID:** A. IXCM06-09 86.3, B. IXCM06-09 106.8, C. IXCM06-09 100.7, D. IXCM06-09 100.7. **Abbreviations:** En - Enargite, IrPy - inclusion-rich pyrite, Mo - molybdenite, RgPy - ragged pyrite, RmPy - rimming pyrite.

## Stage 4 continued

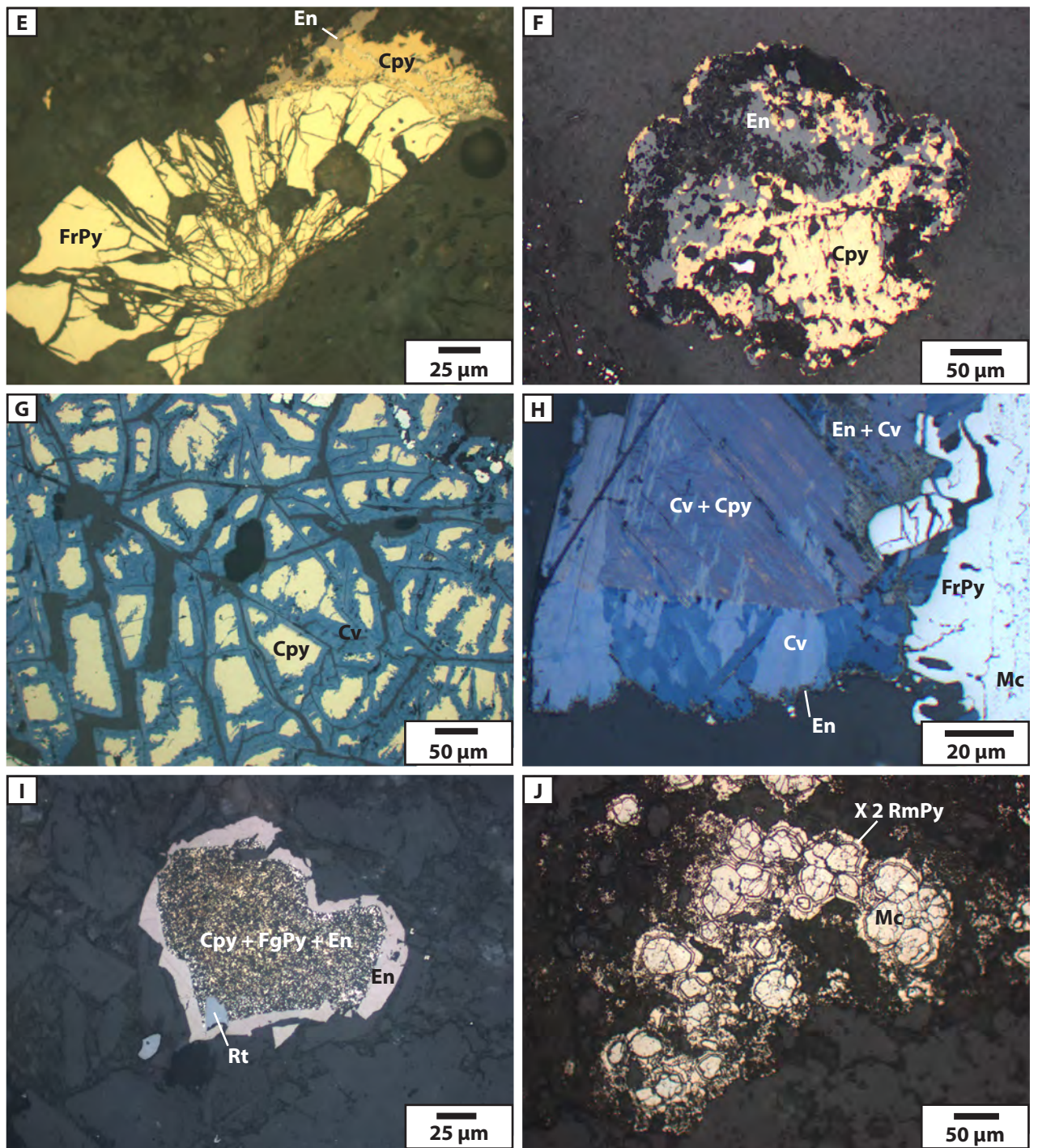


**Figure 6.8** Characteristics of Stage 4 mineralisation continued. **E.** Fractured pyrite (Stage 1) rimmed by chalcopyrite (Stage 2) that is in turn being replaced by enargite (Stage 4). **F.** Enargite replacing chalcopyrite. **H.** Chalcopyrite with covellite developed on its surface is rimmed by covellite which has a fine rim of enargite. Enargite and covellite are inter-grown in the upper right hand corner of the image. **G.** Covellite developed along fractures of chalcopyrite. **I.** Fine grained enargite and fine-grained pyrite forming on the surface of chalcopyrite and a second stage enargite from on the of chalcopyrite in the lower zone explained in text. **J.** Two rims of rimming pyrite forming on early marcasite in the lower zone explained in text. All images are reflected light. Stratigraphic column is explained Chapter 4 and legend is in Figure 4.14. **Sample ID:** E. IXCM06-16.313.4, F. IXCM06-09 86.3, G. IXCM08-48 130.3A, H. IXCM07-20 408.0, I. IXCM08-51 589.3, J. IXCM08-51 599.5. **Abbreviations:** Cpy - chalcopyrite, Cv - covellite, En - enargite, FgPy - fine-grained pyrite, FrPy - fractured pyrite, Mc - marcasite, RmPy - rimming pyrite.

## 6.5 Vein Textures

Late Stage 1 fractured pyrite veins infill early potassic (Stage A) veins and together are brecciated, consistent with pre-breccia pipe formation for Stage A alteration and Stage 1 mineralisation (Figs. 6.9C to D). In addition, a fractured pyrite vein is observed to be crosscut by a sericite (Stage B) altered inclusion-rich pyrite (Stage 2) vein (Figs. 6.9A and B). In addition, late halloysite + kaolinite + marcasite + sphalerite (Stage 3) veins are observed to infill early illite + chalcopyrite + inclusion-rich pyrite + molybdenite (Stage 2) veins (Figs. 6.9E and F). A halloysite-kaolinite (Stage C<sub>HK</sub>) vein with sphalerite-barite-galena bands between halloysite-kaolinite suggests more than one episode of deposition (Figs. 6.9G and H). In addition, this vein suggests that the halloysite-kaolinite is hypogene in origin as sulfide deposition between halloysite-kaolinite formation cannot be explained in a supergene environment.

Rare hydrous and anhydrous phosphate minerals were observed in veins comprising planerite ( $\text{Al}_6(\text{PO}_4)_2(\text{PO}_3\text{OH})_2(\text{OH})_8 \cdot 4(\text{H}_2\text{O})$ ), vivianite ( $\text{Fe}^{2+}_3(\text{PO}_4)_2 \cdot 8(\text{H}_2\text{O})$ ), trolleite ( $\text{Al}_4(\text{PO}_4)_3(\text{OH})_3$ ) and berlinite ( $\text{AlPO}_4$ ; Fig. 6.10). The phosphate minerals are not found in association with other alteration minerals and occur distal to the kandite alteration (Stage C) and crosscut early potassic (Stage A) and sericitic (Stage B) alteration. The timing of phosphate minerals with respect to the kandite alteration (Stage C) is unclear.

A sample hosting a phosphate vein contains botryoidal planerite, trolleite and berlinite identified with XRD (sample IXCM08-45 64.9 m; Fig. 6.10A). SEM imaging indicates that the planerite forms bands extending from the vein wall and the centre of the vein to be infilled with trolleite and berlinite. The planerite is associated with fine-grained pyrite ( $< 20 \mu\text{m}$ ; Fig. 6.10B). Another sample hosts a blue vivianite vein that cross-cuts early potassic and sericitic alteration (Fig. 6.10C). The vivianite was identified using SEM/EDS and thin section petrography.

## 6.6 Spatial Distribution

The distribution of mineralisation is illustrated on four cross sections (A to D; Fig. 6.11 to 6.15). To better illustrate the lateral distribution of mineralisation cross sections A to C were combined along with infill drill holes to make a long section E-E' (Figs. 6.16 and 6.17). The location of the breccia pipe and volcanoclastic wall rock is indicated.

Stage 1 fractured pyrite occurs in veins and in plan view the distribution forms a donut shape centred on the breccia pipe (Fig. 6.12A). In cross section this pyrite is located on the margins of the breccia pipe extending down to 200 m below the surface and 200 m away from the breccia pipe (Figs. 6.16).

Stage 2 inclusion-rich pyrite, chalcopyrite and molybdenite is centred on the southwest breccia pipe with a chalcopyrite + molybdenite + inclusion-rich pyrite core transitioning to inclusion-rich pyrite  $\pm$  chalcopyrite distally (Fig. 6.11A). Inclusion-rich pyrite becomes the most abundant sulfide distal from the core (Fig. 6.16). A molybdenum anomaly in rock sample geochemistry occurs at

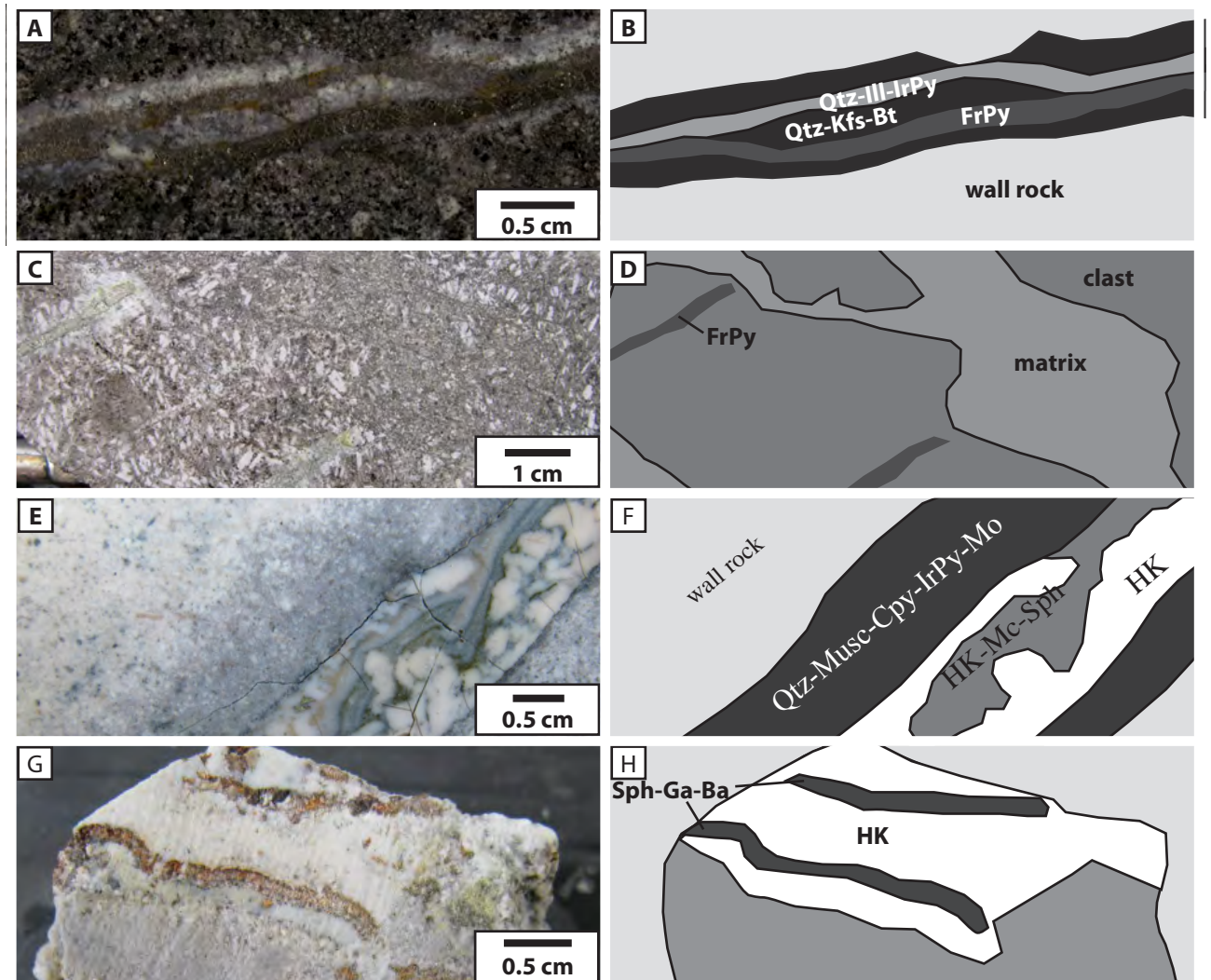


**Figure 6.9** Veins textures of Cerro la Mina. **A/B.** Late fractured pyrite veins infilling early quartz - potassium feldspar - biotite veins which is cross-cut by a illite + inclusion-rich vein. **C/D.** Fractured pyrite veins observed in the clast of the breccia pipe. **E/F.** An earlier sericitic alteration (Stage B) dark grey quartz + muscovite + chalcopyrite + inclusion-rich pyrite + molybdenite vein infilled with a later halloysite-kaolinite + marcasite + sphalerite vein. **G/H.** Vein with alternating bands of halloysite + kaolinite and sphalerite + galena + barite. **Sample ID:** A. IXCM08-55 226.5, C. IXCM08-52 188.0, E. IXCM06-09 214.9, G. IXCM08-51 478.2. **Abbreviations:** Ba - barite, Bt, biotite, Cpy - chalcopyrite, FrPy - fractured pyrite, Ga - galena, HK - halloysite + kaolinite, Ill - illite, IrPy - inclusion-rich pyrite, Kfs - Potassium feldspar, Mc - marcasite, Mo - molybdenite, Musc - muscovite, Qtz - quartz, Sph - sphalerite.

surface, consistent with the observed molybdenite distribution at surface. In cross section the distribution of chalcopyrite and molybdenite is coincident with the breccia pipe orientation (Figs. 6.13 and 6.16). The chalcopyrite + molybdenite core is associated with the high-temperature quartz-muscovite ± illite core of the sericitic alteration (Stage B) described in Chapter 5 (Figs. 5.10, 5.14 and 5.16). Stage 2 mineralisation is found as disseminations (< 5% of rock) and in quartz-sericite (Stage B) altered margins of veins. The molybdenite and chalcopyrite do not extend deeper than 850 m elevation. This may be an artefact of the location of the cross section or a lack of drill holes that extend deeper than 850 m elevation (3 of 67 drill holes). Chalcopyrite is not present or is minor where coarse-grained enargite (> 200-500 µm) occurs in the overprinting quartz-dickite alteration (Stage C<sub>QD</sub>).

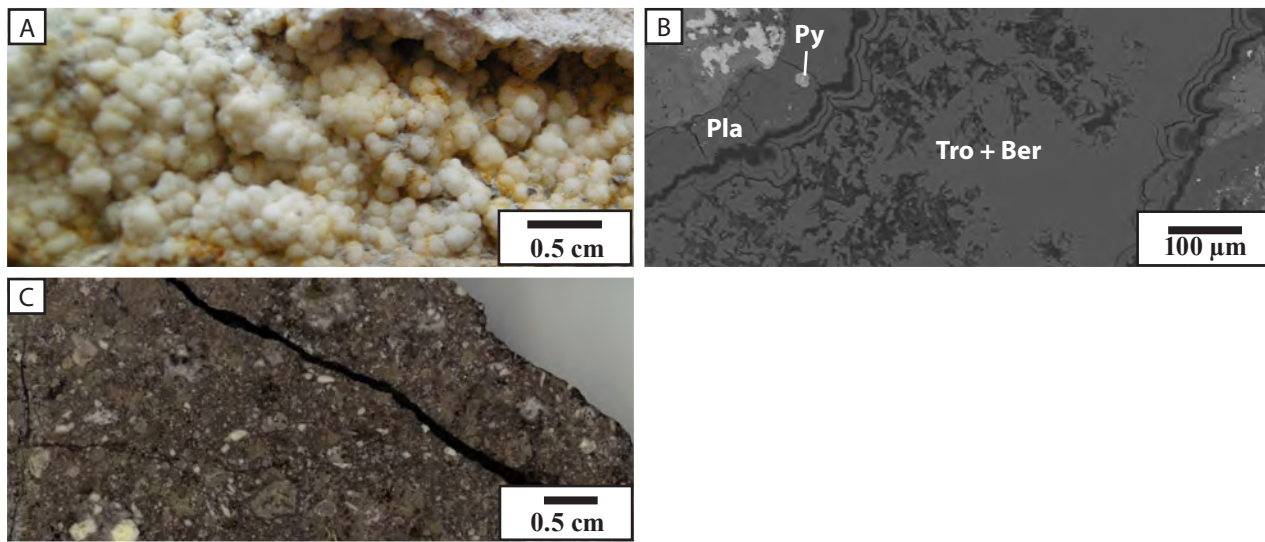


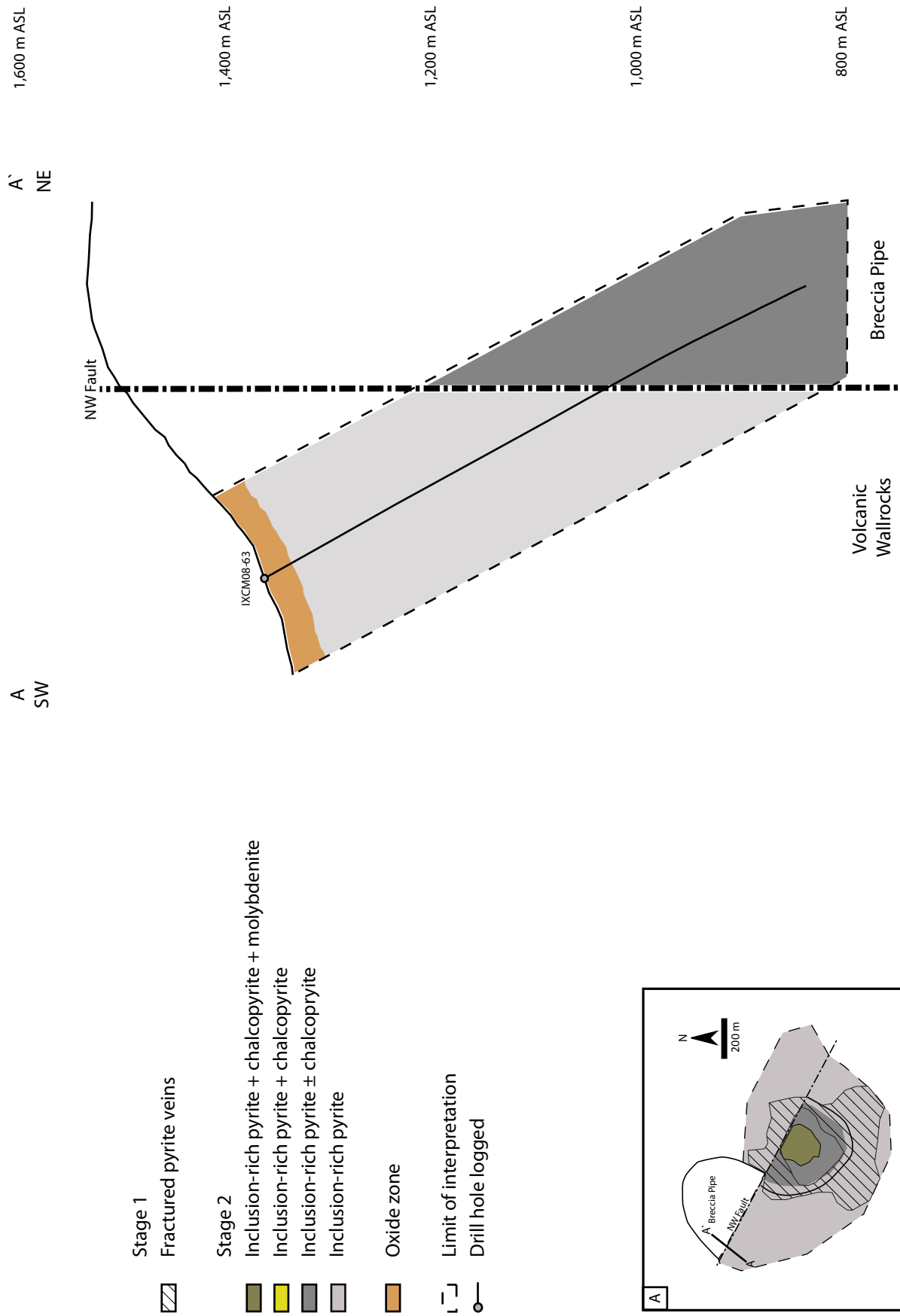
**Figure 6.10** Rare phosphorous veins of Cerro la Mina **A.** Botryoidal planerite occurring in a vein. **B.** Back scattered image of vein shown in A. **C.** Blue vivianite vein cross-cutting early potassic (Stage A) and sericitic alteration (Stage B). **Abbreviations:** Ber - berlinite, Pla - planerite, Tro - trolleite. **Sample ID:** A and B. IXCM08-45 64.9, B. IXCM08-63 454.5.

The distribution of marcasite + sphalerite + galena + barite (Stage 3) occurs mainly in the breccia pipe and is vertically orientated coincident with the breccia pipe (Fig. 6.14 and 6.17). A zone of abundant sphalerite + galena + barite occurs near the surface where it is also coarser grained and becomes less abundant with depth.

Stage 4 is most abundant in two distinct zones classified as the upper and lower arsenic-rich zones (Fig. 6.17). The upper arsenic-rich zone occurs from surface to 200 m depth forming a bowl shape comprising ragged pyrite + rimming pyrite + enargite. The lower arsenic-rich zone comprises rimming pyrite ± enargite that occurs below 1100 m elevation (> 600 m below the surface) forming a sub-horizontal zone (Fig. 6.17). The distribution of mineralisation associated with Stage 3 and 4 mineralisation corresponds to the Au distribution (Fig. 6.17). Stage 4 is less abundant between the upper and lower zones with thin rimming pyrite (< 5 µm; Fig. 6.17).

The Stage 4 mineralisation in the upper arsenic-rich zone is disseminated and is associated mainly with quartz-dickite alteration (Stage C<sub>QD</sub>) and dickite-cemented hydrothermal breccias as described in Chapter 5 (Fig. 5.16). The upper arsenic-rich zone is characterized by a core of quartz + dickite + rimming pyrite (rim thickness 15 to 30 µm) + ragged pyrite + enargite ± covellite that is surrounded by a kaolinite + halloysite + rimming pyrite (rim thickness <15 µm) ± enargite ± fine-grained pyrite ± covellite zone.

The lower arsenic-rich zone has kaolinite + halloysite + rimming pyrite (rim thickness 10 to 20 µm rims) ± enargite ± fine-grained pyrite. The lower zone rimming pyrite contains two rims and enargite that has nearly completely replaced chalcopyrite and is rimmed by a second generation of enargite (e.g. Fig. 6.8I and J). By contrast only one rim occurs in the mid to upper zones (Fig. 6.7D). The sulfides in the lower zone occur mainly as disseminations and in the halloysite-kaolinite cement



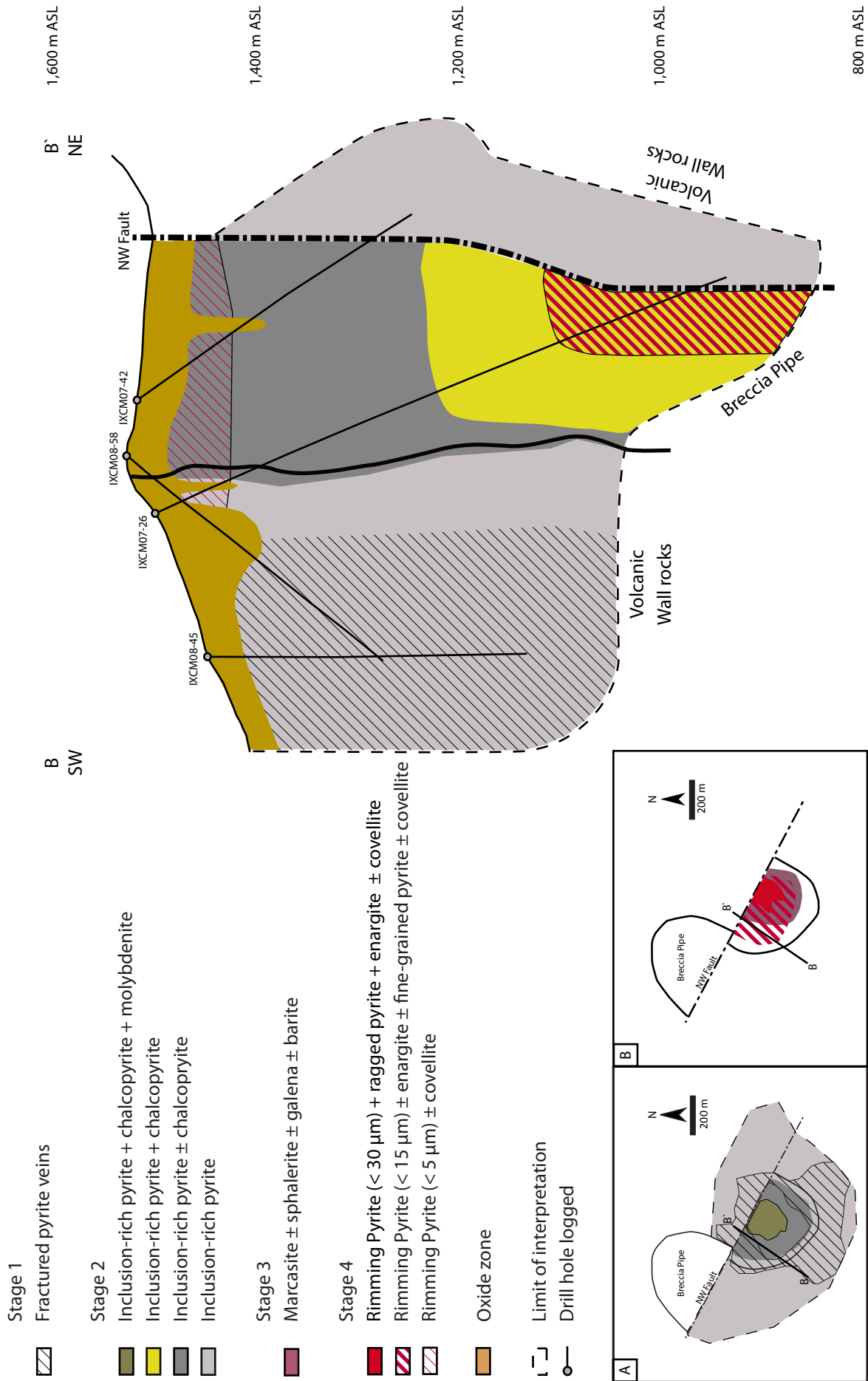


**Figure 6.12** Mineralisation of cross section B-B'. Cross section location shown on plan view in inset A.

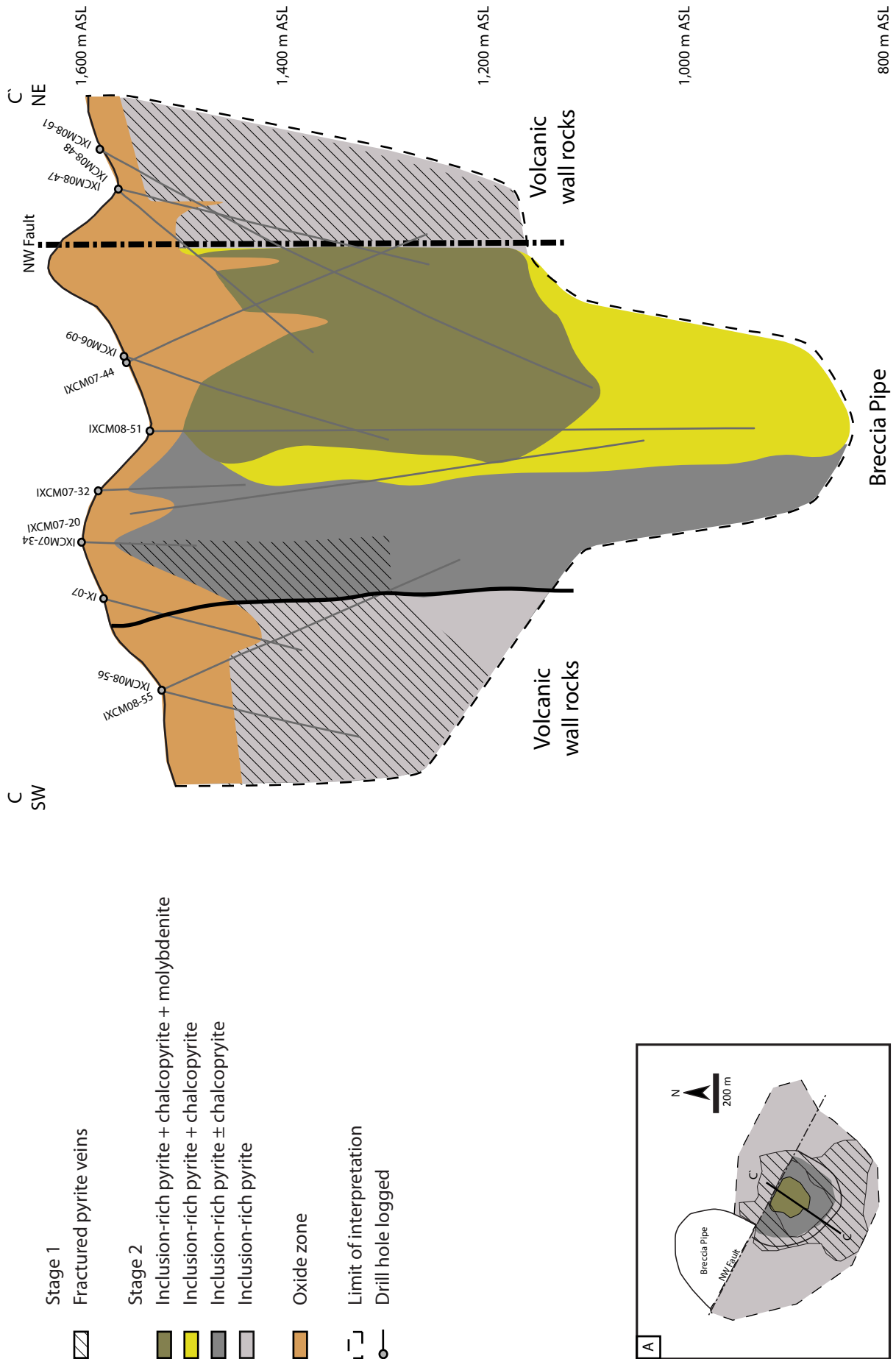
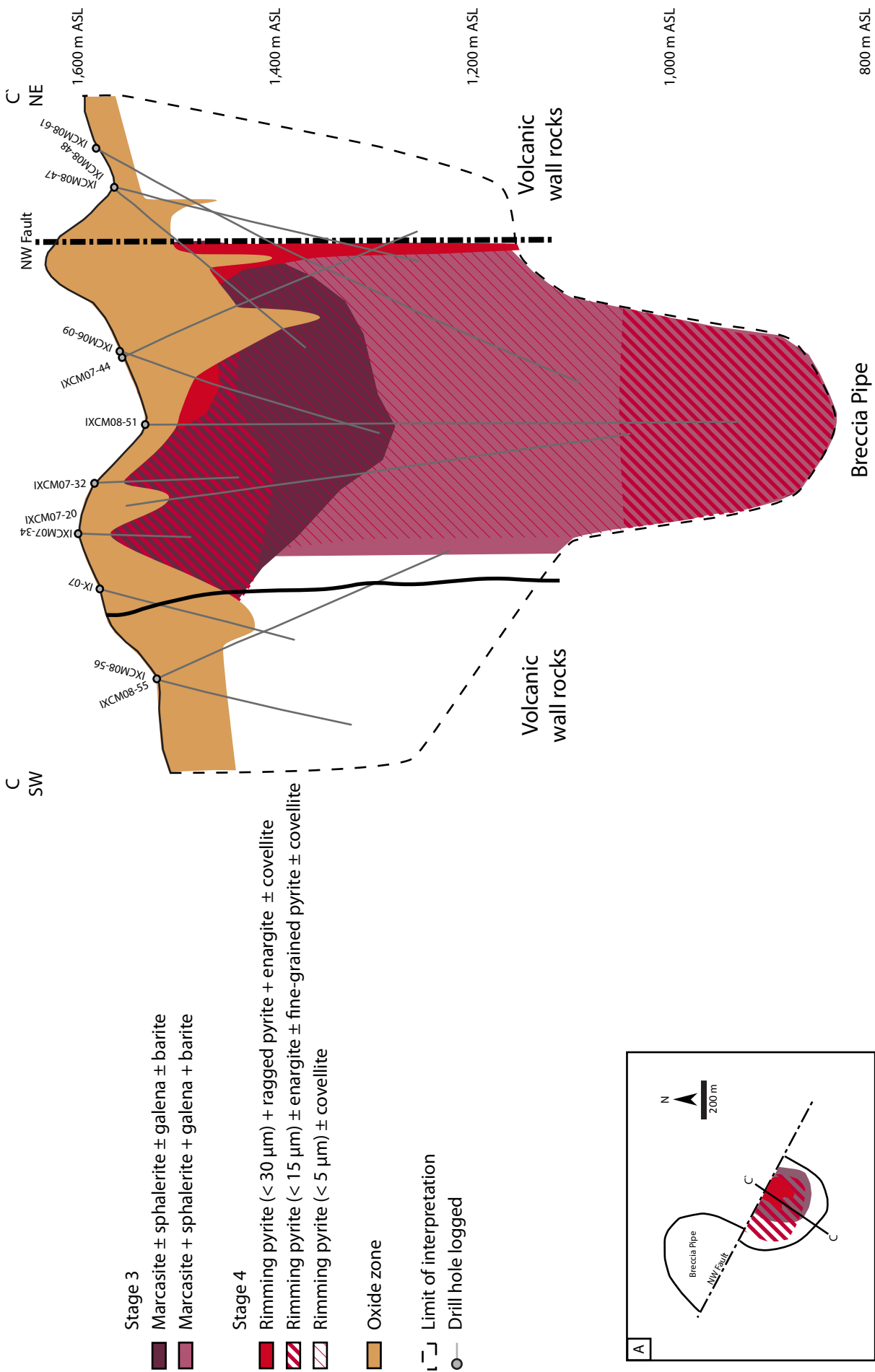
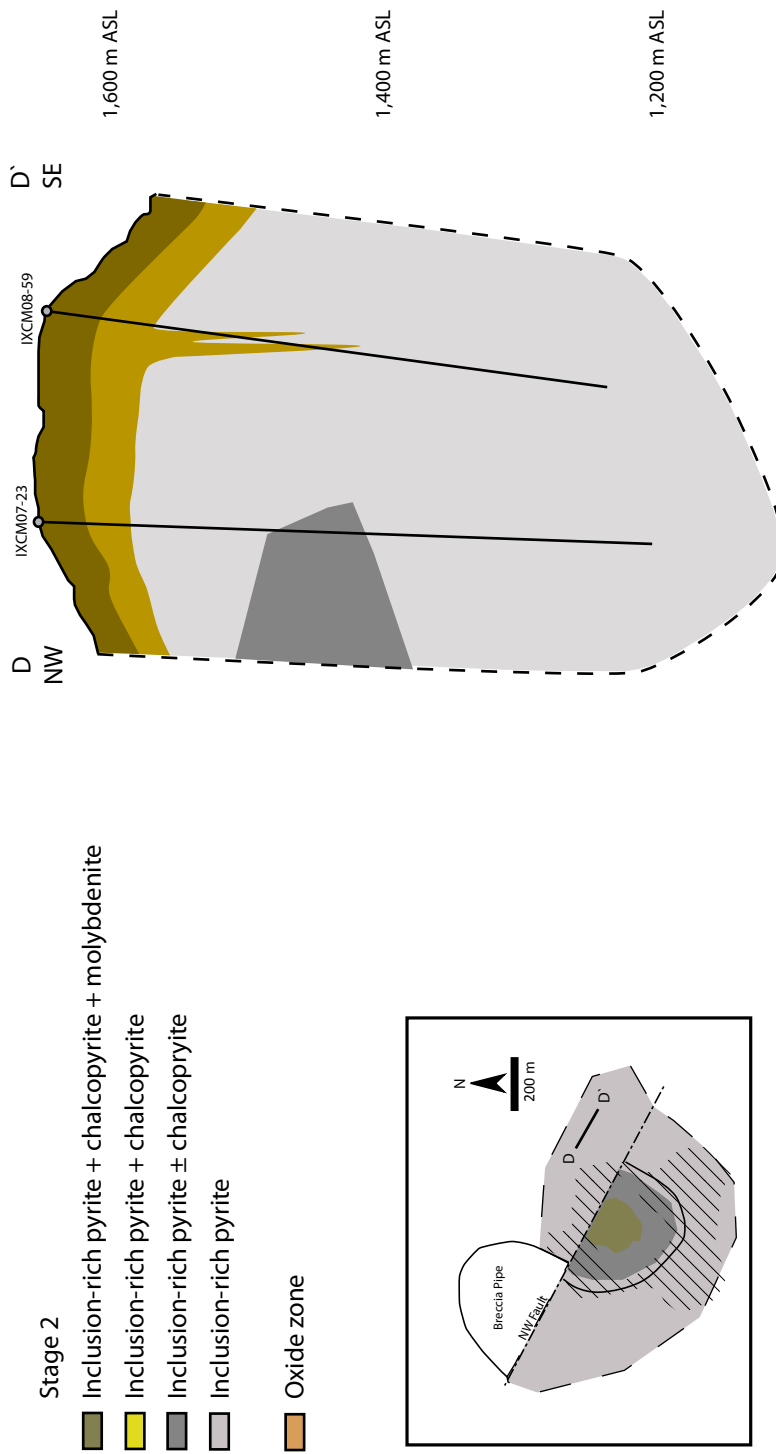
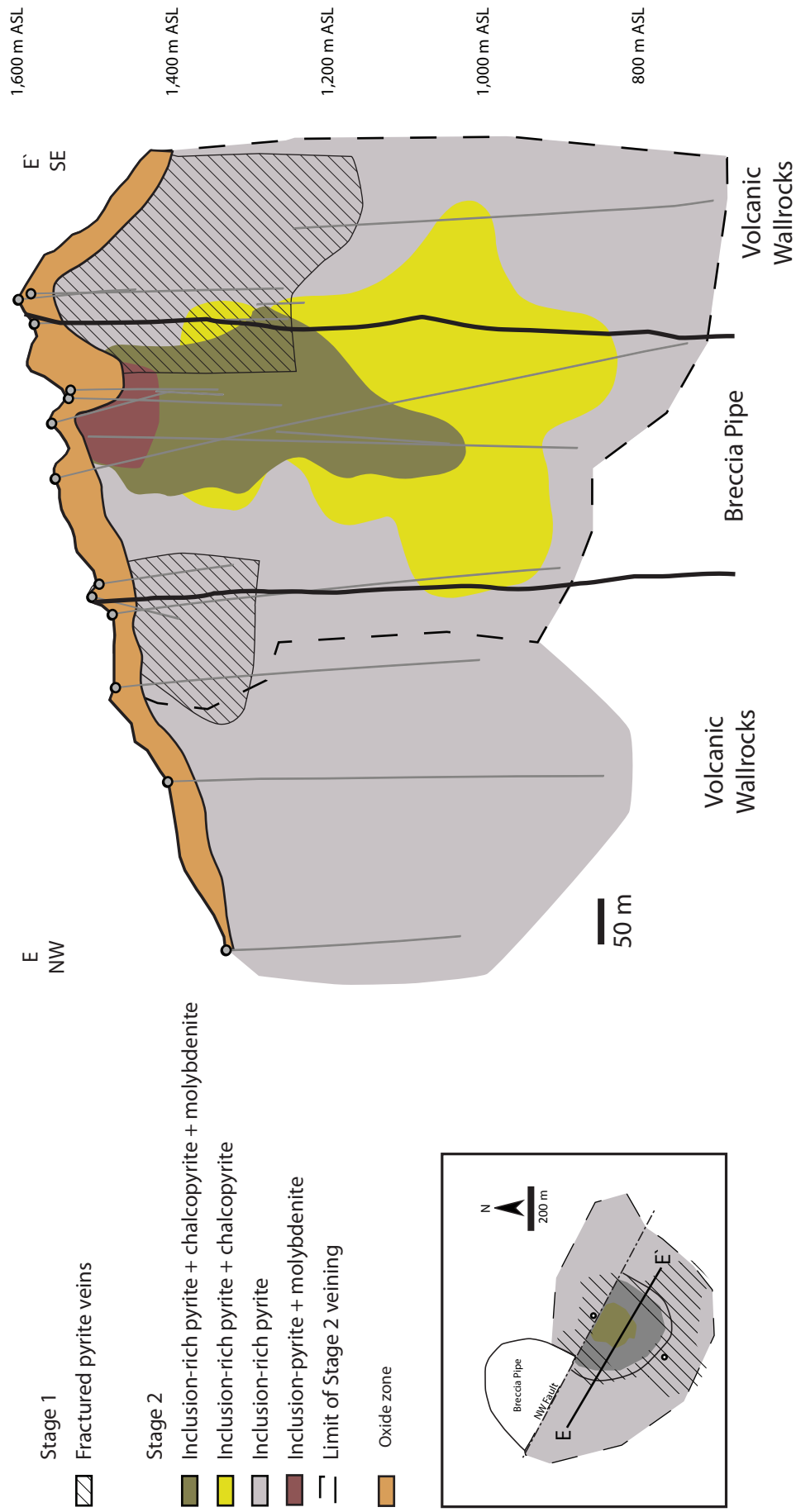


Figure 6.13 Stage 1 and 2 mineralisation of cross section C-C'. Cross section location shown on plan view in inset A.





**Figure 6.15** Mineralisation of cross section D-D'. Cross section location shown on plan view in inset A.



**Figure 6.16** Stage 1 and 2 mineralisation of long section E-E'. Long section location shown on plan view in inset A.

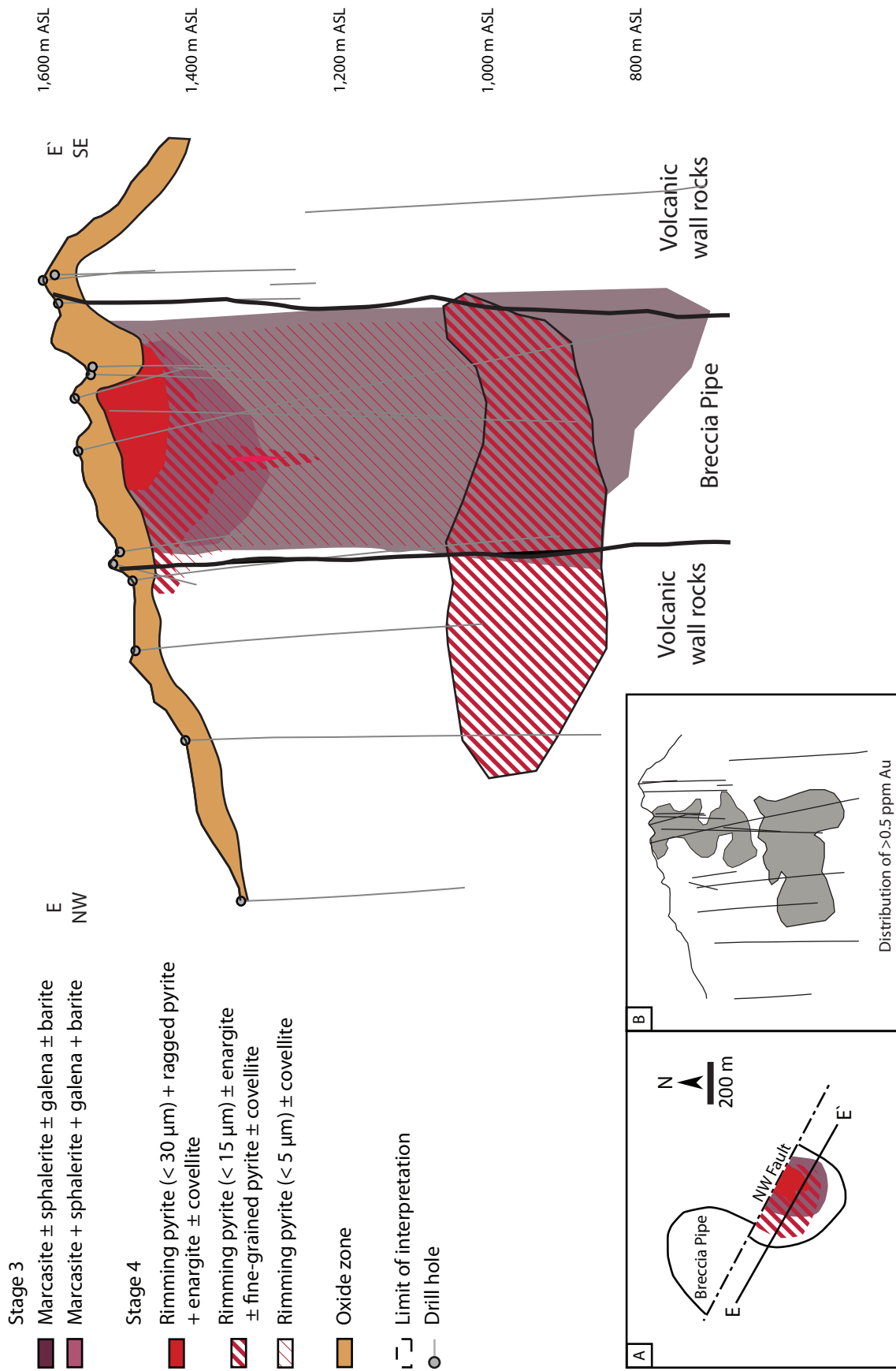


**Figure 6.17** Stage 3 and 4 mineralisation of long section E-E'. Long section location shown on plan view in inset A. Distribution of gold > 0.5 ppm is shown in inset B.

of hydrothermal breccias. Overall, the rimming pyrite is thickest (15 to 30  $\mu\text{m}$ ) at the surface and below 1100 m elevation (10 to 20  $\mu\text{m}$ ; >600 m below surface; Fig. 6.17) and extremely thin rimming pyrite (<5  $\mu\text{m}$ ) occurs between the upper and lower arsenic-rich zones.

The oxide zone, where no sulfides exist, extends on average to 50 m below the surface with a maximum depth of 175 m (Figs. 6.11 to 6.17). Weaker oxidation where pyrite and oxides occur is still present to depths of 545 m below the surface along fractures associated with the northwest fault. The oxide zone comprises goethite, hematite, opal and barite.

## 6.7 Discussion

The mineralisation at Cerro la Mina is hosted entirely in the breccia pipe. Stage 1 and 2 mineralisation is associated with a high temperature phase typically seen in phyllic alteration of porphyry systems (Lowell and Guilbert, 1970; Seedorff et al., 2005). Stage 3 and 4 is associated with low temperature epithermal alteration commonly structurally controlled. A late supergene oxide zone overprints the all of these assemblages.

A schematic diagram to illustrate the four mineralisation stages is shown in Figure 6.18 and a paragenesis diagram is shown in Figure 6.19. The breccia pipe cross-cuts early potassic alteration (Stage A) and the distribution of Stage 1 fractured pyrite providing a fluid pathway for the development of three additional mineralisation stages associated with sericitic (Stage B) and kandite (Stage C) alteration. The stages comprise Stage 2 inclusion-rich pyrite + chalcopyrite + molybdenite associated with the sericitic alteration (Stage B), Stage 3 marcasite + sphalerite + galena + barite associated with kandite alteration (Stage C) and ends with arsenic-rich ragged pyrite + rimming pyrite + enargite + covellite + fine-grained pyrite (Stage 4) that is also associated with the kandite alteration (Stage C).

Stage 1 mineralisation is associated with late fractured pyrite that in-fills early potassic (Stage A) veins. The fractured pyrite probably precipitated as coarse-grained pyrite, and the explosive formation of the breccia pipe moved the pyrite making a donut shape in its distribution (Fig. 6.16) and probably fractured the coarse-grained pyrite into a jig-saw fit texture. The breccia pipe created a fluid pathway for the sericitic (Stage B) and kandite (Stage C) alteration and associated Stage 2 to 4 mineralisation fluids to invade and precipitate.

Stage 2 mineralisation is associated with sericitic alteration (Stage B). The inclusion-rich pyrite + chalcopyrite + molybdenite precipitated along the fluid pathway provided by the breccia pipe, causing the vertical orientation of Stage 2 (Fig. 6.1; Fig. 6.16). The close association of inclusion-rich pyrite and chalcopyrite suggests that they precipitated together. No textural evidence suggests that the molybdenite precipitated with the chalcopyrite + inclusion-rich pyrite, however, its distribution is coincident with chalcopyrite distribution. The association of quartz + muscovite alteration assemblages (Stage B) with chalcopyrite and molybdenite suggests that Stage 2 mineralisation formed at temperatures greater than 300°C, typical of the phyllic stage for a porphyry system (Seedorff et al., 2005).

Distal to the high temperature core, inclusion-rich pyrite becomes the dominant sulfide in association with clay assemblages that indicate decreasing temperature. The inclusion-rich pyrite, chalcopyrite and molybdenite are strongly embayed with cusped edges suggesting these minerals were not in equilibrium with the late kandite alteration (Stage C) fluids. The covellite forms in fractures of chalcopyrite possibly indicating some remobilization of Cu during chalcopyrite replacement. Covellite and enargite have a complex inter-grown texture and are interpreted to have formed together. It is interpreted that Cu has been remobilized mainly from the chalcopyrite and redeposited as enargite.

Stage 3 is associated with kandite alteration (Stage C) and comprises marcasite, sphalerite, galena and barite in a vertical orientation coincident with the breccia pipe. The marcasite rims the inclusion-rich pyrite (Stage 2) and sphalerite rims chalcopyrite (Stage 2) consistent with late timing for Stage 3. As well, the galena is interpreted to replace chalcopyrite (Stage 2).

Stage 4 mineralisation is associated with kandite alteration (Stage C) and kandite cemented hydrothermal breccias, and occurs as two distinct arsenic-rich zones from the surface to 200 m depth and below 600 m depth. The zoning in the upper arsenic-rich zone includes a ragged pyrite + thick rimming pyrite + enargite core, changing distally to a thin rimming pyrite with minor enargite and fine-grained pyrite. This transition is also associated with a quartz-dickite (Stage C<sub>QD</sub>) transition to a kaolinite-rich (relative to halloysite) alteration (Stage C<sub>HK</sub>). The lower arsenic-rich zone at 600 m depth contains thick rimming pyrite and minor enargite + fine-grained pyrite associated with a kaolinite-rich (relative to halloysite) Stage C<sub>HK</sub> alteration. Halloysite-rich (relative to kaolinite) assemblages occur where the rimming pyrite is the thinnest between the upper and lower arsenic-rich zones. The abundance of halloysite clay is therefore changing in association with variations in the distribution of Stage 4 mineralisation, suggesting a hypogene origin.

Enargite can be weakly developed on the surface of chalcopyrite, or as rims, to complete engulfing the chalcopyrite. Where enargite is coarse-grained, chalcopyrite is absent. It is interpreted that the enargite replaced chalcopyrite. Richards (2006) described early chalcopyrite-pyrite-molybdenite assemblages that are partly to completely replaced by covellite, digenite and idaite (Cu<sub>3</sub>FeS<sub>4</sub>) at Cerro la Mina.

The presence of upper and lower arsenic-rich zones suggests that there are two separate Stage 4 mineralisation events. The lower arsenic-rich zone, which lacks quartz-dickite (Stage C<sub>QD</sub>) and abundant enargite, but has kaolinite-rich alteration (Stage C<sub>HK</sub>) and thick rimming pyrite, is probably the top or sides of a quartz + dickite + ragged pyrite + enargite + covellite zone located laterally or deeper (i.e. similar to the upper arsenic-rich zone). In addition, the lower zone has two rims of pyrite, in contrast to one rim in the upper zone suggesting an additional episode of deposition in the lower zone. The two distinct arsenic-rich zones with similar mineralogy could have been formed as the result of significant uplift.

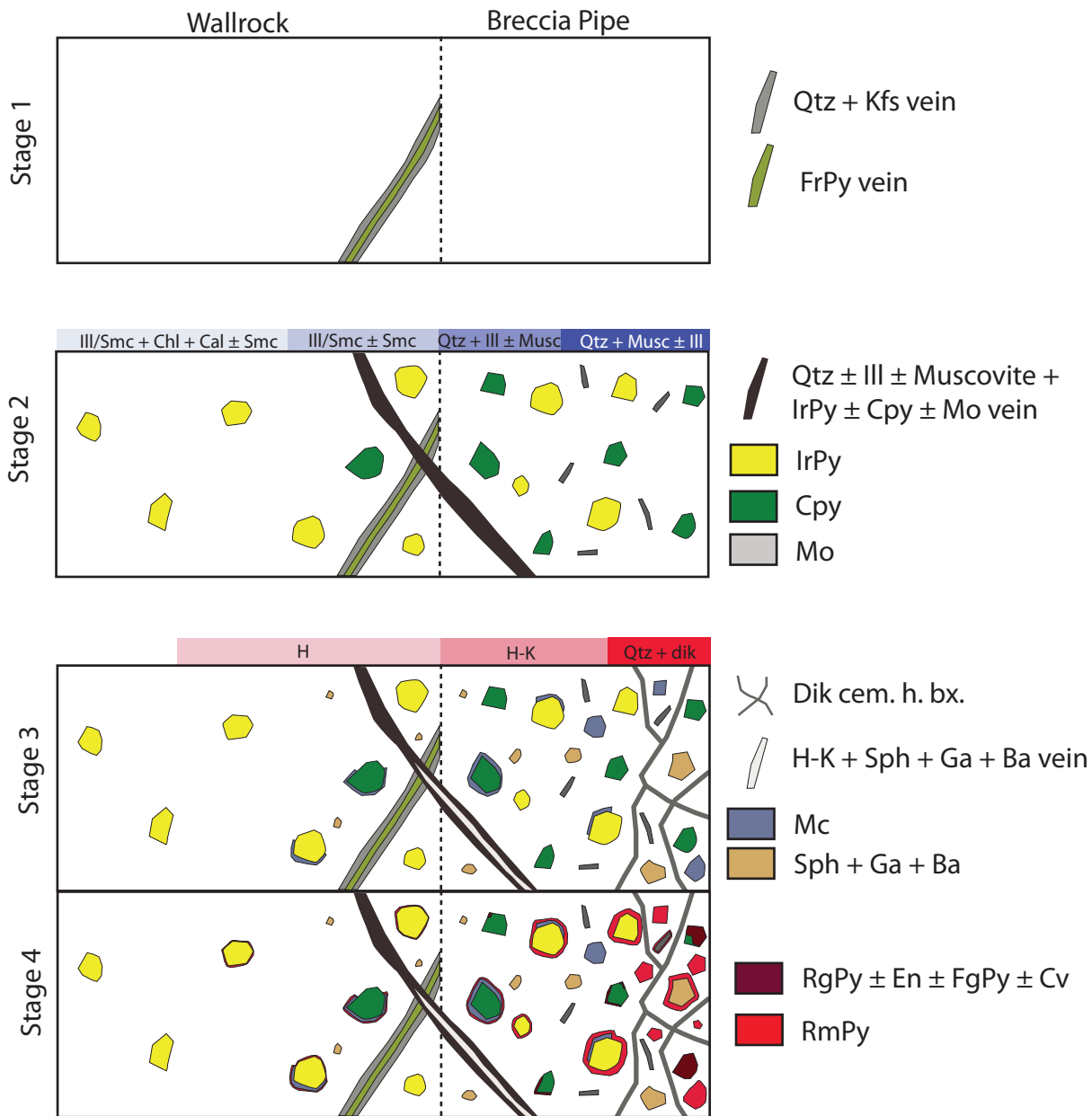


**Figure 6.18** Schematic illustrating the paragenesis of the Cerro la Mina Stages 1 to 4 mineralisation and associated alteration. Explanation is provided in text. **Abbreviations:** Ba - barite, Cal - calcite, Chl - chlorite, Cpy - chalcopyrite, Cv - covellite, Dik - dickite, Dik cem. h. bx. - dickite-cemented hydrothermal breccia, En - enargite, FgPy - fine-grained pyrite, FrPy - fractured pyrite, Ga - galena, H - halloysite, H-K - halloysite + kaolinite, Ill - illite, Ill/smc - illite/smectite, IrPy - inclusion-rich pyrite, Kfs - Potassium feldspar, Mc - marcasite, Mo - molybdenite, Musc - muscovite, Qtz - quartz-dickite, RmPy - rimming pyrite, RgPy - ragged pyrite, Smc - smectite, Sph - sphalerite.

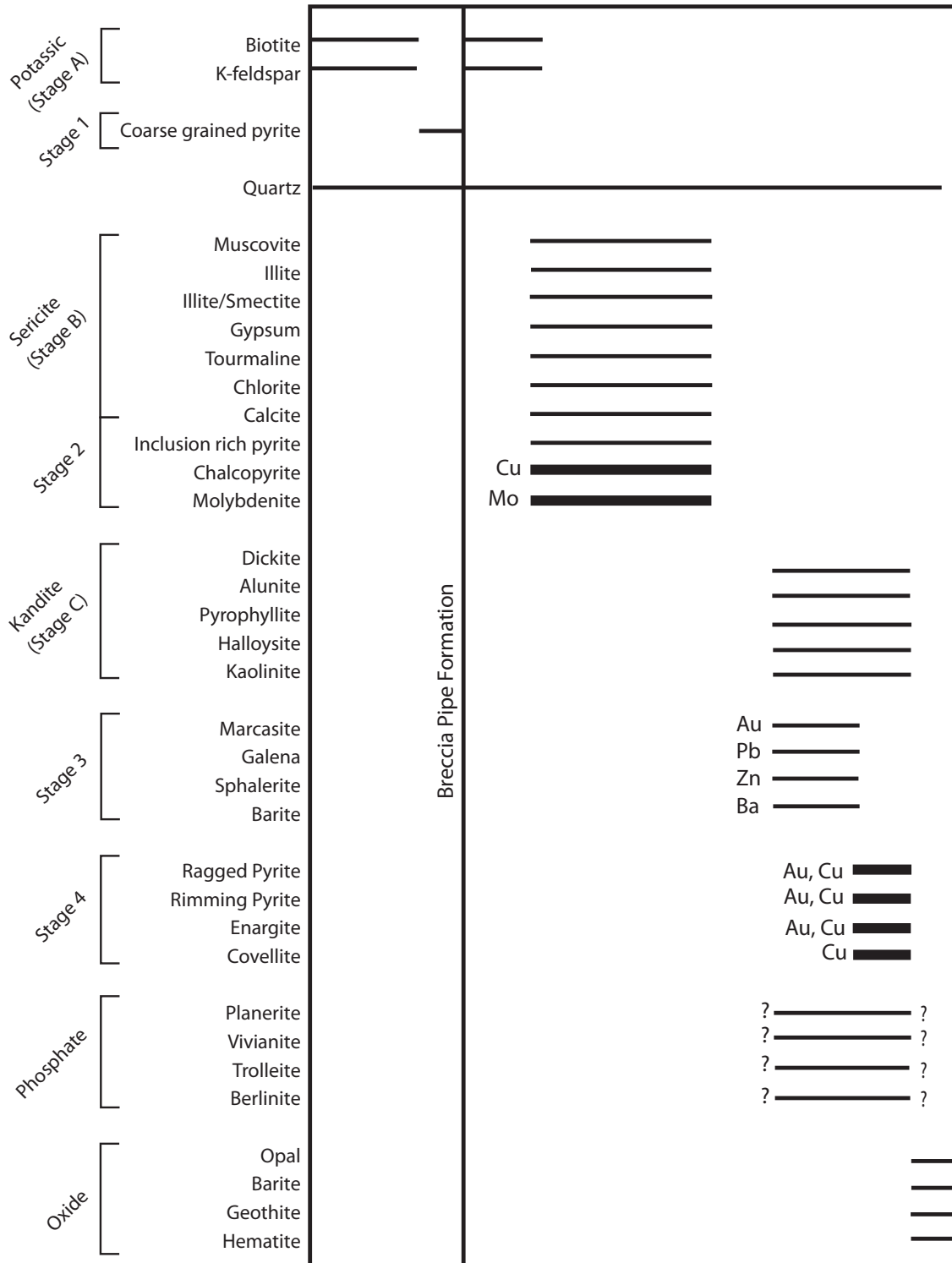


Figure 6.19 Parageneses of mineralisation for the Cerro la Mina prospect.

## 6.8 Sulfide Imaging

Imaging using laser ablation - inductively coupled plasma mass spectrometry (LA-ICP-MS) determined the trace element zoning of fractured pyrite, inclusion-rich pyrite, ragged pyrite, rimming pyrite, marcasite enargite, chalcopyrite and sphalerite from Stages 1 to 4. Imaging constrained the geochemical characteristics of the fluid in which mineralisation was deposited. Examples of trace element zonation for each mineral are shown in Figures 6.21 to 6.36, with the remainder compiled in Appendix IV.3. A total of 43 laser maps were made, with each laser map including at least one or more minerals (Table 6.2).

The pyrite trace element geochemistry was compared with zones that did not contain trace element enrichment during laser mapping (e.g. Appendix IV.3, sample IXCM08-55 95.6). These zones are considered to be the baseline geochemical signature for comparison with enriched zones and is herein called the Cerro la Mina standard pyrite (CSP). The CSP trace element geochemistry was plotted using Tukey box plots and ordered with decreasing median values (Fig. 6.20). The median values for the CSP were used as comparators to determine which elements are enriched. Values considered to be weakly, moderately and strongly enriched are 1, 2 and 3 orders of magnitude greater than CSP respectively. The description of approximate ranges for element concentration are based on the inter quartile range of the Tukey box plot which contains 50% of the data.

### 6.8.1 Stage 1

An example of a fractured pyrite (Stage 1) laser image is contained in Figures 6.21 and 6.22. Fractured pyrite typically contains oscillatory zoning of Co and Se enrichment and rare zones of As enrichment (Figs. 6.21 and 6.22). To distinguish between Co- and Se-rich zones a Co-rich zone was defined by  $\text{Co/Se} > 1$  and a Se-rich zone was defined by a Co/Se ratio of  $< 1$  (Fig. 6.21). Se-rich zones are weakly enriched in Cu, As and Te and in Co-rich zones Ni is weak to moderately enriched (Fig. 6.23). The fractured pyrite also has weakly As enriched zones where Cu, Te and Au are weakly to moderately enriched (Fig. 6.22 and 6.23). Limited distribution of this pyrite type did not permit observation of the spatial distribution of elements in the prospect.

### 6.8.2 Stage 2

Inclusion-rich pyrite (Stage 2) is similar to Stage 1 in that in some examples it show oscillatory zoning of Co or Se enrichment. However, Stage 2 pyrite is distinct from Stage 1 with higher Bi and Ni concentrations. Stage 1, like Stage 2, can be divided into Co-rich ( $\text{Co/Se} > 1$ ; Fig. 6.24) and Se-rich ( $\text{Co/Se} < 1$ ; Fig. 6.24) and As-rich varieties (Fig. 6.25). Tukey plots displaying element concentrations is contained in Figure 6.27.

The Co-rich zones are weakly enriched in Se and Te. The Se-rich zones are strongly enriched in Ni and weakly enriched in Co and Bi. As-rich zones (60-1000 ppm) occasionally occur in Stage 2, however, when observed they are strongly enriched in Pb and Ni, moderately enriched in Sb and Bi, and weakly enriched in Au, Ag and Te. Chalcopyrite does not show element zoning but produces high counts of Se and In (Fig. 6.26).

| Minerals with Laser Maps | Stage | No. |
|--------------------------|-------|-----|
| Fractured pyrite         | 1     | 6   |
| Inclusion-rich pyrite    | 2     | 26  |
| Chalcopyrite             | 2     | 5   |
| Marcasite                | 3     | 11  |
| Sphalerite               | 3     | 1   |
| Ragged pyrite            | 4     | 2   |
| Rimming pyrite           | 4     | 20  |
| Enargite                 | 4     | 6   |

**Table 6.2** Summary of the number of laser maps created for each mineral. A total of 43 laser images were created and one laser image can contain multiple minerals.

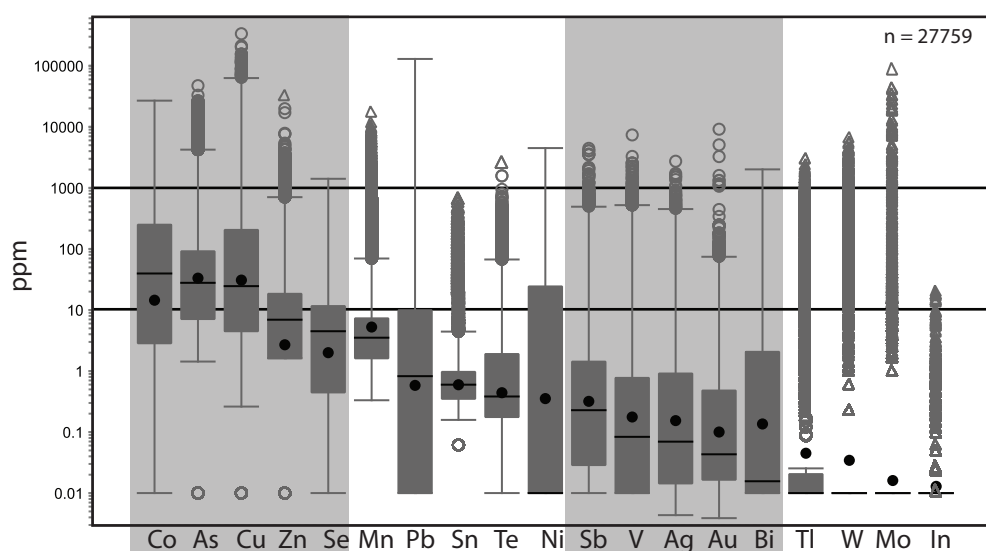
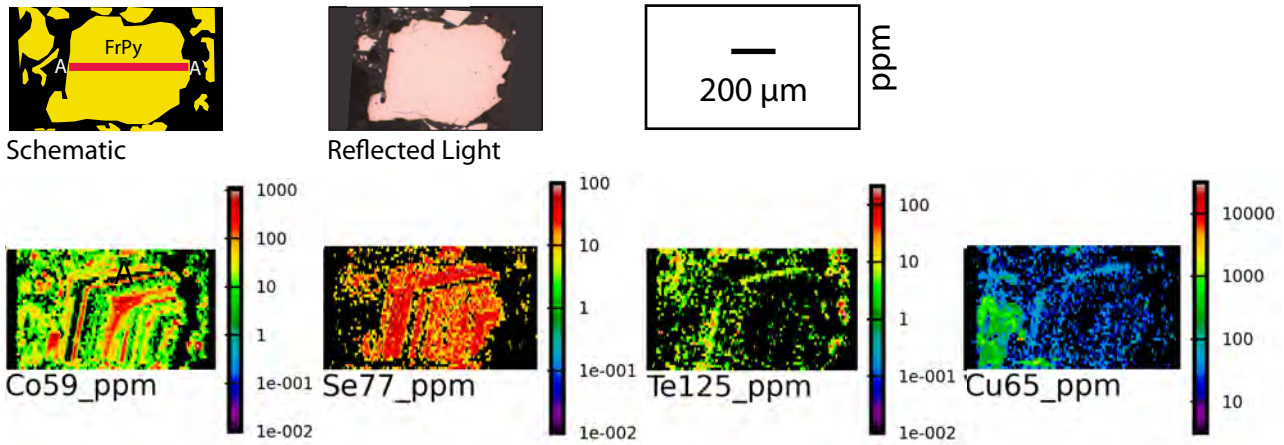


**Figure 6.20** Tukey box plot showing the composition of a Cerro la Mina standard pyrite. Data compiled from laser map points.

The inclusion-rich pyrite (Stage 2) is the most abundant and widespread pyrite type at Cerro la Mina. The concentrations of Co, Ni, Se, Te, Cu and Au in pyrite show an abrupt increase in the breccia pipe compared to the volcanic wall rocks and show increasing concentrations with depth in the breccia pipe (Figure 6.28 and 6.29). Stage 2 pyrite containing zones with no trace element enrichment become less common closer to and deeper in the breccia pipe. Mo and Cu in pyrite also increases toward the breccia pipe and with depth in the breccia pipe; however, the enrichment probably results from an increase of molybdenite and chalcopyrite inclusions in the inclusion-rich pyrite. A Co-Se-Te-Mo-(Cu-Au) anomaly occurs in approximately 850 m horizontally to the northwest of the breccia pipe (sample IXCM08-63 168.1).

A. Stage 1 Fractured Pyrite: Co- and Se-rich zones



B. Cross-section A-A`

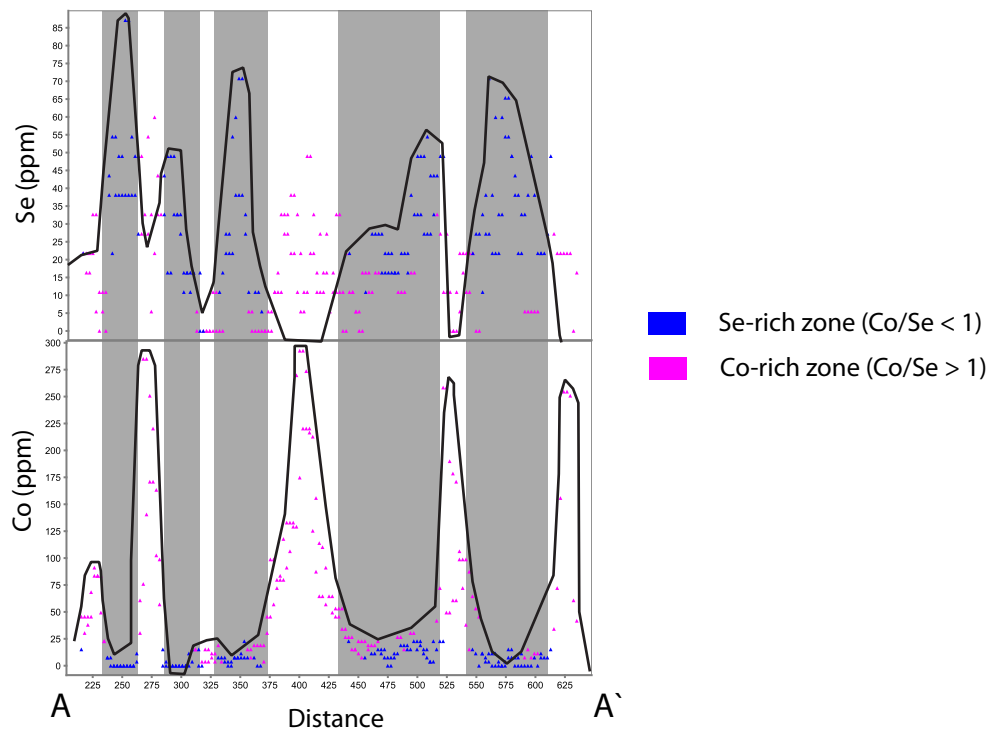


**Figure 6.21** Laser map image of fractured pyrite (Stage 1) with Co- and Se-rich zones (units in ppm). **A.** Laser map image of Stage 1 mineralisation show alternating Co and Se enrichment. Se-rich zones are enriched in Te and Cu. **B.** Cross section A-A` through a fractured pyrite illustrating the alternating bands of Co and Se enrichment that is amplified using a Co/Se ratio. Cross section location is shown in Figure A schematic. **Sample ID:** IXCM08-55 226.5 Image 002. **Abbreviations:** FrPy - fractured pyrite.

## Stage 1 Fractured Pyrite: Arsenic rich core

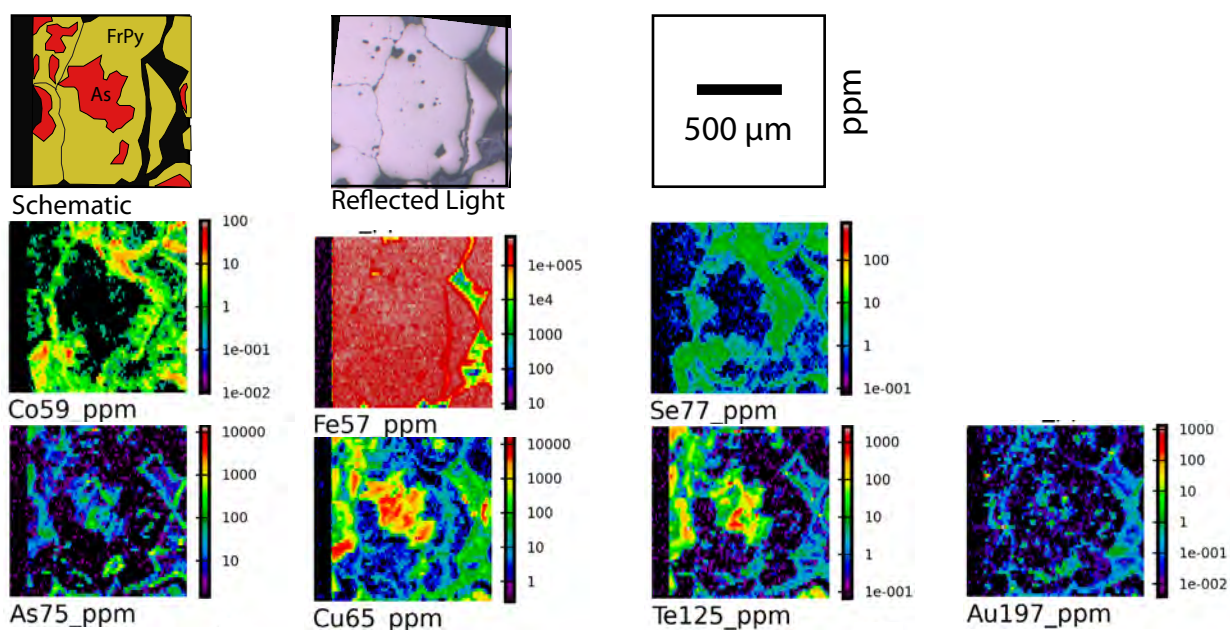


**Figure 6.22** Laser map image of fractured pyrite with an arsenic-rich core (units in ppm). **Sampled ID:** IXCM08-56 68.5B Image 001. **Abbreviations:** As - arsenic-rich zone, FrPy - fractured pyrite.

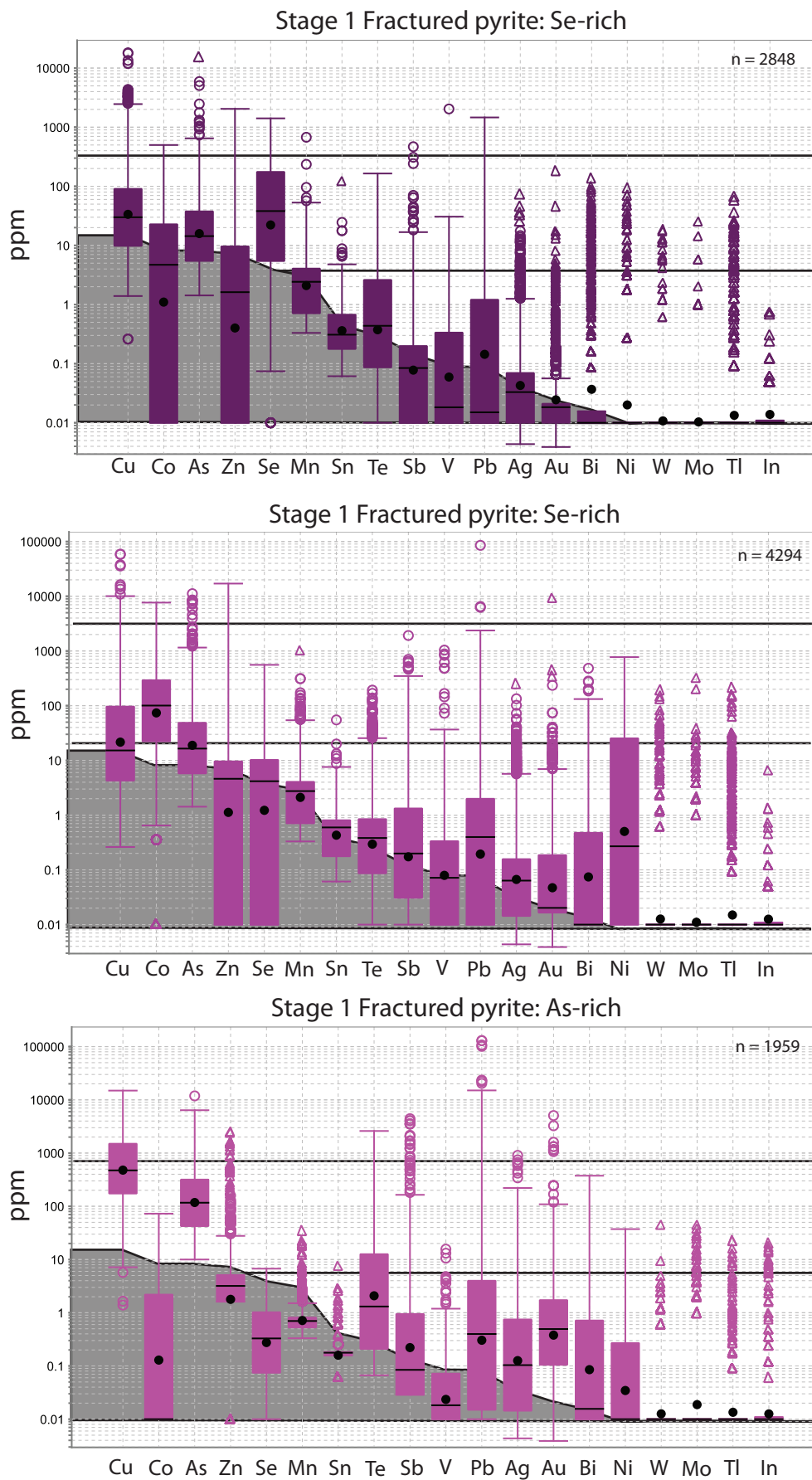


**Figure 6.23** Tukey box plot showing the trace element concentrations for fractured pyrite (Stage 1) mineralisation with Co-, Se- and As-rich zones. The grey zone outlines the median composition of the Cerro la Mina standard pyrite. Data compiled from laser map points.

## Stage 2 Inclusion-rich pyrite: Co- and Se-rich zones

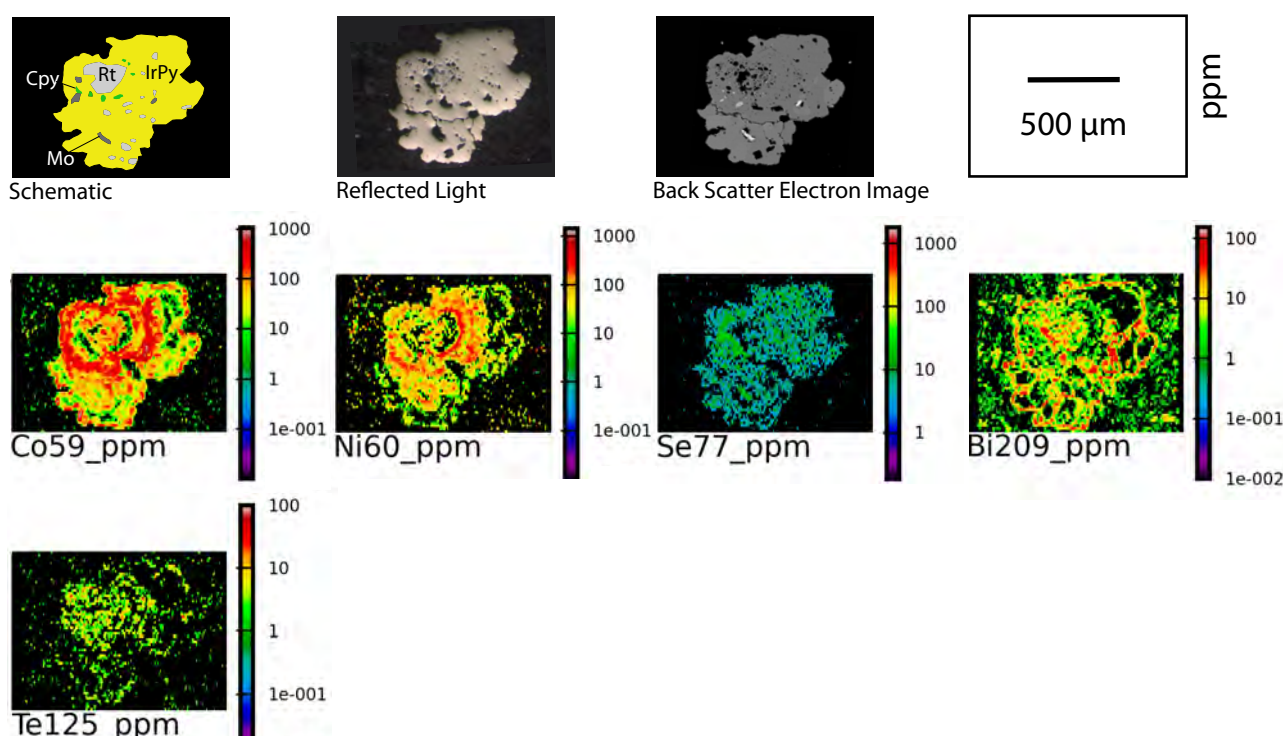


**Figure 6.24** Laser map image of inclusion-rich pyrite (Stage 2; units in ppm). Stage 2 pyrite has an enrichment in Co, Ni, Se, Bi and Te. Co and Se do show alternating bands of enrichment however it is not as pronounced as the fractured pyrite (Stage 1). **Sampled ID:** IXCM06-09 86.3 Image 005. **Abbreviations:** Cpy - chalcopyrite, IrPy - inclusion-rich pyrite, Mo - molybdenite, Rt - rutile.

## Stage 2 Inclusion-rich Pyrite: Arsenic-rich core

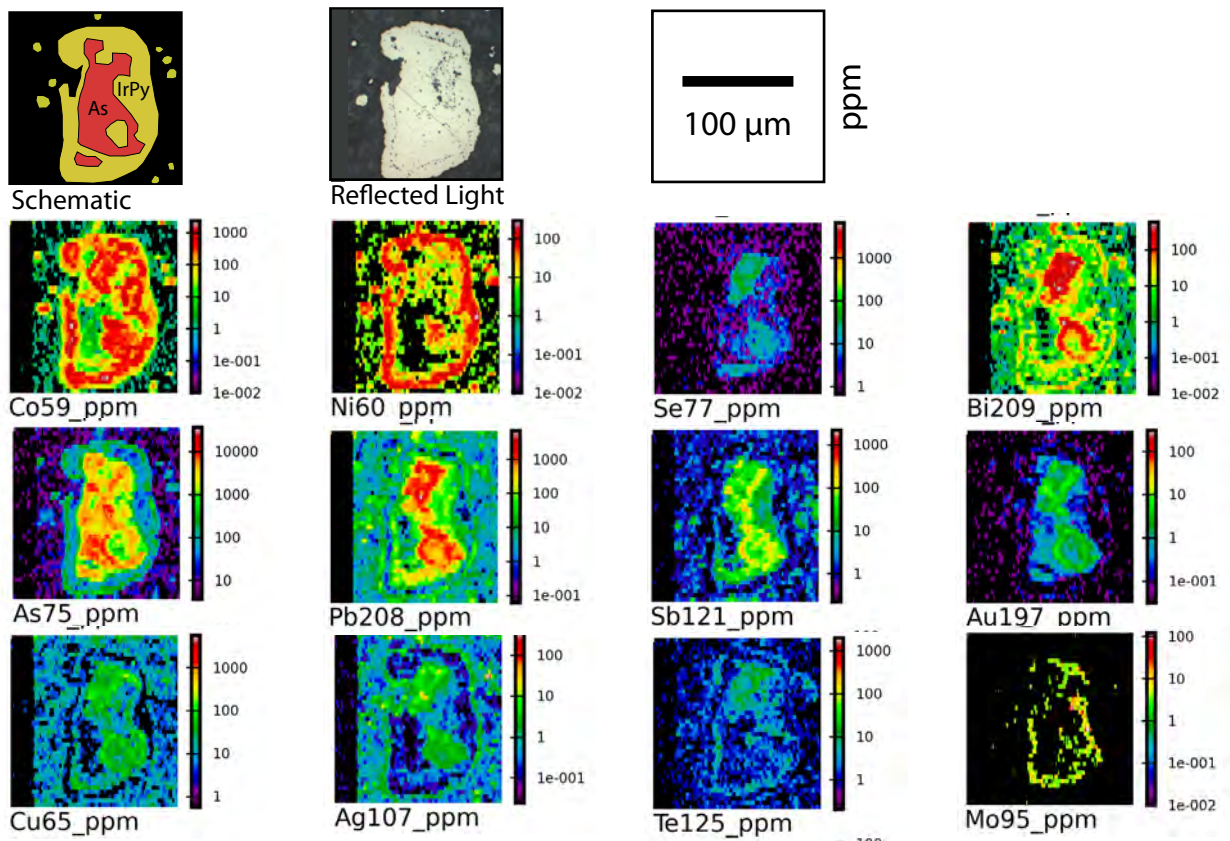


**Figure 6.25** Laser map image of inclusion-rich pyrite (Stage 2) with an arsenic-rich core (units in ppm). The arsenic-rich core is enriched in Bi, Pb, Sb, Au, Cu, Ag, and Te. A molybdenum enrichment band occurs at the junction of the arsenic core and inclusion-rich pyrite rim. **C.** Laser map image of chalcopyrite that has high counts of In and Se. **Sampled ID:** IXCM08-63 168.1 Image 001. **Abbreviations:** As- arsenic-rich zone, IrPy - inclusion-rich pyrite.

## Stage 2 Chalcopyrite

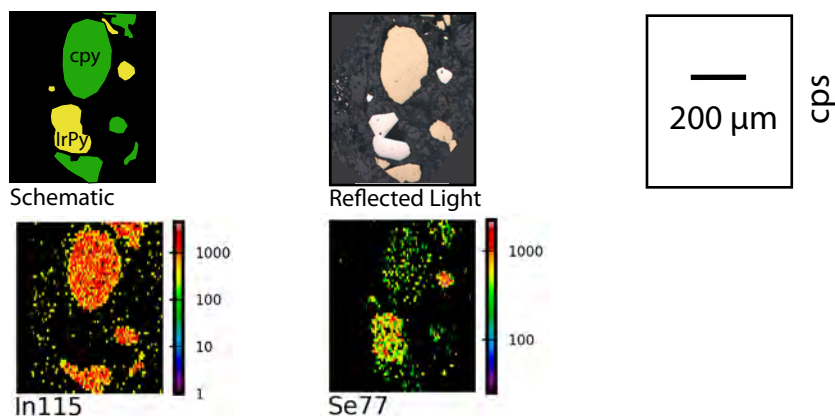


**Figure 6.26** Laser map image of chalcopyrite (Stage 2; units in cps). Chalcopyrite has high counts of In and Se. **Sampled ID:** IXCM07-20 324.5 Image 005. **Abbreviations:** Cpy - chalcopyrite, IrPy - inclusion-rich pyrite.

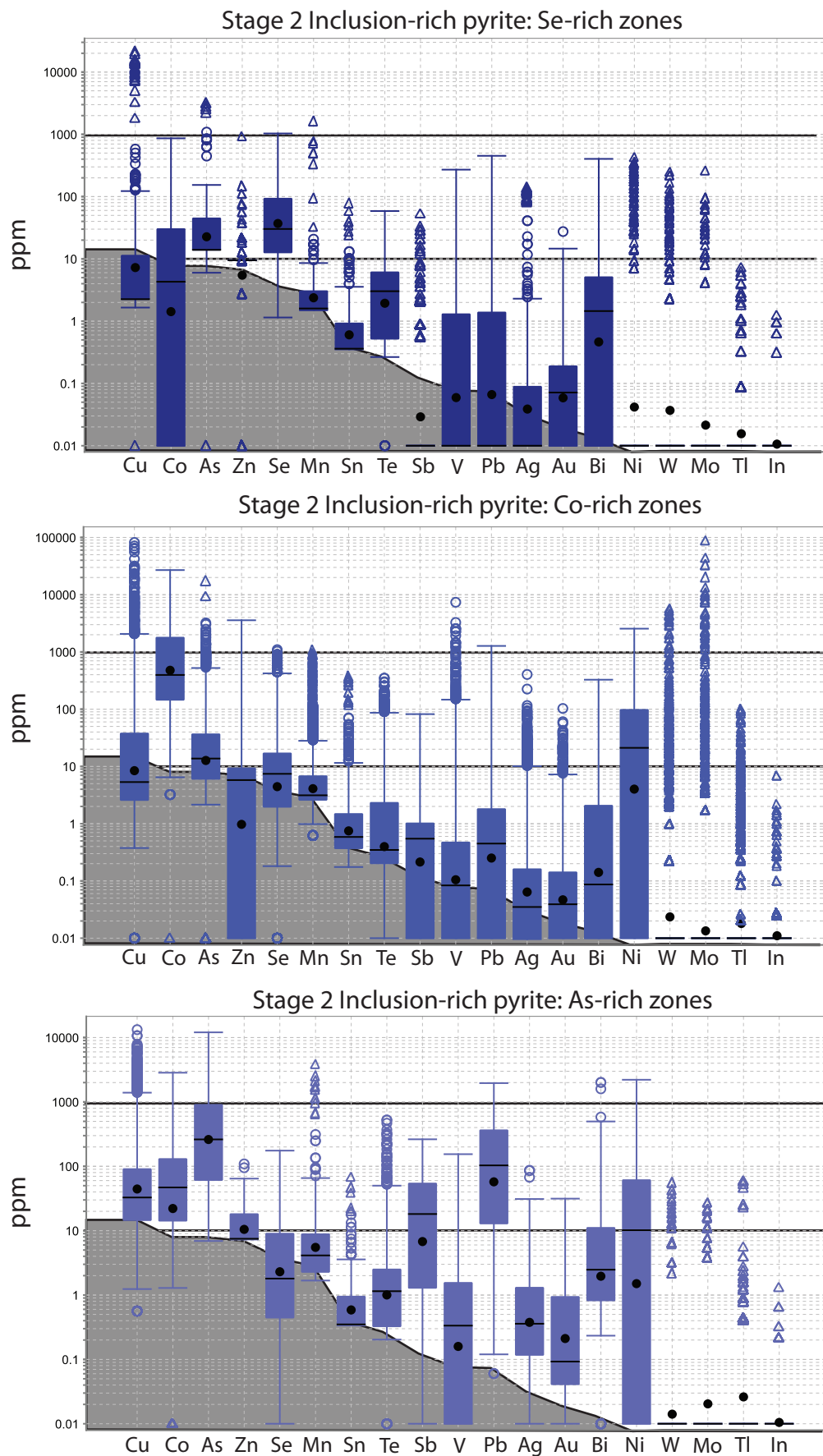


**Figure 6.27** Tukey box plot showing the trace element concentrations for inclusion-rich pyrite (Stage 2) with Co-, Se- and As-rich zones. The grey zone outlines the median composition of the Cerro la Mina standard pyrite. Data compiled from laser map points.

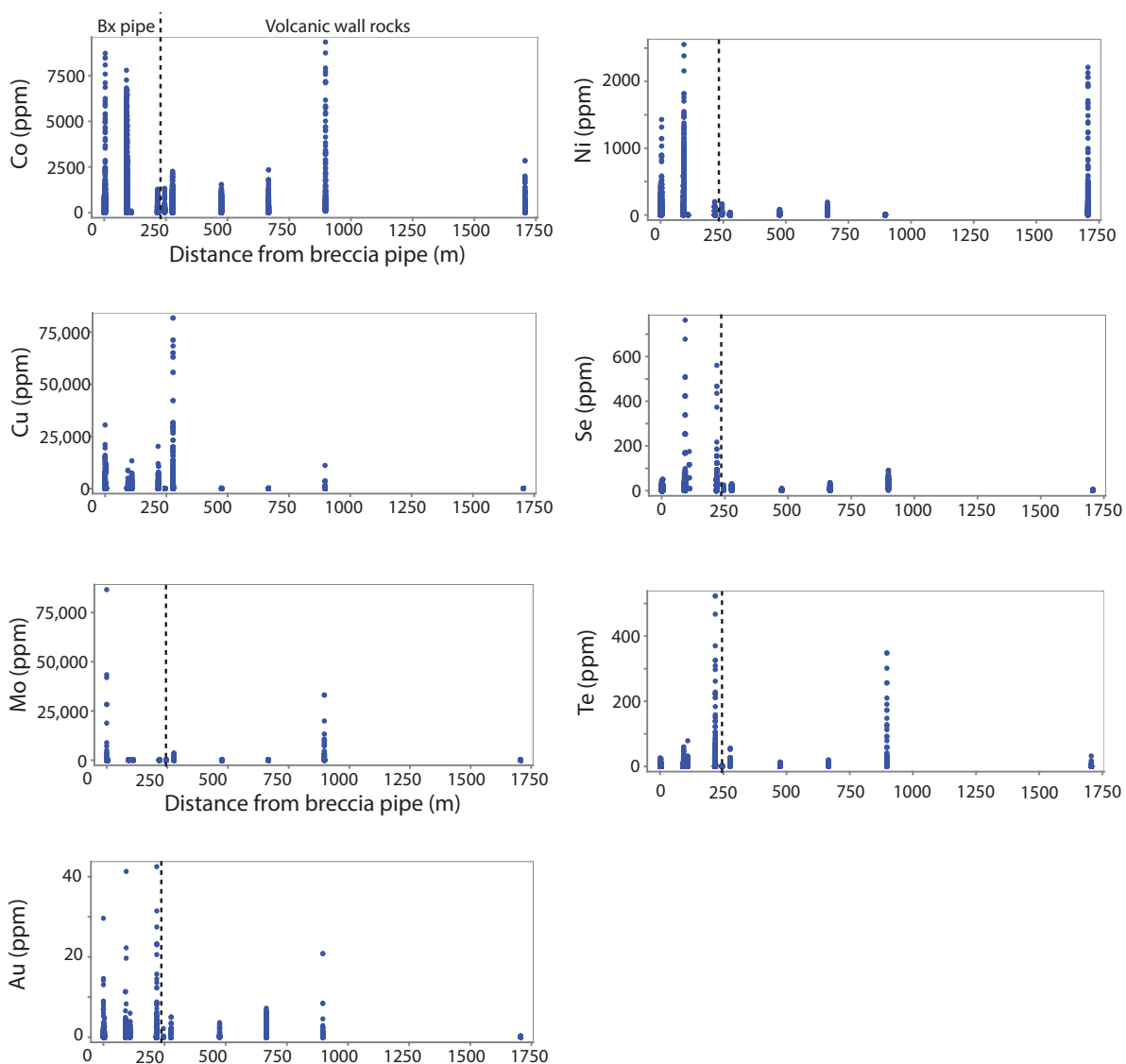


**Figure 6.28** Concentrations of Co, Ni, Cu, Se, Mo, Te, and Au in Stage 2 pyrite versus horizontal distance from breccia pipe.

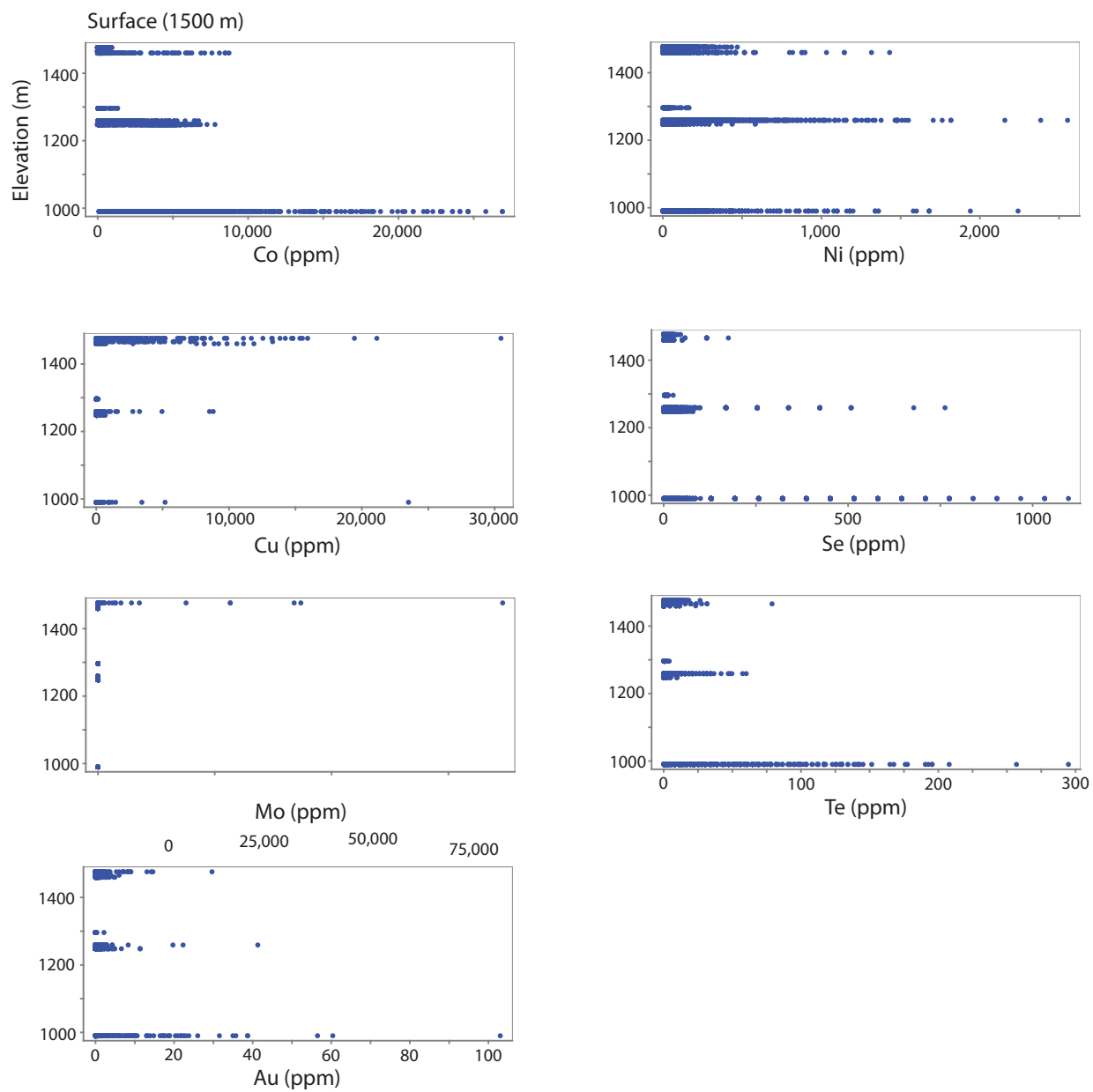


**Figure 6.29** Concentrations of Co, Ni, Cu, Se, Mo, Te, and Au in Stage 2 pyrite versus elevation in the breccia pipe.

### 6.8.3 Stage 3

Stage 3 marcasite is strongly enriched in Pb, Ag, Au and Tl, moderately enriched in As, Zn and Mn, and weakly enriched in Cu and Sb (Fig. 6.30 and 6.32). The fine-grained nature of the marcasite did not allow resolution of any zoning, however, one image contains a weak zonation with Mn, Zn, and Au enriched cores and Cu, Pb and Ag enriched on the rims (Fig. 6.30). One laser map for sphalerite does not show zoning and has high counts of Hg (> 1000 cps; Fig. 6.31).

### 6.8.4 Stage 4

Stage 4 ragged pyrite is strongly enriched in As, Pb, Ag, Bi and Tl, moderately enriched in Cu, Zn, Te, Sb and Au, and weakly enriched in In (Figs. 6.33 and 6.36). Stage 4 pyrite did not show zoning of trace elements.

The rimming pyrites (Stage 4) from the upper and lower arsenic-rich zones (Fig. 6.34 and 6.36) have slightly different geochemistry to the ragged pyrite. The upper arsenic-rich zone is strongly enriched in Bi, moderately enriched in Cu, Pb, Ag, Au, Tl and weakly enriched in As. The lower arsenic-rich zone is strongly enriched in As and Tl, moderately enriched in Mn, Sb, Pb, Ag, and Au, and weakly enriched in Cu, and Zn. The upper zone is characterized by less than 1 % arsenic and the lower zone contains 0.5 to 5% arsenic. In addition, the upper zone has higher concentrations of Bi and Cu than the lower zone and the lower zone has higher Sb, Tl, Zn and Au than the upper zone. Ni is enriched in the lower zone, however this is probably inherited from inclusion-rich pyrite (Stage 2), in which the rimming pyrite (Stage 2) occurs in all analyses. Spatially, the geochemistry of Stage 4 is complicated and does not contain clear trends in or around the deposit. Four laser maps of enargite in the upper zone are characterized by high counts of Sb, Bi, Pb, Ag, Zn, Tl, Te, Au and Se (Fig. 6.35; no zoning).

## 6.9 Discussion of Laser Map Imaging

At Cerro la Mina the high temperature porphyry-related pyrite has oscillatory zoning of Co-Ni-Se with minor arsenic-rich zones (Stages 1 and 2) and chalcopyrite (Stage 2) has high contents of Se. The Co, Ni and Se probably relate to higher temperatures as they are associated with high temperature alteration assemblages (i.e. Stage B sericitic alteration). They also increase in concentration towards the breccia pipe and with depth in the breccia pipe closer to the inferred source of fluids or heat source. A Co-Se-Te-Mo-(Cu-Au) pyrite anomaly occurs approximately 850 m from the breccia pipe and may indicate an exploration target for additional mineralisation.

The fractured pyrite (Stage 1) and inclusion-rich pyrite (Stage 2) are similar, with oscillatory zoning of Co and Se and local zones of As enrichment suggesting that they formed under similar conditions. The significance of the Co-Se oscillatory zoning is not fully understood; it could result from changing  $fO_2$  conditions. The minor arsenic-rich zones in Stages 1 and 2 are typically enriched in Te, Au and Cu and may represent conditions of a high sulfidation epithermal fluid.

## Stage 3 Marcasite

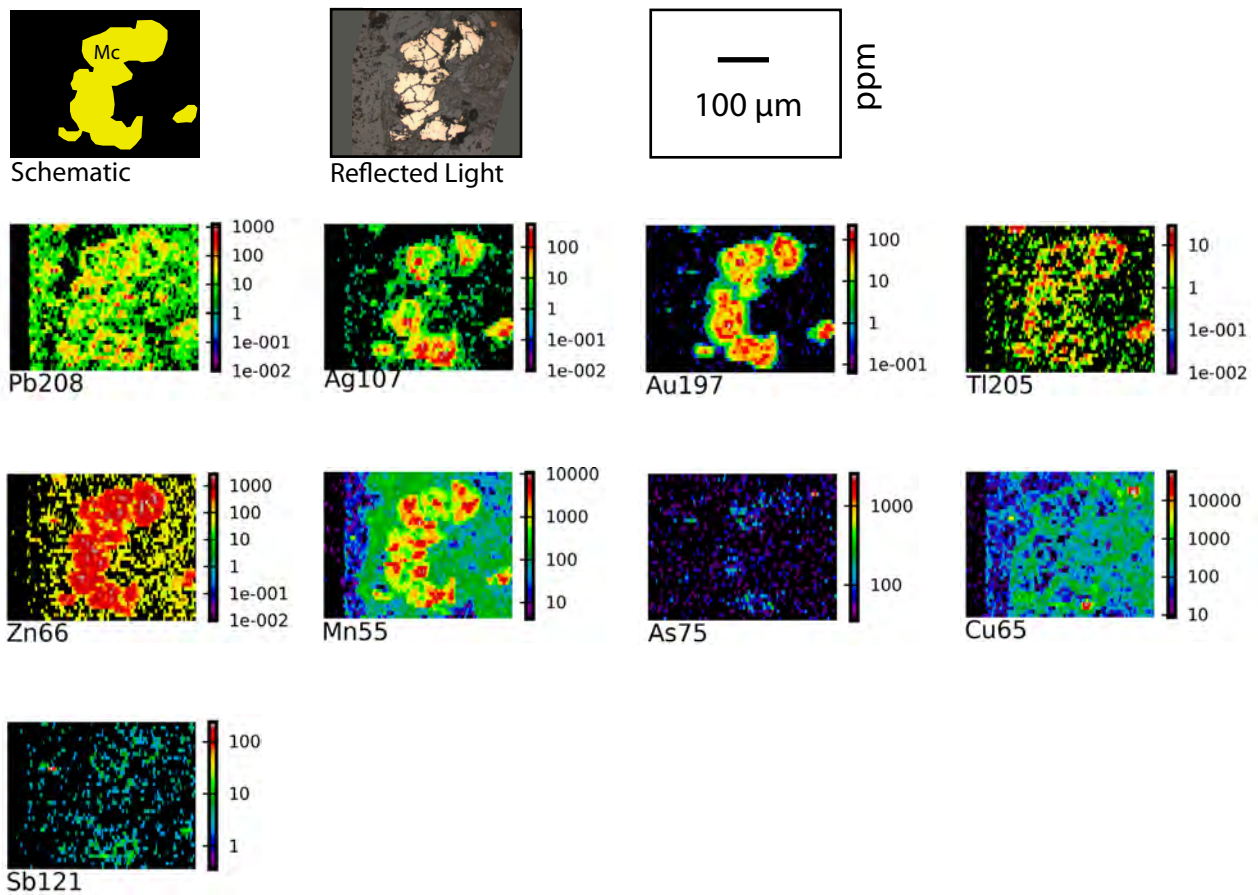


**Figure 6.30** Laser map image marcasite (Stage 3; units in ppm). Marcasite shows enrichment in Pb, Ag, Au, Tl, Zn, Mn, As, Cu and Sb. **Sampled ID:** IXCM07-20 324.5 Image 004. **Abbreviations:** Mc - marcasite.

## Stage 3 Sphalerite

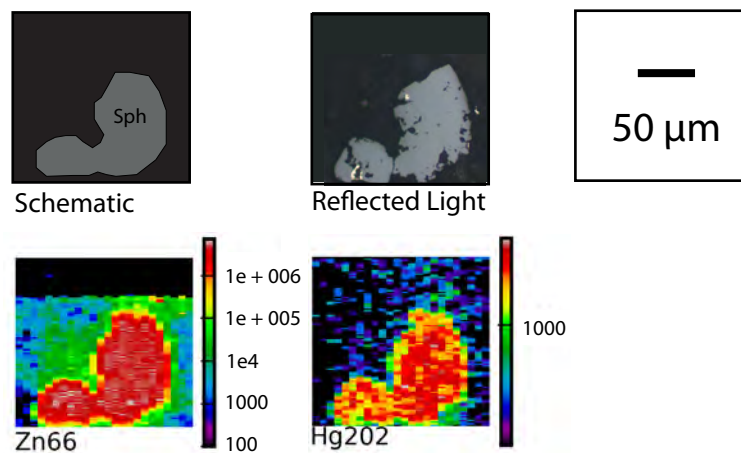


**Figure 6.31** Laser map image sphalerite (Stage 3; units in cps). Sphalerite is enriched in Hg. **Sampled ID:** IXCM06-09 100.7 Image 004. **Abbreviations:** Sph - Sphalerite.

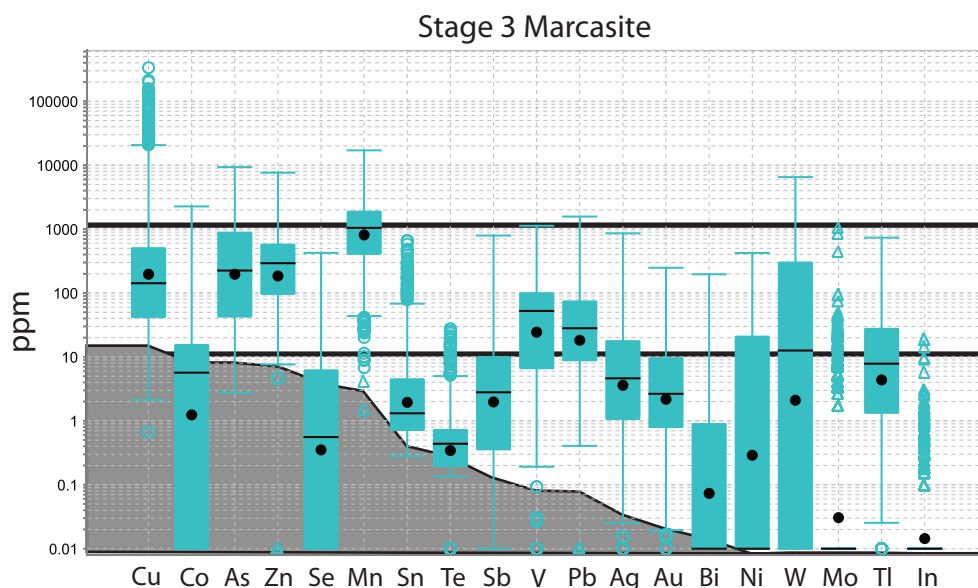


**Figure 6.32** Tukey box plot showing the trace element concentrations for Stage 3 marcasite. The grey zone outlines the median composition of the Cerro la Mina standard pyrite. Data compiled from laser map points.

### Stage 4 Ragged Pyrite

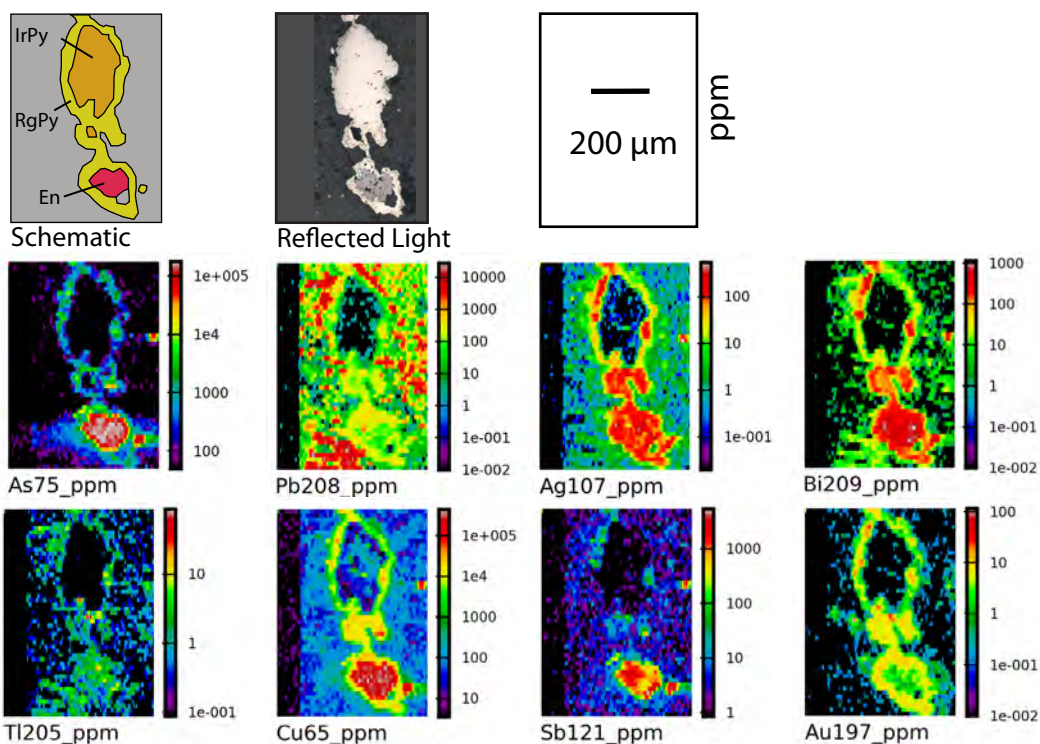


**Figure 6.33** Laser map image ragged pyrite (Stage 4; units in ppm). In this image ragged pyrite is rimming early inclusion-rich pyrite and enargite. The ragged pyrite is enriched in As, Pb, Ag, Bi, Tl, Cu, Sb and Au. **Sampled ID:** IXCM06-09 86.3 Image 006. **Abbreviations:** En - enargite, IrPy - inclusion-rich pyrite, RgPy - ragged pyrite.

## Stage 4 Rimming Pyrite

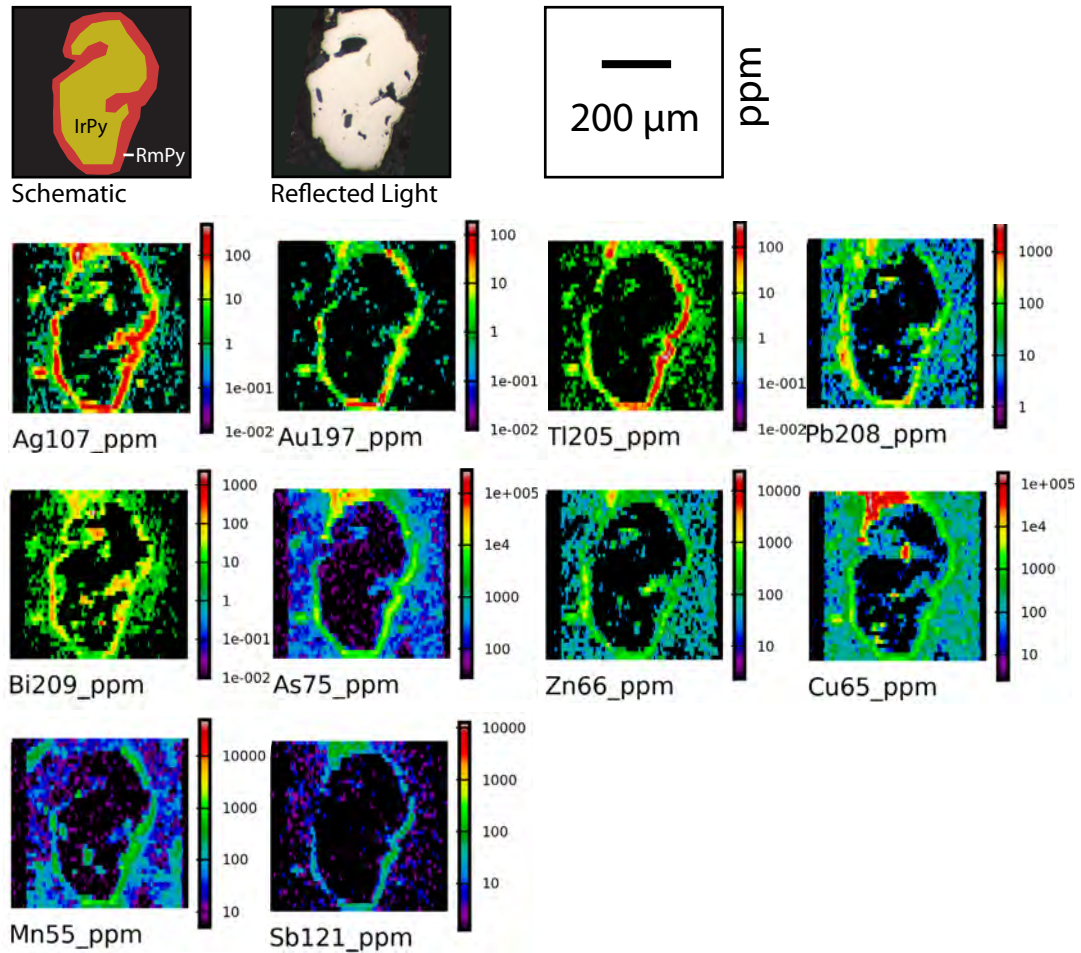


**Figure 6.34** Laser map image rimming pyrite (Stage 4; units in ppm). In this image rimming pyrite is rimming early inclusion-rich pyrite. The rimming pyrite is enriched in Ag, Au, Tl, Pb, Bi, As, Zn, Cu, Mn, and Sb. **Sampled ID:** IXCM08-51 544.2 Image 003. **Abbreviations:** IrPy - Inclusion-rich pyrite, RmPy - Rimming pyrite.

## Stage 4 Enargite

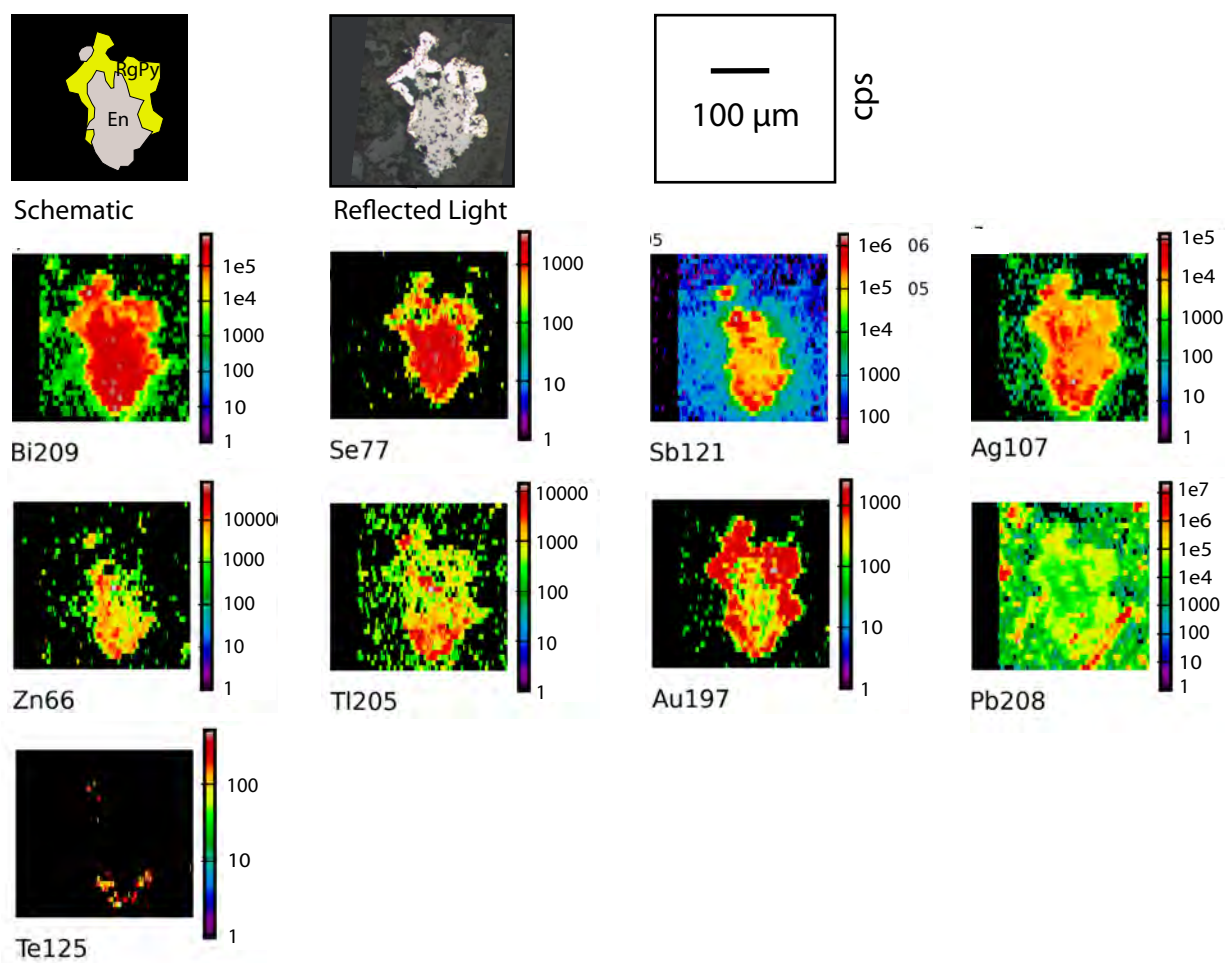


**Figure 6.35** Laser map image enargite (Stage 4; units in cps). Enargite shows high counts of Bi, Se, Sb, Ag, Zn, Tl, Au, Pb, and weak Te. **Sample ID:** IXCM06-09 86.3 Image 001. **Abbreviations:** En - enargite, RgPy - ragged pyrite.

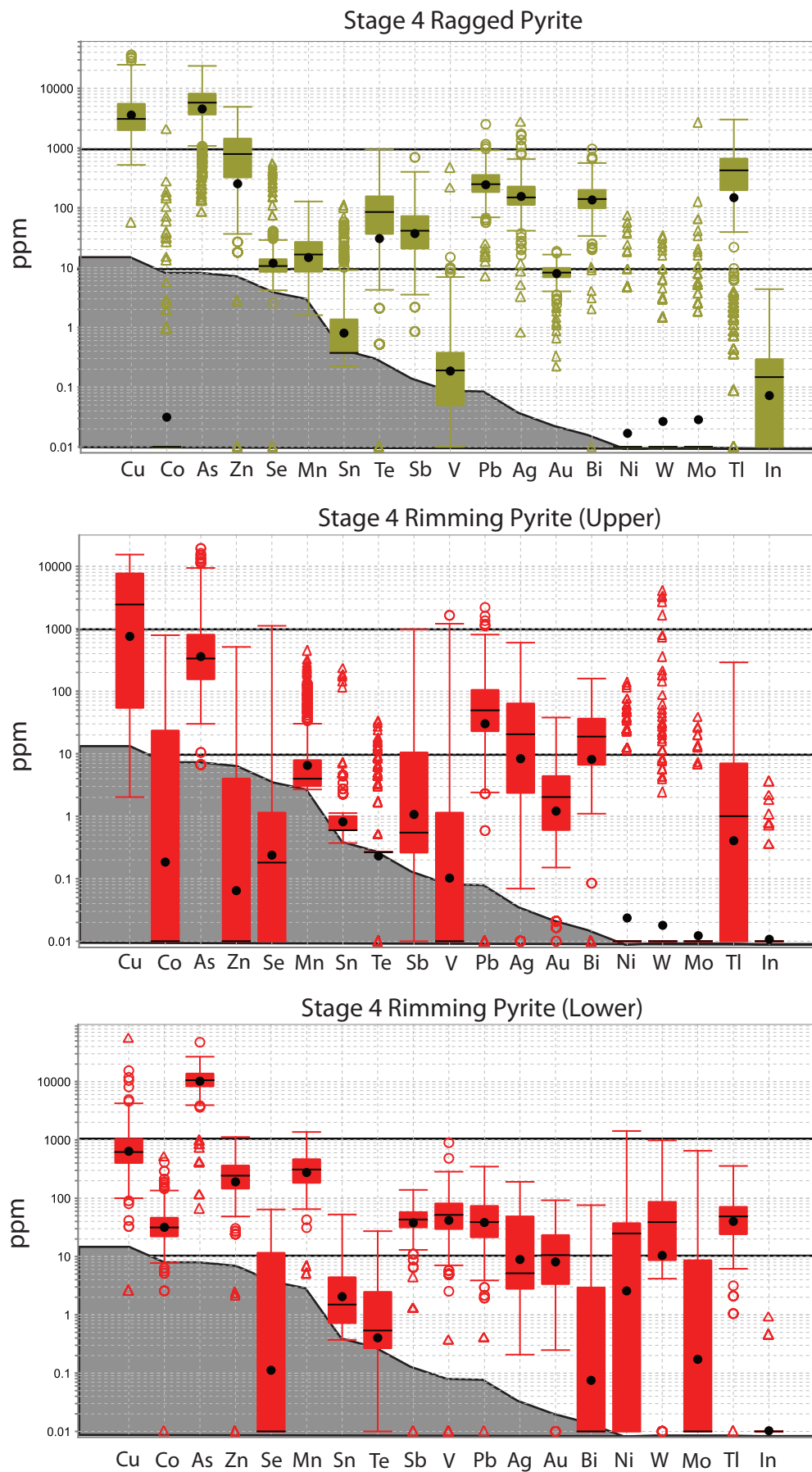


**Figure 6.36** Tukey box plot showing the trace element concentrations for Stage 4 ragged, and rimming pyrite of the upper and lower arsenic-rich zones. The grey zone outlines the median composition of the Cerro la Mina standard pyrite. Data compiled from laser map points.

The lower temperature epithermal style mineralisation (Stage 3 and 4) is arsenic-rich suggesting that lower temperature conditions were suitable for As deposition. Stage 3 and 4 also lack Co and Ni consistent with their association with low temperature kaolinite alteration (Stage C) contrary to Stage 1 and 2 with enriched Co-Ni associated with high temperature alteration assemblages (Stage B). The arsenic concentration increases through Stage 1 to Stage 4 associated with a decrease in temperature of alteration assemblages.

Stage 3 and Stage 4 pyrite and marcasite have similar geochemistry, being enriched in Cu, Au, Zn, Mn, Sb, Pb, Ag, Tl, Te and Bi, suggesting both deposited under similar conditions. Stage 4, however, has higher concentrations than Stage 3 of all these elements except for Mn which is higher in Stage 3. Stages 3 and 4 trace element geochemistry is enriched in trace elements like other high sulfidation deposits such as Hope Brook deposit, Newfoundland, which is enriched in Sb, Bi, Pb and As (Dube et al., 1998). Based on the textural evidence for co-precipitation of ragged pyrite (Stage 4) and enargite (Stage 4), the similar element enrichments suggest that these two minerals, under the prevailing conditions, had similar capacities to absorb trace elements.

The rimming pyrite (Stage 4) of the upper zone, which develops distal to the ragged pyrite and enargite (Stage 4) has lower concentrations of the trace elements previously described, consistent with a more distal location to the source fluids, and was probably deposited from a lower temperature fluid than the fluid that deposited the ragged pyrite + enargite (Stage 4); this is consistent with an association with a lower temperature halloysite (Stage C<sub>HR</sub>) and dickite (Stage C<sub>OD</sub>) alteration, respectively. The rimming pyrite (Stage 4) of the lower zone has composition similar to the ragged pyrite (Stage 4), suggesting its position is close to the source of fluids. Stage 4 introduced the most Cu and Au into the hydrothermal system.

### 6.9.1 As versus Au Plot

Reich et al. (2005) found that there is a solubility limit that can be used to predict the dominant chemical form of Au in arsenian-pyrite and the saturation state of Au in hydrothermal solutions that deposited the arsenian-pyrite. Au-As compositions of arsenian-pyrite configure a wedge shaped distribution in log (Au)-log (As) space where maximum solid-solution Au contents are limited by a slope with Au/As molar ratio of 0.02. In samples located below the limit, the dominant form of Au is solid solution (Au<sup>1+</sup>), whereas anomalous samples plotting above this limit contain significant amounts of Au in the form of native Au nanoparticles (Au<sup>0</sup>).

Pyrites from Stages 1, 2 and 4 at Cerro la Mina contain weak to strong arsenic concentrations which increase from Stage 1 to Stage 4 (Fig. 6.37). The arsenic-rich zones contain high concentrations of Au and Cu in all stages, as previously described. To illustrate whether the Au is in the pyrite lattice or as gold inclusions, an As versus Au plot was made for each pyrite, following the method of Reich et al. (2005; Figs. 6.38 and 6.39). The fractured pyrite (Stage 1) and inclusion-rich pyrite (Stage 2) contain similar distributions, mainly plotting in the gold in lattice zone and partly in gold in inclusions zone (Fig. 6.38 and 6.39). Stage 4 (ragged and rimming pyrite) plots mainly in the gold in pyrite

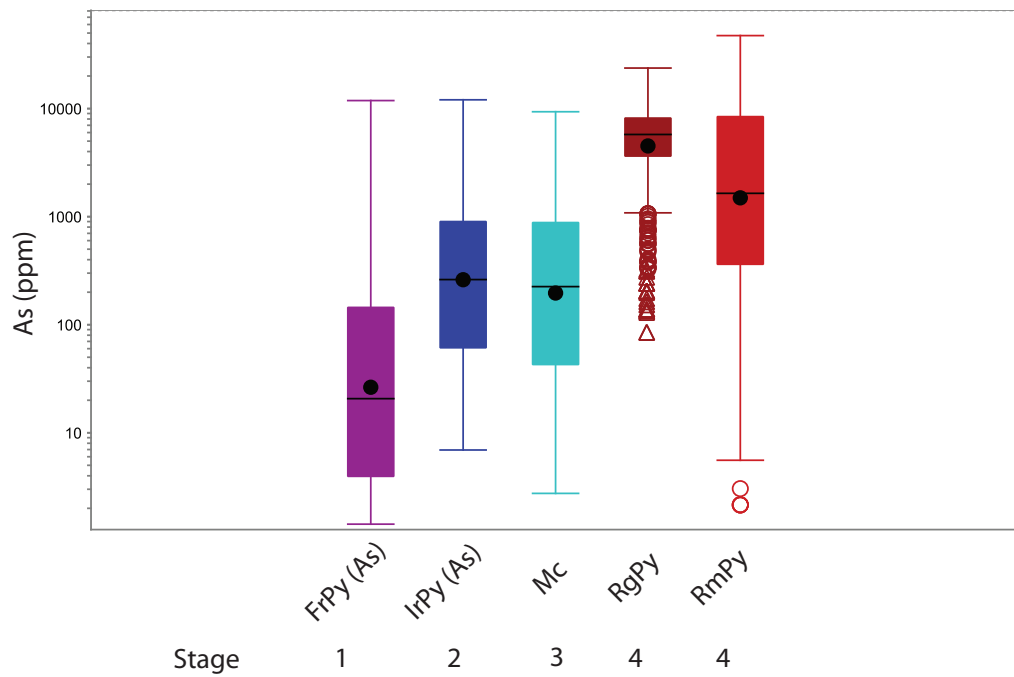


**Figure 6.37** Tukey box plot of the various stages illustrating an increase in As concentration with each stage of mineralisation. Data compiled from laser map points. **Abbreviations:** FrPy - fractured pyrite, IrPy - inclusion-rich pyrite, Mc - marcasite, RgPy - ragged pyrite, RmPy - rimming pyrite.

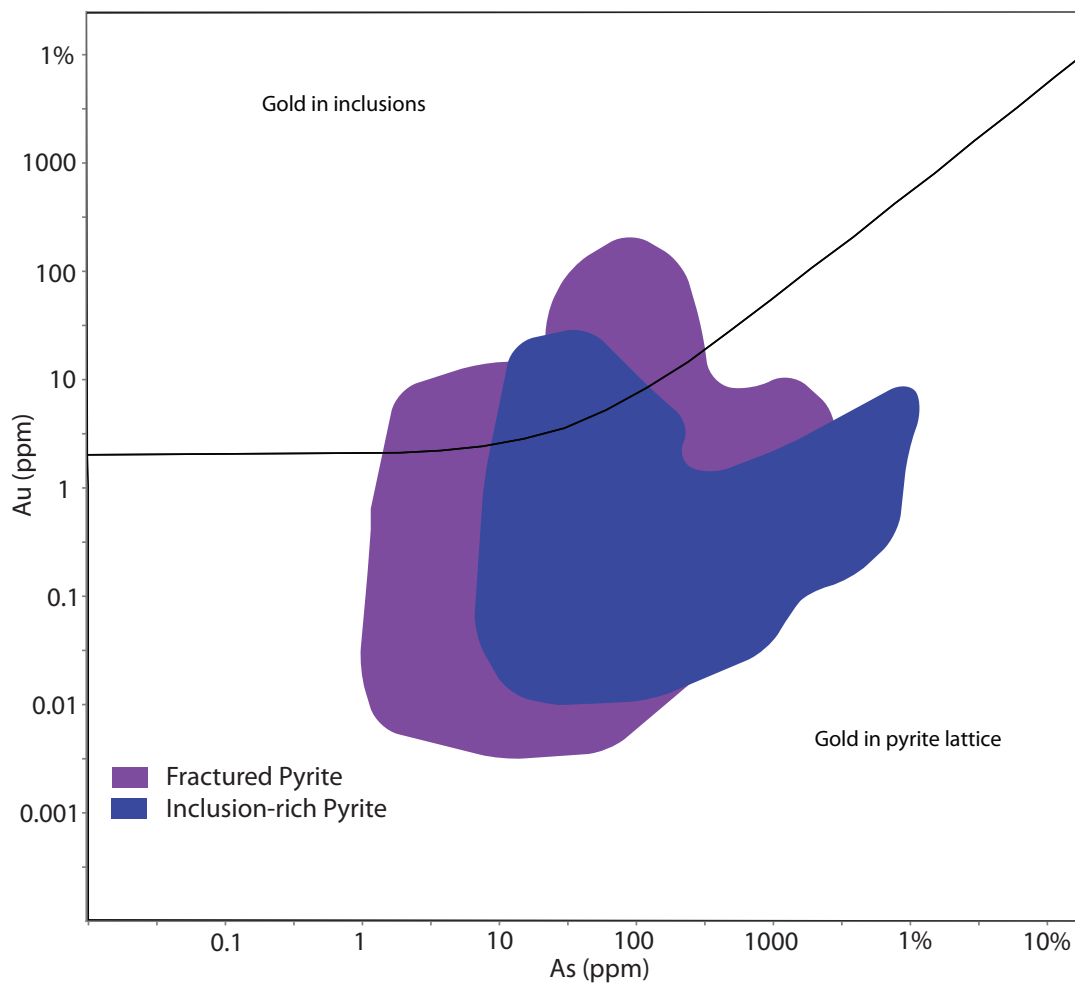


**Figure 6.38** As versus Au diagram showing the distribution of fractured (Stage 1) and inclusion-rich pyrite (Stage 2). Data compiled from laser map points. Modified from Reich et al. (2005).

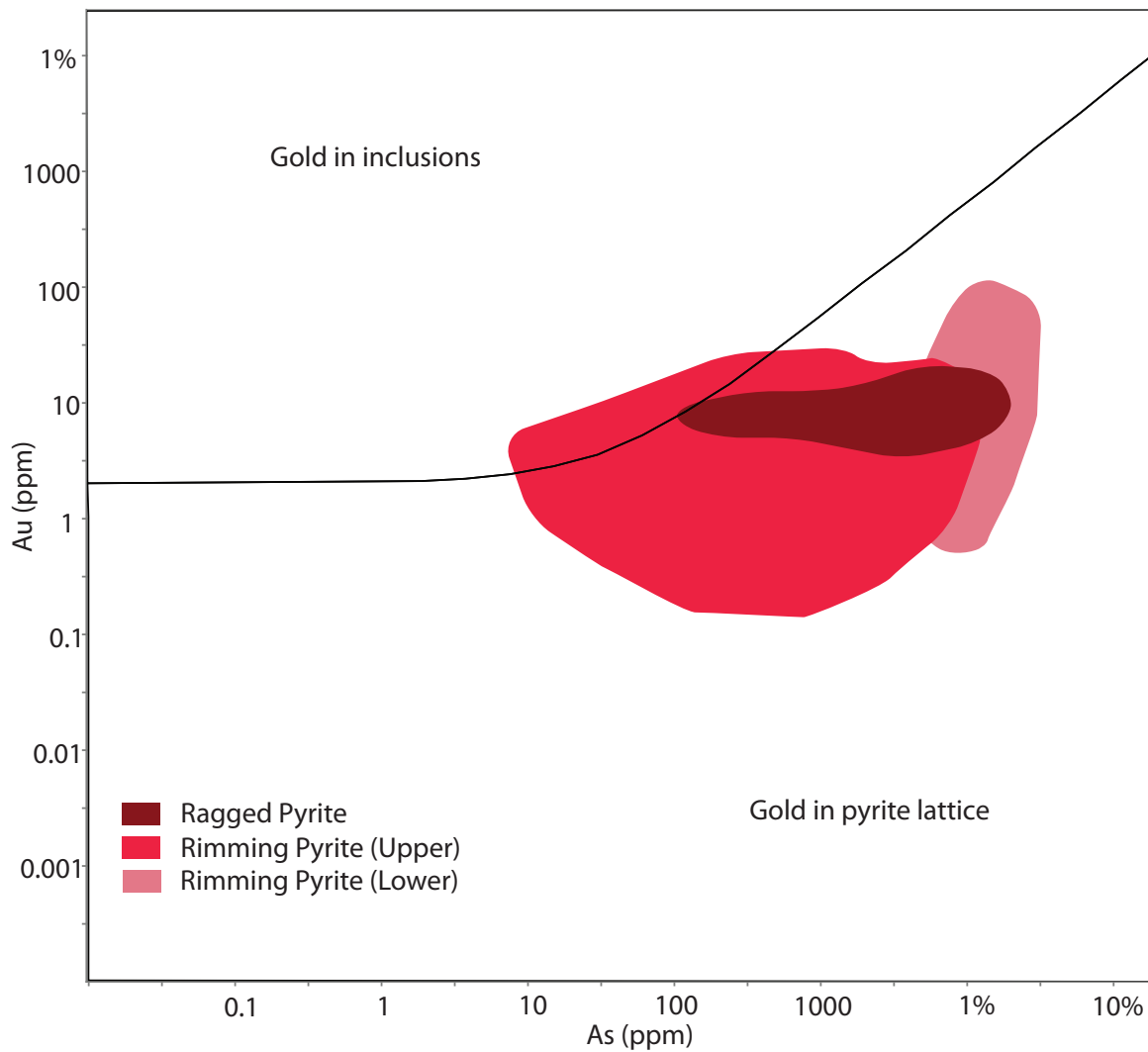


**Figure 6.39** As versus Au diagram showing the distribution of ragged pyrite (Stage 4) and rimming pyrite (Stage 4) from the upper and lower arsenic-rich zones. Data compiled from laser map points. Modified from Reich et al. (2005).

lattice zone with a portion of upper rimming pyrite occurring in the gold in inclusions zone (Fig. 6.39). Fractured pyrite (Stage 1) was the only sulfide observed to have visible gold as inclusions (Fig. 6.5B). The observations are consistent with the parent hydrothermal solutions at Cerro la Mina for Stage 1 to 3 containing solid solution of Au as well also minor amounts of native Au ( $\text{Au}^0$ ) whereas the parent hydrothermal solutions for Stage 4, where the solid solution Au is dominant in arsenian-pyrite, were largely unsaturated with respect to Au.

## 6.10 Conclusions

The Cerro la Mina Au (Cu-Mo) prospect is a high sulfidation epithermal system telescoped onto a porphyry copper system. The mineralisation is structurally and lithologically controlled, with the breccia pipe (Unit 4) hosting significantly higher levels of Au, Cu and Mo compared to the surrounding volcanic wall rocks. Higher grades also occur in structures probably related to the northwest fault.

The quartz-dickite altered rocks, specifically dickite-cemented breccias, host the highest average grades of 0.7 ppm Au and 0.23% Cu.

Four stages of mineralisation were identified at Cerro la Mina comprising Stages 1 and 2 with porphyry affinities and Stages 3 and 4 with epithermal affinities. Stage 1 pyrite infill potassic veins and which are together fractured to a jigsaw-fit texture, consistent with their pre-brecciation timing. Post-brecciation Stage 2 is associated with sericitic alteration (Stage B) comprising inclusion-rich pyrite ± chalcopyrite ± molybdenite veins and disseminations that are most abundant in the quartz-muscovite ± illite core of the sericitic alteration (Stage B). The inclusion-rich pyrite is the dominant sulfur species distally. The Cu and Mo grade shells have a vertical orientation coincident with the shape of the breccia pipe. Stage 3 comprises marcasite + sphalerite + galena + barite, and Stage 4 comprises ragged pyrite + enargite + rimming pyrite + fine-grained pyrite. Stage 3 and 4 are both associated with kandite alteration (Stage C) and occur in breccia cement, veins and disseminations.

Laser mapping indicates that Stage 1 and 2 pyrites have oscillatory zoning of Co, Ni and Se with local arsenic-rich zones and are associated with high temperatures related to the porphyry system. The occurrence of high Co, Ni and Se concentrations in pyrite associated with sericitic alteration (Stage B) and their concentrations increasing towards the breccia pipe, and with depth in the breccia pipe, are consistent with a high temperature of formation. The concentrations of these elements in pyrite could be used to define vectors towards porphyry style mineralisation or heat centres. Stages 1 and 2 pyrites are not associated with significant Au-Cu mineralisation, however Stage 2 has significant Cu-Mo associated with chalcopyrite and molybdenite.

The arsenic concentration increases from early the high temperature and porphyry style Stage 1 to the low temperature and epithermal Stages 3 and 4. Stages 3 and 4 pyrites lack Co and Ni, consistent with their association with low temperature kandite alteration (Stage C). Stage 3 and Stage 4 pyrites have similar geochemistry, being enriched in As, Cu, Au, Zn, Mn, Sb, Pb, Ag, Tl, Te and Bi, typical of high sulfidation epithermal systems (Hedenquist et al., 1994). Enargite has a similar trace element enrichment pattern as pyrite in Stages 3 and 4 and it also has elevated Se. Stages 3 and 4 are the most important contributors of Au and Cu to the system.

Halloysite is associated with Stages 3 and 4 Au-Cu mineralisation and the abundance of halloysite varies with the thickness of rimming pyrite (Stage 4). As a result, the KH index described in Chapter 5, could be used as an exploration vector. The abundance of kaolinite increases in towards Stage C<sub>QD</sub> alteration which hosts the most significant mineralisation drilled to date at Cerro la Mina. Banded veins of alternating halloysite + kaolinite and Stage 3 mineralisation occur at Cerro la Mina; a supergene origin for this vein type would require a complicated scenario of alternating supergene and hypogene conditions. All of the above evidence is consistent with a hypogene origin for halloysite.



# Chapter 7 – Geochronology

## 7.1 Introduction

A geochronology study was undertaken to constrain the age of volcanic rocks, alteration and mineralisation. Chapter 2 discuss the sparse K-Ar age dating completed on volcanic rocks which host mineralisation in the region of Cerro la Mina with ages ranging from 2.29 to 2.17 Ma (Fig. 2.6; Damon and Motesinos, 1978). The full significance of these ages is uncertain, as the K-Ar systematics could have been reset by porphyry-related potassic alteration evident in the region. Thus a reconnaissance zircon U/Pb laser ablation – inductively coupled plasma mass spectrometry (LA-ICP-MS) study was undertaken, using samples of pyroclastic and volcanoclastic rocks from outcrop and drill core. None of the units had been dated by previous studies. In addition, no age dating has been undertaken for the age of mineralisation or alteration in the district, an Ar-Ar and Re-Os study was undertaken.

The chapter starts by describing the research methods for the three dating techniques (U-Pb, Ar-Ar and Re-Os). The methods are followed by a description of the results for each isotopic decay system. A discussion on the context and significance of each age is then discussed. The chapter ends with a conclusion of the main points.

## 7.2 Research Methods

### 7.2.1 U-Pb Geochronology

#### 7.2.1.1 Zircon Separation and Preparation

Approximately 100 g of a geochronology sample was crushed in a tungsten-carbide hydraulic press to gravel size (2 to 4 mm) and repeatedly sieved and crushed in a chrome-steel ring mill to a grain size of <400  $\mu\text{m}$ . Samples that contained high concentrations of pyrite were put into an oven at 400°C for 15 minutes to oxidize the surface of the pyrite so that they could then be removed with a magnet. Non-magnetic heavy minerals were then separated using a gold pan. The zircons were randomly handpicked from the heavy mineral concentrate under the microscope in cross-polarised transmitted light. The selected zircons were mounted in epoxy blocks, polished and washed in distilled water in an ultrasonic bath. Transmitted and reflected light optical microscopy and SEM cathodoluminescence were used to identify crystal zoning and avoid crystals with prominent flaws and/or inclusions.

#### 7.2.1.2 LA- ICP-MS Method

The LA-ICP-MS method is widely used for measuring U, Th and Pb isotopic data (e.g., Fryer et al., 1993; Compston, 1999; Black et al., 2004; Jackson et al., 2004; Chang et al., 2006; Harley and Kelly, 2007). U-Th-Pb isotopic compositions of zircons were measured using an Agilent 7500cs quadrupole ICP-MS with a 193 nm Coherent Ar-F gas laser and the Resonetics M50 ablation cell at the Centre of Excellence in Ore Deposits, University of Tasmania. Each analysis on the zircons began with a 30 second blank gas measurement followed by a further 30 seconds of analysis time when the laser was switched on. Zircons were sampled on 32-35  $\mu\text{m}$  spots using the laser at 5 Hz and a density of

approximately 2 J/cm<sup>2</sup>. A flow of He carrier gas at a rate of 0.6 L/minute carried particles ablated by the laser out of the chamber to be mixed with Ar gas and carried to the plasma torch. Isotopes measured included <sup>49</sup>Ti, <sup>96</sup>Zr, <sup>202</sup>Hg, <sup>204</sup>Pb, <sup>206</sup>Pb, <sup>207</sup>Pb, <sup>208</sup>Pb, <sup>232</sup>Th and <sup>238</sup>U with each element being measured sequentially every 0.16 seconds with longer counting times for the Pb isotopes compared to the other elements.

The ICP-MS was operated in time-resolved mode, collecting one point per mass per sweep of the mass range with a dwell time of 5-20 milliseconds/mass. Spots to be analysed were cleaned with four single laser pulses at 1 Hz before the commencement of mass detection. After cleaning, background count rates on each mass were taken for 30 second before each ablation. Each analysis was followed by a 20 second washout period during which the signal intensities returned to background levels.

### 7.2.1.3 Data Collection and Reduction

The down hole fractionation, instrument drift and mass bias correction factors for Pb/U ratios on zircons were calculated using two analyses on the primary (91500 standard of Wiendenbeck et al. (1995)) and one analysis on each of the secondary standard zircons (Temora standard of Black et al. (2003) and GJ1 of Jackson et al. (2004)) analysed at the beginning of the session and every 12 unknown zircons (roughly every 1/2 hour) using the same spot size and conditions as used on the samples. Additional secondary standards, the Mud Tank Zircon of Black and Gulson (1978) and 15090 of Braxton (2007) were also analysed. The correction factor for the <sup>207</sup>Pb/<sup>206</sup>Pb ratio was calculated using three large spot of NIST610 analysed at the beginning and end of the day and corrected using the values recommended by Baker et al. (2004).

The data was reduced based on the method outlined in detail in Meffre et al. (2008) and similar to that described by Black et al. (2004) and Paton et al. (2010). The common lead component in the zircons was determined using the model of Stacey and Kramers (1975) at the age of the rock or individual zircons for older sedimentary zircons. Element abundances on zircons were calculated using the method outlined by Kosler (2001) using Zr as the internal standard element, assuming stoichiometric proportions and using the 91500 to standard correct for mass bias.

Given the young age of the zircons analysed, the <sup>230</sup>Th disequilibrium was considered as this disequilibrium induces a deficit in <sup>206</sup>Pb for zircons showing Th/U ratio <1 (Schärer, 1984). Considering that zircon usually shows  $f < 1$  ( $f = (\text{Th}/\text{U})_{\text{mineral}} / (\text{Th}/\text{U})_{\text{magma}}$ ), the extent of the effect of <sup>230</sup>Th disequilibrium on the corrected ages is a function of two factors: the lower the  $f$  factor and the younger the grain, the higher the age correction (in relative notation; Schärer, 1984; Cocherie et al., 2009). The raw data was corrected using the methods outlined in Schärer (1984):

$$^{206}\text{Pb}^* = ^{238}\text{U}\{(\text{EXP}(\lambda_{238}T) - 1) + (\lambda_{238}/\lambda_{230}) * (f - 1)\}$$

Where  $\lambda_{238} = 1.55125 \times 10^{-5} \text{ an}^{-1}$ ,  $\lambda_{230} = 9.22 \text{ an}^{-1}$  and <sup>206</sup>Pb\* is the radiogenic <sup>206</sup>Pb (Schärer, 1984). A Th/U<sub>magma</sub> value of 3.471 was used for sample NJ08IX-198, as Th and U whole rock geochemical data is available. A value of 3.192 was used for the other samples and is the average Th/U ratio for the

unaltered Selva Negra volcanic rocks (Chapter 3). Zircon analyses are listed in Appendix V.1.

### 7.2.2 $^{40}\text{Ar}/^{39}\text{Ar}$ Methods

The sample was lightly crushed, sieved with 600 $\mu\text{m}$  mesh, put into an ultra sonic bath to disperse the grains and placed in a graduated cylinder with water. The mixture was stirred vigorously to suspend the less dense impurities which were syphoned off. The remaining dense biotite-rich material was dried in an oven at 60°C overnight. The biotite was further separated using a magnet covered with wax paper and sieved with 500, 125 and 63  $\mu\text{m}$  sieves and acetone. Pure hydrothermal biotite > 125 $\mu\text{m}$  was then handpicked under a microscope.

The samples were then sent to the Western Australian Argon Isotope Facility in Perth, Australia. A second separation was done by separating unaltered, optically transparent and 125 to 500  $\mu\text{m}$  size, hydrothermal biotite. These minerals were separated using a Frantz magnetic separator and then carefully hand-picked under a binocular microscope. The selected hydrothermal biotite minerals were further leached in diluted HF for one minute and then thoroughly rinsed with distilled water in an ultrasonic cleaner.

The sample was then loaded into a large well of one 1.9 cm diameter and 0.3 cm depth aluminium disc. The well was bracketed by small wells that included Fish Canyon sanidine (FCs) used as a neutron fluence monitor for which an age of  $28.305 \pm 0.036$  Ma ( $1\sigma$ ) was adopted (Renne et al., 2010) based on the calibration by Jourdan and Renne (2007). The discs were Cd-shielded (to minimize undesirable nuclear interference reactions) and irradiated for 2 hours in the Hamilton McMaster University nuclear reactor (Canada) in position 5C. The mean J-value computed from standard grains in the small pits range from  $0.00079300 \pm 0.00000397$  determined as the average and standard deviation of the J-values of the small wells for the irradiation disc. Mass discrimination was monitored using an automated air pipette and provided a mean value of  $1.006544 \pm 0.003221$  per dalton (atomic mass unit) relative to an air ratio of  $298.56 \pm 0.31$  (Lee et al., 2006). The correction factors for interfering isotopes were  $(^{39}\text{Ar}/^{37}\text{Ar})_{\text{Ca}} = 7.40 \times 10^{-4}$  ( $\pm 11\%$ ),  $(^{36}\text{Ar}/^{37}\text{Ar})_{\text{Ca}} = 2.82 \times 10^{-4}$  ( $\pm 1\%$ ) and  $(^{40}\text{Ar}/^{39}\text{Ar})_{\text{K}} = 6.76 \times 10^{-4}$  ( $\pm 32\%$ ).

The  $^{40}\text{Ar}/^{39}\text{Ar}$  analyses were performed at the Western Australian Argon Isotope Facility at Curtin University, operated by a consortium consisting of Curtin University and the University of Western Australia. The sample was step-heated in a double vacuum high frequency Pond Engineering© furnace. The gas was purified in a stainless steel extraction line using two AP10 and one GP50 SAES getters and a liquid nitrogen condensation trap. Ar isotopes were measured in static mode using a MAP 215-50 mass spectrometer (resolution of  $\sim 400$ ; sensitivity of  $4 \times 10^{-14}$  mol/V) with a Balzers SEV 217 electron multiplier mostly using 9 to 10 cycles of peak-hopping.

The data acquisition was performed with the Argus program written by M.O. McWilliams and ran under a LabView environment. The raw data were processed using the ArArCALC software (Koppers, 2002) and the ages have been calculated using the decay constants recommended by Renne et al. (2010). Blanks were monitored every 3 to 4 steps and typical  $^{40}\text{Ar}$  blanks range from 1 x

$10^{-16}$  to  $2 \times 10^{-16}$  mol. Ar isotopic data corrected for blank, mass discrimination and radioactive decay are given in Appendix V.2. Individual errors are given at the  $1\sigma$  level. The determination of plateau includes at least 70 percent of  $^{39}\text{Ar}$  and distributed over a minimum of three consecutive steps agreeing at 95 percent confidence level and satisfying a probability of fit (P) of at least 0.05. Plateau ages are given at the  $2\sigma$  level and are calculated using the mean of all the plateau steps, each weighted by the inverse variance of their individual analytical error. Mini-plateaus are defined similarly except that they include between 50 percent and 70 percent of  $^{39}\text{Ar}$ . Integrated ages ( $2\sigma$ ) are calculated using the total gas released for each Ar isotope. Inverse isochrons include the maximum number of steps with a probability of fit  $\geq 0.05$ . All sources of uncertainties are included in the calculation.

### 7.2.3 Re-Os Analysis

Molybdenite was obtained by metal-free crushing of the rock sample, followed by gravity and magnetic concentration methods, to obtain a pure mineral separate. Methods used for molybdenite analysis are described in detail by Selby and Creaser (2004) and Markey et al. (2007). The  $^{187}\text{Re}$  and  $^{187}\text{Os}$  concentrations in molybdenite were determined by isotope dilution mass spectrometry using Carius-tube, solvent extraction, anion chromatography and negative thermal ionization mass spectrometry techniques. For this work, a mixed double spike containing known amounts of isotopically enriched  $^{185}\text{Re}$ ,  $^{190}\text{Os}$  and  $^{188}\text{Os}$  analysis was used. Isotopic analysis was made using a ThermoScientific Triton mass spectrometer by Faraday collector. Total procedural blanks for Re and Os are less than  $<3$  pg and 2 pg, respectively. These procedural blanks are insignificant in comparison to the Re and Os concentrations in molybdenite. The Chinese molybdenite powder HLP-5 (Markey et al., 1998), which is used as an in-house “control sample” by AIRIE, Colorado State University, is also routinely analyzed at the University of Alberta. For this “control sample” over the period of analysis of the sample, we determined an average Re-Os date of  $221.5 \pm 0.3$  Ma ( $1\sigma$  uncertainty,  $n=4$ ). The Re-Os age date is identical to that reported by Markey et al. (1998) of  $221.0 \pm 1.0$  Ma.

## 7.3 Results

### 7.3.1 U/Pb Age Results

Six samples were dated, two trachyandesite fiamme breccias (Unit 1B<sub>c</sub>), two monzodiorites (Unit 2), one trachyandesite matrix-supported breccia (Unit 3C) and a matrix-rich, granule breccia (Unit 4) crosscut by a dickite-cemented hydrothermal breccia (Stage C). A total of 71 zircons were analysed from the six samples of which 40 were used for age calculation. None of the analyses were rejected but many older grains were analysed in volcanoclastic rocks which did not contribute to the final weighted averages of the youngest zircons. The study was hindered by the low concentration of zircons in the rocks. The number of zircons obtained in the separation process for samples ranged from 0 to 24 zircons. All zircons analysed had euhedral crystals with weak to moderate oscillatory zoning (Fig. 7.1). All cathodoluminescence and scanning electron images can be found in Appendix V.1.

LA-ICP-MS geochronology analytical results and grain population statistics are listed in Table 7.1. The zircon U-Pb data are presented in the Tera-Wasserburg diagrams (Fig. 7.2) and  $^{238}\text{Th}$

disequilibrium and  $^{207}\text{Pb}$  corrected  $^{206}\text{Pb}/^{238}\text{U}$  ages are presented in probability plots (Fig. 7.3). The analyses with abundant common Pb fit very closely with the model of Stacey and Kramers (1975). An uncertainty of one percent was placed on this common Pb  $^{207}\text{Pb}/^{206}\text{Pb}$  ratio to take into account small local variations. Propagation of this uncertainty was performed using Isoplot 3.0 of Ludwig (2003). The weighted averages, concordia diagrams and probability plots were calculated and plotted using Isoplot 3.0 (Ludwig, 2003). All of the weighted averages are reported with uncertainty at the  $2\sigma$  level. Individual grain and standard analyses are presented in Appendix V.1. All the samples had U concentrations well below the radiation dose required to cause metamictization and Pb loss for zircons aged less than 1 Ma (Murakami et al., 1991; Geisler et al., 2007) despite sample NJ08IX-198 having

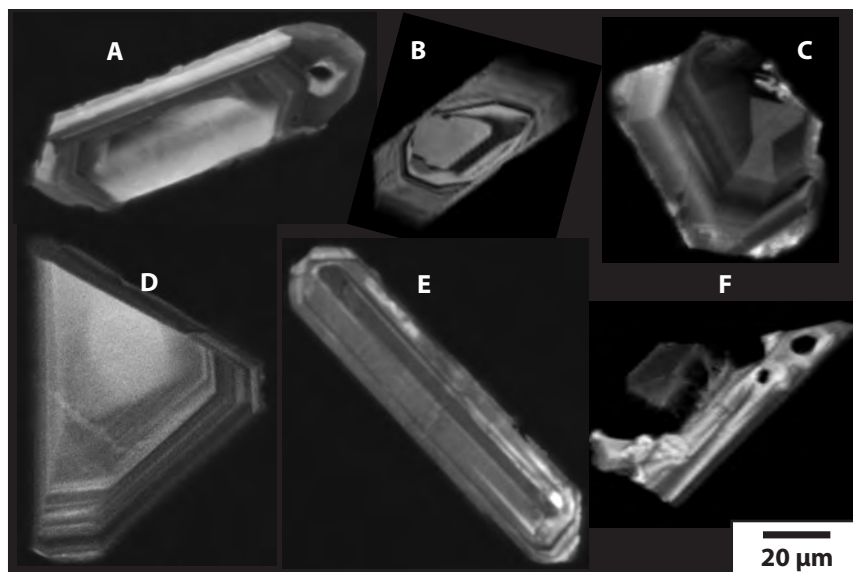


**Figure 7.1** Cathodoluminescence images of typical zircon grains with weak oscillatory zoning. **Sample ID:** A. IXCM07-23 221.0, B. IXCM07-23 327.0 C. IXCA08-18 95.0 D. NJ08IX-198 E. IXCM06-09 100.7 F. IXCM08-62 72.0.

concentrations as high as 1.2 percent. All standards analysed yielded their recommended age within uncertainty values (Table 7. 2). The  $^{238}\text{Th}$  disequilibrium correction caused a shift to older ages by 0.039 to 0.11 Ma.

### 7.3.1.1 *Trachyandesite Fiamme Breccia (Unit 1B<sub>s</sub>)*

Twenty-four zircons were analysed for sample IXCM07-23 221.0 of which 20 were discarded because they yielded old ages (8 to 1158 Ma). The remaining four zircons yielded an age of  $1.18 \pm 0.17$  Ma before the disequilibrium correction. The data spreads away from concordia toward common lead on the Tera-Wasseburg diagram (Fig. 7.2). Twelve zircons were analysed for sample IXCM07-23 327.0 of which 11 were discarded because they yielded old ages (23 to 1146 Ma). One zircon yielded an age of  $1.04 \pm 0.4$  Ma (Fig. 7.2). After  $^{238}\text{Th}$  disequilibrium correction the age increased to  $1.220 \pm 0.085$  Ma associated with a MSWD value of 1.11 and a P value of 0.34 for IXCM07-23 221.0 and an age of  $1.12 \pm 0.20$  Ma for IXCM07-23 327.0 (Fig. 7.3).

### 7.3.1.2 *Monzodiorite (Unit 2)*

Twelve zircons were analysed in sample NJ08IX-198 and yielded an age of  $1.01 \pm 0.04$  Ma. The data

| Description  | Sample ID       | n total | n inh. | n <sup>a</sup> | Mean <sup>206</sup> Pb/ <sup>238</sup> U Age corrected for <sup>230</sup> Th disequilibrium $\pm 2\sigma$ | MSWD | P     |
|--|-----------------|---------|--------|----------------|---|------|-------|
| Unit 1B <sub>s</sub> - Trachyandesite fiamme breccia | IXCM07-23 221.0 | 24      | 20     | 4              | 1.220 $\pm$ 0.085 Ma  | 1.11 | 0.34  |
| Unit 1B <sub>s</sub> - Trachyandesite fiamme breccia | IXCM07-23 327.0 | 12      | 11     | 1              | 1.12 $\pm$ 0.20 Ma  | n.a. | n.a.  |
| Unit 2 - Monzodiorite intrusion                      | NJ08IX-198      | 12      | 0      | 12             | 1.064 $\pm$ 0.043 Ma  | 1.9  | 0.037 |
| Unit 2 - Monzodiorite intrusion                      | IXCM08-18 95.0  | 9       | 0      | 9              | 1.035 $\pm$ 0.036 Ma  | 1.2  | 0.27  |
| Dickite cemented hydrothermal breccia                | IXCM06-09 100.7 | 11      | 0      | 11             | 0.746 $\pm$ 0.082 Ma  | 1.11 | 0.35  |
| Unit 3C - Trachyandesite matrix-supported breccia    | IXCM08-63 72.0  | 3       | 0      | 3              | 0.60 $\pm$ 0.39 Ma  | 0.56 | 0.57  |

**Table 7.1** Summary of new U-Pb geochronology for the Cerro la Mina prospect and Ixhuatán concession.

**Abbreviations:** <sup>a</sup> - Number of zircons used for age calculation, inh. = inherited. Instrumental parameters: 193 nm laser @ 5 Hz, 2 J/cm<sup>2</sup>, 32-35  $\mu$ m spot size, Agilent 7500cs quadrupole ICP-MS.

| Analyses | Standard | n  | Age $\pm 2\sigma$ | MSWD | P     | Recommended Age                                    |
|----------|----------|----|-------------------|------|-------|--|
| My21     | 91500    | 8  | 1068 $\pm$ 15     | 2.3  | 0.023 | 1062.4 $\pm$ 0.4 (TIMS), Wiedenbeck, et. al., 1995 |
| Dc14     | 91500    | 16 | 1063.3 $\pm$ 7.4  | 0.28 | 0.995 |  |
| Au24     | 91500    | 8  | 1062 $\pm$ 6.6    | 0.28 | 0.995 |  |
| My21     | Temora   | 12 | 414 $\pm$ 3       | 1.03 | 0.41  | 416.8 $\pm$ 1.1 (TIMS), Black et. al., 2003        |
| Dc14     | Temora   | 8  | 417 $\pm$ 4.6     | 0.55 | 0.79  |  |
| Au24     | Temora   | 6  | 416 $\pm$ 4.3     | 0.52 | 0.76  |  |
| Dc14     | GJ1      | 8  | 606.1 $\pm$ 5.2   | 0.66 | 0.71  | 600.4 $\pm$ 2.0 (TIMS), Jackson et. al., 2004      |
| Au24     | GJ1      | 6  | 606.9 $\pm$ 5.4   | 0.49 | 0.78  |  |
| My21     | Mud Tank | 6  | 736 $\pm$ 19      | 1.6  | 0.14  | 732 $\pm$ 5 (TIMS), Black and Gulson, 1978         |
| Au24     | Mud Tank | 4  | 710 $\pm$ 21      | 0.73 | 0.53  |  |
| My21     | 15090    | 6  | 2.13 $\pm$ 0.28   | 0.91 | 0.48  | 2.23 $\pm$ 0.05 (SHRIMP), Braxton, 2007            |

**Table 7.2** Summary of standards analysed during U-Pb age dating and their recommended ages.

clusters around concordia with a small amount of common lead detected in a few of the analyses (Fig. 7.2). Sample IXCA08-18 95.0 had nine zircons analysed and yielded an age of  $0.996 \pm 0.044$  Ma. In some analyses significant common Pb was detected (using the <sup>207</sup>Pb method) but most data points plotting close to concordia (Fig. 7.2). The <sup>238</sup>Th disequilibrium correction increased the age to  $1.064 \pm 0.043$  Ma associated with a MSWD value of 1.9 and a P value of 0.037 for NJ08IX-198 and to  $1.035 \pm 0.036$  Ma associated with a MSWD value of 1.2 and a P value of 0.27 for IXCA08-18 95.0 (Fig. 7.3).

### 7.3.1.3 Unit 4 with Dickite-Cemented Hydrothermal Breccia (Stage C<sub>QD</sub>)

Sample IXCM06-09 100.7 contained eleven zircons yielding an age of  $0.661 \pm 0.082$  Ma (Fig. 7.2). Most of the Pb in these analyses is common lead with a few analyses containing a small amount of radiogenic Pb and extend towards concordia on the Tera-Wasseburg diagram. The <sup>238</sup>Th disequilibrium correction increased the age to  $0.746 \pm 0.082$  Ma associated with a MSWD value of 1.11 and a P value of 0.35 (Fig. 7.3).

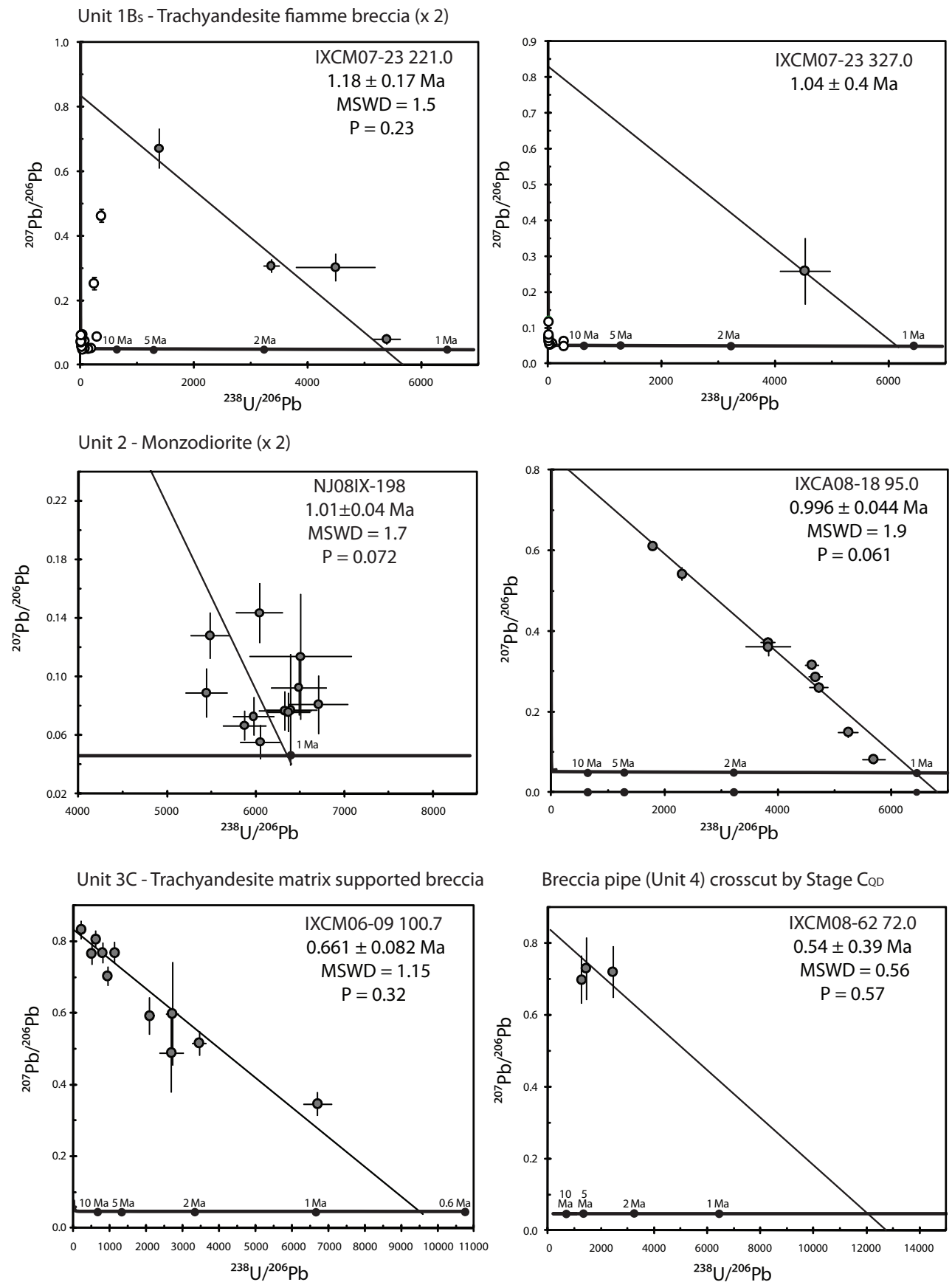


**Figure 7.2**  $^{207}\text{Pb}$  corrected  $^{206}\text{Pb}/^{238}\text{U}$  zircon ages plotted on Tera-Wasserburg concordia diagrams. Open points were excluded from weighted average calculations. Data point crosses are  $1\sigma$  and age errors are  $2\sigma$ .

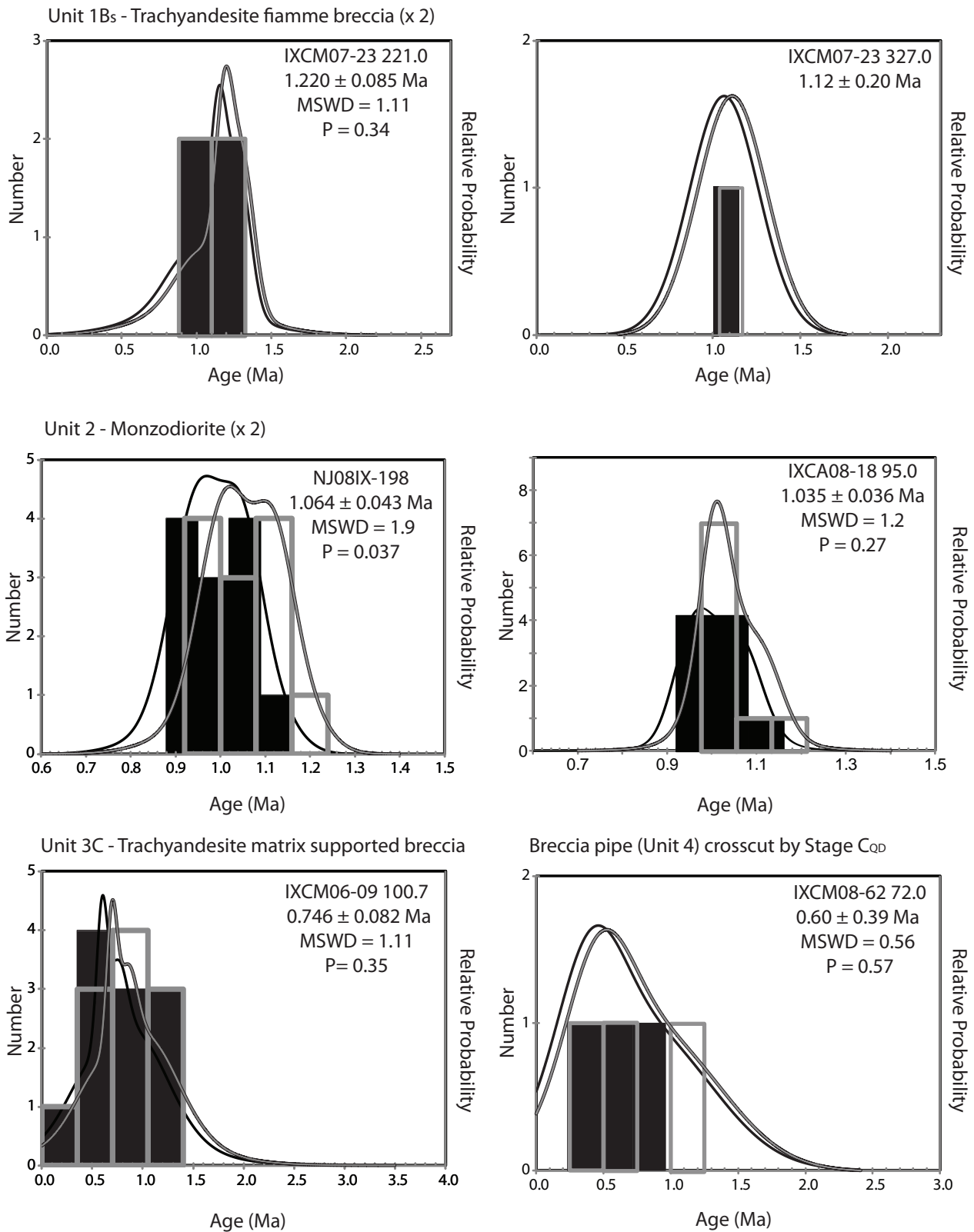


**Figure 7.3**  $^{207}\text{Pb}$  corrected  $^{206}\text{Pb}/^{238}\text{U}$  zircon ages corrected for  $^{230}\text{Th}$  disequilibrium. A slight shift to older ages occurs for all samples. Black is the probability density plot for  $^{207}\text{Pb}$  corrected  $^{206}\text{Pb}/^{238}\text{U}$  age and grey is the  $^{207}\text{Pb}$  corrected  $^{206}\text{Pb}/^{238}\text{U}$  age corrected for  $^{230}\text{Th}$  disequilibrium. Age errors are  $2\sigma$ .

### 7.3.1.4 Trachyandesite Matrix-Supported Breccia (Unit 3C)

Sample IXCM08-62 72.0 is a coarse-grained, matrix-rich, trachyandesite breccia. Nine zircons were analysed and yielded an age of  $0.996 \pm 0.044$  Ma. Many of the zircons contain significant common lead (Fig. 7.2). Only young fresh zircons were analysed from this rock type and therefore no old zircons were recorded for this rock type. The  $^{238}\text{Th}$  disequilibrium correction increased the age to  $0.60 \pm 0.39$  Ma associated with a MSWD value of 0.56 and a P value of 0.57 (Fig. 7.3).

### 7.3.2 $^{40}\text{Ar}/^{39}\text{Ar}$ Results

A sample from the Cerro la Mina prospect containing hydrothermal biotite in veinlets (Fig. 7.4) was analysed with  $^{40}\text{Ar}/^{39}\text{Ar}$  dating techniques to constrain the age of potassic hydrothermal alteration (Stage A).

The age spectrum yielded a plateau age of  $0.689 \pm 0.013$  Ma including 96 percent of the released  $^{39}\text{Ar}$  (Fig. 7.5). The age is associated with MSWD and P values of 0.86 and 0.60 respectively, showing that the steps are concordant within uncertainty. The plateau age conforms well to



**Figure 7.4** Image of sample with hydrothermal biotite veinlets in potassium feldspar altered rock in which biotite was extracted for  $^{40}\text{Ar}/^{39}\text{Ar}$  analysis. **Sample ID:** IXCM07-25 589.3.

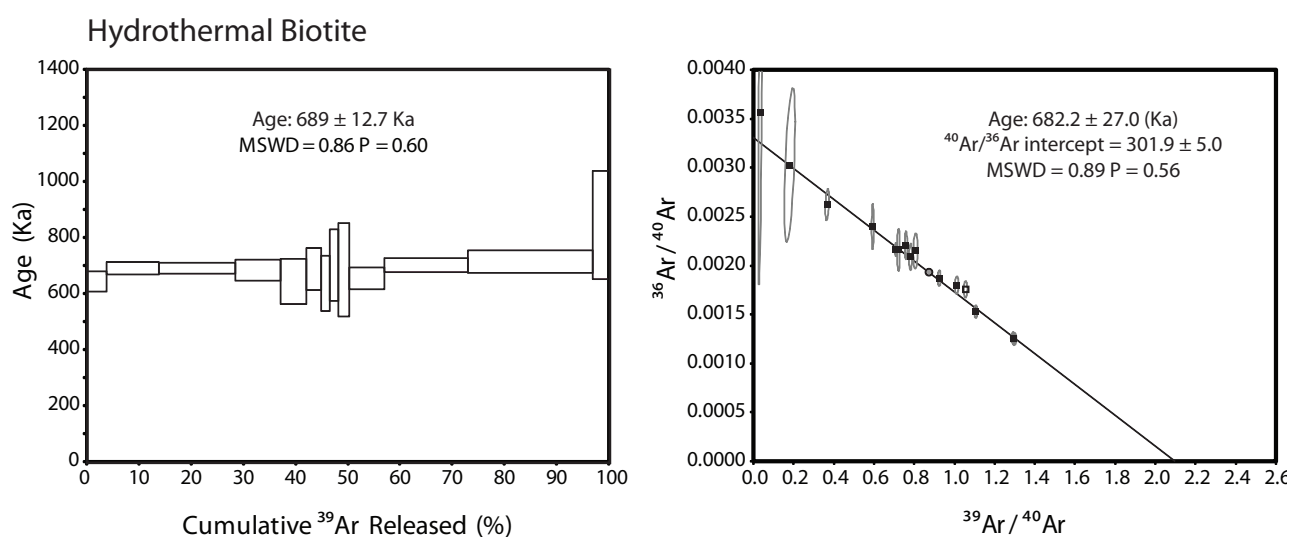


**Figure 7.5** Age spectrum and inverse isochron plots for  $^{40}\text{Ar}/^{39}\text{Ar}$  analysis of hydrothermal biotite **A.** Age spectrum plot showing a uniform plot within error as expected from a sample that remained thermally undisturbed since crystallization and rapid cooling. **B.** Inverse isochron plot with all analysis except one falling on the line of best fit. Error ellipses are and age errors are  $2\sigma$ . **Symbols:** closed square - analysis falling on line of best fit, open square - analysis off the line of best fit. **Sample ID:** IXCM07-25 589.3.

that expected from a sample that remained thermally undisturbed since crystallization and relatively rapid cooling. The age spectrum also does not show any disturbance from excess argon. The inverse isochron plot yielded the same age of  $0.682 \pm 0.027$  Ma and shows a high degree of correlation among all the 15 heating steps (MSWD = 0.89;  $P = 0.56$ ) with all but one sample plotting within  $\pm 2\sigma$ . The  $^{40}\text{Ar}/^{36}\text{Ar}$  intercept value of  $0.302 \pm 0.005$ , indistinguishable from the air ratio of  $0.2986 \pm 0.0001$  Ma from Lee et al. (2006), further demonstrates that no excess  $^{40}\text{Ar}^*$  is present in the biotite. Thus the age of  $0.689 \pm 0.013$  Ma is used for the hydrothermal biotite.

### 7.3.3 Re-Os Results

An age constraint on the Cu-Mo mineralisation (Stage 3) associated with the sericitic alteration (Stage B) was completed by Re-Os dating of molybdenite. Sample IXCM08-51 210.0 was selected for analysis because of the high concentration of disseminated molybdenite.

The molybdenite age was calculated using a  $^{187}\text{Re}$  decay constant of  $1.666 \times 10^{-11} \text{ year}^{-1}$  (Smoliar et al., 1996). Analysed Re and Os concentrations in the sample were 691.6 ppm and 5.651 ppb, respectively (Table 7.3). A Re/Os date of  $0.780 \pm 0.010$  Ma was determined for the Cerro la Mina molybdenite, assuming no initial  $^{187}\text{Os}$ .

| Mineral     | Re<br>ppm | $\pm 2\sigma$ | $^{187}\text{Re}$<br>ppb | $\pm 2\sigma$ | $^{187}\text{Os}$<br>ppb | $\pm 2\sigma$ | Model Age<br>(Ma) | $\pm 2\sigma$ with $\lambda$<br>(Ma) |
|-------------|-----------|---------------|--------------------------|---------------|--------------------------|---------------|-------------------|--------------------------------------|
| Molybdenite | 691.6     | 1.8           | 434715                   | 1125          | 5.651                    | 0.072         | 0.780             | 0.010                                |

**Table 7.3** Summary of data for Re-Os dating of molybdenite. **Sample ID:** IXCM08-51 210.0

## 7.4 Discussion

A comparison of the eight ages obtained is shown in Figure 7.6. The MSWD values for zircon U-Pb ages range from 0.56 to 1.9 and probabilities 0.037 to 0.57 for the rocks dated in this study. Most of the samples occur close to or in hydrothermal alteration and have significant common Pb adding to the uncertainties. The low number of zircons separated from the samples is probably the result of the alkaline composition of the volcanic rocks which tends to inhibit zircon development (Watson and Harrison, 1983) and/or the rocks that have cooled quickly locking the Zr into the glassy matrix inhibiting zircon crystallization. The molybdenite and biotite ages have small errors.

The two ages yielded from two trachyandesite fiamme breccia (Unit 1B<sub>g</sub>) samples are within error of each other consistent with the close distribution (106 m apart) and occur in the same stratigraphic unit. Only one young zircon found out of the 12 crystals was used in sample IXCM07-23 327.0. Without more than one zircon analysis contamination cannot be ruled out. However, as this zircon is within the analytical uncertainty of the four youngest crystals analysed in sample IXCM07-23 221.0 from the same drill hole and geological unit, it suggests that this zircon is reliable and that the age of  $1.220 \pm 0.085$  Ma represents the age of eruption for Unit 1B<sub>g</sub>.

The trachyandesite fiamme breccia (Unit 1B<sub>g</sub>) samples contained zircons that yielded ages

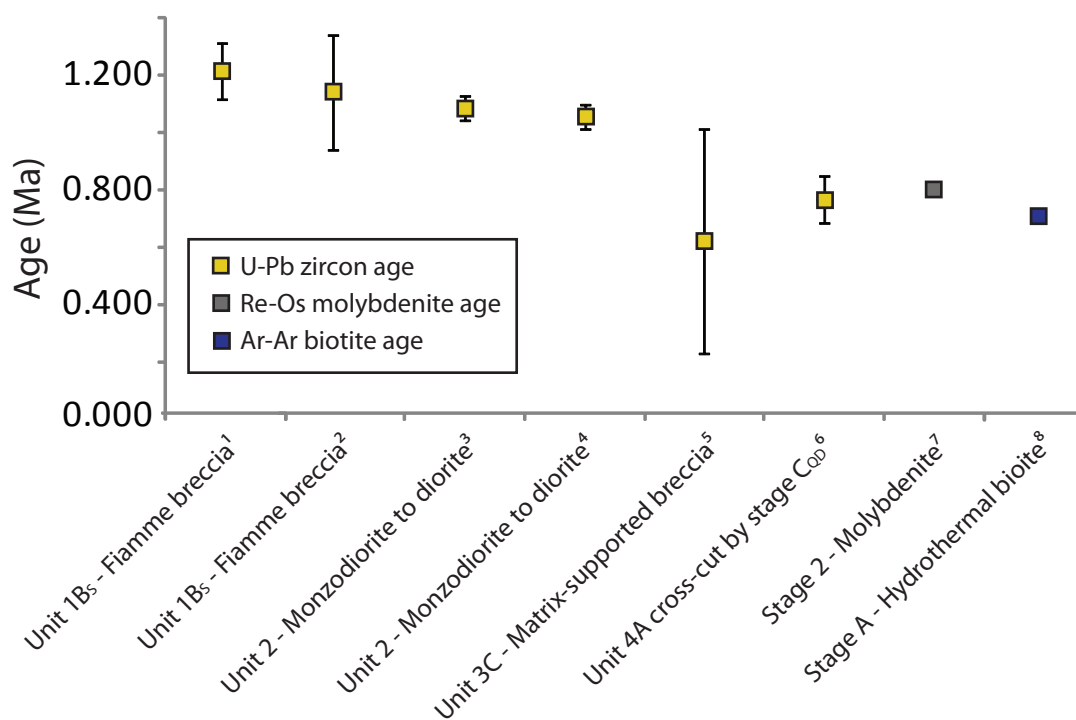


**Figure 7.6** Comparison of U-Pb, Re-Os and Ar-Ar ages completed in this study. Error bars are  $2\sigma$ . **Sample ID:** 1 - IXCM07-23 221.0, 2 - IXCM07-23 327.0, 3 - NJ08IX-198, 4 - IXCM08-95.0, 5 - IXCM06-09 100.7, 6 - IXCM08-63 72.0, 7 - IXCM08-51 210.0, 8- IXCM07-25 589.3.

from 8 to 1158 Ma (Fig. 7.7). The Chiapas Massif (CM) which crops out in the south of Chiapas State probably represents the basement rocks below the Cerro la Mina district. The CM has rocks of Precambrian to Permian age (Schaaf et al., 2002; Weber et al., 2005; Weber et al., 2007). Ortho- and paragneisses of the CM yielded an average of 1.0 to 1.2 and 1.4 to 1.6 Ga and represents Grenville crust (Schaaf et al., 2002; Weber et al., 2005). Mid-Permian plutons intruded the CM at  $271.9 \pm 2.7$  Ma and is followed by a high-grade orogenic thermal event and syn-tectonic granitoid plutons at  $254.0 \pm 2.3$  to  $251.8 \pm 3.8$  Ma (Weber et al., 2007). A cluster of zircon ages from Unit 1B<sub>s</sub> occurs at  $\sim 925$  Ma and probably represents a mixed signal from a Pre-Cambrian core, a mid to later Permian event or young rims from the magma chamber that erupted Unit 1B<sub>s</sub> creating slightly younger ages than 1.0 to 1.2 Ga (Fig. 7.7). A second cluster of ages occurs at  $\sim 425$  Ma for which no ages have been published. A third cluster of ages from Unit 1B<sub>s</sub> that occurs at  $\sim 225$  Ma may represent zircons from the mid to late Permian intrusion and orogenic event (Fig. 7.7). A number of zircons ranged in age from 8.3 to 95.9 Ma could be a mixed signal from inherited cores from the CM and younger rims from the magma chamber that has erupted this rock unit. The old zircons are therefore interpreted to be inherited from crustal contamination during the ascent of a magma before or during eruption and confirm the presence of CM rocks in the basement rocks below Cerro la Mina.

The U-Pb age of zircons from monzodiorites (Selva Negra Group B; Cerro la Mina Unit 2) samples IXCA08-18 95.0 and NJ08IX-198 probably represent the crystallization age of these rocks. Their ages of  $1.064 \pm 0.043$  and  $1.035 \pm 0.036$  Ma are statistically the same (Fig. 7.6) despite the small uncertainty on the measurements ( $<0.043$  Ma) and coming from distinctly different locations (Fig. 7.9).

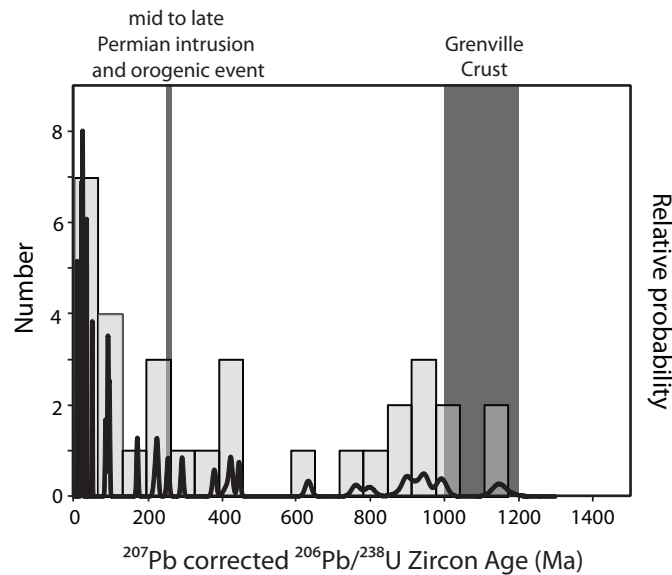


**Figure 7.7** Probability charts for old zircons analysed in Unit 1B<sub>s</sub> (samples IXCM07-23 221.0 and 327.0) and their correlation to basement ages from the Chiapas massif. Mid- to late Permian intrusion and orogenic event from Weber et al. (2007). Grenville crust age from Schaaf et al. (2002) and Weber et al. (2005).

Sample IXCM06-09 100.7 is cross-cut by a dickite-cemented hydrothermal breccia (Stage C<sub>QD</sub>) and the protolith is inferred to be matrix-rich, granule breccia (Unit 4A) which contains clasts of mixed provenance. The age is the youngest age with the smallest error (compared to trachyandesite matrix-supported breccia (Unit 3C; Fig. 7.6) and suggests that volcanism occurred until at least  $0.746 \pm 0.082$  Ma. The age also represents the maximum age at which the kandite alteration (Stage C) could have occurred.

The trachyandesite matrix-supported breccia (Unit 3C) had only three zircons (IXCM08-62 72.0). These zircons contained relatively high common Pb (0.3-1.5 ppm) both hosted in inclusions and on the surface of the relatively small crystals (25 x 50  $\mu$ m). The high common Pb contributed to the large uncertainty for the weighted average age of these zircons ( $\pm 0.39$ ). Unit 3C is polymictic rock of mixed provenance and host the youngest zircons than any other units dated in this study but with large error ( $0.60 \pm 0.39$  Ma; Fig. 7.6). The age suggests that Unit 3C is younger than the Units 1 and 2 consistent with the geology paragenesis (Chapter 4). The age however cannot be used as a deposition age because of the mixed provenance of the clasts in Unit 3C.

A Re-Os age on molybdenite mineralisation (Stage 2) associated with the sericitic alteration (Stage B) formed at  $0.78 \pm 0.010$  Ma. The molybdenite age is younger than Units 1B<sub>s</sub> and 2 is consistent with the breccia pipe (Unit 4), which hosts the molybdenite, cross-cutting Units 1B<sub>s</sub> and 2 (Fig. 7.6). The age suggests that Stage 2 mineralisation occurred near the time volcanism ceased ( $\sim 0.75$  Ma; Fig. 7.6). The age also suggests that the monzodiorite to diorite (Unit 2) is unrelated to mineralisation.

The Cerro la Mina hydrothermal biotite is associated with potassium feldspar (Stage A alteration) and probably formed at high temperatures characteristic potassic alteration that forms in a porphyry system to depths of 1 to 2 km. The hydrothermal biotite is juxtaposed with low temperature

halloysite (< 110°C and < 1 km depth) and is currently sitting ~500 m below the surface. The juxtaposition is all indicative of a rapid uplift environment allowing for the formation and rapid cooling of the hydrothermal biotite after its formation. A relative rapid cooling below ~300°C (closure temperature of biotite; Harrison et al., 1985) is supported by the absence of argon diffusion profile on the age spectrum which results in an undisturbed plateau age of the  $0.689 \pm 0.013$  Ma age developed over 96 percent of the spectrum (Fig. 7.5). The hydrothermal biotite age signifies the time at which the hydrothermal system cooled below ~300°C (Harrison et al., 1985) and the onset of kandite alteration (Stage C). The biotite age is consistent with the maximum age yielded from IXCM06-09 100.7 that is cross-cut by quartz-dickite alteration (Stage C<sub>QD</sub>;  $0.661 \pm 0.082$  Ma). The biotite age is younger than Re-Os age of molybdenite and is consistent with molybdenite forming at temperatures greater than 300°C.

A stratigraphic column is shown in Figure 7.8 and is based on the geological paragenesis described in Chapter 4. The U-Pb dating of zircons is consistent with the paragenesis with the flamme breccia (Unit 1B<sub>s</sub>;  $1.22 \pm 0.085$  Ma; Fig. 7.8) identified as the oldest unit being intruded by the later monzodiorite (Unit 2; ~1 Ma; Fig. 7.8). The youngest samples yielded ages of  $0.746 \pm 0.082$  Ma (Unit 4A cross cut by Stage C<sub>QD</sub>; IXCM06-09 100.7) and  $0.60 \pm 0.39$  Ma (Unit 3C; IXCM08-62 72.0) suggesting volcanism was active from ~1.2 to at least ~0.75 Ma and Unit 3C is younger than Unit 1B<sub>s</sub>. Volcanism was followed by molybdenite mineralisation (Stage 2) associated with the sericitic alteration (Stage B) at  $0.78 \pm 0.010$  Ma (Fig. 7.8) and the hydrothermal system cooling to temperatures below 300°C at  $0.689 \pm 0.013$  Ma and onset of Stage C alteration and Stage 3 and 4 mineralisation (Fig. 7.8).

The ages of the volcanic rocks in the Selva Negra (and Cerro la Mina) are significantly younger than the K-Ar dates for the region produced by Damon and Motesinos (1978) which range from 2.79 to 1.95 Ma (Table 7.4; Fig. 7.9). The K-Ar ages are not expected to be the same as different units were dated in this study. However, the full significance of the ages from Damon and Motesinos (1978) are uncertain as the K-Ar systematics could have been reset by porphyry-related potassic

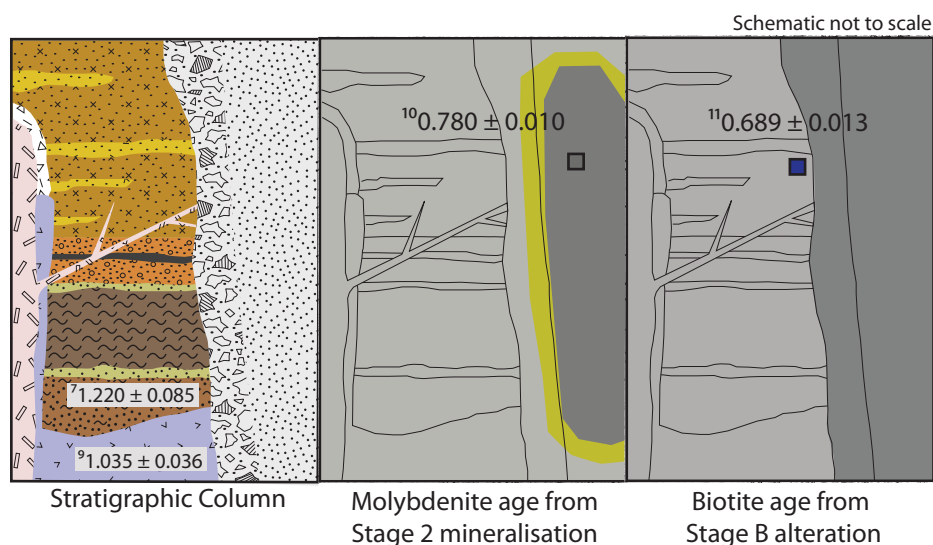


**Figure 7.8** Compilation of geology, mineralisation and alteration ages for the Cerro la Mina prospect. Age errors are  $2\sigma$ . **Notation:** 7,8, 10 and 11 details of each age is listed in Table 7.4. Legends for stratigraphic column in Chapter 4, mineralisation in Chapter 6 and alteration in Chapter 5.

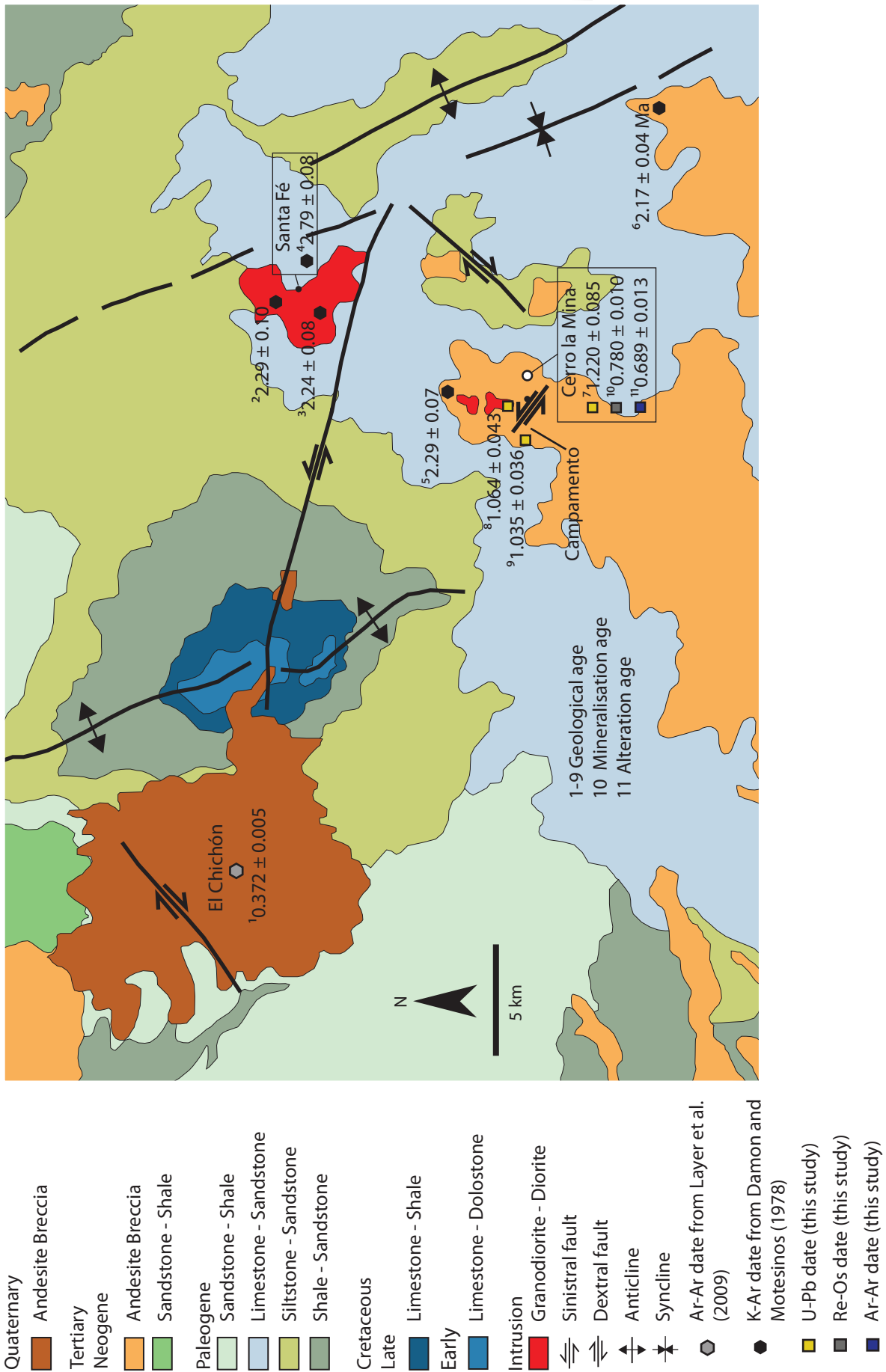


**Figure 7.9** Simplified geologic map indicating the location of ages from the literature and new ages from this study. Details of each age is listed in Table 7.4.

| No. | Source                     | Sample ID       | Long        | Lat         | Dating Method     | Age (Ma) $\pm 2\sigma$ | Description  |
|-----|----------------------------|-----------------|-------------|-------------|-------------------|------------------------|--|
| 1   | Layer et al. (2009)        | CHI-0804-08A    | 93°13'26" W | 17°21'26" N | Ar-Ar whole rock  | 0.372 $\pm$ 0.005      | El Chichón pre Somma   |
| 2   | Damon and Motesinos (1978) | 1               | 93°02'40" W | 17°20'24" N | K-Ar whole rock   | 2.79 $\pm$ 0.08        | Basaltic-andesite dyke   |
| 3   | Damon and Motesinos (1978) | 2               | 93°02'18" W | 17°18'10" N | K-Ar biotite      | 2.29 $\pm$ 0.07        | Dike in Oligocene shale  |
| 4   | Damon and Motesinos (1978) | 3               | 93°02' W    | 17°22' N    | K-Ar biotite      | 2.29 $\pm$ 0.10        | Diorite containing pyrite, bornite, and chalcopyrite, intruded into Oligocene limestone which has been converted to wollastonite |
| 5   | Damon and Motesinos (1978) | 4               | 93°02'16" W | 17°22'12" N | K-Ar biotite      | 2.24 $\pm$ 0.08        | Unaltered, granodiorite dyke in argillic alteration zone, contains, disseminated pyrite,   |
| 6   | Damon and Motesinos (1978) | 5               | 92°58'45" W | 17°10'18" N | K-Ar whole rock   | 2.17 $\pm$ 0.04        | Andesite, tilted and underlying pumiceous ash flow   |
|     |                            |                 | UTME        | UTMN        | Elev. (m)         |                        |  |
| 7   | This Study                 | IXCM07-23 221.0 | 494537      | 1908873     | Zircon U-Pb       | 1.220 $\pm$ 0.085      | Unit 1B <sub>s</sub> - Ignimbrite  |
| 8   | This Study                 | NJ08IX-198      | 491965      | 1908601     | Zircon U-Pb       | 1.12 $\pm$ 0.20        | Unit 2 - Monzodiorite  |
| 9   | This Study                 | IXCM08-18 95.0  | 493543      | 1909511     | Zircon U-Pb       | 1.064 $\pm$ 0.043      | Unit 2 - Monzodiorite  |
| 10  | This Study                 | IXCM08-51 210.0 | 494183      | 1908815     | Re-Os molybdenite | 0.780 $\pm$ 0.010      | High grade molybdenite   |
| 11  | This Study                 | IXCM07-25 589.3 | 494290      | 1908726     | Ar-Ar biotite     | 0.689 $\pm$ 0.013      | Secondary biotite veins  |

**Table 7.4** Summary table of regional dating from literature and new ages from this study. Locations shown in Figure 7.9.

alteration evident in the region. El Chichón volcano 20 km to the northwest is younger than the Cerro la Mina volcanic rocks with an Ar-Ar age of 372,000 years (Layer et al., 2009).

## 7.5 Conclusions

U-Pb ages are consistent with paragenetic relationships of rock units described in Chapter 4. Strong fiamme breccia (Unit 1B<sub>s</sub>) yields an age of  $1.220 \pm 0.085$  Ma (zircon U-Pb age) and the monzodiorite to diorite (Chapter 3 referred to as Group B, Chapter 4 referred to as Unit 2) yields ages of  $1.064 \pm 0.043$  and  $1.035 \pm 0.036$  Ma (zircon U-Pb age). U-Pb ages on volcanic rocks in the Selva Negra (Cerro la Mina) region suggest volcanism occurred from  $\sim 1.2$  Ma to at least  $\sim 0.75$  Ma. Geological units are significantly younger than the K-Ar ages determined by Damon and Motesinos (1978). The full significance of the ages from Damon and Motesinos (1978) are uncertain as the K-Ar systematics could have been reset by porphyry-related potassic alteration evident in the region.

Volcanism was followed by a hydrothermal system which deposited Stage 2 mineralisation and associated sericitic alteration (Stage B) at  $0.780 \pm 0.010$  Ma (molybdenite Re-Os age). The hydrothermal system cooled below  $300^{\circ}\text{C}$  at  $0.689 \pm 0.013$  Ma (hydrothermal biotite Ar-Ar age) that was followed by kaolinite alteration (Stage C) and Stage 3 and 4 mineralisation. The molybdenite age is younger than Units 1B<sub>s</sub> and 2 consistent with the breccia pipe (Unit 4), which hosts the molybdenite, cross-cutting Units 1B<sub>s</sub> and 2 (Fig. 7.6). The molybdenite age also suggests that the monzodiorite to diorite (Chapter 3 referred to as Group B, Chapter 4 referred to as Unit 2) is unrelated to mineralisation.

## Chapter 8 - Stable Isotopes

### 8.1 Introduction

Oxygen-deuterium stable isotope analysis of halloysite characterised the type of fluid that deposited the halloysite and whether it formed in a supergene or hypogene environment. A study on sulfur isotopes complimented the mineral paragenesis interpretation (Chapter 6) and provided further insight into the type of fluid that carried the sulfides and sulfates.

The chapter is organized by describing the research methods, followed by results and a discussion. The chapter concludes with a summary of the oxygen-deuterium and sulfur isotope results.

### 8.2 Research Methods

#### 8.2.1 Oxygen-Deuterium Isotopes

##### 8.2.1.1 Halloysite Separation

Light crushing and sieving to  $< 150 \mu\text{m}$  produced a clay mineral separate from two halloysite bearing samples. Suspension and centrifugation in distilled water with sodium hexametaphosphate (to disperse clay) produced a clay mineral separate of  $< 10 \mu\text{m}$ . Evaporation of the water from the clay/water mixture under ambient temperatures in a fume hood left the desired clay separates.

##### 8.2.1.2 Quantitative X-ray diffraction Analysis

Quantitative X-ray diffraction (QXRD) analysis on the clay separates determined the abundance of halloysite in the sample before oxygen-deuterium analysis. The XRD methods are described in Chapter 5.

##### 8.2.1.3 Oxygen-Deuterium Analysis

The oxygen-deuterium analyses were completed at National Isotope Centre in Lower Hutt, New Zealand. Storage of the samples at  $160^\circ\text{C}$  for one week removed any atmospheric moisture. A  $\text{CO}_2$ -laser and  $\text{BrF}_5$  extracted oxygen from the sample powders (Sharp, 1990). Oxygen isotope values are reported in  $\delta^{18}\text{O}$  notation, relative to VSMOW. Samples were normalized to the international quartz standard NBS-28 using a value of +9.6 per mil. Values for all four NBS-28 analysed with the samples had values that varied by less than 0.15 per mil. Samples and standards were heated overnight to  $150^\circ\text{C}$  before loading into the vacuum extraction line. These were then evacuated for approximately six hours. Blank  $\text{BrF}_5$  runs were done until yield was less than  $0.2 \mu\text{moles}$  oxygen. Oxygen yields were recorded and  $\text{CO}_2$  gas analysed on a Geo20-20 mass spectrometer.

A HEKAtech high temperature elemental analyser coupled with a GV Instruments IsoPrime mass spectrometer analysed for deuterium. Samples were pyrolyzed at  $1450^\circ\text{C}$ , in silver capsules. All samples were analysed in triplicate. All results are reported with respect to VSMOW, normalized to international standards IAEA-CH-7, NBS30 and NBS22 with reported  $\delta\text{D}$  values of -100, 66 and 118

per mil. The precision on the standards is 1.5 per mil.

### 8.2.2 Sulfur Isotope Methods

Sulfides and sulfates were identified with a reflected light microscope in polished slabs and mounts and separated with a micro-drill. Typically five to six grains of the same sulfide/sulfate were drilled per sample to obtain at least 5 mg of material.

The  $\delta^{34}\text{S}$  values for sulfide and sulfate samples were analysed at the Central Science Laboratory, University of Tasmania on the VG SIRA series II mass spectrometer.  $\text{SO}_2$  was extracted from sulfides and sulfates using methods described in Robinson and Kusakabe (1975) and Yanagisawa and Sakai (1983). A cold finger was used when the yield was below 5 mmHg. Standards were in house and calculated against International Atomic Energy Agency (IAEA) standards to  $\pm 0.1$  per mil. In house sulfide standards included galena from Broken Hill and Rosebery deposits with  $\delta^{34}\text{S}$  values of +3.0 and +12.4 per mil, respectively. In house sulfate standards included barite from the Madame Howard deposit and seawater sulfate (Tasul I) with  $\delta^{34}\text{S}$  values of +31.2 and +20.9 per mil, respectively.

## 8.3 Oxygen-deuterium Results

Two samples were selected from the strong halloysite alteration (Stage C<sub>HK</sub>), at least 190 m below the oxide zone, associated with sulfides and 150 m apart (Fig. 8.1). The highest halloysite concentration of 85 percent was obtained through clay separation when separated to  $< 1 \mu\text{m}$  fraction, the balance being orthoclase, albite, quartz and sulfides. In lieu of analysing a pure sample of halloysite ( $> 98\%$ ) for oxygen-deuterium, separation of the samples into four different size fractions created varying amounts of halloysite to impurities (Table 8.1). QXRD analysis obtained the concentrations of halloysite and impurities before the oxygen-deuterium analysis.

The  $\delta^{18}\text{O}$  values for the separates increased with increasing halloysite concentration (Table 8.1; Fig. 8.2). Extrapolation using a line of best fit gave the  $\delta^{18}\text{O}$  value for 100 percent halloysite (Fig. 8.2). The  $\delta^{18}\text{O}$  and  $\delta\text{D}$  values for the two samples are in good accordance being calculated to +20.3 and -59.7 per mil (IXCM08-51 221.5) and +20.2 and -59.1 per mil (IXCM08-51 357.1), respectively. The average composition of  $\delta\text{D}$  was used, as the values varied little and sometimes within error. Analysis of rain water collected 1 km east of the Cerro la Mina prospect in the town of Tapilula yielded  $\delta^{18}\text{O}$  of -2.23 per mil and  $\delta\text{D}$  of -2.7 per mil.

## 8.4 Sulfur Isotope Results

The samples were taken from various stages of the paragenesis and at various distances from the core of the deposit (Fig. 8.1). Sulfur isotope values for sulfides and sulfates from the Cerro la Mina prospect are given in Table 8.2. Twenty-one  $\delta^{34}\text{S}$  analyses on fractured pyrite (Stage 1), chalcopyrite (Stage 2), inclusion-rich pyrite (Stage 2), barite (Stage 3) and ragged pyrite (Stage 4) is indicated in Table 8.2. Marcasite, sphalerite and galena proved to be too fine-grained to obtain a pure sample. To test the accuracy of analysing multiple sulfide grains from the same sample, five separate samples of

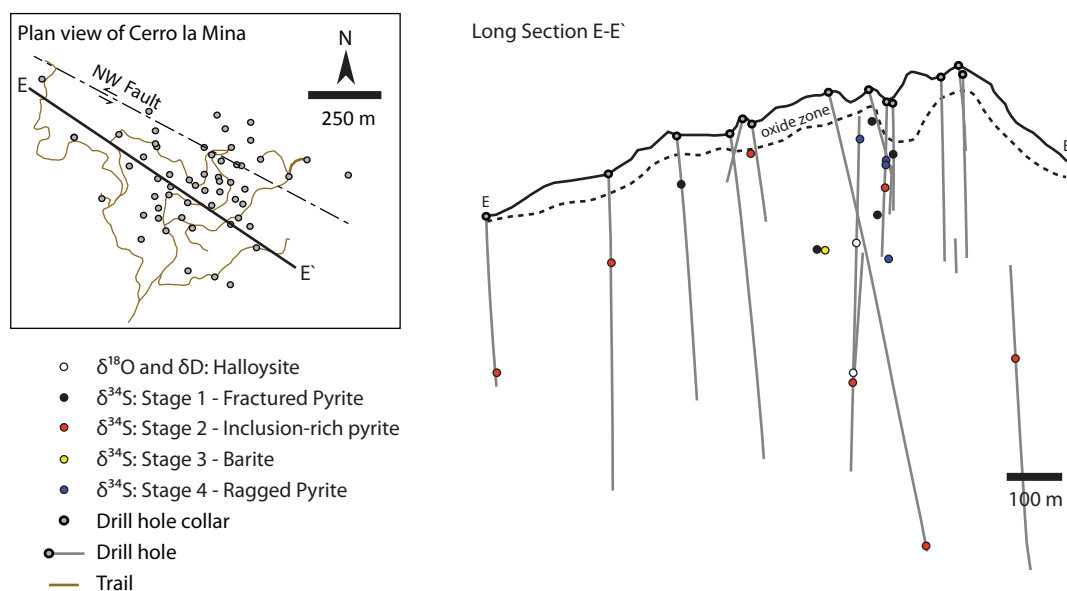


**Figure 8.1** Sample locations for oxygen-deuterium and sulfur isotope analyses on long section E-E'.

| Sample ID                         | Size fraction      | % Halloysite | $\delta^{18}\text{O}$ (‰) | $\delta\text{D}$ (‰) | $\delta\text{D } 1\sigma$ |
|-----------------------------------|--------------------|--------------|---------------------------|----------------------|---------------------------|
| IXCM08-51 221.5 A                 | < 1 $\mu\text{m}$  | 84.8         | +18.9                     | -59.1                | 0.4                       |
| IXCM08-51 221.5 B                 | < 5 $\mu\text{m}$  | 34.7         | +16                       | -60.1                | 0.2                       |
| IXCM08-51 221.5 C                 | < 10 $\mu\text{m}$ | 23.5         | +14.5                     | -58.5                | 1.3                       |
| IXCM08-51 221.5 D                 | Whole Rock         | 19.0         | +10.1                     | -61.2                | 1.3                       |
| IXCM08-51 375.1 A                 | < 1 $\mu\text{m}$  | 74.3         | +18.2                     | -58.8                | 0.8                       |
| IXCM08-51 375.1 B                 | < 5 $\mu\text{m}$  | 23.9         | +14.6                     | -58.4                | 0.4                       |
| IXCM08-51 375.1 C                 | < 10 $\mu\text{m}$ | 17.9         | +12.5                     | -54.1                | 0.2                       |
| IXCM08-51 375.1 D                 | Whole Rock         | 13.1         | +9.1                      | -65                  | 0.3                       |
| Rain water from Tapilula, Chiapas |                    |              | -2.23                     | -2.7                 | 0.8                       |

**Table 8.1**  $\delta^{18}\text{O}$  and  $\delta\text{D}$  data for separated Cerro la Mina halloysite and rain water from Tapilula, Chiapas.

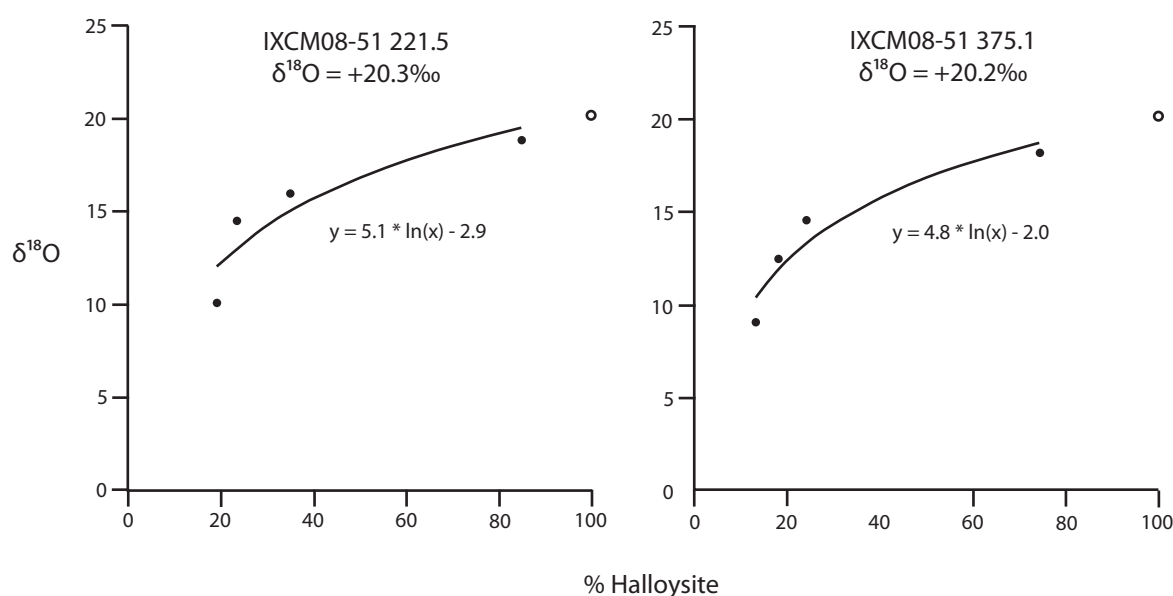


**Figure 8.2** Extrapolation of  $\delta^{18}\text{O}$  values for pure halloysite from samples with varying abundances of halloysite to impurities. Equations for the line of best fit are shown. **Symbols:** closed circle - known  $\delta^{18}\text{O}$  value of halloysite + impurity sample, open circle - extrapolated  $\delta^{18}\text{O}$  value of pure halloysite.

inclusion-rich pyrite (Stage 2) were drilled from sample IXCM08-62 300.1. The results were accurate to  $\pm 0.6$  per mil ( $2\sigma$ ).

The  $\delta^{34}\text{S}$  values for the Cerro la Mina sulfides ranged from -2.49 to +4.89 per mil with a mean of +0.73 per mil (Fig. 8.3). Stage 1 has two populations at approximately -2.5 and +2 per mil with values ranging from -2.49 to +2.24 per mil with a mean of 0.23 per mil (Fig. 8.3). Stage 2 ranged from -0.46 to +0.91 per mil with a mean of +0.29 per mil (Fig. 8.3). One sample of barite from Stage 3 yielded a  $\delta^{34}\text{S}$  of +10.52 per mil. The  $\delta^{34}\text{S}$  for Stage 4 shifts to slightly higher values with a range of +1.07 to +4.89 per mil; mean +2.3 per mil (Fig. 8.3). Stage 2 has the widest distribution of  $\delta^{34}\text{S}$  values and did not show any consistent vertical or horizontal changes in  $\delta^{34}\text{S}$  (Fig. 8.1). Stages 1, 3 and 4 do not have sufficient sample distribution to observe spatial trends (Fig. 8.1).

| Sample ID          | Mineral               | Stage | Weight (mg) | Yield (mmHg) | $\delta^{34}\text{S}$ CDT (‰) |
|--------------------|-----------------------|-------|-------------|--------------|-------------------------------|
| IXCM07-21 281.0    | Fractured pyrite      | 1     | 13.7        | 16.8         | +1.83                         |
| IXCM07-27 97.5     | Fractured pyrite      | 1     | 12.4        | 24.8         | +1.94                         |
| IXCM08-48 130.3    | Fractured pyrite      | 1     | 13.0        | 17.6         | -2.37                         |
| IXCM08-55 225.6    | Fractured pyrite      | 1     | 13.8        | 20.4         | 2.24                          |
| IXCM08-56 68.5     | Fractured pyrite      | 1     | 13.8        | 22.2         | -2.49                         |
| IXCM06-09 136.9    | Chalcopyrite          | 2     | 79.8        | 37.0         | +0.41                         |
| IXCM07-20 798.4    | Chalcopyrite          | 2     | 98.2        | 53.0         | -0.46                         |
| IXCM06-16 528.3    | Inclusion-rich pyrite | 2     | 11.7        | 21.0         | 0.68                          |
| IXCM07-28 487.4    | Inclusion-rich pyrite | 2     | 12.0        | 12.4         | -0.35                         |
| IXCM08-45 42.9     | Inclusion-rich pyrite | 2     | 16.2        | 22.4         | +0.81                         |
| IXCM08-62 182.2    | Inclusion-rich pyrite | 2     | 21.9        | 17.0         | +0.40                         |
| IXCM08-63 300.1 #1 | Inclusion-rich pyrite | 2     | 16.2        | 23.6         | +0.47                         |
| IXCM08-63 300.1 #2 | Inclusion-rich pyrite | 2     | 13.1        | 29.0         | +0.12                         |
| IXCM08-63 300.1 #3 | Inclusion-rich pyrite | 2     | 13.6        | 17.6         | +0.67                         |
| IXCM08-63 300.1 #4 | Inclusion-rich pyrite | 2     | 12.7        | 15.4         | +0.91                         |
| IXCM08-63 300.1 #5 | Inclusion-rich pyrite | 2     | 24.2        | 30.8         | +0.62                         |
| IXCM07-21 284.3    | Barite                | 3     | 54.3        | 30.0         | +10.52                        |
| IXCM08-47 238.4    | Ragged pyrite         | 4     | 1.6         | 2.2*         | +1.67                         |
| IXCM08-51 44.8     | Ragged pyrite         | 4     | 10.3        | 8.8          | +4.89                         |
| IXCM06-09 100.7    | Ragged pyrite         | 4     | 4.9         | 4.8*         | +1.07                         |
| IXCM06-09 106.8    | Ragged pyrite         | 4     | 16.4        | 29.0         | +1.58                         |

**Table 8.2**  $\delta^{34}\text{S}$  data for sulfates and sulfates from the four stages of mineralisation. **Notation:** \* - cold finger used.

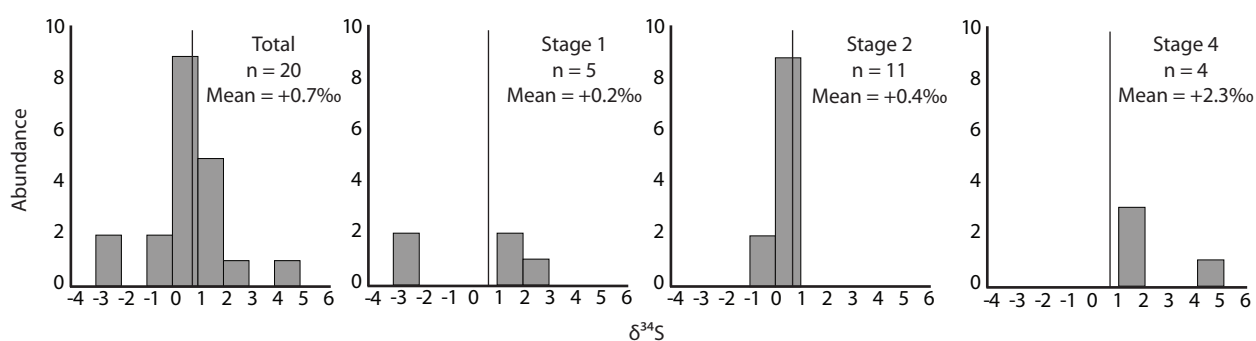


**Figure 8.3** Histograms illustrating the  $\delta^{34}\text{S}$  values for the total, Stage 1, Stage 2 and Stage 4 sulfides. The vertical line at +0.7‰ is the interpreted magmatic  $\delta^{34}\text{S}$  value form Luhr et al. (2002).

## 8.5 Oxygen-Deuterium Discussion

### 8.5.1 Comparison with Supergene and Hypogene Halloysite

The Cerro la Mina halloysite is plotted against known supergene and hypogene halloysite in Figure 8.4. The supergene halloysite field is a compilation by Sheppard and Gilg (1996) of known supergene halloysite. The hypogene halloysite field is determined from an active seafloor hydrothermal system (Marumo and Hattori, 1999). The kaolinite 20°C line on Figure 8.4 represents the isotopic composition of kaolinite in equilibrium with meteoric water at 20°C and is referred to as the “kaolinite line” by Sheppard et al. (1969). Supergene kaolinites either plot on the “kaolinite line” or slightly to the left of it (Sheppard et al., 1969; Taylor, 1974). The kaolinite 35°C line represents the isotopic composition of kaolinite in equilibrium with meteoric waters at a temperature of 35°C. Sheppard et al. (1969) considers the kaolinite 35°C line to be a highly tentative line separating known supergene kaolinite from hypogene or potentially hypogene kaolinite samples. The area to the left of the kaolinite 35°C line is consistent with a higher temperature (hypogene) temperature for kaolinite, with the right-hand side consistent with a supergene origin for kaolinite due to low temperature weathering. The Cerro la Mina halloysite isotopic compositions plot to the right of the kaolinite 35°C line and in the low temperature (supergene) halloysite field. A supergene origin can be assumed given the halloysite has not been enriched in  $\delta^{18}\text{O}$  during post mineralisation exchange with lower temperature meteoric water (e.g. Simone et al., 2005; Ece et al., 2008).

### 8.5.2 Fractionation Factor for Cerro la Mina Halloysite

The fractionation factor for Cerro la Mina was used to determine the probable composition of fluid from which the halloysite precipitated. Isotopic fractionation factors for halloysite are not well defined, but they can be approximated by the values for kaolinite (Sheppard and Gilg, 1996) because both minerals have the same ideal stoichiometric composition; however halloysite contains an additional interlayer of water. The fractionation trend for Cerro la Mina halloysite in equilibrium with water is plotted in Figure 8.5 (line A) using the  $\delta^{18}\text{O}$  fractionation factor expressed by  $1000 \ln \alpha = 2.76 * 10^6/T^2 - 6.75$  and the  $\delta\text{D}$  isotopic fractionation factor expressed by  $1000 \ln \alpha = -7.7 * 10^6/T^2 - 2.7$  (Sheppard and Gilg, 1996).

Spatial coverage is limited for the isotopic composition of meteoric water in Mexico. As a result the isotopic composition of meteoric water for northern Chiapas was calculated using data collected in Veracruz, Veracruz State from 1962 to 1988 and located 385 km to the northwest (IAEA/WMO, 2006). The results of IAEA/WMO study were filtered to the months June to October (rainy season) in which 85 percent of the meteoric water fell to best reflect long-term seasonally weighted precipitation inputs to the landscape. The average composition of rainwater at Veracruz is  $\delta^{18}\text{O} = -4.1 \pm 2.2$  per mil (1 $\sigma$ ; IAEA/WMO, 2006).

Cerro la Mina (1500 m elevation) is located at a higher elevation than Veracruz (16 m elevation). Meteoric water systematically becomes isotopically lighter as moist air masses are forced to rise over mountainous regions, and water condenses at progressively lower temperatures (Chamberlain

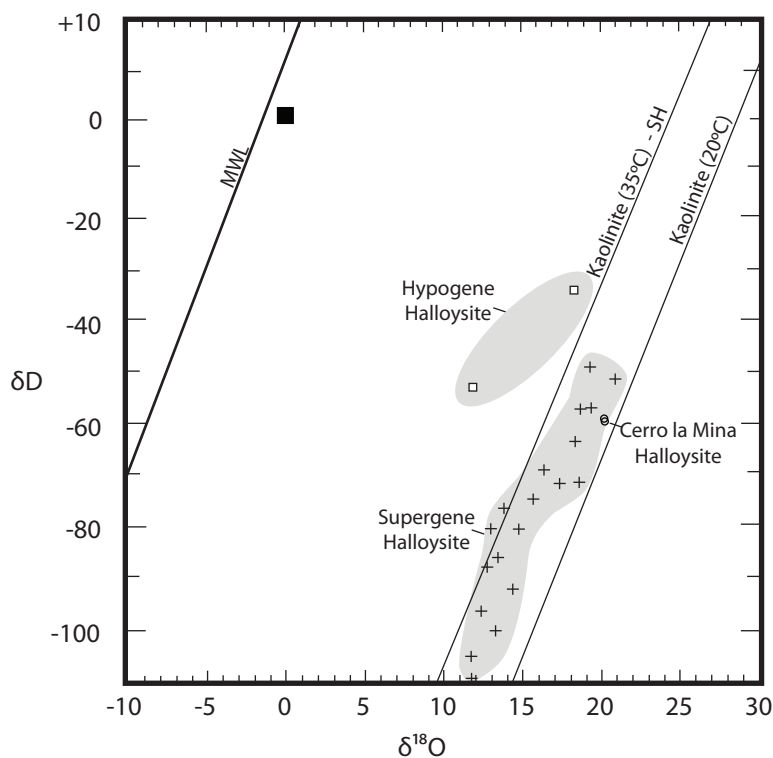


**Figure 8.4**  $\delta^{18}\text{O}$  versus  $\delta\text{D}$  diagram showing the composition of Cerro la Mina halloysite compared to the fields of supergene and hypogene halloysite. Hypogene halloysite field and open squares are from Marumo and Hattori (1999). Supergene halloysite field and crosses are from Sheppard and Gilg (1996). The kaolinite 20°C and 35°C lines are the composition of kaolinite in equilibrium with meteoric water at these temperatures (Sheppard et al., 1969). The kaolinite 35°C line is also considered to be a tentative dividing line between supergene and hypogene clays from Sheppard et al. (1969). **Symbols:** closed square - standard mean ocean water **Abbreviations:** MWL - meteoric water line, SH - supergene/hypogene, SMOW - standard mean ocean water.

and Poage, 2000). A change of  $\delta^{18}\text{O} = -3 \pm 1$  per mil occurs over  $\sim 1500$  m from Veracruz to Cerro la Mina using the  $\Delta \delta^{18}\text{O}$  of surface waters versus net elevation from Chamberlain and Poage (2000). Therefore, the composition of Cerro la Mina meteoric water is calculated to be  $\delta^{18}\text{O} = -7.1 \pm 1.7$  per mil and  $\delta\text{D} = -46.8$  per mil. The  $\delta\text{D}$  value was calculated using  $\delta\text{D} = 8 \cdot \delta^{18}\text{O} + 10$  from Craig (1961).

The isotopic composition calculated is consistent with Wasenaar (2009) who developed a predictive general linear model (GLM) for hydrogen and oxygen isotopic spatial patterns in Mexican groundwater. The GLM used elevation, latitude, drainage basin (Atlantic versus Pacific) and rainfall as the most relevant predictive variables. Wasenaar (2009) predicts northern Chiapas, in the region of Cerro la Mina, to have a composition of  $\delta^{18}\text{O} = -6.25$  to  $-8.75$  per mil. The Tapilula meteoric water sample analysed in this study has heavier isotopes than the range for northern Chiapas, probably because of seasonal variations in rainfall composition (e.g., IAEA/WMO, 2006) and lower elevation of 750 m (e.g., Chamberlain and Poage, 2000).

The fractionation trend for the Cerro la Mina halloysite (Line A) meets the meteoric water line ( $\delta\text{D} = 8 \cdot \delta^{18}\text{O} + 10$ ; Craig, 1961) at a temperature of 25°C and composition of  $\delta^{18}\text{O} = -4.9$  per mil and  $\delta\text{D} = -27.3$  per mil and within the range for Veracruz (16 m) meteoric water (Point C; Fig. 8.5). Point C has a heavier  $\delta^{18}\text{O}$  value ( $\sim 1$  ‰) than the Cerro la Mina (1600 m) meteoric water composition consistent with a hypogene origin if the weathering history occurred at high elevations. However, if

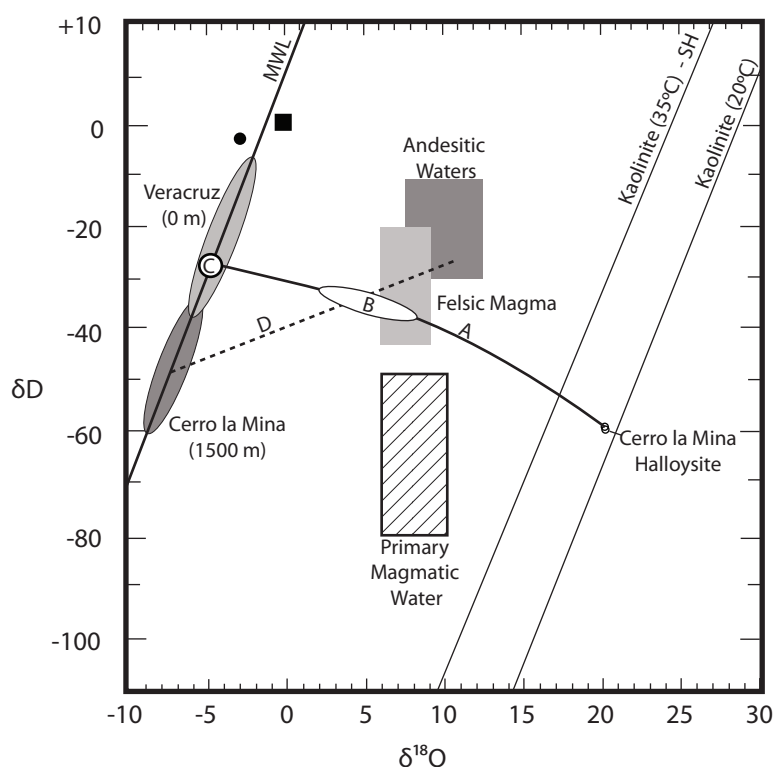


**Figure 8.5**  $\delta^{18}\text{O}$  versus  $\delta\text{D}$  diagram showing the fractionation trend of water in equilibrium with Cerro la Mina halloysite in relation to possible sources of water. Line A is the fractionation trend for Cerro la Mina halloysite. Point B is the composition of fluid in equilibrium with Cerro la Mina halloysite at 60 to 110°C interpreted from mineral associations. Point C is the intersection of fractionation factor for Cerro la Mina halloysite and the MWL occurring at 26°C. Line D is a linear trend between meteoric water and andesitic water commonly observed in acid geothermal waters and steam from hot spring areas (Craig, 1963; Giggenbach, 1992). The magmatic water field is from Sheppard et al. (1969) and Campbell and Larsen (1998), the felsic magmas field is from Taylor (1992), and andesitic water field is from Giggenbach (1992). The Cerro la Mina (1600 m) meteoric water field is extrapolated from Veracruz, Veracruz State (16 m) meteoric water IAEA/WMO (2006) and calibrated for elevation using Chamberlain and Poage (2000). The kaolinite 20°C and 35°C lines are from Sheppard et al. (1969). Meteoric water line from Craig (1961). **Symbols:** closed circle - Tapilula, Chiapas meteoric water composition, closed square - standard mean ocean water. **Abbreviations:** MWL - meteoric water line, SMOW - standard mean ocean water, SH - supergene/hypogene line.

much of the weathering history occurred at lower elevation the discrimination between supergene and hypogene origin is ambiguous. A weathering history at lower elevation is a more complicated scenario, as it would require recent uplift with little erosion.

### 8.5.3 Formation Temperature of Halloysite

To interpret further the oxygen-deuterium results the temperature of formation for the halloysite was considered by reviewing its mineral zonation and assemblages. In high sulfidation systems, where advanced argillic alteration like Cerro la Mina Stage C alteration occurs, temperatures typically range between 160 to 260°C (Hedenquist, 2000). When considering that the Cerro la Mina halloysite (Stage  $C_{\text{HK}}$ ) occurs at a deeper position than the hypogene quartz-dickite alteration (Stage  $C_{\text{QD}}$ ) in association with arsenian-pyrite, marcasite, sphalerite, galena and barite (Stages 3 and 4) the formation temperatures are probably greater than those in a supergene environment and closer to temperatures of 61 to 110°C for hypogene halloysite recorded Marumo and Hattori (1999). As described in Chapter 5, the halloysite abundance changes in response to distance from the high temperature

quartz-dickite core (Stage C<sub>OD</sub>) with halloysite increasing in abundance distally. In the geothermal systems of the Philippines, dickite is recorded to form from 110 to 250°C (Reyes, 1990).

For the purposes of this study a temperature of 60 to 110°C is used as a reasonable assumption for the formation temperature of the Cerro la Mina halloysite. No independent geothermometry is available, e.g. fluid inclusions, sulfur/sulfate or oxygen isotopes. The interpreted temperature of formation for the Cerro la Mina halloysite (60 to 110°C) has  $\delta^{18}\text{O}$  values between 2.1 and +8.2 per mil and  $\delta\text{D}$  values between -32.2 and -37.0 per mil (Point B; Fig. 8.5).

Figure 8.5 also shows the accepted range for isotopic composition of primary magmatic water is  $\delta\text{D} = -40$  to  $-80$  per mil and  $\delta^{18}\text{O} = +6$  to  $+10$  per mil (Sheppard et al., 1969; Campbell and Larsen, 1998). Exsolution of magmatic fluid (degassing) from a typical felsic magma at 3 to 5 weight percent water results in  $\delta\text{D}$  enrichment of about 15 to 20 per mil, but may be as high as 40 per mil (Taylor, 1992). Water that discharges to the surface via volcanic fumaroles termed 'andesitic water' has heavy  $\delta\text{D}$  values of  $-20 \pm 10$  per mil (Giggenbach, 1992) consistent with an initial melt composition of  $-20$  to  $-45$  per mil  $\delta\text{D}$  and a fractionation factor of approximately 20 per mil (Hedenquist et al., 1998).

Water in geothermal systems show a strong correlation with their meteoric water  $\delta^{18}\text{O}$  composition by shifting to heavier  $\delta^{18}\text{O}$  values as a result of isotopic exchange with silicate and carbonate country rocks, all of which start out with  $\delta^{18}\text{O}$  values higher than +5.5 per mil (Craig, 1963; Taylor, 1974; Giggenbach, 1992). In contrast to the  $\delta^{18}\text{O}$ , the  $\delta\text{D}$  values of hot waters in geothermal areas are not controlled by the exchange process because the rocks contain little initial hydrogen compared to the amounts of the  $\text{H}_2\text{O}$  involved. Instead, the  $\delta\text{D}$  values remain constant in near-neutral, chloride-rich geothermal waters, identical to the local meteoric waters (Craig, 1963). Acid geothermal waters and steam from hot spring areas are systematically enriched in deuterium along linear trends between meteoric water and andesitic water (Craig, 1963; Giggenbach, 1992). The latter is due to non-equilibrium evaporation of steam at temperatures of 70° to 90°C (Craig, 1963).

The interpreted composition of fluids in equilibrium with the Cerro la Mina halloysite (Point B; Fig. 8.5) falls on the trend between the Cerro la Mina (1600 m) meteoric water and andesitic water composition; a trend commonly observed in acid geothermal waters (Line D; Fig. 8.5). Therefore, when considering halloysite mineral zonation and assemblages the fluid responsible for the formation of the halloysite is consistent with a hypogene origin comprising a mixture of meteoric and andesitic water at 60 to 110°C.

#### 8.5.4 Halloysite Hydrogen Exchange

Studies have shown that hydrogen isotopes in halloysite are measurably exchangeable with water vapour at room temperature on relatively short time scales (59 to 118 hours; Hsieh and Yapp, 1999). A laboratory study on halloysite detected deuterium/hydrogen isotopic exchange between interlayer and hydroxyl hydrogen and suggests that meaningful deuterium/hydrogen measurements may not be obtained from halloysite (Lawrence and Taylor, 1971). This exchange may be attributed to the immediate contact and hydrogen bonding between interlayer water and surface hydroxyls in halloysite (Giese, 1988). Therefore, it is possible that the Cerro la Mina halloysite has not preserved its

formation deuterium/hydrogen isotopic composition. A meteoric water signal could have also been achieved by not fully dehydrating the interlayer water of the halloysite which could have exchanged with ambient water vapour. The Cerro la Mina halloysite samples however were stored at 160°C for one week before isotopic analyses and are expected to have fully dehydrated their interlayer water.

### *8.5.5 Deep Position of Cerro la Mina Halloysite*

In addition to the oxygen-deuterium analysis, the deep position of the Cerro la Mina halloysite was considered. The maximum depth at which the halloysite is observed is 800 m vertically below the surface (drill hole IXCM07-20) where present day temperatures could be greater than supergene temperatures eliminating the possibility for a supergene origin. However, given the steep topography of the region the halloysite occurs at a minimum distance of 580 m from the nearest surface. Melchiorre et al. (2000), using an oxygen isotope thermometer, suggests that oxidation of massive sulfides deposits can produce shallow subsurface temperatures up to 25°C higher than local mean air temperatures indicating that supergene temperatures at Cerro la Mina can reach as high as 55°C. Minimum temperatures at 580 m below the surface would be approximately 30 to 40°C given a 25°C/km temperature gradient and within the range of supergene temperatures (<55°C; (Melchiorre et al., 2000). This temperature gradient is a conservative estimate, as Cerro la Mina is located in close proximity to an active tectonic boundary and active El Chichón volcano suggesting higher temperature gradients. Therefore, the deep position of the halloysite cannot be used to discriminate a possible hypogene origin for the Cerro la Mina halloysite.

## **8.6 Sulfur Isotope Discussion**

Possible influences on the sulfur isotope signature of sulfides and sulfates at the Cerro al Mina prospect are magmatic sulfur, sulfur in the volcanic rocks and a thick (> 770 m) sequence of Lower Cretaceous evaporites in the basement rocks. At the nearby El Chichón volcano ion-microprobe analyses of  $\delta^{34}\text{S}$  obtained on six ovoid-shaped inclusions of pyrrhotite, chalcopyrite and/or intermediate sulfide solid solution hosted by silicate or oxide crystals yielded  $\delta^{34}\text{S}$  values of -0.1 to +2.7 per mil with a mean of +0.7 per mil and are interpreted to be magmatic (Luhr et al., 2002). Total  $\delta^{34}\text{S}$  values are not available for the Selva Negra volcanic rocks, however, the average  $\delta^{34}\text{S}$  value for total sulfur (sulfide and sulfate) for andesites in island-arc environments have  $\delta^{34}\text{S}$  total values between +5 and +7 per mil (Ueda and Sakai, 1984; Woodhead et al., 1987). The lower Cretaceous contains a thick evaporite sequence with values ranging from approximately  $\delta^{34}\text{S}$  +18 to +24 per mil based on the seawater sulfate curve of Claypool et al. (1980).

Stage 1 and Stage 2 sulfide minerals have mean values of +0.2 to +0.4 per mil and are interpreted as magmatic in origin. Stage 4 sulfides have shifted to slightly heavier  $\delta^{34}\text{S}$  values (mean = +2.3 ‰) suggesting input from meteoric fluids that may have interacted with volcanic rocks or basement evaporites. Stage 3 sulfate probably has involvement of magmatic sulfur and sulfur derived from volcanic rocks or evaporite sequence. There were no sulfides that were stable with the barite for sulfide/sulfate geothermometry.

The sulfur isotope results are consistent with mineralogical observations where Stage 1 and 2 mineralisation are part of a late porphyry sericitic alteration (Stage B) dominated by magmatic waters. Stage 3 and 4 mineralisation is part of the kaolinite epithermal alteration (Stage C) where a mix of magmatic fluids that have interacted with meteoric fluids derived from the volcanic rocks and/or basement evaporites.

## 8.7 Conclusions

The oxygen-deuterium analysis of the Cerro la Mina halloysite was not able to discriminate between a supergene and hypogene origin. Instead it provided a means of describing the composition of water probably involved in the formation of the Cerro la Mina halloysite. Four interpretations can be made from the oxygen-deuterium study: (1) the Cerro la Mina halloysite oxygen-deuterium composition falls in a field typical of supergene kaolinite and halloysite from previous studies (Sheppard et al., 1969) consistent with a supergene origin given that the halloysite has not been enriched in  $\delta^{18}\text{O}$  during post mineralisation exchange with lower temperature meteoric water (e.g. Simone et al., 2005; Ece et al., 2008); (Fig. 8.4); (2) the fractionation trend for the Cerro la Mina halloysite meets the meteoric water line at 26°C and at a heavier composition than the Cerro la Mina meteoric water (~1500 m), and at the same composition as the Veracruz (16 m) meteoric water (Point C; Fig. 8.5). The composition is consistent with a hypogene origin if the weathering history occurred at high elevations. However, if a more complicated scenario of weathering history occurred at lower elevation the discrimination between supergene and hypogene origin is ambiguous; (3) mineral zonation and assemblages of the halloysite described in Chapter 5-6 suggests a temperature of formation between 60 and 110°C. A fluid in equilibrium with the Cerro la Mina halloysite at 60 to 110°C occurs on a trend commonly observed in acid geothermal waters and steam from hot spring areas where  $\delta^{18}\text{O}$  and  $\delta\text{D}$  are systematically enriched along linear trends between meteoric water and andesitic water (Line D; Fig. 8.5; Craig, 1963; Giggenbach, 1992). Therefore, the oxygen-deuterium analysis results are consistent with a hypogene origin comprising a mixture of meteoric and andesitic water at temperatures of 60 to 110°C for the Cerro la Mina halloysite; and (4) the halloysite has undergone major partial deuterium/hydrogen isotope exchange with the local Chiapas meteoric water and the values are meaningless. The author favours the third interpretation that is consistent with a hypogene origin comprising a mixture of meteoric and andesitic water at temperatures of 60 to 110°C for the Cerro la Mina halloysite. This interpretation is consistent with textural observations discussed in the Chapter 5 and 6 that also suggest that the halloysite is hypogene in origin.

Sulfur isotope data suggest that Stage 1 and 2 mineralisation precipitated from magmatic fluids. The sulfur isotopes of epithermal mineralisation Stage 3 and 4 shifts to heavier  $\delta^{34}\text{S}$  values suggesting a mix of magmatic waters and meteoric waters that have interacted with volcanic rocks and/or evaporite units in the basement. Stage 3 and 4 mineralisation are associated Stage C alteration consistent with a hypogene origin for halloysite (Stage  $C_{\text{HK}}$ ). The results of both oxygen-deuterium and sulfur isotope studies are complimentary, suggesting a mixture of meteoric and magmatic water is responsible for the formation of halloysite (Stage  $C_{\text{HK}}$ ) and Stage 4 epithermal mineralisation.

# Chapter 9 - Genesis of the Cerro la Mina Prospect

## 9.1 Introduction

The genetic model of the Cerro la Mina prospect is described here by pulling together the observations made for the igneous geochemistry, geology, alteration, mineralisation in addition to geochronology and stable isotope results. This information is then compared with other porphyry-epithermal deposits and how the Cerro la Mina prospect is distinct. The chapter ends with a conclusion.

## 9.2 Genesis

### 9.2.1 Tectonic Setting and Volcanism

Cerro la Mina is located in a unique setting characterized by a complex triple junction between the North American, Caribbean, and Cocos plates (Nixon, 1982; Burbach et al., 1984). The Cocos plate began subducting below the North American and Caribbean plates during the middle Miocene (Meneses-Rocha, 2001) and initiated volcanism in the Sierra Madre volcanic arc, along the Pacific coast, parallel to the Middle American trench and ceased around 9 Ma (Damon and Motesinos, 1978; Meneses-Rocha, 2001). Around 3 Ma, the volcanic arc moved inland and approximately 30° oblique to the Middle American trench, with the onset of the modern Chiapanecan volcanic arc (CVA) using northwest orientated strike-slip faults as magma conduits (Damon and Motesinos, 1978; García Palomo et al., 2004; Manea and Manea, 2006; Mora et al., 2007). The northwest strike-slip faults are a continuation of the western-most part of the Motagua-Polochic sinistral fault, which separates the North American and Caribbean plates (Guzman-Speziale and Meneses-Rocha, 2000; Meneses-Rocha, 2001).

The Chiapanecan volcanic arc is, with the exception of anomalous high-K El Chichón and shoshonitic Selva Negra volcanic rocks, calc-alkaline in composition and related to the subducting Cocos plate (Mora et al., 2007). The shoshonitic rocks of the Selva Negra are attributed to the inland location (300 to 330 km) of the strike-slip zone from the trench that has allowed low degree partial melts, generated by the deep position (200 to 220 km; Rebollar et al., 1999) of the subducting Cocos plate, to reach the surface. Widespread monzodiorite to diorite intrusions of the Selva Negra region are associated with a large magnetic high and crystallized around 1.0 Ma (zircon U-Pb ages). The ascending magmas interacted with the thick crust (~50 km) through MASH processes giving the rocks radiogenic Nd, Sr, and Pb isotopes and enriched LILE. Assimilation of the crust is consistent with zircons in volcanic rocks that have yielded ages similar to the pre-Mesozoic metamorphic, sedimentary, and igneous basement (Chiapas Massif; Sánchez-Montes De Oca, 1979; Schaaf et al., 2002; Weber et al., 2005) and the occurrence of limestone xenoliths at El Chichón. The combination of low degree partial melts of a heterogeneous mantle enriched in LILE and LREE, and crustal contamination, resulted in a shoshonitic and enriched LILE geochemistry for the Selva Negra volcanic rocks. The effects of the subducting Tehuantepec ridge, whose onshore propagation lies directly below the

Selva Negra, on the geochemistry are uncertain as crustal contamination may be diluting the signal.

### 9.2.2 Geologic Framework

The Cerro la Mina prospect is hosted in the trachyandesitic, Pleistocene Selva Negra volcanic rocks which overlie Mesozoic sedimentary rocks and Cenozoic sedimentary rocks (Fig. 9.1). U-Pb ages on volcanic rocks in the Selva Negra region suggest volcanism occurred from ~1.2 to at least ~0.75 Ma. The Cerro la Mina stratigraphy comprises ignimbrites (Unit 1; pyroclastic flow deposits), syn-volcanic domes (Unit 3A and 3B), debris and mass flows (Unit 3C) and rare basalts (Fig. 9.1). The Cerro la Mina volcanic stratigraphy is similar to the regional volcanism of the Chiapanecan volcanic arc that comprises low profile (< 850 m high), small-volume (3 to 4 km<sup>3</sup>) volcanic domes with associated pyroclastic flow deposits comprising rare basalts, porphyritic hornblende andesites, trachyandesites, and minor rhyodacites and rhyolites (Damon and Motesinos, 1978; Duffield et al., 1984; Mora et al., 2007). The Cerro la Mina prospect probably developed on the flanks of a volcano similar to El Chichón and probably in a graben setting where there is large input of debris flows.

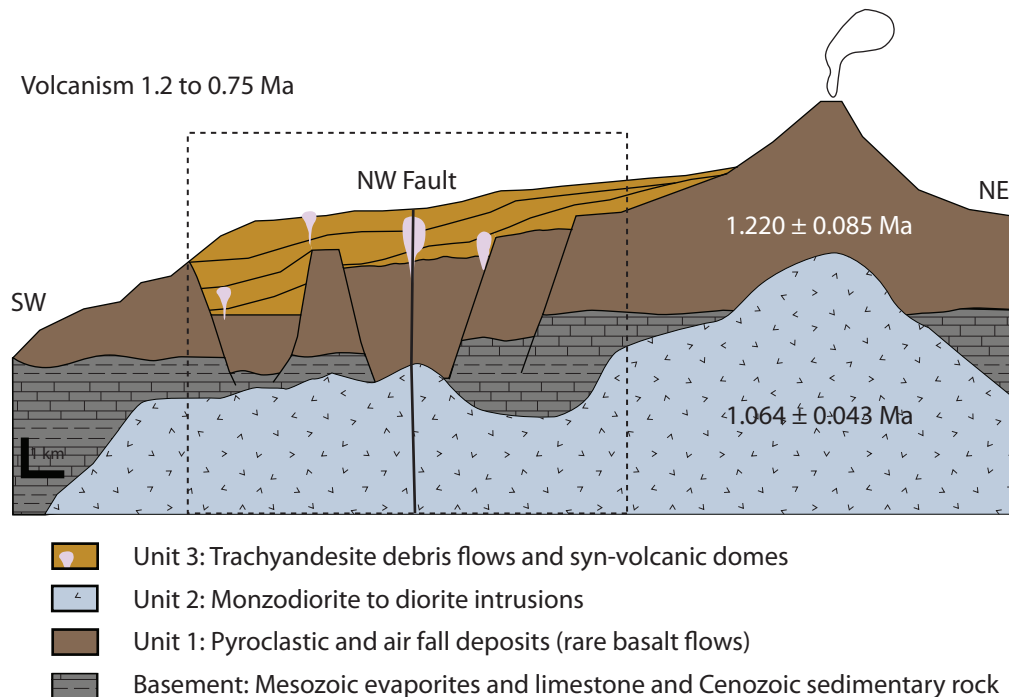


**Figure 9.1** Schematic presentation of the geologic setting for the Cerro la Mina prospect. The prospect developed on the flanks of volcano similar to El Chichón and probably in a graben setting where there was a large input of debris flows. Geologic units described in detail in Chapters 2, 3 and 4. Ages are U-Pb on zircon from Chapter 7. Dashed box is the location of Figure. 9.2.

### 9.2.3 Hydrothermal System

Volcanism was followed by a hydrothermal system consisting of an epithermal superimposed onto a weakly developed porphyry system. The formation of a breccia pipe and the northwest trending sinistral strike-slip fault structure provided the plumbing for the ensuing hydrothermal system. The hydrothermal system consists of four mineralisation stages associated with three stages of alteration

comprising potassic (Stage A), sericitic (Stage B) and kandite (Stage C) alteration.

### 9.2.3.1 Porphyry Cu-Mo Stage

Porphyry style alteration began with quartz, potassium feldspar and biotite (Stage A) and is representative of a potassic zone in a porphyry-Cu alteration (Lowell and Guilbert, 1970; Seedorff et al., 2005). Pre-breccia pipe potassic alteration (Stage A) and Stage 1 pyrite (Fig. 9.2A) is crosscut by the vertically-orientated breccia pipe (Unit 4) formed by the explosive release of hydrothermal fluids from an inferred intrusion at depth causing brecciation of the overlying rocks (Fig. 9.2B). Potassic alteration continued after breccia formation and is followed sericitic alteration (Stage B) typical of a porphyry-Cu phyllic alteration zone (Fig. 9.2C; Lowell and Guilbert, 1970; Seedorff et al., 2005) comprising quartz, muscovite, illite, illite/smectite, chlorite, calcite, gypsum and tourmaline. An inferred porphyry intrusion at depth created a quartz-muscovite altered core centred on the breccia pipe with increasingly lower temperature clay assemblages distally (Fig. 9.2C). The temperature zonation is consistent with decreasing Al-OH and increasing crystallinity in SWIR spectra towards the breccia pipe.

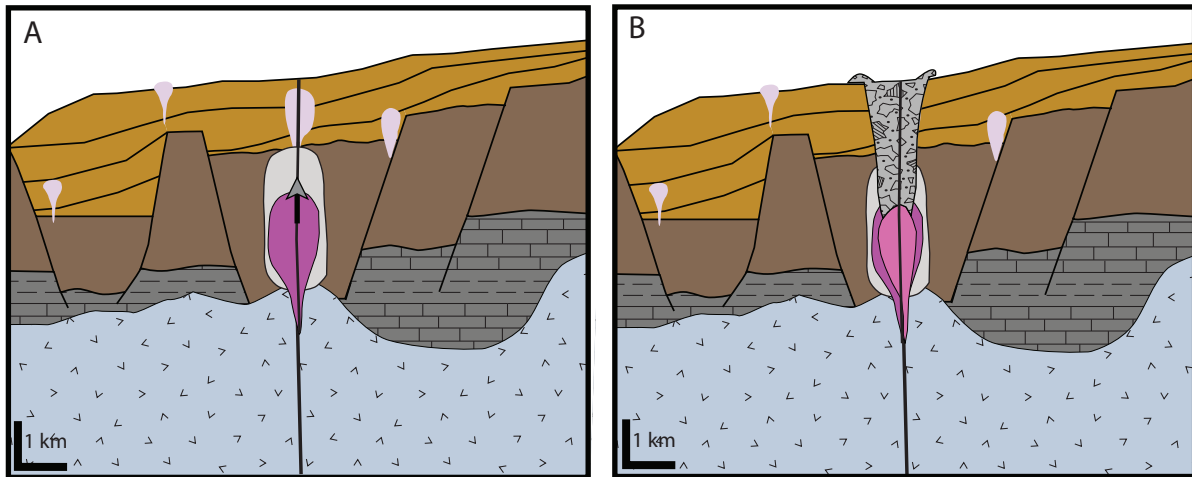
Textures suggest that Stage A alteration was active before and after breccia pipe formation. Stage 1 pyrite infills potassic veins and are together fractured to a jigsaw-fit texture, consistent with a pre-brecciation timing (Figs. 9.2A and B). Stage B alteration is associated with inclusion-rich pyrite  $\pm$  chalcopyrite  $\pm$  molybdenite veins and disseminations (Stage 2 mineralisation) that are most abundant in the quartz + muscovite  $\pm$  illite core. Molybdenite yielded an age of  $0.780 \pm 0.010$  Ma (Re-Os age). Sulfur isotope data suggest that Stages 1 and 2 pyrite precipitated from magmatic fluids and have oscillatory zoning of Co, Ni and Se with local arsenic-rich zones (Figs. 9.2A and C). The high temperature core (quartz + muscovite  $\pm$  illite) is associated with the highest Co, Ni and Se concentrations and decrease distally coincident with decreasing temperature clay assemblages away from the breccia pipe. Stage 2 introduced significant Cu and Mo into the system and their ore grade shells have a vertical orientation coincident with the shape of the breccia pipe.

### 9.2.3.2 Epithermal Au-Cu Stage

The hydrothermal system cooled below 300°C at  $0.689 \pm 0.013$  Ma (hydrothermal biotite Ar-Ar age) with the onset of Stage 3 and 4 mineralisation associated with kandite alteration (Stage C; Fig. 9.2D). Kandite alteration (Stage C) and mineralisation (Stages 3 and 4) represents a high sulfidation epithermal system (e.g., Arribas, 1995; Hedenquist, 2000) that has been telescoped onto a porphyry-Cu system, suggesting significant uplift has occurred or a sector collapse (e.g., Sillitoe, 1994).

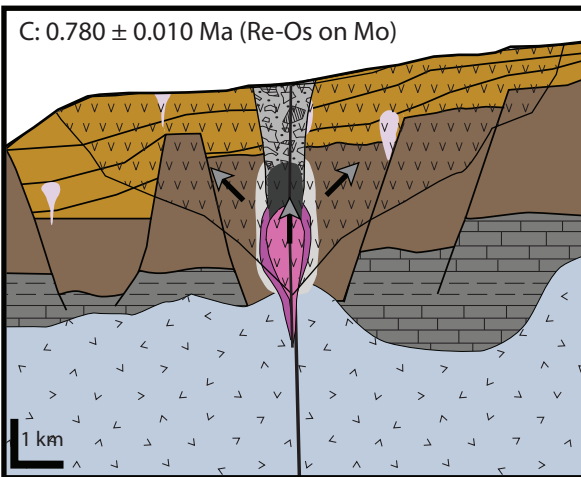
Kandite alteration (Stage C) is separated into two coeval zones, Stage C<sub>QD</sub> comprising quartz, dickite and lesser pyrophyllite, alunite and kaolinite, and Stage C<sub>HK</sub> comprising halloysite and kaolinite. Upper Cretaceous detrital-calcareous units have a wide distribution in the uppermost 4 km of the Chiapas crust (Fig. 2.3; Hernández-García, 1973; Taran et al., 1998) and probably buffered the acidic fluids from producing vuggy quartz typical for most high sulfidation systems.

Arsenic concentrations in pyrite and marcasite increased from the early high temperature and

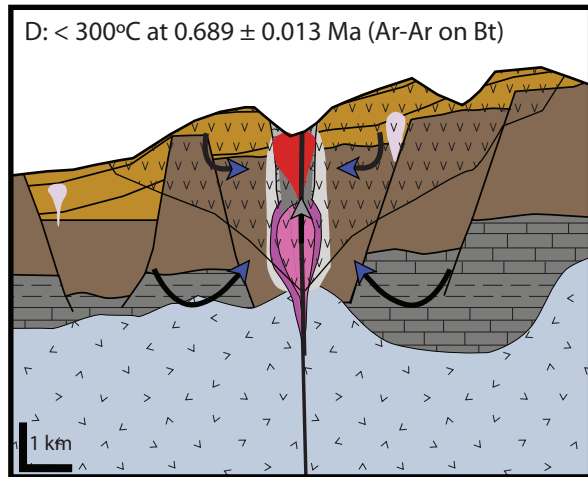


**A**  
Pre-Breccia Pipe: Potassic Alteration and Stage 1 Mineralisation  
Py:  $\delta^{34}\text{S} = +0.7 \text{ ‰}$

**B**  
Breccia Pipe Formation



**C:**  $0.780 \pm 0.010 \text{ Ma}$  (Re-Os on Mo)  
Potassic + Sericitic Alteration + Stage 2 Mineralisation  
Py + Cpy:  $\delta^{34}\text{S} = +0.2 \text{ ‰}$



**D:**  $< 300^\circ\text{C}$  at  $0.689 \pm 0.013 \text{ Ma}$  (Ar-Ar on Bt)  
Kandite Alteration + Stage 3 and Stage 4 Mineralisation  
Py:  $\delta^{34}\text{S} = +2.3 \text{ ‰}$   
Hall:  $\delta^{18}\text{O} = +20.2 \text{ ‰}$   $\delta\text{D} = -59.4 \text{ ‰}$

- Inferred porphyry intrusions
- Pre-breccia pipe potassic alteration and Stage 1 mineralisation
- Post-breccia pipe potassic alteration
- Sericitic alteration + Stage 2 mineralisation
- Kandite alteration + Stages 3 and 4 mineralisation
- Magmatic water
- Meteoric water

**Figure 9.2** Schematic diagrams illustrating the formation of the Cerro la Mina Au (Cu-Mo) prospect. Alteration and mineralisation stages are explained in text. Sulfur isotopes and oxygen-deuterium values from Chapter 8. Location of diagram outlined with a dashed box in Figure 9.1. View is towards the northwest. **Abbreviations:** Bt - biotite, Cpy - chalcopyrite, Hall - halloysite, Mo - molybdenite, Py - pyrite.

porphyry stages (1 and 2) and are highest in the low temperature epithermal stages (3 and 4). Stage 3 comprises marcasite + sphalerite + galena + barite, and Stage 4 consists of ragged pyrite + enargite + rimming pyrite + fine-grained pyrite. Stages 3 and 4 occur in kaolinite cemented hydrothermal breccias, veins and disseminations. Stages 3 and 4 mineralisation have similar geochemistry, being enriched in As, Cu, Au, Zn, Mn, Sb, Pb, Ag, Tl, Te and Bi, typical of high sulfidation epithermal systems (Hedenquist et al., 1994). Sulfur isotope data of epithermal mineralisation Stage 3 and 4 suggests a mix of magmatic waters and meteoric waters that have interacted with volcanic rocks and/or evaporite units in the basement (Fig. 9.2D).

### 9.2.3.3 Halloysite Formation

Extensive halloysite developed in the advanced argillic kaolinite alteration (Stage C). Abundant kaolinite relative to halloysite occurs close to the quartz-dickite alteration (Stage C<sub>QD</sub>) and thick rimmed pyrite (Stage 4) whereas the abundance halloysite relative to kaolinite increased distal to Stage C<sub>QD</sub> in association with increasingly thinner rimming pyrite. SEM imaging shows that halloysite developed as cylindrical tubes predominantly on potassium feldspar and sericite into sheet-like morphology of kaolinite with the progression of alteration. Oxygen-deuterium isotopes suggest a hypogene fluid comprising a mixture of meteoric and andesitic water at temperatures of 60 to 110°C for the formation of the Cerro la Mina halloysite.

### 9.2.4 Present Day

At present the northwest fault, with a strike orientation of 308° and sub-vertical, offsets the stratigraphy, alteration and mineralisation by approximately 200 m horizontally and 500 m vertically (Fig. 9.3). The northwest fault is consistent with the regional, left-lateral, strike-slip structural regime in which it occurs (Meneses-Rocha, 2001; García-Palomo et al., 2004).

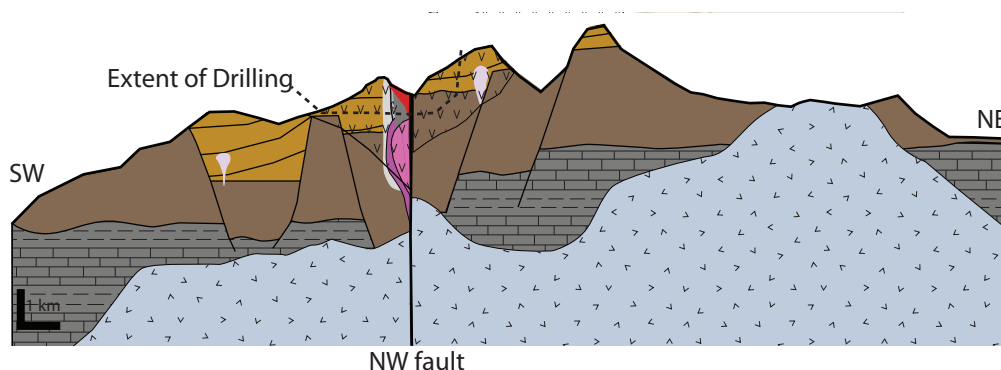


**Figure 9.3** Schematic illustrating Cerro la Mina prospect at present day where geology, alteration and mineralisation are off-set horizontally and vertically by the northwest fault. View towards the northwest. Approximate extent of drilling to date shown. Legend shown in Figures 9.1 and 9.2.

## 9.3 Cerro la Mina in Relation to World Deposits

The Cerro la Mina Au (Cu-Mo) prospect is a weakly mineralised system hosted in alkaline rocks where the alteration and mineralisation mainly occurs in a breccia pipe. The prospect has both porphyry and high sulfidation affinities.

### 9.3.1 Alkalic Affinity

A porphyry stock related to the porphyry mineralisation at Cerro la Mina has not been intersected. However, the composition of the porphyry stock is probably alkaline consistent with the regional volcanic rocks in which it is hosted. Alkalic porphyry deposits are reasonably well-documented from British Columbia (e.g., Lang et al., 1995a; Schroeter, 1995) and eastern Australia (e.g., Heithersay and Walshe, 1995; Lickfold et al., 2003; Wilson et al., 2003; Cooke et al., 2007; Wilson et al., 2007) but few examples have been described from other terrains (Jensen and Barton, 2000). Key characteristics of alkalic rocks associated with gold deposits are their hydrous and oxidized nature, as well as their ability to produce hydrothermal systems with ideal chemistries for transporting gold (Richards, 1995). Alkalic Au (Cu) porphyry deposits include some of the world's highest-grade porphyry gold resources and some of the largest gold accumulations in epithermal environments (Jensen and Barton, 2000; Mungall, 2002).

Calc-potassic assemblages are a distinguishing feature of alkalic porphyry deposits; e.g., Ridgeway (Holliday et al., 2002; Wilson et al., 2003), Mt. Polley (Lang et al., 1995b). Calc-potassic assemblages are enclosed by a propylitic halo that changes from hematite-present to hematite absent outward from the deposit centre (Wilson et al., 2003). Mt. Polley is a silica-undersaturated alkalic Cu-Au system associated with hematite-dusted potassium feldspar – magnetite  $\pm$  biotite (potassic assemblage) and garnet-bearing assemblages (calc-potassic) that pass upwards to biotite – chlorite and downwards to actinolite – epidote (Lang et al., 1995b).

High sulfidation epithermal gold deposits are uncommon for alkaline suites which is interpreted to be a result of highly efficient buffering of acidic fluid by metasomatised alkaline rocks (Sillitoe, 2002). Alkaline suites typically have low-sulfidation affinities, e.g., Ladolam, Lihir island (Müller et al., 2001), Cripple Creek (Thompson et al., 1985; Jensen, 2003), and Porgera (Cooke and Simmons, 2000; Ronacher et al., 2004).

The sulfur isotopic composition of sulfides from alkalic porphyry and epithermal deposits, e.g., Mt. Polley BC, (Deyell, 2005), Northparkes and Cadia, NSW (Heithersay and Walshe, 1995; Wilson et al., 2007), Lihir (Gemmell et al., 2004), Porgera (Richards and Kerrich, 1993) are typically negative, a feature characteristic of sulfides deposited from oxidized (sulfate predominant) magmatic fluids (Rye, 1993; Wilson et al., 2007). These oxidised fluids discriminate alkalic epithermal deposits from their reduced calc-alkalic counterparts, which have sulfide minerals with homogeneous, positive sulfur isotopic compositions, e.g., Kerikil (Wurst, 2004) and Kelian (Davies et al., 2008).

The potassic alteration at Cerro la Mina is consistent with a calc-alkaline porphyry deposit with early, high-temperature potassium feldspar  $\pm$  biotite assemblages to muscovite  $\pm$  chlorite

assemblages (sericitic alteration) and low-temperature, advanced argillic clay-bearing assemblages (Seedorff et al., 2005) unlike calc-potassic assemblages that are a distinguishing feature of alkalic porphyry deposits. A high sulfidation affinity for Cerro la Mina is consistent with a calc-alkaline geochemistry which are uncommon for alkaline suites. The sulfur isotopes at Cerro la Mina range from -2.49 to +4.89 per mil (mean = +0.73‰) consistent with a reduced calc-alkalic system and dissimilar to typically negative, oxidized (sulfate predominant) magmatic fluids for alkalic systems.

### 9.3.2 Breccia Pipes

Breccia pipes are common in the porphyry-epithermal environment. Like Cerro la Mina, porphyry deposits can be emplaced into pre-existing breccia pipes or diatremes, e.g. Boyongan (Braxton, 2007), Grasberg (MacDonald and Arnold, 1994) and Lihir (Müller et al., 2002). Many porphyry deposits have breccia pipes as a significant part of the deposit, either mineralised, e.g., Rio Blanco – Los Bronces (Warnaars et al., 1985); or barren, like El Teniente, where the breccia pipe was the last major magmatic-hydrothermal event (Maksaev et al., 2004). Epithermal deposits are also known to be hosted in breccia pipes, e.g. Cripple Creek (Thompson et al., 1985), Kelian (Davies et al., 2008). Lihir (Müller et al., 2002) and Martabe (Sutopo et al., 2003).

### 9.3.3 Halloysite

Halloysite is not an abundant hypogene mineral in high sulfidation deposits and is traditionally regarded as supergene (e.g., Hedenquist, 2000). However at Cerro la Mina its deep extent and association with sulfides is consistent with a hypogene origin. The halloysite is observed in veins and wall rock alteration associated with gold-bearing sulfides below the oxide zone. **In addition, the halloysite is developed to at least 800 m below the present day surface in the fluid pathway of the breccia pipe, deeper than the hypogene clay minerals dickite, alunite, and pyrophyllite.** A TerraSpec study shows that the relative abundance of halloysite to kaolinite changes in association with the thickness of rimming pyrite (Stage 4) and SEM imaging revealed the transition from halloysite to kaolinite. Banded veins of alternating halloysite + kaolinite and Stage 3 mineralisation occur at Cerro la Mina; a supergene origin for this vein type would require a complicated scenario of alternating supergene and hypogene conditions. All the above evidence indicates that the halloysite is hypogene in origin. Kaolinite is a common mineral in high sulfidation deposits (Hedenquist et al., 1994; Arribas, 1995; Hedenquist et al., 1998). Distinguishing halloysite from kaolinite is complicated by dehydration, as discussed in Chapter 5, and may be underestimated in high sulfidation deposits.

### 9.3.4 Lithocap

Previous workers at the Cerro la Mina prospect proposed that the alteration at Cerro la Mina was typical of lithocap (Miranda-Gasca et al., 2009). Sillitoe (1995) defines a lithocap to comprise advanced argillic alteration with vuggy quartz, chalcedony and crystalline alunite grading outwards to assemblages comprising one or more of kaolinite, dickite, sericite, pyrophyllite and diaspore. The Cerro la Mina prospect does not have vuggy quartz and alunite is not abundant. The Upper Cretaceous detrital-calcareous units have a wide distribution in the uppermost 4 km of the Chiapas crust (Fig.

2.3; Hernández-García, 1973; Taran et al., 1998) and probably buffered the acidic fluids from producing vuggy quartz. Therefore, the Cerro la Mina prospect does not have characteristics consistent with a lithocap but it is consistent with an advanced argillic clay-altered breccia pipe with high sulfidation affinities.

## 9.4 Conclusions

The genesis of the Cerro la Mina prospect is attributed to the complex triple junction setting in which it is situated. The inland extension of the Motagua-Polochic sinistral fault, separating the North American and Caribbean plates, extends into southeastern Mexico and allowed magmas generated by the subducting Cocos plate to the surface with a shoshonitic composition. A hydrothermal system followed also using these sinistral faults with alteration typical of porphyry and high sulfidation systems associated with four stages of mineralisation.

The Cerro la Mina prospect has potassic alteration with an advanced argillic overprint and heavy sulfur isotopic values consistent with a reduced calc-alkaline system. This is unusual as the geochemistry of the volcanic rocks and intrusions are alkaline and may suggest that calc-alkaline magmatism, not yet intercepted in the district, may be related to the alteration and mineralisation. The mineralisation and alteration is hosted in a breccia pipe and these are common attributes in epithermal-porphyry districts. The advanced argillic alteration is not typical of a lithocap with no vuggy quartz and very little alunite consistent with fluids interacting with the basement evaporite and limestone. Abundant hypogene halloysite is also unusual although the identification of halloysite is complicated by dehydration and may be underestimated in high sulfidation deposits.

## Chapter 10 - Conclusions

### 10.1 Tectonic Setting

Cerro la Mina is located in a tectonic setting characterized by a complex triple junction between the North American, Caribbean, and Cocos plates (Nixon, 1982; Burbach et al., 1984). The state of Chiapas consists of a pre-Mesozoic metamorphic, sedimentary, and igneous rocks, overlain by Mesozoic detrital-calcareous units and Cenozoic interbedded sandstone and siltstone (Escandón Valle et al., 2006; Sánchez-Montes De Oca, 1979).

Volcanism in Chiapas began with the onset of subduction of the Cocos plate below the North American and Caribbean plates and the initiation of the Sierra Madre volcanic arc along the Pacific coast, parallel to the Middle American trench and ceased around 9 Ma (Fig. 2.3; Damon and Motesinos, 1978; Meneses-Rocha, 2001). The volcanic arc moved inland and approximately 30° oblique to the Middle American trench with the onset of the modern Chiapanecan volcanic arc around 3 Ma, using the northwest orientated strike-slip fault zone as magma conduits (Fig. 2.2; Damon and Motesinos, 1978; García Palomo et al., 2004; Manea and Manea, 2006; Mora et al., 2007). The strike-slip fault zone is a continuation of the Motagua-Polochic sinistral fault zone which separates the North American and Caribbean plates extending into southeastern Mexico (Guzman-Speziale and Meneses-Rocha, 2000; Meneses-Rocha, 2001).

### 10.2 Selva Negra Geochemistry

The Selva Negra volcanic rocks consist of widespread monzodiorite to diorite intrusions with a crystallization age of around 1.0 Ma (zircon U-Pb), trachyandesite volcanic rocks and rare basalt flows. The shoshonitic and LILE-rich composition of the Selva Negra is the result of low degree partial melts which have ascended along the inland faults of the strike-slip zone 300 to 330 km from the trench. The radiogenic isotope data suggest that the ascending magmas interacted with the thick crust (~50 km) through MASH processes. The combination of low degree partial melts of a heterogeneous mantle enriched in LILE and LREE, and crustal contamination resulted in a shoshonitic and enriched LILE geochemistry for the Selva Negra volcanic rocks.

### 10.3 Cerro la Mina Geology

The Cerro La Mina volcanic succession is divided into four major units that are described using non-genetic terminology. A lower succession of clast-supported to matrix-supported fiamme-bearing volcanoclastic breccias (Unit 1) are intruded by equigranular monzodiorite to diorite bodies (Unit 2). Unit 1 is overlain by feldspar-phyric trachyandesites and associated monomictic breccias that transition distally to abundant, thick beds of polymictic breccias in the middle part of the succession (Unit 3). The final unit cross-cuts all of the previous units and forms a predominantly matrix-rich, granule breccia (Unit 4). This unit is characterized by abundant clasts of the basement monzodiorite to diorite, clasts within clasts, and clasts containing early pyrite veins. It is observed to have a vertical orientation as it is recognized at various elevations from the surface to the maximum drill hole depth

of 800 metres below surface, implying vertical emplacement. On the rims of the matrix-rich, granule breccia, a breccia containing clasts of the wall rock stratigraphy is observed. A major northwest fault that off-sets the stratigraphy 500 m vertically and 200 m left laterally is probably part of the regional strike-slip fault zone which is composed of a set of up thrown and downthrown blocks, bounded by left-lateral strike-slip faults (García-Palomo et al., 2004; Meneses-Rocha, 2001).

Genetically, the volcanic stratigraphy likely represents ignimbrites (Unit 1) that are intruded by monzodiorites to diorites (Unit 2). Unit 1 is overlain by debris flows or lahars and trachyandesite syn-volcanic domes and associated autoclastic rocks (Unit 3). U-Pb ages for volcanic rocks in the Selva Negra indicate volcanism occurred from ~1.2 to at least ~0.75 Ma. The matrix-rich, granule breccia (Unit 4) is inferred to be a breccia pipe formed by the explosive release of hydrothermal fluids from an inferred intrusion at depth causing brecciation of the overlying rocks.

## 10.4 Alteration and Mineralisation

The breccia pipe is important as it hosts all of the significant alteration and mineralisation drilled to date. Higher grades also occur in structures related to the northwest fault. Dickite-cemented breccias, host the highest average grades of 0.7 ppm Au, 0.23% Cu and 131 ppm Mo. No resource estimate has been carried out.

### 10.4.1 Porphyry System

The porphyry-style alteration includes early potassic (quartz + potassium feldspar ± biotite) veins and wall rock alteration (Stage A), and later sericitic alteration (Stage B). The potassic alteration (Stage A) comprises coarse- to fine-grained pervasive potassium feldspar replacement of the volcanoclastic groundmass. Hydrothermal potassium feldspar is intergrown with quartz with lesser very fine-grained biotite occurring as irregular amasses. The potassic veins are infilled with late fractured pyrite (Stage 1) that has been fractured to a jigsaw-fit texture, consistent with its pre-brecciation timing. Potassic alteration occurred after breccia pipe formation, altering the matrix of the matrix-rich, granule breccia (Unit 4). The potassic alteration (Stage A) is not associated with significant mineralisation. Sulfur isotope data suggest that Stage 1 pyrite precipitated from magmatic fluids and are enriched and have oscillatory zoning of Co, Ni and Se with local arsenic-rich zones (LA-ICP-MS mapping).

A late sericitic alteration (Stage B) consists of quartz, muscovite, illite, illite/smectite, chlorite, calcite, gypsum (after anhydrite), and tourmaline. Stage B alteration typically is silicified and grey and occurs as pervasive and vein alteration. Stage 2 molybdenite yielded an age of  $0.780 \pm 0.010$  Ma (Re-Os). The sericitic alteration (Stage B) is zoned, with a quartz + muscovite ± illite ± gypsum centred on the breccia pipe that transitions to quartz + illite ± muscovite ± tourmaline ± gypsum, illite/smectite ± smectite ± gypsum, and illite/smectite + calcite + chlorite ± smectite distally. This zonation reflects decreasing temperature outward from the centre (Corbett and Leach, 1998). Sericitic altered rocks host Cu-Mo mineralisation consisting of inclusion-rich pyrite ± chalcopyrite ± molybdenite veins and disseminations (Stage 2) that are most abundant in the quartz + muscovite ± illite

core of the sericitic alteration (Stage B). The inclusion-rich pyrite becomes the most dominant sulfide distally. The Cu and Mo ore grade shells have a vertical orientation coincident with the shape of the breccia pipe. Sulfur isotope data suggest that Stage 2 pyrite precipitated from magmatic fluids and is enriched and have oscillatory zoning of Co, Ni and Se with local arsenic-rich zones similar to Stage 1. The high temperature quartz-muscovite alteration is associated with the highest Co, Ni and Se concentrations in inclusion-rich pyrite which decrease distally, coincident with decreasing temperature clay assemblages.

#### 10.4.2 Epithermal System

The hydrothermal system cooled below 300°C at  $0.689 \pm 0.013$  Ma (hydrothermal biotite Ar-Ar age) with the onset of Stage 3 and 4 mineralisation associated with advanced argillic kandite alteration (Stage C). The late advanced argillic alteration in this prospect includes abundant quartz and kandite group minerals and minor alunite and pyrophyllite. The strongest kandite alteration (Stage C) occurs in a 500 m wide and 600 m deep zone in the breccia pipe altering the rock to a light grey to white. The kandite alteration (Stage C) grades between the quartz-dickite (Stage C<sub>QD</sub>) and halloysite-kaolinite zones (Stage C<sub>HK</sub>). The Stage C<sub>QD</sub> zone is a small pod of quartz + dickite ± pyrophyllite ± alunite ± kaolinite occurring at the surface to 200 metres depth. The transition from the Stage C<sub>QD</sub> to Stage C<sub>HK</sub> alteration is marked by the loss of dickite and halloysite + kaolinite becoming the dominant species. The lower halloysite + kaolinite zone (Stage C<sub>HK</sub>) extends to at least 800 metres below the surface.

The kandite-altered rocks host Au-Cu mineralisation consisting of arsenian-pyrite, marcasite, enargite, galena, sphalerite, and barite. Mineralisation in the quartz-dickite zone consists of arsenian-pyrite + enargite + galena + sphalerite + barite (Stage 3 and 4). In the halloysite-kaolinite zone mineralisation consists of marcasite + arsenian-pyrite ± sphalerite ± galena ± barite (Stage 3 and 4). The sulfides occur in breccia cement, veins, and disseminations. The breccias range from chaotic, jigsaw-fit to mosaic dickite or halloysite-kaolinite cemented.

Stages 3 and 4 mineralisation have similar geochemistry, being enriched in As, Cu, Au, Zn, Mn, Sb, Pb, Ag, Tl, Te and Bi, typical of high sulfidation epithermal systems (Hedenquist et al., 1994). Sulfur isotope data of epithermal mineralisation Stage 3 and 4 suggests a mix of magmatic waters and meteoric waters that have interacted with volcanic rocks and/or evaporite units in the basement

The advanced argillic alteration is the kandite overprint which consists dominantly of the minerals halloysite 10Å ( $\text{Al}_2\text{Si}_2\text{O}_5(\text{OH})_4 \cdot 2 \text{H}_2\text{O}$ ), halloysite 7Å ( $\text{Al}_2\text{Si}_2\text{O}_5(\text{OH})_4$ ), kaolinite ( $\text{Al}_2\text{Si}_2\text{O}_5(\text{OH})_4$ ), and dickite ( $\text{Al}_2\text{Si}_2\text{O}_5(\text{OH})_4$ ). The kandite minerals were identified with the SWIR spectra and confirmed with XRD and SEM imaging (this study and Kyne, 2009).

#### 10.4.3 Halloysite

The kandite alteration (Stage C) contains abundant halloysite to at least 800 m associated with sulfides below the present day surface. Traditionally the low temperature halloysite clay is thought to

be a supergene mineral (e.g., Hedenquist, 2000). However, at Cerro la Mina the halloysite occurs in veins and wall rock alteration associated with gold-bearing sulfides below the oxide zone. In addition, the halloysite is developed to at least 800 m below the present day surface in the fluid pathway of the breccia pipe, deeper than the hypogene clay minerals dickite + alunite + pyrophyllite. A TerraSpec study shows that the relative abundance of halloysite to kaolinite changes in association with the thickness of rimming pyrite (Stage 4).

A SEM study shows that the halloysite-kaolinite alteration (Stage  $C_{HK}$ ) at Cerro la Mina is predominantly characterised by halloysite tubes that coalesce into aggregates and thin sheets of kaolinite. The halloysite tubes begin with the development of a spheroid on the parent mineral. The spheroid then grows parallel to the parent surface and with continued growth extends away from the surface. Further growth of multiple tubes causes them to interconnect and coalesce into aggregates with the most advanced form producing a sheet-like morphology comprised of kaolinite. The same development and transition of halloysite to kaolinite is observed in the weathering profile of anorthosite (Jeong, 1998) and in hydrothermal alteration (Papoulis et al., 2009). At Cerro la Mina the dominant parent minerals of halloysite were observed to be potassium feldspar and muscovite, indicating that the halloysite-kaolinite alteration (Stage  $C_{HK}$ ) is late stage.

All the above evidence indicates that the halloysite is hypogene in origin. With an increased understanding of this deep kaolinite alteration (Stage C) the exploration window is widened for the discovery of valuable deposits in the epithermal-porphyry environment.

## 10.5 Genesis

The geology and genesis of the Cerro la Mina prospect is attributed to the complex triple junction setting in which it is situated. The inland extension of the Motagua-Polochic sinistral fault, separating the North American and Caribbean plates, extends into southeastern Mexico and allowed magmas generated by the subducting Cocos plate to the surface with a shoshonitic composition. A hydrothermal system followed, also using these sinistral faults, with alteration typical of porphyry and high sulfidation systems associated with four stages of mineralisation.

The Cerro la Mina prospect has a porphyry potassic alteration with a advanced argillic overprint and heavy sulfur isotopic values consistent with a reduced calc-alkalic system. This is unusual as the geochemistry of the volcanic rocks and intrusions is alkalic and may suggest that calc-alkaline magmatism, not yet recognised in the district, may be related to the alteration and mineralisation. The mineralisation and alteration is hosted in a breccia pipe and these are common attributes in epithermal-porphyry districts. The advanced argillic alteration is not typical of a lithocap with no vuggy quartz and very little alunite consistent with fluids interacting with the basement evaporite and limestone. Abundant hypogene halloysite is unusual although the identification of halloysite is complicated by dehydration and may be underestimated in high sulfidation deposits.

## 10.6 Exploration Implications

The Cerro la Mina prospect occurs outside the major metallogenic provinces of Mexico in significantly younger volcanic rocks ( $< 5$  Ma; Damon and Motesinos, 1978). The Santa Fé skarn and Campamento epithermal deposits are the only other mineralisation known. Modern exploration has only taken place since 2000 making the region prospective for epithermal, porphyry and skarn mineralisation.

### 10.6.1 Tectonics and Geology

Well-endowed porphyry and/or epithermal mineral provinces are closely related to the subduction of aseismic ridges which promote flat-slab subduction, crustal thickening, uplift and erosion (Cooke et al., 2005). Hollings (2005) argued that the subduction of a ridge is associated with the formation of giant porphyry deposits, whereby it plays a greater role in changing the mantle source by increased subduction erosion and increased sediment input in the mantle wedge, all of which may contribute to the generation of giant ore deposits. The effects of the subducting Tehuantepec ridge may play an important role on the genesis of the Cerro la Mina prospect, however, its effects were not observed in the geochemistry of the Selva Negra because a thick crust may be diluting the geochemistry.

The geology of Cerro la Mina shows that a northwest fault has off-set the breccia pipe that hosts significant alteration and mineralisation. The breccia pipe along strike in the northeast block remains largely untested for mineralisation with only three drill holes ( $< 500$  m drilling). In addition, geologic mapping suggests a 500 m vertical movement on the fault suggesting the breccia pipe in the northeast block is closer in proximity to a potential underlying porphyry system. With the abundance of evaporites and limestone in the basement one might expect high sulfidation, carbonate replacement polymetallic deposits in the Cerro la Mina district like Colquijirca, and Cerro de Pasco Peru (Einaudi, 1977; Bendezú et al., 2003; Baumgartner et al., 2008).

### 10.6.2 Porphyry Vectors

The zonation patterns of the sericitic alteration point to the heat source of fluids from an inferred porphyry intrusion at depth. At Cerro la Mina a quartz-muscovite alteration is centred in the breccia pipe and lower temperature clay assemblages occur distally suggesting the source of fluids is at depth in the breccia pipe. The temperature zonation is also consistent with decreasing Al-OH and increasing crystallinity in SWIR spectra towards the breccia pipe. The untested breccia pipe in the northeast block shows a similar zonation pattern as the breccia pipe in the southeast block.

The concentrations of Co-Ni-Se in inclusion-rich pyrite also reflect the temperature zonation of the sericitic alteration (Stage B). Consistent with the temperature zonation, the concentrations of Co-Ni-Se increase towards and with depth in the breccia pipe (inferred heat source) and could be used as vectors toward a potential porphyry copper mineralisation or a intrusion centre.

### *10.6.3 High Sulfidation Epithermal Vectors*

An arsenic-rich zone was intersected below 1100 metres with mineralisation and alteration consistent with a distal position to a zone of quartz-dickite alteration (Stage C<sub>QD</sub>) with associated Stage 3 and 4 mineralisation. Additional drilling, laterally or deeper, could intersect Stage C<sub>QD</sub> alteration that is associated with higher grades of Au-Cu drilled to date. In addition, the abundance of halloysite to kaolinite decreases moving closer to quartz-dickite alteration (Stage C<sub>QD</sub>) at the surface. Therefore, the relative abundance of halloysite to kaolinite, using the KH index, could be used as an exploration vector in kaolinite alteration (Stage C) of hydrothermal systems similar to Cerro la Mina.

## **10.7 Further Work**

### *10.7.1 Geology*

A more comprehensive geologic study at the regional and district scale is required using non-genetic descriptions as employed in this study. Information regarding the structure at a regional scale is limited and could help in the exploration of new deposits as the structure plays an important role for mineralisation at Cerro la Mina.

### *10.7.2 Halloysite Isotopes*

To better constrain the origin of the Cerro la Mina halloysite a study could be undertaken to compare the isotopic composition of most intensely oxidized halloysite with the composition of the halloysite associated with sulfides (e.g., Braxton et al., 2009). In addition, the isotopic composition of hypogene dickite and sericite could be used as comparators.

## References Cited

- Arribas, A., 1995, Characteristics of high-sulfidation epithermal deposits, and their relation to magmatic fluid: in Thompson, J. F. H., ed., *Magma, Fluids, and Ore Deposits*, 23, Mineralogical Association of Canada Short Course, p. 419-454.
- Bailey, E. M., and Stevens, R. E., 1960, Selective staining of K-feldspar and plagioclase on rock slabs and thin sections: *American Mineralogist*, v. 45, p. 1020-1025.
- Baker, J., Peate, D., Waight, T., and Meyzen, C., 2004, Pb isotopic analysis of standards and samples using a  $^{207}\text{Pb}$ - $^{204}\text{Pb}$  double spike and thallium to correct for mass bias with a double-focusing MC-ICP-MS: *Chemical Geology*, v. 211, p. 275-303.
- Barton, M. D., Staude, J. M., Zürcher, L., and McGaw, P. K. M., 1995, Porphyry copper and other intrusion-related mineralization in Mexico: in Pierce, F. W., and Bolm, J.G., ed., *Porphyry copper deposits of the American Cordillera* 20, Arizona Geological Society Digest, p. 487-524.
- Baumgartner, R., Fontboté, L., and Vennemann, T., 2008, Mineral zoning and geochemistry of epithermal polymetallic Zn-Pb-Ag-Cu-Bi mineralization at Cerro de Pasco, Peru: *Economic Geology*, v. 103, p. 493-537.
- Bendezú, R., Fontboté, L., and Cosca, M., 2003, Relative age of Cordilleran base metal lode and replacement deposits, and high sulfidation Au-(Ag) epithermal mineralization in the Colquijirca mining district, central Peru: *Mineralium Deposita*, v. 38, p. 683-694.
- Berthier, P., 1826, Analyse de l'halloysite: *Annales de Chimie et de Physique*, v. 32, p. 332-335.
- Black, L. P., and Gulson, B. L., 1978, The age of the mud tank carbonatite, Strangways Range, Northern Territory: *BMR Journal of Australian Geology and Geophysics* 3, p. 227-232.
- Black, L. P., Kamo, S. L., Allen, C. M., Aleinikoff, J. N., Davis, D. W., Korsch, R. J., and Foudoulis, C., 2003, TEMORA 1: A new zircon standard for Phanerozoic U-Pb geochronology: *Chemical Geology*, v. 200, p. 155-170.
- Black, L. P., Kamo, S. L., Allen, C. M., Davis, D. W., Aleinikoff, J. N., Valley, J. W., Mundil, R., Campbell, I. H., Korsch, R. J., Williams, I. S., and Foudoulis, C., 2004, Improved  $^{206}\text{Pb}/^{238}\text{U}$  microprobe geochronology by the monitoring of a trace-element-related matrix effect; SHRIMP, ID-TIMS, ELA-ICP-MS and oxygen isotope documentation for a series of zircon standards: *Chemical Geology*, v. 205, p. 115-140.

- Braxton, D. P., 2007, Boyongan and Bayugo porphyry Cu-Au deposits, NE Mindanao, Philippines: Aeology, geochemistry, and tectonic evolution: Unpub. PhD thesis, University of Tasmania, 277 p.
- Braxton, D. P., Cooke, D. R., Ignacio, A. M., Rye, R. O., and Waters, P. J., 2009, Ultra-deep oxidation and exotic copper formation at the Late Pliocene Boyongan and Bayugo porphyry copper-gold deposits, Surigao, Philippines: Geology, mineralogy, paleoaltimetry, and their implications for geologic, physiographic, and tectonic controls: *Economic Geology*, v. 104, p. 333-349.
- Brindley, G. W., and Comer, J. J., 1956, Structure and morphology of kaolin clay from Eyzies (France): *Clay Minerals*, v. 4, p. 61-66.
- Brindley, G. W., De Souza Santos, P., and De Souza Santos, H., 1963, Mineralogical studies of kaolinite-halloysite clays: Part 1. Identification problems: *American Mineralogist*, v. 48, p. 897-910.
- Burbach, G. V., Frohlich, C., Pennington, W. D., and Matumoto, T., 1984, Seismicity and tectonics of the subducted cocos plate: *Journal of Geophysical Research*, v. 89, p. 7719-7735.
- Burkart, B., 1983, Neogene North American-Caribbean plate boundary: Offset along the Polochic fault: *Tectonophysics*, v. 99, p. 251-270.
- Campbell, A. R., and Larsen, P., 1998, Introduction to stable isotope applications in hydrothermal systems in Richardson, J., and Larsen, P., eds., *Techniques in Hydrothermal Ore Deposit Geology*, 10, *Reviews in Economic Geology*, p. 173-193.
- Camprubí, A., and Albinson, T., 2007, Epithermal deposits in Mexico - Update of current knowledge, and an empirical reclassification: *Geological Society of America Special Papers*, v. 422, p. 377-415.
- Camprubí, A., 2009, Major metallogenic provinces and epochs of México: *SGA News*, p. 7-19.
- Cano Mendoza, A., 2008, Report for Linear Gold Corp. on the Santa Fé Mine, p. 3.
- Capaul, W. A., 1987, Volcanoes of the Chiapas volcanic belt, Mexico: Unpub. Masters Thesis, 93 p.
- Carlson, R. W., and Nowell, G. M., 2001, Olivine-poor sources for mantle-derived magmas: Os and Hf isotopic evidence from potassic magmas of the Colorado Plateau: *Geochemistry, Geophysics, Geosystems*, v. 2, p. 1-17

- 
- Carr, M. J., Rose, W. I., and Stoiber, R. E., 1982, Central America: Andesites: Orogenic andesites and related rocks, p. 149-166.
- Carr, M. J., Feigenson, M. D., and Bennett, E. A., 1990, Incompatible element and isotopic evidence for tectonic control of source mixing and melt extraction along the Central American arc: *Contributions to Mineralogy and Petrology*, v. 105, p. 369-380.
- Castillo, P. R., Janney, P. E., and Solidum, R. U., 1999, Petrology and geochemistry of Camiguin Island, southern Philippines: insights to the source of adakites and other lavas in a complex arc setting: *Contributions to Mineralogy and Petrology*, v. 134, p. 33-51.
- Chamberlain, C. P., and Poage, M. A., 2000, Reconstructing the paleotopography of mountain belts from the isotopic composition of authigenic minerals: *Geology*, v. 28, p. 115-118.
- Chang, Z., Vervoort, J. D., McClelland, W. C., and Knaack, C., 2006, U-Pb dating of zircon by LA-ICP-MS: *Geochemistry, Geophysics, Geosystems*, v. 7.
- Churchman, G. J., and Carr, R. M., 1972, Stability fields of hydration states of an halloysite: *American Mineralogist*, v. 57, p. 914-923.
- Claypool, G. E., Holser, W. T., Kaplan, I. R., Sakai, H., and Zak, I., 1980, The age curves of sulfur and oxygen in marine sulfate and their initial interpretation: *Chemical Geology*, v. 28, p. 199-260.
- Cocherie, A., Fanning, C. M., Jezequel, P., and Robert, M., 2009, LA-MC-ICPMS and SHRIMP U-Pb dating of complex zircons from Quaternary tephras from the French Massif Central: Magma residence time and geochemical implications: *Geochimica et Cosmochimica Acta*, v. 73, p. 1095-1108.
- Compston, W., 1999, Geological age by instrumental analysis; the 29th Hallimond Lecture: *Mineral Magazine*, v. 63, p. 297-311.
- Cooke, D. R., and Simmons, S. F., 2000, Characteristics and genesis of epithermal gold deposits: *Reviews in Economic Geology*, v. 13, p. 221-244.
- Cooke, D. R., Hollings, P., and Walshe, J. L., 2005, Giant porphyry deposits: Characteristics, distribution, and tectonic controls: *Economic Geology*, v. 100, p. 801-818.
- Cooke, D. R., Wilson, A. J., House, M. J., Wolfe, R. C., Walshe, J. L., Lickfold, V., and Crawford, A. J., 2007, Alkalic porphyry Au - Cu and associated mineral deposits of the Ordovician to Early Silurian Macquarie Arc, New South Wales: *Australian Journal of Earth Sciences*, v. 54, p. 445-463.

- Corbett, G., and Leach, T., 1998, Southwest Pacific rim gold-copper systems: Structure, alteration, and mineralization: Society of Economic Geologist, Special Publication, v. 6, 237 p.
- Craig, H., 1961, Isotopic variations in meteoric waters: *Science*, v. 133, p. 1702-1703.
- Craig, H., 1963, The isotopic geochemistry of water and carbon in geothermal areas, in Tongiorgi, E., ed., *Nuclear geology on geothermal areas*, Spoleto: Pisa, Consiglio nazionale delle ricerche, p. 17-53.
- Crawford, A. J., Meffre, S., Squire, R. J., Barron, L. M., and Falloon, T. J., 2007, Middle and Late Ordovician magmatic evolution of the Macquarie Arc, Lachlan Orogen, New South Wales: *Australian Journal of Earth Sciences*, v. 54, p. 181 - 214.
- Cumming, G., 2008, Volcanic facies analysis: Cerro La Mina Prospect, Ixhuatán, Chiapas state, Mexico, Report for Kinross and Linear Gold Corporation, 20 p.
- Damon, P. E., and Motesinos, E., 1978, Late Cenozoic volcanism and metallogenesis over an active benioff zone in Chiapas, Mexico: *Arizona Geological Society Digest*, v. 11, p. 155-168.
- Damon, P. E., Shafiqullah, M., and Clark, K. F., 1983, Geochronology of the porphyry copper deposits and related mineralization of Mexico: in Dawson, K.M. Ed., *Symposium; Metallogeny and tectonics of the North American Cordillera*: *Canadian Journal of Earth Sciences*, v. 20, p. 1052-1071.
- Danyushevsky, L., Robinson, P., Gilbert, S., Norman, M., Large, R., McGoldrick, P., and Shelley, M., 2011, Routine quantitative multi-element analysis of sulphide minerals by laser ablation ICP-MS: Standard development and consideration of matrix effects: *Geochemistry: Exploration, Environment, Analysis*, v. 11, p. 51-60.
- Davies, A. G. S., Cooke, D. R., Gemmell, J. B., van Leeuwen, T., Cesare, P., and Hartshorn, G., 2008, Hydrothermal breccias and veins at the Kelian gold mine, Kalimantan, Indonesia: Genesis of a large epithermal gold deposit: *Economic Geology*, v. 103, p. 717-757.
- De Ignacio, C., Castineiras, P., Marquez, A., Oyarzun, R., Lillo, J., and Lopez, I., 2003, El Chichón Volcano (Chiapas Volcanic Belt, Mexico) transitional calc-alkaline to adakitic-like magmatism: Petrologic and tectonic implications: *International Geology Review*, v. 45, p. 1020-1028.
- De Mets, C., Gordon, R. G., Argus, D. F., and Stein, S., 1990, Current plate motions: *Geophysical Journal International*, v. 101, p. 425-478.

- 
- Defant, M. J., and Drummond, M. S., 1990, Derivation of some modern arc magmas by melting of young subducted lithosphere: *Nature*, v. 347, p. 662-665.
- Defant, M. J., and Drummond, M. S., 1993, Mount St. Helens: Potential example of the partial melting of the subducted lithosphere in a volcanic arc: *Geology*, v. 21, p. 547-550.
- Deyell, C. L., 2005, Sulfur isotope zonation at the Mt Polley alkalic porphyry Cu-Au deposit, British Columbia, Canada, in Mao, J., and Bierlein, F. P., eds., *Mineral deposit research: Meeting the global challenge (8th Biennial SGA meeting)*, p. 375-376.
- Dominguez, S., Lallemand, S., Malavieille, J., and Schnürle, P., 1998a, Oblique subduction of the Gagua ridge beneath the Ryukyu accretionary wedge system: Insights from marine observations and sandbox experiments: *Marine Geophysical Researches*, v. 20, p. 383-402.
- Dominguez, S., Lallemand, S. E., Malavieille, J., and Von Huene, R., 1998b, Upper plate deformation associated with seamount subduction: *Tectonophysics*, v. 293, p. 207-224.
- Dostal, J., Zentilli, M., Caelles, J. C., and Clark, A. H., 1977, Geochemistry and origin of volcanic rocks of the Andes (26°–28°S): *Contributions to Mineralogy and Petrology*, v. 63, p. 113-128.
- Dube, B., Dunning, G. R., and Lauziere, K., 1998, Geology of the Hope Brook Mine, Newfoundland, Canada; a preserved late Proterozoic high-sulfidation epithermal gold deposit and its implications for exploration: *Economic Geology*, v. 93, p. 405-436.
- Duffield, W. A., Tilling, R. I., and Canul, R., 1984, Geology of El Chichón Volcano, Chiapas, Mexico: *Journal of Volcanology and Geothermal Research*, v. 20, p. 117-132.
- Ece, Ö., I., Schroeder, P. A., Smilley, M. J., and Wampler, J. M., 2008, Acid-sulphate hydrothermal alteration of andesitic tuffs and genesis of halloysite and alunite deposits in the Biga Peninsula, Turkey: *Clay Minerals*, v. 43, p. 281-315.
- Edwards, C. M. H., Menzies, M. A., Thirlwall, M. F., Morris, J. D., Leeman, W. P., and Harmon, R. S., 1994, The transition to potassic alkaline volcanism in island arcs: The Ringgit-Beser complex, East Java, Indonesia: *Journal of Petrology*, v. 35, p. 1557-1595.
- Einaudi, M. T., 1977, Environment of ore deposition at Cerro de Pasco, Peru: *Economic Geology*, v. 72, p. 893-924.
- Escandón Valle, F. J., Gómez de la Rosa, E., Salinas Prieto, J. C., De la Calleja Moctezuma, A., Sánchez Rojas, L. E., Barajas Nigoche, L. D., and Salinas Prieto, J. C., 2006, Carta geológico Mexicano estados de Chiapas y Tabasco, Servicio Geológico Mexicano.

- Espindola, J. M., Macias, J. L., Tilling, R. I., and Sheridan, M. F., 2000, Volcanic history of El Chichón volcano (Chiapas, Mexico) during the Holocene, and its impact on human activity: *Bulletin of Volcanology*, v. 62, p. 90-104.
- Ferrari, L., Lopez-Martinez, M., Aguirre-Diaz, G., and Carrasco-Nunez, G., 1999, Space-time patterns of Cenozoic arc volcanism in central Mexico: From the Sierra Madre Occidental to the Mexican Volcanic Belt: *Geology*, v. 27, p. 303-306.
- Foley, S., 1992a, Petrological characterization of the source components of potassic magmas: geochemical and experimental constraints: *Lithos*, v. 28, p. 187-204.
- Foley, S., 1992b, Vein-plus-wall-rock melting mechanisms in the lithosphere and the origin of potassic alkaline magmas: *Lithos*, v. 28, p. 435-453.
- Fryer, B. J., Jackson, S. E., and Longrich, H. P., 1993, The application of laser ablation microprobe-inductively coupled plasma-mass spectrometry (LAM-ICP-MS) to in situ (U)-Pb geochronology: *Chemical Geology*, v. 109, p. 1-8.
- García-Palomo, A., Macías, J. L., and Espíndola, J. M., 2004, Strike-slip faults and K-alkaline volcanism at El Chichón volcano, southeastern Mexico: *Journal of Volcanology and Geothermal Research*, v. 136, p. 247-268.
- García-Palomo, A., Macías, J. L., Arce, J. L., Mora, J. C., Saucedo, R., Espíndola, J. M., Escobar, R., and Layer, P., 2006, Geological evolution of the Tacaná Volcanic Complex, México-Guatemala, *Special Paper of the Geological Society of America*, p. 39-57.
- Gasparon, M., and Varne, R., 1998, Crustal assimilation versus subducted sediment input in west Sunda arc volcanics: An evaluation: *Mineralogy and Petrology*, v. 64, p. 89-117.
- Geisler, T., Schaltegger, U., and Tomaschek, F., 2007, Re-equilibration of zircon in aqueous fluids and melts: *Elements*, v. 3, p. 43-50.
- Gemmell, J. B., Sharpe, R., Jonasson, I. R., and Herzig, P. M., 2004, Sulfur isotope evidence for magmatic contributions to submarine and subaerial gold mineralization: Conical Seamount and the Ladolam Gold Deposit, Papua New Guinea: *Economic Geology*, v. 99, p. 1711-1725.
- Giese, R. F., 1988, Kaolin minerals; structures and stabilities: *Reviews in Mineralogy and Geochemistry*, v. 19, p. 29-66.
- Giggenbach, W. F., 1992, SEG Distinguished Lecture - Magma degassing and mineral deposition in hydrothermal systems along convergent plate boundaries: *Economic Geology and the Bulletin of the Society of Economic Geologists*, v. 87, p. 1927-1944.

- 
- Gill, J. B., 1981, *Orogenic andesites and plate tectonics*: Berlin-Heidelberg, Springer-Verlag, 390 p.
- Gómez-Tuena, A., Orozco-Esquivel, M. T., and Ferrari, L., 2007, Igneous petrogenesis of the Trans-Mexican Volcanic Belt: *Geological Society of America Special Papers*, v. 422, p. 129-181.
- Guzman-Speziale, M., and Meneses-Rocha, J. J., 2000, The North America-Caribbean plate boundary west of the Motagua-Polochic fault system: a fault jog in Southeastern Mexico: *Journal of South American Earth Sciences*, v. 13, p. 459-468.
- Harley, S. L., and Kelly, N. M., 2007, Zircon tiny but timely: *Elements*, v. 3, p. 13-18.
- Harris, A. C., Kamenetsky, V. S., White, N. C., and Steele, D. A., 2004, Volatile Phase separation in silicic magmas at Bajo de la Alumbrera porphyry Cu-Au deposit, NW Argentina: *Resource Geology*, v. 54, p. 341-356.
- Harris, A. C., Bryan, S. E., and Holcombe, R. J., 2006, Volcanic Setting of the Bajo de la Alumbrera porphyry Cu-Au deposit, Farallón Negro volcanics, Northwest Argentina: *Economic Geology*, v. 101, p. 71-94.
- Harris, A. C., 2007, Petrographic descriptions for Cerro la Mina prospect, Ixhuatán project, Mexico, Report for Linear Gold Corporation, 16 p.
- Harrison, T. M., Duncan, I., and McDougall, I., 1985, Diffusion of  $^{40}\text{Ar}$  in biotite: Temperature, pressure and compositional effects: *Geochimica et Cosmochimica Acta*, v. 49, p. 2461-2468.
- Hastie, A. R., Kerr, A. C., Pearce, J. A., and Mitchell, S. F., 2007, Classification of altered volcanic island arc rocks using immobile trace elements: Development of the Th-Co discrimination diagram: *Journal of Petrology*, v. 48, p. 2341-2357.
- Havskov, J., Singh, S. K., and Novelo, D., 1982, Geometry of the Benioff zone in the Tehuantepec area of southern Mexico: *Geofisica Internacional*, v. 21, p. 325-330.
- Hedenquist, J. W., Matsuhisa, Y., Izawa, E., White, N. C., Giggenbach, W. F., and Aoki, M., 1994, Geology, geochemistry, and origin of high sulfidation Cu-Au mineralization in the Nansatsu District, Japan: *Economic Geology*, v. 89, p. 1-30.
- Hedenquist, J. W., Arribas, A., Jr., and Reynolds, T. J., 1998, Evolution of an intrusion-centered hydrothermal system: Far Southeast-Lepanto porphyry and epithermal Cu-Au deposits, Philippines: *Economic Geology*, v. 93, p. 373-404.

- Hedenquist, J. W., 2000, Exploration for epithermal gold deposits: *Society of Economic Geologist Review*, v. 13, p. 245-277.
- Heithersay, P. S., and Walshe, J. L., 1995, Endeavour 26 North: a porphyry copper-gold deposit in the late Ordovician, shoshonitic Goonumbla Volcanic Complex, New South Wales, Australia: *Economic Geology*, v. 90, p. 1506-1532.
- Hernández-García, R., 1973, Paleogeografía del Paleozoico de Chiapas, Mexico: *Asociación Mexicana de Geólogos Petroleros Boletín*, v. 25, p. 77-134.
- Hildreth, W., and Moorbath, S., 1988, Crustal contributions to arc magmatism in the Andes of Central Chile: *Contributions to Mineralogy and Petrology*, v. 98, p. 455-489.
- Holliday, J. R., Wilson, A. J., Blevin, P. L., Tedder, I. J., Dunham, P. D., and Pfitzner, M., 2002, Porphyry gold-copper mineralisation in the Cadia district, Eastern Lachlan Fold Belt, New South Wales, and its relationship to shoshonitic magmatism: *Mineralium Deposita*, v. 37, p. 100-116.
- Holliday, J. R., and Cooke, D. R., 2007, *Advances in geological models and exploration methods for copper ± gold porphyry deposits: Exploration 07*, Toronto, 2007.
- Hollings, P., and Wyman, D., 2005, The Geochemistry of trace elements in igneous systems: principles and examples from basaltic systems, in Linnen, R., and Samson, I., eds., *Rare Element Geochemistry and Ore Deposits*, Geological Association of Canada Short Course Notes, v.17, p. 1-24.
- Hollings, P., Cooke, D., and Clark, A., 2005, Regional geochemistry of Tertiary igneous rocks in central Chile: Implications for the geodynamic environment of giant porphyry copper and epithermal gold mineralization: *Economic Geology*, v. 100, p. 887-904.
- Hollings, P., Wolfe, R., Cooke, D. R., and Waters, P. J., 2011, Geochemistry of Tertiary igneous rocks of northern Luzon, Philippines: Evidence for a back-arc setting for alkalic porphyry copper-gold deposits and a case for slab roll-back?: *Economic Geology*, v. 106, p. 1257-1277.
- Hsieh, J. C. C., and Yapp, C. J., 1999, Hydrogen-isotope exchange in halloysite; insight from room-temperature experiments: *Clays and Clay Minerals*, v. 47, p. 811-816.
- IAEA/WMO, 2006, Global network of isotopes in precipitation. The GNIP database. Accessible at: <http://www.iaea.org/water>.
- Islas Tenorio, J. J., Ramírez García, M. G., Gómez Áviles, A., Moreno Ruíz, J. P., Wingartz Carranza, J. A., and Mendieta Flores, J., 2005, *Carta geológico-minera Villahermosa*

- 
- E15-8 Tabasco, Veracruz, Chiapas y Oaxaca, Servicio Geológica Mexicano.
- Jackson, S. E., Pearson, N. J., Griffin, W. L., and Belousova, E. A., 2004, The application of laser ablation-inductively coupled plasma-mass spectrometry to in situ U-Pb zircon geochronology: *Chemical Geology*, v. 211, p. 47-69.
- Jansen, N. H., 2007, An infrared spectral reflectance study of the hydrothermal alteration minerals from the Campamento Au/Ag deposit, southern Mexico: Unpub. Honours thesis, Saint Mary's University, 92 p.
- Jensen, E. P., and Barton, M. D., 2000, Gold deposits related to alkaline magmatism, gold in 2000. *Reviews in Economic Geology*, 279-314 p.
- Jensen, E. P., 2003, Magmatic and hydrothermal evolution of the Cripple Creek gold deposit, Colorado, and comparison with regional and global magmatic – hydrothermal systems associated with alkalic magmatism: Unpub. PhD thesis, University of Arizona, Tuscon, 801 p.
- Jeong, G. Y., 1998, Formation of vermicular kaolinite from halloysite aggregates in the weathering of plagioclase: *Clays and Clay Minerals*, v. 46, p. 270-279.
- Jones, D. A., Layer, P. W., and Newberry, R. J., 2008, A 3100-year history of argon isotopic and compositional variation at El Chichón volcano: *Journal of volcanology and Geothermal Research*, v. 175, p. 427-443.
- Joplin, G. A., 1968, The shoshonite association: A review: *Journal of the Geological Society of Australia*, v. 15, p. 275-294.
- Jourdan, F., and Renne, P. R., 2007, Age calibration of the Fish Canyon sanidine  $^{40}\text{Ar}/^{39}\text{Ar}$  dating standard using primary K-Ar standards: *Geochimica et Cosmochimica Acta*, v. 71, p. 387-402.
- Joussein, E., Petit, S., Churchman, J., Theng, B., Righi, D., and Delvaux, B., 2005, Halloysite clay minerals - a review: *Clay Minerals*, v. 40, p. 383-426.
- Joussein, E., Petit, S., Delvaux, B., 2007, Behavior of halloysite clay under formamide treatment: *Applied Clay Science*, v. 35, p. 17-24.
- Kay, R. W., and Gast, P. W., 1973, The rare earth content and origin of alkali-rich basalts: *The Journal of Geology*, v. 81, p. 653-682.
- Kerrich, R., and Wyman, D. A., 1996, Trace element systematics of igneous rocks in mineral exploration, an overview, in Wyman, D. A., ed., *Trace element geochemistry of volcanic*
-

- rocks: Application for massive sulphide exploration: Short Course Notes, 12: Geological and Mineralogical Association of Canada, p. 1-50.
- Kinross Gold, 2008, Helimag image of Cerro la Mina Prospect.
- Koppers, A. A. P., 2002, ArArCALC software for  $^{40}\text{Ar}/^{39}\text{Ar}$  age calculations: Computers and Geosciences, v. 28, p. 605-619.
- Kosler, J., 2001, Laser-ablation ICPMS study of metamorphic minerals and processes, in J., S. P., ed., Laser-ablation-ICPMS in the earth sciences; principles and applications: Mineralogical Association of Canada Short Course Handbook, v.29, p. 185-202.
- Kyne, R., 2009, Clay alteration of the Cerro la Mina porphyry-epithermal deposit, Chiapas, Mexico: Unpub. Honours thesis, Lakehead University, 80 p.
- Lang, J. R., Lueck, B., Mortensen, J. K., Kelly Russell, J., Stanley, C. R., and Thompson, J. F. H., 1995a, Triassic-Jurassic silica-undersaturated and silica-saturated alkalic intrusions in the Cordillera of British Columbia: Implications for arc magmatism: *Geology*, v. 23, p. 451-454.
- Lang, J. R., Stanley, C. R., Thompson, J. F. H., and Dunne, K. P. E., 1995b, Na-K-Ca magmatic hydrothermal alteration in alkalic porphyry Cu-Au deposits, British Columbia, Mineralogical Association of Canada Shortcourse, Victoria, v. 23, p. 339-366.
- Large, R. R., Danyushevsky, L., Hollit, C., Maslennikov, V., Meffre, S., Gilbert, S., Bull, S., Scott, R., Emsbo, P., Thomas, H., Singh, B., and Foster, J., 2009, Gold and trace element zonation in pyrite using a laser imaging technique: implications for the timing of gold in orogenic and carlin-style sediment-hosted deposits: *Economic Geology*, v. 104, p. 635-668.
- Lawrence, J. R., and Taylor, H. P., 1971, Deuterium and oxygen-18 correlation: Clay minerals and hydroxides in Quaternary soils compared to meteoric waters: *Geochimica et Cosmochimica Acta*, v. 35, p. 993-1003.
- Layer, P. W., Garcia-Polomo, A., Jones, D., Macias, J. L., Arce, J. L., and Mora, J. C., 2009, El Chichón volcanic complex, Chiapas, México: stages of evolution based on field mapping and  $^{40}\text{Ar}/^{39}\text{Ar}$  geochronology: *Geofisica Internacional*, v. 48, p. 33-54.
- Le Bas, M. J., and Streckeisen, A. L., 1991, The IUGS systematics of igneous rocks: *Journal of the Geological Society*, v. 148, p. 825-833.
- Le Maitre, R. W., 1989, A Classification of igneous rocks and glossary of terms: recommendations of the international union of geological sciences subcommission on the systematics

- of igneous rocks: Oxford, Blackwell Scientific.
- Lee, J.-Y., Marti, K., Severinghaus, J. P., Kawamura, K., Yoo, H.-S., Lee, J. B., and Kim, J. S., 2006, A redetermination of the isotopic abundances of atmospheric Ar: *Geochimica et Cosmochimica Acta*, v. 70, p. 4507-4512.
- Lickfold, V., Cooke, D. R., Smith, S. G., and Ullrich, T. D., 2003, Endeavour copper-gold porphyry deposits, Northparkes, New South Wales: Intrusive history and fluid evolution: *Economic Geology*, v. 98, p. 1607-1636.
- Linear Gold Corp., 2007, Linear Gold Corporation website, Linear Gold Corporation, <http://lineargoldcorp.com>.
- Lowell, J. D., and Guilbert, J. M., 1970, Lateral and vertical alteration-mineralization zoning in porphyry ore deposits: *Economic Geology*, v. 65, p. 373-408.
- Lucassen, F., Wiedicke, M., and Franz, G., 2010, Complete recycling of a magmatic arc: evidence from chemical and isotopic composition of Quaternary trench sediments in Chile (36°-40°S): *International Journal of Earth Sciences*, v. 99, p. 687-701.
- Ludwig, K. R., 2003, User's manual for Isoplot 3.00: Berkeley, California, Berkeley Geochronology Center.
- Luhr, J. F., Carmichael, I. S. E., and Varekamp, J. C., 1984, The 1982 eruptions of El Chichón volcano, Chiapas, Mexico: Mineralogy and petrology of the anhydrite bearing pumices: *Journal of Volcanology and Geothermal Research*, v. 23, p. 69-108.
- Luhr, J. F., 1997, Extensional tectonics and the diverse primitive volcanic rocks in the western Mexican volcanic belt: *The Canadian Mineralogist*, v. 35, p. 473-500.
- Luhr, J. F., Amelia, M., and Logan, V., 2002, Sulfur isotope systematics of the 1982 El Chichón trachyandesite: An ion microprobe study: *Geochimica et Cosmochimica Acta*, v. 66, p. 3303-3316.
- Luhr, J. F., Kimberly, P., Siebert, L., Aranda-Gomez, J.J., Housh, T.B., Kysar Mattiotti, K., 2006, Mexico's Quaternary volcanic rocks: Insights from the MEXPET petrological and geochemical database: in Siebe, c., Macias, J.L., and Aguirre-Diaz, CU., eds., Neogene-Quaternary continental margin volcanism: A perspective from Mexico: *Geological Society of America Special Paper*, v. 402, p. 1-44.
- MacCarthy, E. T., 1897, Mining in the wollastonite ore-deposits of the Santa Fé Mine, Chiapas: *transactions of the Institution of Mining and Metallurgy*, v. 4, p. 169-189.

- MacDonald, G. D., and Arnold, L. C., 1994, Geological and geochemical zoning of the Grasberg Igneous Complex, Irian Jaya, Indonesia: *Journal of Geochemical Exploration*, v. 50, p. 143-178.
- Macías, J. L., Espíndola, J. M., García-Palomo, A., Scott, K. M., Hughes, S., and Mora, J. C., 2000, Late Holocene Peléan-style eruption at Tacaná volcano, Mexico and Guatemala: Past, present, and future hazards: *Bulletin of the Geological Society of America*, v. 112, p. 1234-1249.
- Macías, J. L., Arce, J. L., Mora, J. C., Espíndola, J. M., Saucedo, R., and Manetti, P., 2003, A 550-year-old plinian eruption at El Chichón Volcano, Chiapas, Mexico: Explosive volcanism linked to reheating of the magma reservoir: *Journal of Volcanology and Geothermal Research*, v. 108, p. 2569.
- Maksaev, V., Munizaga, F., McWilliams, M., Fanning, M., Mathur, R., Ruiz, J., and Zentilli, M., 2004, New chronology for El Teniente, Chilean Andes, from U-Pb,  $^{40}\text{Ar}/^{39}\text{Ar}$ , Re-Os and fission-track dating: Implications for the evolution of a supergiant porphyry Cu-Mo deposit: *Society of Economic Geologists Special Publication*, v. 11, p. 15-54.
- Mandujano-Velazquez, J. J., and Keppie, J. D., 2009, Middle Miocene Chiapas fold and thrust belt of Mexico: A result of collision of the Tehuantepec transform/ridge with the middle America trench: *Geological Society Special Publication*, p. 55-69.
- Manea, M., Manea, V. C., Ferrari, L., Kostoglodov, V., and Bandy, W. L., 2005, Tectonic evolution of the Tehuantepec ridge: *Earth and Planetary Science Letters*, v. 238, p. 64-77.
- Manea, M., Manea, V.C., 2008, On the origin of El Chichón volcano and subduction of Tehuantepec ridge: A geodynamical perspective: *Journal of volcanology and geothermal research*, v. 175, p. 459-471.
- Manea, V. C., and Manea, M., 2006, Origin of the modern Chiapanecan Volcanic arc in southern México inferred from thermal models: *Geological Society of America Special Papers*, v. 412, p. 27-38.
- Markey, R., Stein, H., and Morgan, J., 1998, Highly precise Re-Os dating for molybdenite using alkaline fusion and NTIMS: *Talanta*, v. 45, p. 935-946.
- Markey, R., Stein, H. J., Hannah, J. L., Zimmerman, A., Selby, D., and Creaser, R. A., 2007, Standardizing Re-Os geochronology: A new molybdenite Reference Material (Henderson, USA) and the stoichiometry of Os salts: *Chemical Geology*, v. 244, p. 74-87.
- Martinez Lopez, F., 2009, Ixhuatán geologic map, Kinross Gold Corporation.

- Marumo, K., and Hattori, K. H., 1999, Seafloor hydrothermal clay alteration at Jade in the back-arc Okinawa Trough: mineralogy, geochemistry and isotope characteristics: *Geochimica et Cosmochimica Acta*, v. 63, p. 2785-2804.
- McDonough, W.F., Sun, S.-S., Ringwood, A.E., Jagoutz, E. and Hofmann, A.W. (1992). Potassium, rubidium and cesium in the earth and moon and the evolution of the mantle of the earth. *Geochimica et Cosmochimica Acta*, v. 56, p. 1,001-1,012.
- McGee, J. J., Tilling, R. I., and Duffield, W. A., 1987, Petrologic characteristics of the 1982 and pre-1982 eruptive products of El Chichón volcano, Chiapas, Mexico: *Geofísica Internacional*, v. 26, p. 85-108.
- Medina, F., Gonzalez-Moran, T., and Gonzalez, L., 1990, Gravity and seismicity analyses of the El Chichón volcano, Chiapas, Mexico: *Pageoph*, v. 133, p. 149-165.
- Meffre, S., Large, R. R., Scott, R., Woodhead, J., Chang, Z., Gilbert, S. E., Danyushevsky, L. V., Maslennikov, V., and Hergt, J. M., 2008, Age and pyrite Pb-isotopic composition of the giant Sukhoi Log sediment-hosted gold deposit, Russia: *Geochimica et Cosmochimica Acta*, v. 72, p. 2377-2391.
- Melchiorre, E. B., Criss, R. E., and Rose, T. P., 2000, Oxygen and carbon isotope study of natural and synthetic azurite: *Economic Geology*, v. 95, p. 621-628.
- Meneses-Rocha, J. J., 2001, Tectonic evolution of the Ixtapa graben, an example of a strike-slip basin of southeastern Mexico: implications for regional petroleum systems: *American Association of Petroleum Geologists Memoir*, v. 75, p. 183-216.
- Menzies, M. A., and Hawkesworth, C. J., 1987, *Mantle metasomatism*: London, Academic Press, 472 p.
- Mercado, R., and Rose, W. I., 1992, Reconocimiento geológico y evaluación preliminar de peligrosidad del Volcán Tacaná, Guatemala/México: *Geofísica Internacional*, v. 31, p. 205-237.
- Miranda-Gasca, M. A., Pyle, P., Roldán, J., Ochoa-Camarillo, H. R., Arias, R., and Jaimez, A., 2009, Los depósitos de oro-plata y cobre-oro en Ixhuatán y Santa Fé, Chiapas, México, in Clark, F. C., Salas-Pizá, G.A. and Cubillas-Estrada, R., ed., *Geología Económica de México*, 2, Asociación de Ingenieros de Minas, Metalurgistas y Geólogos de Mexico, A.C., Servicio Geologico Mexicano, p. 953.
- Mora, J. C., Jaimes-Viera, M. C., Garduno-Monroy, V. H., Layer, P. W., Pompa-Mera, V., and Gondinez, M. L., 2007, Geology and geochemistry characteristics of the Chiapanecan Volcanic Arc (Central Area), Chiapas Mexico: *Journal of Volcanology and Geothermal*

- Research, v. 162, p. 43-72.
- Morrison, G. W., 1980, Characteristics and tectonic setting of the shoshonite rock association: *Lithos*, v. 13, p. 97-108.
- Müller, D., Franz, L., Herzig, P. M., and Hunt, S., 2001, Potassic igneous rocks from the vicinity of epithermal gold mineralization, Lihir Island, Papua New Guinea: *Lithos*, v. 57, p. 163-186.
- Müller, D., Kaminski, K., Uhlig, S., Graupner, T., Herzig, P., and Hunt, S., 2002, The transition from porphyry- to epithermal-style gold mineralization at Ladolam, Lihir Island, Papua New Guinea: A reconnaissance study: *Mineralium Deposita*, v. 37, p. 61-74.
- Mungall, J. E., 2002, Roasting the mantle: Slab melting and the genesis of major Au and Au-rich Cu deposits: *Geology*, v. 30, p. 915-918.
- Murakami, T., Chakoumakos, B. C., Ewing, R. C., Lumpkin, G. R., and Weber, W. J., 1991, Alpha-decay event damage in zircon: *American Mineralogist*, v. 76, p. 1510-1532.
- Narcía-López, C., Castro, R. R., and Rebollar, C. J., 2004, Determination of crustal thickness beneath Chiapas, Mexico using S and Sp waves: *Geophysical Journal International*, v. 157, p. 215-228.
- Nelson, S. A., and Gonzalez-Caver, E., 1992, Geology and K-Ar dating of the Tuxtla Volcanic Field, Veracruz, Mexico: *Bulletin of Volcanology*, v. 55, p. 85-96.
- Nelson, S. A., Gonzalez-Caver, E., and Kyser, T. K., 1995, Constraints on the origin of alkaline and calc-alkaline magmas from the Tuxtla Volcanic Field, Veracruz, Mexico: *Contributions to Mineralogy and Petrology*, v. 122, p. 191-211.
- New York Times, 1889, English Money in Mexico - A large transfer of copper mine property in Chiapas, *The New York Times*.
- Nixon, G. T., 1982, The relationship between Quaternary volcanism in central Mexico and the seismicity and structure of subducted ocean lithosphere: *Geological Society of America Bulletin*, v. 93, p. 514-523.
- North American Magnetic Anomaly Group (NAMAG), 2002, Magnetic Anomaly Map of North America, in Brunstein, F. C., ed., U.S. Geological Survey Open-File Report 02-414, U.S. Geological Survey.
- Pantoja, A., 1991, The Santa Fé Mine, Chiapas, in Salas, G. P., ed., *The Geology of North America*, P-3. Economic Geology, Mexico: Boulder, Colorado, Geological Society of

---

America.

- Papoulis, D., Tsolis-Katagas, P., Kalampounias, A. G., and Tsikouras, B., 2009, Progressive formation of halloysite from the hydrothermal alteration of biotite and the formation mechanisms of anatase in altered volcanic rocks from Limnos Island, northeast Aegean Sea, Greece: *Clays and Clay Minerals*, v. 57, p. 566-577.
- Pardo, M., and Suárez, G., 1995, Shape of the subducted Rivera and Cocos plates in southern Mexico: Seismic and tectonic implications: *Journal of Volcanology and Geothermal Research*, v. 100, p. 12357-12373.
- Patino, L. C., Carr, M. J., and Feigenson, M. D., 2000, Local and regional variations in Central American arc lavas controlled by variations in subducted sediment input: *Contributions to Mineralogy and Petrology*, v. 138, p. 265-283.
- Paton, C., Woodhead, J. D., Hellstrom, J. C., Hergt, J. M., Greig, A., and Maas, R., 2010, Improved laser ablation U-Pb zircon geochronology through robust downhole fractionation correction: *Geochemistry, Geophysics, Geosystems*, v. 11, p. 1-36.
- Pearce, J. A., and Peate, D. W., 1995, Tectonic implications of the composition of volcanic arc magmas: *Annual Review of Earth and Planetary Sciences*, v. 23, p. 251-285.
- Peccerillo, A., and Taylor, S. R., 1976, Geochemistry of Eocene calc-alkaline volcanic rocks from the Kastamonu area, Northern Turkey: *Contributions to Mineralogy and Petrology*, v. 58, p. 63-81.
- Peccerillo, A., 1992, Potassic and ultrapotassic rocks: compositional characteristics, petrogenesis, and geologic significance: *Episodes*, v. 15, p. 243-251.
- Peccerillo, A., 1999, Multiple mantle metasomatism in central-southern Italy: geochemical effects, timing and geodynamic implications: *Geology*, v. 27, p. 315-318.
- Polve, M., Maury, R. C., Jego, S., Bellon, H., Margoum, A., Yumul Jr, G. P., Payot, B. D., Tamayo Jr, R. A., and Cotten, J., 2007, Temporal geochemical evolution of neogene magmatism in the Baguio gold-copper mining district (Northern Luzon, Philippines): *Resource Geology*, v. 57, p. 197-218.
- Pontual, S., 2001, Implementing field-based and HyLogging spectral datasets in exploration and mining, AusSpec International.
- Pyle, P., 2009, Personal Communication.
- Rainbow, A., and Kyser, K., 2005, Mineral paragenesis and gold distribution at the Ixhuatán

- gold deposit, Chiapas, Mexico, Report for Linear Gold Corporation, 14 p.
- Rebollar, C. J., Espíndola, V. H., Uribe, A., Mendoza, A., and Pérez-Vertti, A., 1999, Distributions of stresses and geometry of the Wadati-Benioff zone under Chiapas, Mexico: *Geofísica Internacional*, v. 38, p. 95-106.
- Reich, M., Kesler, S. E., Utsunomiya, S., Palenik, C. S., Chryssoulis, S. L., and Ewing, R. C., 2005, Solubility of gold in arsenian pyrite: *Geochimica et Cosmochimica Acta*, v. 69, p. 2781-2796.
- Renne, P. R., Mundil, R., Balco, G., Min, K., and Ludwig, K. R., 2010, Joint determination of  $^{40}\text{K}$  decay constants and  $^{40}\text{Ar}^*/^{40}\text{K}$  for the Fish Canyon sanidine standard, and improved accuracy for  $^{40}\text{Ar}/^{39}\text{Ar}$  geochronology: *Geochimica et Cosmochimica Acta*, v. 74, p. 5349-5367.
- Reyes, A. G., 1990, Petrology of Philippine geothermal systems and the application of alteration mineralogy to their assessment: *Journal of Volcanology and Geothermal Research*, v. 43, p. 279-309.
- Richard, P., Shimizu, N., and Allègre, C. J., 1976,  $^{143}\text{Nd}/^{146}\text{Nd}$ , a natural tracer: An application to oceanic basalts: *Earth and Planetary Science Letters*, v. 31, p. 269-278.
- Richards, J. P., and Kerrich, R., 1993, The Porgera gold mine, Papua New Guinea; magmatic hydrothermal to epithermal evolution of an alkalic-type precious metal deposit: *Economic Geology*, v. 88, p. 1017-1052.
- Richards, J. P., 1995, Alkalic-type epithermal gold deposits—a review, in Thompson, J. F. H., ed., *Magma, fluids, and ore deposits*: Mineralogical Association of Canada, Short Course Series, 23, p. 367-400.
- Richards, J. P., 2006, Petrographic report on eight samples of argillic alteration from the Ixhuatán gold deposit, Southern Mexico, Report for Linear Gold Corporation, 14 p.
- Richards, J. P., 2006a, Confidential report to Linear Gold Corp.: Reconnaissance study of fluid inclusions in carbonate vein samples from the Ixhuatán gold deposit, southern Mexico, 13 p.
- Richards, J. P., 2006b, Petrographic report on eight samples of argillic alteration from the Ixhuatán gold deposit, southern Mexico, Report for Linear Gold Corporation, 14 p.
- Richards, J. P., and Kerrich, R., 2007, Special paper: Adakite-like rocks: Their diverse origins and questionable role in metallogenesis: *Economic Geology*, v. 102, p. 537-576.

- Robin, C., and Tournon, J., 1978, Spatial relations of andesitic and alkaline provinces in Mexico and Central America: *Canadian Journal of Earth Sciences*, v. 15, p. 1633-1641.
- Robin, C., 1982, Mexico, in Thorpe, R. S., ed., *Andesites: Orogenic andesites and related rocks*: Chichester, John Wiley & Sons, p. 137-147.
- Robinson, B. W., and Kusakabe, M., 1975, Quantitative preparation of sulfur dioxide, for  $^{34}\text{S}/^{32}\text{S}$  analyses, from sulfides by combustion with cuprous oxide: *Analytical Chemistry*, v. 47, p. 1179-1181.
- Robinson, P., Townsend, A. T., Yu, Z., and Münker, C., 1999, Determination of scandium, yttrium and rare earth elements in rocks by high resolution inductively coupled plasma-mass spectrometry: *Geostandards Newsletter*, v. 23, p. 31-46.
- Rogers, N. W., Hawkesworth, C. J., Matthey, D. P., and Harmon, R. S., 1987, Sediment subduction and the source of potassium in orogenic leucitites: *Geology*, v. 15, p. 451-453.
- Ronacher, E., Richards, J. P., Reed, M. H., Bray, C. J., Spooner, E. T. C., and Adams, P. D., 2004, Characteristics and evolution of the hydrothermal fluid in the north zone high-grade area, Porgera gold deposit, Papua New Guinea: *Economic Geology*, v. 99, p. 843-867.
- Rose, W. I., Bornhorst, T. J., Halsor, S. P., Capaul, W. A., Plumley, P. S., Dela Cruz-Reyna, S., Mena, M., and Mota, R., 1984, Volcán El Chichón, Mexico: Pre-1982 S-rich eruptive activity: *Journal of Volcanology and Geothermal Research*, v. 23, p. 147-149, 155-167.
- Rye, R. O., Luhr, J. F., and Wasserman, M. D., 1984, Sulfur and oxygen isotopic systematics of the 1982 eruptions of El Chichón Volcano, Chiapas, Mexico: *Journal of Volcanology and Geothermal Research*, v. 23, p. 109-123.
- Rye, R. O., 1993, The evolution of magmatic fluids in the epithermal environment; the stable isotope perspective: *Economic Geology*, v. 88, p. 733-752.
- Sánchez-Montes De Oca, R., 1979, Geología petrolera de la Sierra de Chiapas: *Boletín de la Asociación Mexicana de Geólogos Petroleros*, v. 31, p. 67-97.
- Schaaf, P., Weber, B., Weis, P., Gross, A., Ortega-Gutiérrez, F., and Köhler, H., 2002, The Chiapas Massif (Mexico) revised: New geologic and isotopic data for basement characteristics, in Miller, H., ed., *Contributions to Latin American Geology: Neues Jahrbuch für Geologie und Paläontologie Abhandlung*, v.225, p. 1-23.
- Schärer, U., 1984, The effect of initial  $^{230}\text{Th}$  disequilibrium on young U-Pb ages: the Makalu case, Himalaya: *Earth and Planetary Science Letters*, v. 67, p. 191-204.

- Schroeter, T. G., 1995, Porphyry deposits of the northwestern cordillera of North America: Canadian Institute of Mining, Metallurgy and Petroleum, v.46, p. 888.
- Seedorff, E., Dilles, J. H., Proffett, J. M., Jr., Einaudi, M. T., Zurcher, L., Stavast, W. J. A., Johnson, D. A., and Barton, M. D., 2005, Porphyry deposits: Characteristics and origin of hypogene features: Economic Geology 100TH Anniversary Volume, p. 251-298
- Selby, D., and Creaser, R. A., 2004, Macroscale NTIMS and microscale LA-MC-ICP-MS Re-Os isotopic analysis of molybdenite: Testing spatial restrictions for reliable Re-Os age determinations, and implications for the decoupling of Re and Os within molybdenite: *Geochimica et Cosmochimica Acta*, v. 68, p. 3897-3908.
- Sharp, Z. D., 1990, A laser-based microanalytical method for the in situ determination of oxygen isotope ratios of silicates and oxides: *Geochimica et Cosmochimica Acta*, v. 54, p. 1353-1357.
- Sheppard, S. M. F., Nielson, R. L., and Taylor, H. P., 1969, Oxygen and hydrogen isotope ratios of clay minerals from porphyry copper deposits: *Economic Geology*, v. 64, p. 755-777.
- Sheppard, S. M. F., and Gilg, H. A., 1996, Stable isotope geochemistry of clay minerals: *Clay Minerals*, v. 31, p. 1-24.
- Sillitoe, R. H., 1976, Reconnaissance of the Mexican porphyry copper belt: *Transactions of the Institution of Mining and Metallurgy, Section B: Applied Earth Science*, v. 85, p. 170-189.
- Sillitoe, R. H., 1994, Erosion and collapse of volcanoes: Causes of telescoping in intrusion-centered ore deposits: *Geology*, v. 22, p. 945-948.
- Sillitoe, R. H., 1995, Exploration of porphyry copper lithocaps. In: J.L. Mauk, J.D. St. George (Eds.) *Proceedings of the 1995 PacRim Congress: Australasian Institute of Mining and Metallurgy*, v. 5, p. 527-532.
- Sillitoe, R. H., 1999, Styles of high-sulphidation gold, silver and copper mineralisation, PAC-RIM '99: Bali, Indonesia, p. 29-44.
- Sillitoe, R. H., 2002, Some metallogenic features of gold and copper deposits related to alkaline rocks and consequences for exploration: *Mineralium Deposita*, v. 37, p. 4-13.
- Sillitoe, R. H., and Hedenquist, J. W., 2003, Linkages between volcanotectonic settings, ore-fluid compositions, and epithermal precious metal deposits: *Society of Economic Geologists, Special Publications Series*, v. 10, p. 314-343.

- 
- Simeone, R., Dilles, J. H., Padalino, G., and Palomba, M., 2005, Mineralogical and stable isotope studies of kaolin deposits: Shallow epithermal systems of Western Sardinia, Italy: *Economic Geology*, v. 100, p. 115-130.
- Simmons, S. F., and Christenson, B. W., 1994, Origins of calcite in a boiling geothermal system: *American Journal of Science*, v. 294, p. 361-400.
- Singh, B., and Gilkes, R. J., 1992, An electron optical investigation of the alteration of kaolinite to halloysite: *Clays and Clay Minerals*, v. 40, p. 212-229.
- Smoliar, M. I., Walker, R. J., and Morgan, J. W., 1996, Re-Os Ages of Group IIA, IIIA, IVA, and IVB iron meteorites: *Science*, v. 271, p. 1099-1102.
- Stacey, J. S., and Kramers, J. D., 1975, Approximation of terrestrial lead isotope evolution by a two-stage model: *Earth and Planetary Science Letters*, v. 26, p. 207-221.
- Sun, S. S., and McDonough, W. F., 1989, Chemical and isotopic systematics of oceanic basalts: implications for mantle composition and processes: *Magmatism in the ocean basins*, p. 313-345.
- Sun, W. D., Ling, M. X., Yang, X. Y., Fan, W. M., Ding, X., and Liang, H. Y., 2010, Ridge subduction and porphyry copper-gold mineralization: An overview: *Science China Earth Sciences*, v. 53, p. 475-484.
- Sutopo, B., Jones, M.L., and Levet, B.K., 2003, The Martabe gold discovery: A high sulphidation epithermal gold-silver deposit, North Sumatra, Indonesian Proc. NewGenGold 2003 Conference, Louthean Media, Perth, Australia, p. 147-158.
- Syracuse, E. M., and Abers, G. A., 2006, Global compilation of variations in slab depth beneath arc volcanoes and implications: *Geochemistry, Geophysics, Geosystems*, v. 7, p. 1-18.
- Taran, Y., Fischer, T. P., Pokrovsky, B., Sano, Y., Aurora Armienta, M., and Macias, J. L., 1998, Geochemistry of the volcano-hydrothermal system of El Chichón Volcano, Chiapas, Mexico: *Bulletin of Volcanology*, v. 59, p. 436-449.
- Tatsumoto, M., Knight, R. J., and Delevaux, M. H., 1972, Uranium, thorium, and lead concentrations in three silicate standards and a method of lead isotopic analysis: U.S.G.S. Professional Paper 800-D, p. 111-115.
- Taylor, H. P., 1974, The application of oxygen and hydrogen isotope studies to problems of hydrothermal alteration and ore deposition: *Economic Geology*, v. 69, p. 843-883.

- Taylor, B. E., 1992, Degassing of H<sub>2</sub>O from rhyolite magma during eruption and shallow intrusion, and the isotopic composition of magmatic water in hydrothermal systems: Japan Geological Survey Report 279, p. 190-194.
- Tepley, F. J., Davidson, J. P., Tilling, R. I., and Arth, J. G., 2000, Magma mixing, recharge and eruption histories recorded in plagioclase phenocrysts from El Chichón volcano, Mexico: *Journal of Petrology*, v. 41, p. 1397-1411.
- Thompson, T. B., Trippel, A. D., and Dwelley, P. C., 1985, Mineralized veins and breccias of the Cripple Creek District, Colorado: *Economic Geology*, v. 80, p. 1669-1688.
- Thorpe, R. S., 1982, *Andesites : Orogenic andesites and related rocks*: Chichester, Wiley.
- Todt, W., R., Cliff, A., Hanser, A., and Hofmann, A. W., 1984, <sup>202</sup>Pb -<sup>205</sup>Pb spike for Pb isotopic analysis: *Terra Cognita*, v. 4, p. 209.
- Tukey, J. W., 1977, *Exploratory data analysis*: Reading, Mass., Addison-Wesley Publishing Co.
- Ueda, A., and Sakai, H., 1984, Sulfur isotope study of Quaternary volcanic rocks from the Japanese Islands Arc: *Geochimica et Cosmochimica Acta*, v. 48, p. 1837-1848.
- Valencia-Moreno, M., Ochoa-Landín, L., Noguez-Alcántara, B., Ruiz, J., and Pérez-Segura, E., 2007, Geological and metallogenetic characteristics of the porphyry copper deposits of Mexico and their situation in the world context: *Geological Society of America Special Papers*, v. 422, p. 433-458.
- Varne, R., 1985, Ancient subcontinental mantle: A source for K-rich orogenic volcanics: *Geology*, v. 13, p. 405-408.
- Verma, S. P., 2006, Extension-related origin of magmas from a garnet-bearing source in the Los Tuxtlas volcanic field, Mexico: *International Journal of Earth Sciences*, v. 95, p. 871-901.
- Vigouroux, N., Wallace, P. J., and Kent, A. J. R., 2008, Volatiles in high-k magmas from the western Trans-Mexican Volcanic Belt: Evidence for fluid fluxing and extreme enrichment of the mantle wedge by subduction processes: *Journal of Petrology*, v. 49, p. 1589-1618.
- Wallén, C. C., 1955, Some characteristics of precipitation in Mexico: *Geografiska Annaler*, v. 37, p. 51-85.
- Warnaars, F. W., Holmgren D, C., and Barassi F, S., 1985, Porphyry copper and tourmaline breccias at Los Bronces-Rio Blanco, Chile: *Economic Geology*, v. 80, p. 1544-1565.

- Wassenaar, L. I., Van Wilgenburg, S. L., Larson, K., and Hobson, K. A., 2009, A groundwater isoscape ( $\delta D$ ,  $\delta^{18}O$ ) for Mexico: *Journal of Geochemical Exploration*, v. 102, p. 123-136.
- Watson, E. B., and Harrison, T. M., 1983, Zircon saturation revisited: temperature and composition effects in a variety of crustal magma types: *Earth and Planetary Science Letters*, v. 64, p. 295-304.
- Weber, B., Cameron, K. L., Osorio, M., and Schaaf, P., 2005, A Late Permian tectonothermal event in Grenville crust of the southern Maya terrane: U-Pb zircon ages from the Chiapas massif, southeastern Mexico: *International Geology Review*, v. 47, p. 509-529.
- Weber, B., Iriondo, A., Premo, W., Hecht, L., and Schaaf, P., 2007, New insights into the history and origin of the southern Maya block, SE México: U-Pb-SHRIMP zircon geochronology from metamorphic rocks of the Chiapas massif: *International Journal of Earth Sciences*, v. 96, p. 253-269.
- Welton, J. E., 1984, SEM petrology atlas: Tulsa, USA, The American Association of Petroleum Geologists.
- White, W. M., and Patchett, J., 1984, Hf-Nd-Sr isotopes and incompatible element abundances in island arcs: Implications for magma origins and crust-mantle evolution: *Earth and Planetary Science Letters*, v. 67, p. 167-185.
- Wiedenbeck, M., Allé, P., Corfu, F., Griffin, W. L., Meier, M., Oberli, F., Quadt, A. V., Roddick, J. C., and Spiegel, W., 1995, Three natural zircon standards for U-Th-Pb, Lu-Hf, trace element and REE analyses: *Geostandards Newsletter*, v. 19, p. 1-23.
- Wilson, A. J., Cooke, D. R., and Harper, B. L., 2003, The Ridgeway gold-copper deposit: A high-grade alkalic porphyry deposit in the Lachlan Fold Belt, New South Wales, Australia: *Economic Geology*, v. 98, p. 1637-1666.
- Wilson, J. W., Cooke, D. R., Benjamin, J. H., and Deyell, C. L., 2007, Sulfur isotopic zonation in the Cadia district, southeastern Australia: exploration significance and implications for the genesis of alkalic porphyry gold-copper deposits: *Mineralium Deposita*, v. 42, p. 465-487.
- Wilson, M., 1989, *Igneous petrogenesis: A global tectonic approach*: London, Oxford University Press, 466 p.
- Woodhead, J. D., Harmon, R. S., and Fraser, D. G., 1987, O, S, Sr, and Pb isotope variations in volcanic rocks from the Northern Mariana Islands: Implications for crustal recycling in intra-oceanic arcs: *Earth and Planetary Science Letters*, v. 83, p. 39-52.

- Yanagisawa, F., and Sakai, H., 1983, Thermal decomposition of barium sulfate-vanadium pentoxide-silica glass mixtures for preparation of sulfur dioxide in sulfur isotope ratio measurements: *Analytical Chemistry*, v. 55, p. 985-987.
- Yu, Z., Robinson, P., Townsend, A. T., Münker, C., and Crawford, A. J., 2000, Determination of high field strength elements, Rb, Sr, Mo, Sb, Cs, Tl and Bi at  $\text{ng g}^{-1}$  levels in geological reference materials by magnetic sector ICP-MS after  $\text{HF/HClO}_4$  high pressure digestion: *Geostandards Newsletter*, v. 24, p. 39-50.
- Yu, Z., Robinson, P., and McGoldrick, P., 2001, An evaluation of methods for the chemical decomposition of geological materials for trace element determination using ICP-MS: *Geostandards Newsletter*, v. 25, p. 199-217.